

Inverted Shell Foundation Performance In Soil

Remo Rinaldi

A Thesis

In the Department

of

Building, Civil & Environmental Engineering

Presented in Partial Fulfillment of the Requirements

for the Degree of

Doctor of Philosophy (Civil Engineering) at

Concordia University

Montreal, Quebec, Canada

April 2012

© Remo Rinaldi, 2012

CONCORDIA UNIVERSITY
SCHOOL OF GRADUATE STUDIES

This is to certify that the thesis prepared

By: **Remo Rinaldi**

Entitled: **Inverted Shell Foundation Performance in Soil**

and submitted in partial fulfillment of the requirements for the degree of

DOCTOR OF PHILOSOPHY (Civil Engineering)

complies with the regulations of the University and meets the accepted standards with respect to originality and quality.

Signed by the final examining committee:

_____	Chair
Dr. R. Ganesan	
_____	External Examiner
Dr. M.A. Meguid	
_____	External Examiner
Dr. S.H. Rizkalla	
_____	External to Program
Dr. G. Vatistas	
_____	Examiner
Dr. L. Lin	
_____	Examiner
Dr. O. Pekau	
_____	Thesis Supervisor
Dr. A. Hanna	

Approved by _____
Dr. M. Elektorowicz, Graduate Program Director

October 19, 2012

Dr. Robin A.L. Drew, Dean
Faculty of Engineering and Computer Science

ABSTRACT

Inverted Shell Foundation Performance In Soil

Remo Rinaldi, Ph.D.
Concordia University, 2012

The use of shells in foundation structures over traditional forms has grown steadily since their inception in the early nineteen-fifties. Shell foundations outperform conventional flat footings and are reputable performers especially when heavy superstructural loads are to be transmitted to weak bearing soil. The geotechnical performance of shells in an elastic continuum concerns their bearing capacities and settlement behaviour, whose study has been trailing behind that of their structural performance. Bringing contact pressures closer to uniformity at the soil-shell structure interface is essential in developing a viable behavioural response under vertically concentric and monotonic loading conditions. This study encapsulates the development of new shell foundation geometries employing shell inversion under such loading conditions. Experimental investigation involves validation of the numerical phase in a comparative study following a two-dimensional analysis of shell models using commercially available geotechnical software with finite element analysis. New inverted triangular footings embedded in sand composed of ultra-high performance iShell Mix concrete using fiber-reinforced polymeric (FRP) microfibers are analyzed. A parametric analysis examines key sensitivity elements including shell angle and shell thickness in granular soil for both upright shells and their inverted counterpart. Linearly-elastic behaviour of concrete material is assumed while soil media is modeled under nonlinear elastic perfectly-plastic conditions following the Mohr-Coulomb yield criterion for loose, medium and dense sand states. Theoretical modeling was developed to generate inverted shell bearing capacity factors to predict ultimate bearing capacities of the shell footings. Simulation efforts scrutinized reveal comparable performance with bearing capacity increase of 3 – 5% for the inverted shells over upright shell models and notable improvements of 42 – 45% over conventional flat footings. The developed models investigated represent forefront configurations of superior performance signifying that shells in foundations be highly regarded and fully exploited whenever feasible.

KEYWORDS: shell, contact pressure, bearing capacity, settlement, finite element analysis

ACKNOWLEDGEMENTS

First and foremost, I would like to thank God for the time, strength and wisdom He has given me to allow for the completion of this thesis. The challenging research work undertaken in the development of this academic piece would not have been possible without the contributions and support of the following people:

My supervisor, Dr. Adel Hanna, for his inspiration, guidance and feedback throughout this research endeavor. This research topic was first introduced by Dr. Hanna in the early 1980's and has since seen rapid development through studies undertaken by preceding scholars. The opportunity to contribute to the extension of knowledge on the subject under his expert tutelage is greatly acknowledged. My sincere gratitude to Dr. Marco Bertola, at Concordia University for his time and research consultations in mathematics. Geotechnical engineer, Dr. Daniel Pradel, from the University of California in Los Angeles (UCLA) US, for the stimulating discussions on numerical modeling. The experimental work would not have been possible without the assistance and invaluable insight of Dr. Khaled Galal and exceptional technical knowledge of laboratory technicians Joe Hrib, Jamie Yeargans, Luc Demers and Mark Elie with whom I had the privilege of working with. A special thanks to colleagues and administrative staff in the Department of Building, Civil and Environmental Engineering at Concordia University for their support and unremitting assistance.

My wife, for her unconditional love and understanding whom has spent countless hours listening to me ramble on about a topic that was really of vague interest to her. This work would never have come to fruition without her compassion and flexibility in allowing me the time to complete it.

My parents and brother for their love, patience and kindness throughout the course of my academic studies. The Berlingieri, Di Pietro, Guerrera, Longo, Masciotra and Rinaldi families for their encouragement and support.

Thank you all,

Remo Rinaldi

DEDICATION

To my wife, daughter & son:

Vanessa, Briana & Luca Rinaldi for their love & patience.

&

In loving memory & tribute to:

My grandparents Concetta Longo, Antonio Guerrera, Nicolina Longo, Fiore Rinaldi and late aunt Nicolina Guerrera.

FOREWORD

“Initial enthusiasm in employing shell footings as the most bold & daring foundation structures must not be squandered by the scarcity of its scientific study, for their conception is an amalgamation of theory, experience and judgement.”

© Remo Rinaldi, Ph.D.
Concordia University
Canada

TABLE OF CONTENTS

LIST OF FIGURES	xii
LIST OF TABLES	xix
NOMENCLATURE	xxi
CHAPTER 1 : INTRODUCTION	1
1.1 General.....	1
1.2 Shells in Engineering	3
1.2.1 Shell Applications	5
1.2.2 Shell Definition	6
1.3 Shell Foundations	8
1.3.1 Shell Classification.....	8
1.3.2 Shell Components.....	10
1.4 Thesis Layout	12
CHAPTER 2 : LITERATURE REVIEW	16
2.1 Shell Foundation History.....	16
2.1.1 Primitive Footings	21
2.1.2 Modern Shell Footings.....	23
2.2 Special Shell Footing Cases.....	31
2.2.1 Combined Shell Footings.....	31
2.2.2 Composite Shell Footings	33
2.3 Shell Structural Strength.....	34

2.3.1 Shell Model Studies	37
2.3.2 Research Needs	41
2.4 Problem Statement	44
2.4.1 Scope of the Thesis	45
2.4.2 Study Objectives and Motivation.....	46
CHAPTER 3 : NUMERICAL iSHELL MODELING.....	47
3.1 Introduction	47
3.2 Shell Model Rendering.....	47
3.3 Soil–Shell Structure Modeling.....	51
3.4 Finite Element Modeling Using PLAXIS	54
3.4.1 Shell Material Properties.....	55
3.4.2 Soil Material Properties	56
3.4.3 Safety Analysis in PLAXIS.....	56
3.4.4 PLAXIS Sample Input and Output	57
3.4.5 Load–Settlement Behaviour	81
3.4.6 Finite Element Mesh Generation	83
3.4.7 Summary of Results.....	87
3.5 Non–linear 3D Finite Element Analysis	94
3.5.1 Discretization and Validation of FE Shell Models	94
3.5.1.1 Pyramidal Shell Footing – 3D Model	95
3.5.1.2 Triangular Strip Footing.....	101
3.5.2 Inverted Shell Triangular Strip Footing Models	104
3.5.3 iShell Footing Performance.....	107

3.6 Parametric Study.....	110
3.7 Summary of Results	114
CHAPTER 4 : EXPERIMENTAL iSHELL MODELING	116
4.1 Introduction.....	116
4.2 iShell Footing Models	118
4.3 iShell Fabrication.....	119
4.3.1 iShell Model Casting	120
4.3.2 iShell Model Observations	123
4.4 Experimental Setup	134
4.4.1 Test Facility Setup	134
4.4.2 Loading System.....	141
4.4.3 Test Tank Layout.....	145
4.4.4 Pressure Transducers	150
4.4.5 Data Acquisition System.....	153
4.5 Soil Models	155
4.5.1 Mohr–Coulomb Failure Criterion.....	155
4.5.2 Soil Properties and Characteristics	156
4.5.2.1 Grain Size Distribution	156
4.5.2.2 Compaction and Permeability	160
4.5.3 Sand Bed Preparation	167
4.5.4 In–Situ Stresses in Sand.....	173
4.6 Soil–Shell Structure Interface	179
4.7 Summary.....	194

CHAPTER 5 : THEORETICAL iSHELL MODELING	196
5.1 Introduction	196
5.1.1 Shell Behaviour	197
5.2 Shell Footing Contact Pressure	201
5.2.1 Contact Pressure Distribution	204
5.3 Bearing Capacity for iShell Footings	206
5.3.1 Ultimate Bearing Capacity Theory	206
5.4 Theoretical Triangular iShell Model	209
5.5 iShell Bearing Capacity Coefficients	235
5.5.1 iShell Depth and Shape Factors	235
5.6 Concluding Remarks	238
 CHAPTER 6 : iSHELL INNOVATION	 239
6.1 Introduction	239
6.2 iShell Economy	239
6.3 iShell Construction Methods	240
6.4 iShell Concrete Mix	241
6.4.1 Innovation Incentives	242
6.4.2 iShell Footing Innovation	243
6.4.3 iShell Mix Design	244
6.4.3.1 Research and Development	247
6.4.3.2 Batch Composition	248
6.4.3.3 Increase of Dry–Compact Density	249
6.4.3.4 Microstructure Improvement	250

6.4.4 iShell Mix Characteristics	251
6.4.4.1 Homogeneity Improvement.....	253
6.4.4.2 Dimensional Stability	254
6.4.4.3 Heat Treatment.....	255
6.4.4.4 Capillary Porosity.....	256
6.4.4.5 Acid, Fire and Corrosion Resistance.....	258
6.5 Concluding Remarks	259
CHAPTER 7 : CONCLUSIONS & RECOMMENDATIONS	260
7.1 Summary	260
7.1.1 Geotechnical Behaviour of iShell Footings	261
7.2 Conclusion.....	263
7.3 Recommendations for Further Research.....	265
REFERENCES	268
APPENDIX I : iShell Prototypes	278
APPENDIX II : iShell Bearing Capacity Program	289
APPENDIX III : iShell Bearing Capacity Factor Tables	329

LIST OF FIGURES

CHAPTER 1	Page
Figure 1.1 : Sydney Opera House: Shell Roof Structure	3
Figure 1.2 : Hoover Dam	4
Figure 1.3 : Shell Anchors & Shoring Wall Applications	5
Figure 1.4 : Shell Classification	9
Figure 1.5 : Shell Components	10
Figure 1.6 : Shell Study Chart	12
Figure 1.7 : Flowchart Analysis	13
CHAPTER 2	
Figure 2.1 : Hypar Footing for St. Vincent's Chapel	17
Figure 2.2 : Hypar Footing for a Factory for Lamex	18
Figure 2.3 : Hypar Footings	19
Figure 2.4 : Stone Arch Foundations	22
Figure 2.5 : Inverted Masonry Arch Foundations	23
Figure 2.6 : The Nonoalco Tower Foundation	24
Figure 2.7 : Folded-Plate Shell Footings	25
Figure 2.8 : Folded-Plate Shell Footings	26
Figure 2.9 : Dome Shell Footings	26
Figure 2.10 : Conical Shell Footings	27
Figure 2.11 : Inverted Circular Shells	28
Figure 2.12 : The Hyperbolic Paraboloid 'Hypar' Footing	29
Figure 2.13 : Elliptical Paraboloid Shells	30
Figure 2.14 : Parabolic Pyramidal Dome Footing	30
Figure 2.15 : Combined Shell Footing: O.H. Water Tank	32
Figure 2.16 : Composite Shell Footing	33
Figure 2.17 : Hypar Shell General Diagonal Failure Mode	34
Figure 2.18 : Hypar Shell Footing Model	35

Figure 2.19 : Crack Pattern of the Hypar Shell Footing Model	36
Figure 2.20 : Conical Shell Model	37
Figure 2.21 : Normal Contact Pressure Distribution Diagrams	38
Figure 2.22 : Contact Pressure Diagrams: Conical Models	39
Figure 2.23 : Contact Pressure Diagrams: Spherical Models	39
Figure 2.24 : Settlement Diagrams	40
Figure 2.25 : Load vs. Settlement Diagrams	40

CHAPTER 3

Figure 3.1 : Plain Flat Footing Model Rendering	47
Figure 3.2 : Triangular Shell Model Rendering.....	48
Figure 3.3 : Cylindrical Shell Model Rendering.....	49
Figure 3.4 : Combined Shell Model Rendering.....	50
Figure 3.5 : Mohr–Coulomb Yield Surface in Principal Stress Space.....	52
Figure 3.6 : Upright Shell Modeling Using Shape Designer (SAAS) 2011.....	53
Figure 3.7 : FEM Mesh Generation for Embedded Shell	55
Figure 3.8 : Parameters Tab Sheet for Soil and Interface Data Set Window ...	58
Figure 3.9 : PLAXIS Data Input Fields – Shell Modeling	59
Figure 3.10 : PLAXIS Data Input – Flat Footing Model.....	60
Figure 3.11 : Flat Footing Model Output.....	61
Figure 3.12 : Flat Footing Rupture Surface Model.....	62
Figure 3.13 : Upright Shell Model – PLAXIS Soil–Structure Interface.....	63
Figure 3.14 : Total Displacements for Upright Shell Model	64
Figure 3.15 : Connectivities for Upright Shell Model.....	65
Figure 3.16 : Effective Stresses for Upright Shell Model	66
Figure 3.17 : Upright Shell Footing Model: Total Soil Displacements	67
Figure 3.18 : Upright Shell Footing Model: Generated Soil Displacements	68
Figure 3.19 : Upright Shell Footing Model: Generated Soil Displacements	69
Figure 3.20 : Sinusoidal Footing Model: Total Displacements	70
Figure 3.21 : Sinusoidal Footing Model: Contour Line Displacements	71
Figure 3.22 : Close–up View iShell Footing Model	72

Figure 3.23 : iShell Footing Model iS4: Deformed Mesh	73
Figure 3.24 : iShell Footing Model iS4: Effective Stresses.....	74
Figure 3.25 : iShell Footing Model iS4: Connectivities & Nodal Points.....	75
Figure 3.26 : iShell Footing Model iS4: Total Stresses.....	76
Figure 3.27 : iShell Footing Model iS4: Total Displacements.....	77
Figure 3.28 : iShell Footing Model iS4: Contour Displacements	78
Figure 3.29 : iShell Footing Model iS3: Initial Loading Conditions.....	79
Figure 3.30 : iShell Footing Model iS3: Effective Stresses.....	80
Figure 3.31 : Load–Settlement Curves for iShell Models	81
Figure 3.32 : Finite Element Meshes for Flat & Upright Shell Footing	84
Figure 3.33 : Finite Element Meshes for Sinusoidal & iS9 Shell	85
Figure 3.34 : Finite Element Meshes for iS2 & iS3 Shell	86
Figure 3.35 : FE Model of Upright Pyramidal Shell – Plan View	96
Figure 3.36 : FE Model of Upright Pyramidal Shell.....	97
Figure 3.37 : FE Model of Inverted Pyramidal Shell.....	98
Figure 3.38 : FE Model of Upright Pyramidal Shell with Soil Media.....	99
Figure 3.39 : FE Model of Inverted Pyramidal Shell with Soil Media	100
Figure 3.40 : Load vs. Displacement for Upright and iShell Footings	101
Figure 3.41 : FEM 3D Discretization of Strip Shell and Soil Media	102
Figure 3.42 : FEM 3D Discretization of Upright Triangular Strip Shell.....	103
Figure 3.43 : Load vs. Settlement for Upright & iShell Footings	104
Figure 3.44 : Elevation & Isometric FE iShell Triangular Model.....	105
Figure 3.45 : iShell FE Isometrics of Shell Footing Models.	106
Figure 3.46 : Load vs. Settlement – iShell Triangular Strip Footings	106
Figure 3.47 : Upright vs. Inverted Shell Model Discretization	107
Figure 3.48 : FEM Results for iShell 36° vs. Upright Triangular Shell	108
Figure 3.49 : Mesh Deformation: (a) Upright (b) iShell Footing Models.....	108
Figure 3.50 : Displacement Contours – Upright Shell 36°	109
Figure 3.51 : Displacement Contours – iShell 36°	109
Figure 3.52 : Effect of Shell Thickness (t_s) on Load–Carrying Capacity	112
Figure 3.53 : Effect of Shell Thickness (t_s) on Load–Carrying Capacity	112
Figure 3.54 : Effect of Shell Thickness (t_s) on Load–Carrying Capacity	113

Figure 3.55 : Effect of Shell Angle (θ) on Load-Carrying Capacity	113
--	-----

CHAPTER 4

Figure 4.1 : Shell Footing Foundation Models	117
Figure 4.2 : Summary of iShell Model Prototypes Cast.....	119
Figure 4.3 : Wood Box Moulds for iShell Model Casting.....	120
Figure 4.4 : Compression Test Apparatus	121
Figure 4.5 : Compression Strength of iShell Mix Concrete.....	122
Figure 4.6 : Flexural Strength of iShell Mix Concrete	122
Figure 4.7 : Flat Foundation Model of iShell Mix Concrete	123
Figure 4.8 : Upright Triangular Shell Model of iShell Mix Concrete	124
Figure 4.9 : Inverted Sinusoidal Shell of iShell Mix Concrete	124
Figure 4.10 : iShell Footing Models of iShell Mix Concrete.....	125
Figure 4.11 : iShell Overall Plan Dimensions	126
Figure 4.12 : Shell Inversion vs. Upright Shell Model	126
Figure 4.13 : Metallic vs. Concrete Upright Strip Shell Footing Models	127
Figure 4.14 : iShell Model – Frictionless Capping	128
Figure 4.15 : Localization of Contact Pressure Transducers at Depth ‘B’	130
Figure 4.16 : Plexiglass Templates for Sensor Layout & Wash-Bore Drilling.....	131
Figure 4.17 : Concrete Drill Bit (1/2" dia.) and Slot-Plug Adapters.....	132
Figure 4.18 : Wash-Boring Procedure : iShell Footing Model.....	132
Figure 4.19 : Perforated iShell Footing Models	133
Figure 4.20 : Loading Frame & Test Tank Setup	136
Figure 4.21 : Self-Reacting A-Frame & Loading Assembly	137
Figure 4.22 : Transverse Loading Beam Plans	138
Figure 4.23 : Loading Yoke Plans	139
Figure 4.24 : Test Tank Internal Dimensions	140
Figure 4.25 : LVDT Displacement Measuring Device	141
Figure 4.26 : Universal Flat Load Cell Schematic.....	142
Figure 4.27 : Universal Flat Load Cell and Ball-Pinion for Loading Jack.....	144
Figure 4.28 : Loading Yoke, Load-Cell, Jack Cylinder & Ball-Pinion Setup	144

Figure 4.29 : Test Frame and Tank Setup	145
Figure 4.30 : Layered Sand Test – Rupture Surface Simulation.....	146
Figure 4.31 : In–Progress Testing of Shell Footing Model	147
Figure 4.32 : Rupture Surfaces for Flat and Upright Shell Footings	148
Figure 4.33 : Bearing Capacity Failure for Sinusoidal and iShell Footings.....	149
Figure 4.34 : Miniature Pressure Transducer Models: PDB–PA.....	151
Figure 4.35 : Pressure Transducer Insertion – iShell Footing Model.....	153
Figure 4.36 : Sensor Calibration Charts	154
Figure 4.37 : Grain Size Distribution for TECH-Mix® Sand.....	157
Figure 4.38 : Standard Proctor Test Compaction Curve for TECH-Mix Sand	160
Figure 4.39 : Direct Shear Box Test, $\gamma = 15 \text{ kN/m}^3$	161
Figure 4.40 : Direct Shear Box Test, $\gamma = 16 \text{ kN/m}^3$	162
Figure 4.41 : Direct Shear Box Test, $\gamma = 17 \text{ kN/m}^3$	162
Figure 4.42 : Direct Shear Box Test, $\gamma = 18 \text{ kN/m}^3$	163
Figure 4.43 : Direct Shear Box Test, $\gamma = 19 \text{ kN/m}^3$	163
Figure 4.44 : Shear Stress vs. Normal Stress.....	164
Figure 4.45 : Unit Weight vs. Angle of Friction.....	164
Figure 4.46 : Angle of Shearing Resistance vs. Relative Density	165
Figure 4.47 : Sieve Sand Rainer.....	168
Figure 4.48 : Dry Sand Pluviation.....	169
Figure 4.49 : Rolling and Impact Mechanisms.....	170
Figure 4.50 : Elevated Storage Bin & Funnel System for Sand Pluviation	171
Figure 4.51 : Sand Pluviation Distribution Method.....	172
Figure 4.52 : Sand Compaction Results for Vertical & Lateral Stresses.....	177
Figure 4.53 : OCR & $k_0(\text{oc})$ Distribution from Sand Compaction	178
Figure 4.54 : Normal Contact Distribution.	182
Figure 4.55 : Load–Settlement Graph – Flat Footing Model.....	184
Figure 4.56 : Load–Settlement Graph – Upright Footing Model	185
Figure 4.57 : Load–Settlement Graph – Sinusoidal Footing Model.....	185
Figure 4.58 : Load–Settlement Graph – iS4 Inverted Shell Footing Model. ...	186
Figure 4.59 : Load–Settlement Graph – iS6 Inverted Shell Footing Model. ...	186
Figure 4.60 : Ultimate Load (Q_u) vs. Angle of Shearing Resistance, $\phi(^{\circ})$	187

Figure 4.61 : Ultimate Load (Q_u) vs. Angle of Friction, $\phi(^{\circ})$ – Varia.....	188
Figure 4.62 : Ultimate Load (Q_u) vs. Settlement Factor, (F_{δ}).....	188
Figure 4.63 : Contact Pressure Distribution for Flat Footing Model	191
Figure 4.64 : Contact Pressure Distribution for Upright & Sinusoidal Shell Footings.	192
Figure 4.65 : Contact Pressure Distribution for iShell18°(iS4) & iShell36°(iS6) Footings.	193

CHAPTER 5

Figure 5.1 : Shell Foundations	196
Figure 5.2 : Inverted Spherical Shell Footing.....	198
Figure 5.3 : Spherical Shell Footing Behaviour	199
Figure 5.4 : Contact Pressure Components	201
Figure 5.5 : Shell Reactive Pressures.....	202
Figure 5.6 : Contact Pressure Distribution Beneath Rigid Footings.....	204
Figure 5.7 : General Shear Failure Mode	206
Figure 5.8 : Foundation Failure Modes for Footings on Sand	207
Figure 5.9 : Mohr–Coulomb’s Failure Criterion.....	212
Figure 5.10 : iShell Footing Rupture Surface.....	213
Figure 5.11 : iShell–Soil Interface Equilibrium using Kötter’s Parameters.....	215
Figure 5.12 : iShell–Soil Interface Equilibrium Model.....	228
Figure 5.13 : iShell Depth Factors ($F_{dq}, F_{d\gamma}$) _{Shell}	237
Figure 5.14 : Flat Footing Depth Factors ($F_{dq}, F_{d\gamma}$)	238

CHAPTER 6

Figure 6.1 : Economical Contrast in Opting for Shell Footing Foundations ..	240
Figure 6.2 : iShell Mix Constituents Composition.....	248
Figure 6.3 : Load–Deflection Curve for Various Concrete Mixes	249
Figure 6.4 : Matrix Consolidation Optimization Strategy	250
Figure 6.5 : Micro–Crack Reinforcement Behaviour.....	251

Figure 6.6 : Shrinkage of iShell Mix Concrete	255
Figure 6.7 : Creep of iShell Mix Concrete	256
Figure 6.8 : Capillary Porosity of iShell Mix Concrete.....	257
Figure 6.9 : iShell Mix Permeability	257

CHAPTER 7

N/A

LIST OF TABLES

CHAPTER 1	Page
N/A	
CHAPTER 2	
Table 2.1 : Cracking and Ultimate Loads of Precast ‘Hypar’ Footings	36
CHAPTER 3	
Table 3.1 : Cross–Sectional Properties of Model Shell Footings	55
Table 3.2 : Soil (Sand) Properties – Mohr–Coulomb Model	56
Table 3.3 : Horizontal Strain, ϵ_{xx} (m/m) for iShell Footing Models	88
Table 3.4 : Vertical Strain, ϵ_{yy} (m/m) for iShell Footing Models	89
Table 3.5 : Horizontal Stress, σ_{xx} (kPa) for iShell Footing Models	90
Table 3.6 : Vertical Stress, σ_{yy} (kPa) for iShell Footing Models	91
Table 3.7 : Horizontal Displacements, Δx (m) for iShell Footing Models	92
Table 3.8 : Vertical Displacements, Δy (m) for iShell Footing Models	93
Table 3.9 : Soil Media Properties for 3D Models	100
Table 3.10 : Load–Settlement Results for Variable Shell Thickness	111
CHAPTER 4	
Table 4.1 : New iShell Footing Model Weights	128
Table 4.2 : Concrete iShell Footing Model Properties	129
Table 4.3 : Load Cell Specifications	143
Table 4.4 : Physical Properties of TECH-Mix® Sand	158
Table 4.5 : TECH-Mix Sand Soil Parameters	159
Table 4.6 : Different Sand Soil Parameters	159
Table 4.7 : Property Variance of TECH-Mix Sand	166
Table 4.8 : Angle of Shearing Resistance for Various Sand States	172
Table 4.9 : Elastic Parameters of Various Soils	174

Table 4.10 : OCR for Loose Sand Compaction.....	176
Table 4.11 : OCR for Loose Medium–Dense Sand Compaction	176
Table 4.12 : OCR for Dense Sand Compaction	176
Table 4.13 : Shell Model Cases Analyzed	179
Table 4.14 : Bearing Capacity, Settlement and Contact Pressures.....	180
Table 4.15 : Load–Settlement Results for iShell Footing Models	183
Table 4.16 : Contact Pressures for Axisymmetrical Condition for Embedded Flat Footings	189
Table 4.17 : Contact Pressures for Axisymmetrical Condition for Embedded iShell Footings	190
Table 4.18 : Ultimate Load Results for Numerical and Experimental Phase..	195

CHAPTER 5

Table 5.1 : Angle $\alpha(^{\circ})$ vs. FOS _r	200
Table 5.2 : Shell Ratio's for Different Footing Configurations	210

CHAPTER 6

N/A

CHAPTER 7

N/A

NOMENCLATURE

a = area

A_{Shell} = flat base shell surface area

A_p = base area of planar projection

b = half of foundation width

B = foundation width (2b)

c = cohesion of soil

C_c = coefficient of curvature of soil

C_u = coefficient of uniformity of soil

d_c = depth of foundation column

D = diameter of the soil particle

D_r = relative density (%)

D_f = depth of embedment from ground surface to shell base

D_{fb} = distance from ground surface to bottom of rupture surface

D_s = depth of shell

e = base of natural logarithm

e = void ratio or eccentricity

E = Young's Modulus

ER = embedment ratio

$(F_{cs}, F_{qs}, F_{\gamma s})_{Shell}$ = shell shape factors

$(F_{cd}, F_{qd}, F_{\gamma d})_{Shell}$ = shell depth factors

F = resultant force acting on rupture surface

$F_{\delta(iS)}$ = settlement factor for inverted shell footing

F_h = horizontal component of forces acting on rupture surface

F_v = vertical component of forces acting on rupture surface

FEM = finite element method

FOS = factor of safety

g = acceleration due to gravity

G_s = specific gravity of soil solids

H = distance from the ground surface to point of intersection between circular and plane parts of rupture surface

I = integration constant

I_x, I_y = moment of inertia about the corresponding axis

$k_{o,nc}$ = coefficient of earth pressure for normally consolidated soil

$k_{o,oc}$ = coefficient of earth pressure for overconsolidated soil

k_x, k_y, k_z = permeability coefficients

l_b = lever arm to center of rupture circle for weight of backfill (w_b)

$l_{1,2,3}$ = lever arms due to segmental weight of foundation (w_c)

l_w = lever arm to center of rupture circle for weight of soil prism (w_T)

$l_{\gamma,c}$ = lever arm to center of rupture circle for earth pressure force (R_γ, R_c)

M = substitution for integration

M = bending moment

M_o = overturning moment

M_s = stabilizing moment

Mw_b = moment of total weight of soil backfill

Mw_c = moment of total weight of shell foundation

Mw_T = total moment of the total weight of soil prism

M_{Rp} = moment of total horizontal earth pressure

M_T = moment of forces acting on rupture surface under foundation

M_F = moment of total shear stress acting on rupture surface

n = porosity

N = substitution for integration

$(N_c, N_q, N_\gamma)_{iS}$ = shells bearing capacity coefficients

OCR = overconsolidation ratio

P = normal contact pressure

q_u = ultimate bearing capacity

$q_{u,Shell}$ = ultimate bearing capacity for a shell footing

Q_b = bearing capacity load

Q_l = local shear failure load

Q_u = ultimate load

r = radius of circular part of rupture surface

R = resultant

R_γ = horizontal earth pressure force due to soil unit weight

R_c = horizontal earth pressure force due to soil cohesion

R_p = total horizontal earth pressure force

S_f = shell factor

S_i = shell index value in savings

S_r = shell ratio

t_s = shell thickness

T_i = transducer at the base of foundation model ($i = 1$ to 6)

T_h = horizontal component of resultant force

T_v = vertical component of resultant force

T_{vc} = vertical component of force acting on circular part of rupture surface

T_{vp} = vertical component of force acting on plane part of rupture surface

V = shear

w = moisture content (%)
 w_b = total weight of soil backfill
 w_{bi} = parts of total weight of soil backfill
 w_f = total weight of foundation
 w_{fi} = parts of total weight of foundation ($i = 1$ to 3)
 w_i = weight for soil prism ($i = 1$ to 8)
 w_t = total weight of soil prism in the rupture surface
 w_w = weight of soil wedge between shell surface and rupture surface
 x, y, z = triaxial coordinate system
 x_o, z_o = coordinates of center of rupture circle
 Z = soil depth
 α = wedge failure angle or vertical angle ($^\circ$)
 β = inner shell angle ($^\circ$)
 γ = soil unit weight
 γ_c = unit weight of concrete
 ∂ = partial derivative
 δ_u = settlement at ultimate load
 δ_x = horizontal displacement calculated from FEM analysis
 δ_y = vertical displacement calculated from FEM analysis
 ε = strain
 ε_{xx} = horizontal strain calculated from FEM analysis
 ε_{yy} = vertical strain calculated from FEM analysis
 η_{is} = inverted shell efficiency factor
 θ = shell angle ($^\circ$)
 ϕ = angle of shearing resistance of soil ($^\circ$)

ω = deflection

λ_1, λ_2 = integration constants

μ = friction coefficient or a function of (ψ, τ_{cir}) used for integration

ν = Poisson's ratio

π = pi

ρ = ratio between radius and half foundation width (r/b)

σ = stress

σ_x = measured lateral stress

σ_0 = theoretical lateral pressure at rest

σ_y = measured vertical stress

σ_{xx} = horizontal stress calculated from FEM analysis

σ_{yy} = vertical stress calculated from FEM analysis

σ_z = theoretical vertical stress

τ = shear stress at tangent point on Mohr–Coulomb's envelope

τ_{cir} = shear stress over circular part of rupture surface

τ_{pl} = shear stress over planar part of rupture surface

τ_{xy} = shear stress at point (x, y)

ψ = dilatancy angle ($^\circ$)

ψ_1 = slope of tangent at point of intersection with ground surface

ψ_2 = slope of tangent at point of intersection with circular curve

ω_n = constants ($n = 1$ to 3)

ξ_i = constants ($i = 1$ to 24)

ζ_n = substitution for integration ($n = 1$ to 3)

\int = integral

CHAPTER 1

INTRODUCTION

1.1 General

An economic alternative to traditionally plain shallow foundations especially where heavy superstructural loads are to be transmitted to weaker soil is opportune incentive to use shell foundations. Shell footings as foundations rely heavily on their geometrical shape and streamlined continuity to induce strength and perform efficiently in soil. As such, shells are thin-slab structures whose performance capabilities as a supporting element rely heavily upon their form and quality of construction materials used. Responsible for mainly compressive forces, shell foundations are composed of one or more curved slabs or folded plates whose relative thickness is inferior to its overall planar dimensions. To obtain maximum structural performance, shell foundations have been prevalently designed in arched, circular, triangular, conical, cylindrical, spherical, pyramidal, square and strip shapes. This investigation proposes to evaluate the geotechnical performance of new shell foundation models in stochastic sandy soil using reinforced concrete test specimens following embedded conditions employing triangular strip variations. In evaluating performance of the specimens coupled with the soils behavioural response, the settlements, contact pressures, working stresses in the footings are determined and compared with data from previously tested models.

The historical success of shells performance as a structure has motivated further research in its application and performance with the objective of exploiting cost savings benefit applied in a geotechnical engineering context. The ingenuity of shell footings as foundations has all the ingredients any design engineer should look to satisfy; that of optimum strength at minimal cost that is both safe and elegant, yet endures. This combination of economy and efficiency coupled with long-term durability is the epitome of a sustainable structure. The inherent versatility, structural efficiency, economy and constructability of shells as desired features make its form worthy of pursuing further research. This study purposes to introduce new shell footings as having superior performance as a cost-effective alternative from a geotechnical perspective.

There exists an invariant set of physical principles founded in the field of foundation engineering that can be used by designers and engineers as aids to understanding the behaviour of existing structural forms and in devising new approaches. The development of these principles has disseminated during the past three centuries to the extent that analytical tools have become extensive and an enormously powerful resource. Thus, the real challenge in the field of foundation engineering lies not so much in developing new analytical tools, but in bringing those currently in existence to bear in the design and formulation of new shapes with the ultimate goal of designing better foundations in pursuit of improved performance. In the case of shell foundations, the major challenge and source of influence is the non-planar and often times curved interface surface existing between the structure and the soil, whereas flat foundations having typically planar rectangular contact surface area with the underlying soil. The underlying idea behind the concept of the shell footing is to maximize use of the entire bearing soil spectrum by generating reduced stress at any one point for a given load in contrast to a plain foundations inefficient generation of local stress concentration.

Since the geotechnical behaviour of shell foundation research has been undermined considerably behind that of structural performance, new shell models are studied numerically to obtain a more uniform contact pressure distribution on the bearing soil on which they rest. Particularly, shell inversion orientation with variation of shell angle of the proposed models are investigated with variable soil strength parameters and correlations to its effect on confining pressure envelopes evaluated. The results of the numerical research are used as a comparable with similar experimental and theoretical models and are validated to confirm performance. The present study includes an analysis of the shell structure and soil using geotechnical software PLAXIS 8.6 – 2D: FOUNDATION. Static conditions of concentric vertical and eccentric loading for the three-dimensional analysis will assess shell behaviour based on finite-difference and finite-element analysis. Accordingly, results of the geotechnical behaviour in terms of the soil-structure interaction beneath the shells will shed light on its influence on bearing capacity and settlement thereby allowing for selection of the best shell shape in efforts to optimize footing design and achieve material cost savings.

1.2 Shells in Engineering

Reinforced concrete shell footings have been increasingly used in engineering projects as structural support members beneath buildings, towers, masts, tunnels, arch dams and cognate structures. The study of their structural performance has developed during the past half century to the extent that they are amazingly established as being superior foundation performers compared to traditional flat foundations in homogenous, non-homogenous and even weak or problematic soils. Essentially three fundamental engineering concepts conducive in opting for shells include a relentless drive to limit depletion of natural resources sustaining conservation, ethics of sound economics and innovative aesthetic appeal.

Shells have not only seen rapid rate of development in foundation structures but have also been previously exploited and used as domes and vaults in roofing, anchors, automobile bodies, ships hull, aircraft fuselage, turbine blades, loudspeaker cones, balloons/parachutes, bottles/cans, to name a few. A sophisticated application of roof shells is shown in the famous Sydney Opera House constructed in 1971 in Sydney, Australia. The intricate geometry exemplifies the most contemporary use of shell structures. A frontal view snapshot of the multi-venue arts centre is depicted in Figure 1.1 as follows.



Figure 1.1. Sydney Opera House: Shell Roof Structure, Australia (Wikipedia.org, 2008).

A shell as a structural shape has an almost infinite range of size and grandeur depending on its application. Another successful example in the use of shell structures includes that of the world renowned massive arch gravity dam known as the Hoover Dam in Las Vegas, USA measuring 221.3 m in height and 379.2 m in length. The generally high strength-to-weight ratio of this shell form along with its inherent stiffness is the reasoning behind its admirable success as an earth-type retaining structure. Structural strength is extracted from this mega-shell form said to be one of the greatest civil engineering marvels. Aerial photos taken upon its completion in 1935 are presented in Figure 1.2 to illustrate the sizable nature of this shell structure as one of the world's largest dams intersecting the Colorado River at Nevada and Arizona states border.

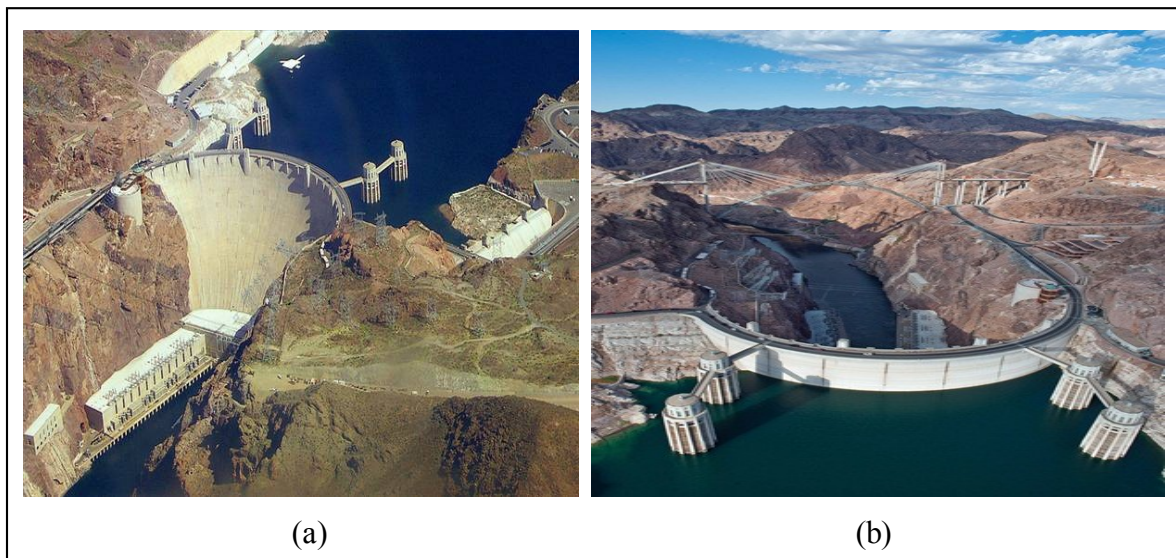


Figure 1.2. Hoover Dam: (a) Upstream (b) Downstream, USA (Wikipedia.org, 2008).

While roofs and tunnels abound in literature as being formidable structural performers against impact such as that experienced in World War II bombings, their application is by no means restricted to such enclosures. Still in its infancy, however, shells have not been fully exploited as foundation engineering structures since much testing and development remains to be undertaken. Other foundation applications of shell-type structures can be seen in the form of shell anchors, retaining walls and pile structures as presented in the next section. Fascinated by the shells superstructural capabilities and spatial versatility, this study harnesses this historical precedent to explore its utility as a versatile substructure.

1.2.1 Shell Applications

In efforts to design foundations with minimal material thereby contributing to cost savings, shells were found to carry forces well with slab thicknesses as thin as 38 mm [1.5 in.] having been reported (Holzer, Garlock, Prevost, 2008); an indication of the incredible strength attributes and rigidity that shells inherently exhibit. Lately, structural conduits employing shell principals have been exploited by industry on account of their convenient lightweight nature and high strength. Embedded earth structures such as culverts, caissons, arches and tunnels have been rehabilitated using shell-type liners. Portals and canopies are applications using corrugated steel plate panelling utilizing shell principles whose overall shape may be that of a shell. Shell forms may be used in retaining earth structures in monolithic form or component parts. Shell anchors and precast cambered shell planks, for example, are conceivable earth retention solutions as illustrated in Figure 1.3.

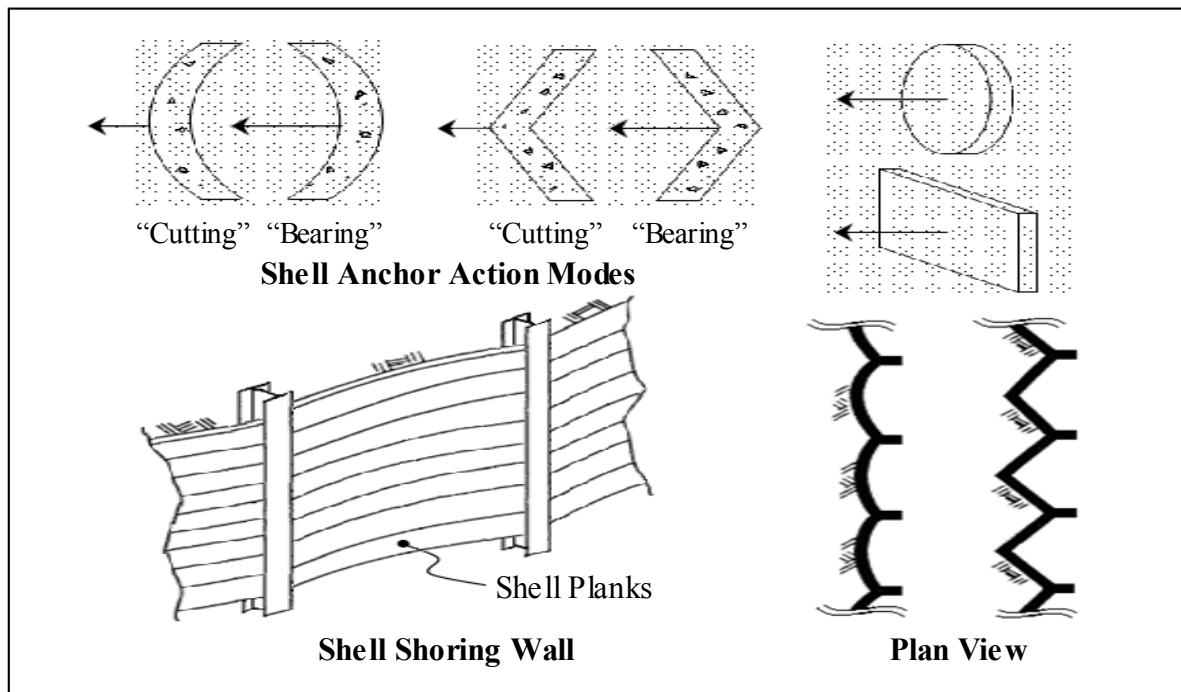


Figure 1.3. Shell Anchors & Shoring Wall Applications.

The aforementioned list of shell applications is by no means exhaustive. The resilience and versatility of shell structures lend themselves as impressive performers and may be employed in a variety of settings. In exposed settings, the elegance shells offer may add architectural benefit from an aesthetic point of view.

1.2.2 Shell Definition

Shells are remarkable performers as a load transmittal structure to founding soil. Their main advantage is closely related to their lightweight nature since, by definition, they are thin-wall structures requiring reduced quantities of concrete material in their construction. Responsible for mainly compressive forces, much like traditional shallow foundations they replace, a shell foundation is perhaps the anti derivative of the plain form and is typically made of reinforced concrete material. Consequently, the American Concrete Institute has defined a thin shell according to ACI 318–19 as:

“A three-dimensional spatial structure made up of one or more curved slabs or folded plates whose thicknesses are small compared to their other dimensions. Thin shells are characterized by their three-dimensional load-carrying behavior, which is determined by the geometry of their forms, by the manner in which they are supported, and by the nature of the applied load.”

The subdued quantity requirement translates to reduced costs as far as their materialization and makeup is concerned. Their structural capacities relying heavily on geometrical considerations as opposed to mass, make them extremely efficient in carrying larger loads than traditional structures. Undoubtedly, structural shell strength originates from form rather than mass, an underlying viewpoint shared with that of preceding researchers. Consequently, unlike typical structures, which are composed of beams, trusses and columns connected at nodal points, shells take advantage of continuity in their form for inducing strength. In terms of geotechnical requirements, this translates to increased bearing capacity and reduced settlement.

Pre-casting and pre-stressing are two major advantages shells offer. The ability to construct shell sub-structures such as footings, anchors, panelling, and piles, easily transported to site on account of their lightweight would have potentially significant time and cost saving implications for a project. Pre-stressed in-house construction of either full-scale or elemental component parts of shell footings offering controlled and temperate conditions is definitely an advantageous mainstream technique.

On the other hand disadvantages of shell use in foundation structures are undeniably present. First and foremost, high labour costs associated with erection and, in terms of constructability, shells require specialized formwork contractors with skilled and experienced labour force. Shell foundation designers should bear serious thought to construction methods involved which has a major impact on cost functions at times and under extreme circumstances rendering their use unfeasible. Idealized geometries coupled with soil cutting techniques in the excavation phase of construction are possible first-hand solutions. Initial enthusiasm in employing shell footings as the most bold and daring foundation structures must not be squandered by the scarcity of its scientific study, for their conception is an amalgamation of theory, experience and judgement. Present-day unavailability of code for design and construction, unskilled labour, inexperience and lagging construction methodologies are all major shortfalls requiring well-deserved attention in using shell foundations. This is perhaps due to their recent inception as the latest newcomers to the applied soil sciences.

While interest in originality exists at the onset of design, opting for improved performance based on new curious models should not feel like a monumental task. Shell shape composition may conveniently be selected from typical material options including timber, steel, and concrete or a novel combination thereof. As far as creativity is concerned, combination of materials may not necessarily be limited to simply those that have been broadly used in the past. Fiber-based materials and composites for example, are increasingly being researched and developed for adoption as major trends demonstrate their tendency to outperform even traditional “engineered materials” available. Experimenting and testing with these new materials leads to innovation and technological advances to further maximize the use of clever shapes.

Researchers have easily come to consensus and have accepted that shell shapes may include a countless variety and so dimensional analysis is typically used as a suitable categorization method. In continued development of shell order, an attempt is made to clearly classify shells on basis of curvature rather than symmetry considerations.

1.3 Shell Foundations

If significant loads are transferred through piers resting on problematic soil such as soft mud, saltmarsh ground, or quicksand, such structures tend to sink to an undesirable depth, proportional to their own weight. If, however, the pier rests on a larger platform or on posts, such as cast-in-place barrette piles drilled through mud or marsh to firmer ground, its weight is better distributed over a larger area in the first case and carried down to an improved soil strata in the second. The platform over which a wall, column or uniformly distributed loads rest in direct bearing with the supporting soil is referred to as the foundations footing. By spreading the load including the dead weight of the structure over a larger bearing surface area, the superstructural loads are evenly distributed, and the likelihood of settlement due to soil consolidation is greatly diminished. For years such a solid footing base has been designed in convenient rectangular formats defining the traditional footprint pattern.

1.3.1 Shell Classification

A shell as a foundation footing can be generally classified based on its curvature and thus fall within three major categories: uncurved, singly-curved and doubly-curved. An uncurved shell is that of a plate or flat footing case which is folded in an upright or inverted position where a radius of curvature does not exist. Singly-curved shells have one set of curves in one direction and are known to have zero Gaussian curvature. By forcing a singly-curved surface into a planar surface characterizes it as being developable whereas doubly-curved shells resist this tendency and are referred to as non-developable having curvature in two directions. The higher rigidity of the doubly-curved shell reflects a stiffer form and thus a conceivably stronger shell. Considering the two curvatures of either the same or opposite directions for the doubly-curved shell further subdivides them into being synclastic or anticlastic, respectively. Synclastic shells are formed by two sets of bent lines curving in the same direction, also known as shells of positive Gaussian curvature. Anticlastic shells are shells of negative Gaussian curvature. A secondary subdivision depends upon whether the developing shell surface is one of translation, revolution and/or ruled type. For example, a cone surface is developed by revolution of a ruled surface and a hyperbolic paraboloid is a shell of translation and a ruled surface. The straightline property

is one in which a section of zero curvature exists typically in anticlastic shells where lines of positive and negative curvatures are straight lines. All ruled surfaces, therefore, exhibit the straight-line property. The conoid, hyperboloid of revolution and the hyperbolic paraboloid are prime examples as illustrated in the classification regime of Figure 1.4.

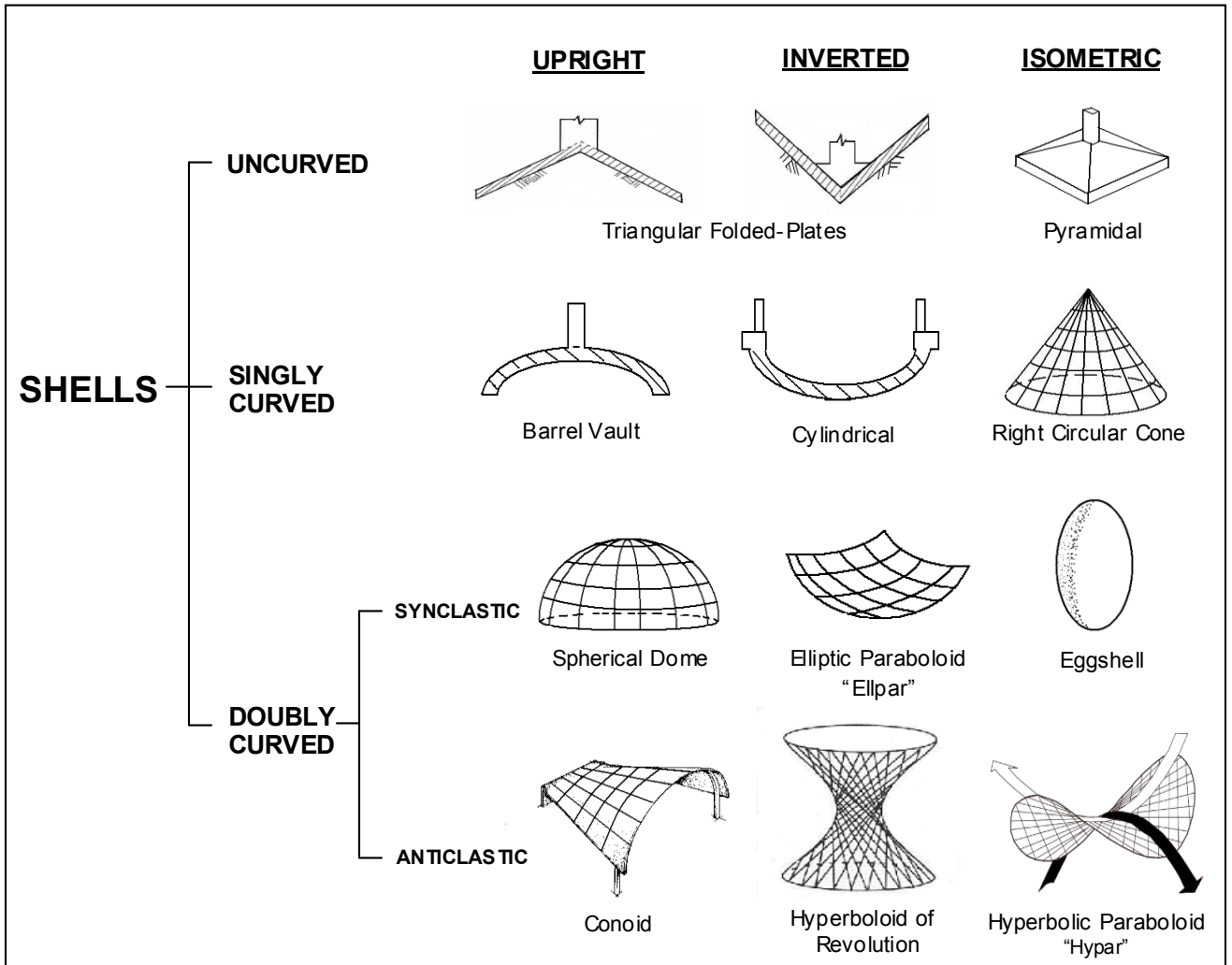


Figure 1.4. Shell Classification.

Membrane analysis on the simplest type of shells including the circular cylinder and the cone which are termed singly-curved shells, have zero Gaussian curvatures and are shells of revolution. Double-curvature shells have non-zero Gaussian curvatures in both principal directions and tend to resist higher magnitudes of load due to their closed-box geometries than do singly-curved shells. Open-box geometries, as the name suggests, are not as rigid and hence deformable under applied external loads.

Positive Gaussian curvatures referred to as synclastic shells have the highest structural performance ratings due to their ability to span substantial distances with very little concrete thickness and/or steel reinforcement and are therefore commonly used for covering large stadiums, arenas and other mass-gathering building structures.

1.3.2 Shell Components

The main composition of any shell foundation may be broadly divided into three main components. Namely, the girder, shell and toe (edge) are well-defined elements and illustrated in Figure 1.5(a) below. The girder beam often referred to as the column base or ring beam of the shell is typically first in line to absorb super-structural loads. In an inverted position the girder may be termed an edge beam in linear cases and ring beams in nonlinear cases. The girder element transfers the load to the actual shell component with the shell element itself being typically where material savings is best exploited.

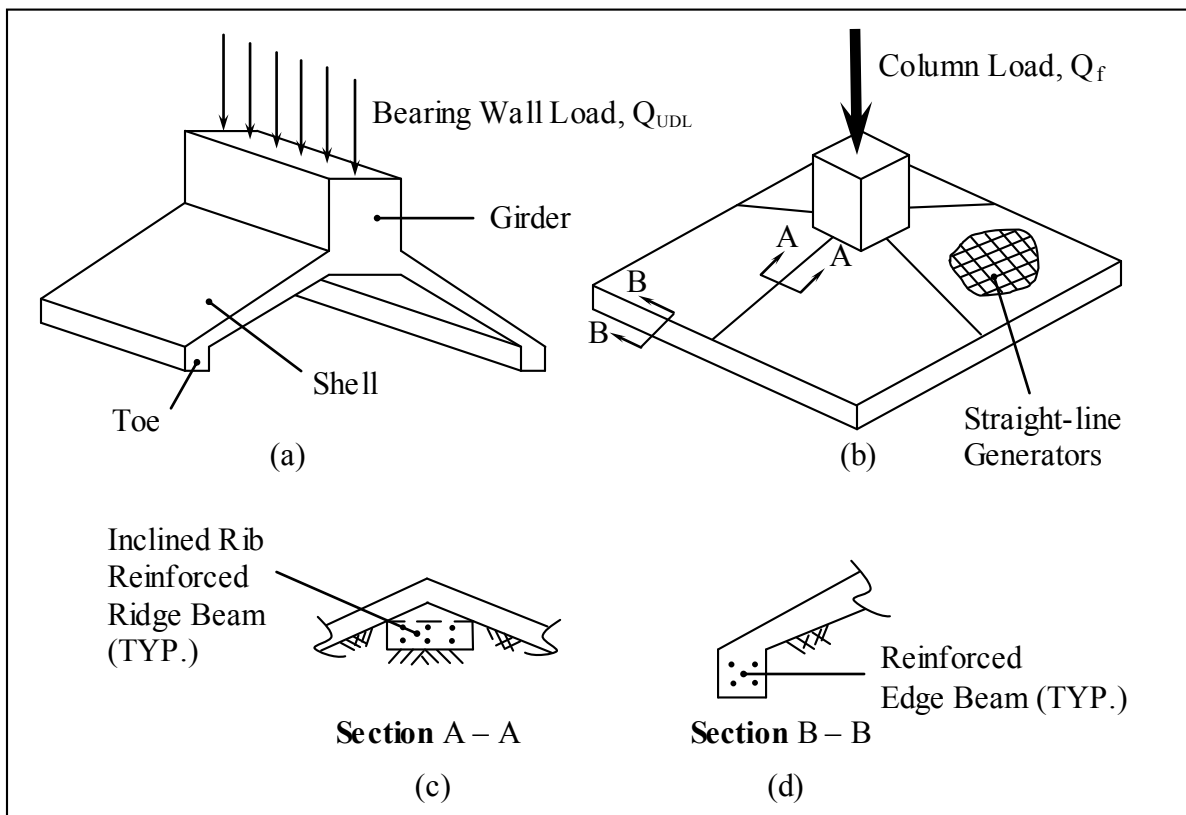


Figure 1.5. Shell Components: (a) Strip Shell Footing (b) Isolated Shell Footing
(c) Ridge Beam Detail (d) Edge Beam Detail.

The shell element is analogous to a fin acting as the primary load transferral mechanism between beam elements. Unlike roofing structures, shell components in foundations must be reinforced to absorb tension loads developing such as in load reversal, overturning, sliding or uplift failure cases.

Finally, the toe element of shell footings are formed by reinforced edge beams following the shells perimeter. The girder, sloped ridge and edge beams would intuitively seem to be taking primary stresses from an applied load, whereas the shell fins themselves absorb secondary stresses. Adding edge beams and increasing their depth of embedment has seemingly demonstrated to have improved stress transferral with increased load carrying capacities of shell footings (Huat *et al.*, 2006). While only conceptual forms have been proposed as far as edge beams are concerned, further exploration into this realm may prove to play an important role in increasing shell footing capacities without substantially adding to overall design complexity nor material cost of the structure. This may become particularly critical as high stress concentrations are known to be found at the peripheries of several geometric shell footing models.

1.4 Thesis Layout

If the suggestion of shells has intrigued you as much as it has myself in being admirable structures more than capable of satisfying basic requirements for foundations, then this introduction forms the reasoning behind advancing their behavioural knowledge and performance. Since shell footings are the latest newcomers to the foundation engineering vocation their studies are generally scarce with very limited investigations attributed to their cause particularly on soil-shell structure interaction front.

The research conducted in this study on shell foundations includes existing and new shape exploration subject to similar field loading conditions as met in practical design situations. The tactical breakdown of shell analysis depicts the critical path embarked in the organizational development of this thesis following a top-down approach. Particularly, the methodology of work undertaken was analyzed and is explained graphically in the shell analysis chart shown in Figure 1.6.

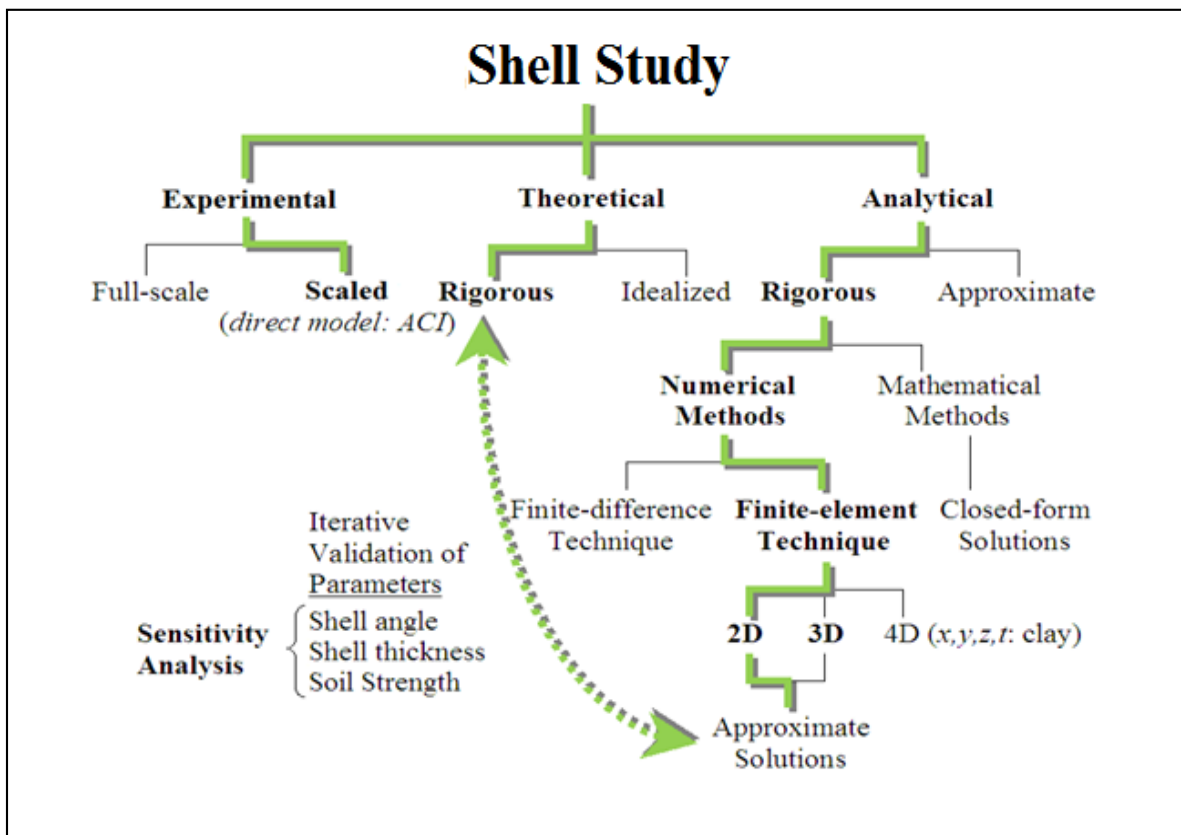


Figure 1.6. Shell Study Chart – Critical Path for Research Work on Shell Footings.

It should be noted that numerical solutions are compared to experimental work of direct models which are scaled from full-scale models to meet constraints of laboratory tests, typically the test tank encasing of the test bed soil media. When scaled models are unavailable, full-scale models should be used in validating solutions, however, that said, it is generally accepted that the former precede the latter if practicable. The flowchart presented in Figure 1.7 shows the stream of data flow between three phases of shell analysis in attempt to validate the findings drawing when necessary on existing data.

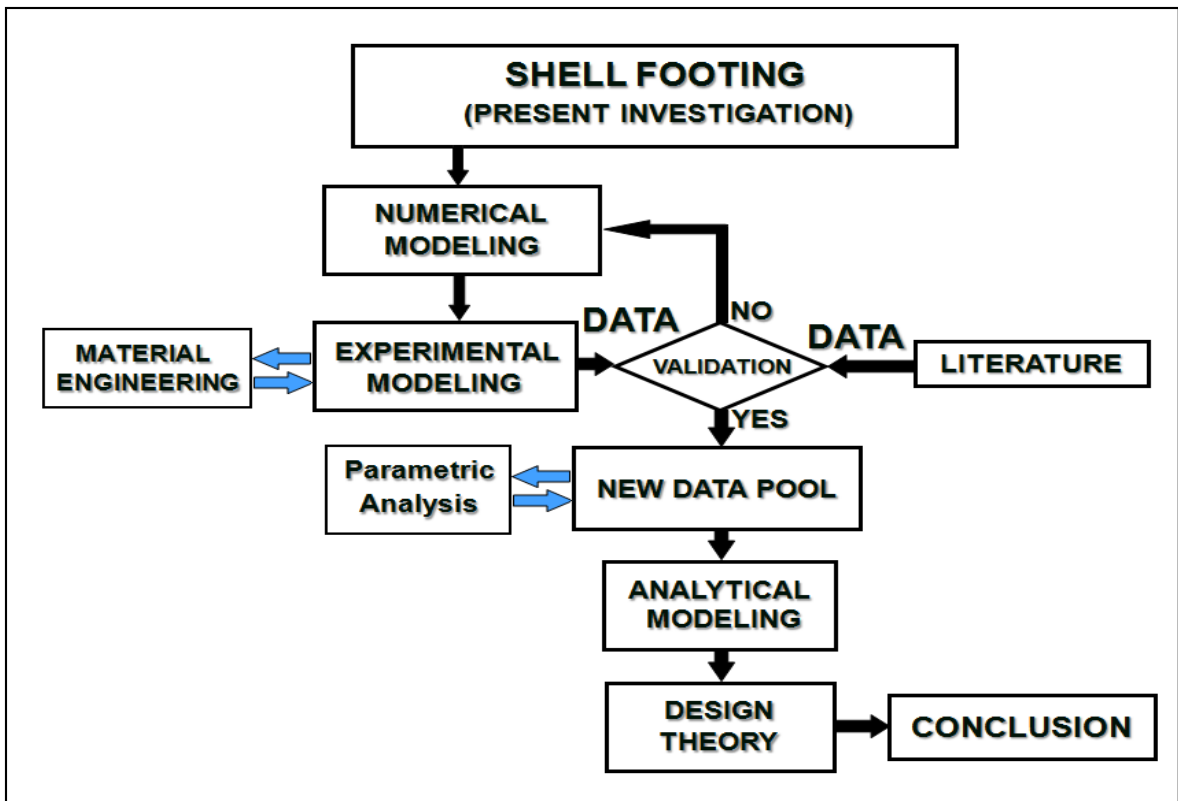


Figure 1.7. Flowchart Analysis – Shell Footing Investigation.

Given the complex nature of soil behaviour, rigorous mathematical approaches are rather difficult to derive. Naturally found soil deposit variations in the field coupled with assumptions of approximated arguments in modeling theories invoke complexities inherent with the shell argument. For example, reasonably accurate mathematical modeling of shell foundation footings on strong sand overlaying a weak sand stratum would be an extremely tedious and daunting task. Moreover, experimentation for comparison sake is best suited to a homogenous soil such as sand strata as contemplated in the present investigation to help evaluate individual results more accurately and facilitate validation.

In Chapter 2 of this study, a literature review is conducted to emphasize critical research milestones ascertained providing a boundary of existing knowledge on the subject. A brief history of shell applications in foundation structures as applied to soil behaviour is also presented to bring forefront terminology and mechanisms previously used. This will help explain and evaluate shell behaviour such as the prediction of soil failure patterns for instance. This chapter highlights the scope of the thesis and the need to better understand contact pressure distributions developing based on geometrical considerations affecting the soil–structure relationship. Extension of knowledge on a shell footings improved behavioural response over existing forms given the marked structural performance exhibited is the premise for furthering shell modeling research as discussed in the subsequent chapters.

A breakdown of the numerical modeling approach is discussed in Chapter 3 including the functional use of several software packages including Shape Designer 2011 and the geotechnical software PLAXIS 2D v.8.6: FOUNDATION. The formulation of structural models as well as description of material parameters for the structure and soil continuum is provided. In addition, the proposed stochastic properties of soil are evaluated and presented. The implementation of the constitutive soil models and overview of the PLAXIS software and its analysis capabilities is discussed. An overview of the finite–element technique with aid of illustrative soil–structure fields employing shell models developed and investigated in the software is discussed.

An experimental modeling phase is implemented to study first–hand behavioural response of shell footings in a laboratory setting as outlined in Chapter 4. Shells have been systematically tested experimentally to determine representative failure mechanisms, load–settlement response and their ultimate capacities. Presentation of the new shell models is provided using computer–aided design software AutoCAD where three–dimensional modeling and renditions are illustrated. Output results include deflection, soil stresses, and contact pressures which are analyzed and presented. The two–dimensional analysis would be limited to plane–strain conditions for shells such as those exhibited in strip footing cases. Three dimensional footing tests shed light on shape factor and its influence on the bearing capacity for the shells. Performance of the newly proposed shell models are

analyzed and validated in a comparative study to that of existing experimental and numerical work, whenever applicable and available. Since the dynamic module for the software is currently being developed, at the present time horizontal loading conditions are considered beyond the scope of this present investigation.

The developments relating to the loading conditions and varying shell forms is commensurate to the central theme of this study. The investigative research previously conducted will serve as a platform for validating and furthering the boundary of knowledge pertaining to shell orientation, shell angularity and loading state. Their importance and influence on sandy soil material is examined.

Theoretical modeling of soil behaviour beneath inverted shell foundations is discussed in Chapter 5. Stress–strain relationships defined by mathematical laws forms the basis of any constitutive soil model such as the Mohr–Coulomb which is explained explicitly. Essentially soil behaves as a multiphase material with nonlinear path–dependant response under load. Moreover, soil deformation is subdued to irrecoverable plastic strains where soils typically dilate or compact. Finally, soil response is influenced by its load history where natural soils are anisotropic and typically exhibit time–dependant behaviour. Overcoming the challenges typical soils present in shell–soil analysis and presenting details of the newly devised rupture surfaces for upright shells and their inverted partner is the focus of this section. Combined shell failure patterns is also analysed and presented.

A presentation of innovation in shell technology as applied to construction and material engineering is covered in Chapter 6. Shell construction methods with particular focus on innovative concrete mix developed especially for shell footing form applications is the topic of discussion. Shell economy from material cost–savings perspective as well as reduction in project execution time is rationalized to justify their novelty and effectiveness with final concluding remarks.

In Chapter 7, a summary of the major findings of this study is outlined and underlying conclusions are drawn as well as recommendations for further research is presented.

CHAPTER 2

LITERATURE REVIEW

2.1 Shell Foundation History

Over time shells have experienced marked development in foundation engineering, especially throughout the past half century from its initial inception in the early nineteen-fifties, particularly in the aftermath of World War II. Intrigued researchers have gained interest in their form as enclosures such as bunkers and refugee strongholds, having withstood the destruction and devastation of the time and found to remain largely intact. In a continued effort to explore a shells interesting performance attributes in footing applications a literature review on shell foundations has been conducted and is presented.

The first recognized use of shell foundations dates back to the early 1950's where Spanish architect, Felix Candela (1955) has undisputedly been regarded as conceptual pioneer and forefather of the shell footing foundations notion. Experimenting with shell shapes, Candela's concern for elegance and style were his underlying motivations in opting for a structural shell. This conviction led to an extensive exploration of shell structural forms many of which are still in existence today. The Hyperbolic paraboloid otherwise known as "Hypar" shell footings, for example, was one he envisioned and used repeatedly on Mexican soil. This geometric shell was implemented successfully in a vast majority of his works in light of other experimental work on barrels and funicular vaults he was using. These shapes were further developed to support column loads in many parts of the world (Sondhi and Patel, 1961). Soon later, the Hypar shell form was suited for high-rise buildings and outfitted for water tank structures founded on poor soil (Kaimal, 1967).

Historically, many Hypar foundations have been reported, particularly by design-builder Candela himself who also firmly believed that strength should come from form and not mass. Two examples of his formidable work employing shells in buildings are reproduced as illustrated in Figures 2.1 and 2.2. The successful applications have surely led to the development of other structural forms where knowledge on their resilience had disseminated.

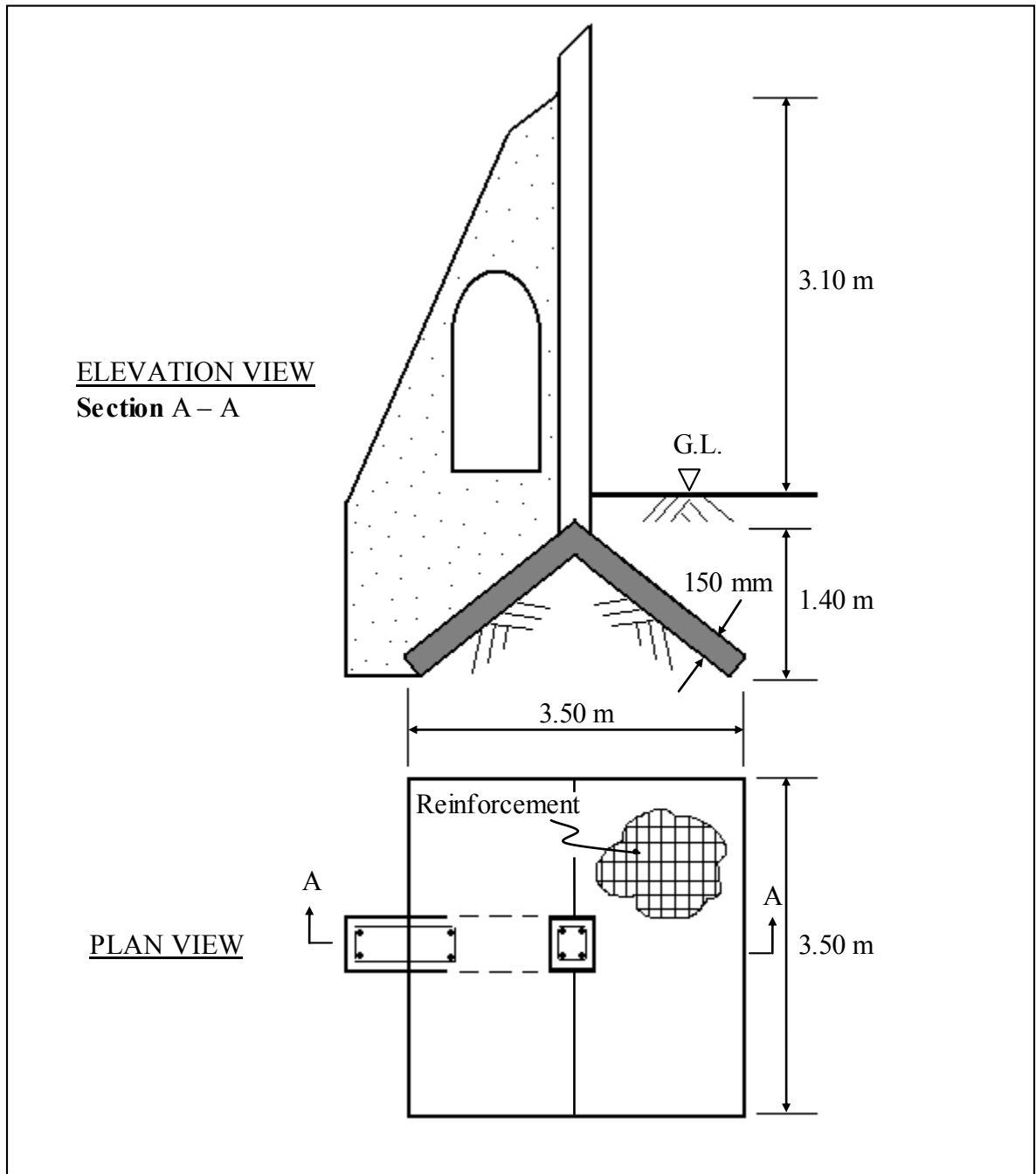


Figure 2.1. Hypar Footing for St. Vincent's Chapel, Coyoacan, Mexico (Joedicke *et al.*, 1963).

The challenge and opportunity is to bring scientific study of the shell used as a footing up to speed justifying its performance with added benefit of its established aesthetic appeal. The literature abounds with examples of varying types of shell foundations such as the conical shell substructure supporting Moscow's famous telecommunications tower in Ostankino, Russia. Economic analyses of residential buildings showed that the use of shell

foundations replacing pile foundations reduced reinforced concrete expenditure by 40%, and construction time of at least two months was saved with labor productivity increased by 148% (Goncharov *et al.*, 1983).

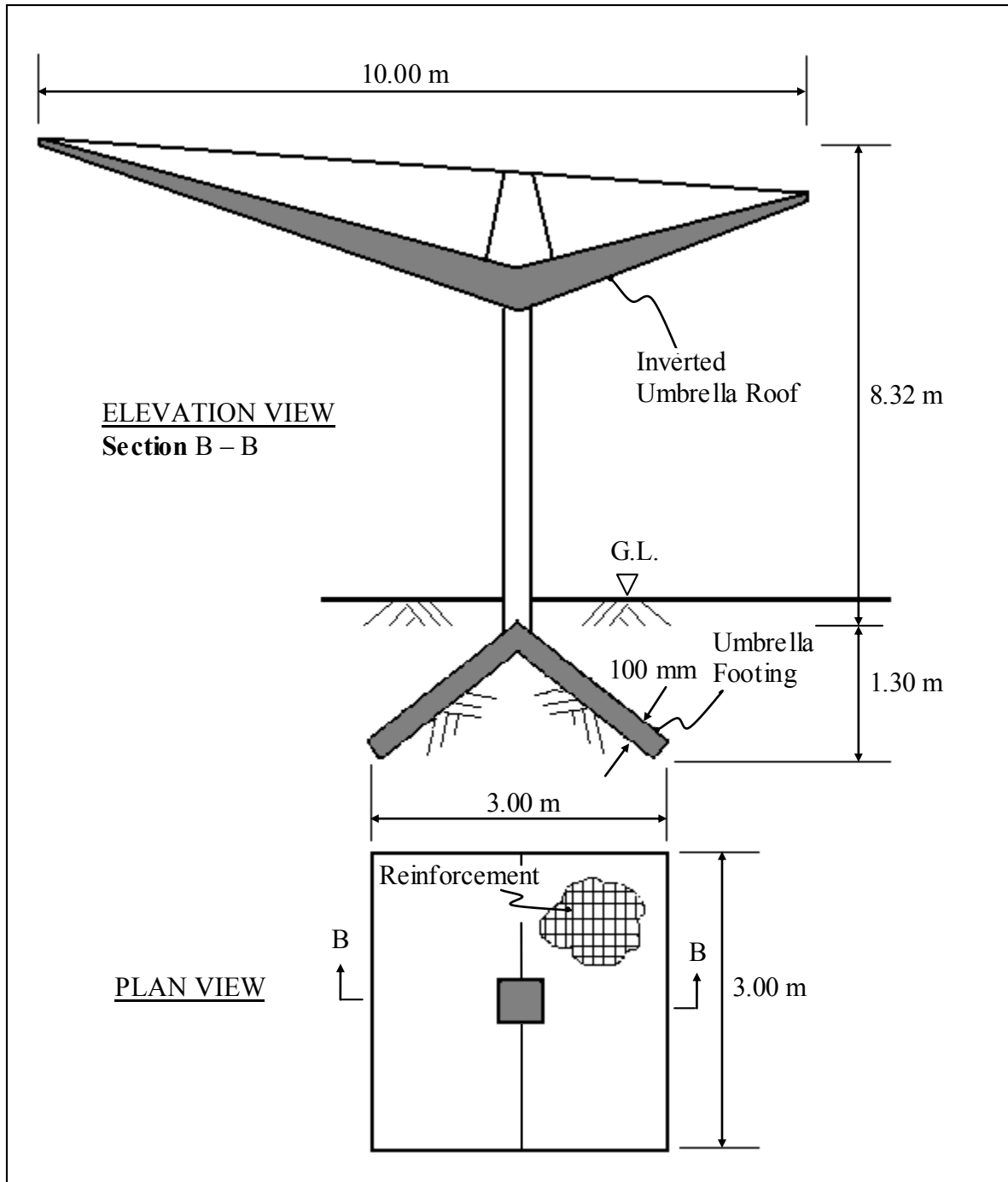


Figure 2.2. Hypar Footing for a Factory for Lamex, S.A., Mexico (Joedicke *et al.*, 1963).

Another example is the implementation of shell-shaped footings for a two-storey building reported as having been constructed in Mombasa Africa, Kenya. It has been determined that the local soil there is soft clay, highly susceptible to the adverse effects of moisture variation. The choice of footing selected was the ‘Hypar’ type shell footing as a solution. Figure 2.3 illustrates the elevation and plan views of the as-built shell footings.

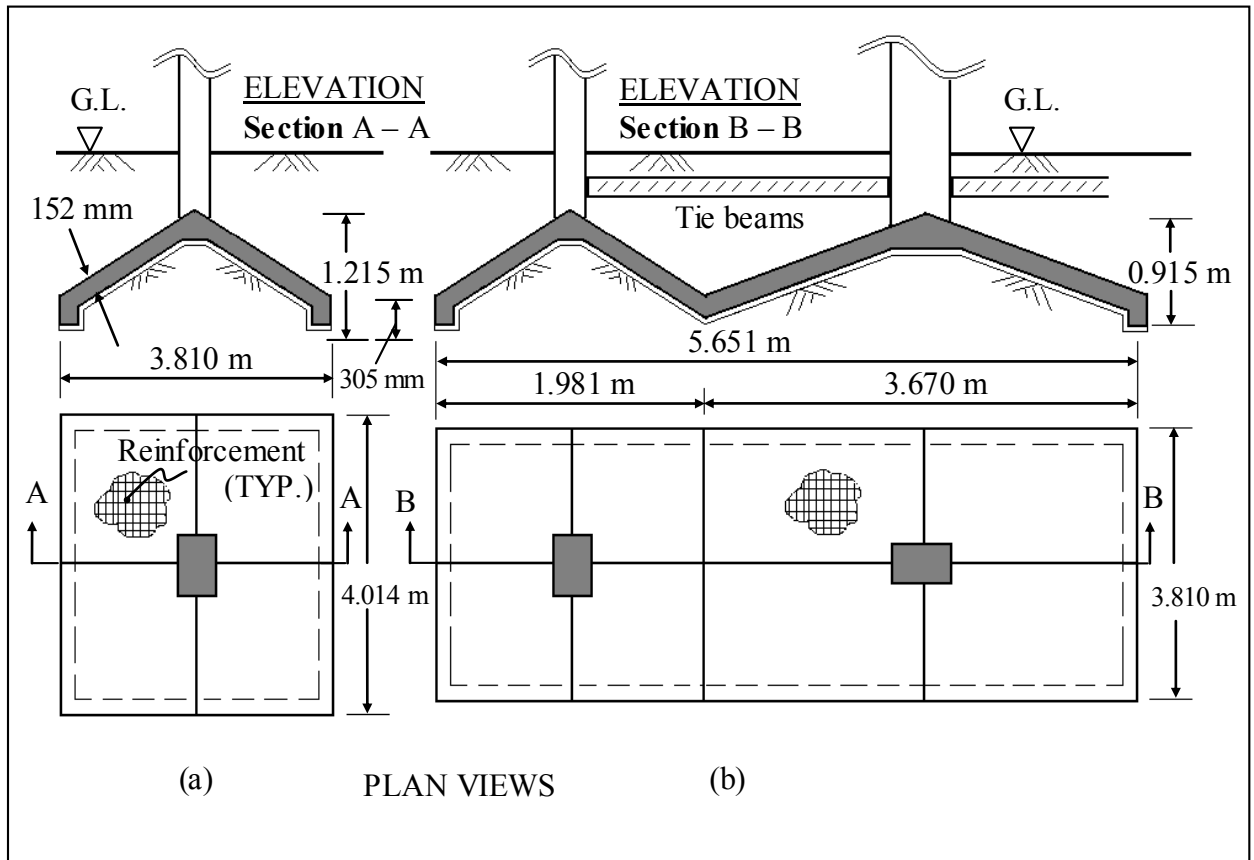


Figure 2.3. Hypar Footings: (a) Isolated (b) Combined (Sondhi *et al.*, 1961).

Earth pressures on curved surfaces have been studied by Mackey (1966) who has reported that passive pressures acting on the convex earth face are considerably greater than those on plane faces. Hanley (1964) had reported similar results on static and dynamic pressures. Hypar shells have been extensively studied at the Indian Institute of Technology, Madras (Kurian, 1971; Mohan, 1980). Some guidelines have been established concerning shell design based on their ultimate strength (Kurian, 1973 and Isi, 1980). A consequent study of the contact pressures under shell foundations has been undertaken for individual ‘Hypar’ shells in square and rectangular forms and ‘combined-Hypar’ footings and rafts were also investigated (Kurian and Mohan, 1981).

Hanna and Abdel-Rahman (1988 and 1990) reported experimental results on strip shell foundations on sand for plain strain condition. Four shell type footings were investigated with peak angle θ varying from 60° to 180° . Testing was conducted in a plexiglass tank with dimensions ensuring plain strain conditions. For sand compaction, the drop technique was adopted. Footings were tested at the surface and in buried conditions (i.e. depth-to-breadth ratio was 0.75). Model footing were subjected to vertical compression load acting on the center by means of a compression machine. The load acting on the footing and corresponding settlements were recorded until failure. The experimental results showed the triangular shell footings had higher bearing capacity and better settlement characteristics than the flat foundation with an equivalent footing width. At a certain load level, the smaller the peak angle of the foundation, the higher the bearing capacity and lower the measured settlement.

Theoretically, the classical solution of the bearing capacity of a flat shallow foundation was extended for the upright case of triangular shell strip footings. The results for surface footings showed that the ultimate bearing capacity for the triangular shell model with a peak angle of 60° was 40% higher over the flat model (Adel-Rahman, 1998).

Studies using mathematical models were undertaken to evaluate the best possible contact surface on a given bearing soil. The new shell surfaces were modeled assuming normalized and homogenous soil conditions. The optimum mathematical model was found to be the harmonic S-sin wave function having a curved base surface (Hadid, 1983).

Many other countries have utilized shells as footings for particularly weak soil conditions, normally weak clays. Russia, India and the United States however, have been predominant users of the shell form in such structures. Great achievement in strength was surprisingly achieved based on aesthetics and ability to construct these structures economically. Since the quantity of both concrete and steel material in shell construction is minimal, their economy aids in reducing costs related to forming as was found in repetitive configurations such as in raft-shell foundation designs (Kurian, 2006).

Over time, designers have seemingly benefited not only from shells strength but from substantial cost-savings. For example, in Havana, the New City Hall was a 24-storey building constructed on a bearing soil of 287.3 kPa [6000 psf] capacity. The two options available to designers were a flat slab with deep beams and a raft formed by folded plate slab. The folded plate slab was selected as the preferred solution due to cost effectiveness of that option. The net savings experienced was reported to be 30% on the construction of such foundations (Martin and Ruiz, 1955).

In the United States, the Summer High School in Washington, a classical example of a large stadium, was constructed of precast prestressed concrete units in attempt to seat some two thousand spectators. The site was reportedly a fill underlain by a deep deposit of soft mud. Thin reinforced concrete Hypar shell footings were adopted for this project to satisfy the established engineering requirements while maximizing space and optimize cost-savings from construction materials used (Anderson, 1960).

2.1.1 Primitive Footings

The most basic and primitive of shapes used as footings have been derived from arches used in roof structures such as entrances of buildings and walkways of ancient buildings. The horseshoe, gothic and roman stone arch styles being by far the mostly widely adopted and constructed shell forms. The material of roman stone arch foundations were initially composed of brick and stone masonry sprung across the soil to support wall loads at shallow depths. The inverted footing was initially used to support pier loads.

Both systems had drawbacks especially at corners where concrete blocks and iron rod ties were used to counteract the outward thrust at the ends. These similar challenges are faced in barrel vaults and bridge arches where buttresses and abutments are used as solutions respectively. These classical threshold roof forms were founding geometries which gave naissance to contemporary roof structures composed of barrel vaults, octagonal domes and hyperbolic paraboloid shapes for instance. These new concrete shell enclosures are found to be today's ideal solution for spanning large unobstructed spaces such as

arenas, stadiums and auditoriums eliminating the need for obsolete secondary members such as rafters, purlins and heavy trusses.

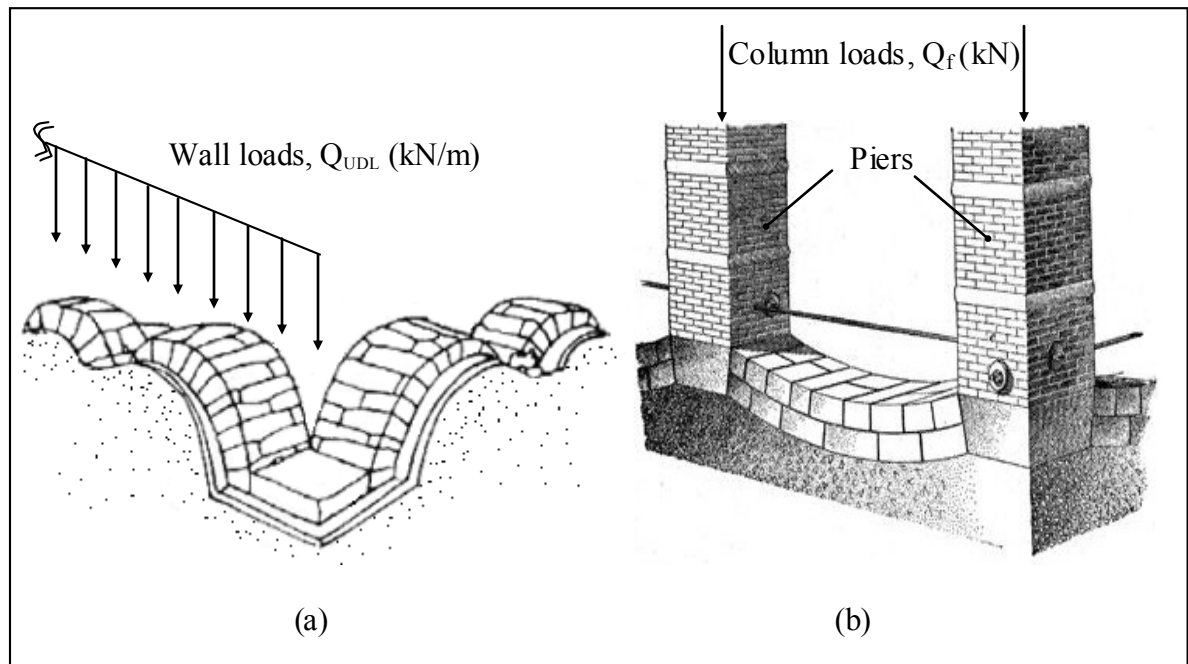


Figure 2.4. Stone Arch Foundations: (a) Upright (b) Inverted (Kidder, 1905).

In Figure 2.4, wall loads are supported by foundations made of brick or stone masonry arches emanating from a series of cement concrete bases which restrain lateral thrust. The method was thought to have helped cut down on material use such as cement, coarse rubble stone and sand etc. Seemingly, a very labor intensive system, the arch foundation was best used if the condition of the soil was firm and the structure being supported was low rise. Single storey homes and office complexes such as that shown in Figure 2.5 were normally found to be the best suited structures to receive shell foundations.

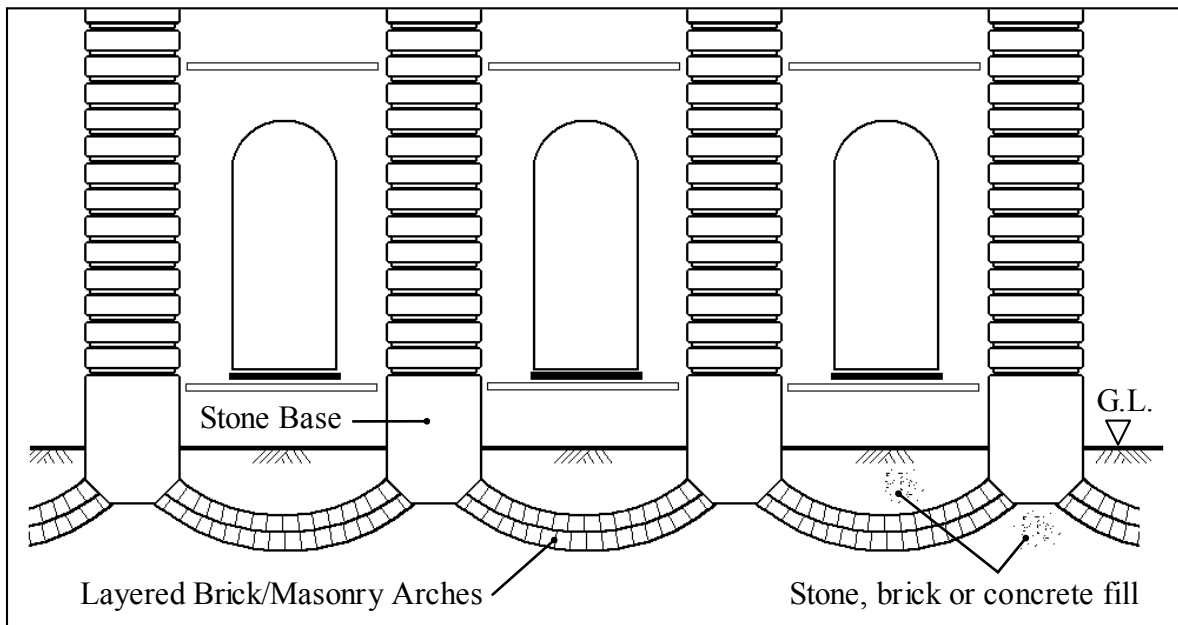


Figure 2.5. Inverted Masonry Arch Foundations (Kidder, 1905).

Underdeveloped countries such as Mexico, India and Africa have benefited most from low labour-to-material cost ratios associated with shell foundations. Nonetheless, developed countries such as Canada, the United States, Germany and Japan have used shells successfully especially when the shell foundation structure was found applicably to be an effective and feasible solution.

2.1.2 Modern Shell Footings

Intuitively shells almost instantly create a curved spatial surface depiction in our mind as to what a shell would look like. One instantly emulates its thin form to that of an eggshell, seashell or a turtles shell affirming its aesthetic appeal. From basic to their most intricate forms, shells are consistently thought of as being elegant, eloquent, inspirational structures creating an undefined harmony between physical and ideological worlds. Ironically, our efforts as designers is to use the intricacies shells offer, capitalize and idealize them, then bury them for no one to ever see or even appreciate. One example of a highly ambitious development of a complex shell foundation system was used in support of the Nonoalco Office Tower as illustrated in Figure 2.6.

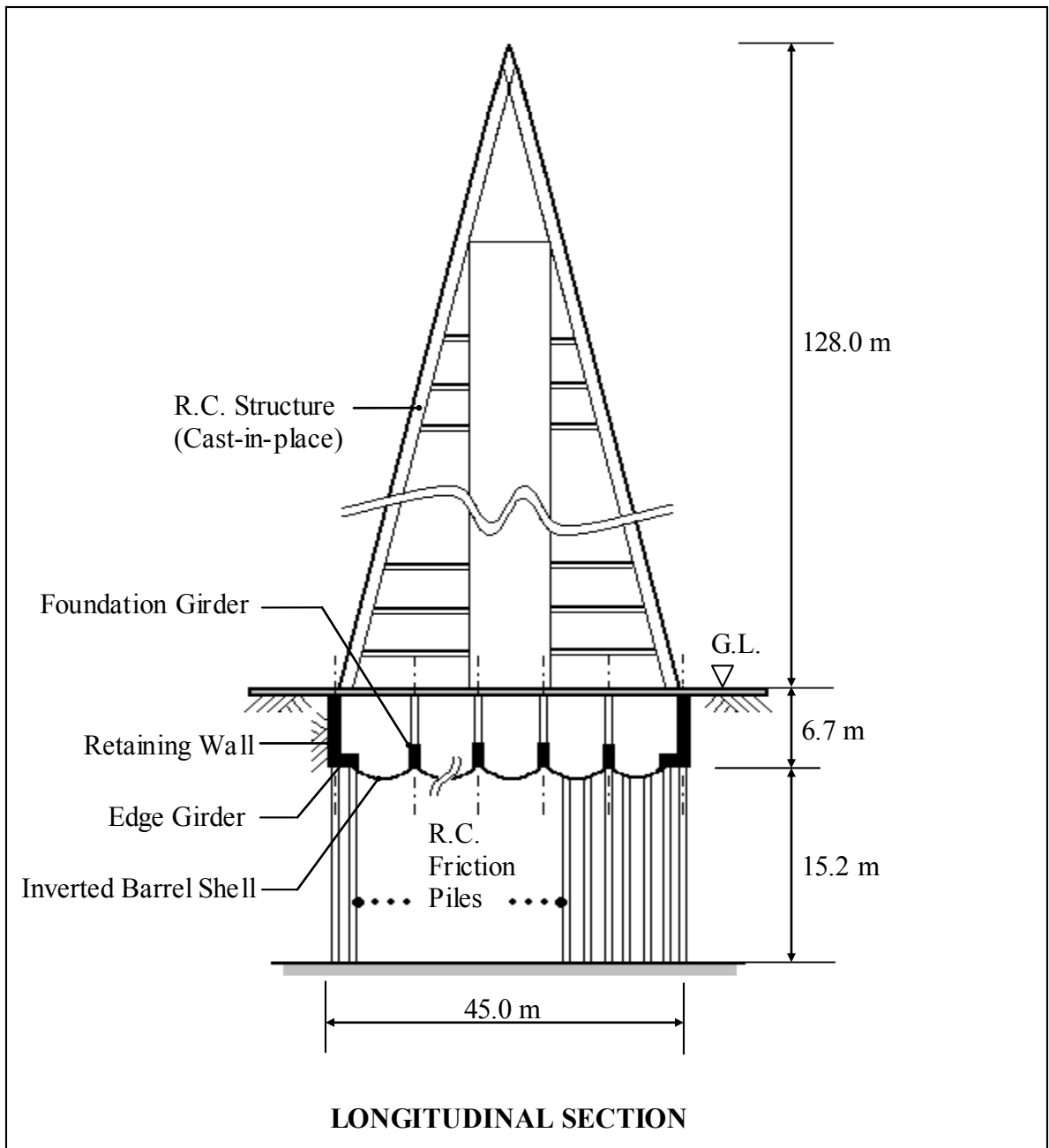


Figure 2.6. The Nonoalco Tower Foundation, Mexico (Enriquez and Fierro, 1963).

The inverted barrel shells were linked by reinforced concrete girders supported overall by cast-in-place friction piles. This foundation system was esteemed to have saved 50% in material costs over the conventional two-way slab foundation it replaced. Moreover, for a given volume of excavated soil, the barrel shell system exhibited increased stiffness and reduced weight (Enriquez *et al.*, 1963).

An M-type composite conoidal shell footing alternative replacing a pile foundation was used in China. It was constructed to support a spheroidal tank in a high seismic region with low allowable soil bearing capacity. The outer conoidal shell was built with a 30° shell angle whereas the inner conoidal shell had a 21.68° slope with overall shell thickness range of 35 – 55 cm. The shell design shows considerable economy of materials including timber falsework and labour. Savings of 24.3% and 22.8% in concrete and steel reinforcement material was reportedly attained with this shell foundation (Wang, 1985).

The most basic concrete shell geometries used in shell foundation structures include the uncurved folded-plate types typically in strip or isolated configurations. Such shapes have a naturally practical advantage over complex curved surfaces from a constructability point of view. A typical folded-plate strip shell foundation is depicted without edge beams in Figure 2.7 below in both the upright and inverted positions.

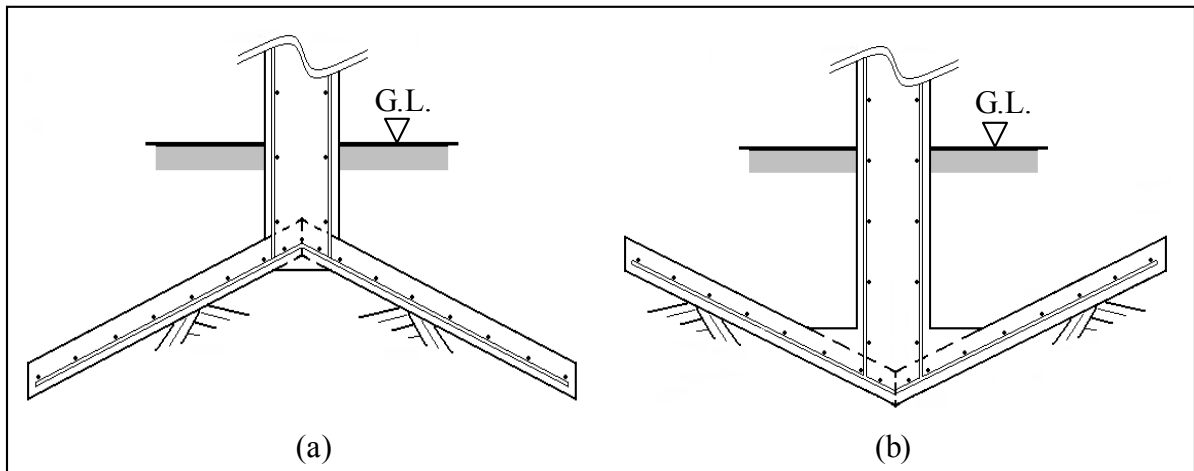


Figure 2.7. Folded-Plate Shell Footings: (a) Upright (b) Inverted.

One example of the folded-plate is the pyramidal shell used mainly as an isolated, strip or combined footing configuration. The following figure illustrates an example of a cast-in-place concrete folded-plate strip shell footing. The photograph was taken at the Potash Corp. in New Brunswick, Canada. Upon inquiry, these shells were used as isolated division walls in an industrial warehouse setting. They were subject to mostly horizontal loads used intuitively to resist overturning and sliding forces generated by containment storage of potash material.



Figure 2.8. Folded-Plate Shell Footings. Potash Corp., Sussex, NB, Canada.

Other simple shell geometries include the cone (conical) and domes known as shells of revolution including spherical, elliptical, parabolic and cycloid types. These are confined, unfortunately, to mostly individual footings supporting isolated column loads. They may, however, be designed sufficiently large enough to become an entire structural system for a larger superstructure such as chimney columns and water tanks. The next two figures illustrate a dome and cone shell in their upright and inverted positions respectively.

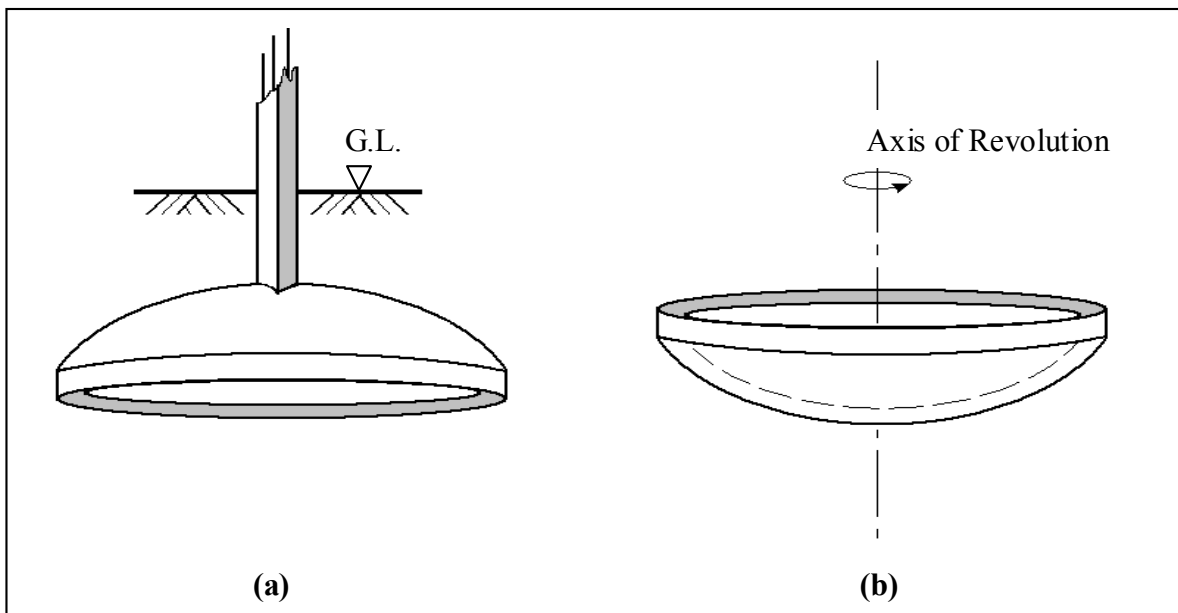


Figure 2.9. Dome Shell Footings: (a) Upright (b) Inverted.

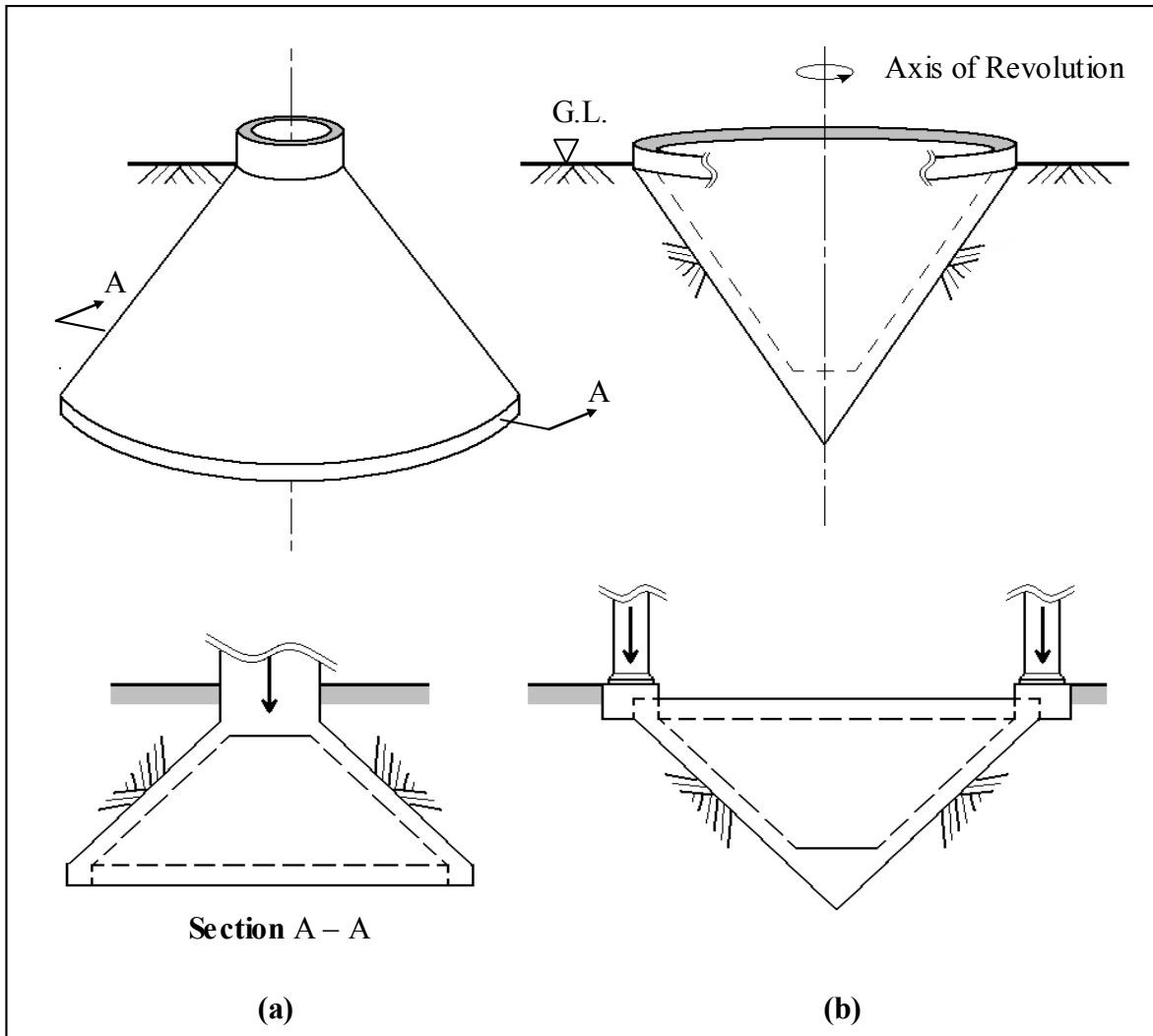


Figure 2.10. Conical Shell Footings: (a) Upright (b) Inverted.

The inverted counterparts may be used to support cylindrical superstructures such as water tanks and silos. They may also be used to support a series of column loads that follow a circular or elliptical pattern as prerequisite for the foundation shell required. For example, an inverted circular cone may be used to support a guyed mast or towering structure whereas an inverted spherical dome may be used in support of water tank basins and/or silos containing agricultural soft commodities for example, such as wheat, grain, rice or hard commodities such as mined ores, coal, salt, etc. Such structures generally have uniform loading effects that follow the said circular or elliptical pattern as illustrated in Figures 2.11 and 2.13 respectively.

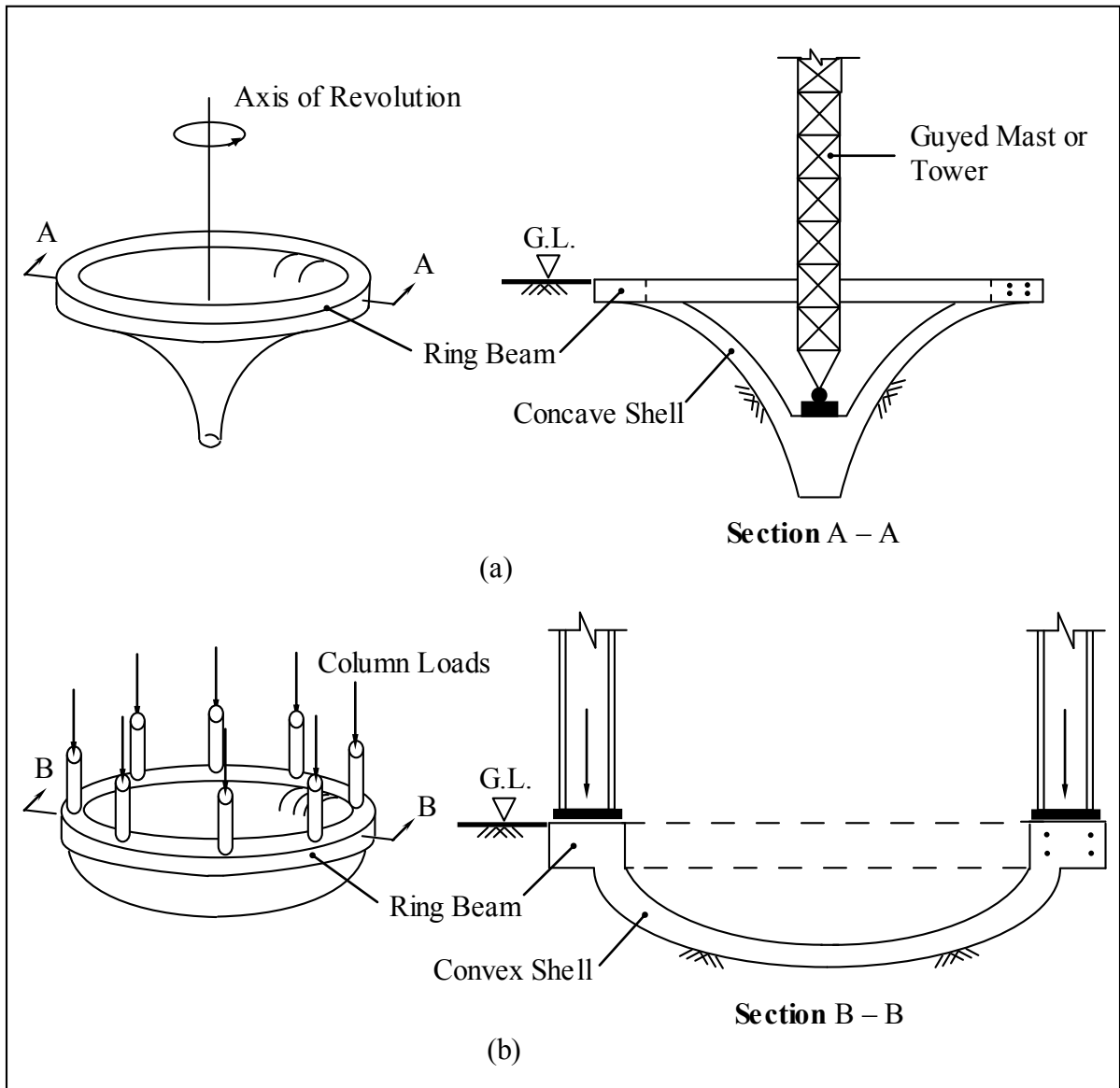


Figure 2.11. Inverted Circular Shells: (a) Cone (b) Dome.

A widely applied geometry is that of the hyperbolic paraboloid referred to as a “Hypar” shell which may be used as an isolated footing or combined in raft/mat configuration. The translational surface of the Hypar shell is known to exhibit great strength due to straight-line property they exhibit. The ruled surface is made up of straight lines known as ‘generators’ that run parallel and are at right angles to each other in plan view. These lines are present over each of the four quadrants and would be seen along directions inclined at 45° to the two principle parabolae: the concave and convex parabola.

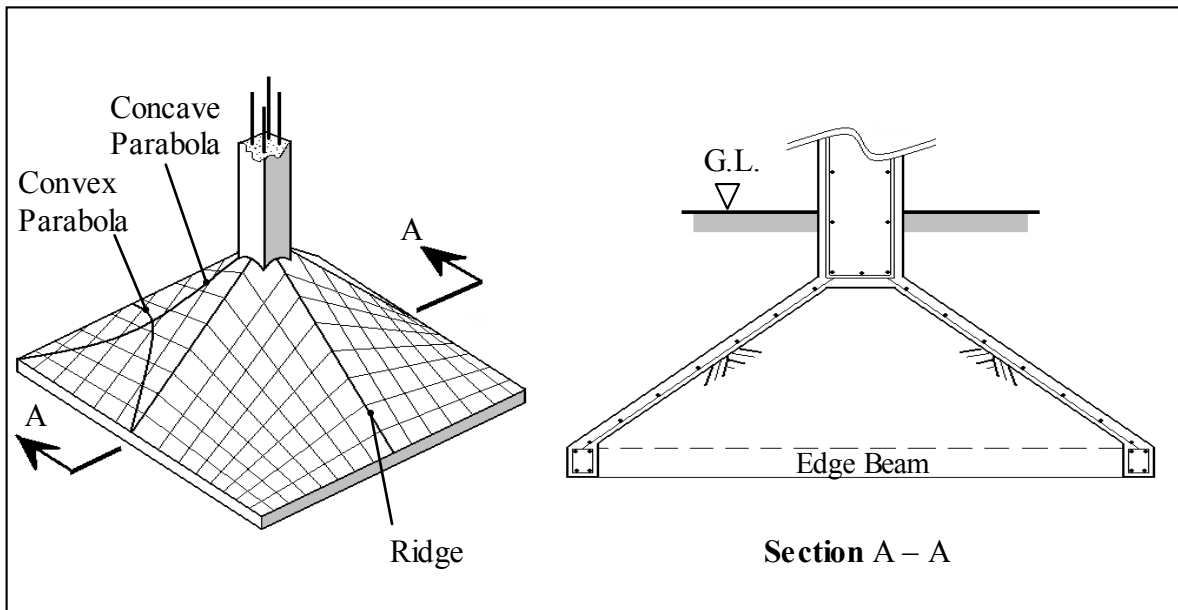


Figure 2.12. The Hyperbolic Paraboloid ‘Hypar’ Footing (Enriquez and Fierro, 1963).

The rectangular hyperbolic paraboloid foundation, for example, shown in Figure 2.12, consists of straight lines over its surface at increasing inclinations while approaching the crest of the shell.

Elliptic paraboloids otherwise known as “Ellpar” shells are another example of a translational surface obtained by running one parabola over another in orthogonal directions. These types of shells are doubly curved synclastic shells graphically presented in Figure 2.13 below which derive their name from the fact that horizontal planes intersect surfaces along an elliptical trajectory for a rectangular shell and along a circular one for a square shell. As an isolated footing, singular and multiple loading conditions may be supported by varying the shells orientation. In either case, the provision of edge beams may be introduced to satisfy additional strength requirements.

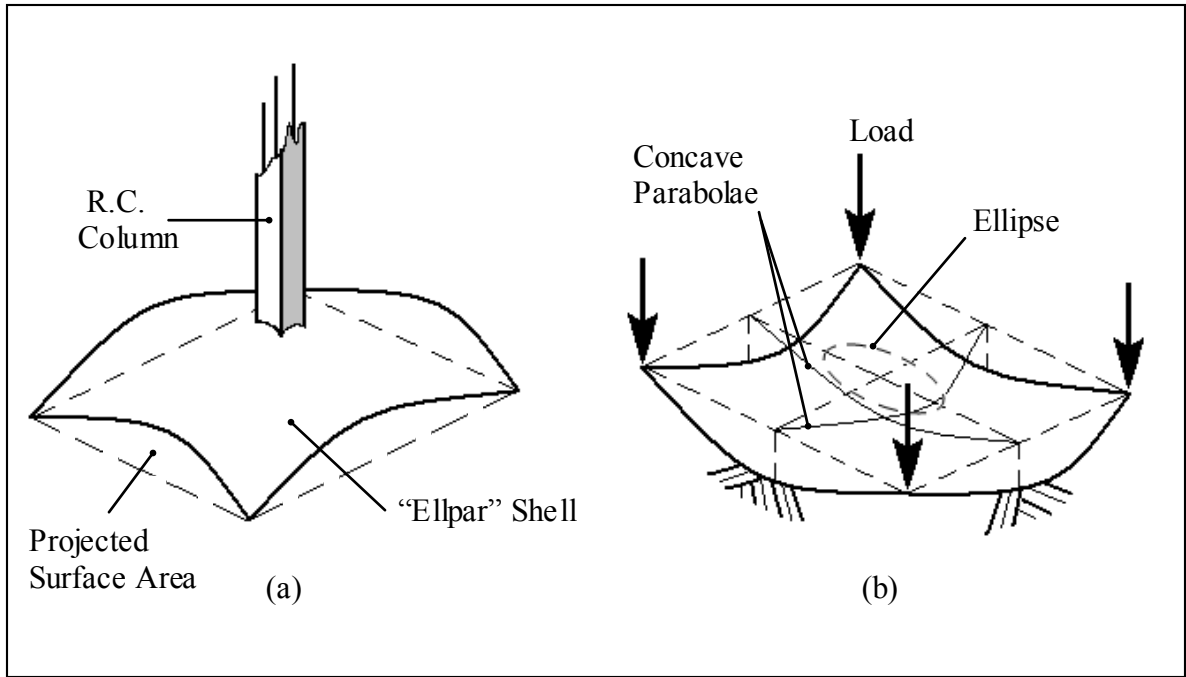


Figure 2.13. Elliptical Paraboloid Shells: (a) Upright (b) Inverted.

Perfectly spherical and cylindrical types are also used. The use of such shapes have shown to maximize the effectiveness of concrete, allowing them to form thin light spans embracing large volumes of soil due to the larger contact surface areas shells have to offer.

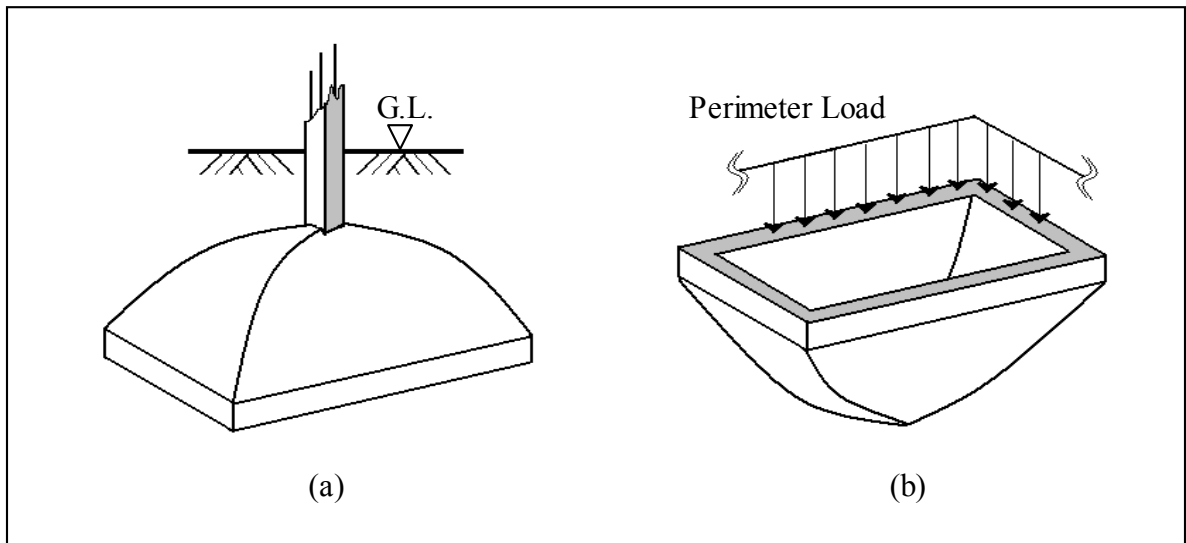


Figure 2.14. Parabolic Pyramidal Dome Footing: (a) Upright (b) Inverted.

2.2 Special Shell Footing Cases

Shell footings have generally taken the form of isolated structures. Notwithstanding their dismal popularity and lagging use, connoisseurs have taken up challenging feats of employing shells beyond conventional methods but only for warranted venues. Consequently, shell footings may take composite form, the likes of which have proven to be successfully embraced in challenging soil conditions. Initially, shell elements of isolated footings of varying geometry may be combined to form '*Combined Shell Foundation*' systems. Next, by varying materials used in combination may form the second special shell footing case known as a '*Composite Shell Foundation*' system. Typically shallow, a shell foundation footing may be combined with piles as deep foundation elements to form a prime example of the latter system. As such, the valuable properties of the shell may be exploited even when the desirable soil strata is at appreciable depth. In either case, the upright orientation or its shell inversion counterpart may be successfully employed. Perusal through literature on shell footings has left readers with much void in scientific information. It was noted, for instance, that construction of an inverted composite shell foundation has yet to be attempted neither in strip nor isolated orientation forming yet another window of possibility. The following sections describe both the combined shell and composite shell footing arrangements as two special shell footing cases.

2.2.1 Combined Shell Footings

Interestingly, the boundaries of conceptual shell footings are as far and wide as ones imagination. In the most demanding and challenging of soil conditions shell shapes may be combined to further enhance footing performance. This may achieved by superposition, where a full spherical shell is modified to include the frustum of an upright cone at either outer shell limit. Since sufficient contact area required beneath footings is of great geotechnical concern, for bearing capacity and settlement to be satisfied, combined shells offer this added surface.

The combined special case shell footing includes combinations of more than one singular element mutually combined to form the composite shell footing. For example, an inverted dome shell segment may be modified to include elements of a conic shell appended to the extremities of the otherwise isolated dome. An overhead water tank structure is depicted in Figure 2.15 below which demonstrates the use of a combined shell foundation. The cylindrical water tank sits on a supporting tower of the same geometry. It is particularly intriguing to note that the shell foundation walls were constructed of the same order of magnitude, in terms of thickness as that of its superstructure it supported. Perhaps yet another indication of material savings and economy expected to be achieved with these footings.

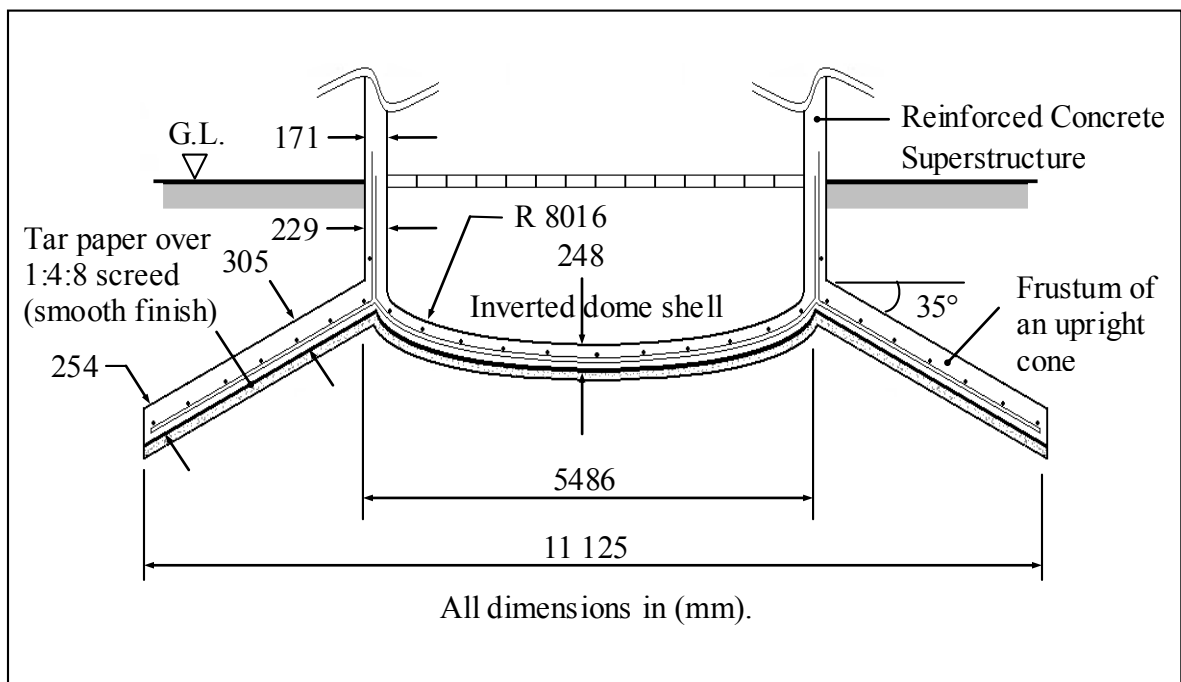


Figure 2.15. Combined Shell Footing: O.H. Water Tank (Bangalore, India, 1987).

This inverted dome-cum-cone combined shell foundation structure, shown above, was designed by STUP Ltd. based in India for a new helicopter factory for the Hindustan Aeronautics Ltd. company. As a general consideration, if peripheral column loads were symmetrical in nature with uniform intensity, the shell appenditures may be omitted to obtain simply an inverted spherical dome configuration. Such is the case for silos and

water tanks containing liquid, fluid or gas substance typically retaining material producing a symmetrical loading patterns where horizontal loading is deemed negligible.

2.2.2 Composite Shell Footings

The second special case of shell footings includes those of several materials forming the composite shell foundation system. The best example is that of a shallow hyperbolic paraboloid shell constructed overtop a deep timber-piled foundation in the soft clay having an average safe bearing pressure of only 109 kPa. The poor soil conditions representative of the site in Khurdah, an industrial suburb of Calcutta, is synonymous with high-settlement prone regions forming a challenging and problematic soil. In effort to control settlement, timber piles were first driven to a stronger soil strata overtop which a 50 mm [2 in.] concrete mat was poured followed by a brick filled core. The numerous shell footings had varied dimensions from 1.52 m square to 5.49 x 4.27 m rectangular having maximum shell thickness of 381 mm [15 in.]. Footings were outfitted with stout ridge beams counteracting any moment effect (Anonymous, 1965).

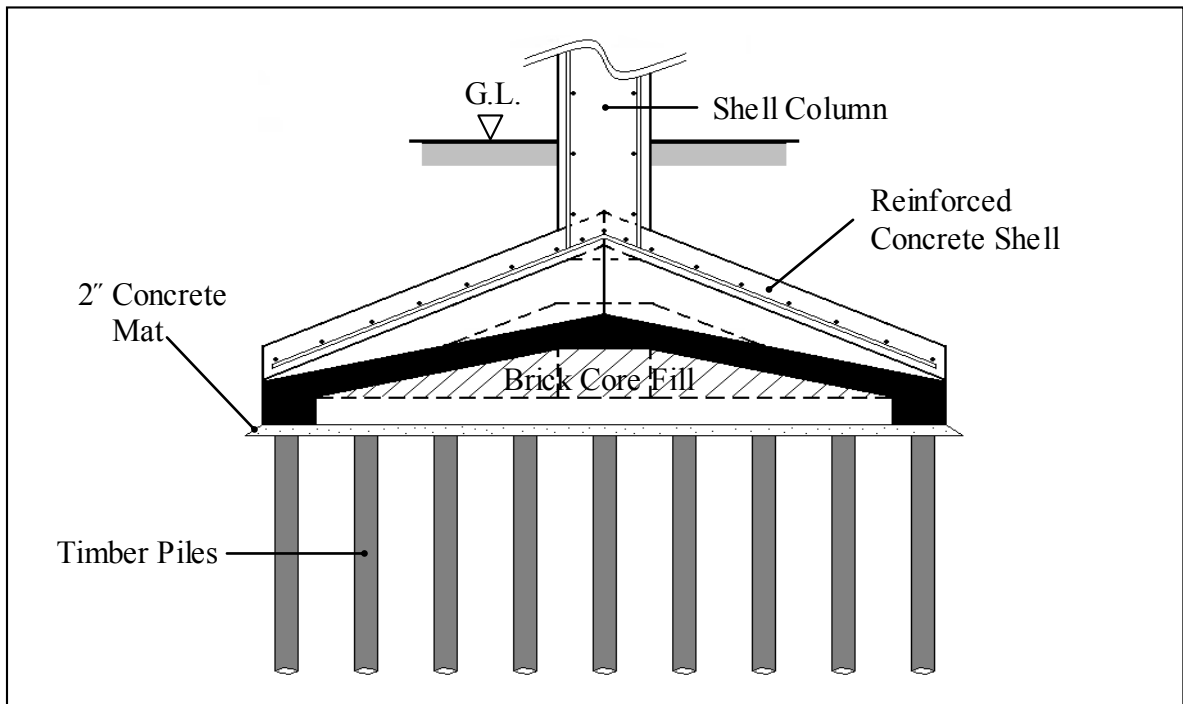


Figure 2.16. Composite Shell Footing: Caustic Soda Factory (Anonymous, 1965).

Present review of shell footing anatomy is by no means limited to customary shapes and geometries for existing shallow or special case types as described above. The scope of other shell forms may be further examined as research allows discovery of new ideologies for their use, whenever their inherent advantages may be effectively and fully exploited.

2.3 Shell Structural Strength

Shell strength performance takes into account bending and shear stresses, cracking and ultimate strength of the footing. A case study on experimental investigation of strength on a 'Hypar' type umbrella shell is described as conducted by Varghese (1971). The following figure shows typical shell failure patterns on micro-concrete shell models as tested on sand.

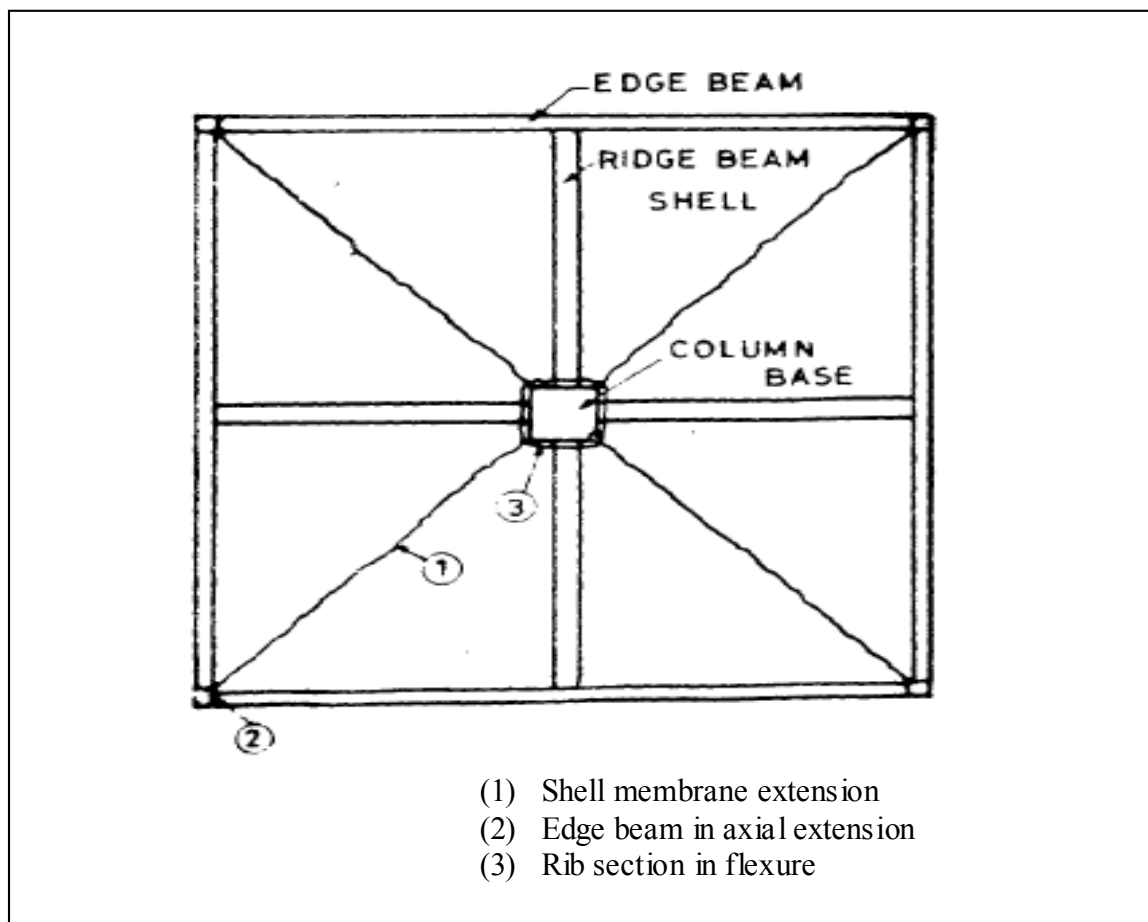


Figure 2.17. Hypar Shell General Diagonal Failure Mode (Varghese and Kurian, 1971).

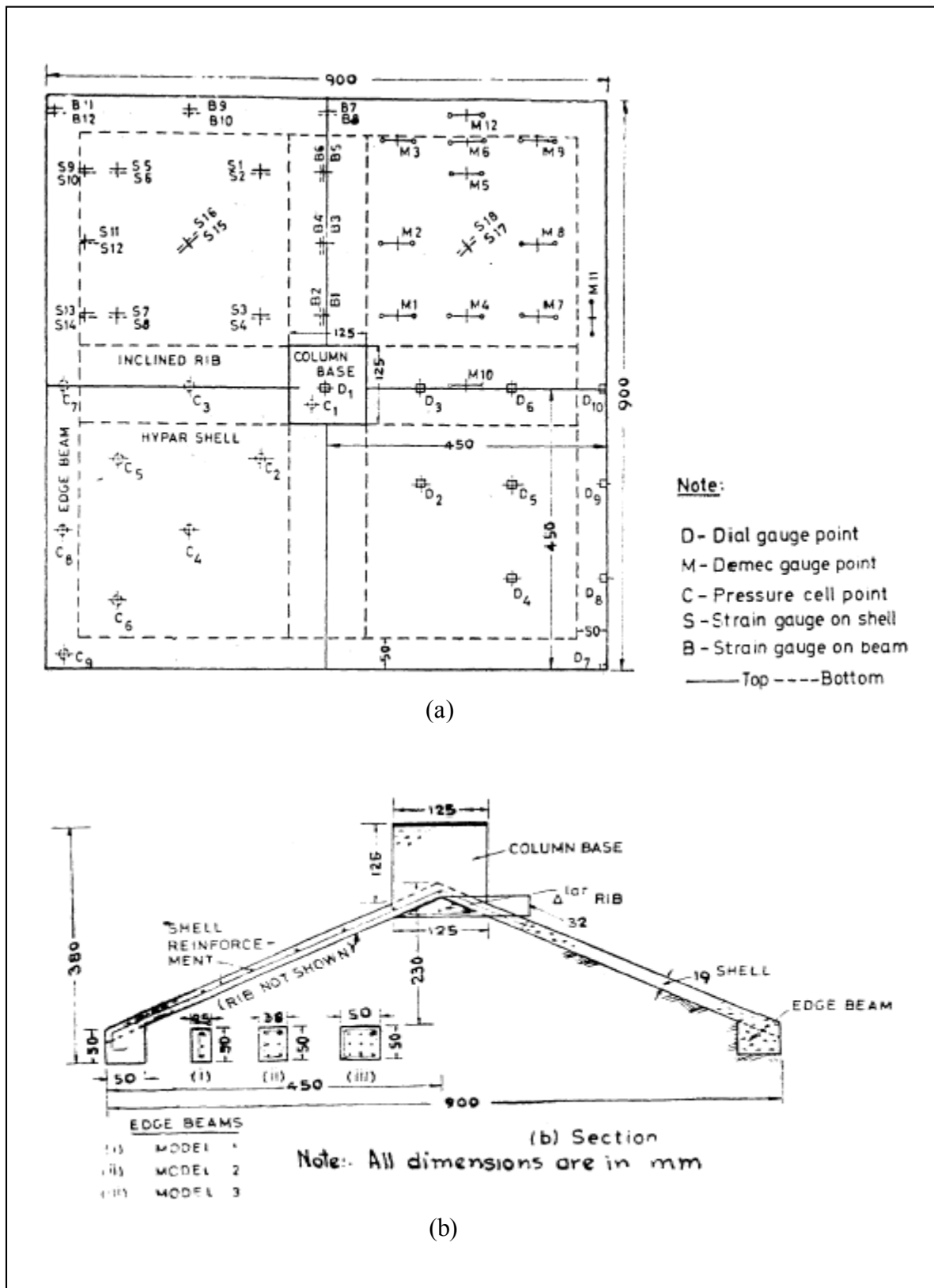


Figure 2.18. Hypar Shell Footing Model: (a) Plan view showing instrumentation (b) Cross-sectional view (Varghese and Kurian, 1971).

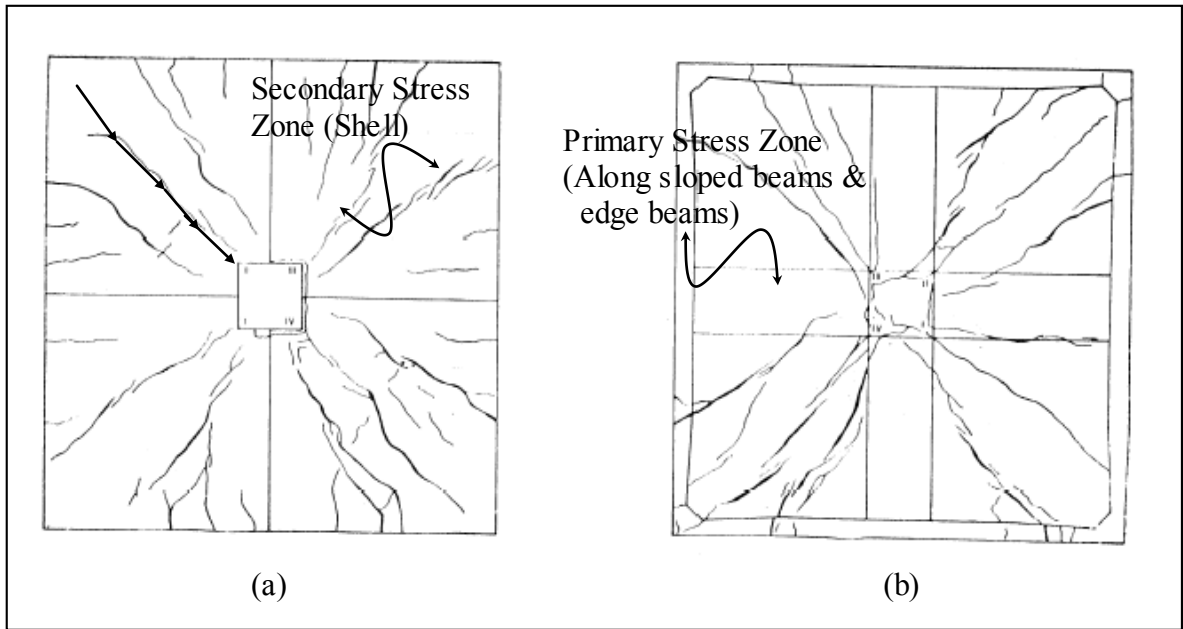


Figure 2.19. Crack Pattern of the Hypar Shell Footing Model (Varghese and Kurian, 1971).

The loads at which footings collapsed are summarized in the following table for the three models:

Model No.	Cracking Load (T)	Ultimate Strength (T)	
		Theoretically	Experimentally
1	7.70	10.25	14.00
2	7.15	14.50	15.45
3	8.80	18.70	18.80

Table 2.1. Cracking and Ultimate Loads of Precast ‘Hypar’ Footings.

In summary, the researchers concluded that the general structural behaviour was in broad agreement with the membrane theory and that there was considerable bending in both the shell elements and the beam elements. The bending was found to be causing tension in the bottom while membrane forces in the shell were in line with the axial forces in the beams. Moreover, the bending action was found to be ‘composite’ and was not directly attributed to the individual shells as given by theory. Visually, this can be represented in terms of shell footing failure which has been noted to fail from their peripheries inward with sloped beams taking primary stresses and shell proper conditioned as the secondary stress zone. Finally, the study suggests provision for added strength of the edge beams and corners and to prevent premature punching failure of the column.

2.3.1 Shell Model Studies

At present, little experimental research on the contact pressure distribution beneath shells has been investigated. Some attempts were made at measuring contact pressures in an experimental setting and found that the problem is essentially one of non-planar geometrical influence at the soil-structure interface coupled with the rigidity/flexibility of the shell itself (Kurian and Jeyachandran, 1972). These researchers' attempts were confined to the first aspect, which is the shape effect, and therefore investigated contact pressures under the extreme case of perfect rigidity. Rigid cast iron shell footing models of various geometrical shapes which would settle uniformly at all points on the shell under a concentric load. This would not only ensure perfect rigidity, but also retention of shape at all stages of loading. Cells developed by Kurian were used to measure the normal component of the contact pressures with sand as the bearing soil.

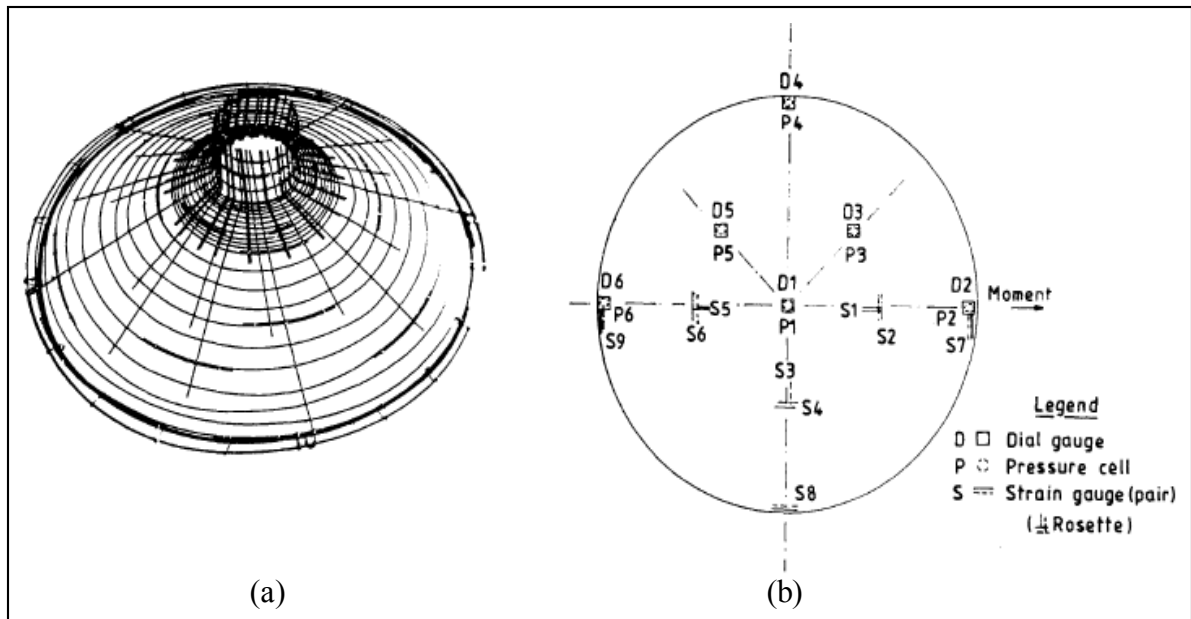


Figure 2.20. Conical Shell Model: (a) Reinforcement Cage (b) Instrumentation Placement (Kurian and Shah, 1984).

Experimental model testing was undertaken on conical and spherical shells. The authors used 20 models of the conical and 10 models of the spherical types using reinforced micro-concrete. The overall steel cage-reinforced shell configuration and instrumentation placement is shown in Figure 2.20 above followed by a summary of their findings on a variety of shell shapes.

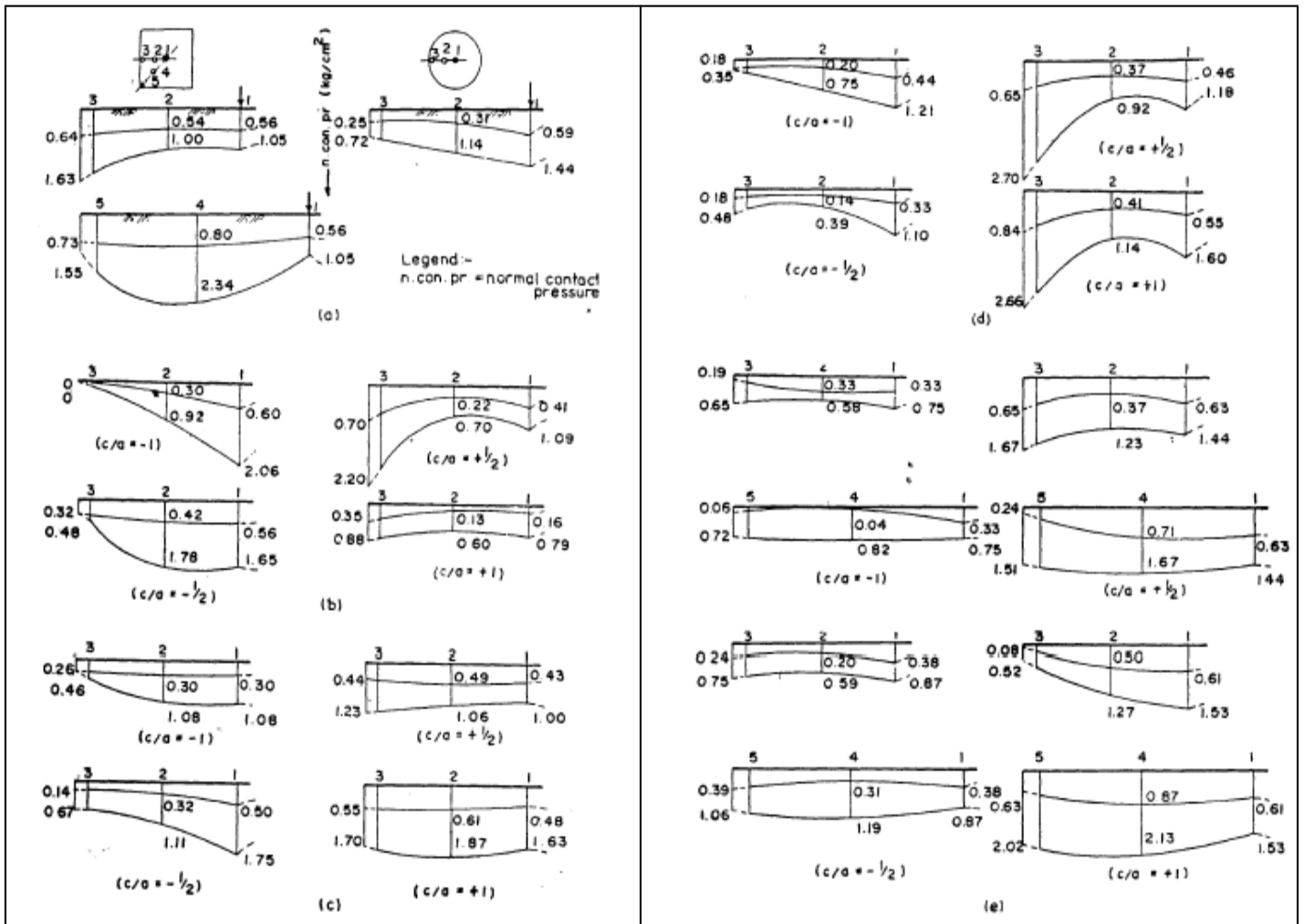


Figure 2.21. Normal Contact Pressure Distribution Diagrams (at $\frac{1}{3}$ and full bearing capacities):

(a) Flat model (b) Cylindrical (c) Folded plate (d) Cone (e) Hypar (Kurian, 1973).

Contact pressure measurements revealed a tendency for edge concentration in the elastic stages and shift towards the center in the inelastic stages. Failure of the cone was therefore from outer perimeter inward (Kurian and Shah, 1984). On the basis of their investigations on varied shell geometries, the shell performance as compared to flat footings showed a more uniform contact pressure distribution for the cone and Hypar cases as reported. Four typical models of each set are presented next using 3D distribution to help visualize the response of contact pressure and settlement along the shell-soil contact surface as presented in Figures 2.22 – 2.25.

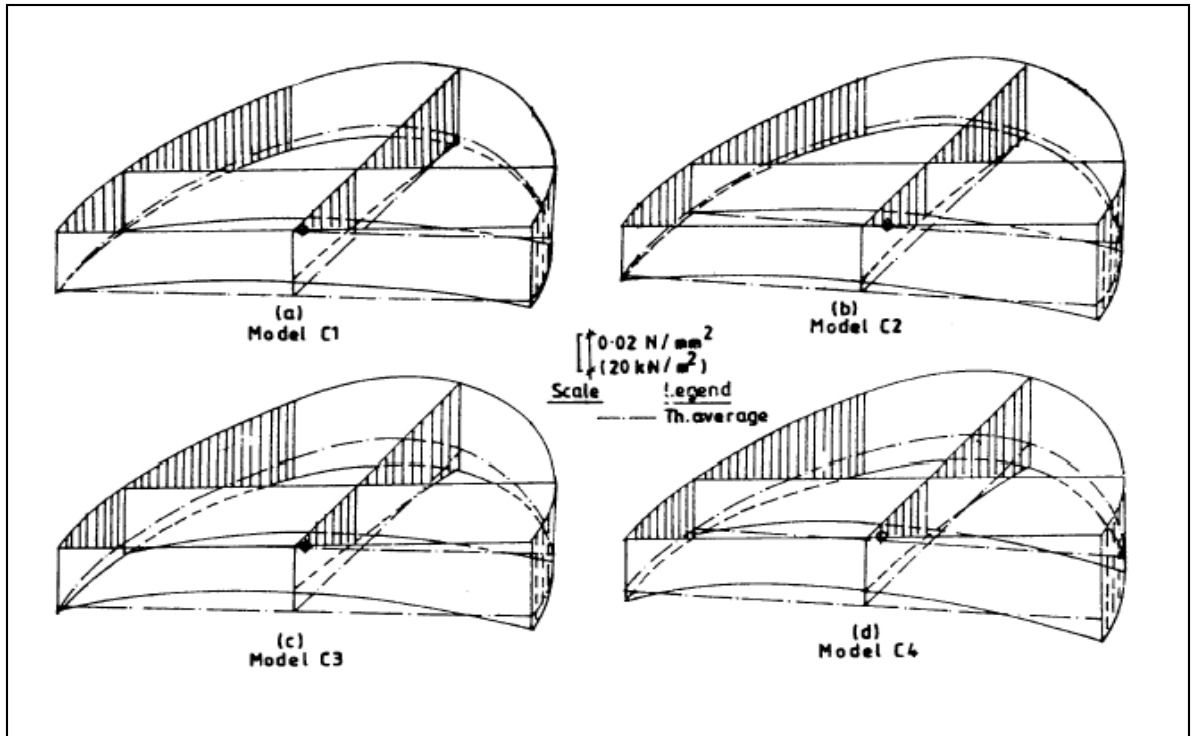


Figure 2.22. Contact Pressure Diagrams: (a) – (d) Conical Models at Working Loads (Kurian and Shah, 1984).

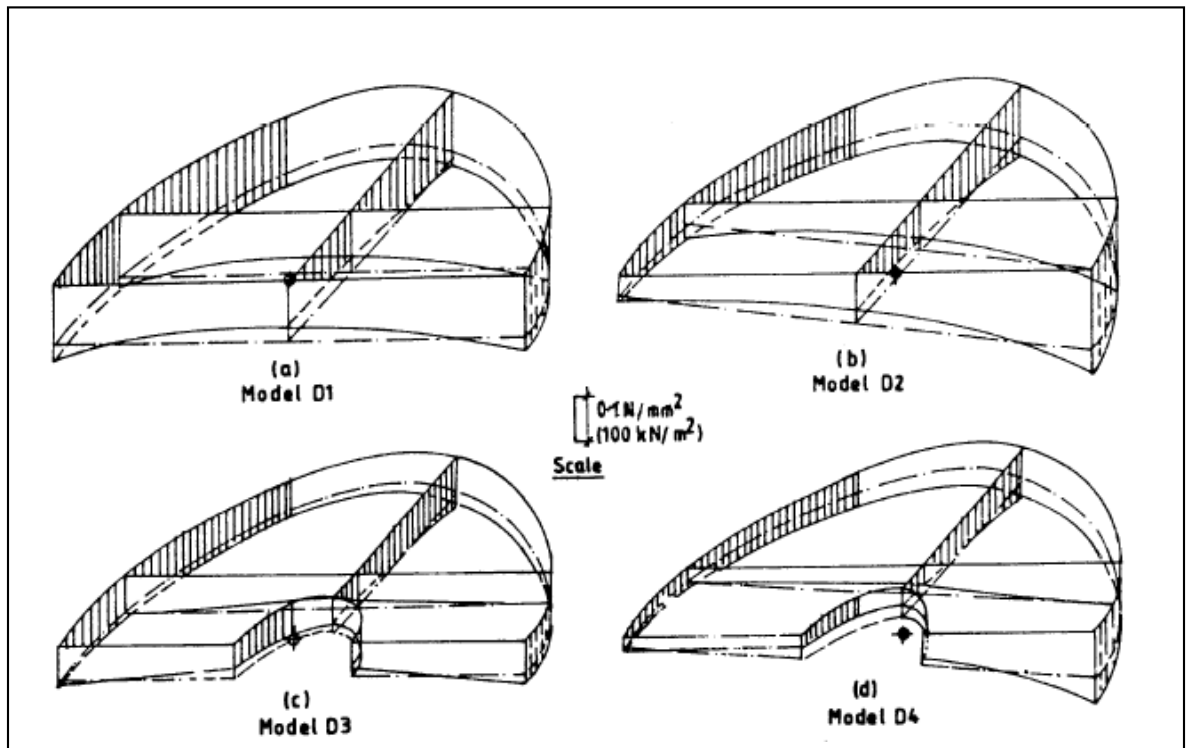


Figure 2.23. Contact Pressure Diagrams: (a) – (d) Spherical Models at Working Loads (Kurian and Shah, 1984).

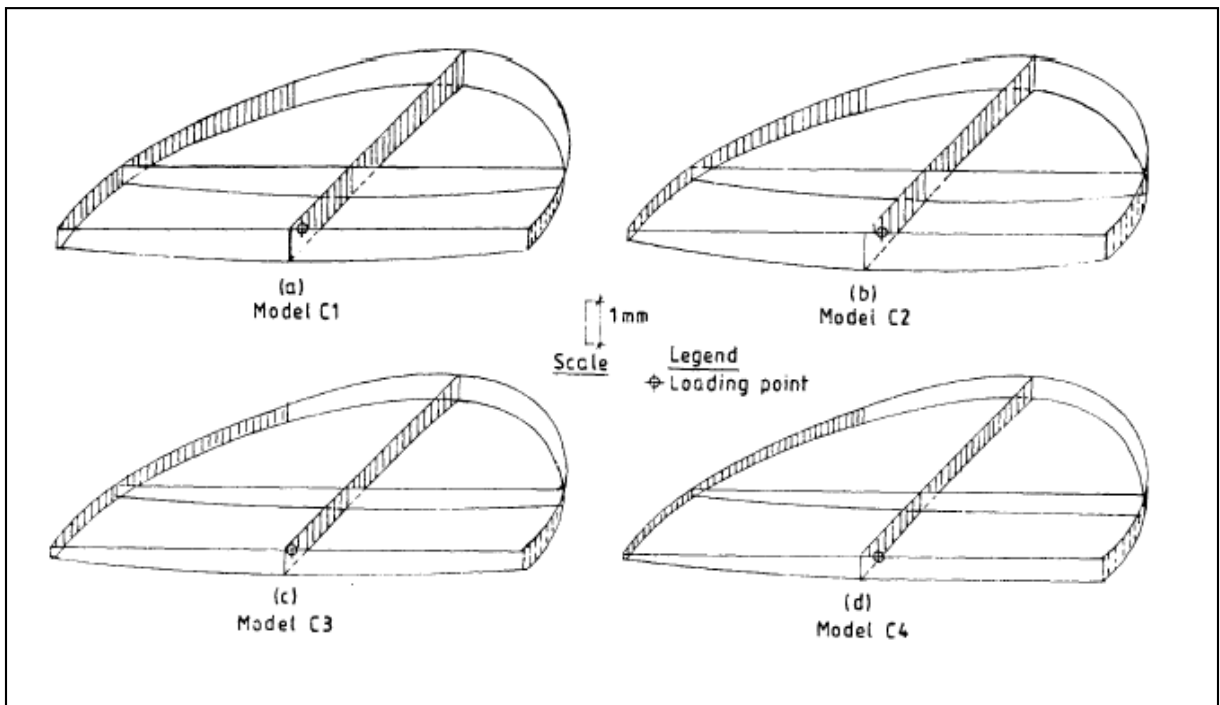


Figure 2.24. Settlement Diagrams: (a) – (d) Spherical models at Working Loads (Kurian and Shah, 1984).

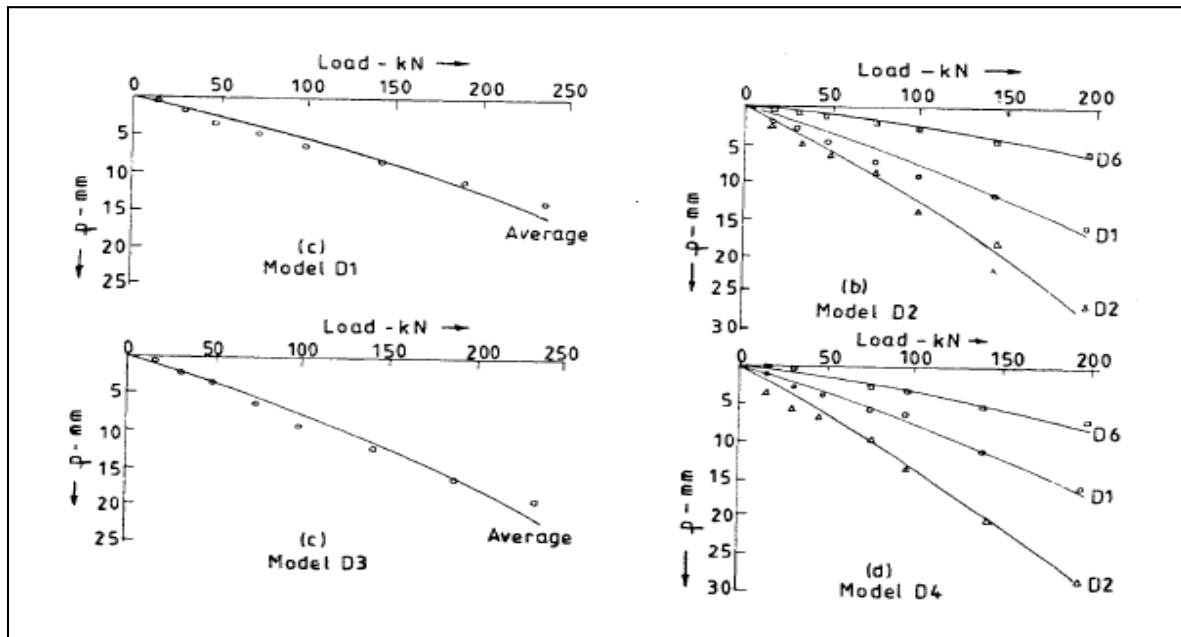


Figure 2.25. Load vs. Settlement Diagrams: (a) – (d) Spherical Models (Kurian and Shah, 1984).

Another experimental investigation was conducted using 15 wire-reinforced micro-concrete models in hyper shapes for isolated, combined and raft formations. Miniature Glözl cells were used operating on air pressure. The findings concluded a substantial

deviation from linear contact pressures initially suggested and that assumed by membrane theory design. The contact pressures show a definite tendency for edge concentration in the elastic stages. A progressive shift towards central shell region was observed in the inelastic stages. The results of contact pressure in this study on hyperbolic paraboloidal shells indicate a more realistic distribution of pressure than what was earlier thought which would lead to better shell foundation design (Kurian and Mohan, 1981). The research conducted remains confined to the Hypar shell shape type.

A similar experimental investigation was made using prefabricated stainless steel Atlas alloys without using bolts nor welds and sandpaper glued to the base of the models to provide representative surface roughness condition. Pressure transducers were used measure contact pressures. In this study, nine shell models were investigated for loose, medium and dense sand states for embedded and surface footing conditions. The results obtained indicate trends of higher contact pressures at 1/3 and 2/3 the width of the base of the footings with a noticeable drop at the edges for simple conical and pyramidal shell footings (Abdel-Rahman, 1996).

2.3.2 Research Needs

The art of designing adequate foundation structures requires a proper understanding of the interface action and reaction between the two load-transferring elements, namely the concrete shell and the underlying soil. Notably in foundation engineering, the primary function of any substructure design is to accommodate the loads transferred to them from the superstructure and distribute these loads to the bearing soil such that the stresses induced neither exceed the allowable bearing stresses nor cause excessive settlement potentially causing either overall or worse yet, differential settlement. Thus the foundation structure is conventionally designed with respect to the contact interface between the concrete material of the foundation and the bearing soil it comes into contact with. The dimensioning and the proper calculation of the strength of shell footings cannot be accurately designed without better knowledge of the following four factors:

1. Magnitude of the load (shear and bending stresses)
2. Direction/position & load type (point, line, horizontal, vertical, eccentric, etc.)
3. Deformation of underlying soil
4. The soil reaction pressure induced by the load

In this research, the reaction pressure which is typically the most difficult to determine, will be referred to as the contact pressure which consist of the normal stress, eccentricity of the normal stress and shear stress. A very limited number of studies found in literature have been devoted efforts to the development of contact pressure distribution beneath shell footings. Select studies have looked at simple soil models, such as the linear Winkler and Pasternak models to simulate soil behaviour at the soil–shell interface. A non–uniform contact pressure distribution has been indicative of the results obtained and often an average value protected by a factor of safety is extracted for design considerations. The structural design of shells is still primarily based on membrane theory with the contact pressures assumed to be uniform (Pandian and Ranganatham 1970; Varghese and Kurian 1971; Bhattachary and Ramaswamy 1977; Jain *et al.* 1977; Das and Kedia 1977; Fareed and Dawoud 1979; Dierks and Kurian 1981; He Chongzhang 1984; Huang–Yih 1984; Nath and Jain 1985; Paliwal *et al.* 1986; Paliwal and Sinha 1986; Paliwal and Rai 1987; Melerski 1988 and Dierks and Kurian 1988).

At any point of contact between a structural foundation and a natural foundation or bearing soil, contact pressures exist which are the reactive pressures exerted by the soil on the foundation. In any shell foundation structure, both the contact pressures offered by the soil and the structural loads must be incorporated to have a safe design. Soil elasticity depends on soil properties including strength parameters (c) and (ϕ), which dictate the actual contact pressure distribution. Moreover, the structural and flexural rigidities of the footings themselves contribute to the distribution of contact pressure and as such are a function of the shell structure–to–soil interaction.

Traditionally, shell foundation designs have been based on a conservative approach using membrane theory in which uniform soil pressures are assumed depending on the position of the resultant vertical load or eccentricity with respect to the centroid of the planar area of the contact surface between the structural foundation and the soil. The simplification of assuming that the contact pressures may be purely normal or vertical to the foundation at all points of contact along the surface is the basis for obtaining a statically determinate rigid design. In other words, shell foundations are designed for linear soil reaction distributions or linearly varying distributions that are ideally uniform or rectangular taken as an 'average uniform value' under a concentric load, and of trapezoidal form under eccentric load.

Inherently in shell foundations, the contact pressure distribution can take varying forms due to the complexities in shell geometries and varying interaction of soil elements and therefore is accordingly non-linear. Consequently, a contact pressure distribution beneath a shell foundation can be determined only by an interactive analysis being highly complex and statically indeterminate. Using complex theoretical formulation, the distribution and nature of contact pressures beneath shell foundations is an exhaustive and intricate subject which has rarely been addressed with representative accuracy.

2.4 Problem Statement

We know that the performance of flat footings is poor as it does not make efficient use of the entire continuum of soil. This is evident in the positive parabolic soil response of such a foundation resting on granular soil. Stress concentration is funneled in the active region of the triangular wedge formed directly beneath the flat foundation. This shortfall of an industry-accepted footing constitutes the main inefficiency as the outstanding problem. Our awareness that shells perform exceedingly well in varied forms as superstructures motivates one to bring this concept to use as a substructure: as a shell foundation footing. The following problem definition is prompted. That is, to investigate the possibility of effectively replacing traditional flat footings with a shell configuration for the purpose of optimizing the full bearing soil continuum by producing a more uniform contact pressure. This must be achieved by safely transferring superstructural loads to the ground while respecting conditions for soil bearing capacity and mitigating settlement.

A variety of shell shapes exist and have been studied in the past. Izadi and Nicholls (1968) have studied cone and hyper footings. Kurian (1977) has studied hyper shell footings. Conical and spherical shells have been investigated by Sharma (1973). The designs of these shell foundations are all based on the working assumption that the soil reaction beneath them is uniform, as previously indicated. It has progressively been realized that the soil pressure distribution will truly be non-uniform. Based on the absence of reliable measurements an ideal analysis on the topic is still lagging behind. An appreciable study in the area of contact pressure distribution below shell foundations requires further investigation. Additionally, new shell shapes using reinforced-concrete models should be studied to obtain a more uniform contact distribution.

2.4.1 Scope of the Thesis

The scope of this thesis has as its primary focus to research contact pressure distributions beneath new shell shapes and conceivably optimize existing ones. A comprehensive investigation will be undertaken to help improve the soil–structure behavioural response. Accordingly, the main objective is to increase shell load–carrying capacity by varying shell dimensions in hopes of extending the knowledge base from a geotechnical perspective, for optimum design of shell footing structures as a broader goal.

At present still, there is no extensive research conducted on experimenting with varying geometries in establishing an optimum contact pressure distribution beneath the structures using practical and constructible shell shapes. Recommendations prescribed in literature for design have no bearing or contribution to any code requirements since shell design codes are practically non–existent. Reference has been made in literature to Building Code Requirements for Reinforced Concrete (ACI 318), which gives some general guidelines, but nothing specific. Perhaps the only available code is that available at the Bureau of Indian Standards pertaining to the design and construction of conical and hyperbolic paraboloid types of shell foundations (Code IS 9456: 1980) reaffirmed back in 2003. Moreover, all designs are based on assumptions that soil contact pressure reaction is uniform as suggested by researchers. Pandian, N. S. (1968) for example, found theoretically that contact pressure distribution has a profound influence on the type and magnitude of shell stresses which govern their design.

Experimental studies, as found by Iyer *et al.* (1970) indicate the absence of the contribution of contact pressure in their investigations due to the lack of instrumentation and study. In accordance with this need, this experimental investigation is undertaken to study the effect and the importance of contact pressure distribution on shell capacity and for their economical design. The variables considered include: shell inversion (upright or inverted), shell angle and size, shell shape factor of several shapes for the shell models and angle of shearing resistance for the sand soil, all to be compared with the limited published data as well as laboratory testing and validation using PLAXIS geotechnical software.

2.4.2 Study Objectives and Motivation

Having conducted an exhaustive literature review and in lieu of the premise for improved soil–structure performance stemming from a comprehensive investigation into inverted shell foundation footings, the objectives of the present research are:

- a) To study the geotechnical behaviour of shells performance in terms of bearing capacity and settlement and determine existing boundary of knowledge on the topic
- b) To develop foundation model configurations which will produce a more uniform contact pressure distribution and conceivably optimize structural shell design (ie. achieve higher bearing capacities and produce less settlement than existing foundation designs)
- c) To study and evaluate the performance of flat, upright and inverted shell orientation including a new Sinusoidal model with varying sand conditions including loose, medium and dense soil states to determine optimum shape
- d) To examine soil's behavioural response numerically considering varied shell model configurations acting on an elastic perfectly–plastic soil using Mohr–Coulomb's failure criterion utilizing finite element method to compare with experimental data
- e) To conduct experimental investigations on prototype shell footings in an especially designed test facility setup to evaluate the soil contact pressure distribution on new shell footing models of varying thickness
- f) To develop a theory for inverted shell footing foundation performance based on the soil's behavioural response by predicting the general rupture surface utilizing bearing capacity coefficients for this case
- g) To promote shell footings as an economic alternative to conventional foundations

CHAPTER 3

NUMERICAL iSHELL MODELING

3.1 Introduction

Numerical shell modeling exploits mainstream use of modern day computing power over traditional methods. When costly and complex field tests and/or tedious mathematical modeling are no longer feasible due to burdensome nature and anisotropic conditions of soil, the present-day approach of choice is the numerical modeling technique. Time constraints in execution of physical tests and the fact that costly models may yield ambiguous results of questionable value as stand-alone quantities to the problem at hand, they are used more-so as validation tools to what powerful program algorithms may propose as solutions assuming validity of the input data.

3.2 Shell Model Rendering

To evaluate shell-soil interaction models numerically, well-defined shell forms for study must be used. Here, twenty-four proposed shell models and two plain shapes are presented as prototypes using AutoCAD graphics software. They include the plain, triangular, cylindrical and combined shell models in upright and inverted orientations, as contemplated, modeled and rendered. Renditions aid in visualization of the overall physical shape as illustrated in Figures 3.1 – 3.4. In the present study, of the group presented and after perusal of intricacy associated with the physical forming, construction and time constraints, the eight models retained were (a), (c) – (i) with one Sinusoidal model added. A total of nine models were tested with geometrical properties presented.

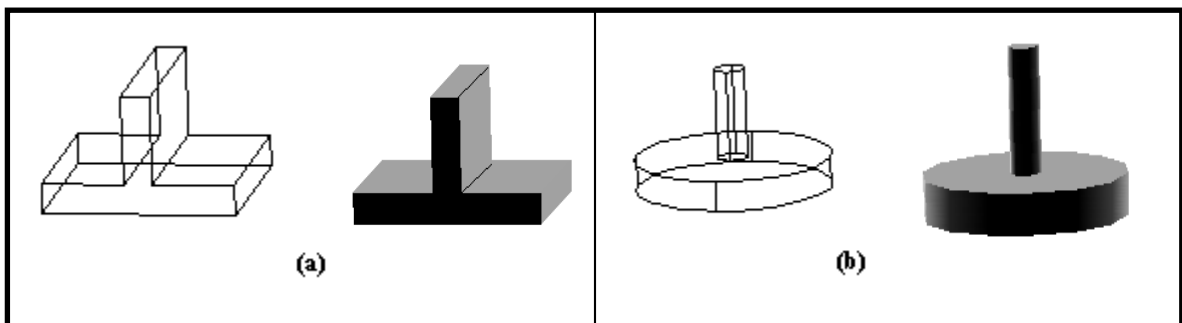


Figure 3.1. Plain Flat Footing Model Rendering: (a) Square (b) Circular.

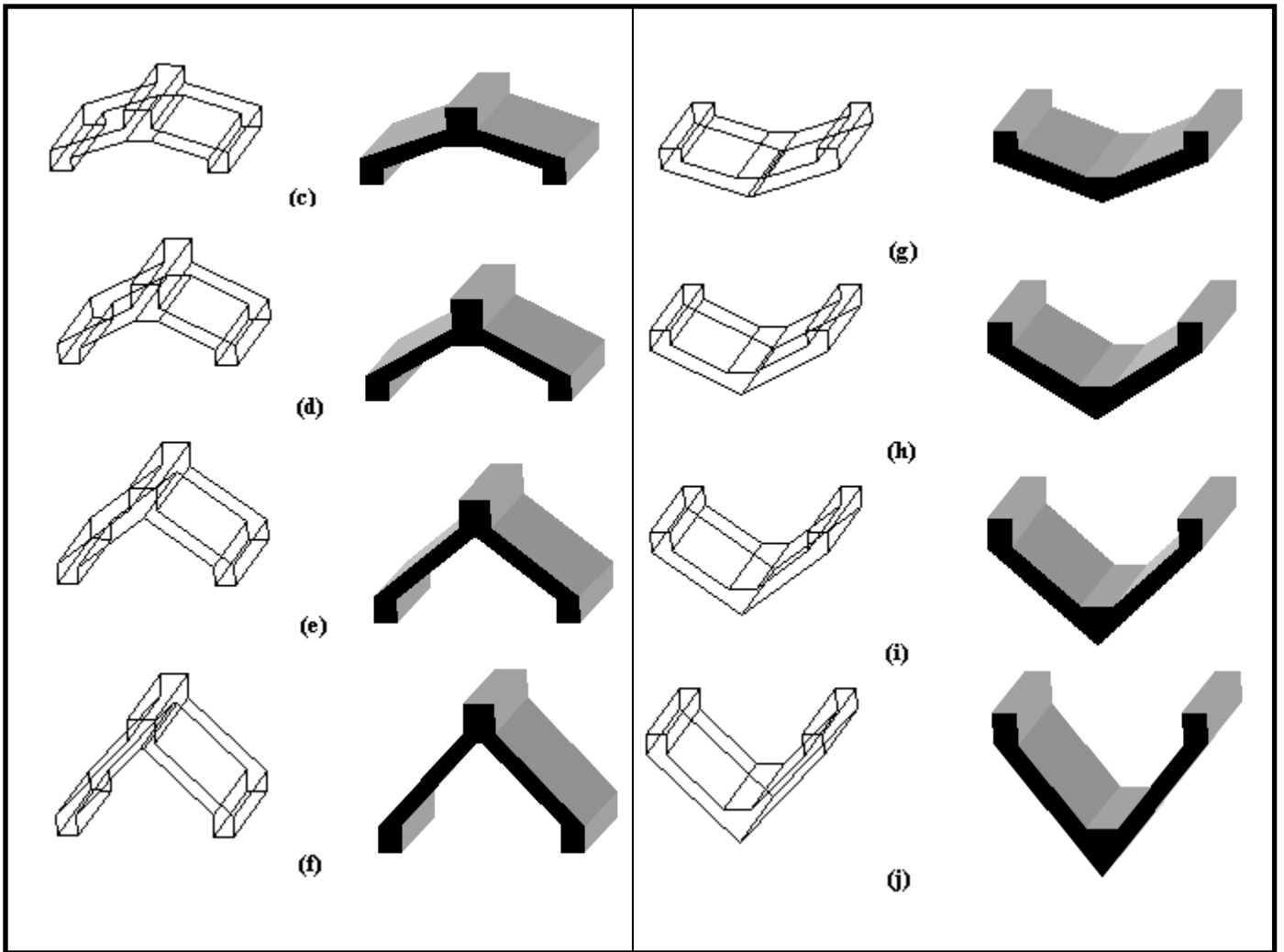


Figure 3.2. Triangular Shell Model Rendering: (c) – (f) Upright. (g) – (j) Inverted.*

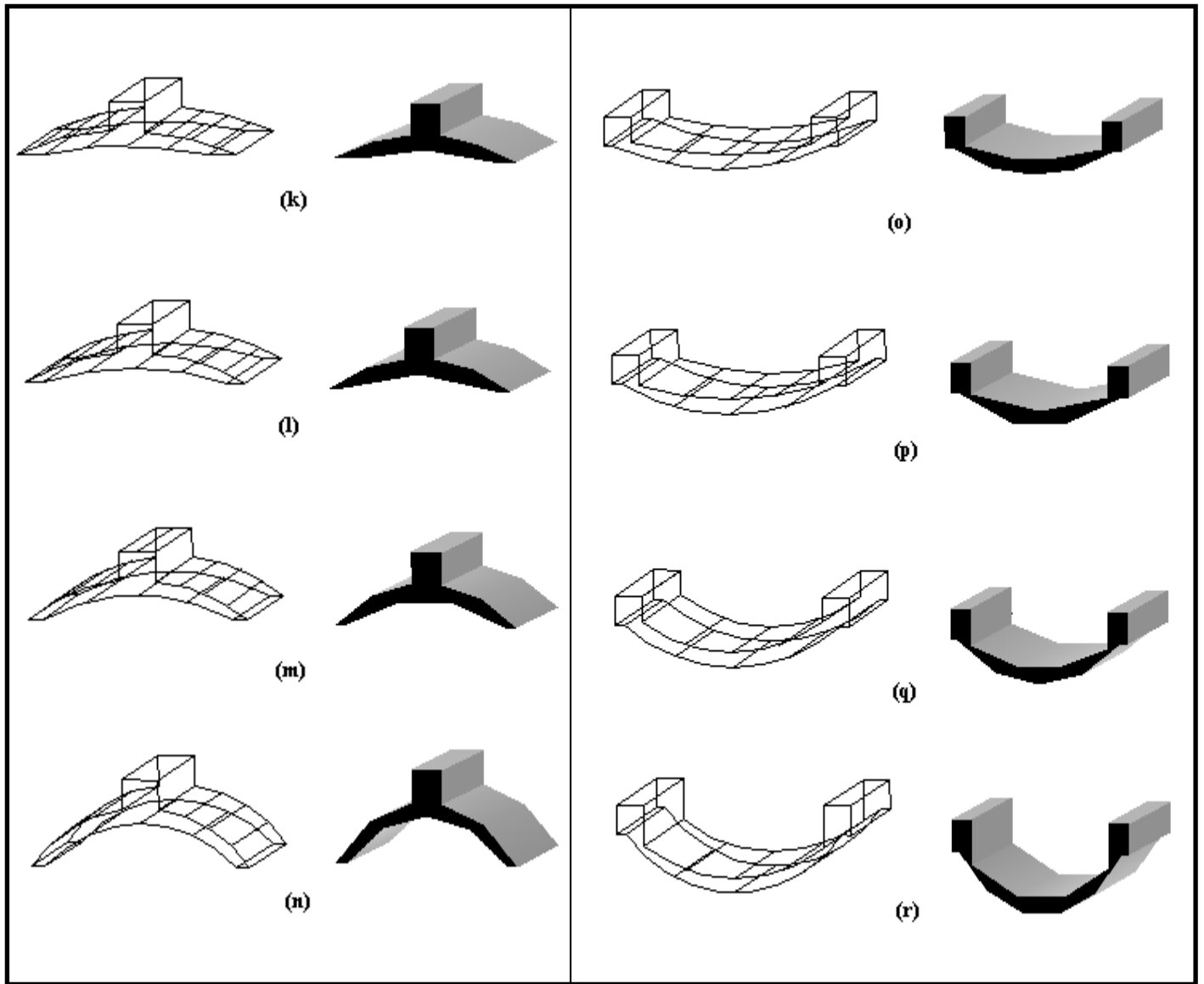


Figure 3.3. Cylindrical Shell Model Rendering: (k) – (n) Upright. (o) – (r) Inverted.*

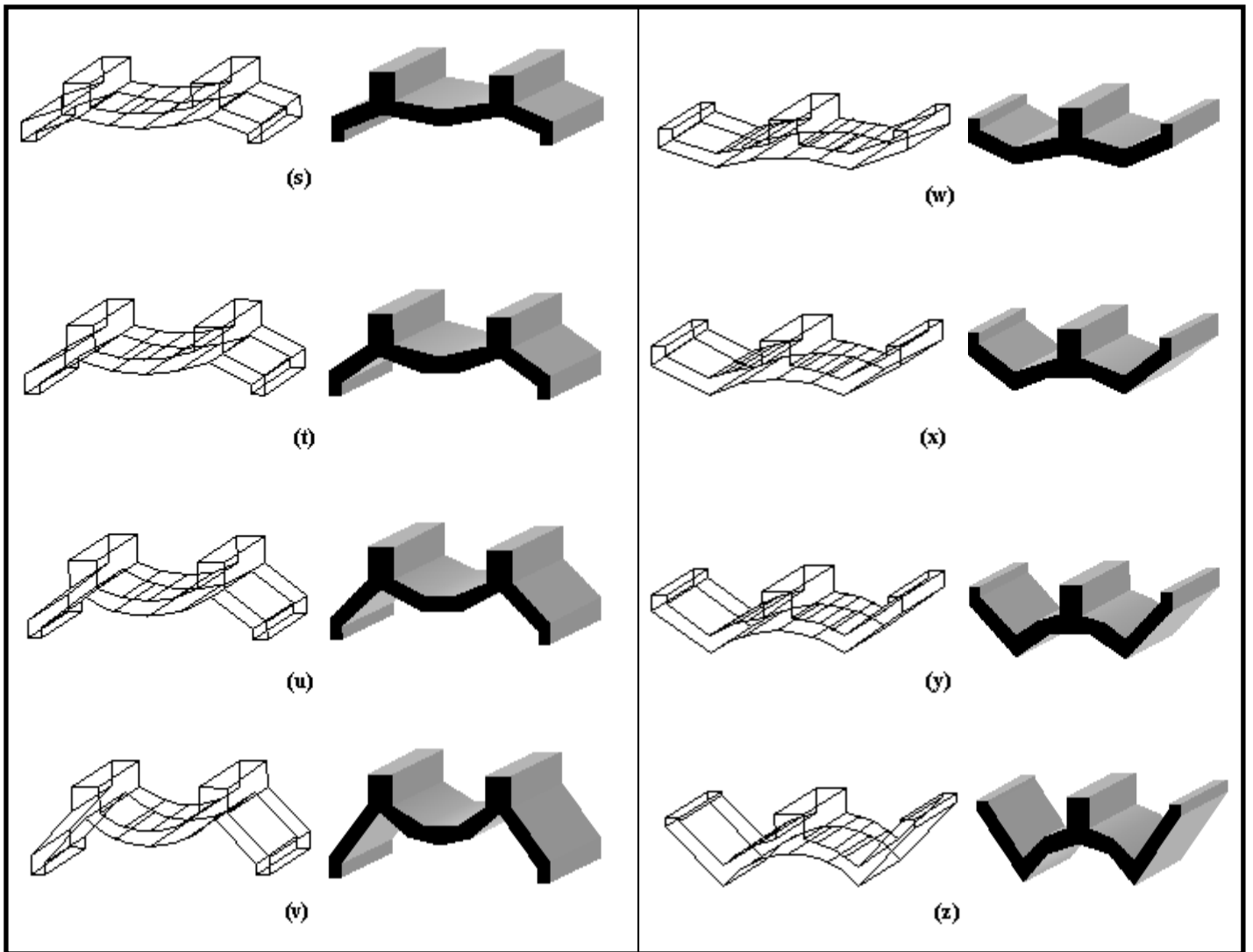


Figure 3.4. Combined Shell Model Rendering: (s) – (v) Upright. (w) – (z) Inverted.

The cylindrical shells (k) – (r) and the combined shells (s) – (z) were not retained however are presented as shapes conceived and options contemplated at the outset for study.

3.3 Soil–Shell Structure Modeling

Since over the years there has never been one standard numerical modeling strategy for implementation of non–linear models, one must rely on perhaps the simplest modeling approach for sake of simplicity. An acceptable and well established model in efforts to unify research findings particularly for the complex nature of the soil–structure behaviour inherent with shell footings is desired and contemplated as a relevant modeling platform.

Several soil models were used by researchers including Cam–Clay and modified Cam–Clay (MCC). The most widely used was found to be the elastic–perfectly plastic model following Mohr–Coulomb yield criterion and is the one retained in the present study. Other widely used yield criterion include the Drucker–Prager, Tresca and the Von Mises models which are often applied in brittle applications such as metallic models. It is acknowledged that the Mohr–Coulomb allows for proper representation of soil parameters: cohesion (c), soil friction angle (ϕ), dilatancy (ψ), Young’s modulus (E), and Poisson’s ratio (ν) and thus its use is warranted.

In numerical modeling using PLAXIS software, the Mohr–Coulomb yield condition is an extension of Coulomb’s friction law to general states of stress. This condition ensures that Coulomb’s friction law is obeyed in any plane within a material element. The yield condition generally consists of six yield functions when formulated in terms of principal stresses, σ_1' , σ_2' and σ_3' . The two plastic model parameters as defined by the yield function are c and ϕ . The defined yield surface in principal stress space for no cohesion which is typical in the present investigation is represented by a hexagonal cone as illustrated in the following figure. The third plasticity parameter is the dilatancy angle (ψ). This parameter allows for modeling of positive plastic volumetric strain increments or dilation as actually observed in soil, particularly for dense sand.

PLAXIS also offers advanced options for input of clay, layered soil conditions and effects of water table. Other soil models are also available such as the Hardening Soil and Soft Soil models. Finally there is an option for a user–defined model. It is worth

mentioning that none of these options mentioned were explored further to maintain focus of the present investigation on shell geometry using the Mohr–Coulomb yield criterion.

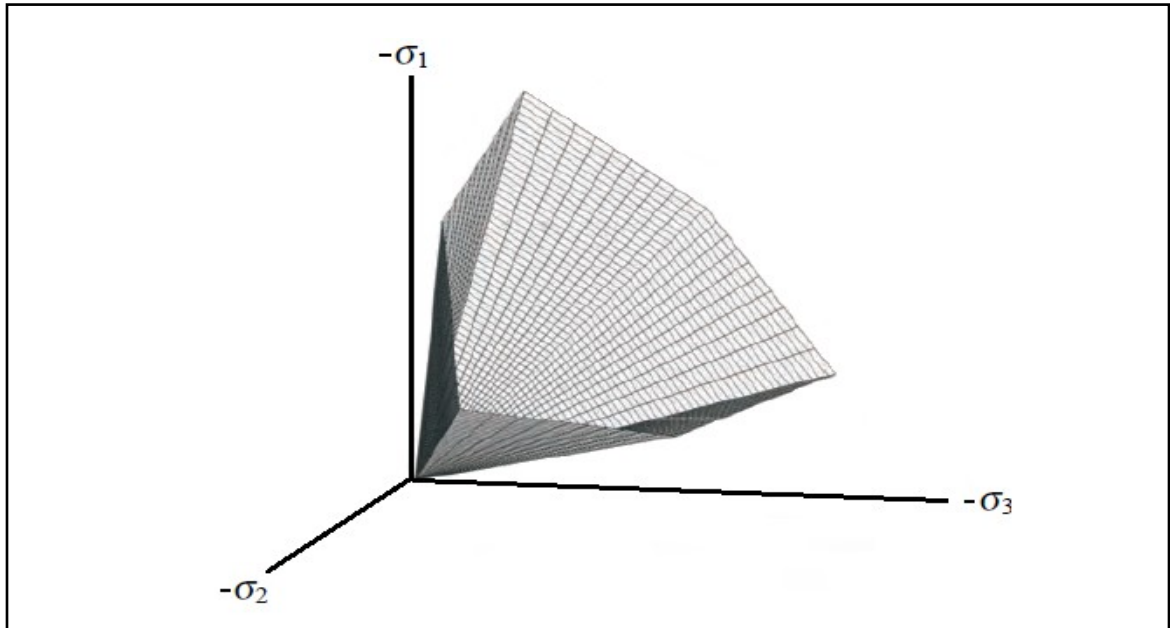
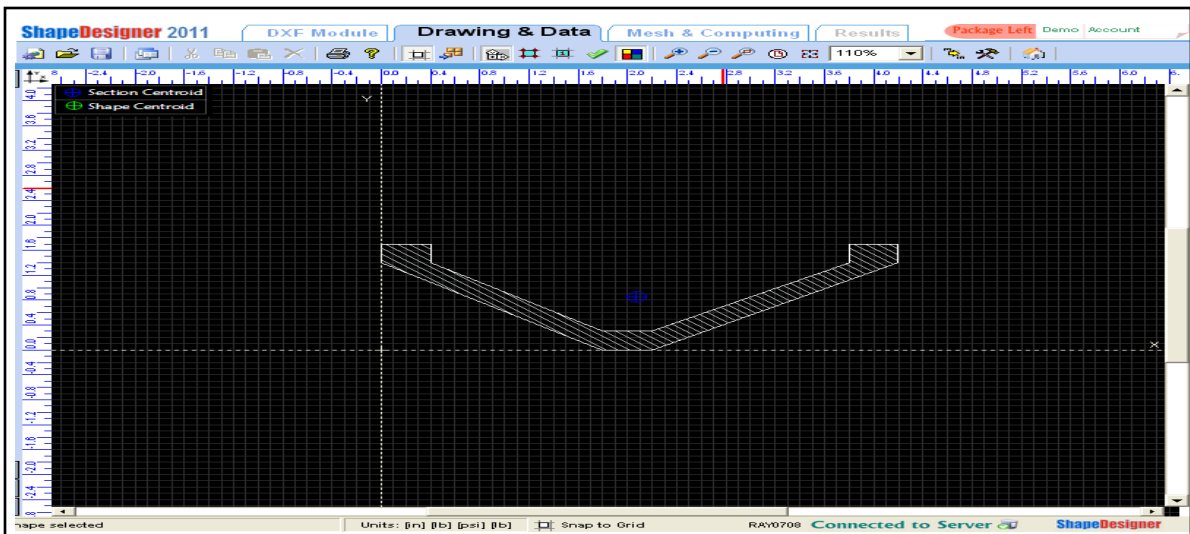


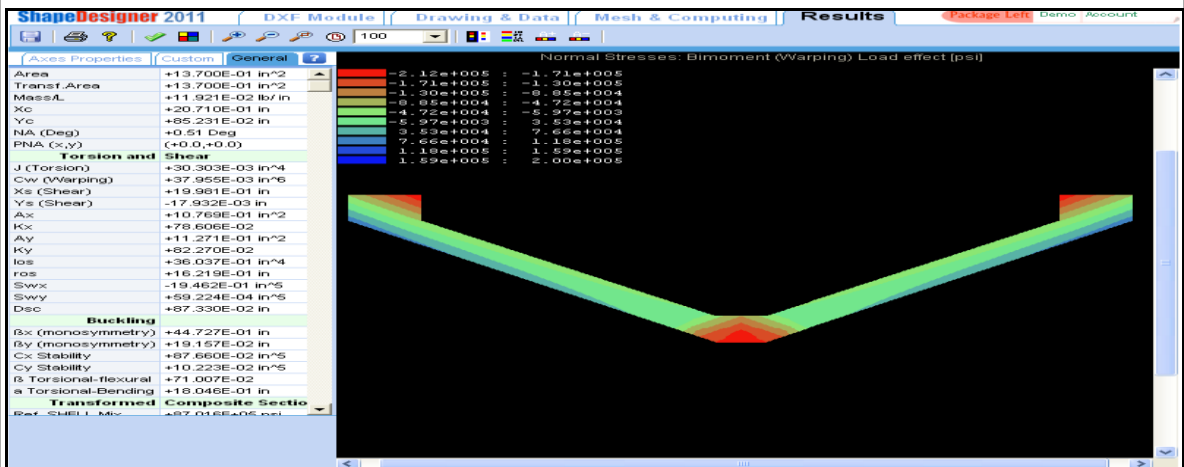
Figure 3.5. Mohr–Coulomb Yield Surface in Principal Stress Space ($c = 0$).

The soil phase, as discussed above is the first of two materials sets under investigation. The second, and equally as important, is the structural shell proper. The structural phase was represented using a linear elastic model using properties of a high–performance concrete designed in the experimental phase. The experimental investigation of this study describes in detail the physical characteristics and elastic properties of similitude input into PLAXIS for modeling the concrete used.

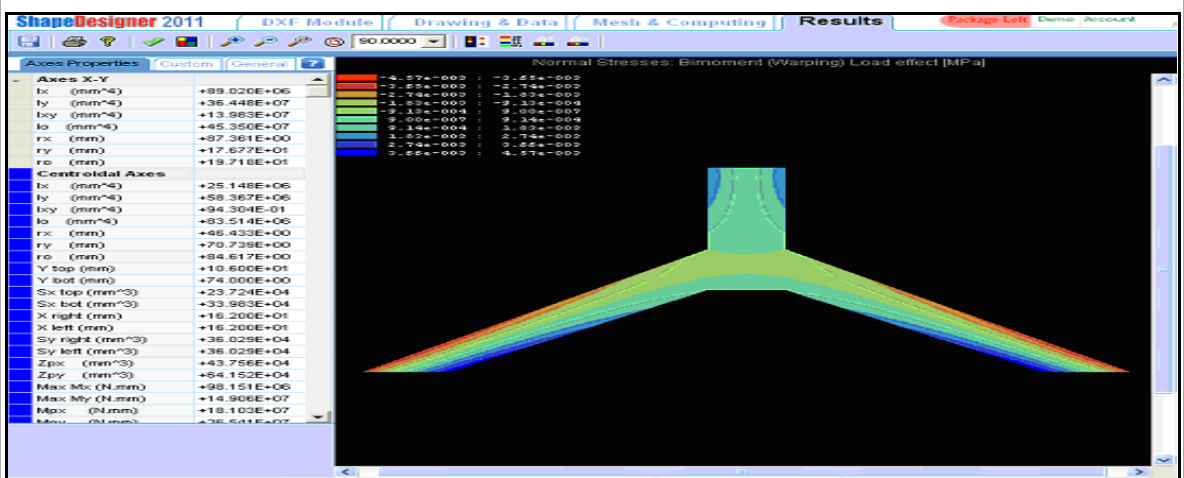
As a starting point other software was explored to help model intrinsic shapes such as that inherent with shell footings. AutoCAD and Shape Designer are two examples. The advantage and reasoning of this exercise is to explore and obtain favorable physical characteristics associated with the shell geometry including their structural attributes for construction. Historical shapes and constructability issues help converge on plausible shapes envisioned for study. The following figures illustrate typical use of computer models for the anticipated form of the new shell footings. Exploration with use of



(a)



(b)



(c)

Figure 3.6. Upright Shell Modeling Using Shape Designer (SAAS) 2011: (a) Inverted Shell (b) Inverted Shell (c) Upright Shell.

3.4 Finite Element Modeling Using PLAXIS

The shell footing models and sand bed medium would be modeled and analyzed using commercially available finite element software PLAXIS. Plaxis is a special purpose two-dimensional finite element computer program used to perform deformation and stability analyses for various types of geotechnical applications. In the evaluation of the contact pressure distribution beneath shell foundations, the stresses and strains within the bearing soil mass must be obtained and rationalized. In order to achieve this goal, a soil of homogenous and isotropic consistency is considered. The theory of elasticity is used as the basis for the analysis. For the case of column loadings above the shells, a 3D problem is encountered and the tri-axial coordinate system (x, y, z) must be used. In the case of strip conical or triangular strip folded-plate shells where a line loading is idealized from that of a wall superstructure, a 2D stress problem may be solved. Real situations are modeled either by a plane strain or axisymmetric model. A 3D version of Plaxis would be used for three-dimensional modeling.

PLAXIS uses an incremental tangent stiffness approach in the analysis, in which the load is divided into a number of smaller increments, which are applied simultaneously. During each load increment, the stiffness properties appropriate for the current stress level are employed in the numerical analysis. The analytical work conducted by (Kurian, 2001) may be used to validate the finite element modeling of the present investigation in terms of load-settlement for axial loading conditions.

Since analytical investigations of the distribution of contact pressures have been mildly attempted, at best, there is very little basis for comparison. This lack of research is presumed to be based on the degree of complexity in developing closed-form solutions. Since new powerful computer programs are available, attempts at developing solutions have been greatly facilitated.

Geometrically, the mesh for plane-strain condition is symmetrical about the centerline, therefore only half the cross-sectional area is considered. The standard fixities, as required by the program along the two sides and bottom have been pin-modeled to allow

rotation but no free translation in the horizontal and vertical directions. Figure 3.7 shows a folded-plate shell model embedded in the surrounding soil mesh generated by the LUCAS software. As an example output, the same figure illustrates the generated and deformed shapes of the mesh with pin fixities along the perimeter for an upright folded-plate shell.

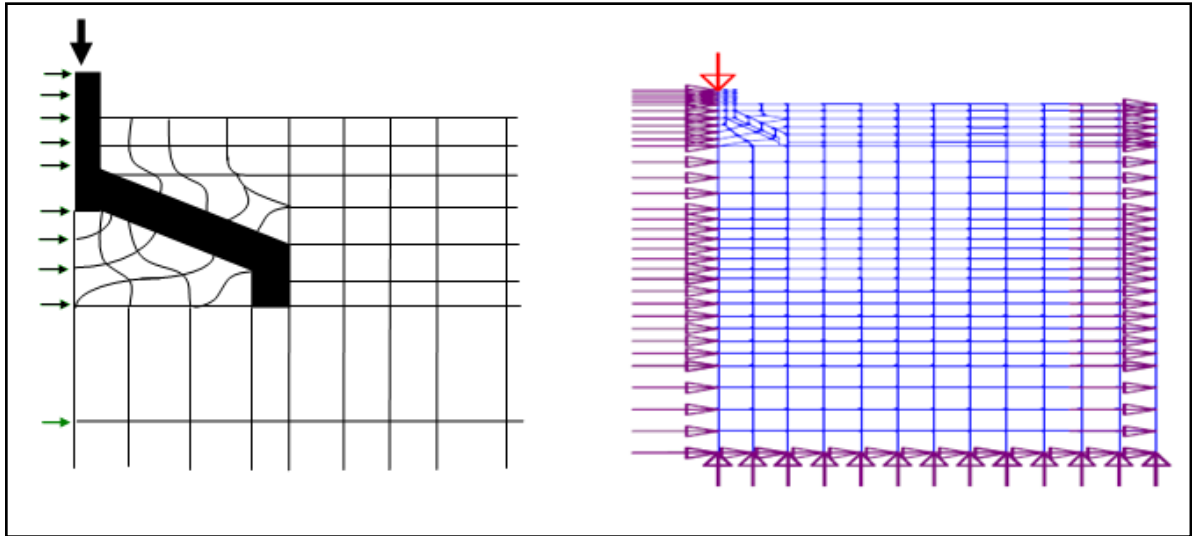


Figure 3.7. FEM Mesh Generation for Embedded Shell.

3.4.1 Shell Material Properties

Shell material properties are crucial and are influenced when scaling of the models is invoked dependant on the test setup and testing conditions. Some typical cross-sectional properties of the finite element shell footing models are presented in the following table.

Shell Properties	Flat	Triangular(upright)	Triangular(inverted)
Cross-Sectional Area (mm^2)	8,375	10,167	6,778
Moment of Inertia, I (mm^4)	8.224E6	13.847E6	1.521E6
Modulus of Elasticity, E_{shell} (GPa)	60	60	60
Poisson ratio, ν	0.3	0.3	0.3
Material Type	Elastic	Elastic	Elastic
Flexural Rigidity, EI ($\text{N}\cdot\text{mm}^2$)	493.40E9	830.85E9	91.26E9
Axial Stiffness, EA/L (N/mm)	2.09×10^6	2.54×10^6	1.80×10^6

Table 3.1. Cross-Sectional Properties of Model Shell Footings.

3.4.2 Soil Material Properties

Variations in soil material properties were used as input into the geotechnical software. Of interest, the soil friction angle (ϕ) and density of soil (γ) will serve as part of the parametric study in tandem with shape exploration. Drained soil properties for sand typically input into PLAXIS software are presented in Table 3.2 as follows.

Soil Properties	Value	Units
Unsaturated Unit Weight, γ	17	kN/m^3
Saturated Unit Weight, γ_{sat}	18	kN/m^3
Permeability Coefficient, $k_x = k_y$	1.0	m/hr
Young's Modulus, E	4×10^4	kPa
Poisson ratio, ν	0.3	–
Cohesion Coefficient, c	0.001	kPa
Friction Angle, ϕ	33.68	<i>degrees, ($^\circ$)</i>
Dilatancy Angle, ψ	2.0	<i>degrees, ($^\circ$)</i>

Table 3.2. Soil (Sand) Properties – Mohr–Coulomb Model.

Soil properties were varied and reflect typical values obtained in the laboratory as a basis for comparison. Namely, values representing loose, medium–dense and dense sand states soil have been examined. The relationship between the three density phases is described in detail in the experimental section of this study and implemented here as a comparable.

3.4.3. Safety Analysis in PLAXIS

Phi– c reduction is an option available in PLAXIS to compute factors of safety (FOS). This approach resembles the method of calculating safety factors as conventionally adopted in slip–circle analyses. In the Phi– c reduction approach the strength parameter $\tan\phi$ and c of the soil are successively reduced until structural shell footing failure occurs. The total multiplier $\sum M_{sf}$ is used to define the soil strength parameters value at the local stage in the analysis given as:

$$\sum M_{sf} = \frac{\tan\phi_{input}}{\tan\phi_{reduced}} = \frac{c_{input}}{c_{reduced}} \quad (3.1)$$

where the strength parameters with the subscript input refer to the material set properties entered and parameters with the subscript reduced refer to the reduced values used in the analysis. In contrast to other total multipliers, $\sum M_{sf}$ is set to unity at the start of a calculation to set all material strengths to their unreduced values. Strength parameters are successively reduced automatically until structural failure of the shell footing occurs. At that point, the factor of safety is given by:

$$\text{FOS} = \frac{\text{available strength}}{\text{failure strength}} = \text{value of } \sum M_{sf} \text{ at failure} \quad (3.2)$$

Should a failure mechanism not develop, then the calculation was repeated with a larger number of additional steps.

3.4.4 PLAXIS Sample Input and Output

The PLAXIS environment allows for ease of user input of data to define the geotechnical problem under investigation. Typical shell and soil material set properties described previously are input in well-defined data sets. The overall geometry of the soil-structure domain is drawn using a combination of mouse and pre-defined tabs. Loading conditions, for instance, are input from pre-defined load tabs including point, line and uniformly distributed load and can be further quantified by user-input magnitudes. Overall input was quantified and tabulated for evaluation of performance from successive runs of the program to determine an optimal solution for a given shape yielding optimum soil profile for the soils contact pressure distribution.

The results obtained were from a two-phase load plot. The initial phase is synonymous with construction of the footing and manipulation of the soil domain including soil embedment, soil backfill and soil boundary confinement. The second phase implements a uniform monotonic vertical force applied to the edge beams in the case of inverted shells and the vertical central column load for the flat and upright shells. Loading on the footing-soil system was applied at 2 kPa load increments till soil media shear strength failure. The following screen shots shows the typical input interface for project

definition, material set designations and their respective characteristic properties to be implemented in the analysis.



Figure 3.8. Parameters Tab Sheet for Soil and Interface Data Set Window (PLAXIS).

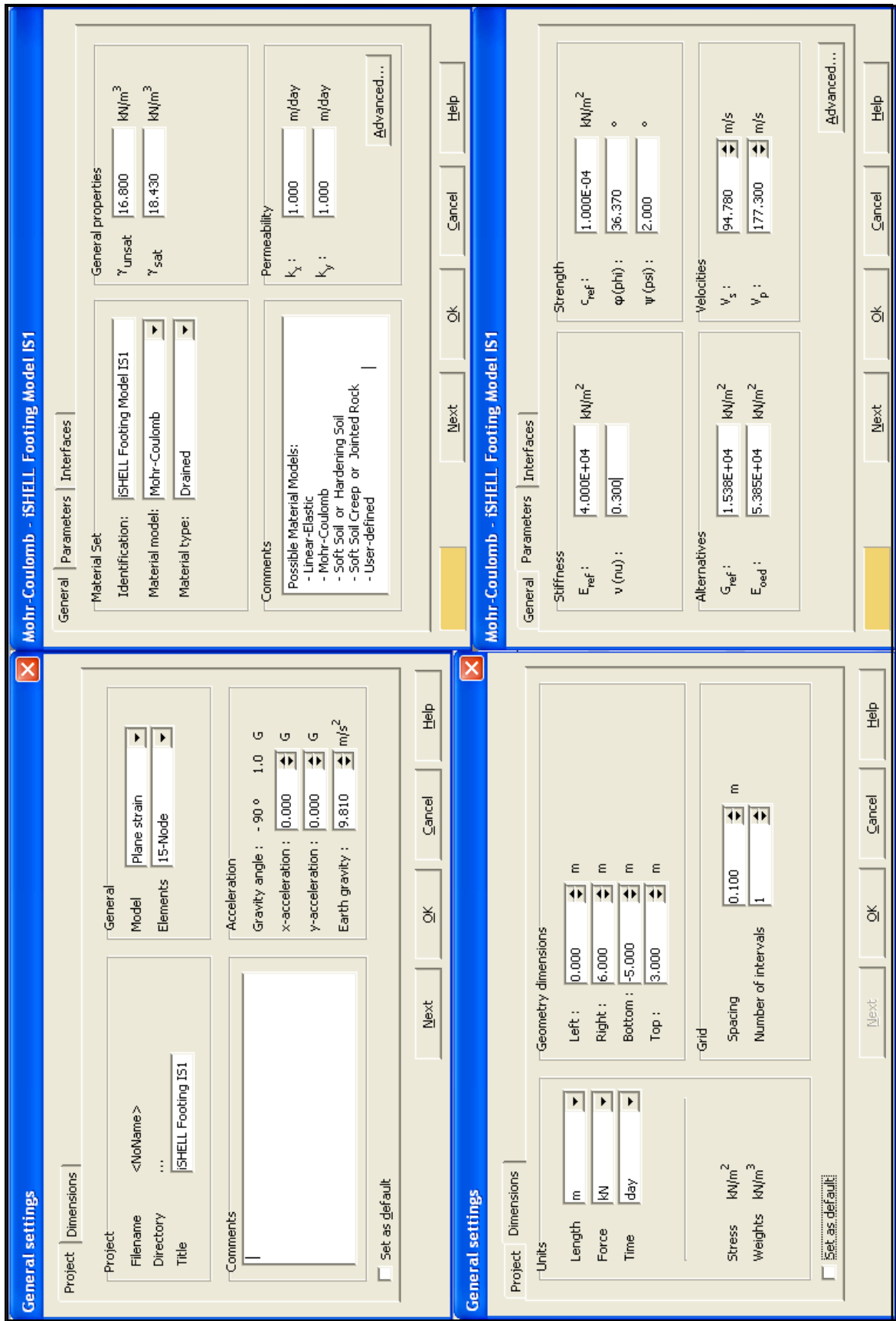


Figure 3.9. PLAXIS Data Input Fields – Shell Modeling.

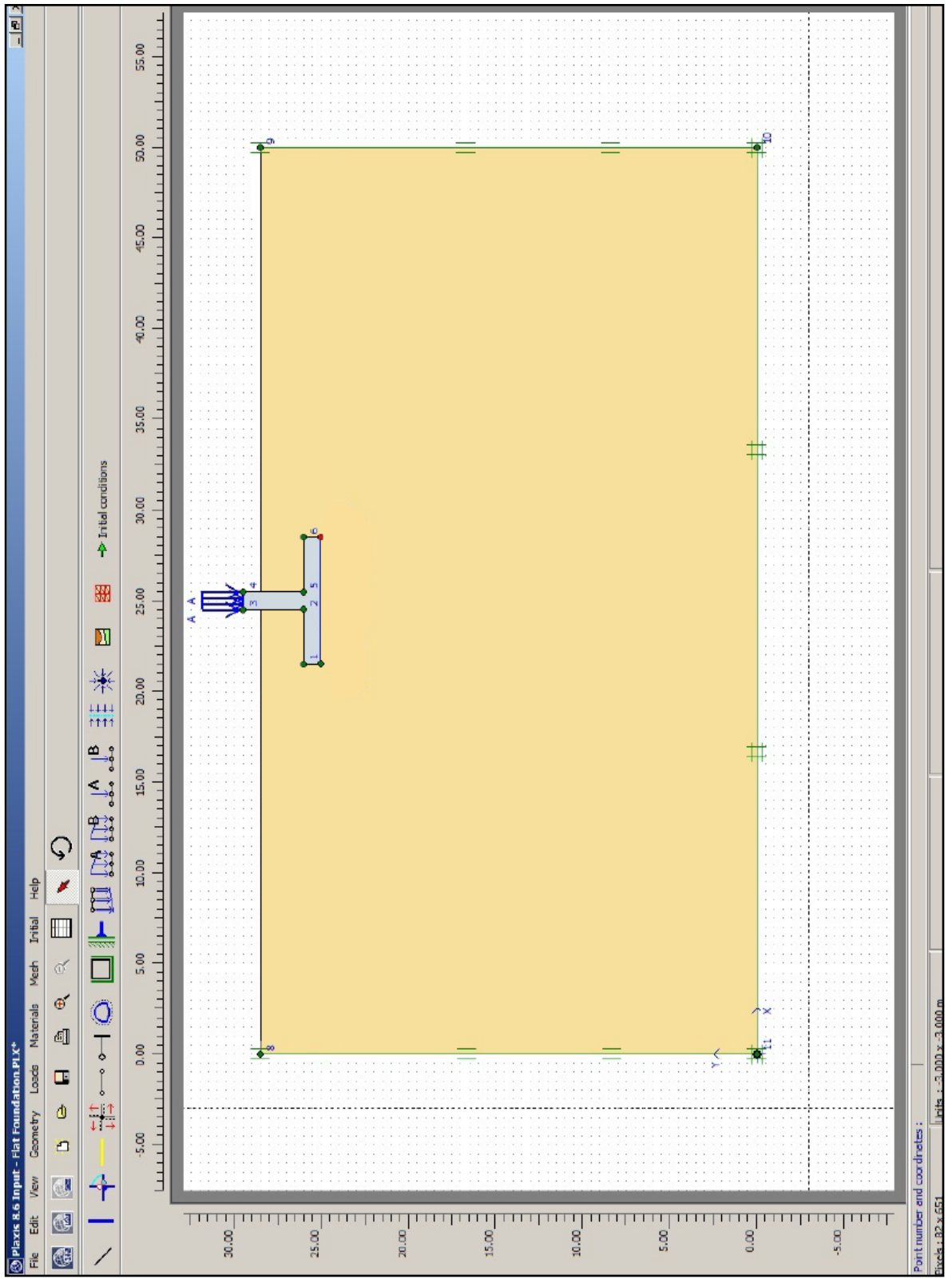


Figure 3.10. PLAXIS Data Input – Flat Footing Model.

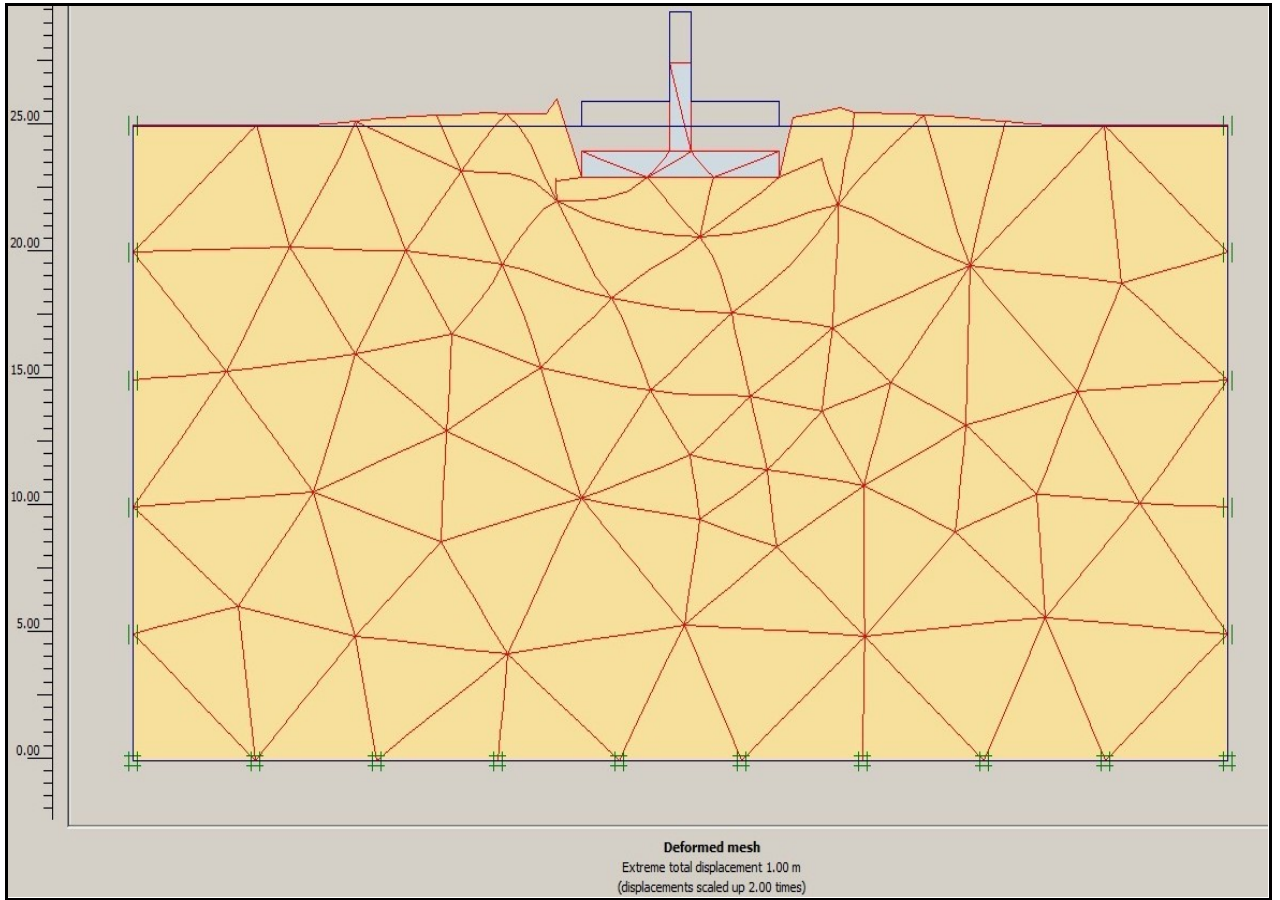


Figure 3.11. Flat Footing Model Output: Generated Soil and Mesh Deformation.

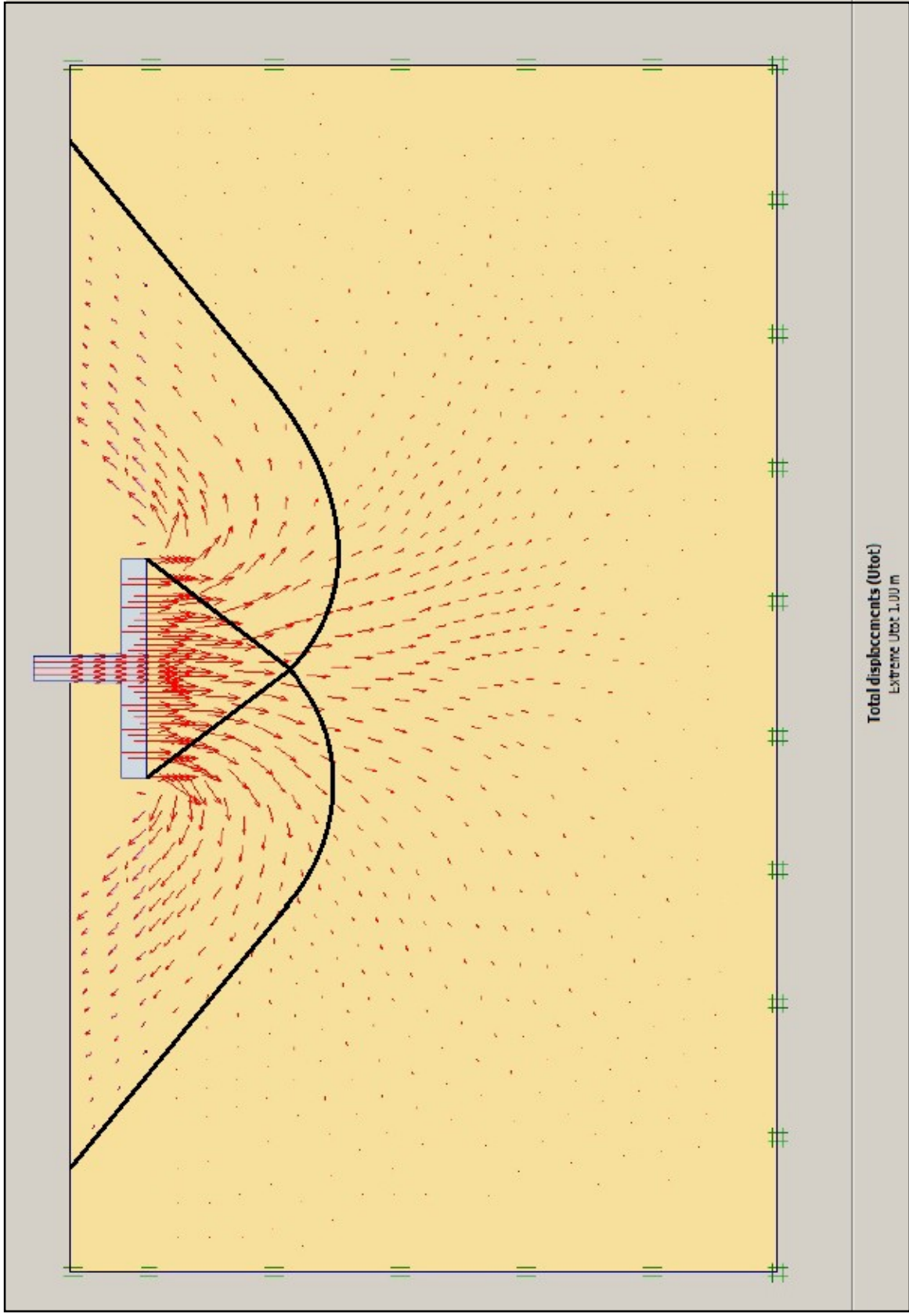


Figure 3.12. Flat Footing Rupture Surface Model - PLAXIS Data Input.

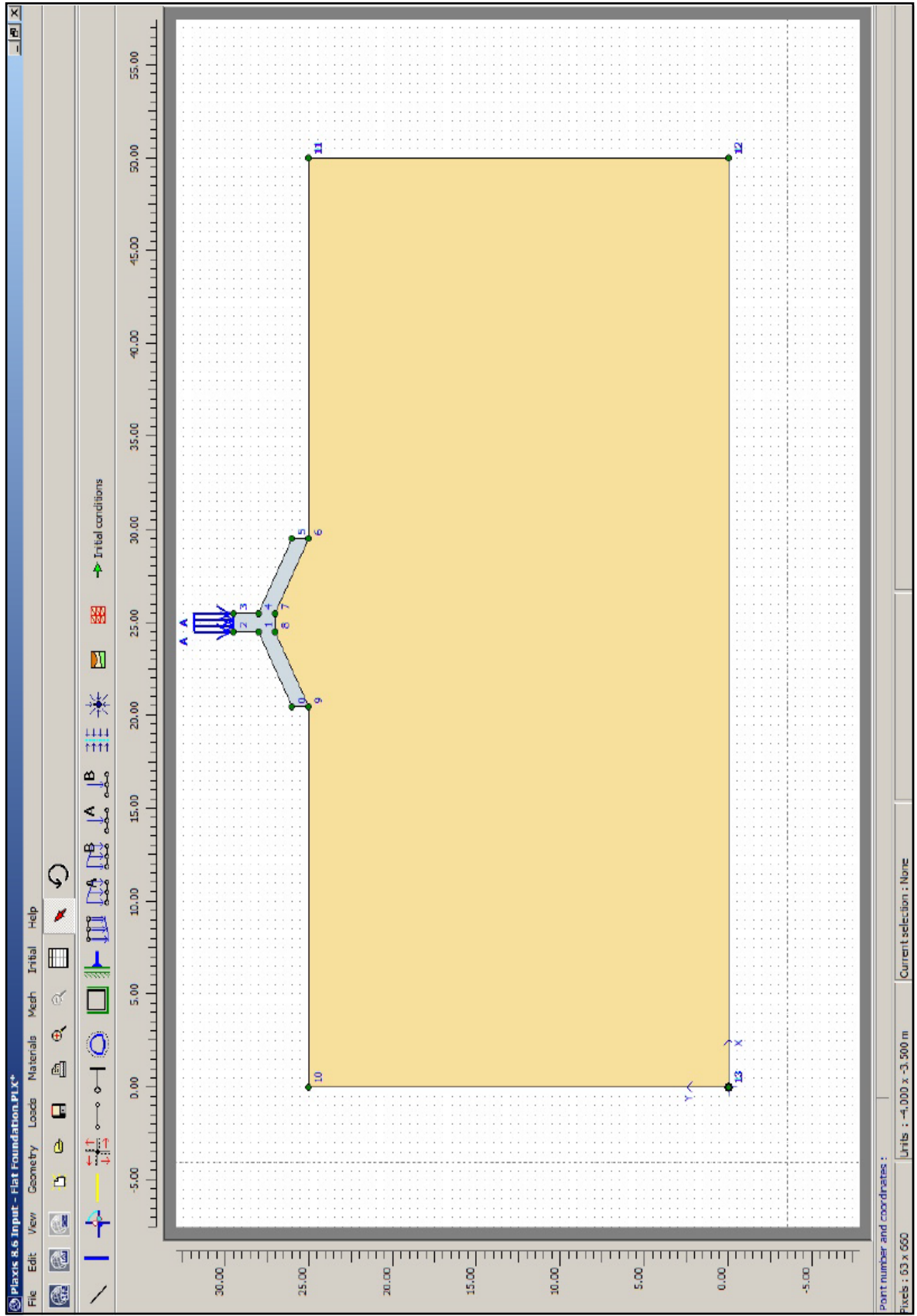


Figure 3.13. Upright Shell Model – PLAXIS Soil-Structure Interface.

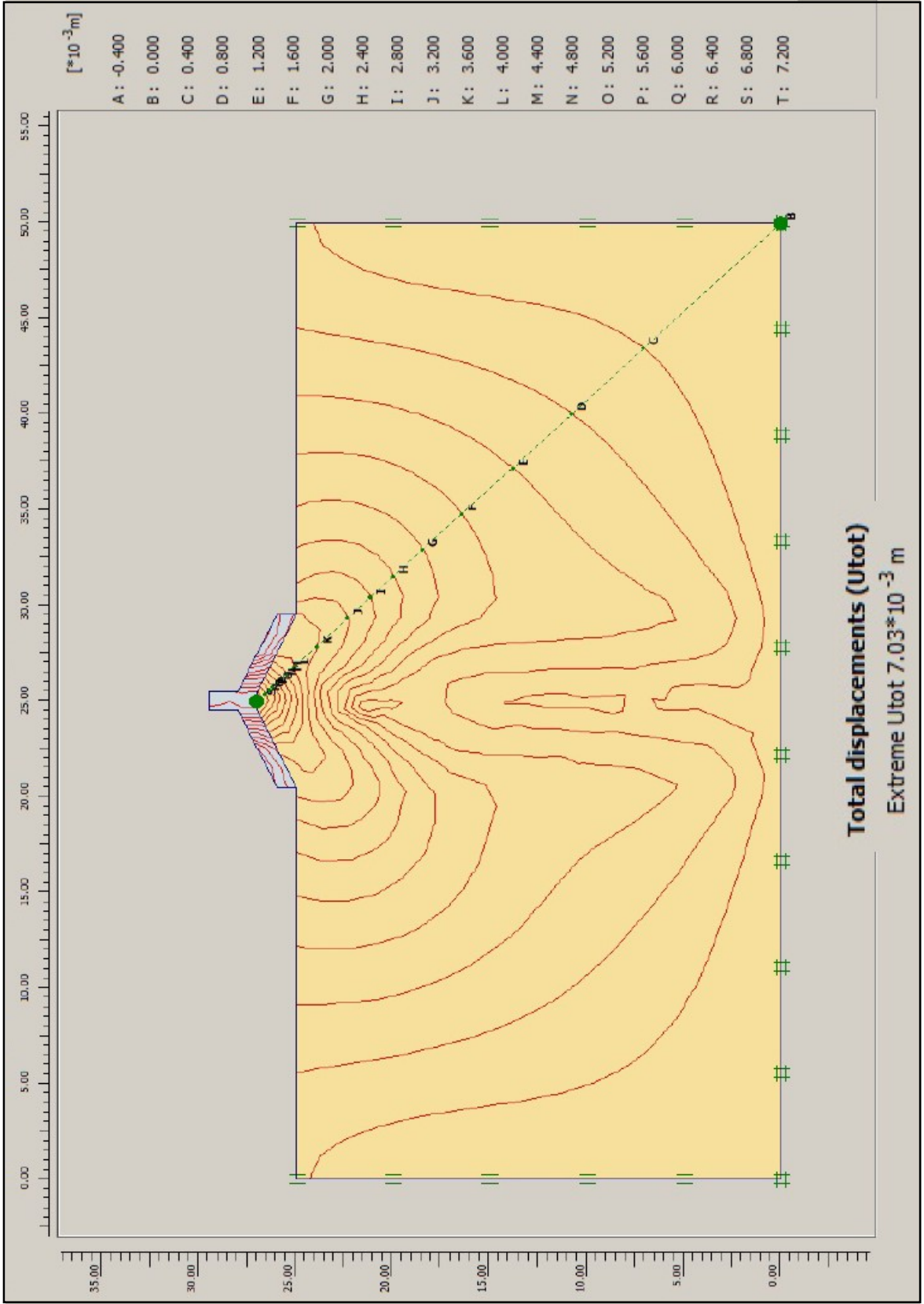


Figure 3.14. Total Displacements for Upright Shell Model.

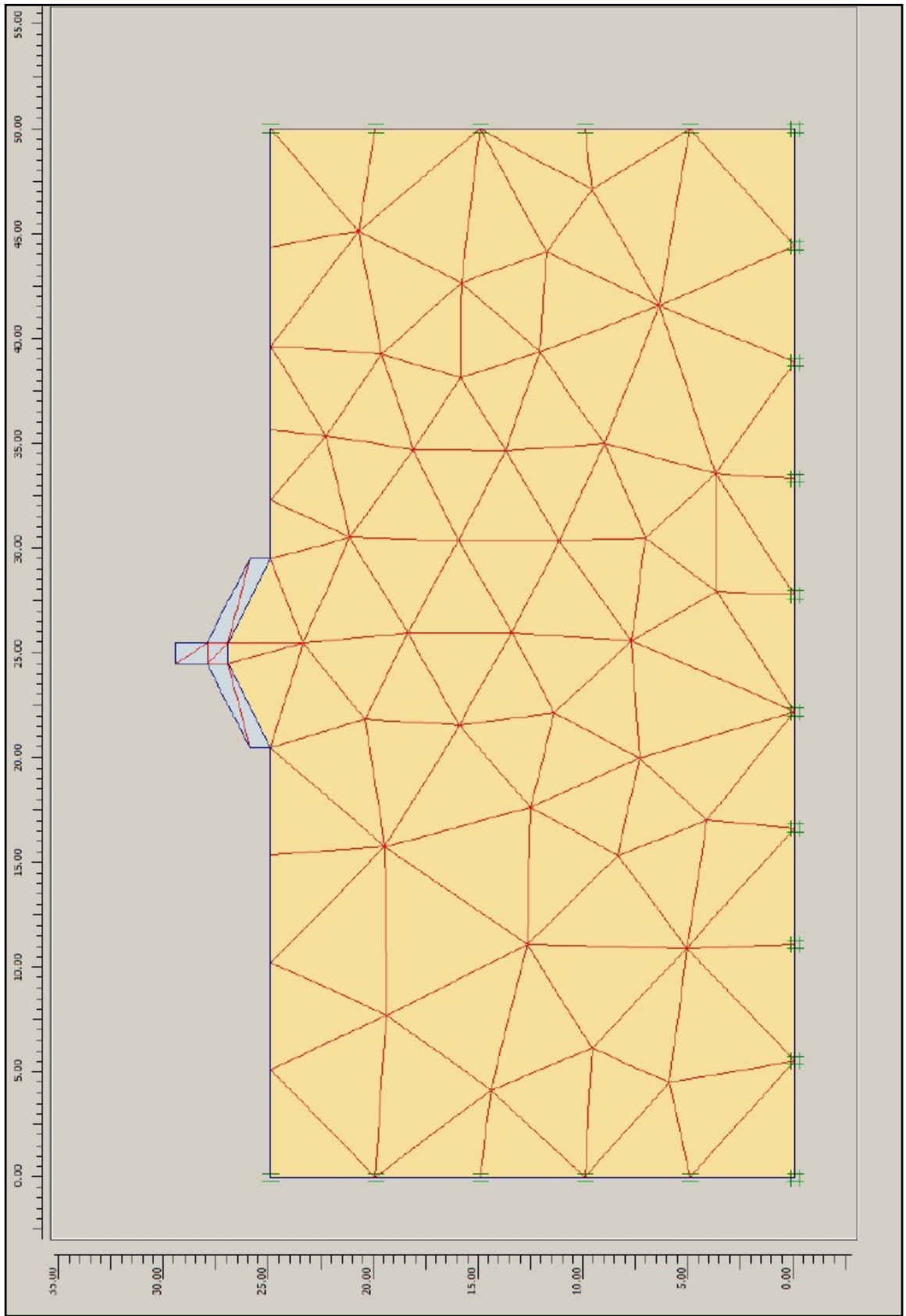


Figure 3.15. Connectivities for Upright Shell Model.

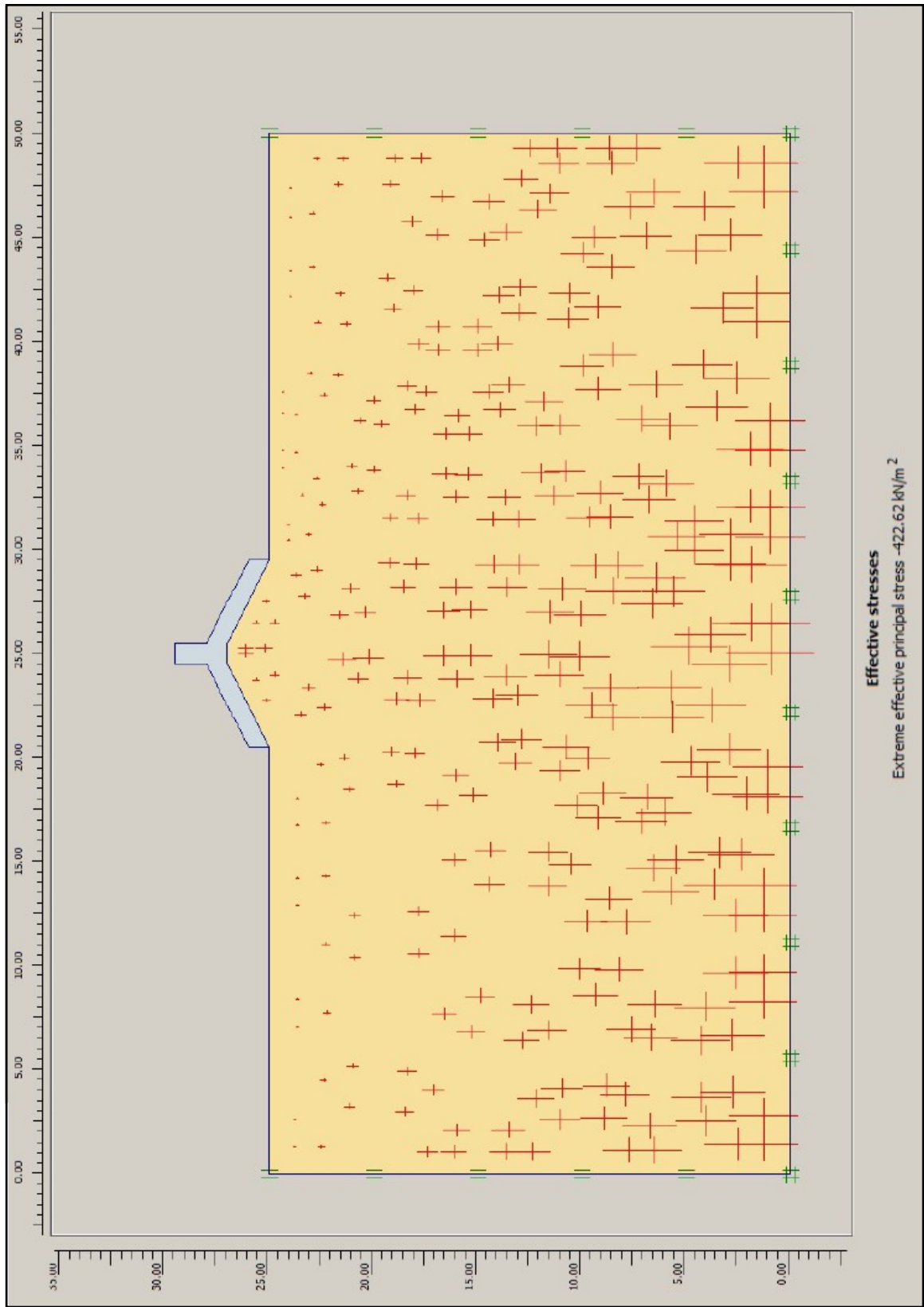


Figure 3.16. Effective Stresses for Upright Shell Model.

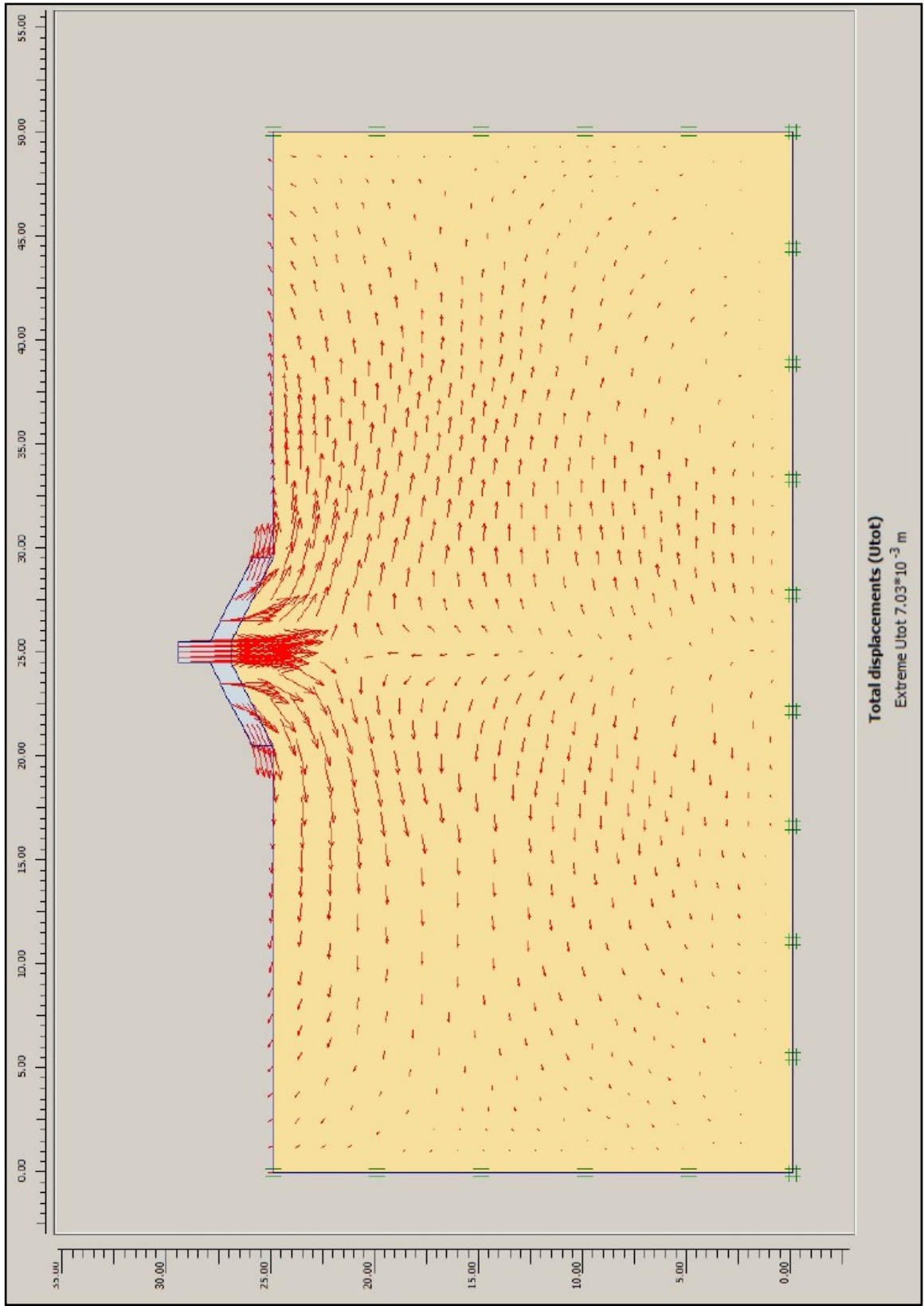


Figure 3.17. Upright Shell Footing Model: Total Soil Displacements.

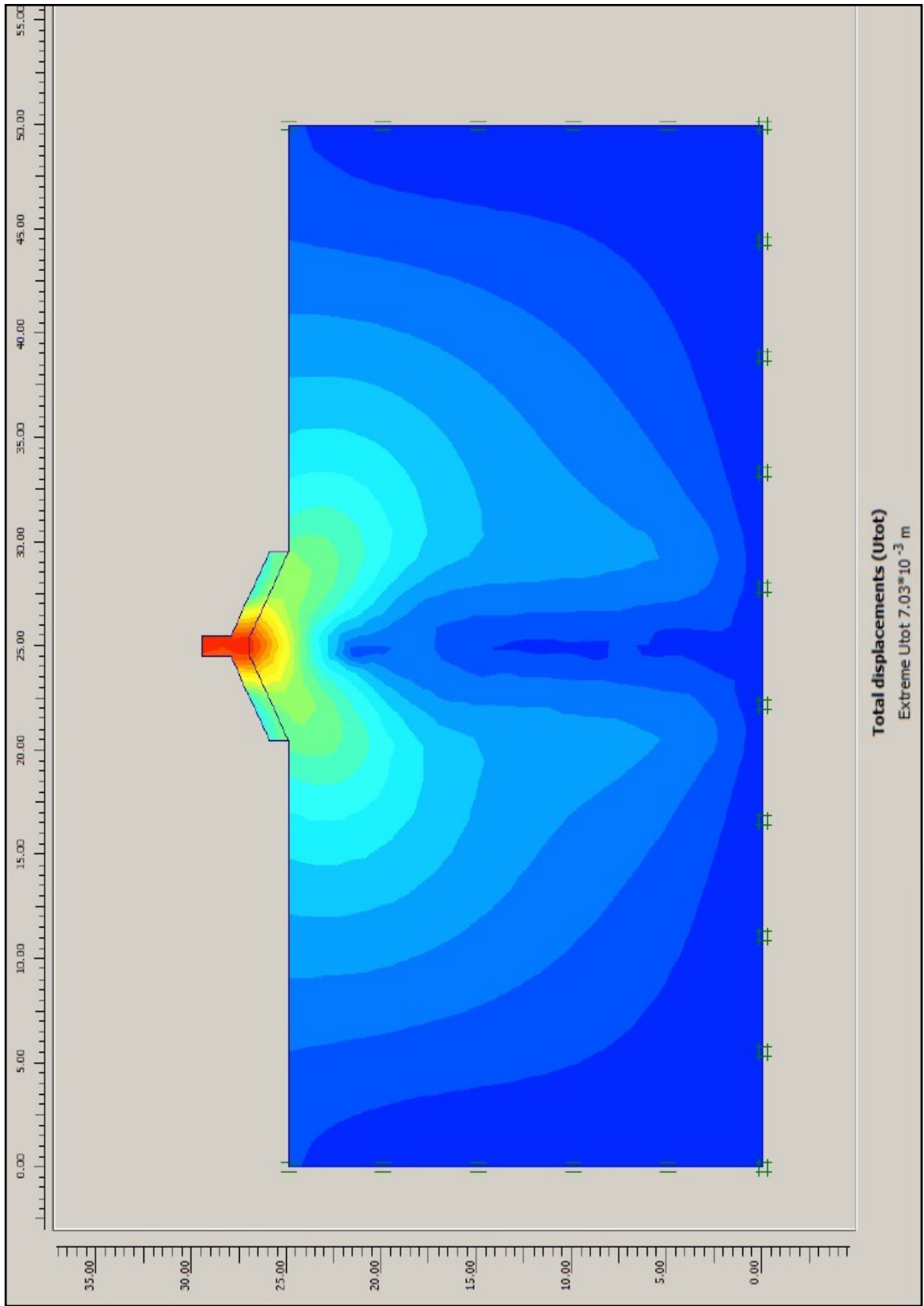


Figure 3.18. Upright Shell Footing Model: Generated Soil Displacements.

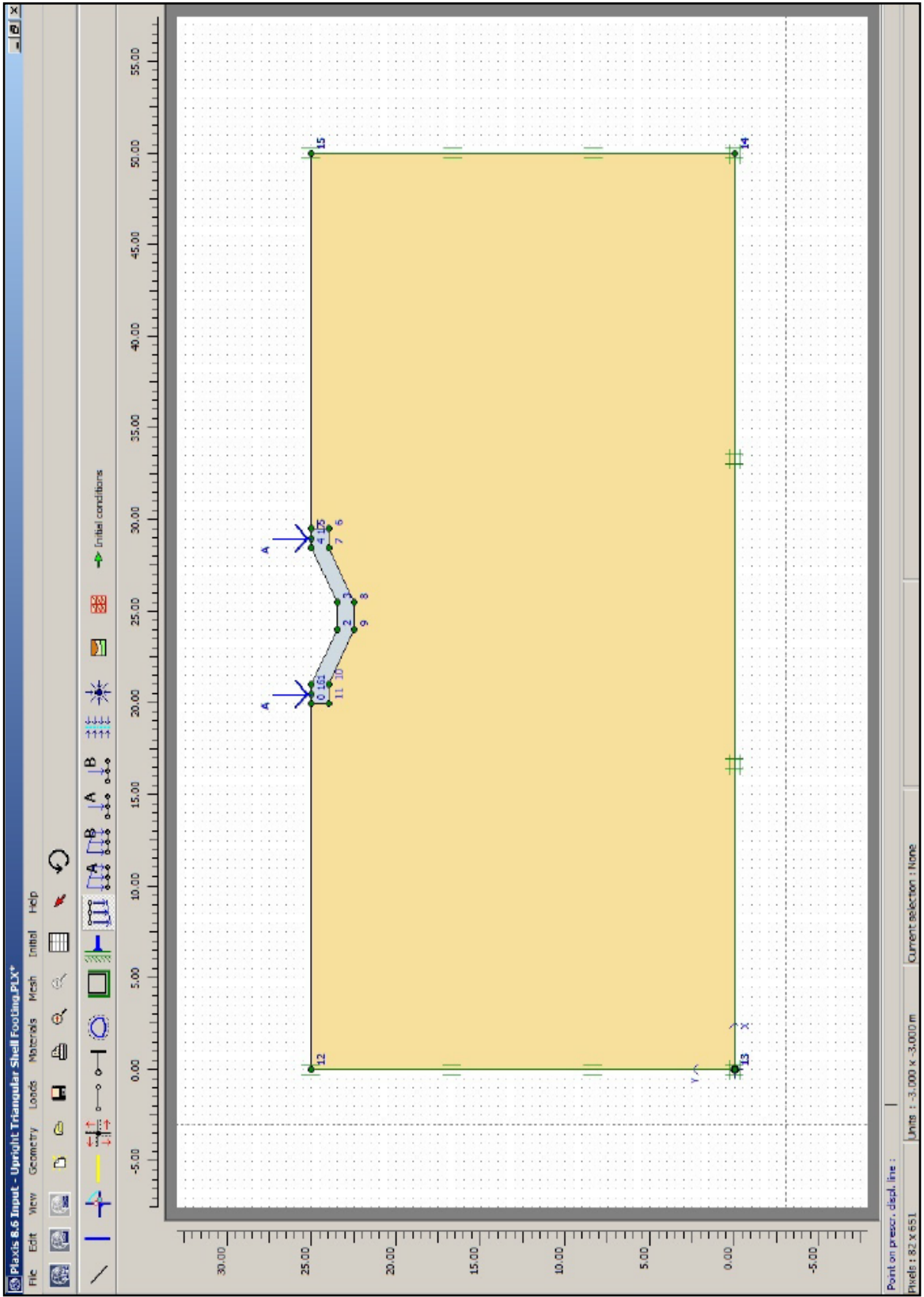


Figure 3.19. Upright Shell Footing Model: Generated Soil Displacements.

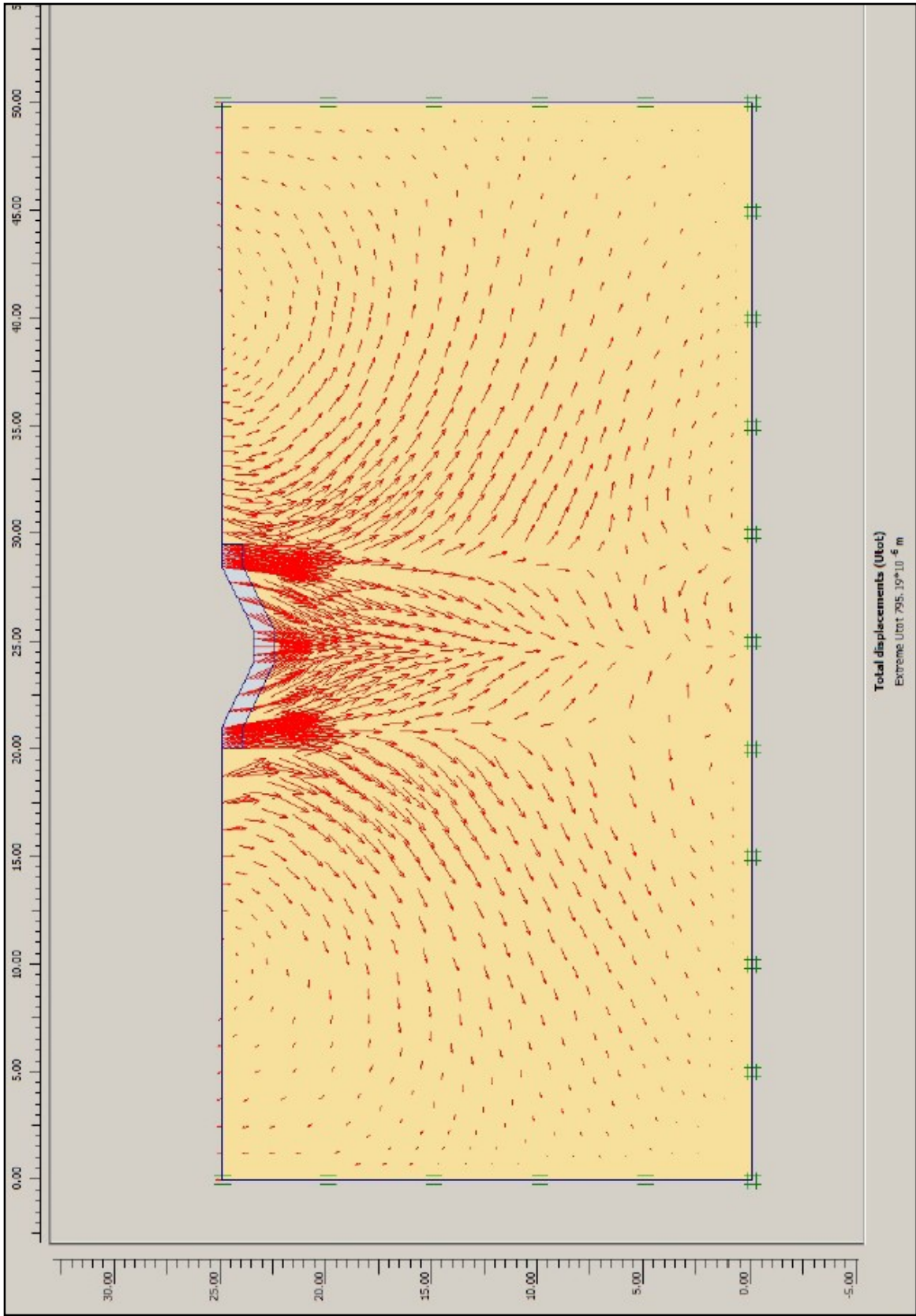


Figure 3.20. Sinusoidal Footing Model: Total Displacements.

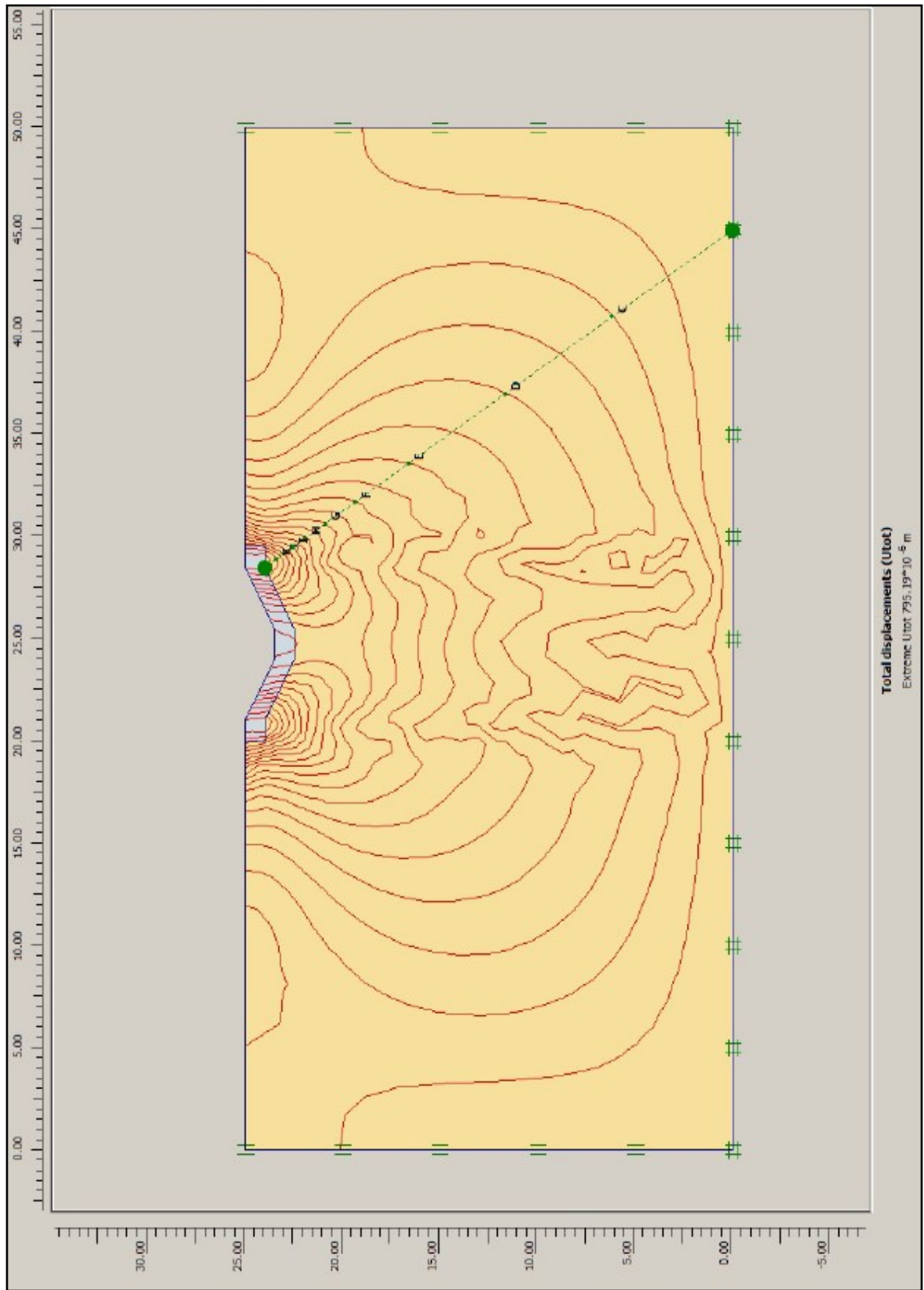


Figure 3.21. Sinusoidal Footing Model: Contour Line Displacements.

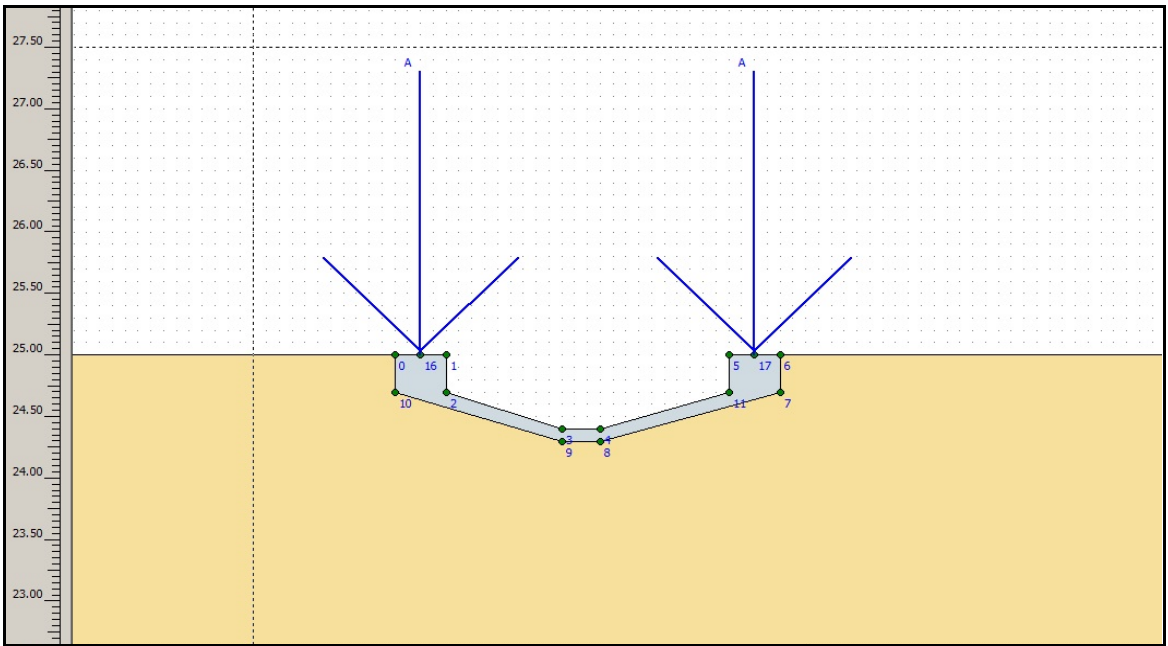


Figure 3.22. Close-up View iShell Footing Model : iS4 Initial loading conditions.

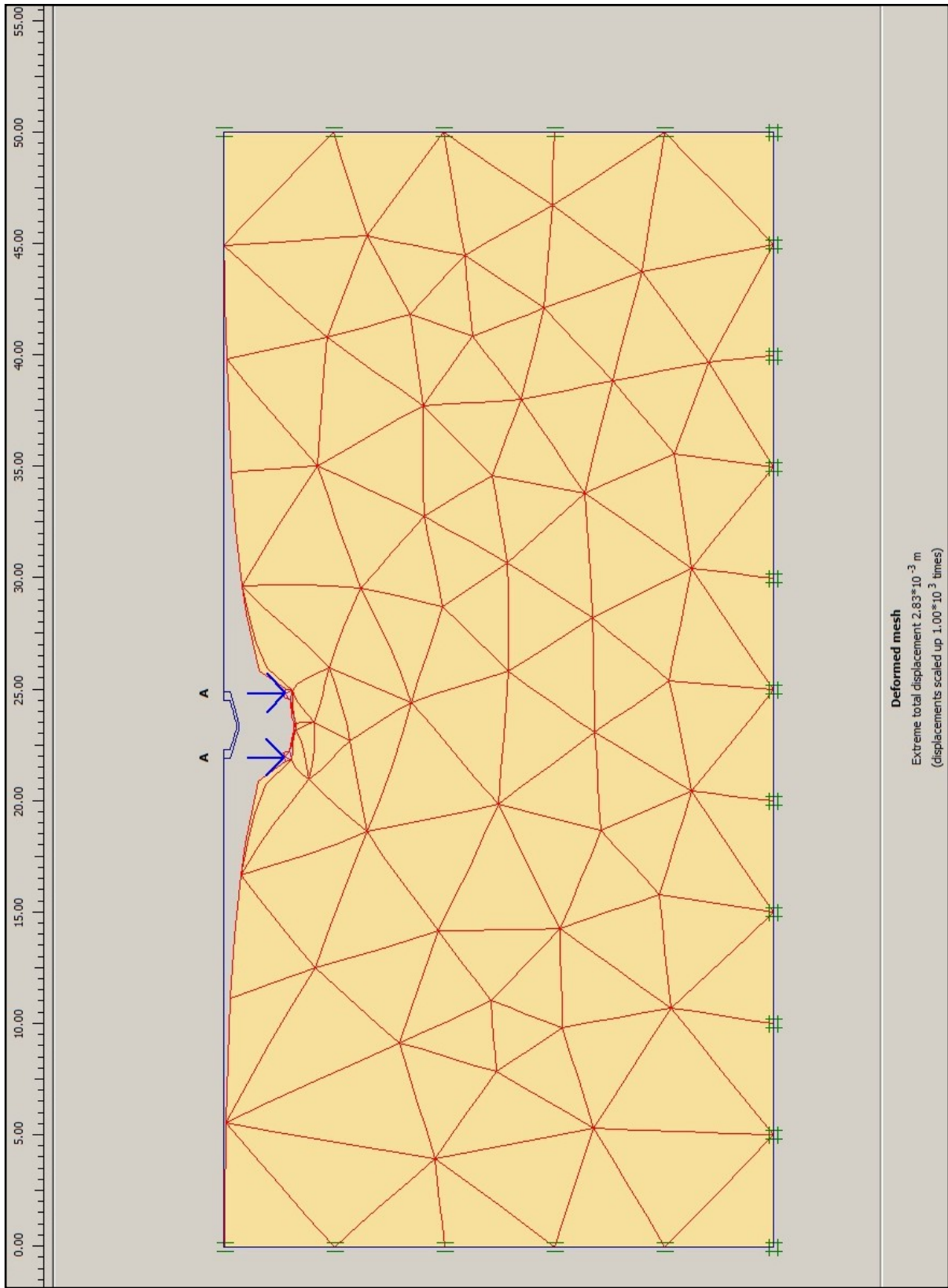


Figure 3.23. iShell Footing Model iS4: Deformed Mesh.

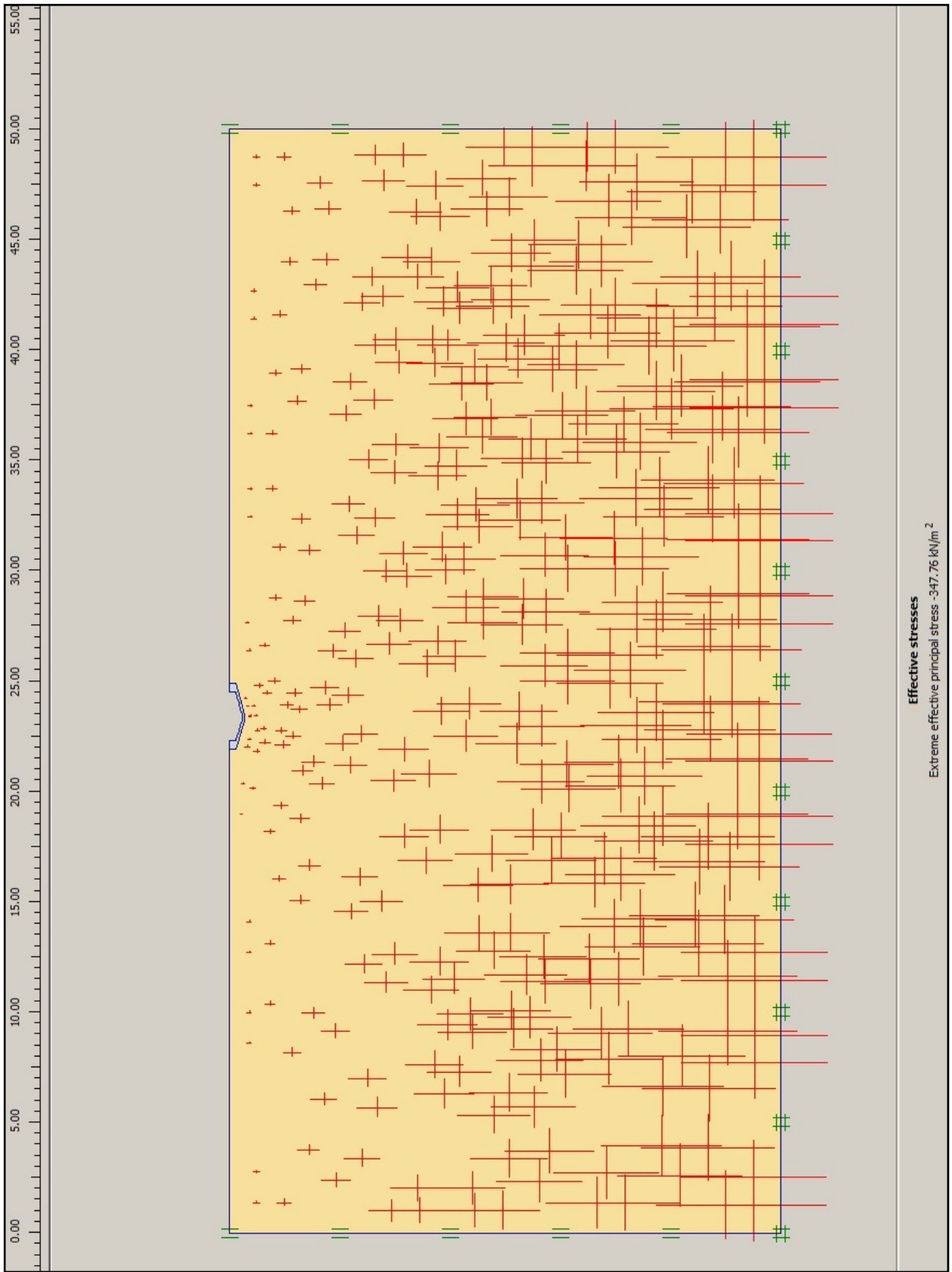


Figure 3.24. iShell Footing Model iS4: Effective Stresses.

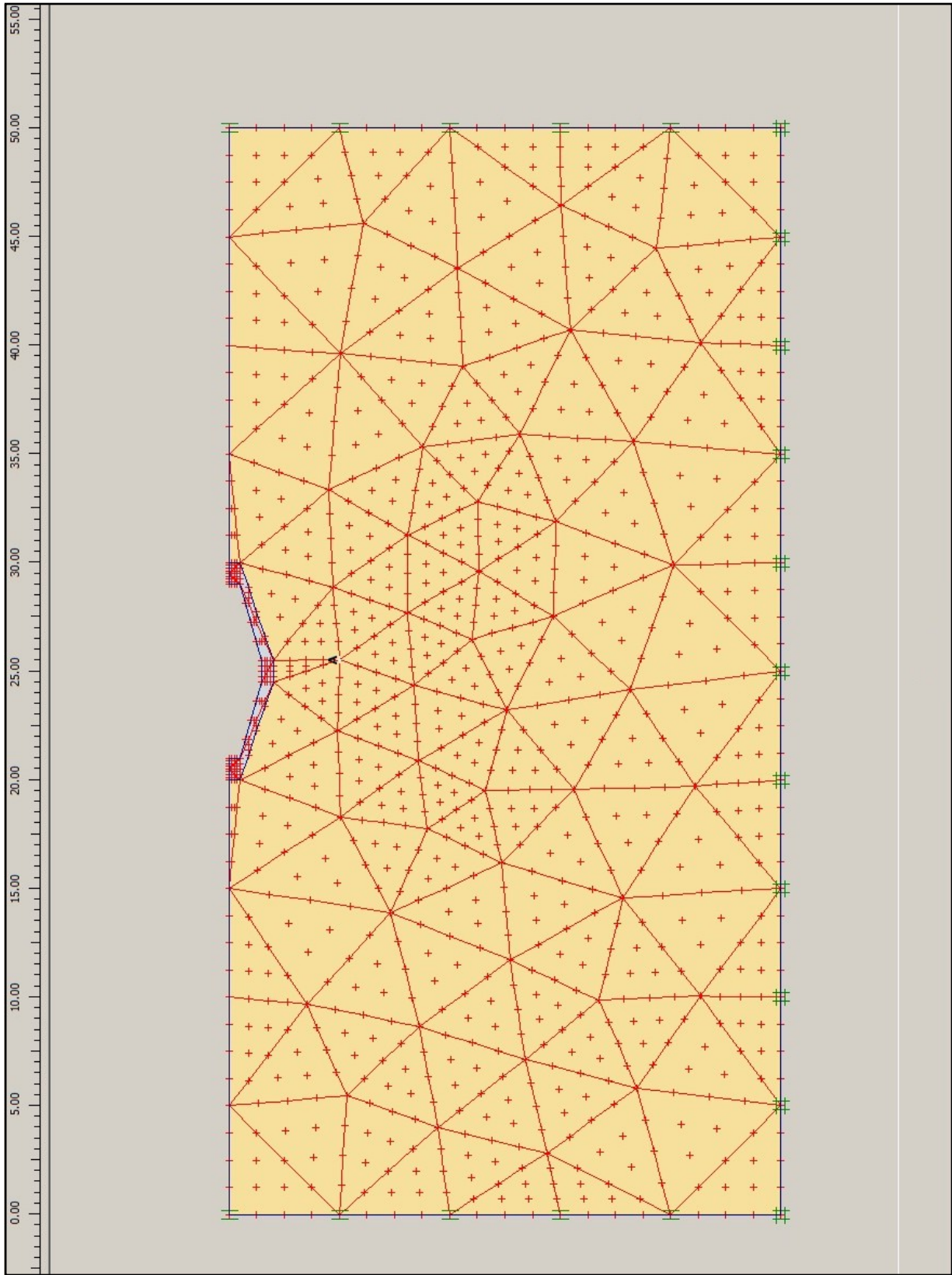


Figure 3.25. iShell Footing Model iS4: Connectivities & Nodal Points.

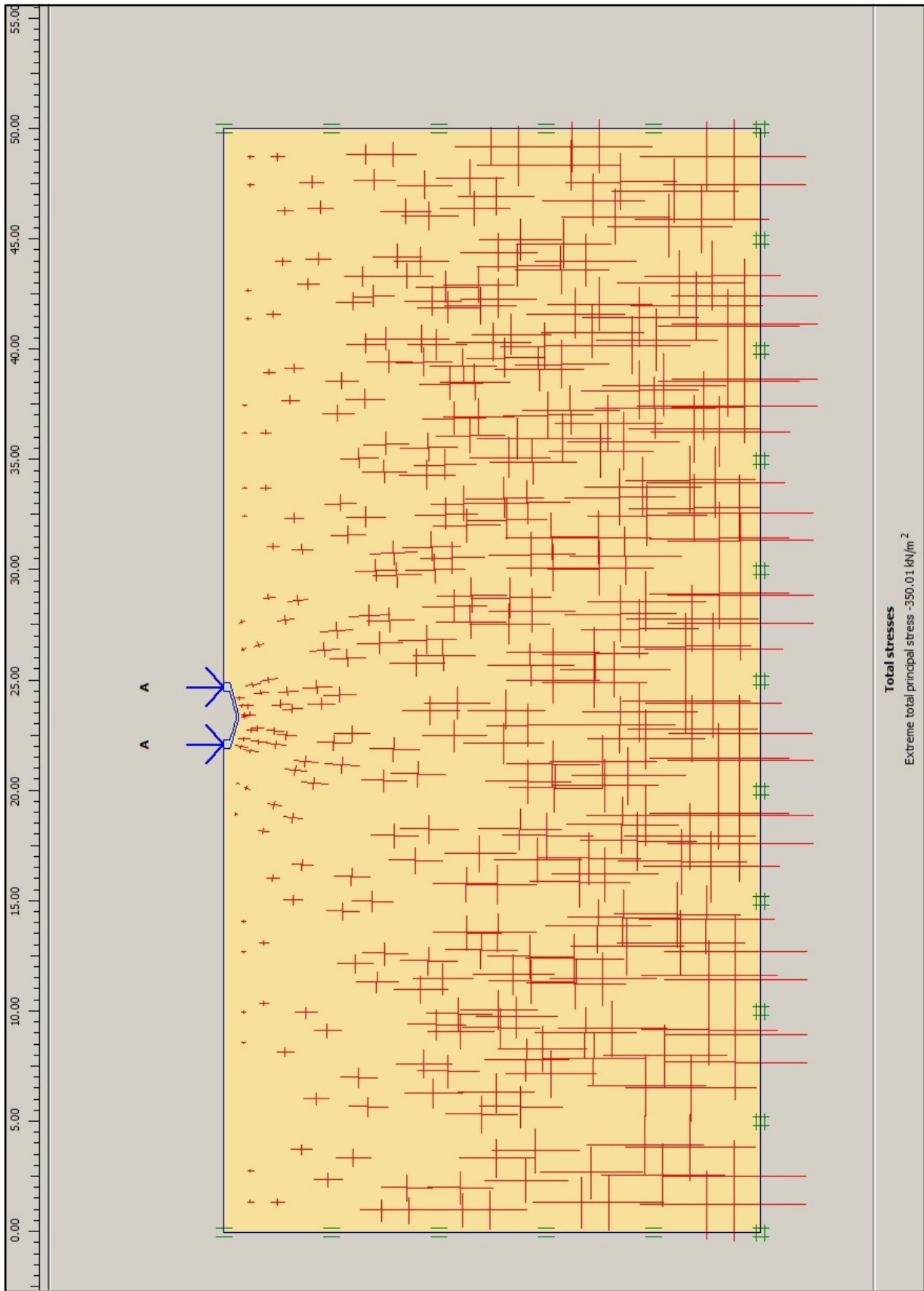


Figure 3.26. iShell Footing Model iS4: Total Stresses.

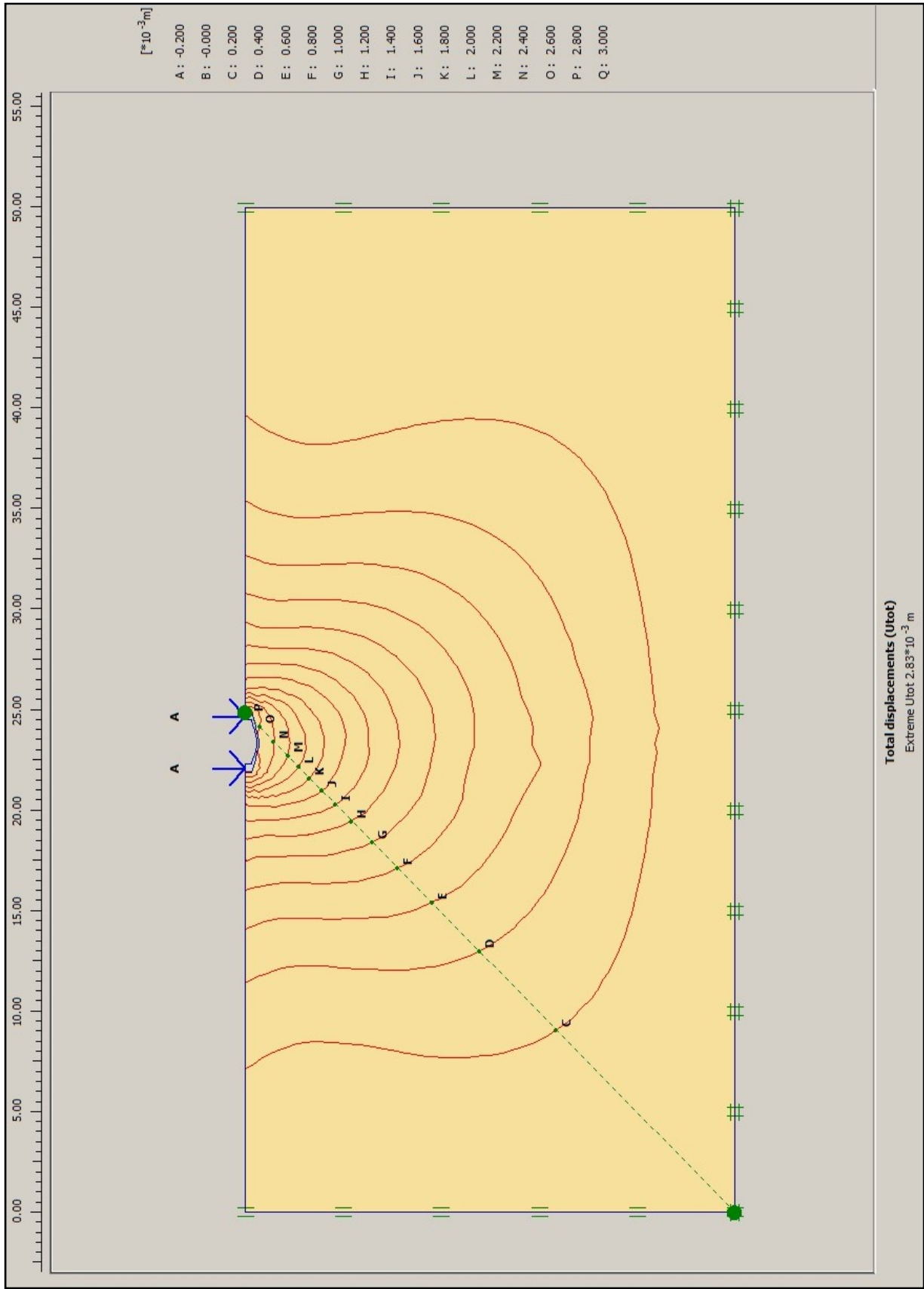


Figure 3.27. iShell Footing Model iS4: Total Displacements.

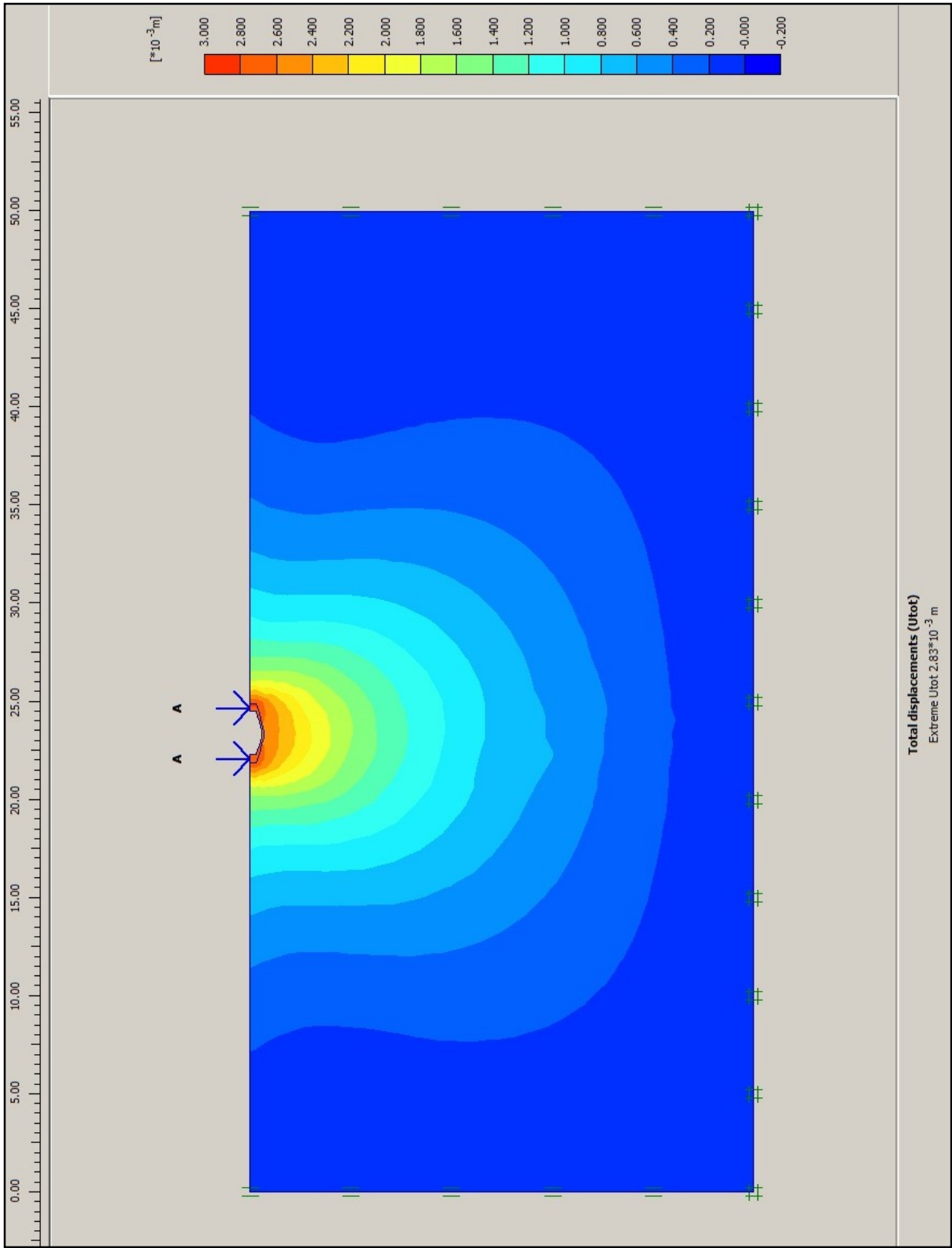


Figure 3.28. iShell Footing Model iS4: Contour Displacements.

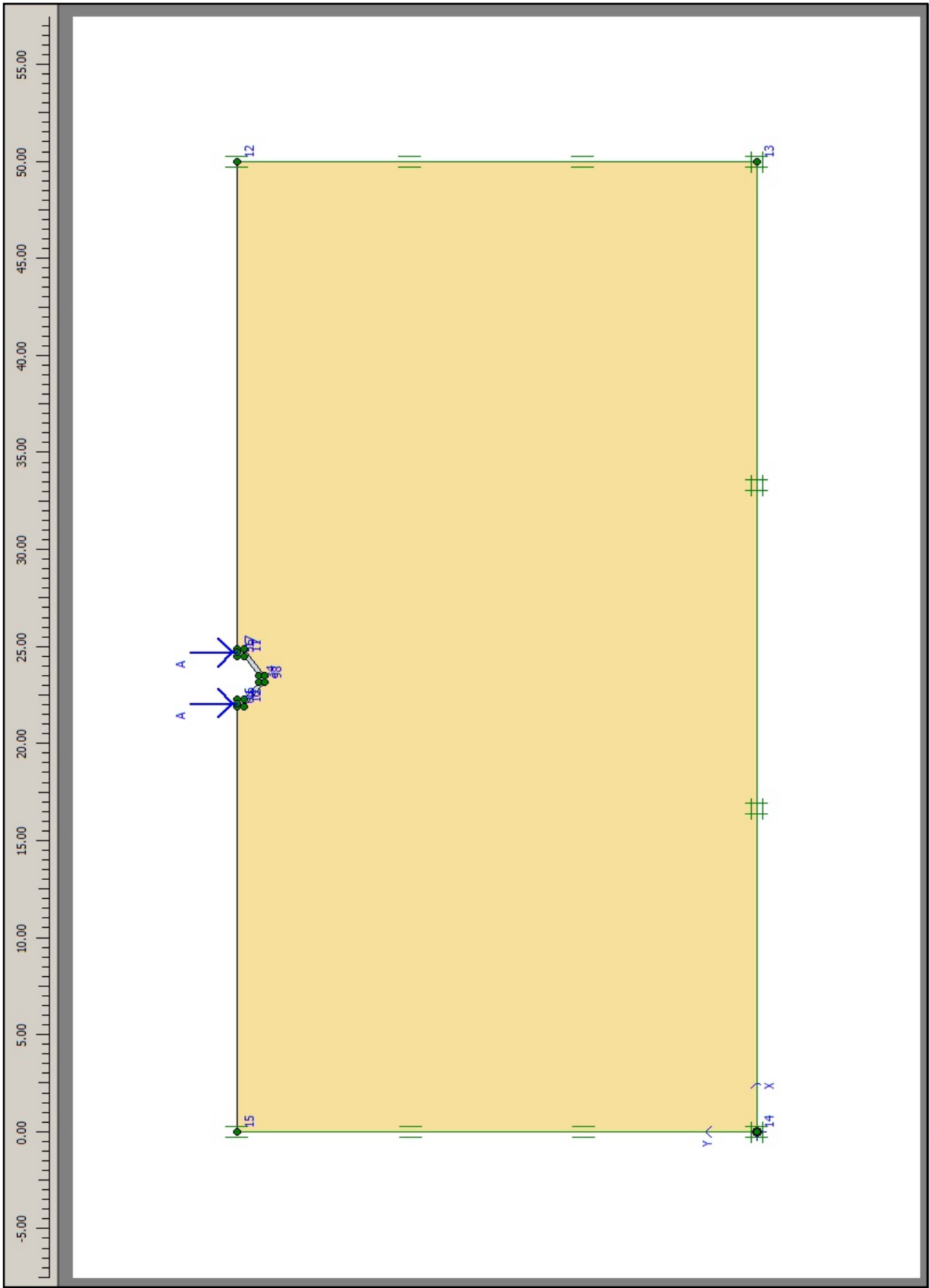


Figure 3.29. iShell Footing Model iS3: Initial Loading Conditions.

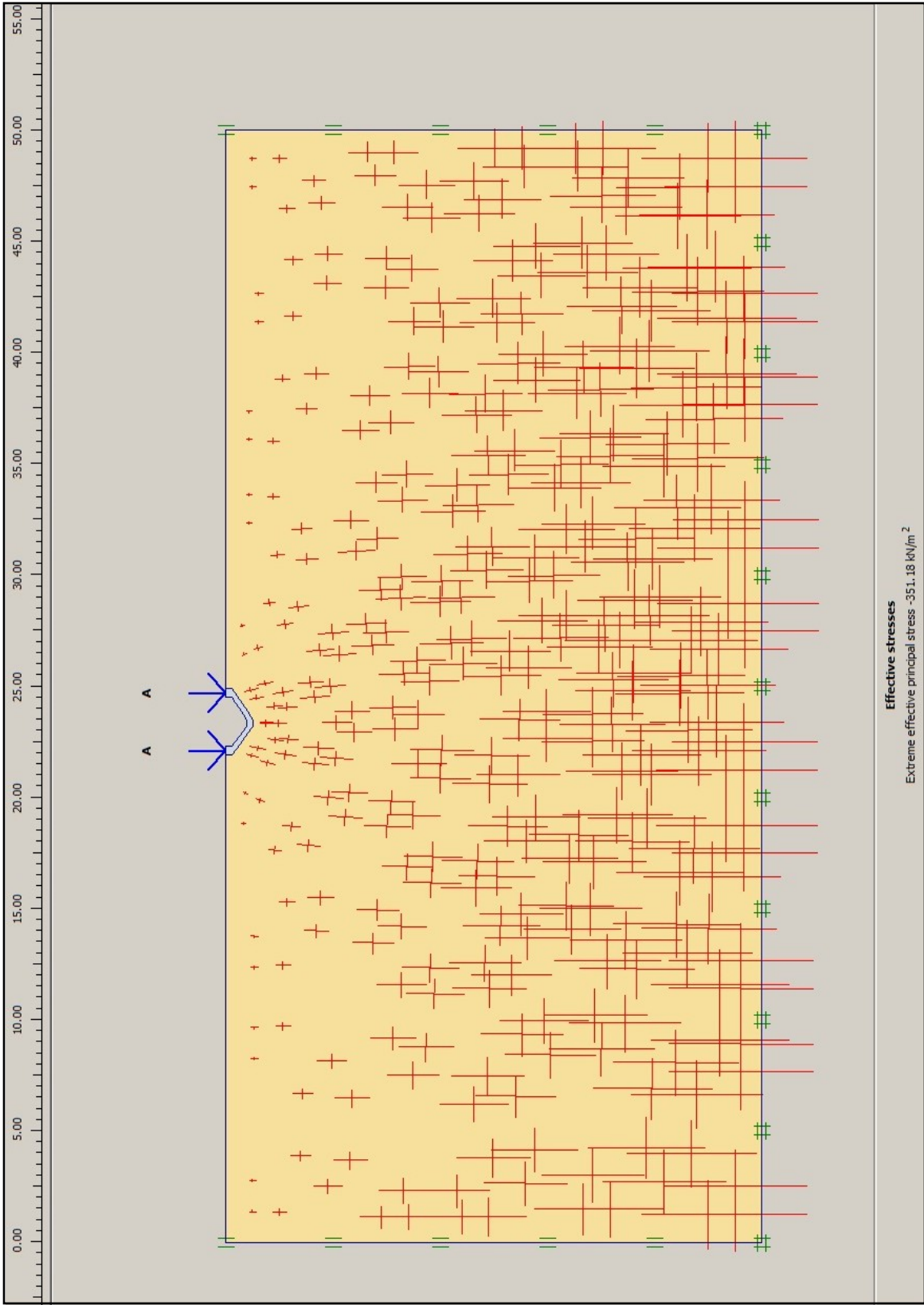


Figure 3.30. iShell Footing Model iS3: Effective Stresses.

3.4.5 Load–Settlement Behaviour

A homogeneous soil with typical shell surface roughness and confined embedment depths helped evaluate performance of the inverted shells modeled. From the numerical investigation the soil response is generated for each shell tested in the form of load–settlement curves as presented in Figure 3.31 below.

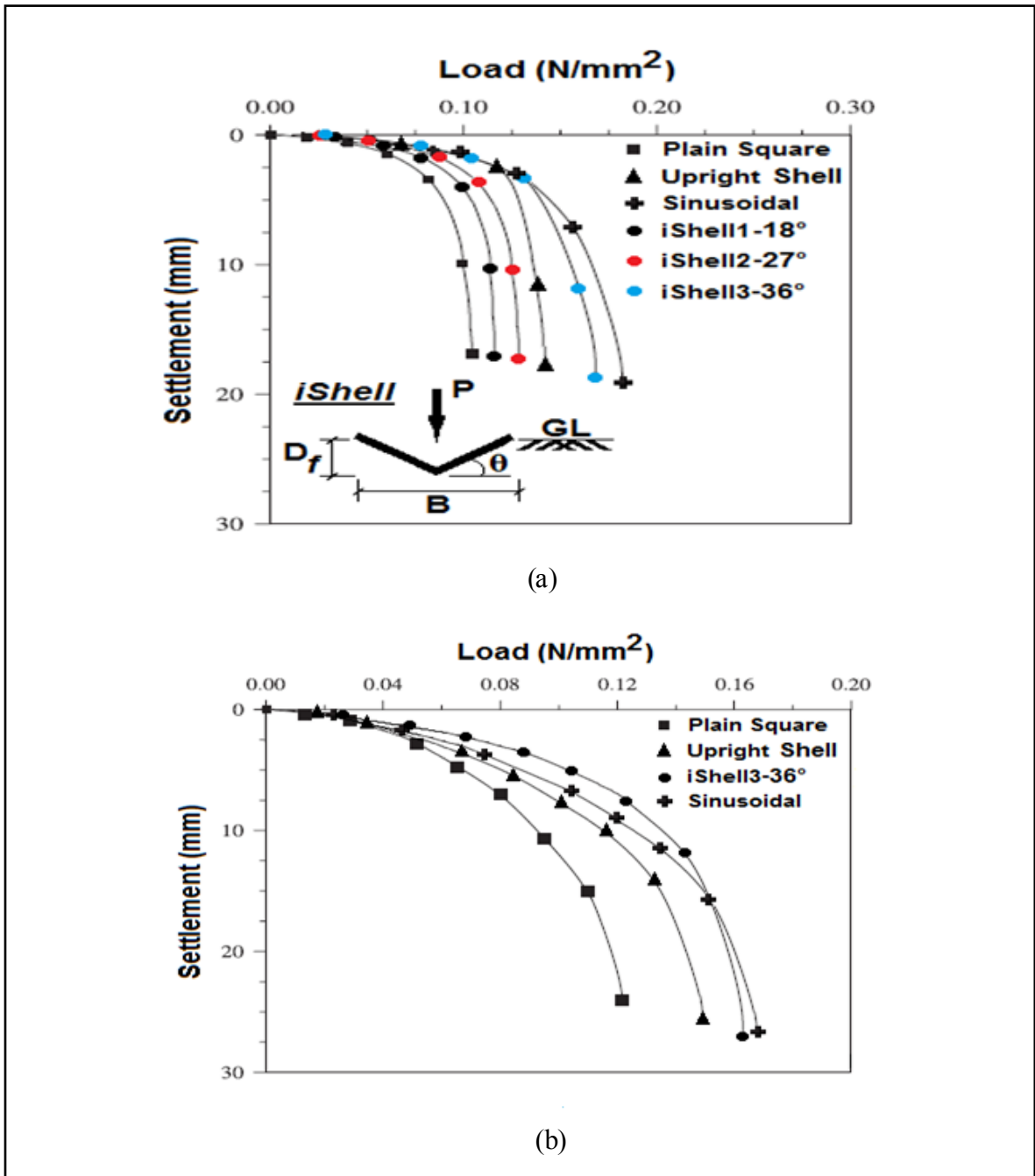


Figure 3.31. Load–Settlement Curves for iShell Models.

Based on the values obtained, Figure 3.31(a) indicates best performance in terms of settlement coming from the Sinusoidal model and iShell36°. iShell models iS1 and iS2 were found to have shown improvement over the flat plain model as reproduced in Figure 3.31(b). The shells also demonstrated having commensurate performance suggesting that the shell response is in good agreement (within 5% margin of error) when compared with other similar geometries. It is worth noting that interface roughness of the models with the soil has remained constant having a coefficient of friction ($\mu = 1$) for perfectly rough condition as simulated by concrete in the field.

From the results of the load–settlement curves presented, the following major conclusions on shell model runs can be drawn, which have been put into quantitative form to the extent possible:

- (a) The load–carrying capacity of the shell (in the inverted position) shows approximately 42% higher load–carrying capacity than its plain counterpart with slightly better improvement of 5% over the upright shell case under identical soil and loading conditions, thereby establishing the superiority of the shell performance over its plain and upright counterparts
- (b) Beneath shell footings, as under plain foundations, an increase in capacity is experienced with increasing density of sand (based on $c-\phi$ soil strength parameters)
- (c) Effect of shell angle on the footings capacity is a major factor in performance as an increase of only 18° in shell angle translated to a 12% increased load–carrying capacity
- (d) Shell thickness had limited variation on the numerical findings rendering this parameter negligible assuming the footing breadth is large having geometry ratio of breadth–to–thickness of at least 20:1
- (e) Depth of embedment increases from 0.50 to 0.75 showed a 2% increase suggesting deeper shell footings having increased capacity on account of denser soil

3.4.6 Finite Element Mesh Generation

The finite element mesh generation utilizes an incremental tangent stiffness approach in the analysis in which the load is divided into a number of small increments, applied simultaneously. For each load increment, the stiffness properties appropriate for the current stress level are employed in the numerical analysis. A typical soil media of 150 elements using 15-nodal points per element were modeled under drained conditions. Figures 3.32 – 3.34 show a typical finite-element mesh generated with idealized boundary conditions for flat, upright and inverted shell orientation with superimposed rupture surface for the respective case.

The resulting rupture surfaces for the inverted shell orientation had comparable depth of penetration, due mainly to its lower center-of-gravity at the onset of loading. Both the inverted shell and upright version have deeper rupture surfaces than the flat shell which seemingly would explain the higher bearing capacity values obtained. Thus, for a similar cross-sectional planar area, the shell footings had higher load-carrying capacity characteristics than those of conventional form. The results also showed some variance between the numerical and experimental results with the latter having 10 – 15% higher capacities as discrepancy. The inverted Sinusoidal shell was found to have highest capacity suggesting that implementation of edge beam is beneficial to overall performance of the shells.

Previous studies found that vertical displacements was reduced by as much as 10% (Hanna and Rahman, 1994) in the case of upright shell footings. This trend in reduction was found to be similar for both the surface and embedded footings up to a cut-off point where rise-to-base ratio (D/B) influence became negligible for vertical soil displacement. The embedment ratio's ranging between 0.35 – 0.50 for the footings has influence on the carrying capacity as the overburden pressure and lateral support offered by the soil looks to stabilize the structure as typically found in practice. On this basis, surface conditions where ($D/B = 0$) for the shell, has been intentionally omitted was thought to have minor significance even from a practical design point of view.

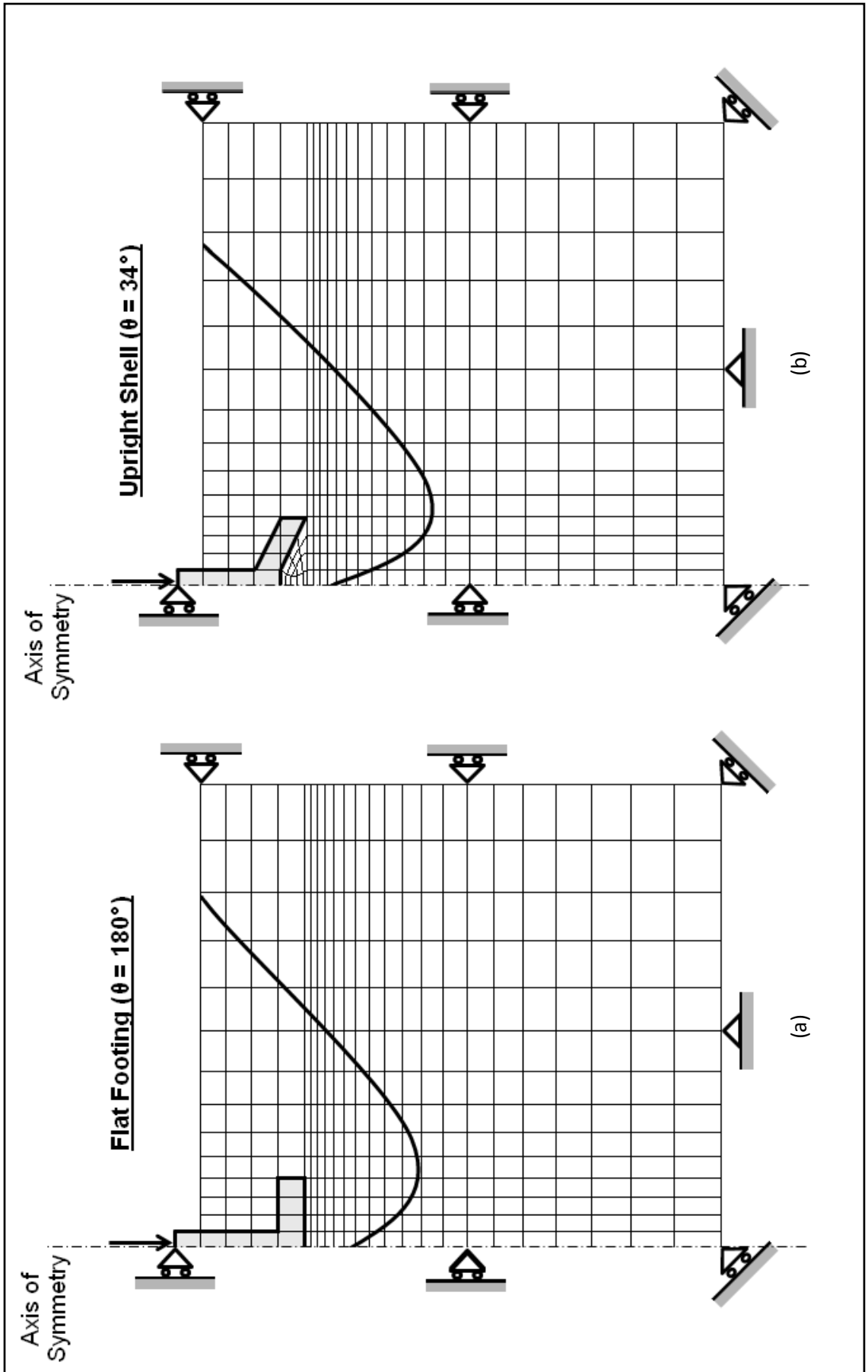


Figure 3.32. Finite Element Meshes for (a) Flat Footing (b) Upright Shell Footing.

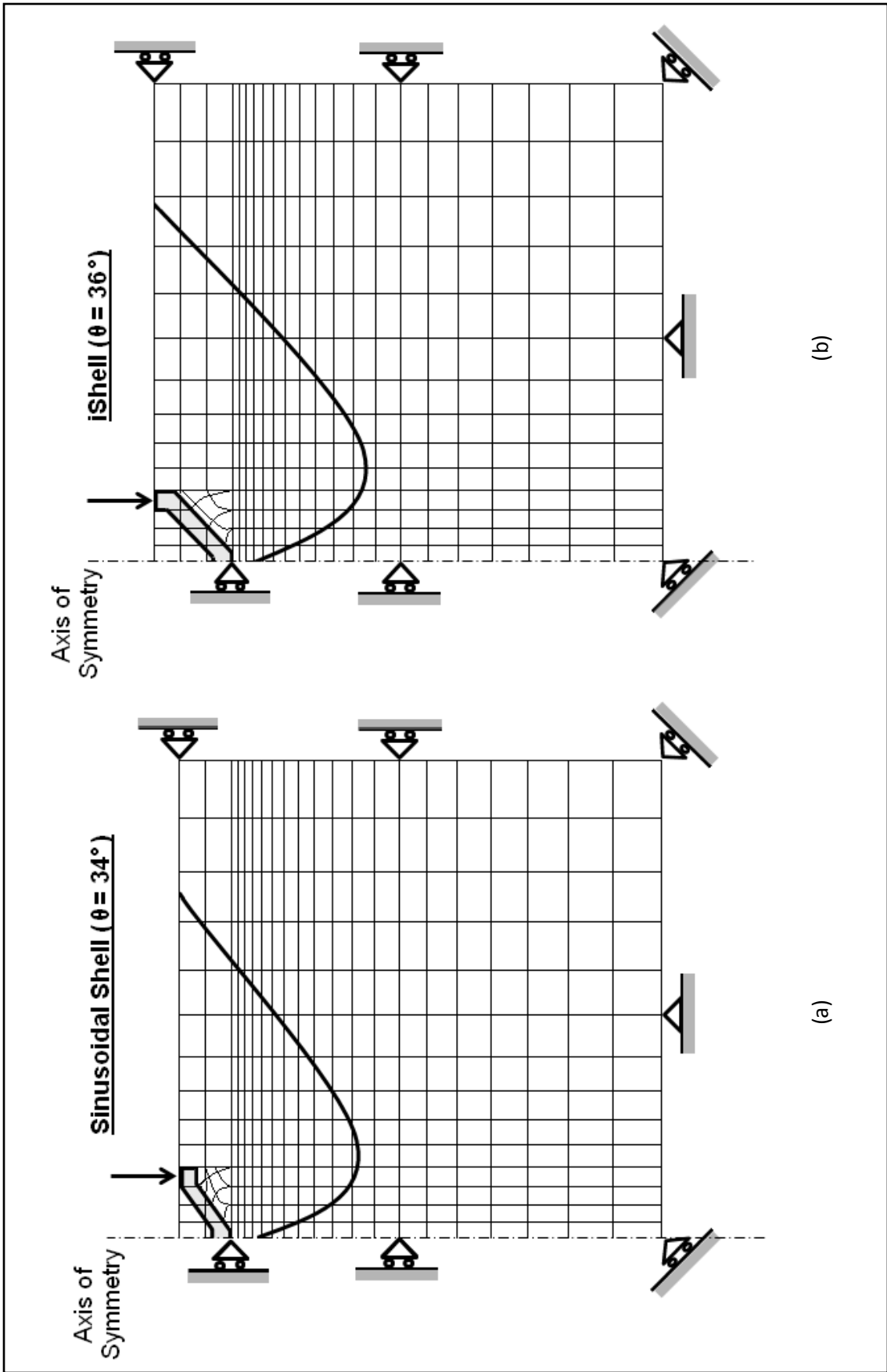


Figure 3.33. Finite Element Meshes for (a) Sinusoidal Shell (b) Inverted Shell Footing-iS3.

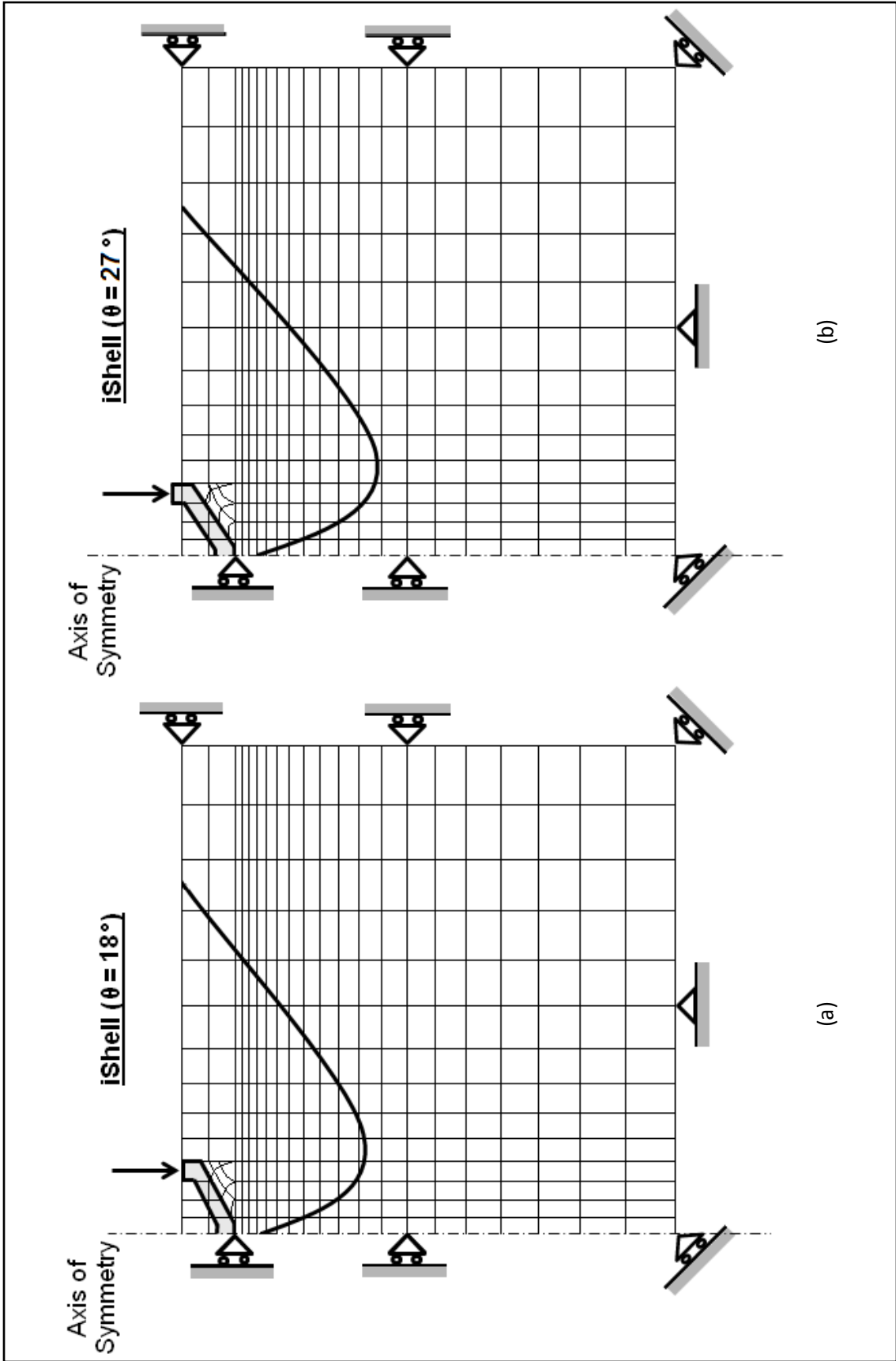


Figure 3.34. Finite Element Meshes for (a) Inverted Shell-iS2 (b) Inverted Shell Footing-iS3.

3.4.7 Summary of Results

Graphical plots of typical output results as those presented in Figures 3.10 – 3.34 helped establish plausible shapes for study in an experimental setting. The numerical results from the PLAXIS software were obtained in the form of plots from nodal elements utilizing the following parameters:

- Deformed meshes using 15-noded triangular elements with 12 stress points
- Displacement vectors using arrows (\rightarrow)
- Horizontal and vertical strains (ϵ_{xx} , ϵ_{yy})
- Horizontal and vertical stress (σ_{xx} , σ_{yy})
- Horizontal, Vertical and Total Displacements (Δ_{xx} , Δ_{yy} , Δ_{tot})

Generally, the figures show the footings displacement behaviour to be vertically downward with the underlying bearing soil being concentrated into a compression wedge in a triangular stress zone. Triangular wedges of high stress concentrations are typically located immediately beneath the footings. The flat shape has the shallowest wedge followed by the upright shell footing ($\theta = 34^\circ$) while the Sinusoidal and inverted shell models with shell angle ($\theta = 36^\circ$) having the steepest wedges. The rupture surface limits for the radial shear zones were also found to have penetrated at a greater depth for the inverted shells suggesting possibly higher bearing capacity threshold. As for horizontal and vertical strains, stresses and displacements the following tables are presented as sample output utilizing contour lines obtained from output report generation. In the case of inverted footings, the maximum negative strains were observed to occur at the edge beams. Positive horizontal strains were observed beyond the planar projection of the shells with highest values at the ground levels and immediately adjacent to the shells. The positive and negative strains were observed similarly to decrease with increasing soil depth with maximum values found at the edge beams of the shells. As one would expect, maximum horizontal displacements were observed at the edge beams of the shells. Overall, vertical soil displacements were in the positive upward directions outside the planar projection region of the shell while negative vertical movement downward was experienced by the shell and vertical soil column found within the limits of the edge beams.

Soil State	Footing		Contours for Model Shell Footings - Numerical Results				
	Model	Embedment Ratio (D/b)	A	B	C	D	E
Loose	Flat	0.75	-0.0387	-0.00411	-0.00123	0.00934	0.01833
	Upright	0.83	-0.0872	-0.00576	-0.00359	0.00273	0.02675
	Sinusoidal	0.82	-0.1134	-0.00845	-0.00429	0.00439	0.03212
	iShell18°	0.52	-0.0789	-0.00496	-0.00196	0.00334	0.02674
	iShell36°	0.61	-0.0953	-0.00693	-0.00385	0.00434	0.03958
Medium-Dense	Flat	0.75	-0.0443	-0.00463	-0.00137	0.00954	0.01839
	Upright	0.83	-0.0989	-0.00648	-0.00399	0.00279	0.02684
	Sinusoidal	0.82	-0.1299	-0.00951	-0.00477	0.00448	0.03223
	iShell18°	0.52	-0.0904	-0.00558	-0.00218	0.00341	0.02683
	iShell36°	0.61	-0.1091	-0.00779	-0.00428	0.00443	0.03972
Dense	Flat	0.75	-0.0518	-0.00520	-0.00148	0.00986	0.01890
	Upright	0.83	-0.1156	-0.00729	-0.00432	0.00288	0.02755
	Sinusoidal	0.82	-0.1479	-0.01069	-0.00517	0.00453	0.03318
	iShell18°	0.52	-0.1081	-0.00628	-0.00236	0.00352	0.02751
	iShell36°	0.61	-0.1292	-0.00876	-0.00464	0.00437	0.04804

Table 3.3. Horizontal Strain, ϵ_{xx} (m/m) for iShell Footing Models.

Soil State	Footing		Contours for Model Shell Footings - Numerical Results				
	Model	Embedment Ratio (D/b)	A	B	C	D	E
Loose	Flat	0.75	-0.01063	-0.00394	-0.001573	0.01046	0.02045
	Upright	0.83	-0.02396	-0.00575	-0.004626	0.00284	0.02982
	Sinusoidal	0.82	-0.03116	-0.00843	-0.005442	0.00452	0.03591
	iShell18°	0.52	-0.02094	-0.00495	-0.002478	0.00337	0.02978
	iShell36°	0.61	-0.02619	-0.00678	-0.004768	0.00442	0.00449
	Flat	0.75	-0.0222	-0.00444	-0.00175	0.01068	0.02052
Medium-Dense	Upright	0.83	-0.0275	-0.00647	-0.00514	0.00290	0.02992
	Sinusoidal	0.82	-0.1187	-0.00949	-0.00605	0.00462	0.03604
	iShell18°	0.52	-0.0240	-0.00558	-0.00276	0.00344	0.02988
	iShell36°	0.61	-0.0300	-0.00762	-0.00530	0.00452	0.00451
	Flat	0.75	-0.0259	-0.00499	-0.00189	0.01103	0.02109
	Upright	0.83	-0.0321	-0.00728	-0.00557	0.00299	0.02755
Dense	Sinusoidal	0.82	-0.1351	-0.01067	-0.00655	0.00461	0.03318
	iShell18°	0.52	-0.0287	-0.00627	-0.00298	0.00356	0.02751
	iShell36°	0.61	-0.0355	-0.00857	-0.00574	0.00426	0.04788

Table 3.4. Vertical Strain, ϵ_{yy} (m/m) for iShell Footing Models.

Soil State	Footing		Contours for Model Shell Footings - Numerical Results				
	Model	Embedment Ratio (D/b)	A	B	C	D	E
Loose	Flat	0.75	2.21	7.11	36.75	5.23	18.75
	Upright	0.83	2.36	8.17	37.54	6.01	21.54
	Sinusoidal	0.82	5.56	25.53	63.23	18.76	29.63
	iShell18°	0.52	3.97	14.28	41.93	10.50	37.64
	iShell36°	0.61	4.04	23.45	48.93	11.58	34.34
Medium-Dense	Flat	0.75	3.22	8.01	49.29	8.43	30.10
	Upright	0.83	3.44	9.20	48.13	10.72	34.58
	Sinusoidal	0.82	8.10	28.74	120.91	34.93	47.57
	iShell18°	0.52	5.79	16.08	61.56	13.46	37.68
	iShell36°	0.61	7.69	27.94	107.13	33.15	46.37
Dense	Flat	0.75	5.78	14.69	66.41	13.04	40.51
	Upright	0.83	6.17	16.88	64.85	16.68	46.54
	Sinusoidal	0.82	14.55	52.71	162.89	50.52	64.02
	iShell18°	0.52	10.39	29.50	82.94	22.14	44.63
	iShell36°	0.61	13.53	51.25	154.28	47.95	62.40

Table 3.5. Horizontal Stress, σ_{xx} (kPa) for iShell Footing Models.

Soil State	Footing		Contours for Model Shell Footings - Numerical Results				
	Model	Embedment Ratio (D/b)	A	B	C	D	E
Loose	Flat	0.75	5.26	16.93	87.46	12.44	44.62
	Upright	0.83	7.84	27.17	124.78	19.97	71.59
	Sinusoidal	0.82	18.79	86.28	213.70	63.42	139.34
	iShell18°	0.52	7.26	26.12	76.69	19.20	68.85
	iShell36°	0.61	16.08	84.14	212.21	46.09	138.62
Medium-Dense	Flat	0.75	12.35	39.76	205.37	29.22	104.78
	Upright	0.83	18.92	63.80	293.01	46.89	168.13
	Sinusoidal	0.82	44.13	202.62	501.84	148.92	327.21
	iShell18°	0.52	15.68	61.35	180.10	45.09	161.67
	iShell36°	0.61	37.76	197.59	498.34	108.22	325.52
Dense	Flat	0.75	21.56	69.40	358.47	51.00	182.89
	Upright	0.83	22.11	74.54	342.35	54.78	196.43
	Sinusoidal	0.82	72.58	333.28	624.44	244.95	438.22
	iShell18°	0.52	8.96	32.22	94.60	23.68	84.92
	iShell36°	0.61	70.10	308.28	622.54	243.19	426.84

Table 3.6. Vertical Stress, σ_{yy} (kPa) for iShell Footing Models.

Soil State	Footing		Contours for Model Shell Footings - Numerical Results				
	Model	Embedment Ratio (D/b)	A	B	C	D	E
Loose	Flat	0.75	-0.00277	-0.00411	-0.00123	0.00093	0.00183
	Upright	0.83	-0.00607	-0.00576	-0.00359	0.00027	0.00268
	Sinusoidal	0.82	-0.00810	-0.00845	-0.00429	0.00044	0.00321
	iShell18°	0.52	-0.00485	-0.00496	-0.00196	0.00033	0.00267
	iShell36°	0.61	-0.00652	-0.00693	-0.00385	0.00043	0.00396
Medium-Dense	Flat	0.75	-0.0045	-0.0068	-0.0020	0.0015	0.0030
	Upright	0.83	-0.0100	-0.0095	-0.0059	0.0004	0.0044
	Sinusoidal	0.82	-0.0133	-0.0139	-0.0070	0.0007	0.0053
	iShell18°	0.52	-0.0080	-0.0081	-0.0032	0.0005	0.0044
	iShell36°	0.61	-0.0107	-0.0114	-0.0063	0.0007	0.0065
Dense	Flat	0.75	-0.0065	-0.0096	-0.0029	0.0022	0.0043
	Upright	0.83	-0.0141	-0.0134	-0.0083	0.0006	0.0062
	Sinusoidal	0.82	-0.0193	-0.0202	-0.0102	0.0010	0.0077
	iShell18°	0.52	-0.0112	-0.0114	-0.0045	0.0008	0.0062
	iShell36°	0.61	-0.0154	-0.0164	-0.0091	0.0010	0.0094

Table 3.7. Horizontal Displacements, Δx (m) for iShell Footing Models.

Soil State	Footing		Contours for Model Shell Footings - Numerical Results				
	Model	Embedment Ratio (D/b)	A	B	C	D	E
Loose	Flat	0.75	-0.0135	-0.00411	-0.000445	-0.000392	-0.000362
	Upright	0.83	-0.0872	-0.00576	-0.000354	-0.000342	-0.000316
	Sinusoidal	0.82	-0.1898	-0.00845	-0.000414	-0.000382	-0.000353
	iShell18°	0.52	-0.0165	-0.00496	-0.000175	-0.000169	-0.000156
	iShell36°	0.61	-0.0174	-0.00693	-0.000291	-0.000273	-0.000252
Medium-Dense	Flat	0.75	-0.019755	-0.006019	-0.000651	-0.000574	-0.000530
	Upright	0.83	-0.126822	-0.008377	-0.000515	-0.000497	-0.000460
	Sinusoidal	0.82	-0.281736	-0.012543	-0.000615	-0.000567	-0.000524
	iShell18°	0.52	-0.023380	-0.007015	-0.000247	-0.000239	-0.000221
	iShell36°	0.61	-0.025457	-0.010148	-0.000426	-0.000400	-0.000369
Dense	Flat	0.75	-0.022632	-0.006895	-0.000746	-0.000658	-0.000608
	Upright	0.83	-0.144029	-0.009514	-0.000584	-0.000565	-0.000522
	Sinusoidal	0.82	-0.325534	-0.014493	-0.000710	-0.000655	-0.000605
	iShell18°	0.52	-0.026225	-0.007869	-0.000277	-0.000268	-0.000248
	iShell36°	0.61	-0.029132	-0.011613	-0.000487	-0.000457	-0.000423

Table 3.8. Vertical Displacements, Δy (m) for iShell Footing Models.

3.5 Non-linear 3D Finite Element Analysis

There are numerous geotechnical problems that can be solved using numerical methods. The solutions are thereby approximated using either plane-strain or axisymmetric conditions. A fair portion of problems in modeling geotechnical hurdles are three dimensional and so the appropriateness of computer simulations generating solutions in a full three dimensional numerical platform. An extension of the 2D analysis, is a 3D attempt made for upright and inverted pyramidal shell.

This section presents the soil-structure interaction of 3D shell foundations under concentric static axial load in the finite element analysis. The applicability was first validated using the model test data presented earlier. The flat, upright and inverted shell orientation have been used to simulate settlement and stress distributions below the shell footings at two separate distances from the vertex of the shell footings. These parameters have been obtained and are used to verify the uniformity distribution represented by stress variation beneath the models. Comparisons were drawn between the six models at variable shell angles between 18 and 36 degrees as well as a Sinusoidal model. These newly proposed iShells were then presented in contrast with the upright and traditional planar footings used previously which have shown notable performance results.

3.5.1 Discretization and Validation of FE Shell Models

The finite element models proposed were validated in the context of ultimate bearing capacity failure of the shells. The models were tested in plane-strain as well as 3D case for dimensional proportionality and to shed insight on influence of performance based on shell shape factor F_{sq} , F_{sy} considerations.

The initial axial compressive load of 0.2 kN applied directly to the loading yoke transferred forces to the edges beams at the toe of the shells. The load was incrementally applied at uniform rate of 0.15 kN/sec for several minutes. During that time forces are transferred from the edge-beams to the shell proper elements and finally converging towards the apex of the inverted shell. All the while, this load transferral induces stress at

the soil–structure contact surface developing the resulting contact pressure as reaction to the applied load. The load was carefully increased at a gradual rate till deformations of the soil began and climaxed with resulting soil rupture surface as theorized.

3.5.1.1 Pyramidal Shell Footing – 3D Model

The discretization of the pyramidal shell footing and the soil medium included the use of 20–nodded isoperimetric finite element quadrants throughout the mesh simulation as depicted in Figures 3.35, 3.36 and 3.37. The incremental loading technique was used for the nonlinear analysis of the soil–shell system with more than 10 variable load increments applied. During each load increment, up to 20 iterations were required to achieve convergence during the nonlinearity response of the soil–shell footing system. The load was applied incrementally from 0.5 kN up to 8 kN at 0.02 kN intervals.

The axial load versus deflection profile is obtained experimentally coupled with the FE model of the upright pyramidal shell footing. The soil properties used in either test are presented in Table 3.9 followed by the shell footing graphical behavioural plot in Figure 3.40. Throughout the elastic–linear stage, it has been observed that the two results are well correlated exhibiting favourable similarity. The FE model displacement values were found to overlap experimental values with discrepancies between the two being negligible. However, through the non–linear stage, the numerical model displayed deflection values 10 – 15% higher than the experimental results. This difference may be due to the scaling factor employed in the lab during testing as well as soil preparation methods which may have affected specimen alignment during the loading phase. Lastly, the fact that finite element results generally employ controlled soil variables and other constants, these may be influenced somewhat in the laboratory setting. One example is that of soil density. While it is customary to simulate proper soil density, time delays associated with setup and test runs have impact on soil parameters whereas these are considered constant in a numerical analysis run.

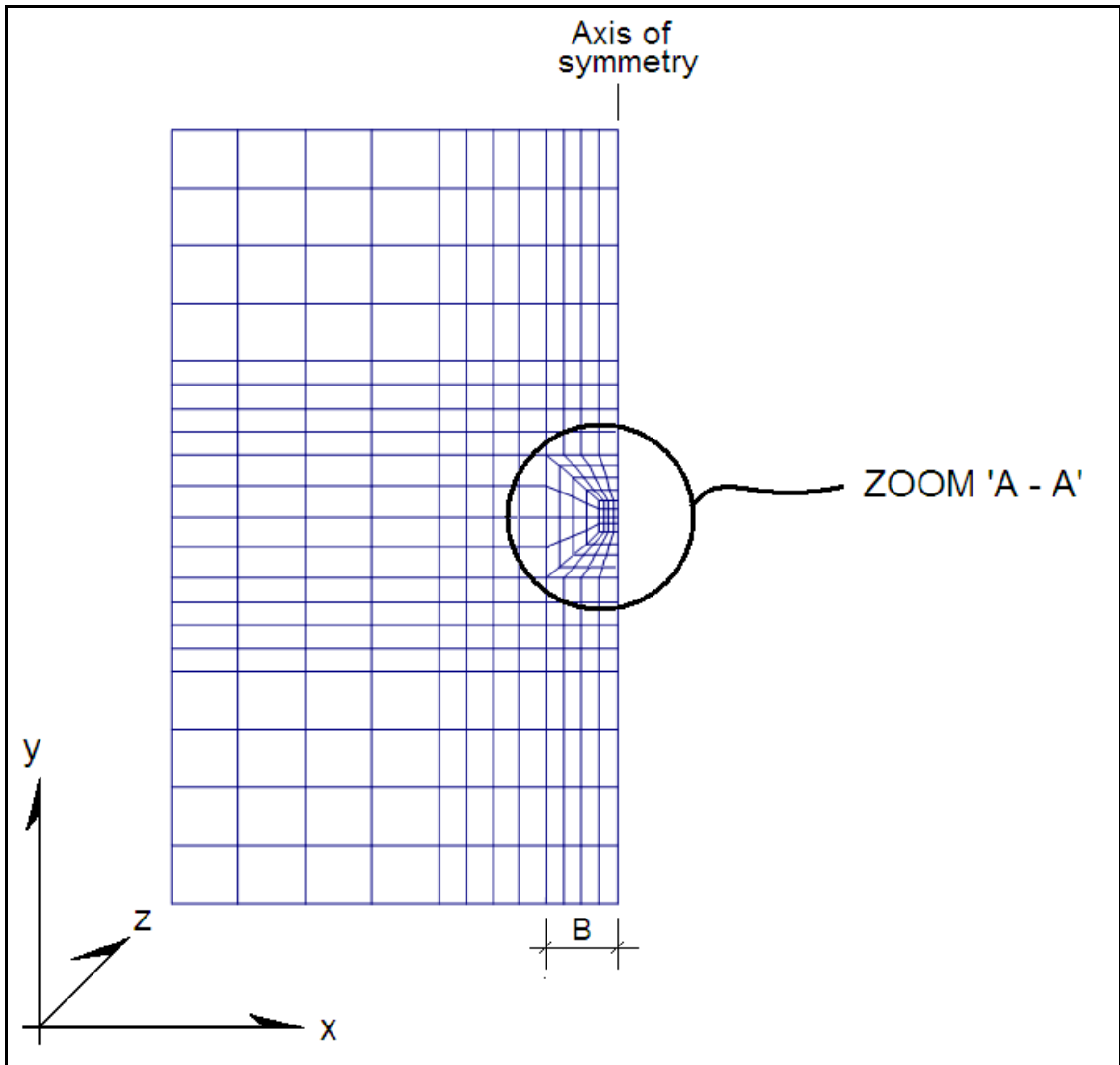


Figure 3.35. FE Model of Upright Pyramidal Shell – Plan View.

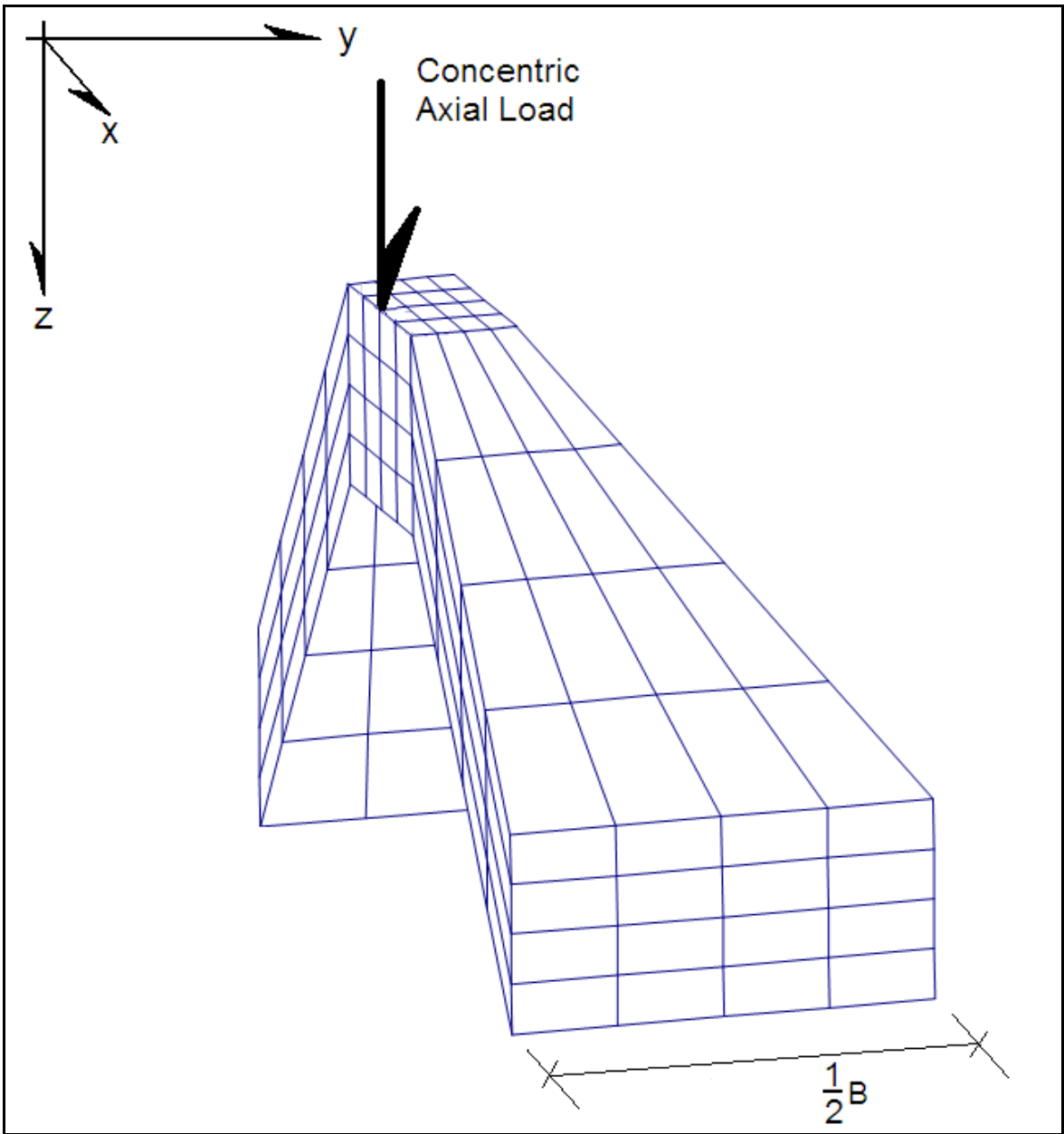


Figure 3.36. FE Model of Upright Pyramidal Shell – Zoomed View ‘A – A’.

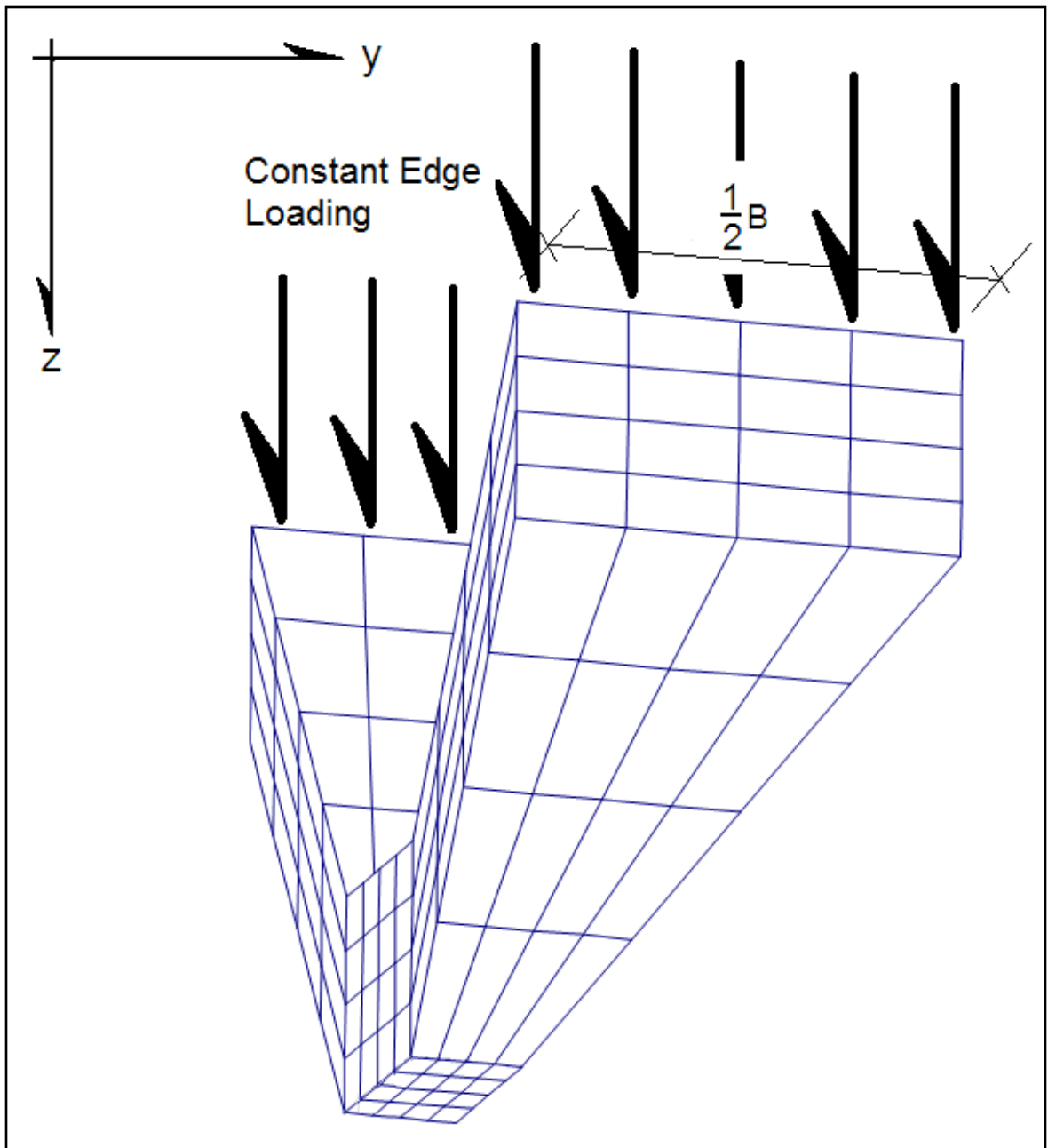


Figure 3.37. FE Model of Inverted Pyramidal Shell – Zoomed View 'A – A'.

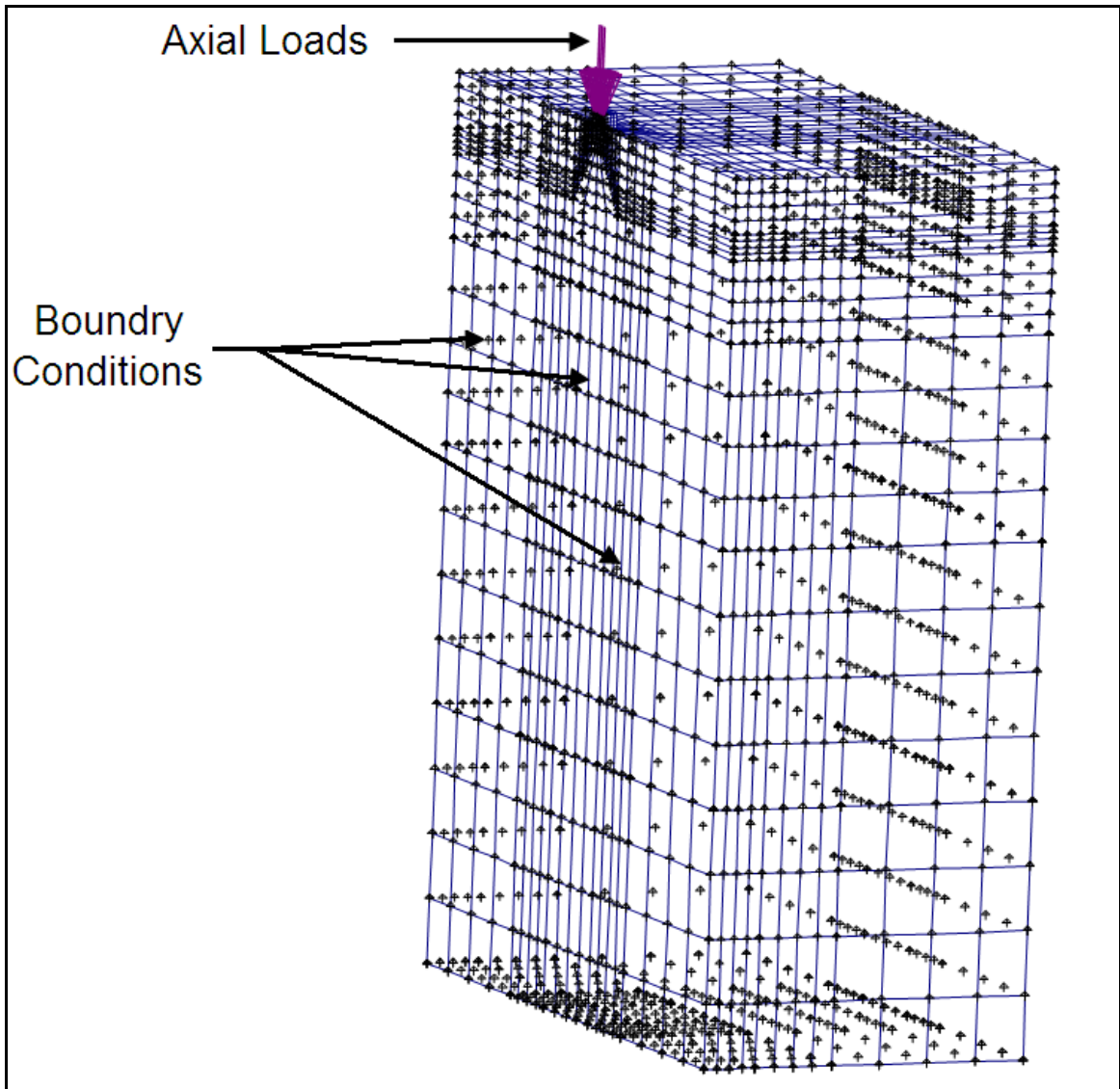


Figure 3.38. FE Model of Upright Pyramidal Shell with Soil Media.

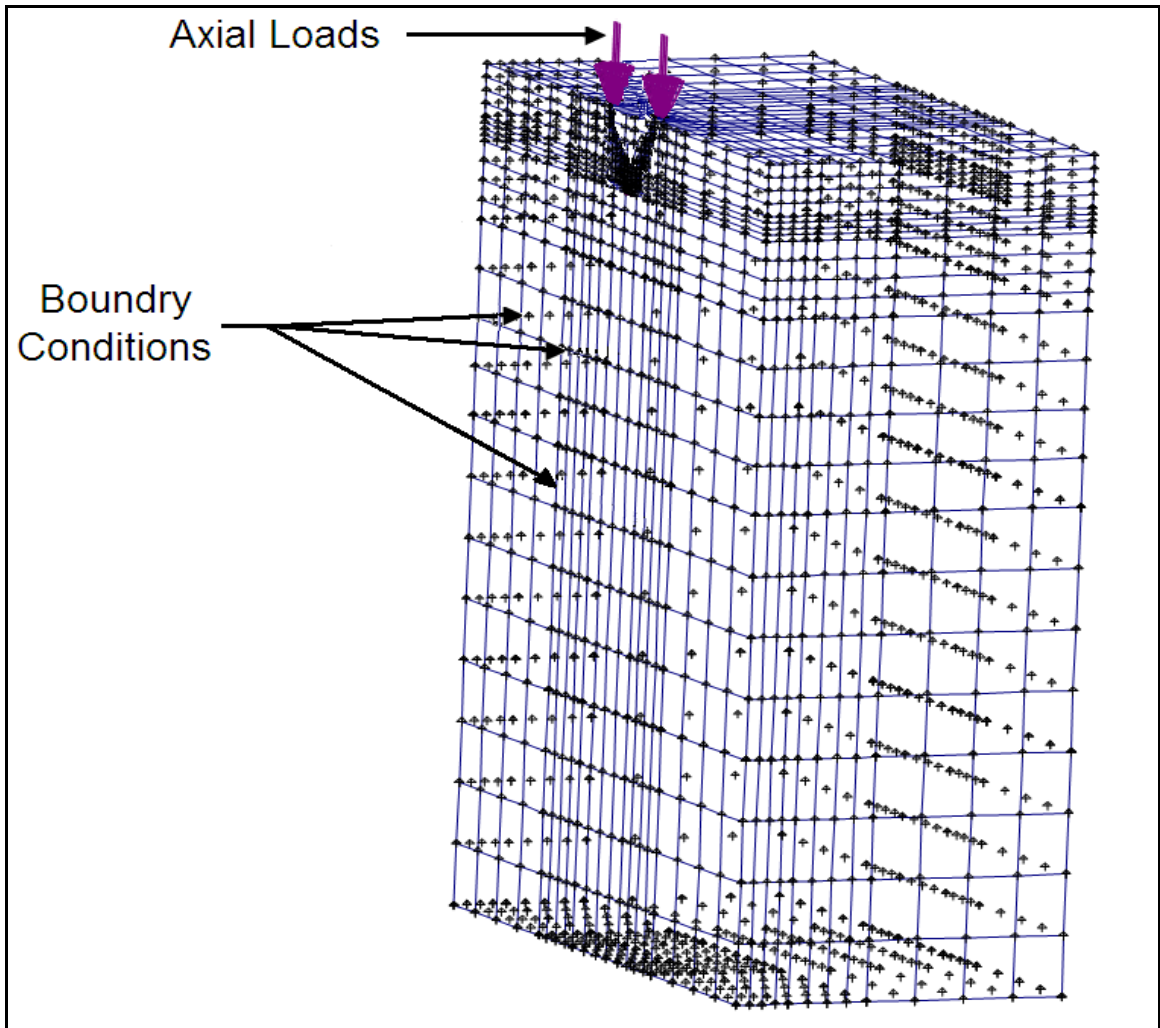


Figure 3.39. FE Model of Inverted Pyramidal Shell with Soil Media.

Property	Symbol	Value
Dry unit weight, (kN/m ³)	γ_d	16.25
Relative density, (%)	D_r	28.32
Angle of shearing resistance, (°)	ϕ	30.25
Cohesion, (kPa)	c	0.20
Angle of Dilatancy, (°)	ψ	2.0
Poisson's ratio	ν	0.30
Soil Elasticity Modulus, (N/mm ²)	E_s	50.2
Concrete Elasticity Modulus, (N/mm ²)	E_{shell}	206×10^3

Table 3.9. Soil Media Properties for 3D Models.

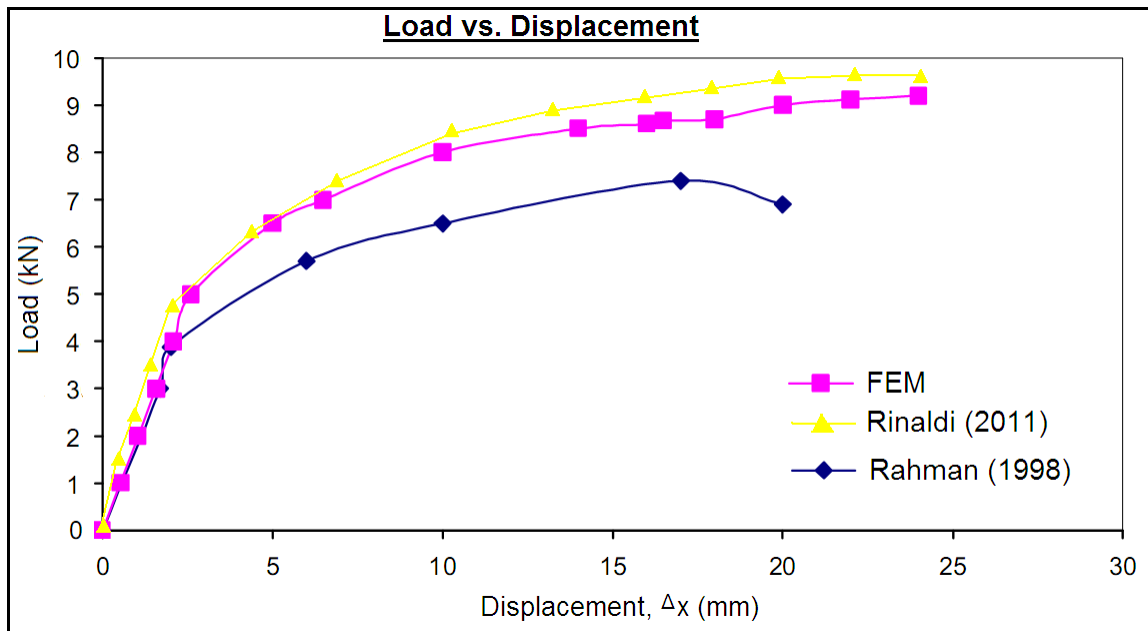


Figure 3.40. Load vs. Displacement for Upright and iShell Pyramidal Footings.

3.5.1.2 Triangular Strip Footing

The discretization of the upright and inverted shell footings for the triangular orientation are presented in Figures 3.41 and 3.42. Therein 20-nodded isoperimetric finite elements were used throughout the mesh generation. Incremental loading was applied for non-linear analysis of the soil-shell system with more the six variable load increments. As before, each increment was composed of 30 iterations for convergence for elasto-plastic soil behaviour modeled with the respective shell footing. The incremental load ranges between 0.5 kN upto 60 kN in 0.25 kN increments. Similar to the pyramidal case, the findings indicate good correlation between at the outset with 10 – 15 % deviation in the later stages of loading. The discrepancies generated mostly to scaling effects and human error in soil placement in the lab.

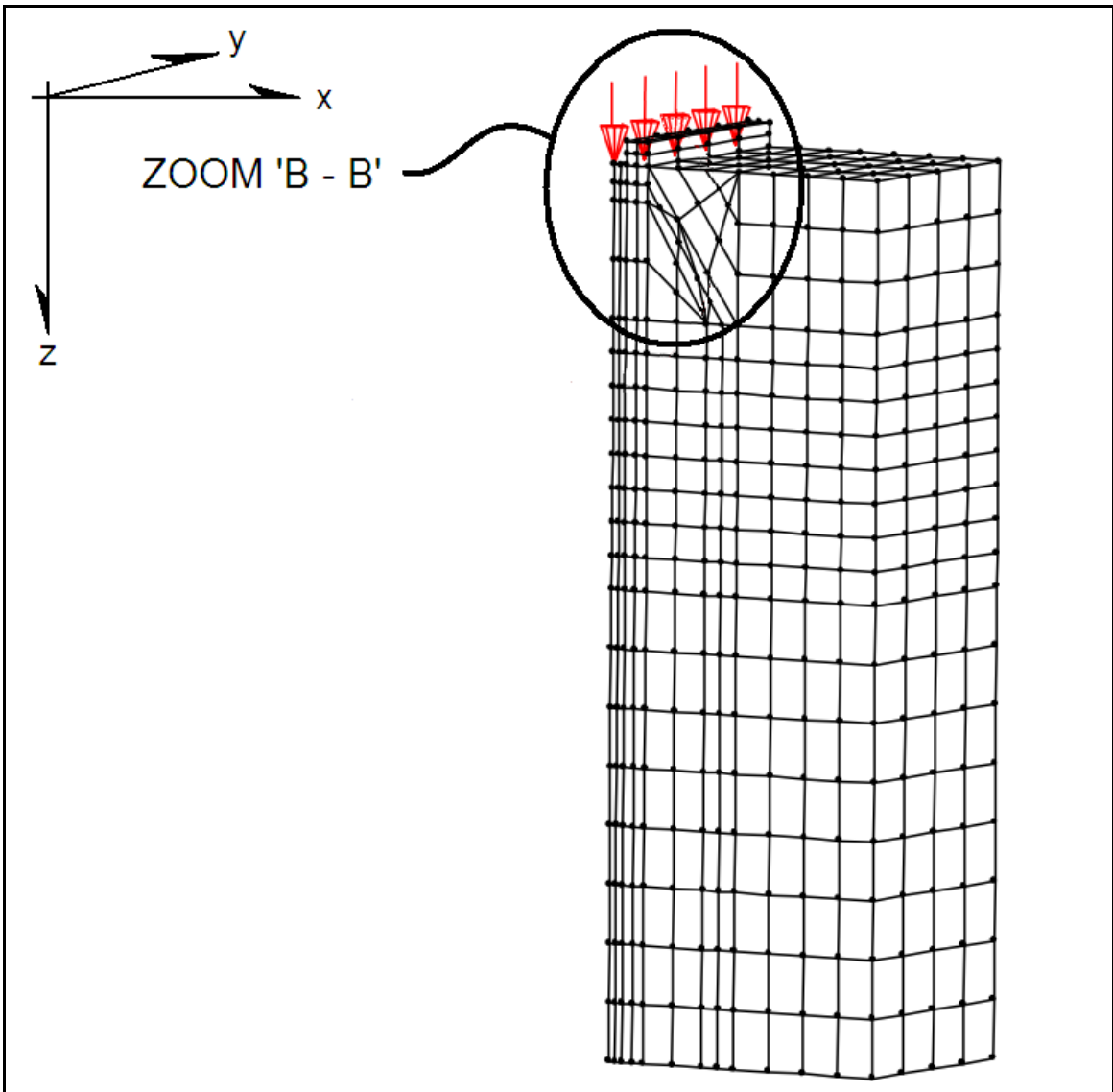


Figure 3.41. FEM 3D Discretization of Strip Shell and Soil Media.

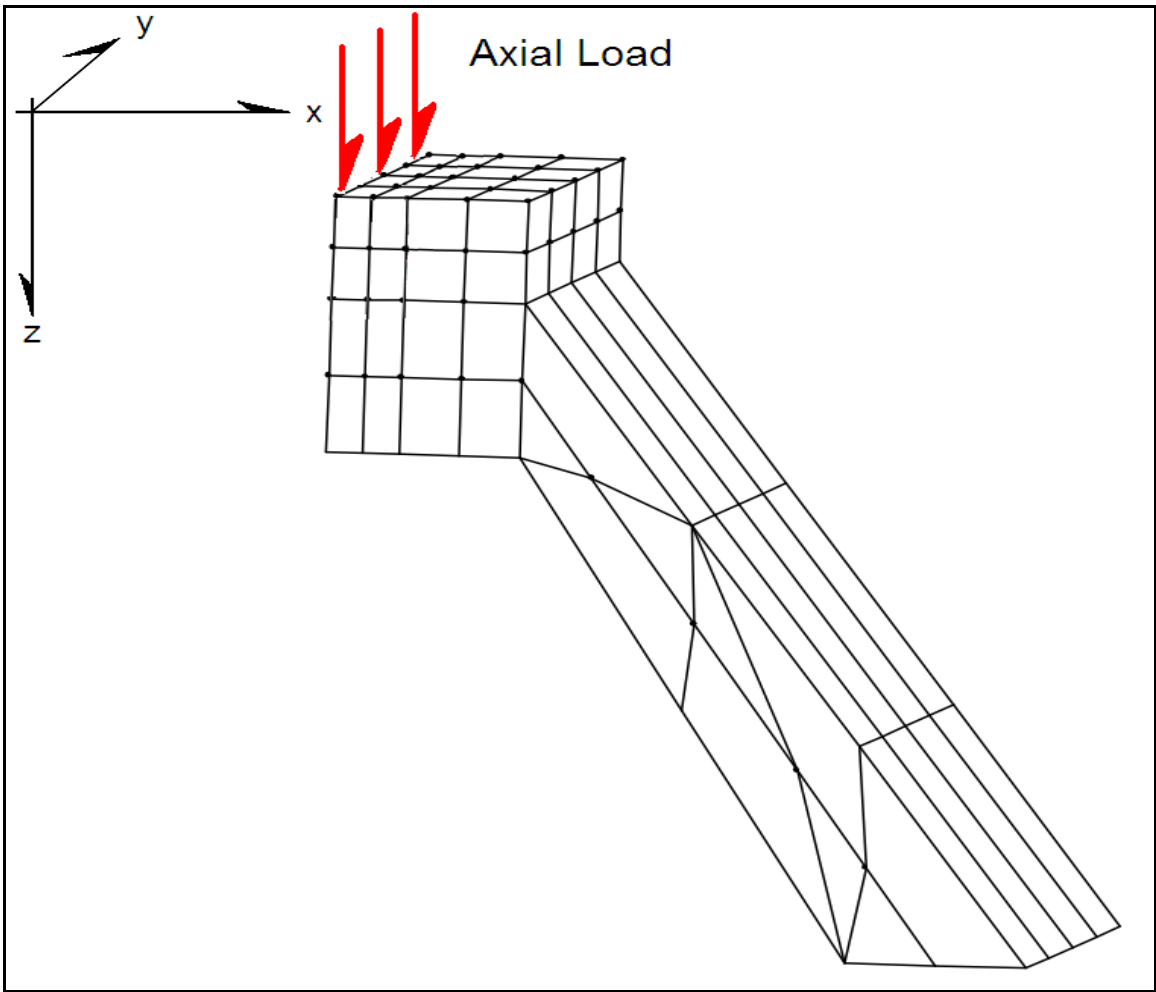


Figure 3.42. FEM 3D Discretization of Upright Triangular Strip Shell.

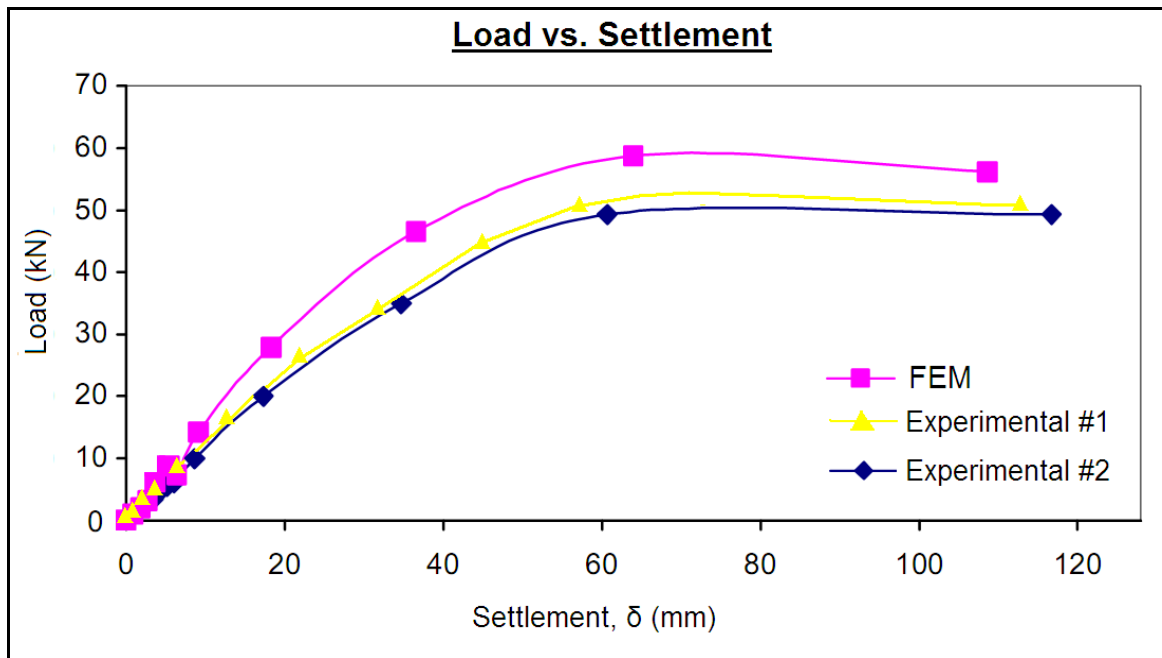


Figure 3.43. Load vs. Settlement for Upright and iShell Triangular Strip Footings.

3.5.2 Inverted Shell Triangular Strip Footing Models

The profile obtained in the experimental phase is plotted as load versus settlement for the inverted shell model. The soil media properties being constant as tabulate in Table 3.1. Two experimental tests were conducted offering almost similar results and correlating well with the finite element model tested. Here the load was induced incrementally from 0.5 kN upto 50 kN at 0.25 kN intervals. The footing and soil media discretization of the mesh was composed of 20-nodded isoperimetric finite elements. The soil-shell system had 8 variable load increments and 5 iterations were required in achieving convergence. Discrepancies between all three tests range between 5 – 10 % error due perhaps to soil placement activity accounting for discrepancies in the unit weight of soil. As well human factors, such as loading and measurement readings may have resulted in deviations.

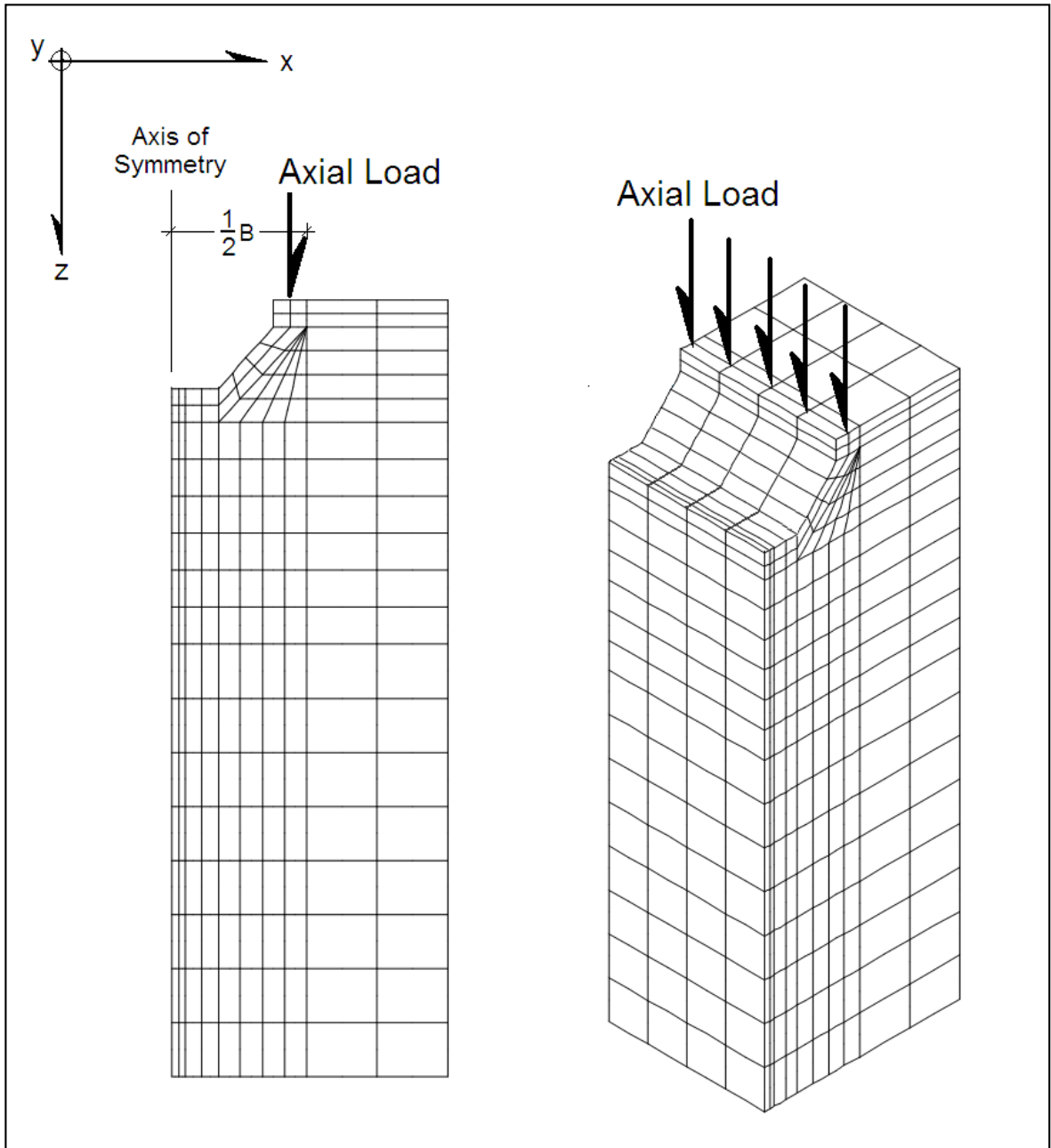


Figure 3.44. Elevation and Isometric FE iShell Triangular Model.

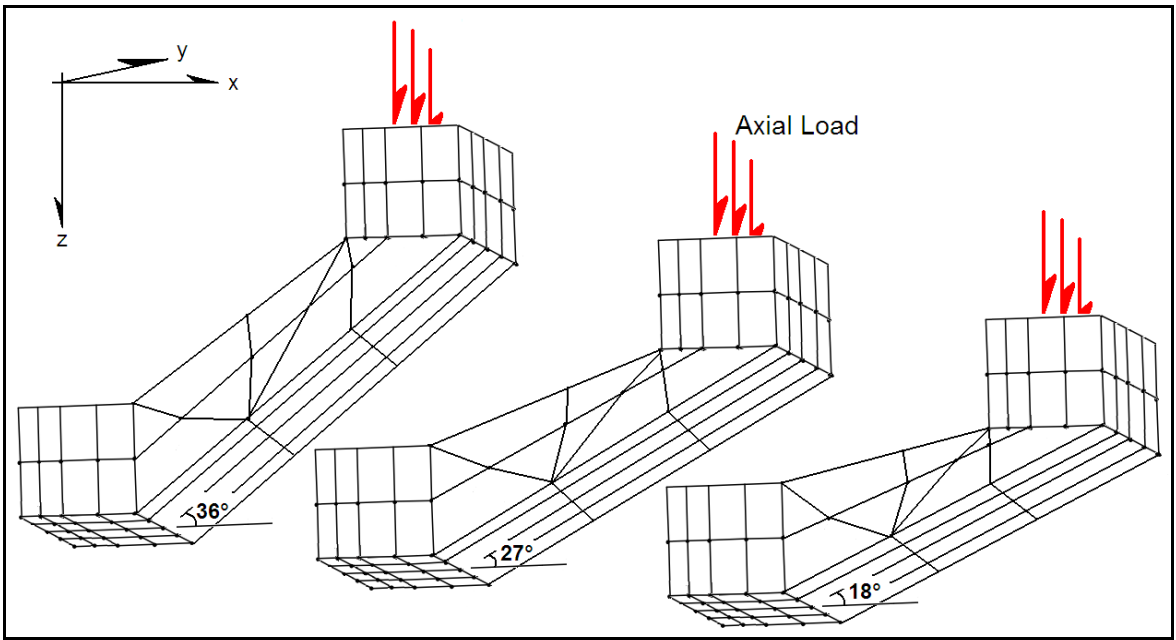


Figure 3.45. iShell FE Isometrics of Shell Footing Models.

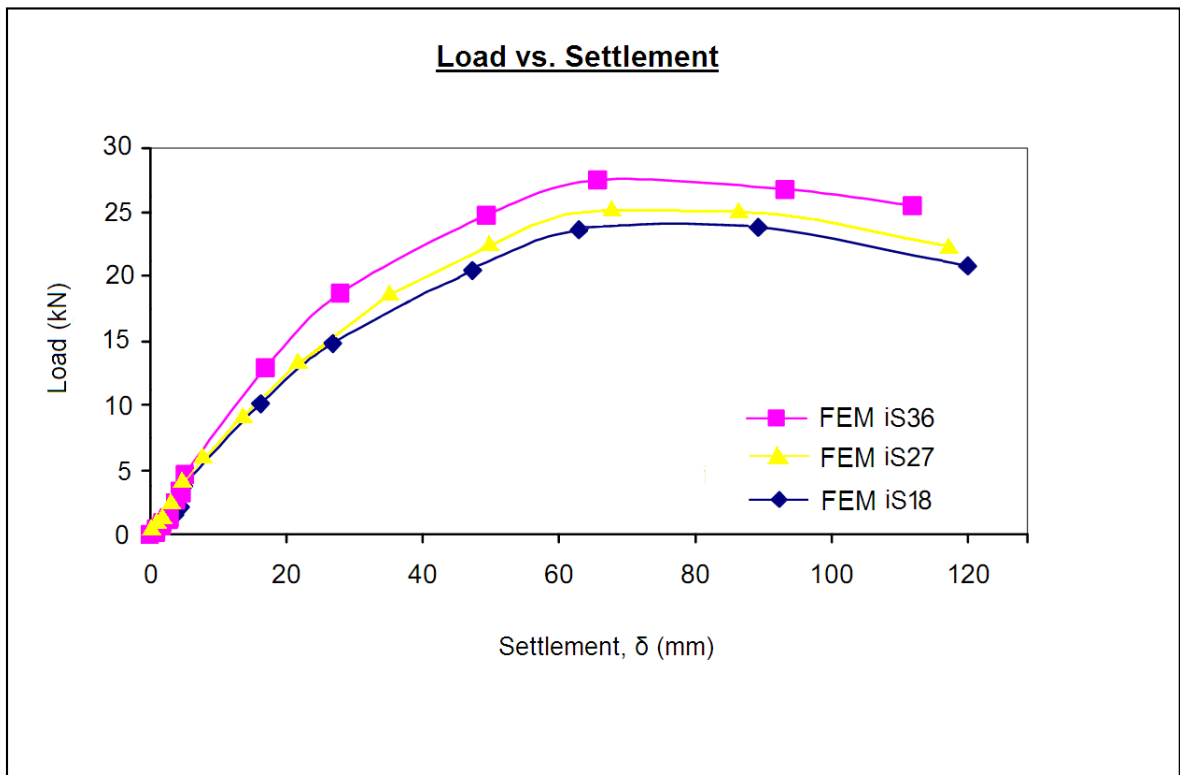


Figure 3.46. Load vs Settlement – iShell Triangular Strip Footings.

3.5.3 iShell Footing Performance

In this section, the performance of the upright and inverted triangular shell footings are presented including load–settlement stress distributions, concentrated core stress below the center of the footings as well as end and edge stress at the toe of the shells. Figure 3.47 shows the FE model discretization for both orientation scenarios.

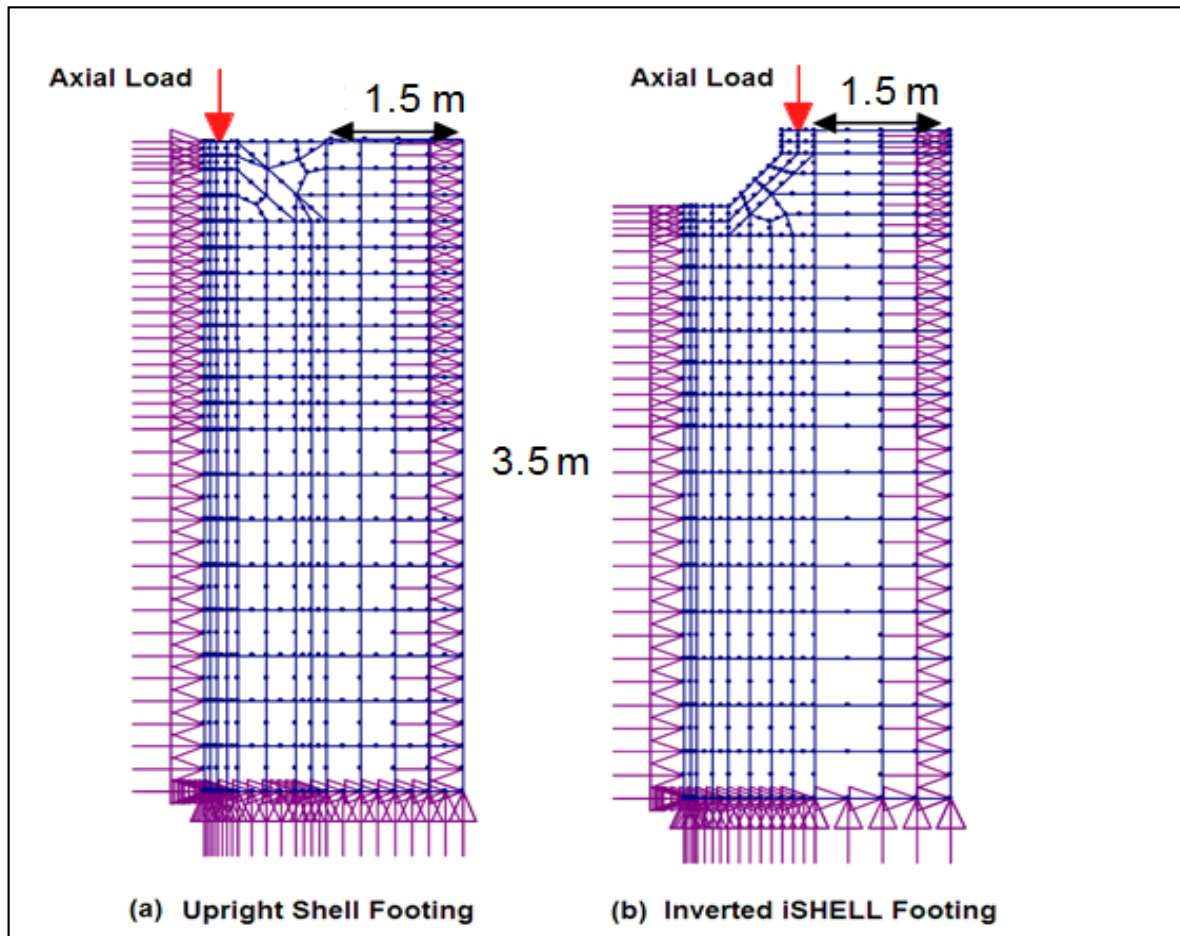


Figure 3.47. Upright vs. Inverted Shell Model Discretization.

The distribution observed in the load–settlement curve for the upright and inverted shell footings is shown in Figure 3.48. It can be noted that the load carry capacity of the inverted shell case are in the order of 22 – 35% higher than that of the upright shell case as typically found previously from PLAXIS output from load–settlement curves.

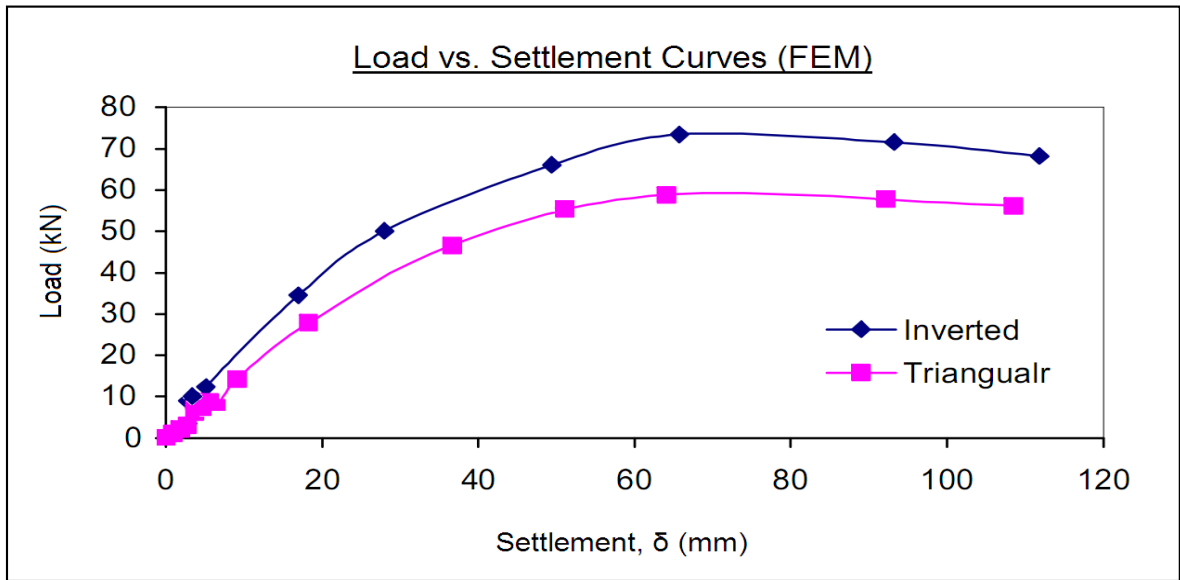


Figure 3.48. FEM Results – iShell 36° vs. Upright Triangular Shell Model.

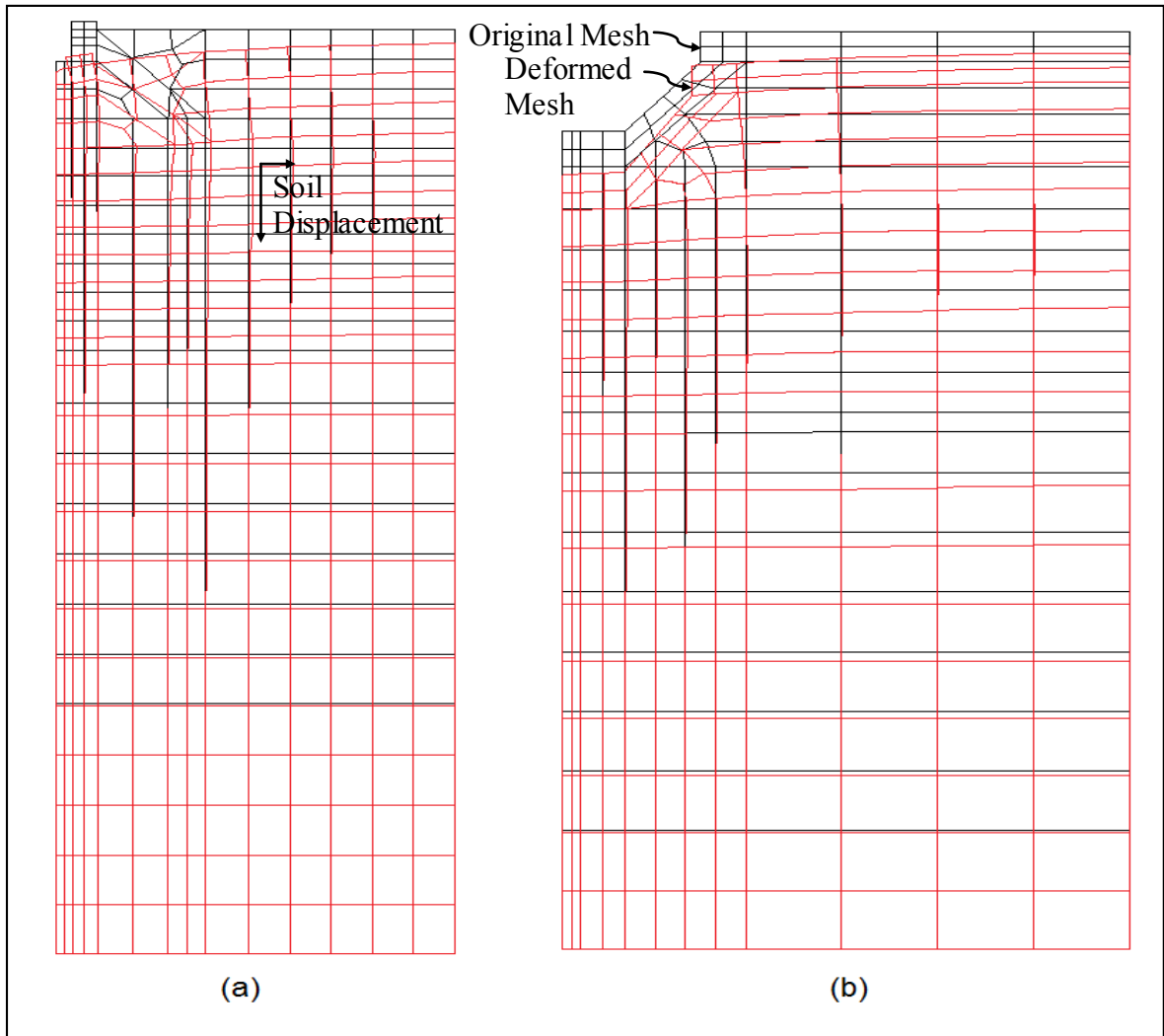


Figure 3.49. Mesh Deformation: (a) Upright (b) iShell Footing Models.

Displacement variation and distributions with respect to depth for the upright and inverted shells demonstrate settlement decreasing with increasing vertical depth. The maximum vertical settlement was observed in vertical alignment with the apex of the shells towards the center of the soil mass corresponding to center of shell footings.

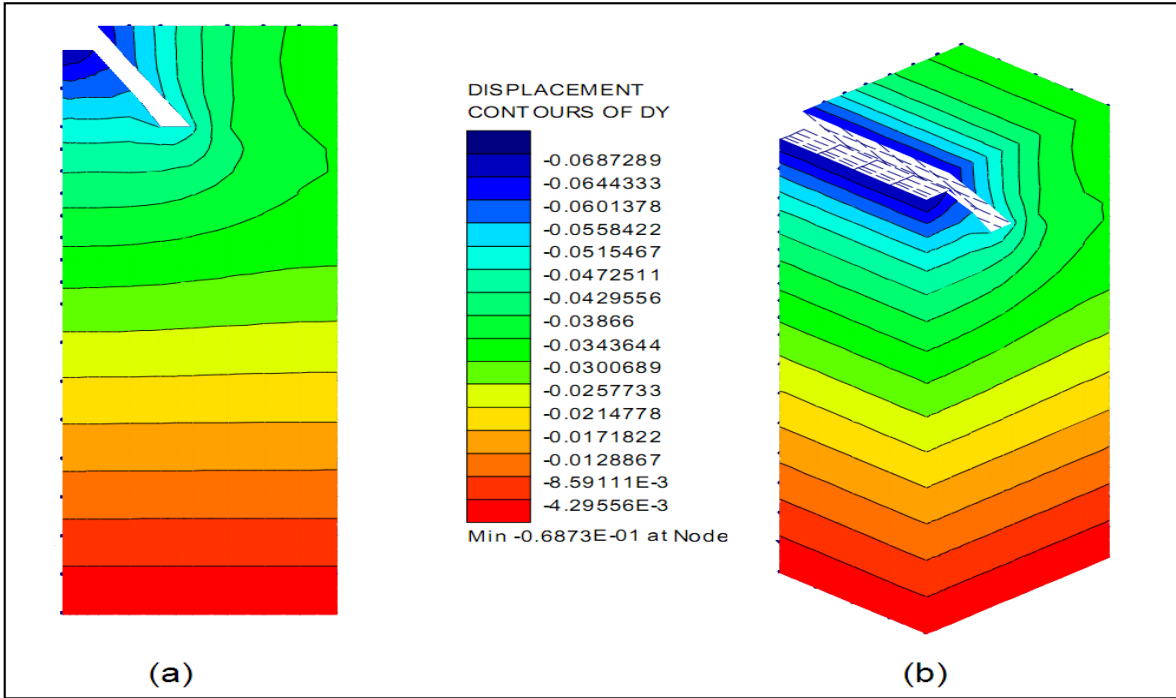


Figure 3.50. Displacement Contours – Upright Shell 36° (a) Elevation (b) Isometric View.

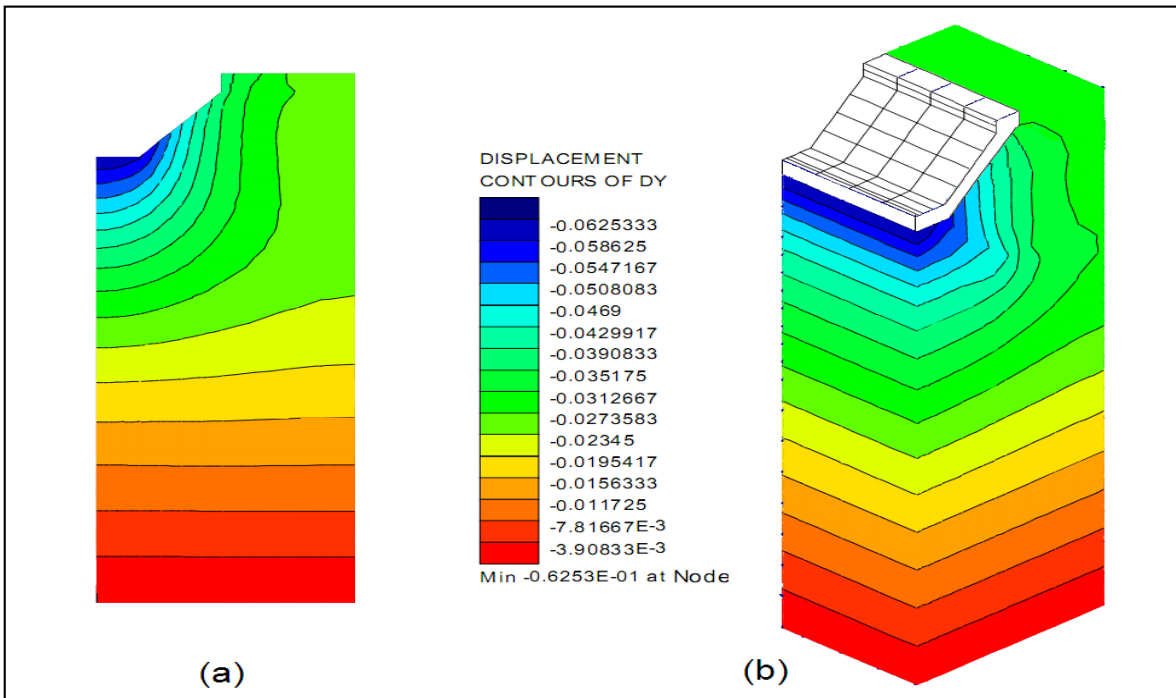


Figure 3.51. Displacement Contours – iShell 36° (a) Elevation (b) Isometric View.

3.6 Parametric Study

Understanding relationships between structural shell parameters and soil parameters and how their shapes influence load carrying capacity provides insight into their behaviour. At this point, intuitively from a soil perspective, the angle of friction, ϕ (ϕ) is independent of soil cohesion, (c), however, does depend on the angle of dilation, ψ (ψ) which in turn depends on the density, (γ_s), and soil pressures such as those of water inclusion for instance. Since soil in the shell footing interaction problem is assumed to be dilating, it therefore has effect on the solution to the problem. This is particularly true for heavily constrained soils such as those found beneath flat and upright shells. It would seem of lesser importance (except for its effect on strength) in the inverted shell case however as these shells seemingly cut into the soil media as opposed to confining it.

Nonetheless, the soil parameters implemented account for the $c - \phi - \psi$ variability of the sand for both the upright shell and the inverted shell as explored in the foregoing section of the numerical analysis. Their arbitrary use at the outset served as starting point for this investigation where variables assigned were based on common values extrapolated from literature. As a concluding remark, this framework provides a better appreciation for the next set of variables introduced in the study, those offered by the shell fin component. The soil parameters are now imposed and maintained constant for the present shell analysis where typical values are those found in Table 3.3. Upon observation, there is a relatively large number of influencing geometric parameters that come into play such as width of shell footing, embedment depth, shell thickness variability and the shell angle. Thus, as far as geometric proprietary elements of the shell is concerned, the two variables retained for closer investigation in this parametric study are those of shell thickness, (t_s), of 19 mm [3/4 in.] and 25 mm [1 in.] and shell angle, (θ) varying between 18° and 36°. The results obtained are scrutinized from load–settlement charts from Table 3.10 and Figures 3.52 – 3.55 as follows.

Footing Models	Upright Shell	Inverted Shells					
		iShell1	iShell2	iShell3	iShell4	iShell5	iShell6
Parameter	Shell Thickness, t_s (mm) / Settlement, δ (mm)						
Load (kN)	25	19	19	19	25	25	25
0	0.00	0.00	0.00	0.00	0.00	0.00	0.00
5	2.95	4.61	4.09	3.91	3.76	3.68	3.07
10	7.19	8.72	7.49	7.60	7.73	7.61	6.73
15	11.86	14.28	12.34	12.25	12.47	11.78	10.49
20	17.69	20.24	17.66	18.16	17.72	16.52	15.27
25	23.73	27.13	22.64	23.45	22.79	21.52	20.38
30	30.23	34.42	29.65	29.81	29.38	27.88	26.23
35	37.61	42.24	36.45	36.59	36.62	34.42	32.59
40	45.12	50.21	44.32	43.76	43.11	41.59	39.43
45	52.76	59.45	53.22	52.42	50.92	48.74	46.84
50	60.94	69.27	63.04	61.29	59.18	57.07	54.25
55	70.45	79.92	72.84	70.02	67.33	64.91	62.14
60	79.83	91.48	82.82	79.54	76.21	73.26	71.08
65	89.98	104.36	95.19	90.63	86.03	82.79	79.77
70	100.04	117.24	106.34	101.30	96.29	92.48	89.91
75	111.34	130.59	119.75	113.25	106.77	103.75	100.38
80	124.45	143.92	132.79	125.76	118.62	115.61	112.59
85	137.22	157.85	144.81	138.27	131.79	128.38	124.12
90	153.55	171.45	158.84	152.98	146.11	141.86	136.63

Table 3.10. Load–Settlement Results for Variable Shell Thickness.

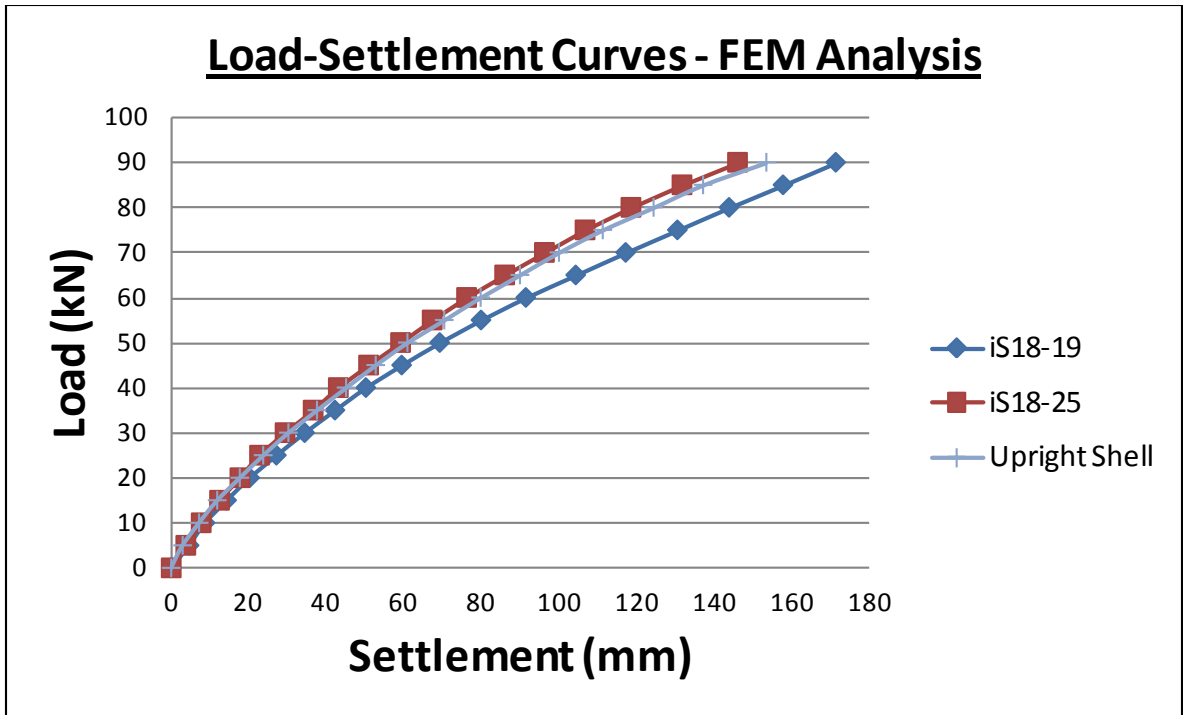


Figure 3.52. Effect of Shell Thickness (t_s) on Load-Carrying Capacity.

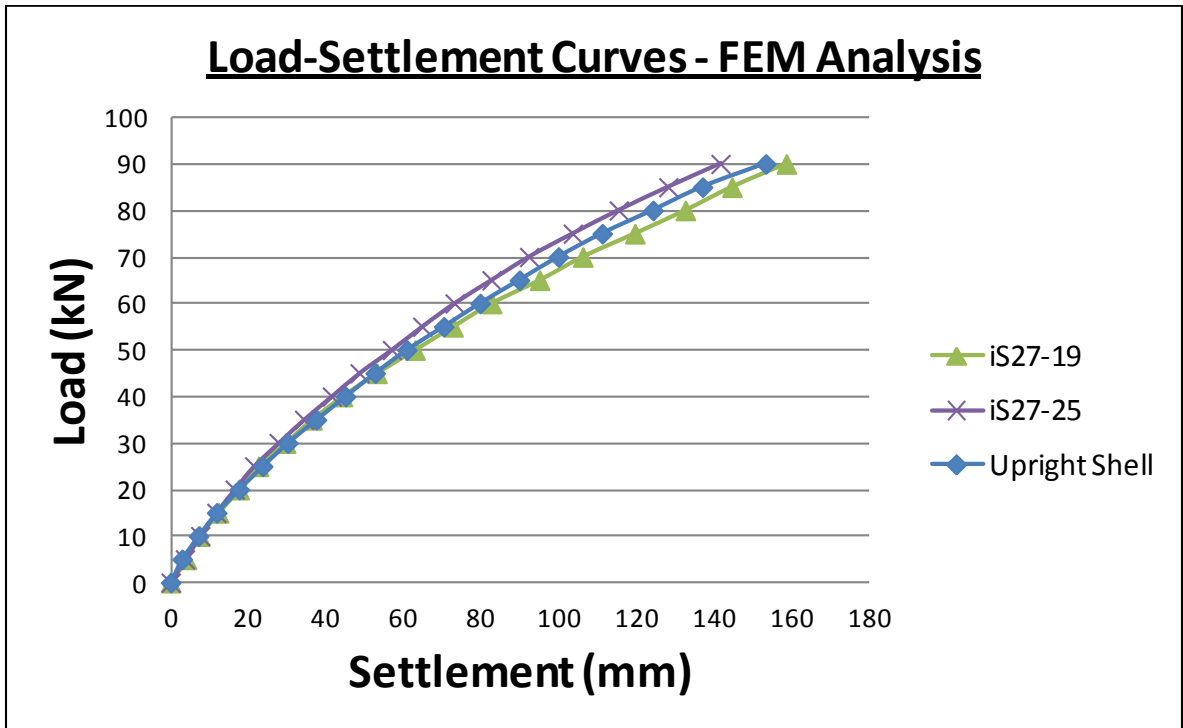


Figure 3.53. Effect of Shell Thickness (t_s) on Load-Carrying Capacity.

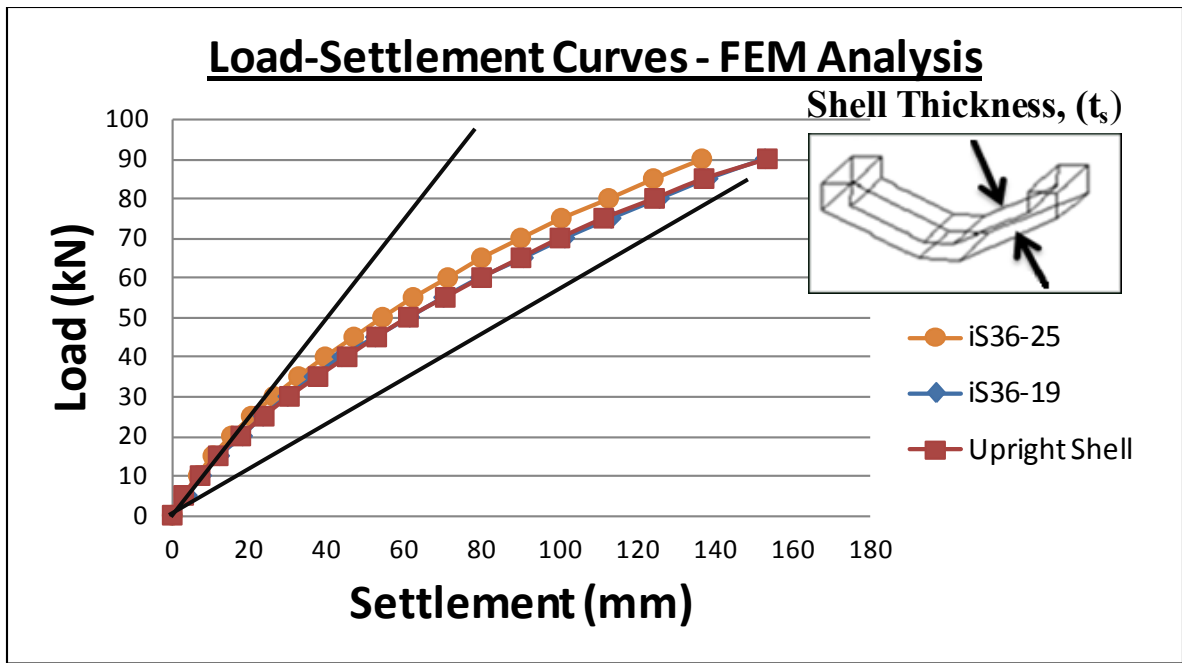


Figure 3.54. Effect of Shell Thickness (t_s) on Load-Carrying Capacity.

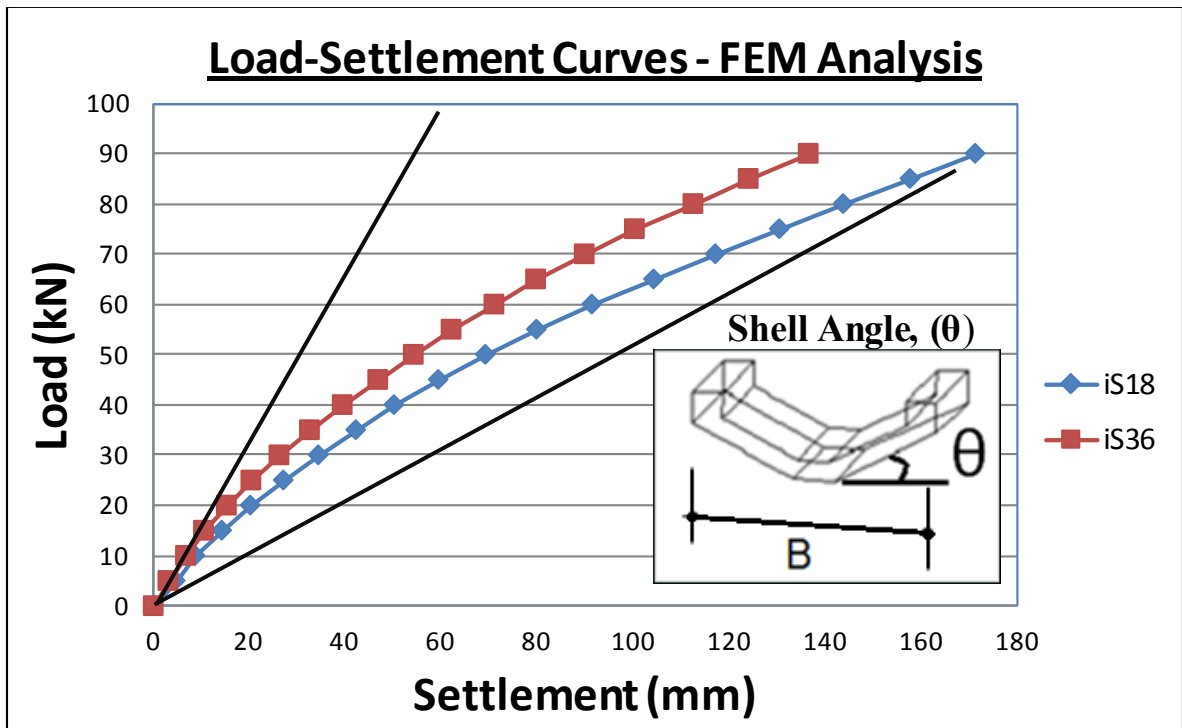


Figure 3.55. Effect of Shell Angle (θ) on Load-Carrying Capacity.

3.7 Summary of Results

A study of the geotechnical behaviour of shell footings was conducted using PLAXIS software employing non-linear finite element analysis. The program uses an incremental tangent stiffness approach in the analysis, in which the load is divided into a number of small increments, which are applied simultaneously. For each load increment, the appropriate properties of stiffness for the current stress level are employed in the numerical analysis. Experimental work was used in comparison to validate the finite element modeling of the current numerical study. From the finite element results, in terms of load-settlement behaviour, the numerical analysis revealed typically higher results as compared to the experimental findings, the details of which are explained.

The inverted shells demonstrated higher load carrying capacity for increasing shell angle with $\theta = 36^\circ$ having best performance of the three tested in the group and as presented in the figures. Overall, in terms of numerical analysis only, the iShells showed just over 14% improved load-settlement characteristics for the same soil conditions. Important to note is the similarity in response between the two orientations for similar loading pattern. Their behaviour is seen to be synonymous which is basis for confirmation that the results are found to be in good agreement between tests. As for the pyramidal iShell footings, they demonstrate a 15 – 20% increase in load-carrying capacity over the upright type particularly in the elastic range and a 10 – 13% increase in the ultimate stages. One can conclude, that for similar planar surface area, breadth of footing and footing angle for same soil conditions, the inverted shell footings offered better load-carrying capacity as compared to the upright shells.

From the parametric study, for same planar sectional area of footing and same soil conditions, the load-carrying capacity was found to increase with both increasing shell thickness (t_s) and increasing shell angle (θ). Increasing shell thickness by 32% from 19 to 25 mm had a 5 – 9% improvement whereas increasing shell angle from 18 to 36° showed approximately 13% improvement. This demonstrates that shell angle is the over-riding parameter over shell slab thickness however the shell thickness parameter itself should not be underestimated and carefully considered in design.

Both tested shell orientations have optimal performance characteristics over the flat footing counterparts. The finite element analysis also showed reasonably good agreement with the experimental results with discrepancies falling within the 12 – 20% range. It is meaningful to mention finally that the addition of edge beams at the shell toes as studied has added benefit of preventing local crushing, improved load–transfer to the fin or shell proper and exhibits positive tendency in increasing shell load–carrying capacity. The addition of edge beams to the shell footings studied numerically demonstrate an increase in load carrying capacity due to an overall increase in rigidity of the footing and its consequent ability to counteract soil pressure concentrations exerted on the shell periphery.

CHAPTER 4

EXPERIMENTAL iSHELL MODELING

4.1 Introduction

Experimental modeling is a valuable research tool to ascertain the validity of tests and confirm authenticity of data to develop new theory. A rather labor intense alternative but frequently used to obtain confirming results, as data is often scarce particularly in shell footing modeling, often times simply inexistent. The objective is to obtain experimental results to evaluate and compare with numerical and theoretical based solutions on the soil's behavioural response of the new shells. This forms the basis for validation creating a new data pool to support the theory developed herein. To achieve this objective, the concrete mix developed insures sustained rigidity of the shell models cast. The soil properties and experimental setup as well as test procedure used are described and presented.

The experimental phase of the present foundation footing investigation attempts to study the performance of scaled models of inverted triangular shells in stochastic sand. Model tests conducted aim at developing shell behaviour under monotonic loading conditions in a controlled indoor environment. The contact pressures obtained for varied conditions will help explain the influence certain shell parameters have on the behaviour of shell footings. The objective is to study the influence of shell angles and shell thickness of the developed shell models using an ultra-high performance concrete mix which has never been attempted. The results are then compared to the upright case by simulating variable soil conditions including bearing soil shear strength and void ratio including loose, medium and dense sand states. The contact pressure distribution envelope is developed for the bearing areas contact surface at the soil-structure interface. The findings generated from the testing program are geared to develop insight on the bearing capacity and settlement behaviour of these foundation footings.

To acquire valid uniform contact pressure measurements, a variety of shell models are required for testing and comparison. Such are those presented in Figure 4.1. By experimentally testing the models and producing load–settlement curves and contact pressure distribution blocks one can determine the influence shape has on the behaviour of contact pressures beneath the shell.

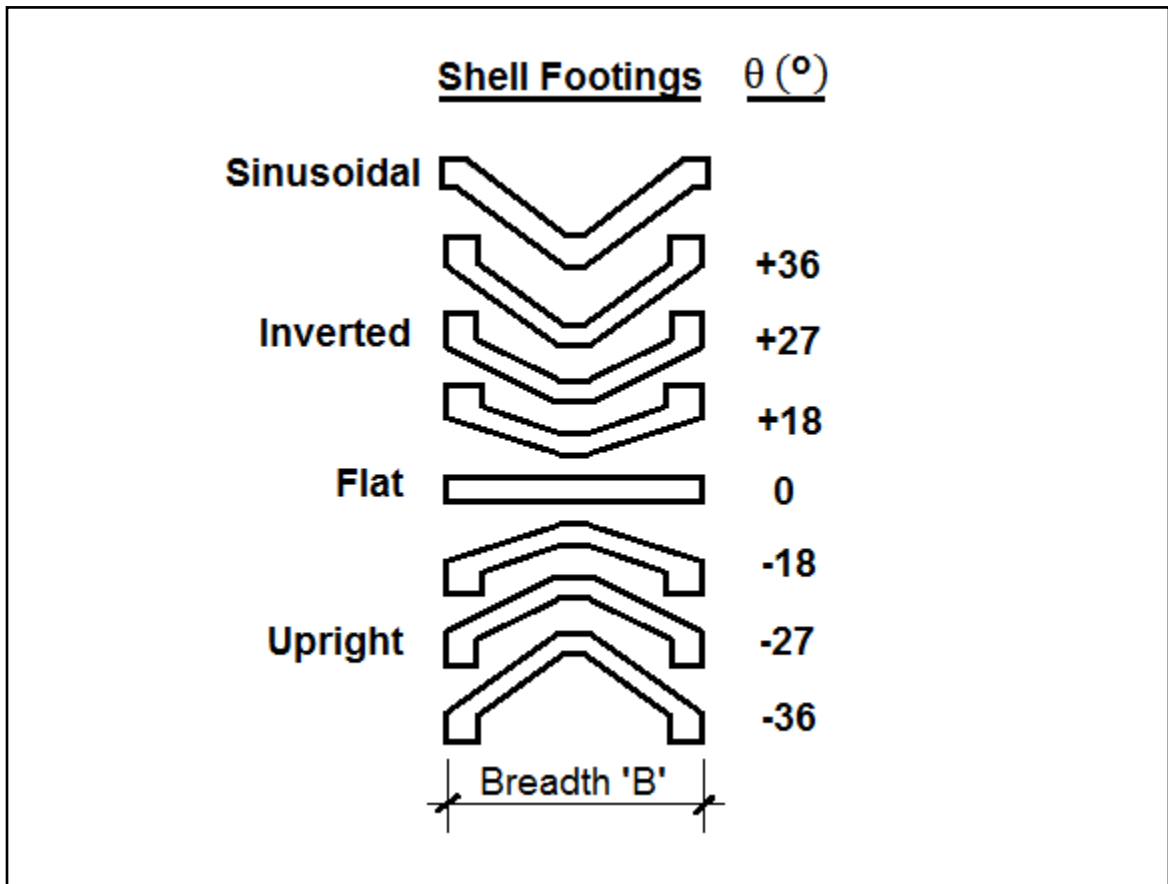


Figure 4.1. Shell Footing Foundation Models.

In a parametric study, variation in shell angle and soil densities including loose, medium and dense is proposed by variation of the angle of friction, ϕ (ϕ) soil strength parameter. Additionally, contact pressure measurements can be made at various stages of loading and settlement including local failure, bearing capacity and ultimate load ranges. Lastly, a comparison between the upright and inverted specimens is examined for the triangular shell shape incorporating the latest Sinusoidal model.

4.2 iShell Footing Models

In this next section shell footing model development is described. In this study nine models were cast using a newly developed blend of ultra-high performance concrete (UHPC), the details of which are further described in subsequent section. A flat foundation represents traditional planar contact surface footing. The second shape is that of the upright triangular type similar to those tested by preceding scholars having a rise-to-half width ratio (D/b) of unity keeping with standard shallow foundation construction practices.

Unlike use of metallic specimens which are perhaps slightly easier to manipulate and develop and possibly the method of choice for repeated testing, concrete models are limited to single tests. Retesting of metallic prototypes is possible without inducing additional stresses thereby adversely affecting experimental results. One thing certain, overall rigidity is key and plays the most pivotal role in influencing test results. Perfect model rigidity ensures maximum variation in the possible variability of the reactive soil pressures generated for a given applied load. This contrasts with perfectly flexible footings where they would all have to be identically matched for comparison sake. To date, both concrete and stainless steel or cast aluminum models have been employed. Other possible materials include elastic models made of Perspex or plexiglass but are deemed unfeasible from a cost perspective. As shells come back into vogue by attracting new generation of architects and engineers, new materials will follow. Advanced materials such as fibercrete and fiber reinforced polymer (FRP) composites may be used in model testing of shells.

The most widely used material as found in literature, for model specimens has been reinforced micro-concrete. In particular, due to scale reduction, the aggregate component of the concrete merits further consideration. That is, normal aggregate sizes of 12.0 – 19.0 mm [1/2 – 3/4 in.] are scaled down to 4.8 – 6.4 mm [3/16 – 1/4 in.] in size and use of microconcrete is warrant. The moulding and wood-working process as a prerequisite requires considerable time to fabricate and the reinforcements, mimicked by using 8 – 12 gauge M.S. wires (Mild Steel wires) typically would require material and bond similitude. Deformations in the form of indentations through an indentation device would be required to replicate reinforcement bar surface roughness conditions.

4.3 iShell Fabrication

To produce the physical shell model prototypes using iShell Mix concrete (discussed in further detail in Chapter 6), shop drawings were developed in AutoCAD and presented in prototypes 1 through 9 in Appendix (I). The nine shell footings are summarized in Figure 4.2. The first is a flat foundation used primarily as a basis for comparison and to scale its underperformance as compared to that of the shells. The triangular upright and inverted shells are constructed to show behavioural soil response in their respective contact surfaces. It is worthwhile to note the inverted shell also was used in attempt to develop a sin-wave type also referred hereafter as the inverted Sinusoidal shell in an effort to harmonize contact pressures in a quasi-linear constant distribution beneath the base. The remaining six shells were developed in two sets as part of the sensitivity analysis. The first set using 25 mm shell thickness while the second using 19 mm shell thickness. Moreover, shell angles were varied between 18° and 36° .

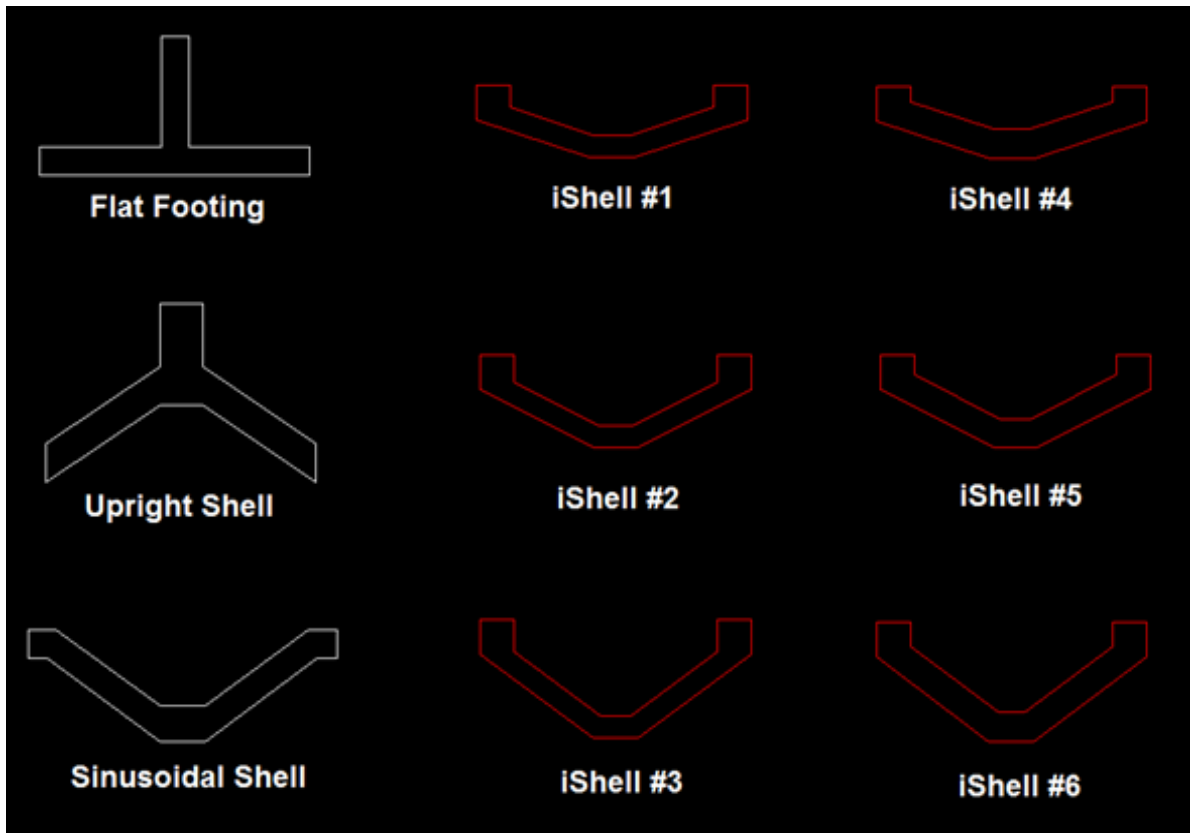


Figure 4.2. Summary of iShell Model Prototypes Cast.

4.3.1 iShell Model Casting

The iShell Mix batch was mixed on April 20, 2011 in a traditional drum mixer of 1m³ capacity. The shell footing models were cast using wood forms of medium-density fiberboard (MDF) as illustrated in Figure 4.3. The MDF panels were mechanically fastened using high strength screws with nut and bolts to encourage surface smoothness thereby limiting voids. Once cured after a 24 hour period the models were un moulded and heat treated in steam at 150°C for 48 hours followed by curing process of 72 hours in a humidity chamber at 23°C and 100% relative humidity. Shop drawings for form construction were prepared beforehand and prepared using debonding agents to facilitate form removal. The concrete mix used was monolithic cast in a controlled setting at room temperature to simulate pre-cast conditions as conceivably constructed in house.



Figure 4.3. Wood Box Moulds for iShell Model Casting.

To produce the inverted shell prototypes the composition of the iShell Mix batch is as follows: 29% cement and 9% Silica fume with balance of mix composed of ultrafine ground glass fibers and fine sand. The premix is a light grey powder available in 60 kg bags. The metallic fibers used were furnished by Lafarge Canada Inc. and measure 0.2 mm in diameter by 13 mm in length. The plasticizing admixture is Chrysofluid Premia 150 having a volume of 910 mL. Water was measured at a volume of 4000 mL and metallic fibers weighing 4.3 kg.

Compression resistance tests were conducted on April 26, May 03 and May 17 for the 7, 14 and 28 day strengths respectively. The latest recommendations and standard industry practices were used in producing representative test specimens and strength results. Due to equipment limitations, traditional 100 mm [4 in.] diameter test cylinders were replaced with 75 mm [3 in.] diameter cylinders. Such samples are deemed representative and interchangeable for determination of compressive strength, particularly for ultra-high performance fiber-reinforced concretes such as this mix (Graybeal *et al.*, 2008). It was estimated that after 7 days of initial curing, the specimens would attain a minimum of 75% of the maximum compression resistance rating. The projected compressive resistance of the mix was expected to attain 180 MPa. Figure 4.4 below illustrate the moulded iShell mix concrete cylinder test specimens and the compression test equipment used.

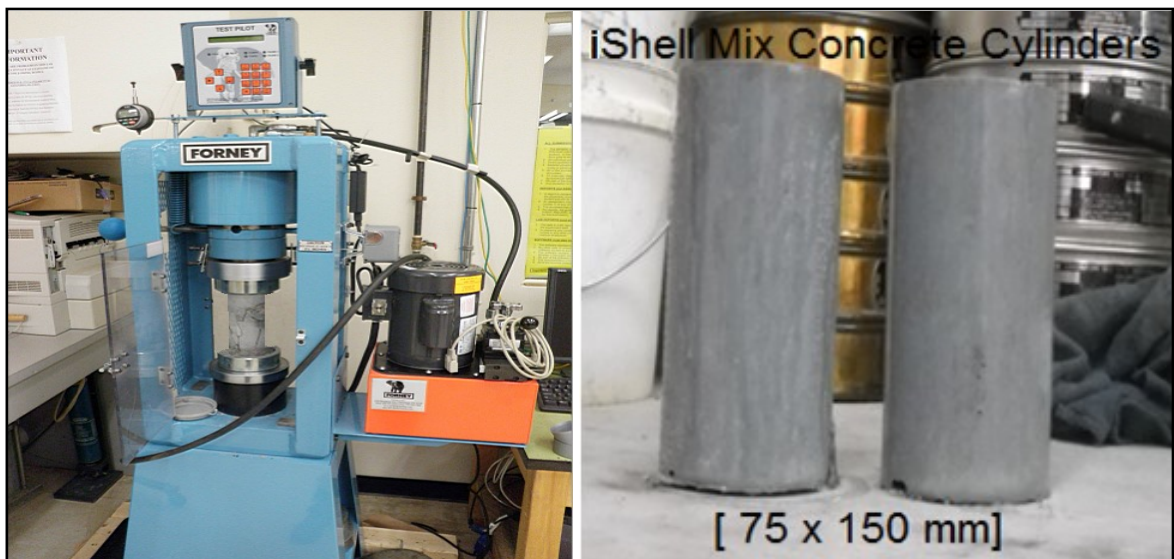


Figure 4.4. Compression Test Apparatus – Soils Laboratory, Concordia University.

The compression resistance test results obtained after 7, 14 and 28 days curing revealed 104.3 MPa, 121.2 MPa and 178.2 MPa values respectively. Finally, flexural strength tests were conducted which showed a peak strength of 52.2 MPa. In keeping with good design practice an allowable bending strength of 80% or 41.8 MPa is proportionate strength and so a good design value would be 40 MPa conservatively. Compression and flexural strength results are summarized in Figures 4.5 and 4.6 respectively.

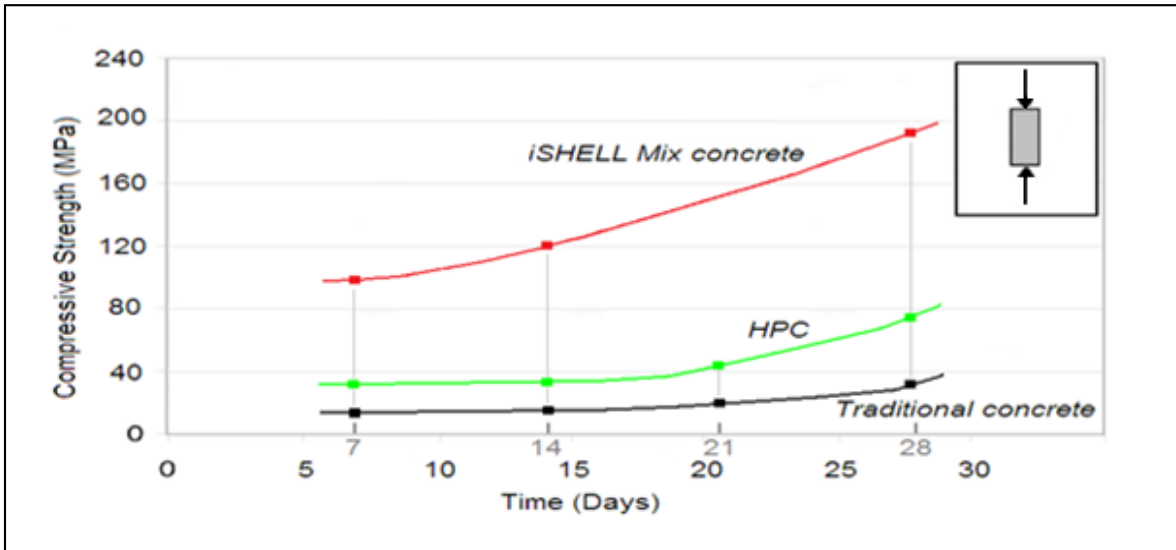


Figure 4.5. Compression Strength of iShell Mix Concrete.

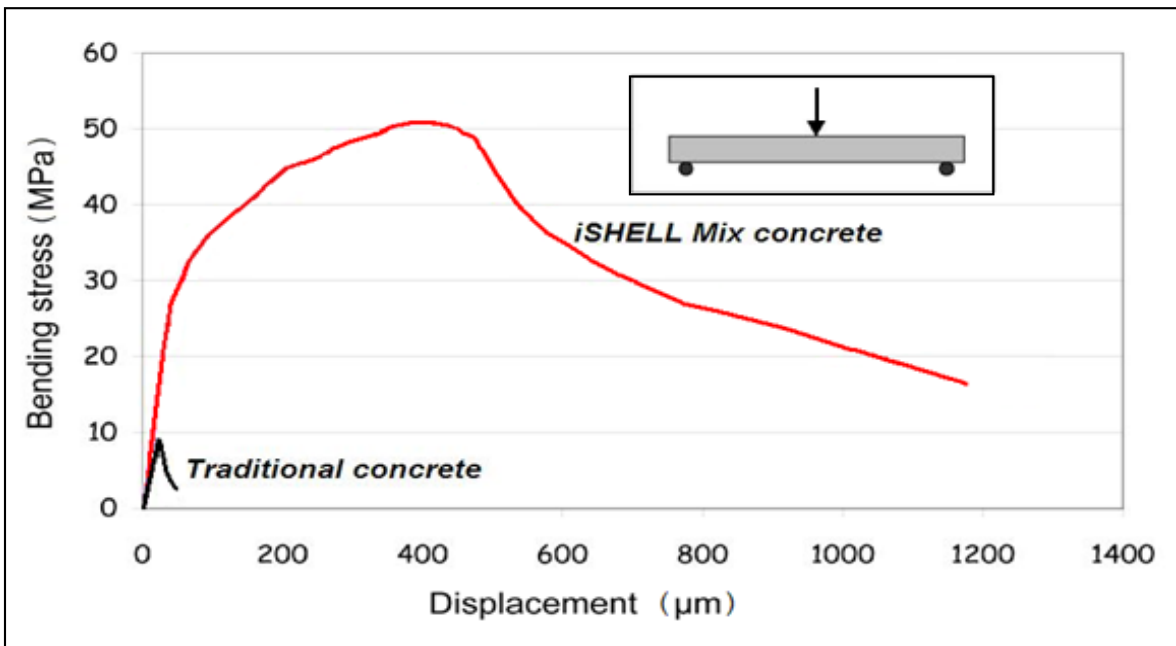


Figure 4.6. Flexural Strength of iShell Mix Concrete.

4.3.2 iShell Model Observations

The cured models are a light-grey color of relatively smooth to the touch surface texture favoring impermeability. The smoothness reflects negligible voids associated with the pour. The edges are well-defined but rough to the touch. Metallic fibers are seen protruding at the peripheries as typical fiber lengths of 19 mm were used being almost the width of the shell model. This is the main limiting factor in consideration of thinner shell thicknesses. Figures 4.7 through 4.23 show the overall view of the ten models including previously tested metallic model following overall similitude in Figure 4.13.



Figure 4.7. Flat Foundation Model of iShell Mix Concrete, $t_s = 25$ mm, $\theta = 180^\circ$.

The second prototype model shown in Figure 4.8 depicts the upright footing case. The model illustrated in Figure 4.9 was the inverted Sinusoidal shell type proposed in attempt to investigate geometrical impact namely the orientation of end beams in the horizontal position on shell performance.



Figure 4.8. Upright Triangular Shell Model of iShell Mix Concrete, $t_s = 25$ mm, $\theta = 34^\circ$.



Figure 4.9. Inverted Sinusoidal Shell of iShell Mix Concrete, $t_s = 25$ mm, $\theta = 36^\circ$.

Finally, two sets of three inverted shells were cast using shell thicknesses of 19 mm and 25 mm with varying shell angles of 18, 27 and 36°, again, keeping within typical construction sizes of full-scale footings. All models generated simulate the plane strain condition in the soil keeping the analysis in check with the numerical study as well. The models were drawn to scale using AutoCAD and then modeled in Shape Designer(SAAS) as described previously to validate size, dimensional properties and geometrical parameters of each section. The new shell model prototypes developed including sketches and photos are illustrated in Figures 4.10 through 4.13.

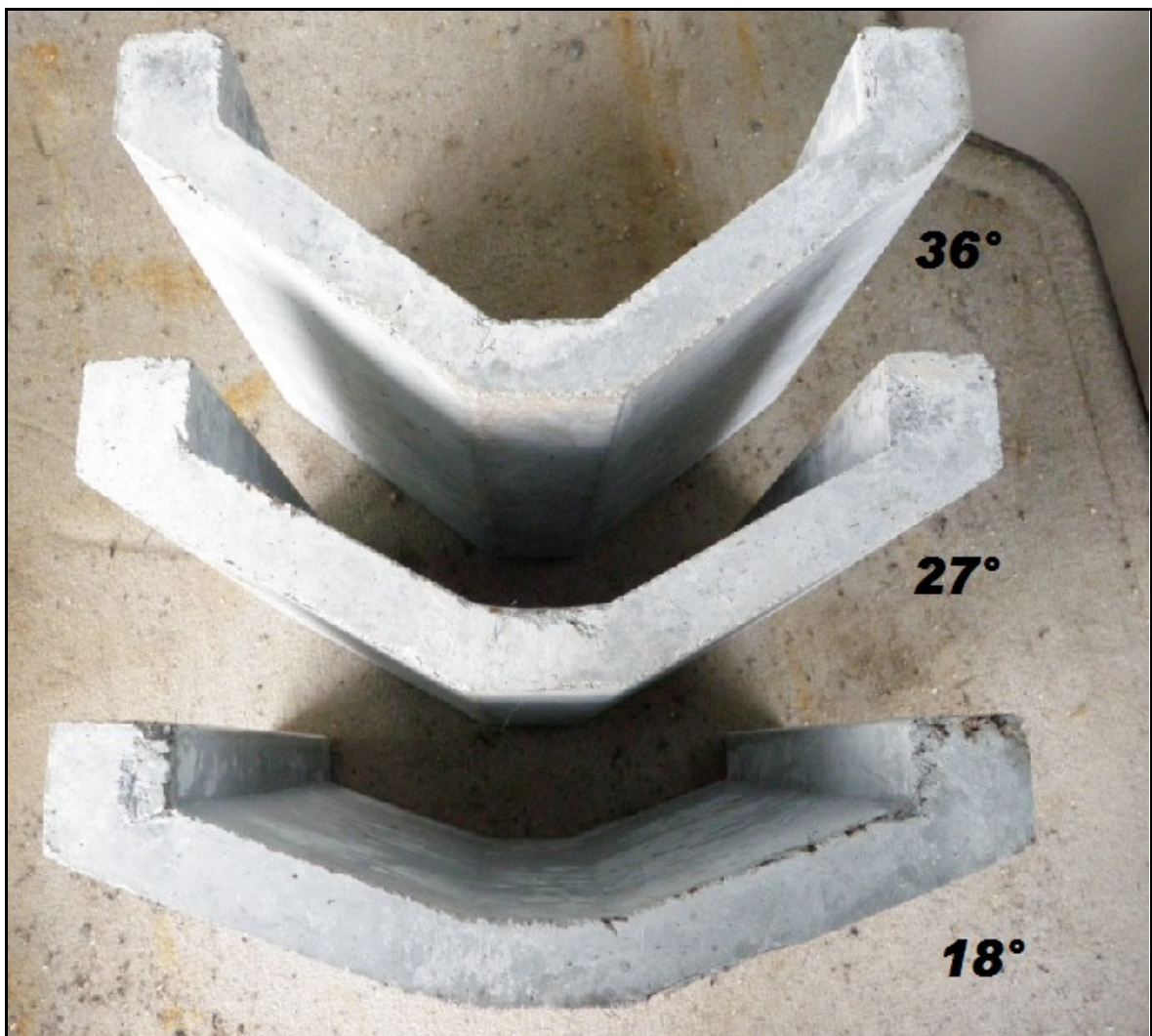


Figure 4.10. iShell Footing Models of iShell Mix Concrete ($t_s = 19$ mm, $\theta = 18, 27, 36^\circ$).



Figure 4.11. iShell Overall Plan Dimensions (240 mm x 240 mm).



Figure 4.12. Shell Inversion vs. Upright Shell Model.

The metallic specimens use sandpaper adhered to the bearing surface to simulate rough concrete surface conditions. The new concrete models mimic and bring to closer reality the conditions of full-scale structures minimizing experimental errors thereby increasing reliability of test results. A close-up view shows scaled comparison between the concrete and metallic counterpart.



Figure 4.13. Metallic vs. Concrete Upright Strip Shell Footing Models.

In perspective, Figure 4.13 above shows a typical metallic specimen previously tested using sandpaper adhered to the base to simulate concrete surface roughness while the adjacent specimen offers real-time response of actual concrete material. The purpose is to validate testing conditions and model based on some existing experimental data available.

The problematic in predicting the performance of concrete structures is complicated by the complexity of the material, which has, at its core, a heterogeneous microstructure and displays composite behaviour at a series of length and strength scales. In particular, the overall transport and mechanical behaviour of concrete is strongly conditioned by its heterogeneous microstructure, which determines the randomness of the overall transport and mechanical variables. Permeability, diffusivity, crack initiation, progression and propagation control within the concrete are significantly reduce this randomness.

Multi-scale modeling is an approach which has attempted to follow and assess the large-scale performance of concrete and address durability issues. In that regard, multi-scale modeling as applied to traditional beams, girders and columns has assisted in providing a methodology to systematically incorporate detailed information about

processes experienced in smaller scales into governing equations at larger scales. This traditional approach in assessing typical concrete is finally replaced with the introduction of composite material that works similar regardless of scale. iShell Mix is envisioned to be a revolutionary product in that not only eliminates scaling errors, but also enables geometric properties of complex shapes such as the shell to thrive from both a construction and durability point of view. In order to limit friction along plexiglass side walls a cut of polyvinyl–chloride strip of 3 mm thickness was epoxy adhered to both ends of the shell models. A typical inverted model is depicted in Figure 4.14 with overall shell dimensions and that of the edge modifications implemented.

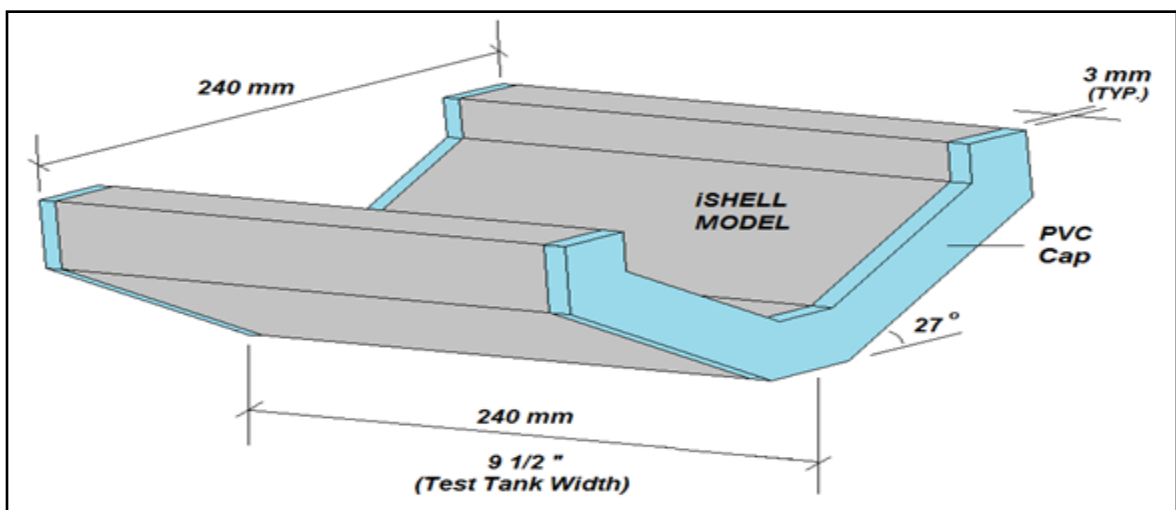


Figure 4.14. iShell Model – Frictionless Capping.

In this study, a flat model and eight shell model properties as tested are summarized and tabulated in Table 4.1 for structural overburden and dead weight considerations and Table 4.2 for structural shell characteristic property identification.

No.	Shell Shape ID (Holed)	Shell Model Mass (g)	Shell Model Dead Load (N)
1	Flat	4803.6	47.1
2	Upright Triangular	5748.2	56.4
3	Inverted Sinusoidal	4164.3	40.9
4	Inverted Shell #1 (iS1)	3226.1	31.6
5	Inverted Shell #2 (iS2)	3445.4	33.8
6	Inverted Shell #3 (iS3)	3719.0	36.5
7	Inverted Shell #4 (iS4)	3837.9	37.7
8	Inverted Shell #5 (iS5)	4080.0	40.0
9	Inverted Shell #6 (iS6)	4141.3	40.6

Table 4.1. New iShell Footing Model Weights.

No. Shape ID	Area (mm ²)	Perimeter (mm)	Shell Angle (°)	Shell Thickness (mm)	Centroid		Radii of gyration		Moment of Inertia		Young's Modulus E (GPa)	Flexural Rigidity EI (10 ⁵ N-mm ²)	Axial Stiffness EA/L (10 ⁶ N/mm)	Material Type	Poisson ratio (ν)
					x (mm)	y (mm)	r _x (mm)	r _y (mm)	I _x (10 ⁶ mm ⁴)	I _y (10 ⁶ mm ⁴)					
1 Flat	8375.0	720.0	180	25	120.0	29.5149	43.0478	133.6173	8.224071	28.9236970	60	493.444260	2.093750	Elastic	0.2
2 Upright Triangular	10167.0	738.9	34	25	120.0	70.7656	79.8109	135.0472	13.847529	39.0184519	60	830.851740	2.541750	Elastic	0.2
3 Inverted Sinusoidal	8212.0	688.0	36	25	136.9	49.4605	56.1155	157.1219	5.770056	4.8879620	60	346.203360	2.053000	Elastic	0.2
4 Inverted Shell #1	5652.3	597.3	18	19	120.0	28.4945	32.6592	142.0276	1.439561	32.6239493	60	86.373682	1.413065	Elastic	0.2
5 Inverted Shell #2	6014.6	630.6	27	19	120.0	38.6135	44.451	142.1612	2.916413	34.9434551	60	174.984784	1.503641	Elastic	0.2
6 Inverted Shell #3	6529.5	679.8	36	19	120.0	50.6225	58.4192	142.1694	5.551194	37.9504799	60	333.071656	1.632380	Elastic	0.2
7 Inverted Shell #4	6777.6	584.8	18	25	120.0	29.0494	32.6846	140.2345	1.521023	35.6880851	60	91.261405	1.694410	Elastic	0.2
8 Inverted Shell #5	7205.1	617.5	27	25	120.0	38.5675	43.7923	140.3704	3.100440	38.2145946	60	186.026371	1.801267	Elastic	0.2
9 Inverted Shell #6	7828.1	665.9	36	25	120.0	49.9719	57.1058	140.3859	5.979686	41.5528382	60	358.781167	1.957016	Elastic	0.2

Table 4-2. Concrete iShell Footing Model Properties.

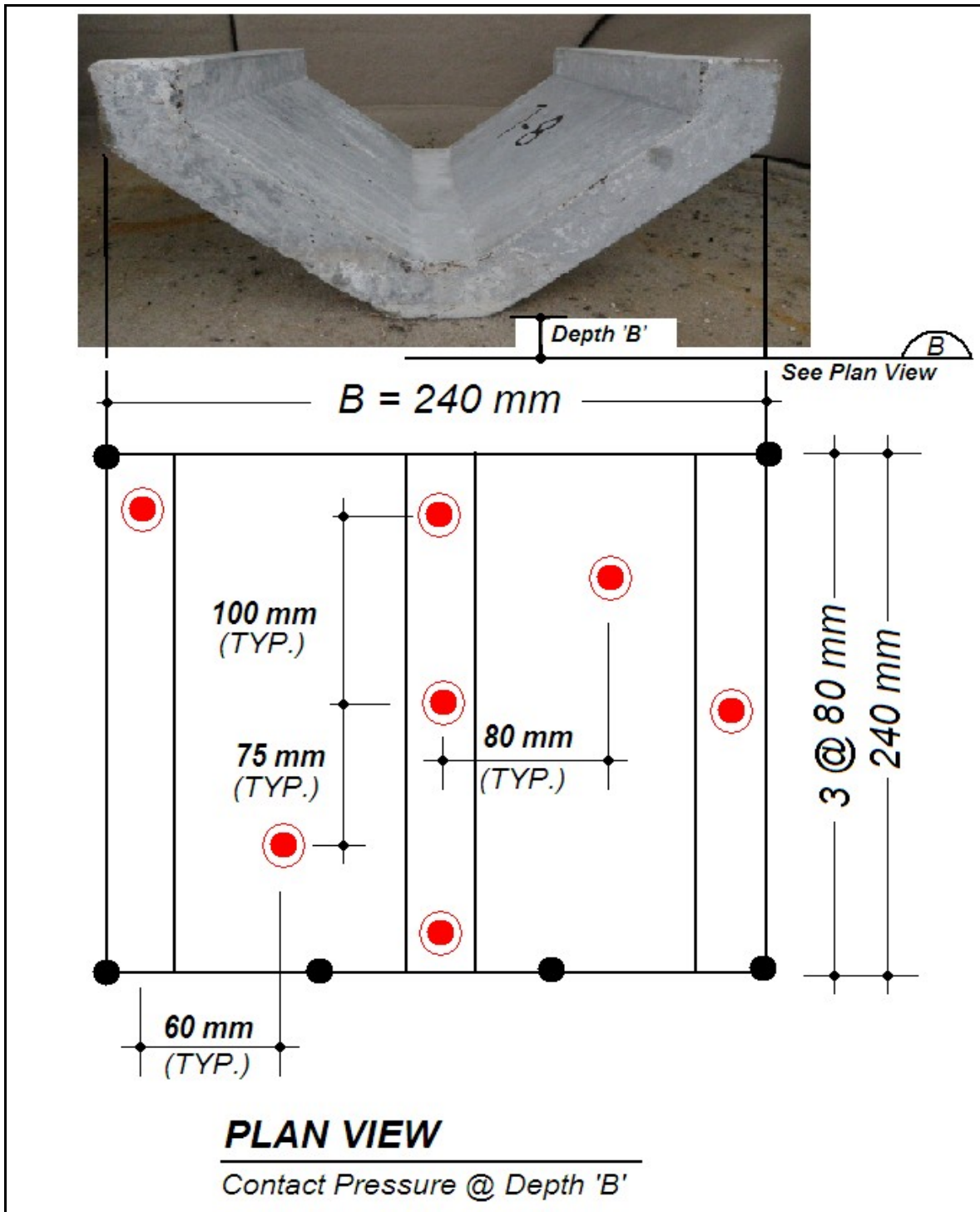


Figure 4.15. Localization of Contact Pressure Transducers at Depth 'B.'

Localization of the bore holes was facilitated by using plexiglass templates of 6.0 mm [$\frac{1}{4}$ in.] thickness to keep point readings coherent between all test models of concern. The convenient sensor locate procedure was accurately defined using the template as illustrated in Figure 4.16 to keep data recording coordinates constant for all models tested as follows.

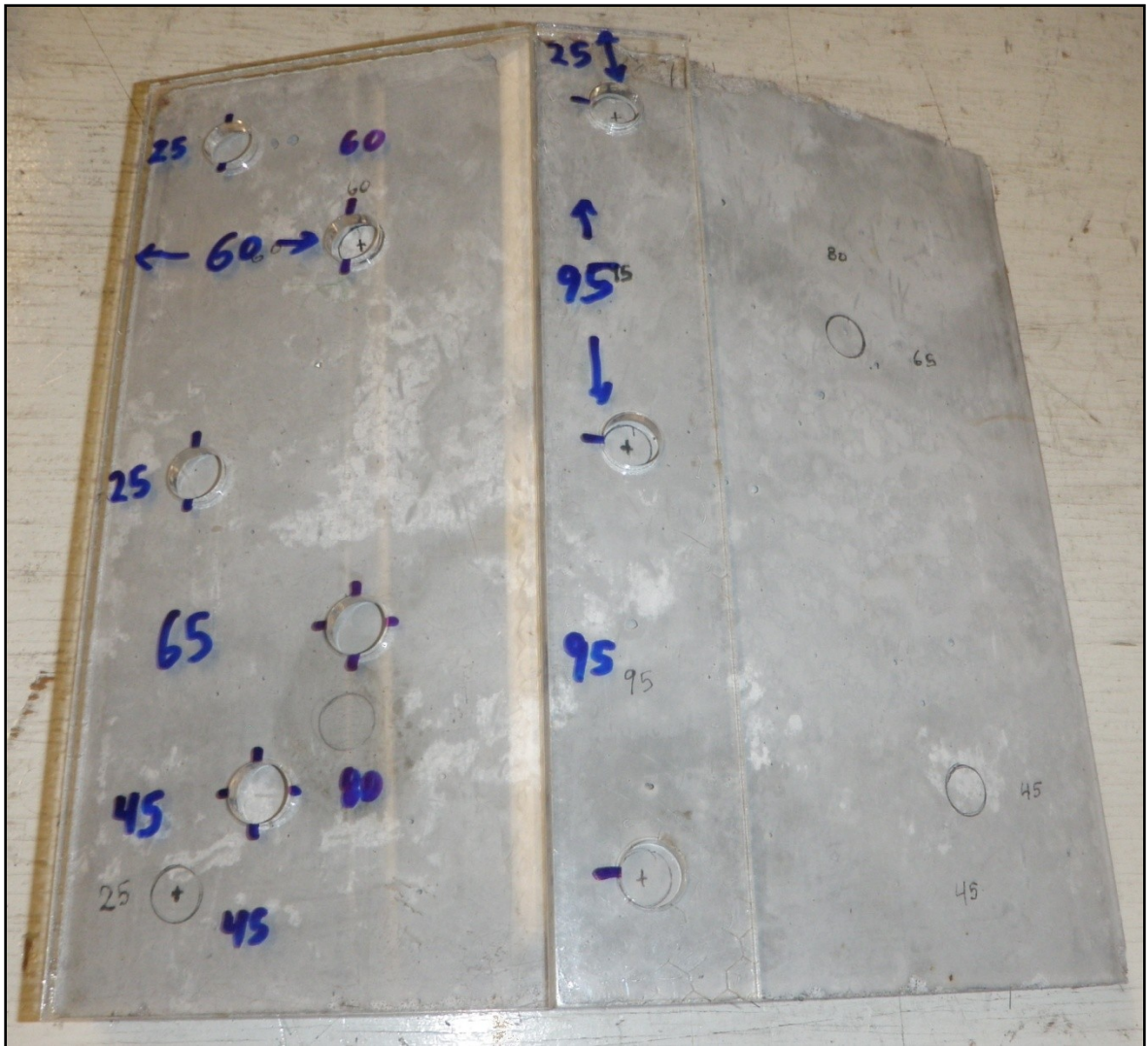


Figure 4.16. Plexiglass Templates for Sensor Layout and Wash-Bore Drilling.

Wash-bore coring method was used to accurately pinpoint the desired locations which were arbitrarily yet strategically selected to obtain feasible results for reasonable contact pressure profiling. The boring efforts required the use of a diamond-tipped hole saw to penetrate the fibers and also yielding a smooth finish. Illustrations of the drill bit that accommodate the transducer housing adapters as well as the wash-boring procedure itself are depicted in Figures 4.17 and 4.18 with the resulting eight shell models developed illustrated in Figure 4.19.



Figure 4.17. Concrete Drill Bit (1/2" dia. – left) and Slot-Plug Adapters (varia).

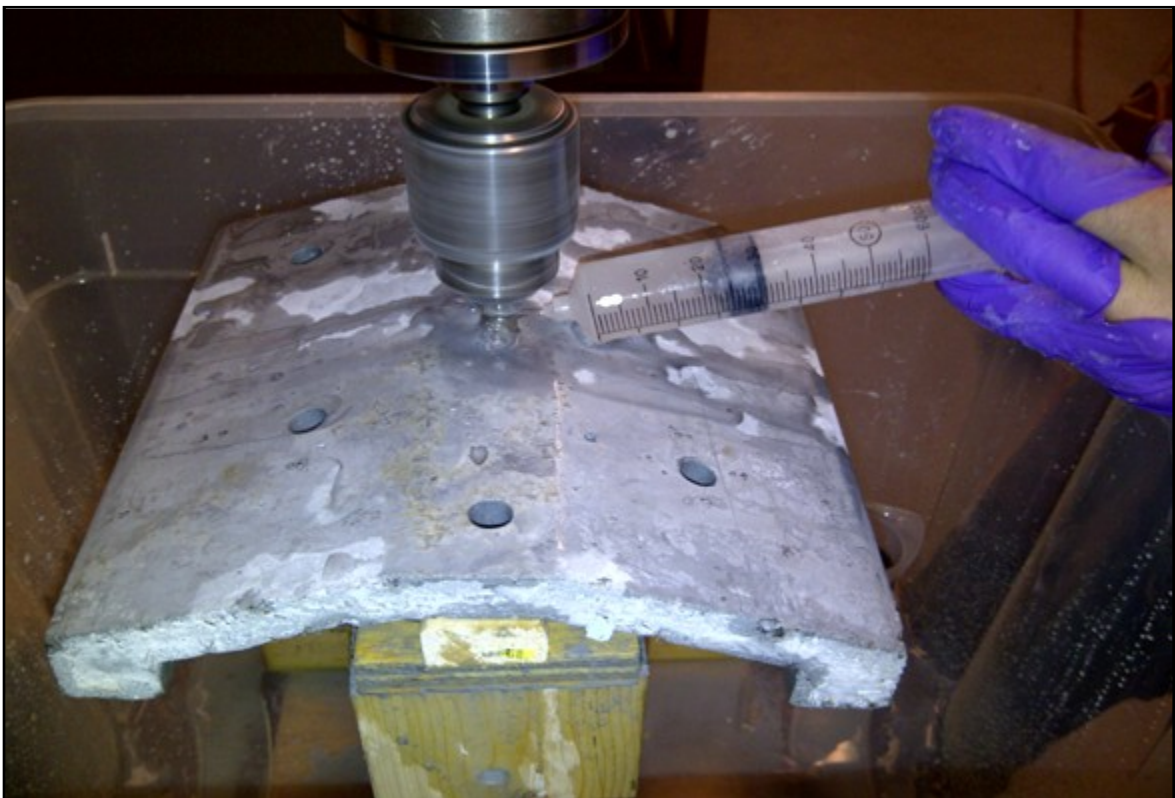


Figure 4.18. Wash-Boring Procedure : iShell Footing Model.



Figure 4.19. Perforated iShell Footing Models.

From a geotechnical perspective, it is worthwhile to note, the micro-structural models used here are to compare contact pressures of traditional upright models to their inverted counterparts. In particular a pressure distribution envelope is investigated to predict soil interface behaviour at depth ‘B’ within stochastic soil media. In part, the microstructure and evolution of failure mechanism will help highlight the advancement in technology of the new iShell Mix which is proposed to exhibit advantageous mechanical properties over traditionally used concrete prototypes. In tandem, the models allow for assessing factors that affect settlement and bearing capacity and performances can be assessed in light of existing data. Secondary results may indicate the probability of cracking or failure paths and resulting impact on its effectiveness in shell footings in terms of durability; that is resistance to alkali and chemical attack the primary adversary to concrete in the natural environment.

4.4 Experimental Setup

The experimental setup used in the program is an original design stemming from concurrent research. It comprises a narrow plexiglass double-sided test tank to simulate plane-strain conditions of the shell footings. The models are loaded concentrically in the vertical direction by a hydraulically controlled piston loading jack set at constant rate. Carefully placed uniform sand beds of varying densities were deposited from a tank mounted on a steel support frame located at fixed height above the test tank. Loading capacities and displacements were monitored using a flat universal load cell and dial gauges respectively.

4.4.1 Testing Facility Setup

Before proposed shells were tested, an adequate load testing apparatus system setup was conceived. The setup for the experimental phase and shell testing methodology follows conventional testing methods employing a sand box reservoir and loading mechanism on the sand bed with distinct proprietary characteristics as described in the following section.

The loading frame should support a rectangular sand-box container of ample size. A tank dimension maximizing the use of a standard 4 ft x 8 ft plexiglass panels was optimal for height and length respectively. A single rectangular test tank composed of two plexiglass sheets (for the sides) connected along six seams by metallic aluminum channels form the main components of tank. Final internal tank dimensions measured 2299 mm [90.5 in.] x 1149 mm [45.25 in.] x 241 mm [9.5 in.] for length, height and width, respectively. The total soil volume capacity is thus 0.6376 m³ [22.5 ft³]. The tank used was designed to simulate the plane-strain conditions of the strip triangular inverted shells for the tests for validation of numerical results and follow suit.

The tank walls have been channel braced to prevent lateral buckling of the steel walls which themselves should be of ample thickness. Full plans were developed in modifying an existing tank frame to accommodate the FRP shell models satisfying plane-strain (2D)

loading conditions. The adaptors developed for the sensors along with plexiglass templates were designed and constructed from shop-drawings as well.

The overall experimental setup employs use of a steel loading frame as shown in Figure 4.20. The base wheels used primarily for mobility were removed and remaining base plates shimmed and secured to the concrete floor during the test phase. The supporting frame is outfitted with a loading jack which transfers load via a steel loading yoke to the shell model located within a sand test tank. Figure 4.28 shows a close-up of the loading jack and ball-pinion used in load transfer setup. It is worthwhile to mention that loading was controlled using a valve system to gauge loading rates as well as carefully applying constant hydraulic pressure with motor driven setup of the loading control system.

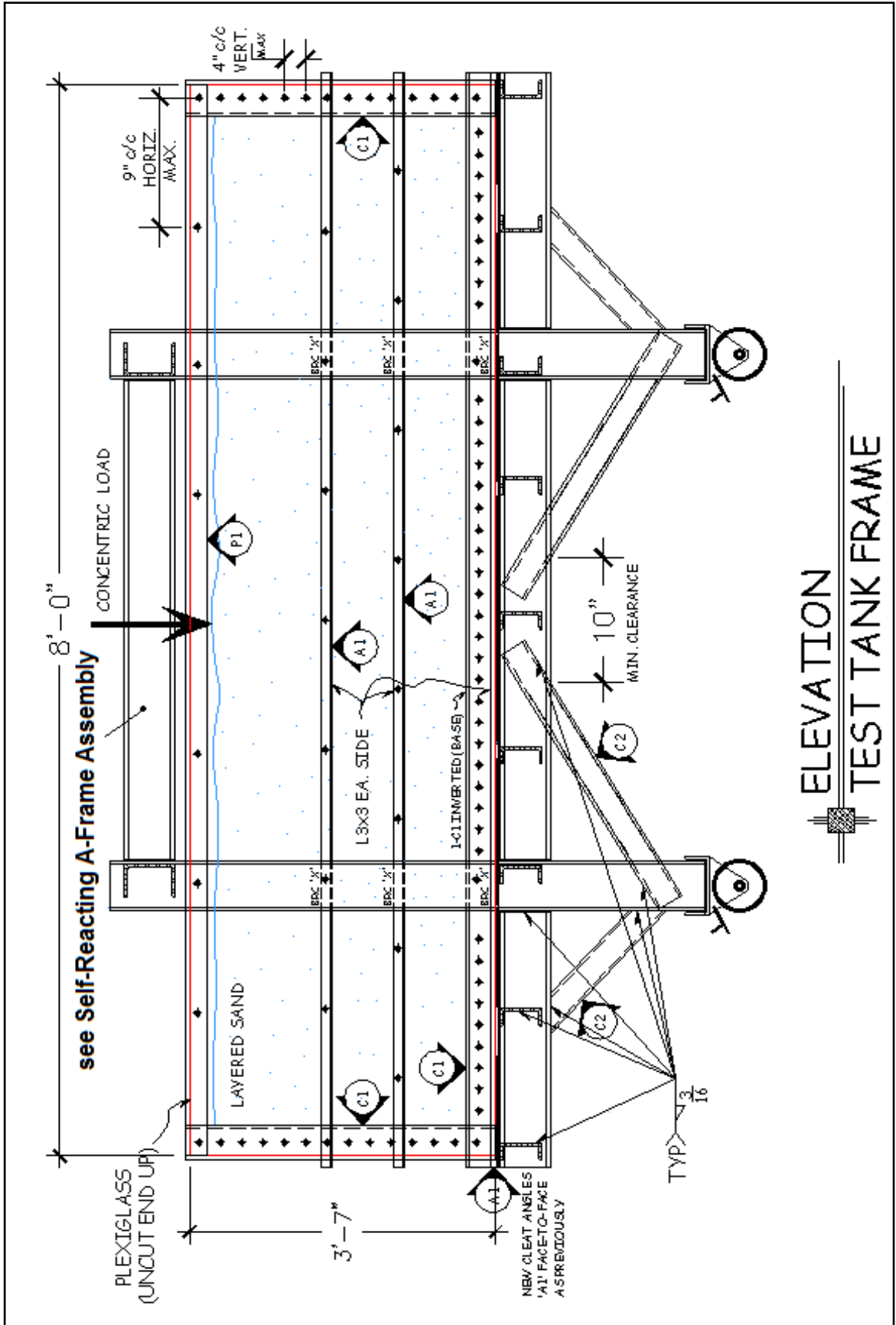


Figure 4.20. Loading Frame and Test Tank Setup.

SELF-REACTING A-FRAME HEAD

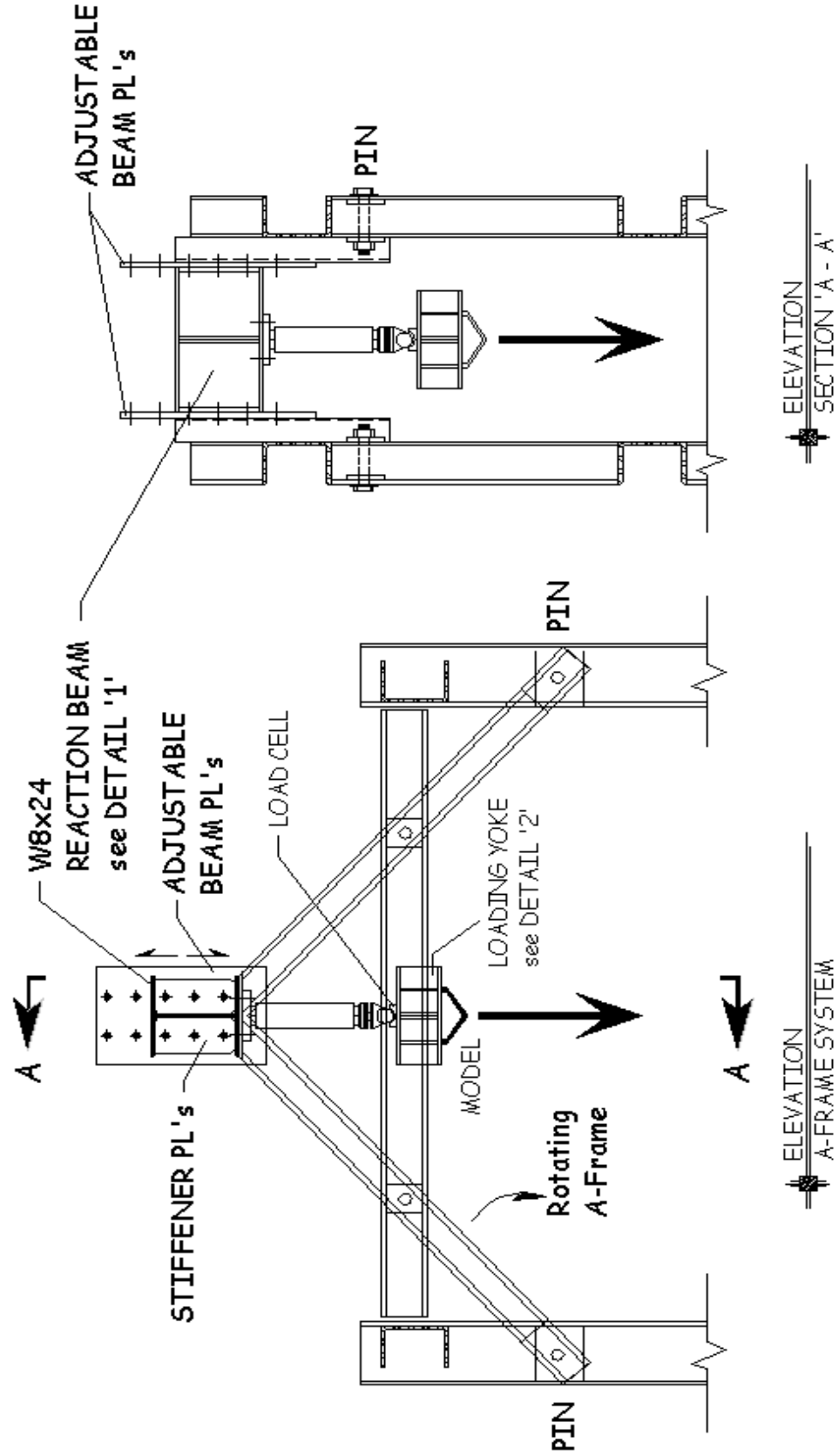


Figure 4.21. Self-Reacting A-Frame & Loading Assembly.

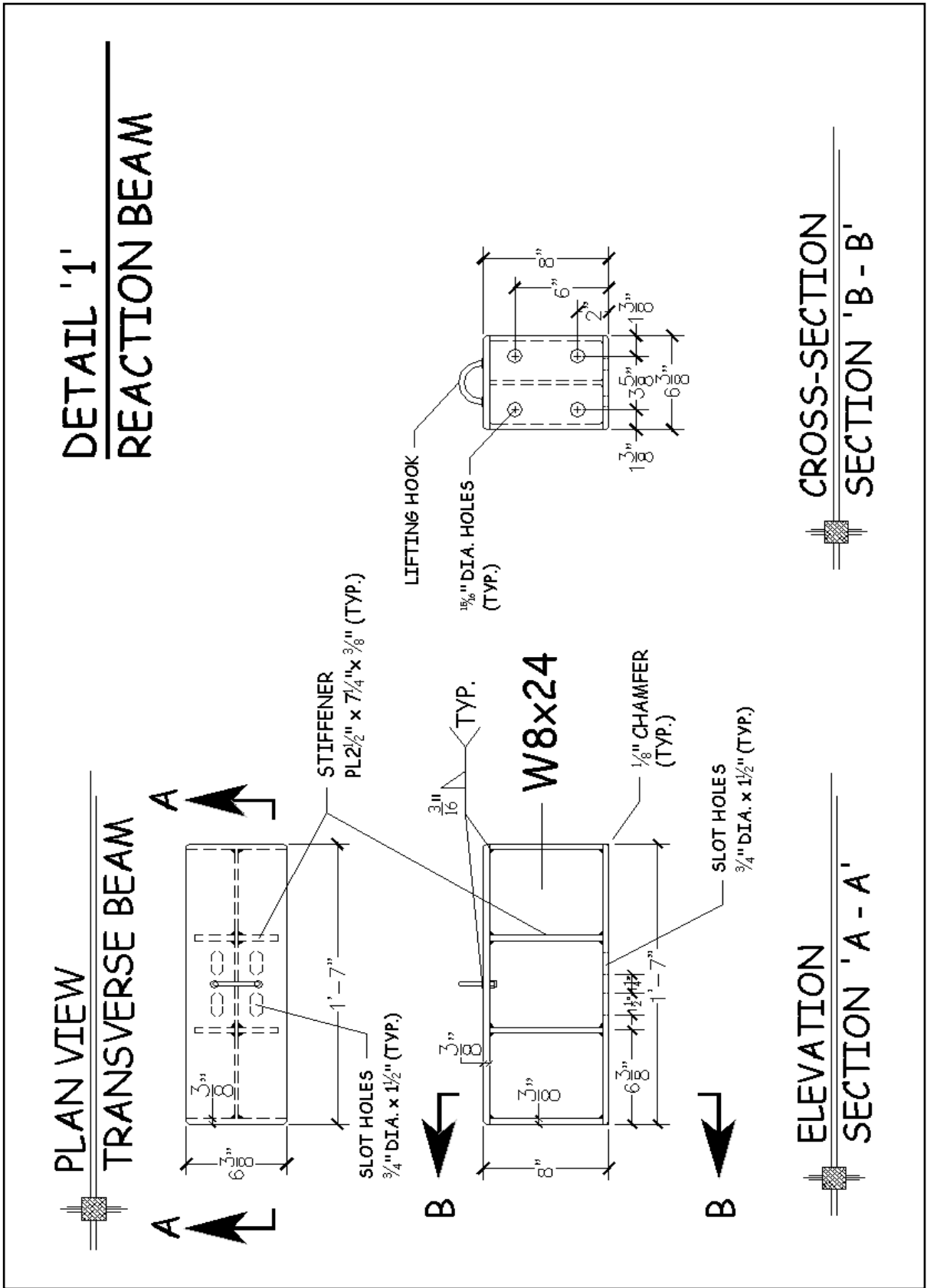
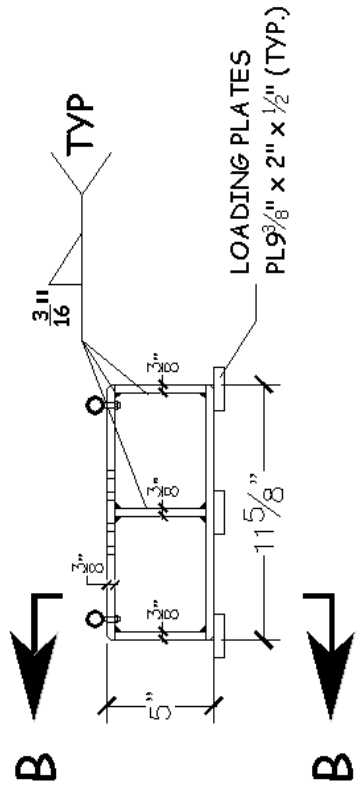
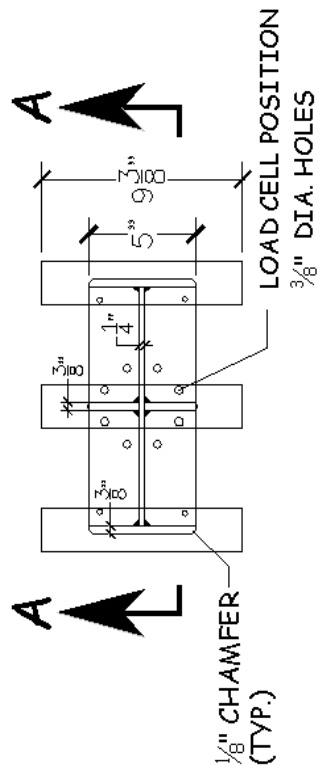
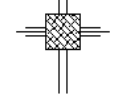


Figure 4.22. Transverse Loading Beam Plans.

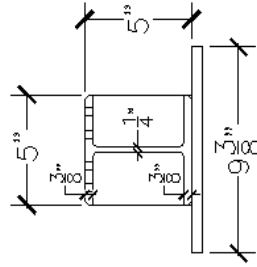
PLAN VIEW
LOADING YOKE



ELEVATION
SECTION 'A - A'



DETAIL '2'
LOADING YOKE



CROSS-SECTION
SECTION 'B - B'

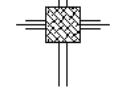


Figure 4.23. Loading Yoke Plans.

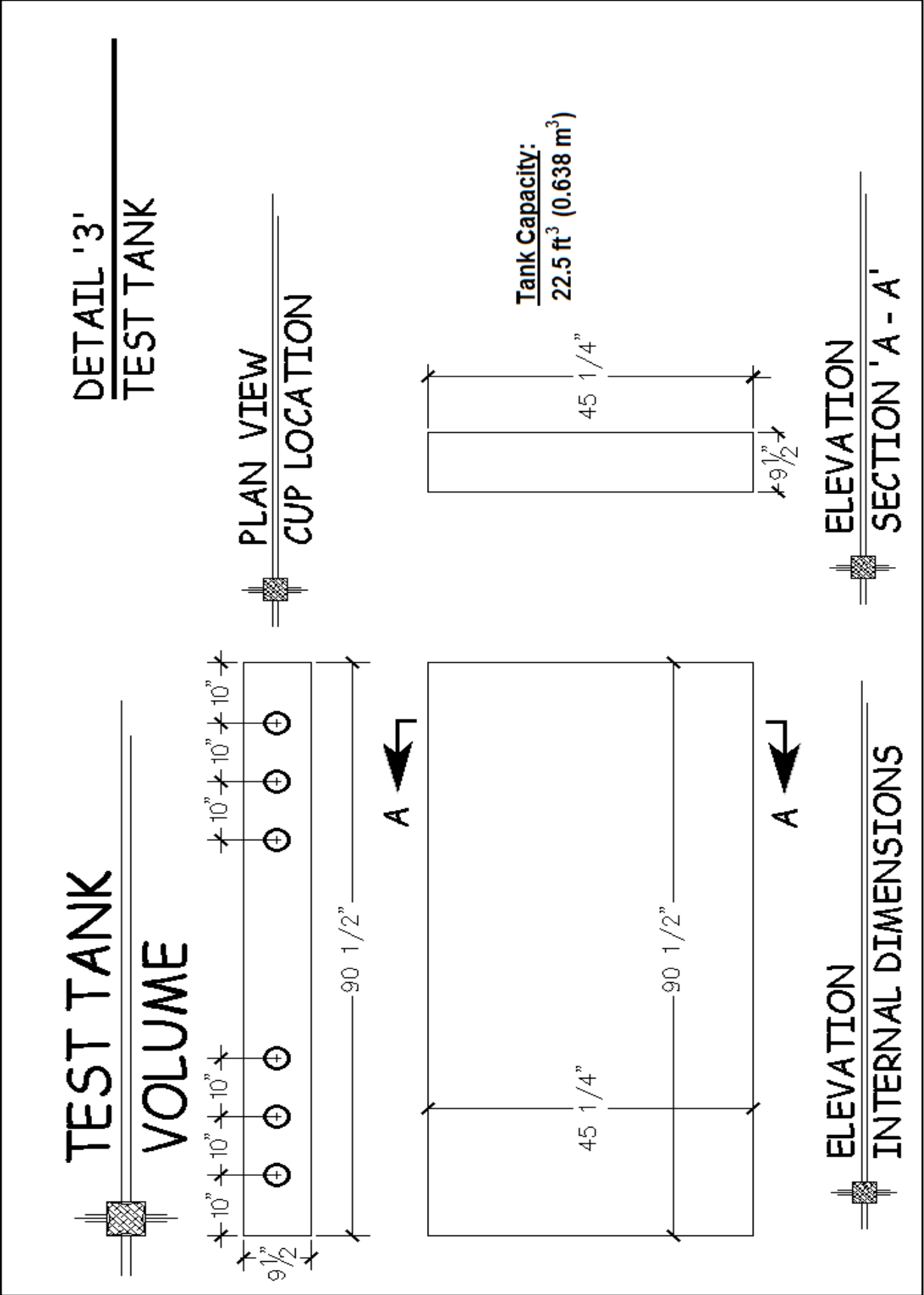


Figure 4.24. Test Tank Internal Dimensions.

4.4.2 Loading System

The loading mechanism is mechanically driven and consists of motorized gear-box capable of loading models at a rate of 0.5 – 5.0 mm/minute as found in the literature. The median rate used during the tests were inducing a downward displacement of 2 mm/minute resulting in development of a maximum applied force on the loading yoke of 19,000 lbf. The load cell used had a maximum capacity of 111.2 kN [25,000 lbs] whereas 40.0 kN was upper limit for similar tests conducted. The uniform displacement transfers an axial force to the shell models where a loading yoke is positioned.

The application of load would be maintained beyond that of bearing capacity till the model would jerk or release the load. A linear variable displacement transducer (LVDT) was installed on the loading system to record the displacement of the shell footing models during testing. The model used was an Omega, Model LD610–50 as illustrated in Figure 4.25 that follows. It was held in place with metallic clamps and an aluminum housing to ensure a positively fixed position for accurate measurement reading. A conventional tape measure was used on the plexiglass tank face for verification of the readings.

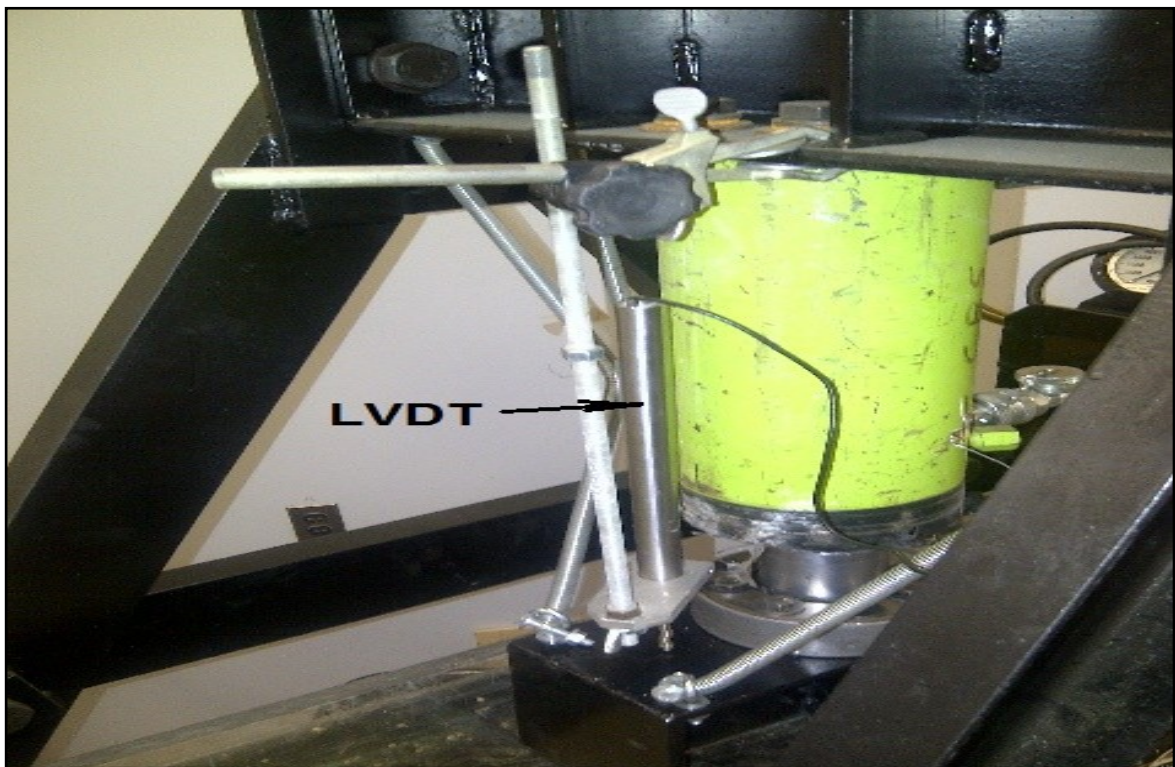


Figure 4.25. LVDT Displacement Measuring Device & Hydraulic Loading Jack.

The STRAIN SERT™ model of the universal flat load cell used had 25,000 lbf capacity representing 40% of projected maximum load of 10,000 lbf. The excess capacity leaves ample room for added loading capability. Tabulation of the load cells technical specifications is provided in Table 4.3 with a graphical illustration of the load cell provided for in Figure 4.26 and Figure 4.27 shown outfitted with a ball-pinion adaptor attachment.

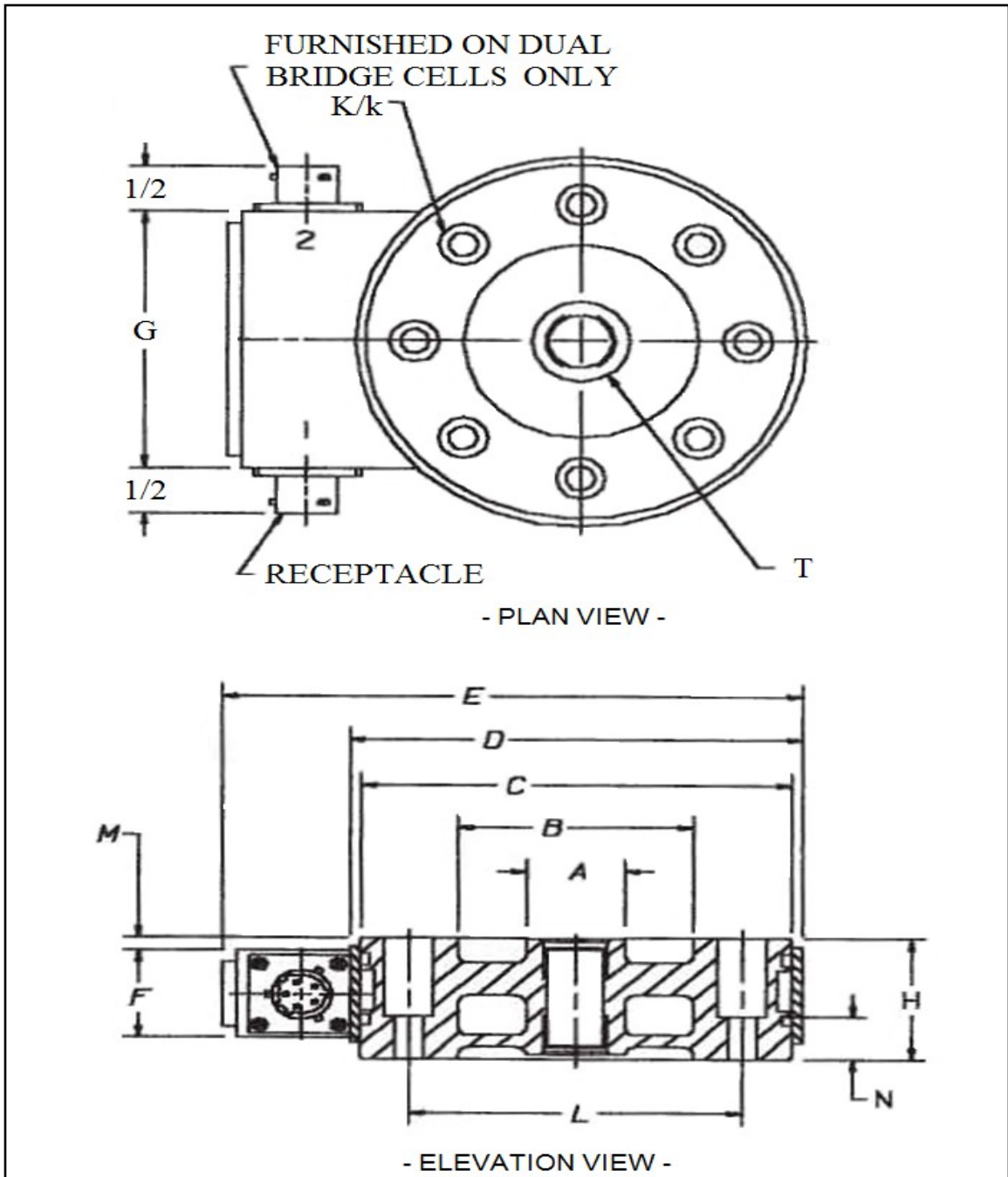


Figure 4.26. Universal Flat Load Cell Schematic.

Strain Sert - Universal Flat Load Cell

Model: FL25U-3SPKT

Serial No.: 06169-1

Features

- precision load sensing, single bridge
- rugged, compact and lightweight
- internally sealed strain gauges
- direct force measurement

Specifications

Capacity	Rated Output	Non-Linearity	Excitation Voltage	Bridge Resistance (Ohms)	Zero Balance
25,000 lbs (11.35 ton)	3mv/V (Standardized Output)	Precision 0.10% F.S.	15V AC or DC (Max.)	350 Ω (Nominal)	+/- 2% F.S.

Dimensions

A - dia.	1-5/8"	Y - full load deflection	0,00148 inch
B - dia.	2-27/32"	K - spring rate	16,900,000 lb/in
C - dia.	4-7/8"	w - load cell weight	5.9 lb
D - dia.	5-1/8"	Mb - bending Moment	16,000 il-in
E - length	6-7/16"	Mt - Torque	33,600 lb-in
F - height	1-3/8"		
G - width	3-3/4"		
H - height	1-1/2"		
K - O. dia.	41/64"		
k - l. dia.	13/32"		
L - dia.	3-3/4"		
M - length	1/16"		
N - hole depth	1/2"		
T - hole	1-14UNF-2B		

Mechanical Properties

Y - full load deflection	0,00148 inch
K - spring rate	16,900,000 lb/in
w - load cell weight	5.9 lb
Mb - bending Moment	16,000 il-in
Mt - Torque	33,600 lb-in

Table 4.3. Load Cell Specifications.



Figure 4.27. Universal Flat Load Cell and Ball-Pinion for Loading Jack.



Figure 4.28. Loading Yoke, Load-Cell, Jack Cylinder and Ball-Pinion Setup.

4.4.3 Test Tank Layout

The main test tank was built of plexiglass material measuring 2.0 x 2.0 m in plan area by 1.8 m height and 25.4 mm [1 in.] thickness easily accommodated by the loading frame. The entire tank was braced against wall buckling under loading conditions developing lateral thrust on the side perimeter walls. This was achieved using a combination of steel angles and lateral braces strategically positioned to resist out-of-plane bending. The resulting internal dimensions of the soil strata are 2.0 x 2.0 x 1.8 m in overall height. Figure 4.24 illustrates the conceptual tank size and internal dimension requirements for construction in the lab while Figure 4.29 that follows depicts the actual as-built tank respecting these necessary internal dimensions to accommodate the test specimens. Overall construction to accommodate the test tank follows the preceding plans of Figures 4.20 – 4.24.



Figure 4.29. Test Frame and Tank Setup.

In preliminary testing phase and as part of the setup certain pre-testing conditions were normalized. Uniform sand-placement technique was perfected, the sensors and load-setup was tested to confirm operation and constant loading speed operation was mastered to warrant test results. The first test objective was to obtain a representative rupture surface for the inverted shell footings required by alternating layered soil in color each having 100 mm thickness. A green dye pigment was premixed in with the TECH-Mix sand to visualize the soil displacement within the media under plane-strain load conditions without changing its physical mechanical soil properties. Idealization of the resulting rupture surface is shown in the ultimate stages for various shell footings including the inverted, upright and flat foundation footings. The deeper penetration of the wedged rupture portion dictates higher bearing capacity when compared to its upright counterpart. Either shell orientation confirms that higher bearing capacities are achieved over that of the shallower wedge obtained from traditionally flat footing models.



Figure 4.30. Layered Sand Test – Rupture Surface Simulation under Plane Strain.

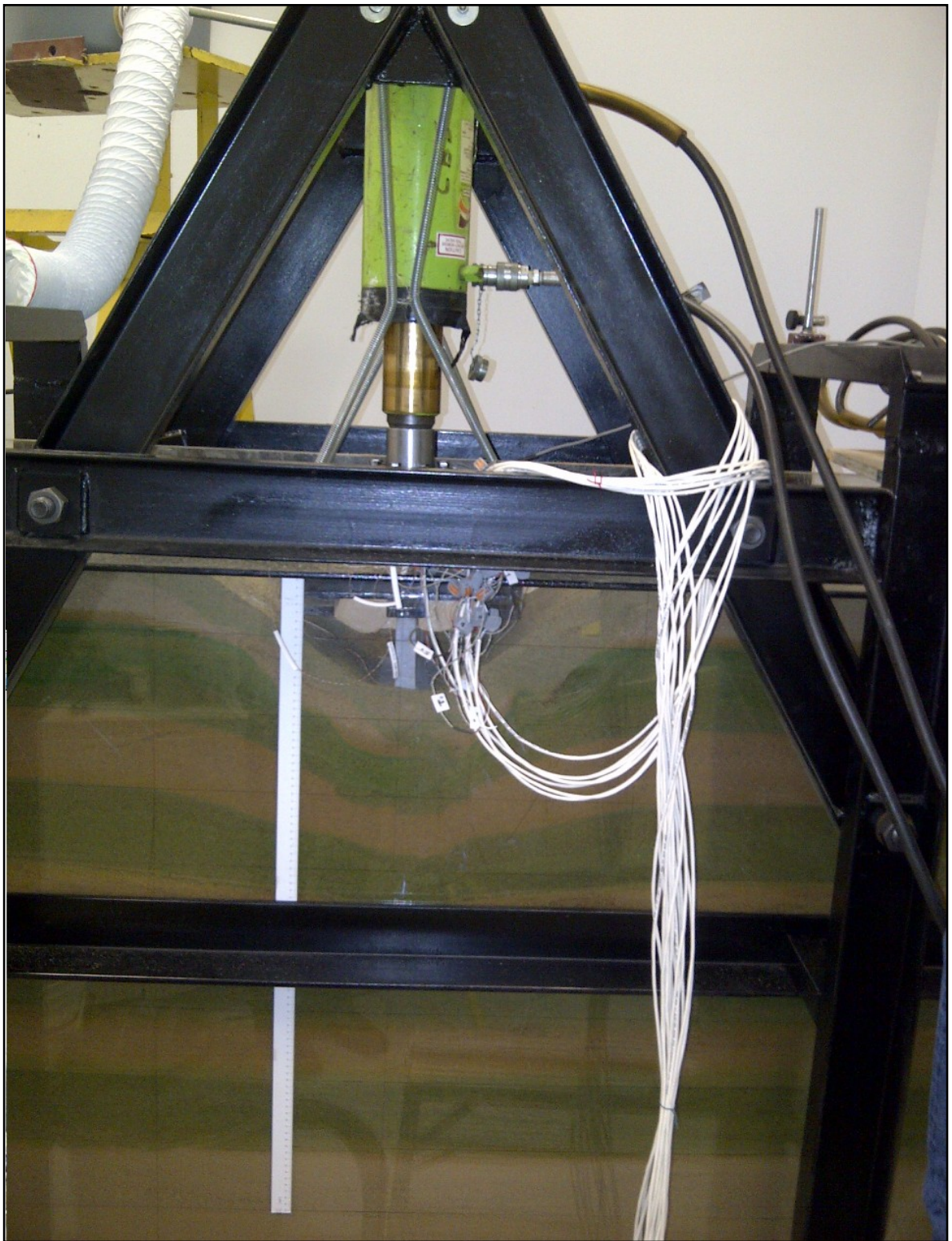


Figure 4.31. In-Progress Testing of Shell Footing Model.

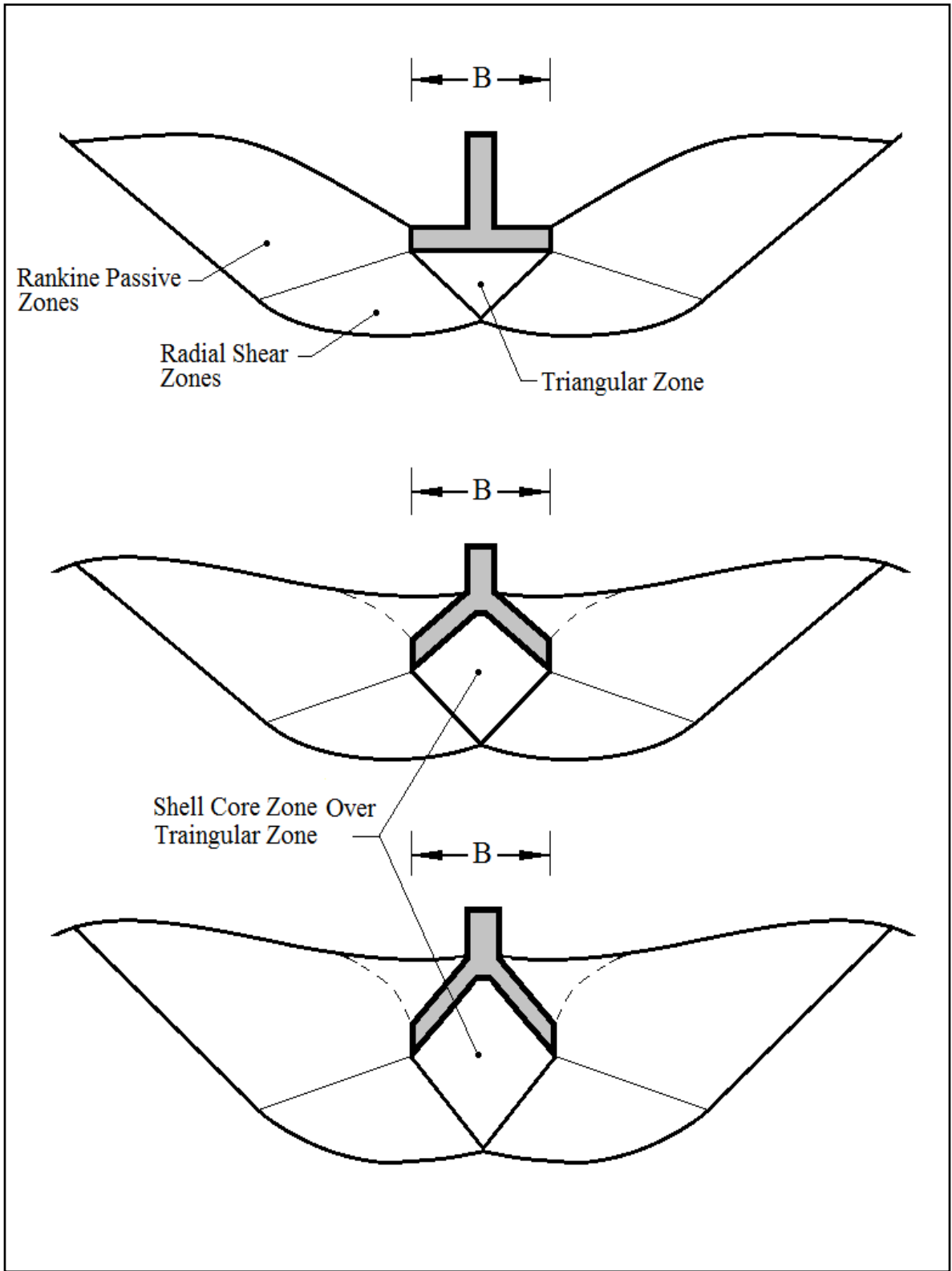


Figure 4.32. Rupture Surfaces for Flat and Upright Shell Footings.

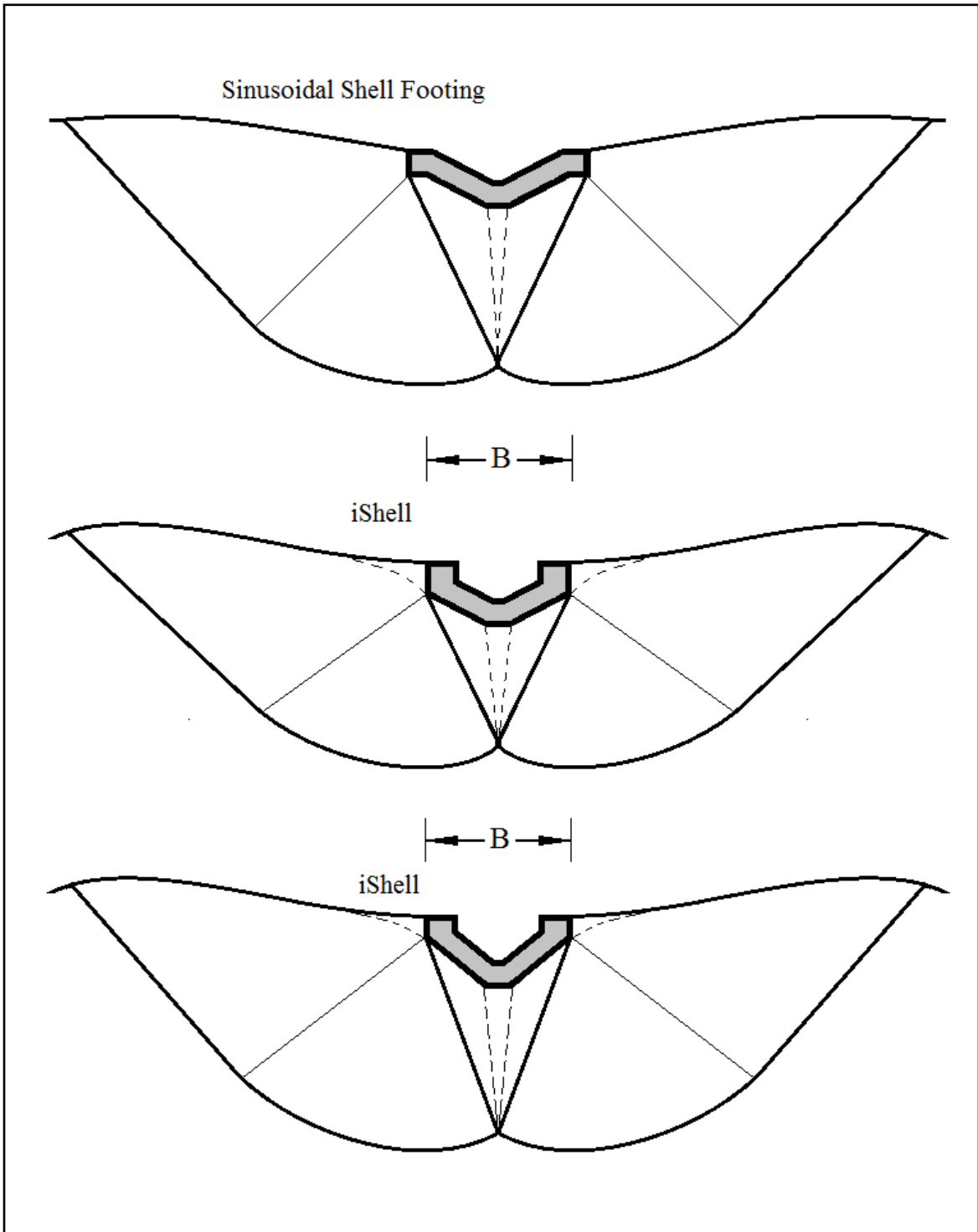


Figure 4.33. Bearing Capacity Failure for Sinusoidal and iShell Footings.

4.4.4 Pressure Transducers

The measurement of contact pressures in shells is of a higher difficulty than that of beams, piles, etc. since the pressure values cannot be deduced nor reduced directly from measured values of stresses. Thus, to accurately obtain a pressure reading, the normal contact pressure must be obtained directly at that point using pressure cells. Pressure is obtained using soil pressure transducers which measure the strain, using an electrical resistance strain gauge, in a thin circular diaphragm which is itself subject the soil pressure. A major flaw in the diaphragm type is that since the diaphragm body is allowed to swell or deflect under pressure, arching may develop in the surrounding soil, which may eventually lead to an underestimated reading of pressure cell at that point. To overcome the arching drawback from this cell, others have been developed operating on the principle of back pressure, in which air or oil, as the cell operation may be, under pressure on the opposite side. Pressure cells are also available which work on the principle of electrical inductance and also capacitance.

Care was foreseen and taken whenever surrounding soil in proximity with the cell was adjusted to allow for full contact. Pockets of higher or lower local densities of sand would greatly influence the results registered and was avoided. There are also cells developed at Cambridge, UK which can measure tangential contact pressures, even though contact pressure measurements are invariably limited to the normal component. In fixing the cells at the bottom of the model, a screw type or slot insertion can be made. The number of dial gauges, strain gauges or pressure cells used will be limited to eight per model. This is to keep the rigidity of the concrete model at its highest potential and limit the contact interface friction regime.

The dimensioning of the pressure transducer used is presented in the detailed sketch of Figure 4.34 with a 6.5 mm diameter and 9 mm shaft representing its overall dimensions. For a slot insertion type into the shell model, type PDB-PA was used. By strategically locating the transducers on the model as that suggested and proposed on the AutoCAD drawings one can obtain readings from a data acquisition system which would register

voltage for each transducer separately and give a pressure reading based on calibration parameters, depending on the calibration chart system provided.

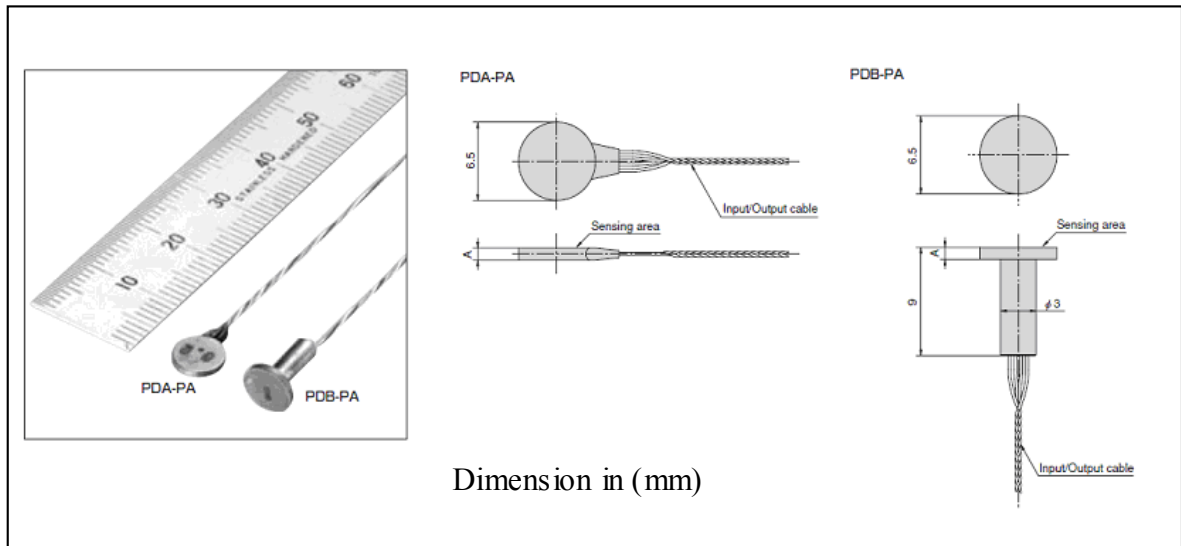


Figure 4.34. Miniature Pressure Transducer Models: PDB-PA (Bestech Ltd, 2009).

Of significant importance is that the transducers should be of high stiffness and insensitive to any temperature variations they may subject to once in the sand box. The PDB-PA model suggested has an acceptable temperature range of -20 to $+70^{\circ}\text{C}$ and capacity of 3 MPa. As well, soil density must be uniform to avoid forming air pockets of higher or lower densities neither at the cell nor the surrounding soil. This would cause an under or over registration and adversely influence the readings. The transducers themselves should also be placed flush with the shell foundation base to avoid any density variations leading to either stress concentration or relaxation, adversely affecting results. In extreme case where no contact exists, especially in the core section of the shell, obviously zero pressure registration will occur. Seven pressure transducers and seven pressure sensors for measurements at the iShell-soil interface and within soil bed were used respectively.

Since stress measurement directly in any structure is currently impossible the strain is measured since it is based on displacement. A number of techniques exist to measure strain but the two more common are extensometers which monitors the distance between two points and strain gages.

The pressure transducer model used in this experimental investigation were miniature sensors in keeping with scale of the experimental setup. A close-up view of the sensor and the metallic housing adaptor is shown in Figure 4.35. The pressure cells were metallic type flush mounted normal to the base of shell models and mechanically secured using bonding adhesive as per manufacturers recommendations. This was done to avoid possibility of incurring any variability in pressure measurements on account of stress concentration or reduction due to local soil densification or relaxation respectively. Pressure cell operates using a liquid diaphragm to generate an electrical signal which is converted to pressure loading signals. A data acquisition unit connected to a computer records contact pressures sent through electrical cables of the pressure cell. The normal pressure is calculated using calibration coefficients obtained from the results at the base of the cell is then plotted and contact pressure distribution curves are generated. It is important to note that prior to testing the pressure transducers required calibration following manufactures recommendations. Routine testing was conducted to monitor and insure cells were operational and in proper position to make sure the calibration factor was being respected by physical pressure tests.

In summary, a measurement of the test results will yield the parameters of response of the model to the applied load. Loading at measured increments will provide: a) deformations, b) stresses and c) contact pressures. The deformations or deflections (usually vertical only) are in most instances measured using dial gauges while the stresses are deduced from the strains ($\sigma = \epsilon \cdot E$), which are measured using electrical resistance strain gauges. Strain gauges will be used in pairs and will be inserted into slots produced in the metallic specimens. The greatest difficulty that can be anticipated is the experience of placing the gauges properly to be flush with the undersides of the model shells and to achieve accurate results from the readings. Although minimal, gross errors may result as due to problems such as temperature variations, contact angle of particles, strength parameters, sand voids in the shell core, etc. Verification with the theory should be examined. The unit stresses (one normal and two shearing) at any section of the shell can be determined from the stress resultants, both membrane and bearing, obtained from the theoretical analysis. These can be verified against the stress values extracted from measurement.



Figure 4.35. Pressure Transducer Insertion – iShell Footing Model.

4.4.5 Data Acquisition System

A computer based data acquisition system known as VISHAY Micro Measurement system was used to convert electrical signals to load values, displacement and pressure using a computer program called StrainSmart™ 5000 (v.4.31). This was achieved using calibration factors for each of the individual transducers, sensors and load cell used in the setup. While the sensors came pre-calibrated, the specifications data sheet information were preserved with data input into the system to identify each sensor on the appropriate channels on the data acquisition unit. The load cell however, was dismantled and tested independently using a Tinius-Olsen loading system at 22.24 kN [5000 lbf] interval for proper calibration.

The results of the calibration tests conducted on the universal flat load cell and sensors are presented in Figure 4.36(a) and (b), respectively. The software automatically records data input at a prescribed time interval minimizing room for discrepancies and possible human error. Sample results of sensor calibration tests conducted are tabulated and presented in graphical form in sensor calibration charts.

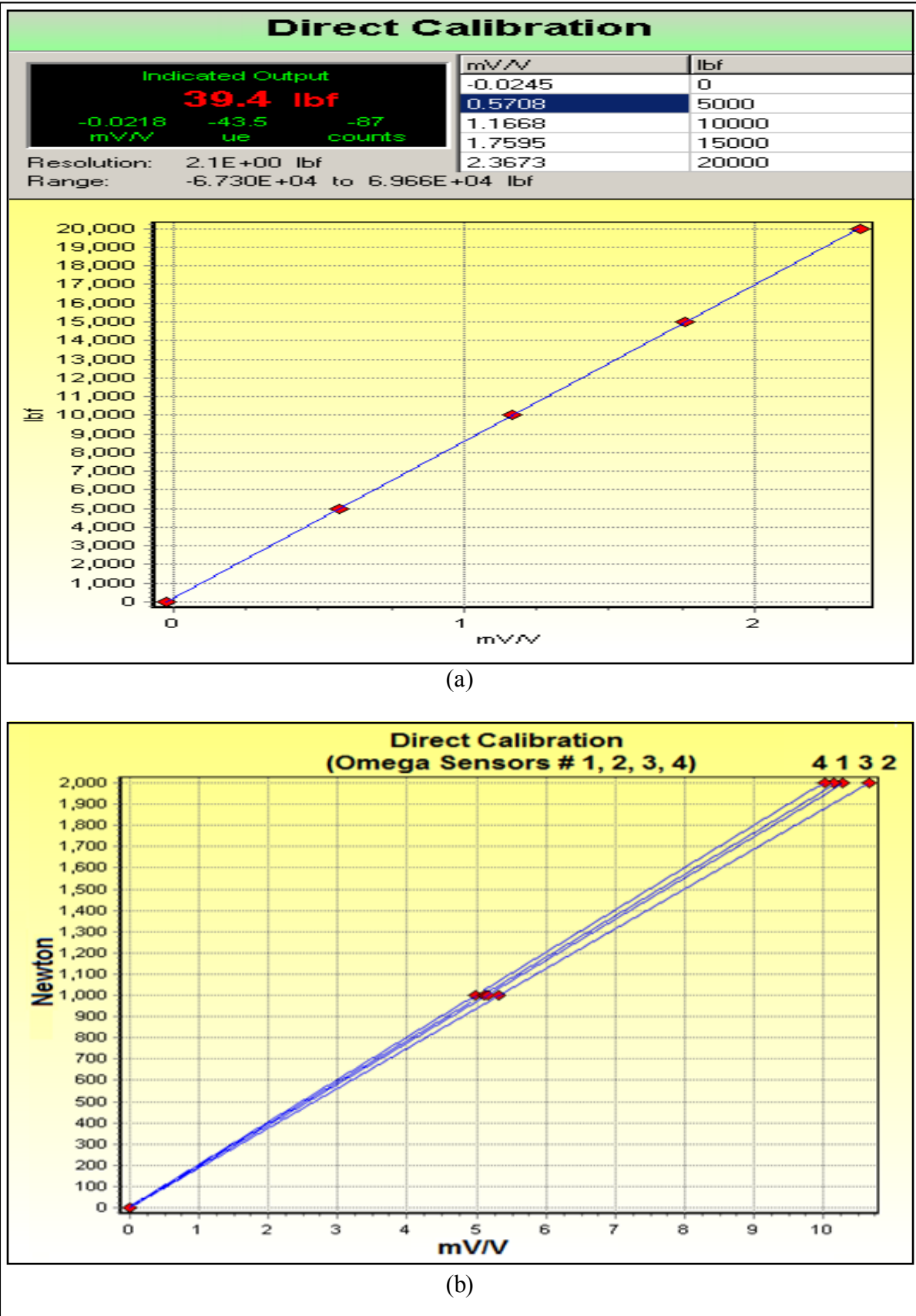


Figure 4.36. Sensor Calibration Charts: (a) Direct Load Cell (b) Omega Sensors.

4.5 Soil Models

Soil is a complex engineering material, and its properties are never unique nor constant. The fact is they vary along and beneath the earth's surface due to many generally uncontrollable environmental factors such as stress history, watertable fluctuations, geologic and chemical processes, time, etc. Due to the complexities of soil behaviour, let alone the curved and/or inclined nature of the shell proper, empirical correlations with proven performance records may be used extensively in evaluating soil parameters particularly for design. For the present investigation, sand is used as opposed to mixed clay–sand or inundated soil to focus our attention on the shell–soil interaction problem by eliminating the time–dependency related to such soil continuum.

4.5.1 Mohr–Coulomb Failure Criterion

The sand soil was modeled to behave as a linear elastic perfectly plastic material, with its yield function defined by Mohr–Coulomb's failure criterion. Aside from its wide use in literature, this model was selected based on its applicability, reasonable accuracy and simplicity of use under the type of analysis being investigated. Mohr's criterion is defined by the following relationship:

$$\tau = f(\sigma) \quad (4.1)$$

where the limiting shear stress, τ , in a plane depends on the normal stress, σ , acting in the said plane. The normal stress function, $f(\sigma)$ corresponds to the failure envelope whose trajectory is tangent to Mohr's circle of stress and defined as

$$\tau = c + \sigma \tan \phi \quad (4.2)$$

where c and ϕ are soil strength parameters of cohesion and angle of shearing resistance respectively. The Mohr–failure criterion associated with Coulomb's equation is referred to as the Mohr–Coulomb's equation and is clearly illustrated later in the next section as employed in the theoretical model.

4.5.2 Soil Properties and Characteristics

Dry sand has been the test method used repetitively in literature since clay is very difficult to obtain in terms of quantity and at a uniform density and consistency. In keeping with practice, the soil used in testing the shell models is chosen to be dry sand to reduce water content and thereby eliminating effects connected to the presence of a groundwater table. The sand maybe sprayed to have minimal water to aid in compaction processes and limit dust propagation during placement. The sand used in the present study is called TECH-Mix® dry sand from the company Bauval Inc. as obtained locally.

These sands are generally classified as being either calcareous or siliceous in nature depending on the chemical composition of the grains. Elastic deformation of the soil and rearrangement of the grains occur in both calcareous and siliceous sands, however crushing and cementation has been found to be characteristically higher in calcareous sands. Grain crushing has benefit of increasing the uniformity coefficient of the soil due to the smaller crushed grains filling the void space between larger grains. Consequently, the increase in the uniformity coefficient of the soil increases the ϕ' of the soil. The problems encountered is that of applying an available failure criterion when modeling numerically. Since this is a time-dependant phenomenon cognate with creep it is not readily representative to use the Mohr-Coulomb failure criterion as performed in PLAXIS. Since the grain-size distribution was found to be well-graded and uniform as shown in the next section, the TECH-Mix sand used minimizes such crushing impact as grains will adjust naturally.

4.5.2.1 Grain Size Distribution

The sand soil material used underwent a mechanical sieve analysis to obtain the grain size distribution curve. Mechanical vibratory sieve equipment such as that used in this test ensures best results. In literature, the sand used in laboratory tests is typically found to be well-graded (SW) type according to the Unified Soil Classification System (USCS). Other sands such as river or sea-bed sand used in similar studies have been reported according to studies conducted by Iyer *et al.* (1970). A sieve analysis graph illustrates the grain size distribution curve for the TECH-Mix sand as presented in Figure 4.37 and compared to the otherwise popular Ottawa sand type commonly used in similar experimental tests.

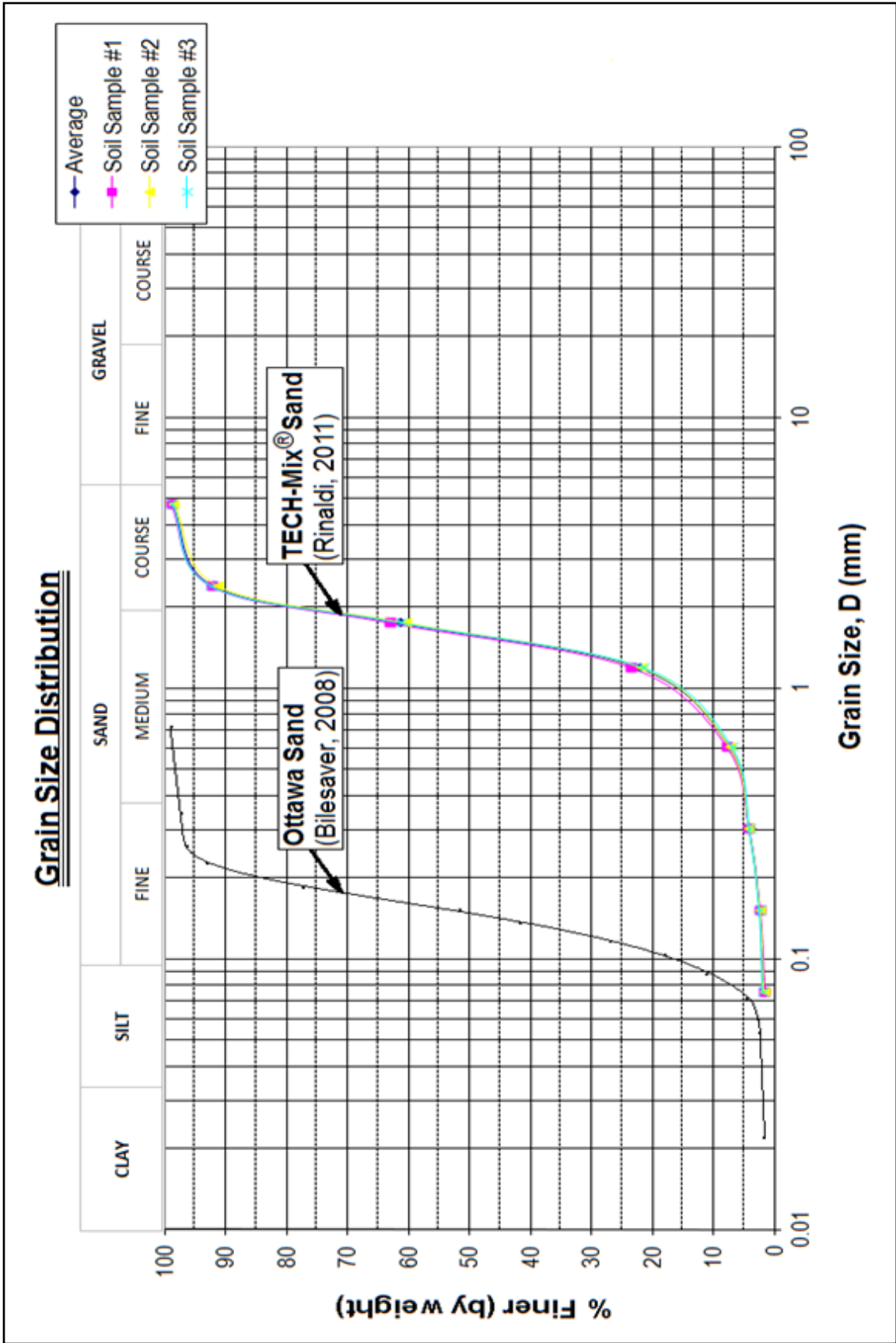


Figure 4.37. Grain Size Distribution for TECH-Mix Sand.

The grain size distribution data revealed medium, uniform sand composed of subangular quartz particles primarily with uniformity coefficient and coefficient of curvature of 2.42 and 1.83, respectively. Laboratory tests revealed an effective grain size of 0.70 mm. The sand material used in this investigation was well-graded (due to high value of C_u) medium to coarse subangular siliceous-quartz sand. Feldspar sands tend to offer higher shear strength values over quartz sands although simple laboratory tests should be invoked as routine measure (Bolton, 1986). As a verification of the theory developed in Chapter 5, a testing program was conducted using scaled concrete shell models bearing on dense, medium-dense and loose sand layers whose main physical characteristics are presented in the Table 4.4 as follows:

Properties	Value
Specific Gravity, G_s	2.60
Coefficient of Uniformity, C_u	2.42
Coefficient of Curvature, C_c	1.83
Grain Diameter at 10% passing, D_{10} (mm)	0.70
Grain Diameter at 60% passing, D_{60} (mm)	1.71
Grain Diameter at 30% passing, D_{30} (mm)	1.48
Maximum Dry Density, γ_{max} (kN/m ³)	16.80
Minimum Dry Density, γ_{min} (kN/m ³)	14.03
Maximum Void Ratio, e_{max}	1.70
Minimum Void Ratio, e_{min}	1.43
Optimum Water Content, w_{OPT} (%)	12.30

Table 4.4. Physical Properties of TECH-Mix® Sand.

Similar findings are that of Ottawa sand type often used in similar soil investigations involving monotonic concentric loading laboratory tests. Interestingly, both sands exhibit well sorted distributions of fines with TECH-Mix sand having proportionately larger sized particles along the spectrum of grain size.

Soil Type	Alwhite sand	Capital silt	Alwhite/Kaolin mixture	Ottawa sand	TECH-Mix® sand ⁽²⁾
G _s	2.75	2.6	N/A	2.65	2.6
D ₅₀ (mm)	0.3	0.06	0.25	0.13	1.69
D ₁₀ (mm)	0.1	0.02	0.06	0.08	0.7
K (cm/s) ⁽¹⁾	0.01	4x10 ⁻⁴	3.6x10 ⁻³	6x10 ⁻³	0.5

(1) $K = c \times d_{10}^2$; $c = 1$ (Budhu, 2007)
(2) (Rinaldi, 2011)

Table 4.5. TECH-Mix Sand Soil Parameters (Bilesavar, 2008).

A recent study describes Ottawa sand visually as being bulky and in general, angular, but clean, having physical properties for that particular batch contrasted with findings in the present investigation to that of the alluvial Mai-Liao sand (Feng T. W., 2009). A comparison is drawn between these and the TECH-Mix sand used in this research study as outlined in Table 4.6.

Soil Type	e _{max}	e _{min}	G _s	D ₅₀ (mm)
Mai-Liao sand	1.11	0.68	2.71	0.17
Ottawa sand	0.702	0.55	2.65	0.31
TECH-Mix® sand ⁽¹⁾	0.6243	0.4902	2.60	1.69

(1) (Rinaldi, 2011)

Table 4.6. Different Sand Soil Parameters (Feng T. W., 2009).

Additional sand soil properties are given in the subsequent table including the shear strength parameters and maximum dry unit weight of the sand obtained traditionally from a direct shear and proctor tests, also conducted. The densities in the direct shear tests should be maintained such that they are the same as those in the sandbox when testing the shell models.

4.5.2.2 Compaction and Permeability

Compaction is the process of increasing the density of a soil by packing the particles closer together with a reduction in the volume of air. The most suitable case of compaction is obtained with the addition of water, known as the optimum water content at which a maximum dry unit weight is reached. Standard proctor compaction tests were performed on TECH-Mix® sand material obtained from supplier BAUVAL Inc. to determine the compaction parameters as maximum dry density and optimum water content. The test results were obtained by compacting three equal layers with 25 blows per layer exerting $600 \text{ kN}\cdot\text{m}/\text{m}^3$ [$12,400 \text{ ft}\cdot\text{lb}/\text{ft}^3$] of compactive energy following standard ASTM D698. The data obtained from the compaction tests are plotted as shown in Figure 4.38 and the resulting average values of maximum dry density and optimum water content were found to be $16.8 \text{ kN}/\text{m}^3$ and 12.3%, respectively.

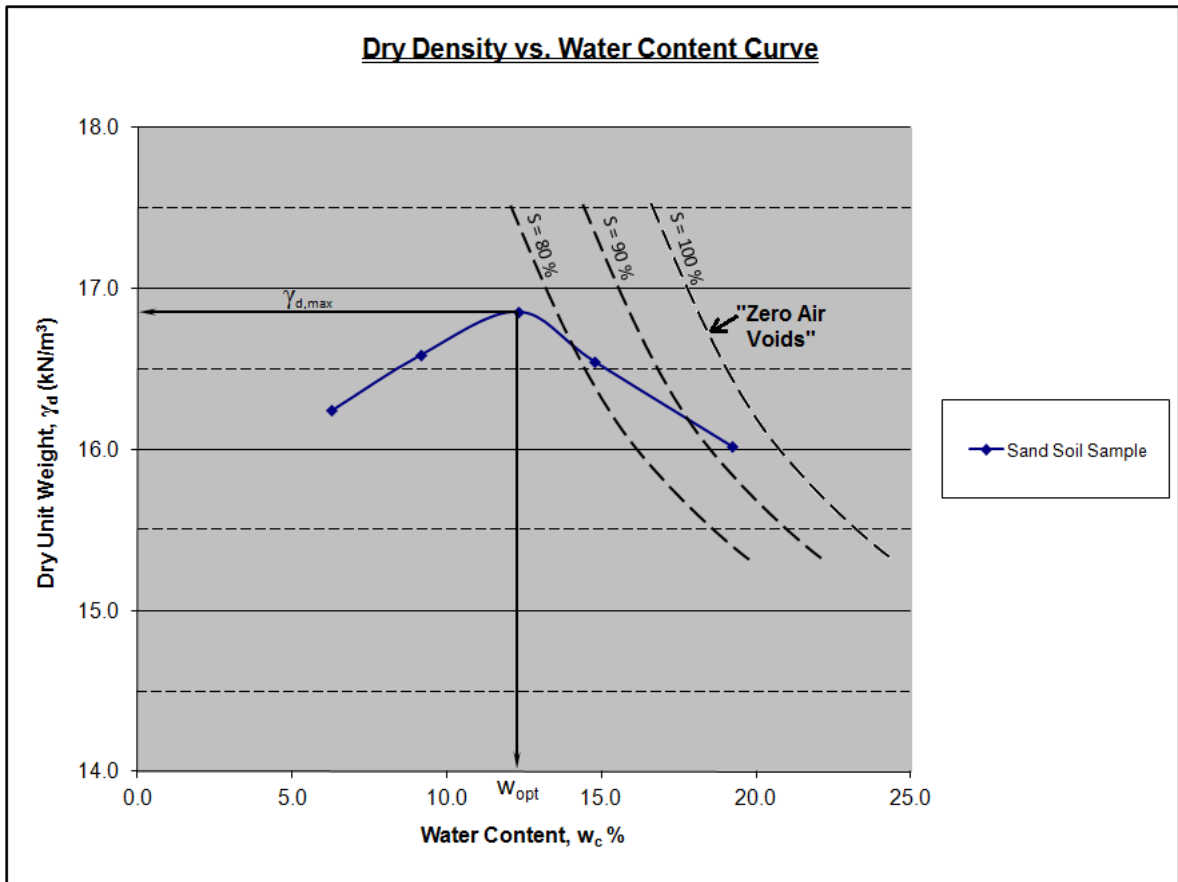


Figure 4.38. Standard Proctor Test Compaction Curve for TECH-Mix® Sand.

Following the experimental compaction curve obtained, the saturation curves for 80%, 90% and 100% were plotted.

The permeability of the same sand batch taken as representative samples were determined using the falling head permeability tests (ASTM D2434) performed on 10 compacted samples. The permeability coefficients obtained from the results of these tests varied from 4.6×10^{-7} to 3.3×10^{-9} cm/s, with an average value of 3.6×10^{-8} cm/s. Following these permeability test values obtained, materials are categorized in the very low permeable–impermeable class (Bell, 1993). This results in a suitable and convenient soil test material for the purposes of testing shallow shell foundation models.

The angles of shearing resistance of the three soil packing states under consideration were obtained from direct shear box and triaxial compression shear tests, and presented as shown in Figures 4.39 – 4.46 which follow.

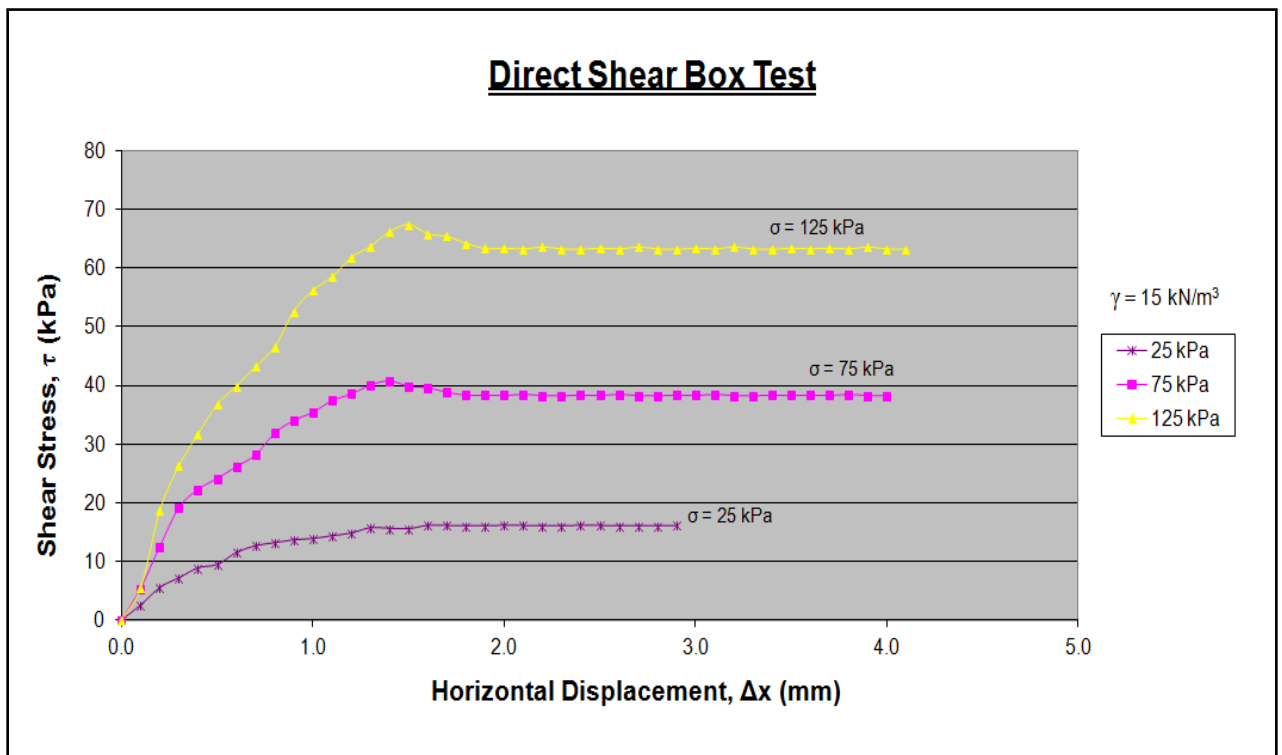


Figure 4.39. Direct Shear Box Test, $\gamma = 15 \text{ kN/m}^3$ on TECH-Mix® Sand.

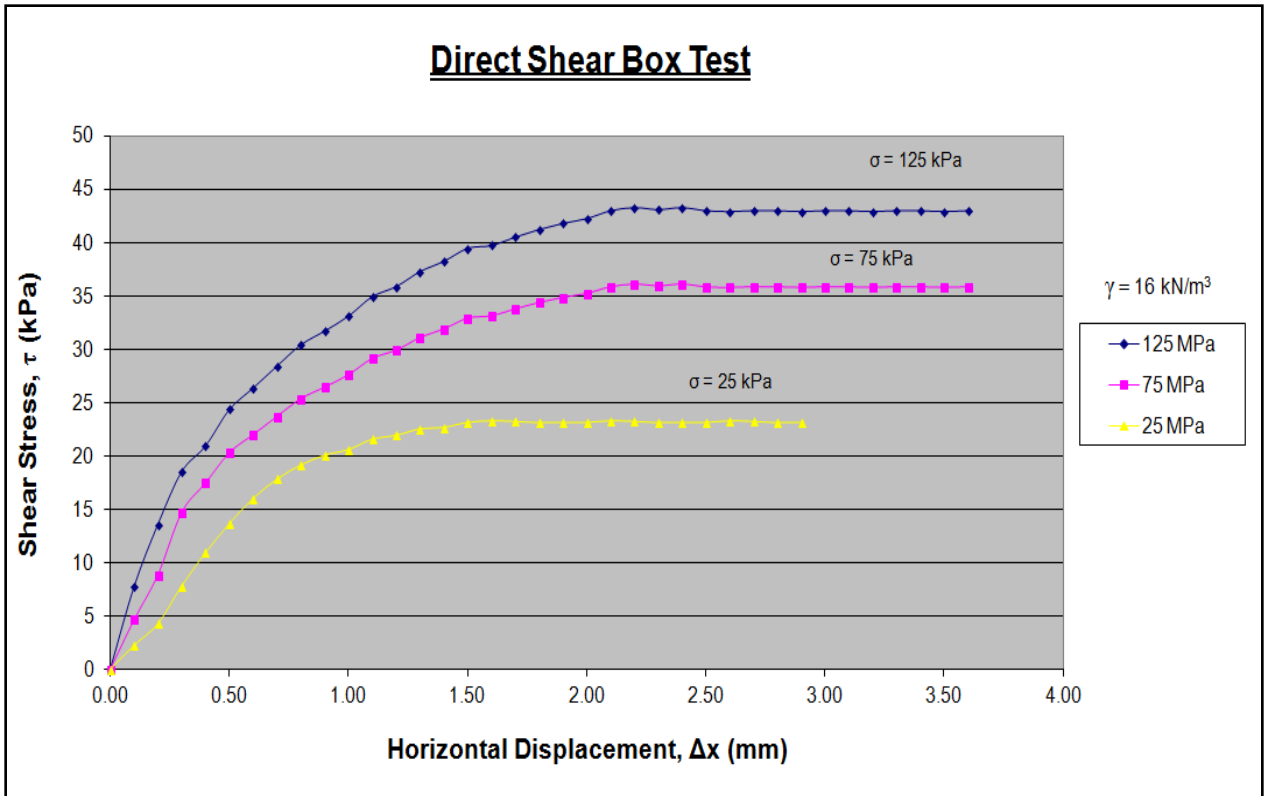


Figure 4.40. Direct Shear Box Test, $\gamma = 16 \text{ kN/m}^3$ on TECH-Mix® Sand.

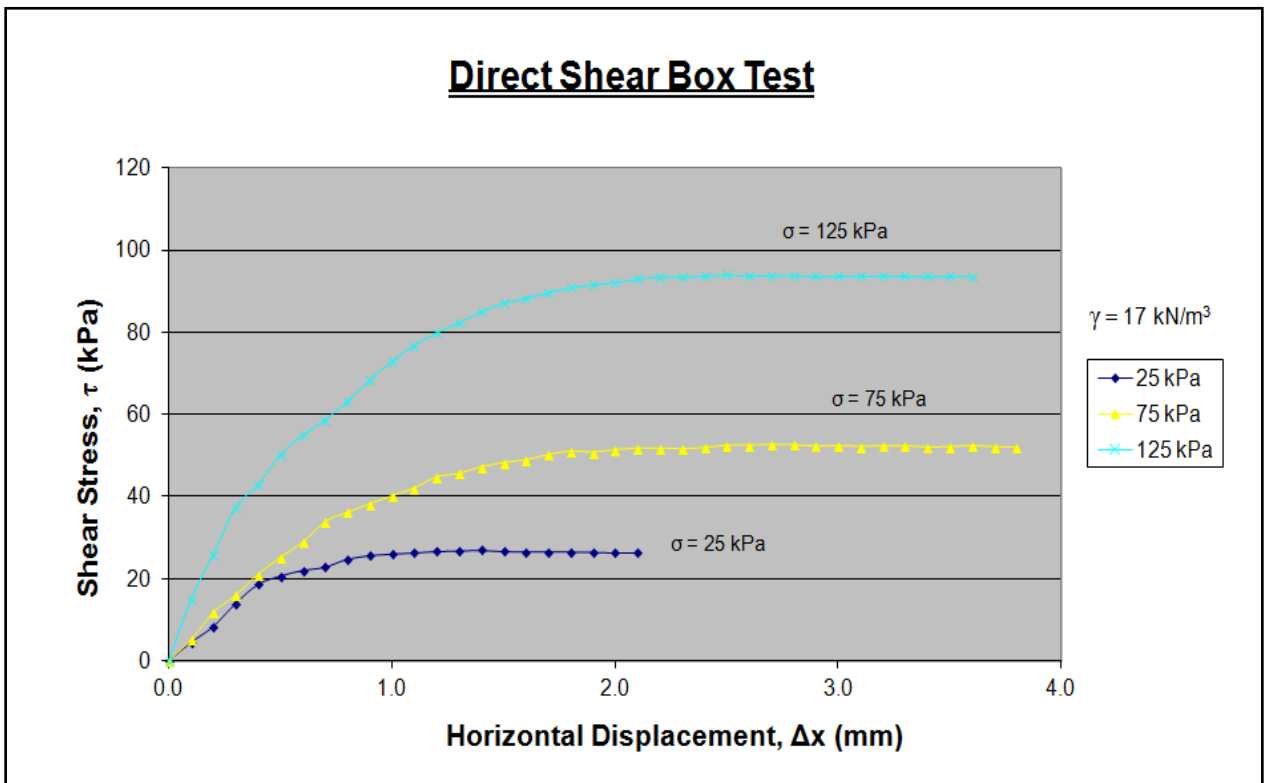


Figure 4.41. Direct Shear Box Test, $\gamma = 17 \text{ kN/m}^3$ on TECH-Mix® Sand.

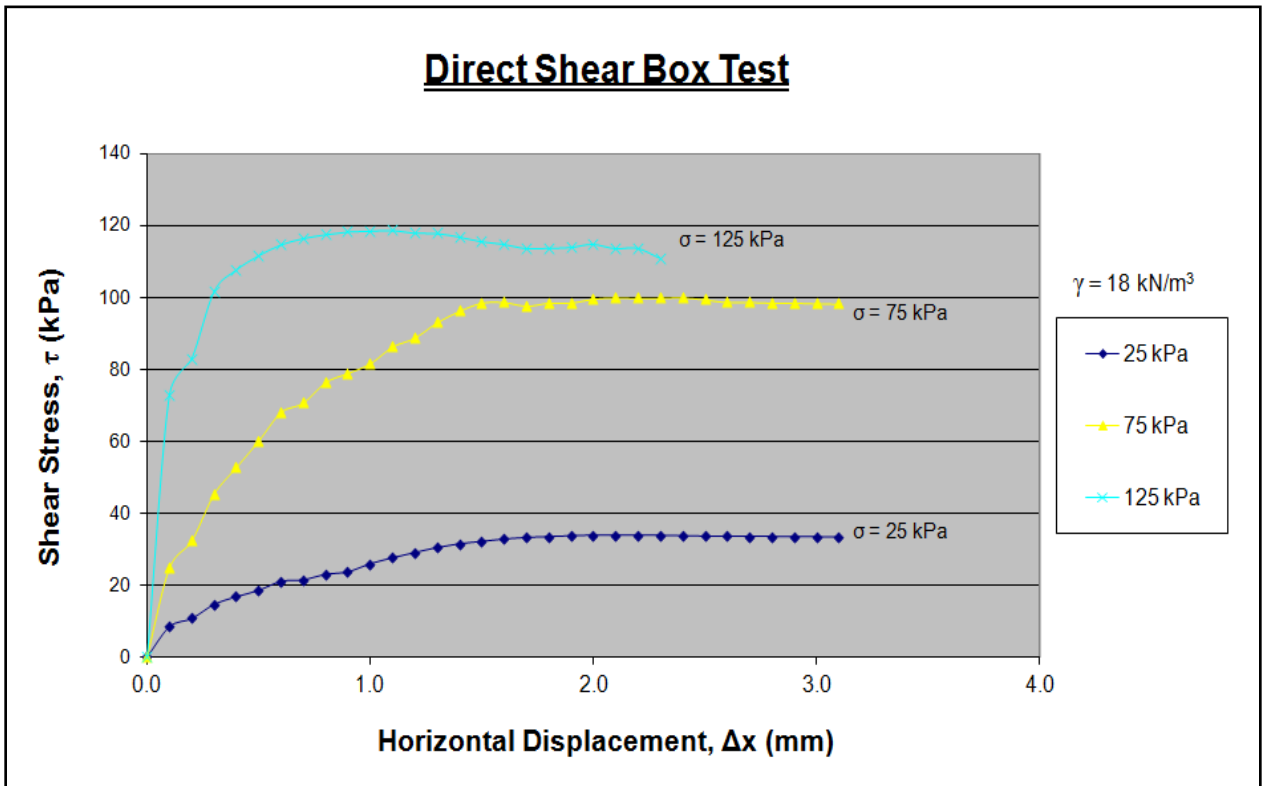


Figure 4.42. Direct Shear Box Test, $\gamma = 18 \text{ kN/m}^3$ on TECH-Mix® Sand.

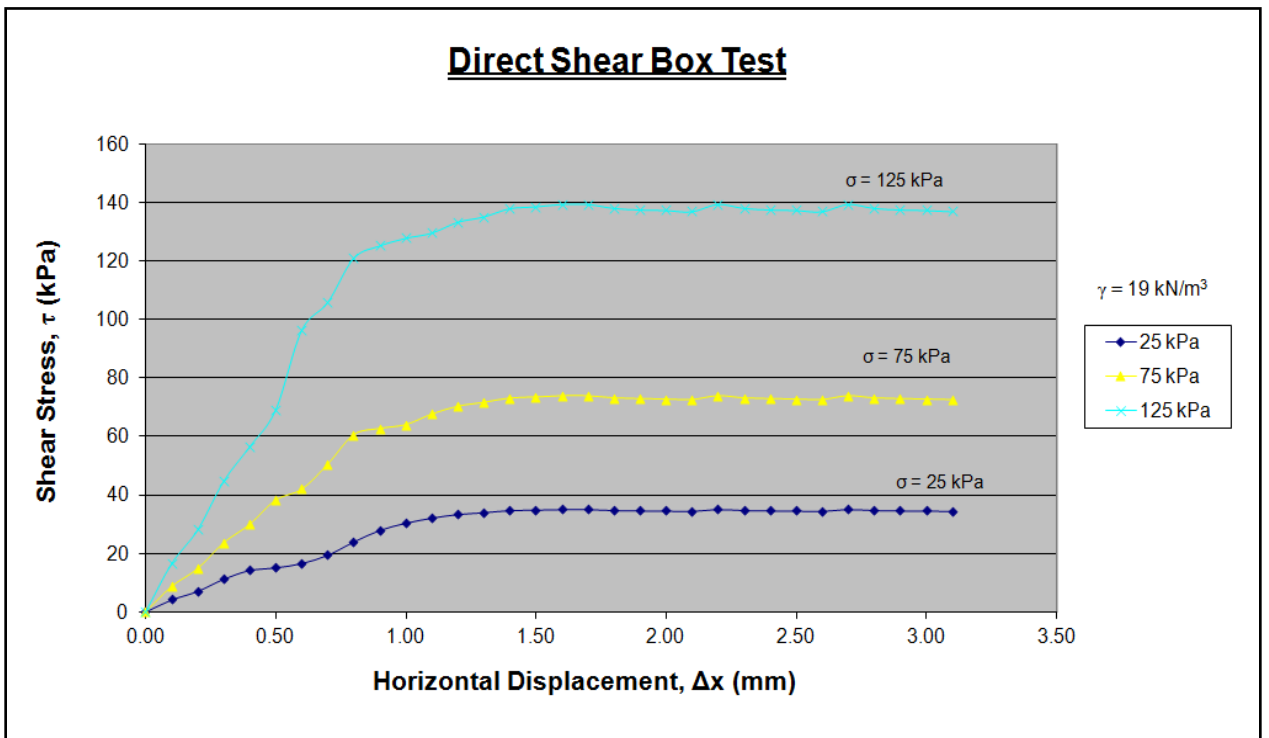


Figure 4.43. Direct Shear Box Test, $\gamma = 19 \text{ kN/m}^3$ on TECH-Mix® Sand.

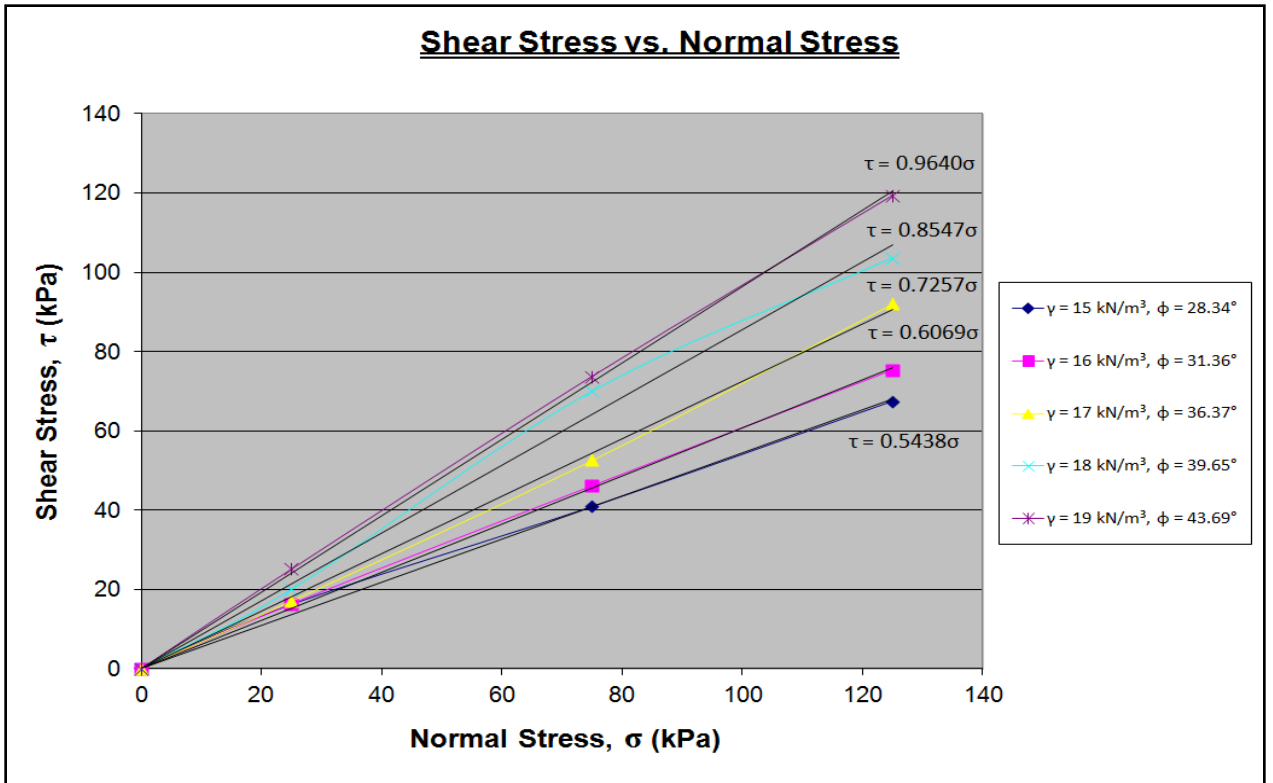


Figure 4.44. Shear Stress vs. Normal Stress on TECH-Mix® Sand.

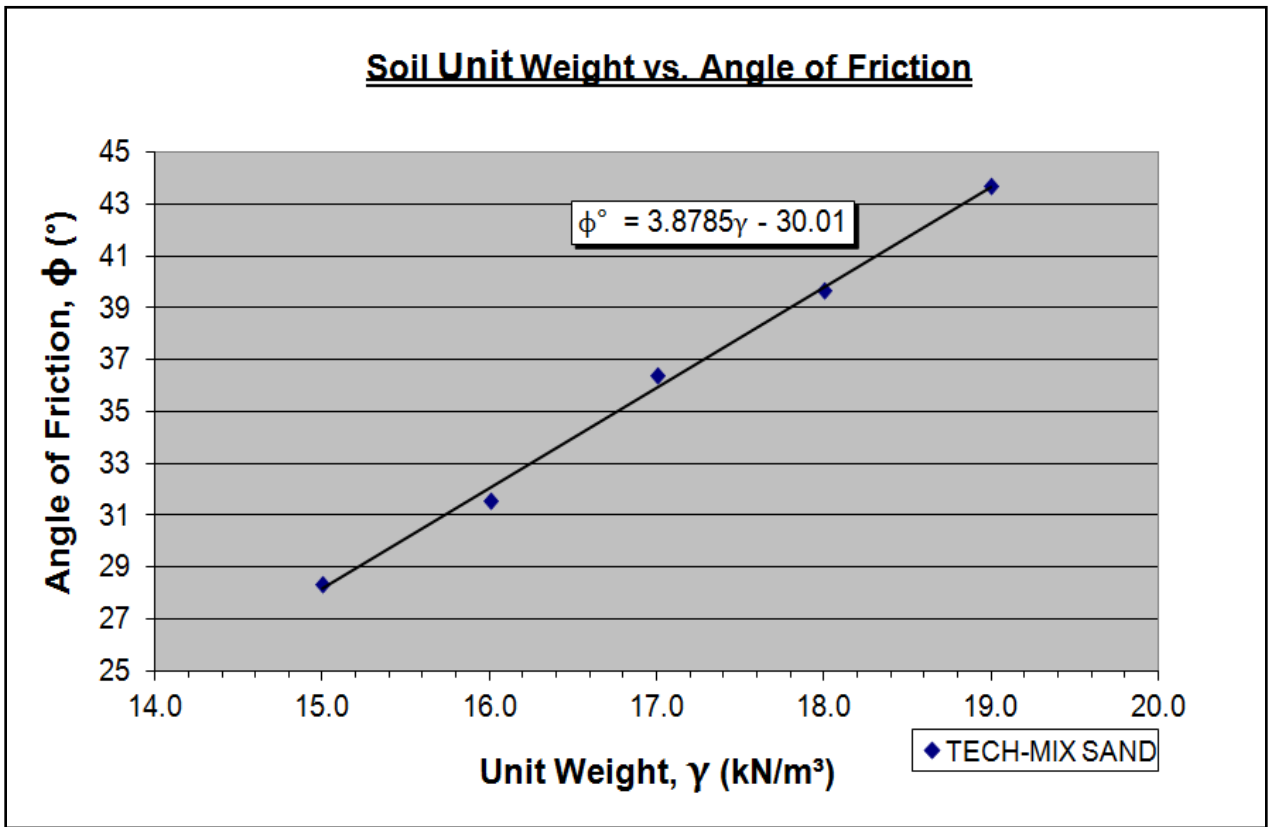


Figure 4.45. Unit Weight vs. Angle of Friction on TECH-Mix® Sand.

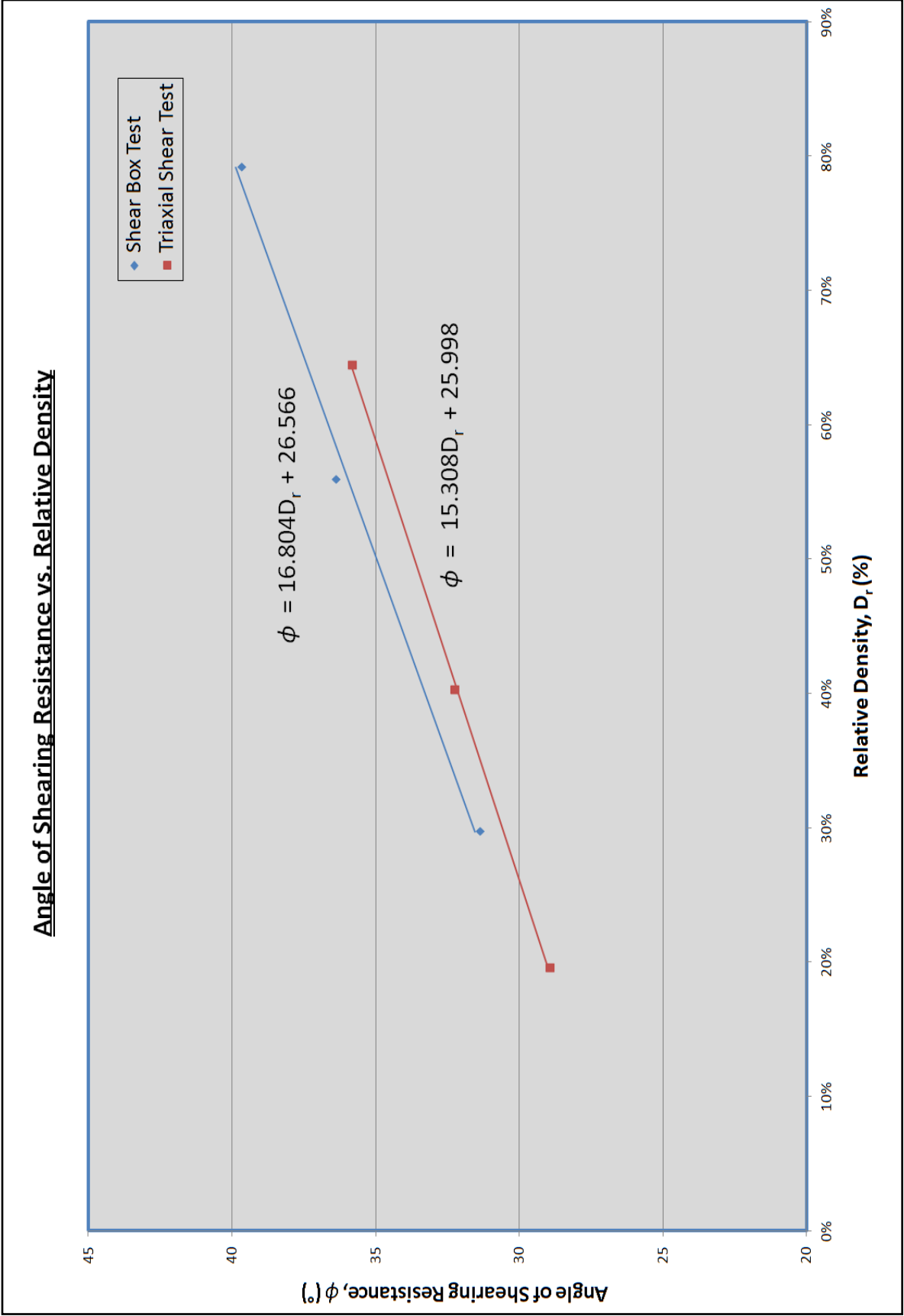


Figure 4.46. Angle of Shearing Resistance vs. Relative Density for TECH-Mix® Sand.

The results show an angle of shearing resistance from the shear box test was 10.7% and 8.4% higher over the triaxial test for dense and loose states respectively. On average the shear box tests render 9.6% higher values than the triaxial tests from which one can conclude a more conservative design from the latter over the former. Results from plane-strain tests may have otherwise been obtained yielding perhaps more conservative results.

Summary of Results :

Properties	Soil State		
	Loose	Medium–Dense	Dense
Sand Parameters			
Cohesion, c (kPa)	0.0001	0.0001	0.0001
Peak angle of internal friction, ϕ (°)	32.63	39.22	42.71
Maximum dry unit weight, $\gamma_{d \max}$ (kN/m ³)	16.76	16.80	16.84
Optimum water content, w_{opt} (%)	12.28	12.30	12.32
Dry unit weight, γ_d (kN/m ³)	16.15	17.85	18.75
Minimum dry unit weight, $\gamma_{d \min}$ (kN/m ³)	14.0	14.03	14.06
Uniformity Coefficient, C_u	2.42	2.42	2.42
Coefficient of Curvature, C_c	1.83	1.83	1.83
Average Specific Gravity, G_s	2.60	2.60	2.60
Relative Density, D_r (%)	33.6	55.8	79.2

Table 4.7. Property Variance of TECH-Mix® Sand.

4.5.3 Sand Bed Preparation

A prerequisite for sand bed preparation is infilling a testing reservoir of sufficient size to limit unwanted boundary condition and size effects. Fixed wall calibration chambers impose zero soil strain as the lateral boundary condition. The used placement technique in this study aimed at achieving greatest possible uniformity in pouring sand can be attained if the sand is allowed to fall into the tank slowly. While there may be several techniques to distribute the sand, the importance of uniformity is of significance. A good method uses vibro-compaction technique in several sand layers to maintain uniform soil conditions. Simple compaction of the entire sand bed at the surface provides non-uniform soil conditions which will adversely affect the result and thus was avoided. The method used in this study is explained in the next section and is prescribed to ensure reproducibility of the sand density throughout the testing program itself as reference for future studies.

Several methods were considered to be used to create sand-bed medium of dense, medium-dense and loose densities as developed by the experimental testing program. Popular sand bed preparation methods include tamping, sieve rainer and sand pluviation methods. The method used in the present investigation involves the rainfall method from a prescribed height to produce uniform and desirable density of the sand. It does however, involve certain elements of all three methods mentioned and therefore a brief description is provided for each before the sand bed preparation descriptive used in the present investigation is outlined.

In the tamping method, the sand is moistened prior to pouring in the sandbox container mainly for dust control. The sand is then deposited in the container in layers. Each layer is compacted by tamping with a specific, and even, force. Hand tamping or vibratory compaction can be used with the former used in this study. Sand samples with a relative density ranging between 40% up to as much as 80% have been created by wet tamping (Konrad, 1998).

Stuit (1995) constructed sand samples for testing in a centrifuge. He used the sieve rainer method on two different sands, namely the Dune and Eastern Scheldt sands in order to obtain the homogeneous sand samples required for his tests. The sieve rainer or pepperbox method is based on pouring sand in the sample container through a sieve which is located at a certain distance above the sample container as shown in Figure 4.47. The sieve is characterized by a low aperture area reducing the sand flow so that the sand flux can be controlled accurately. Generally, the set-up consists of three main parts:

- The pepperbox, in which the sand is stored. A sieve is attached at its bottom
- The lifting system, which makes it possible to change the height of the pepperbox and control the falling height of the sand
- A sand transportation and vacuum system

The vacuum system is connected with the pepperbox. The pepperbox is airtight, which allows the vacuum system to regulate the “opening” of the sand sieve by changing the vacuum pressure and thus the airflow in the pepperbox. The sand transportation system which is on one side connected to an external sand storage and on the other side to the pepperbox can also be regulated by the vacuum system.

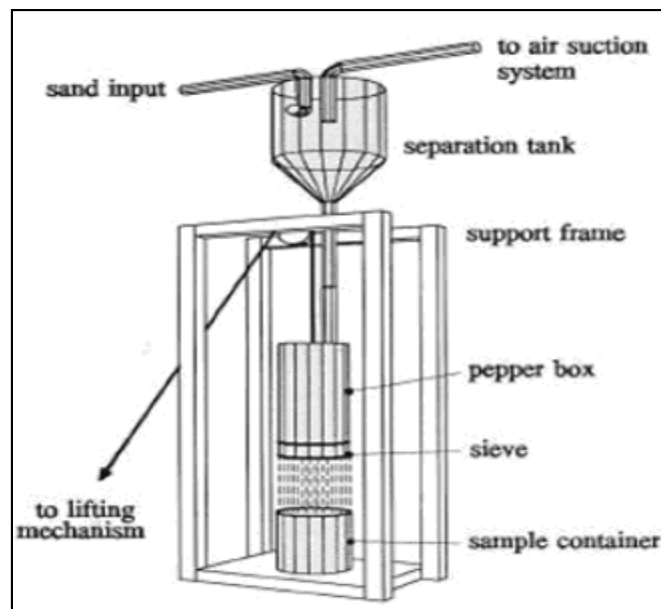


Figure 4.47. Sieve Sand Rainer (Stuit, 1995).

The falling height is the actual distance between the sand surface and the falling point where the sand starts to fall (ie. from the sieve). Since a lower falling height gives a relatively higher porosity to that of the already rained sand it is important to keep the falling height constant when a homogenous sand sample is desired. During the construction of a homogenous sand sample, the lifting system therefore increases the height of the sieve as the sand surface rises. Falling heights ranging from 0 mm up to 400 mm are used. During the test, a guiding cylinder is placed on top of the sample container preventing the falling sand from external air turbulence. The excess sand above the container surface is removed with a sand scraper.

The pluviation method is widely used and an acceptable method to create sand beds of uniform density. Sand pluviation is based on the same theory as the sand raining method; the falling height of the sand determines the density of the sample created (Rad and Tumay, 1987). Instead of the sieve, a funnel is used. The sand is stored above the funnel. The height of the funnel can be adjusted by hand or mechanically. Two different sand pluviation methods are used; dry sand pluviation and wet pluviation. A setup of dry pluviation is shown in Figure 4.48. Sand is stored in the funnel (A). The sand falls through an optional pipe (B), to avoid air turbulence influencing the sand flow, in the sample container (C). The falling height (H) is measured with the help of a long ruler (D).

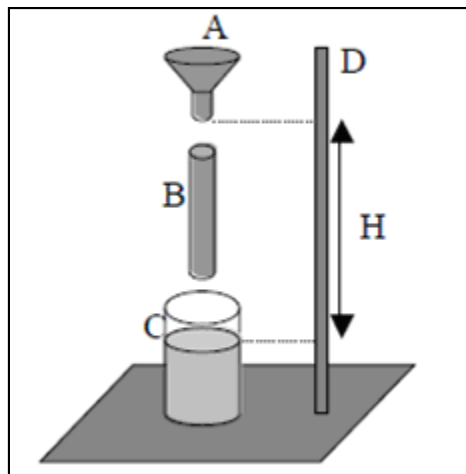


Figure 4.48. Dry Sand Pluviation.

The density of the sand specimen is related to the drop in height, volume of the sand deposited per unit time, funnel size and sand grain properties. A drawback of this method,

however, is that dry pluviation may cause particle segregation by rolling or impact as described by (Stuit, 1995) who investigated the dry pluviation method in more detail and so a constrained funnel system was not used in this study. Specifically, he defined two kinds of mechanisms observed during sand pluviation; the “rolling” and the “impact” mechanisms as shown in Figure 4.49 below. The rolling mechanism is best explained by the shape of a cone. When the sand falls onto the surface, a cone is formed. Compaction takes place at the point of the cone. However a large part of the sand rolls down the slope of the cone, which will not compact the underlying sand. These cone shapes have to be avoided since they have tendency to increase the variation of the density within a sample.

The impact mechanism occurs when the sand hits the sand surface with a high speed resulting in compaction of a large area. A sample, which is prepared with short falling distances, will be built up mainly by the rolling mechanism. The impulse of falling sand will be small at the point of contact with the sand surface. Therefore, the area which is compressed is small and the impulse is too low to fully compress the developed sand cone. Naturally, with increasing falling heights the energy of the sand stream increases. Due to the greater diameter of the sand stream at the time of contact with the sand surface a larger area will directly be compressed. Dry sand pluviation is a technique often used to prepare sand samples for centrifuge tests.

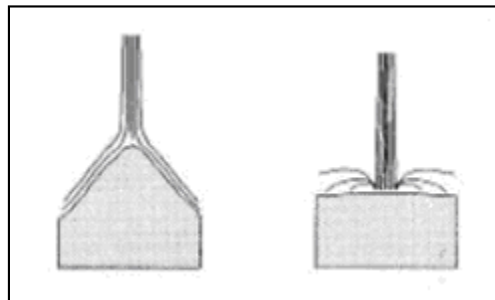


Figure 4.49. Rolling (left) and Impact (right) Mechanisms Occurring During Dry Sand Pluviation (Stuit, 1995).

Wet pluviation is similar to dry pluviation, but de-aired water is used instead of air. This ensures specimen saturation. Since the terminal velocity of the sand through water is lower than through air, lower sample relative densities are achievable. The range of

densities, which can be obtained, is also very small because the terminal velocity in water for sand with a D_{50} of 0.4 mm is reached in 2.0 mm (Vaid & Negussey, 1984).

Dense sand packing was obtained by raining the sand from a height of 914 mm [36 in.] for each 102 mm [4 in.] layer aided by a metallic sieve 241 mm [9.5 in.] in diameter. Medium-dense sand packing was achieved by raining the sand from a 152 mm [6 in.] height for each layer aided by a flexible rubber hose outfitted with an end-sieve. Loose sand packing was achieved using the same equipment for medium-dense sand placement only very slowly and at low height following the dry sand pluviation method of placement. Figure 4.50 illustrates the storage bin at height and hose funnel system used for sand placement to achieve the desired uniform soil distribution and density.



Figure 4.50. Elevated Storage Bin & Funnel System for Sand Pluviation.

A mesh made from 3 mm thick PVC grid having 4 mm diameter perforations located 6 mm and 12 mm center-to-center in each of the planar directions enabled 100% passage of sand to freely disperse and further create uniformity for each layer. This added measure prevented any unwanted particles from entering the test tank potentially hindering results.



Figure 4.51. Sand Pluviation Distribution Method.

The average dry density (γ_d), porosity (n), and relative density (D_r) of the TECH-Mix sand used in this investigation are provided in Table 4.8 as follows.

Sand State	Dry Density, γ_d (kN/m ³)	Porosity, n (%)	Relative Density, D_r (%)	Angle of Shearing Resistance, ϕ (°)	
				Direct Shear Box Test Results	Triaxial Compression Test Results
I Loose	16.15	48.9%	33.6%	32.63	28.94
II Medium dense	17.85	43.7%	55.8%	39.22	32.24
III Dense	18.75	38.1%	79.2%	42.71	35.82

Table 4.8. Angle of Shearing Resistance for Various Sand States.

The canned density method provided a suitable way of determining the specified densities at any location within the test tank. Eight aluminum cans of known mass and volume were placed level on a sand bed line coherent with soil-shell structure interface. Following each test, the cans were carefully removed and excess sand was shed. Each can-soil specimen was weighed to obtain the required confirmation of density calculated and representative of those enlisted in the preceding table.

4.5.4 In-Situ Stresses in Sand

From a modeling perspective, establishing in-situ stresses is of fundamental importance. This requires that the initial stress state in the sand be known. Generally for soils, vertical stresses can be readily determined, while horizontal stresses are much more difficult to ascertain. The ratio of horizontal to vertical effective stresses in soil is defined by the coefficient of earth pressure at rest, k_o , or simply:

$$k_o = \frac{\sigma_h'}{\sigma_v'} \quad (4.3)$$

Coefficient of earth pressure at rest for normally consolidated and overconsolidated soils is given by $k_{o,nc}$ and $k_{o,oc}$ respectively. The value of k_o during one-dimensional normal compression or consolidation under which no lateral deformation occurs is known as $k_{o,nc}$ and has been determined empirically to be constant for a given soil. The most generally accepted relationship in estimating $k_{o,nc}$ is represented by the equation:

$$k_{o,nc} = \left(1 + \frac{2}{3} \sin\phi'\right) \left(\frac{1 - \sin\phi'}{1 + \sin\phi'}\right)$$

which can be approximated in the widely accepted form as:

$$k_{o,nc} = 1 - \sin\phi' \quad (\text{Jaky, 1944}) \quad (4.4)$$

Other relationships have been developed including

$$k_{o,nc} = 0.95 - \sin\phi' \quad (\text{Brooker \& Ireland, 1965}) \quad (4.5)$$

$$k_{o,nc} = \left(\frac{1 - \sin(\phi' - 11.5^\circ)}{1 + \sin(\phi' - 11.5^\circ)} \right) \quad (\text{Bolton, 1991}) \quad (4.6)$$

$$k_{o,nc} = \left(\frac{\sqrt{2} - \sin\phi'}{\sqrt{2} + \sin\phi'} \right) \quad (\text{Brick model: Simpson, 1992}) \quad (4.7)$$

For overconsolidated soils, k_o can be calculated from known values of $k_{o,nc}$ and the over consolidation ratio (OCR). The overconsolidation ratio is defined as the largest vertical effective stress ever experienced by the soil deposit (σ_p'), known as the preconsolidation pressure, divided by the existing vertical effective stress (σ_v'). Widely accepted relationships found in literature include:

$$\text{OCR} = \frac{\sigma_p'}{\sigma_v'} \quad (4.8)$$

$$k_o = k_{o,nc} \text{OCR} - \left[\frac{v}{1-v} \right] (\text{OCR} - 1) \quad (\text{Wroth, 1972}) \quad (4.9)$$

Several researchers suggest that k_o is related to OCR by an expression of the form

$$k_o = k_{o,nc} (\text{OCR})^\alpha \quad (\text{Schmidt, 1966; Alpan, 1967}) \quad (4.10)$$

where $\alpha = 1.25 \sin\phi'$

alternatively,

$$\alpha = \sin\phi' \quad (\text{Mayne and Kulhawy, 1982}) \quad (4.11)$$

$$\alpha = 0.46 \pm 0.06 \quad (\text{Jamiołkowski, et al. 1979}) \quad (4.12)$$

$$\alpha = 0.5 \quad (\text{Meyerhof, 1976}) \quad (4.13)$$

Typical values of coefficient of earth pressure at rest (k_o) and poisson's ratio (v):

No.	Soil State Type	k_o	v
1	Dense Sand	0.35	0.30 – 0.45
2	Medium Sand	0.45	0.25 – 0.40
3	Loose Sand	0.60	0.20 – 0.40
4	Normally consolidated clays	0.5 – 0.6	0.20 – 0.30
5	Lightly overconsolidated clays	1.00	0.30 – 0.50
6	Heavily overconsolidated clays	3.00	0.30 – 0.50

Table 4.9. Elastic Parameters of Various Soils (Das, 2005).

Pressure transducers were used to measure the vertical and lateral stress within the sand bed before and after compaction effort was applied. As expected at the onset, compaction of each progressive sand layer would lead to an increase in both the vertical σ_{yy} and lateral stresses σ_{xx} within the previous sand mass due to the cumulative mechanical effort. These stresses would exceed theoretical values calculated for the sand before compaction as the sand bed would be in a normally consolidated state as follows:

$$\sigma_o = \sigma_z k_{o,nc} \quad (4.14)$$

$$\text{where} \quad \sigma_z = \gamma z \quad (4.15)$$

and $k_{o,nc}$ is that given by (Jaky, 1944) mentioned above. After completing compaction the vertical and lateral stresses would gradually decrease in effort to stabilize until they attained values slightly higher than the overburden pressure σ_z and the at rest earth pressure σ_o , respectively. Consequently, mechanical compaction effort of layered sand soil develops an overconsolidated sand state.

For the prescribed depth of embedment immediately after placing and compaction of the sand layer we can calculate the overconsolidation ratio (OCR) using Equation (4.9) proposed by (Wroth, 1972). As such, establishing $k_{o,nc}$ from Equation (4.4) and using the experimental results for $k_{o,oc}$, one can calculate OCR as follows:

$$\text{OCR} = \left(\frac{k_{o,oc} - (v / 1 - v)}{k_{o,nc} - (v / 1 - v)} \right) \quad (4.16)$$

where poisson's ratio, v were taken as the average values of 0.30, 0.33 and 0.36, from Table 4.9 above as proposed by (Das, 2005) for the loose, medium and dense sand states respectively. The results in a tabulated form are presented and concluding remarks in the summary is made.

LOOSE SAND

$$\phi = 32.63^\circ, \gamma = 16.15 \text{ kN/m}^3$$

Depth (m)	σ_x (kPa)	σ_y (kPa)	σ_z (kPa)	σ_o (kPa)	$k_{o(oc)}$	$k_{o(nc)}$	v	OCR
0	0	0	0	0	0	0	0.30	0.00
-0.10	0.80	1.73	1.62	0.74	0.462	0.461	0.30	1.05
-0.20	1.65	3.51	3.23	1.49	0.470	0.461	0.30	1.29
-0.30	2.51	5.32	4.85	2.23	0.472	0.461	0.30	1.34
-0.40	3.24	6.83	6.46	2.98	0.474	0.461	0.30	1.42
-0.50	3.89	8.18	8.08	3.72	0.476	0.461	0.30	1.46
-0.60	4.69	9.84	9.69	4.47	0.477	0.461	0.30	1.49

Table 4.10. OCR for Loose Sand Compaction.

MEDIUM-DENSE SAND

$$\phi = 39.22^\circ, \gamma = 17.85 \text{ kN/m}^3$$

Depth (m)	σ_x (kPa)	σ_y (kPa)	σ_z (kPa)	σ_o (kPa)	$k_{o(oc)}$	$k_{o(nc)}$	v	OCR
0	0	0	0	0	0	0	0.33	0.00
-0.10	0.82	2.48	1.79	0.66	0.331	0.368	0.33	1.30
-0.20	1.69	5.18	3.57	1.31	0.326	0.368	0.33	1.33
-0.30	2.55	7.93	5.36	1.97	0.322	0.368	0.33	1.37
-0.40	3.35	10.65	7.14	2.63	0.315	0.368	0.33	1.43
-0.50	3.99	13.52	8.93	3.28	0.295	0.368	0.33	1.58
-0.60	4.87	16.53	10.71	3.94	0.295	0.368	0.33	1.59

Table 4.11. OCR for Medium-Dense Sand Compaction.

DENSE SAND

$$\phi = 42.71^\circ, \gamma = 18.75 \text{ kN/m}^3$$

Depth (m)	σ_x (kPa)	σ_y (kPa)	σ_z (kPa)	σ_o (kPa)	$k_{o(oc)}$	$k_{o(nc)}$	v	OCR
0	0	0	0	0	0	0	0.36	0.00
-0.10	0.89	3.88	1.88	0.60	0.229	0.322	0.36	1.38
-0.20	1.71	7.69	3.75	1.21	0.222	0.322	0.36	1.41
-0.30	2.62	12.91	5.63	1.81	0.203	0.322	0.36	1.49
-0.40	3.38	16.79	7.50	2.41	0.201	0.322	0.36	1.50
-0.50	4.02	23.02	9.38	3.02	0.175	0.322	0.36	1.61
-0.60	4.89	28.18	11.25	3.62	0.174	0.322	0.36	1.62

Table 4.12. OCR for Dense Sand Compaction.

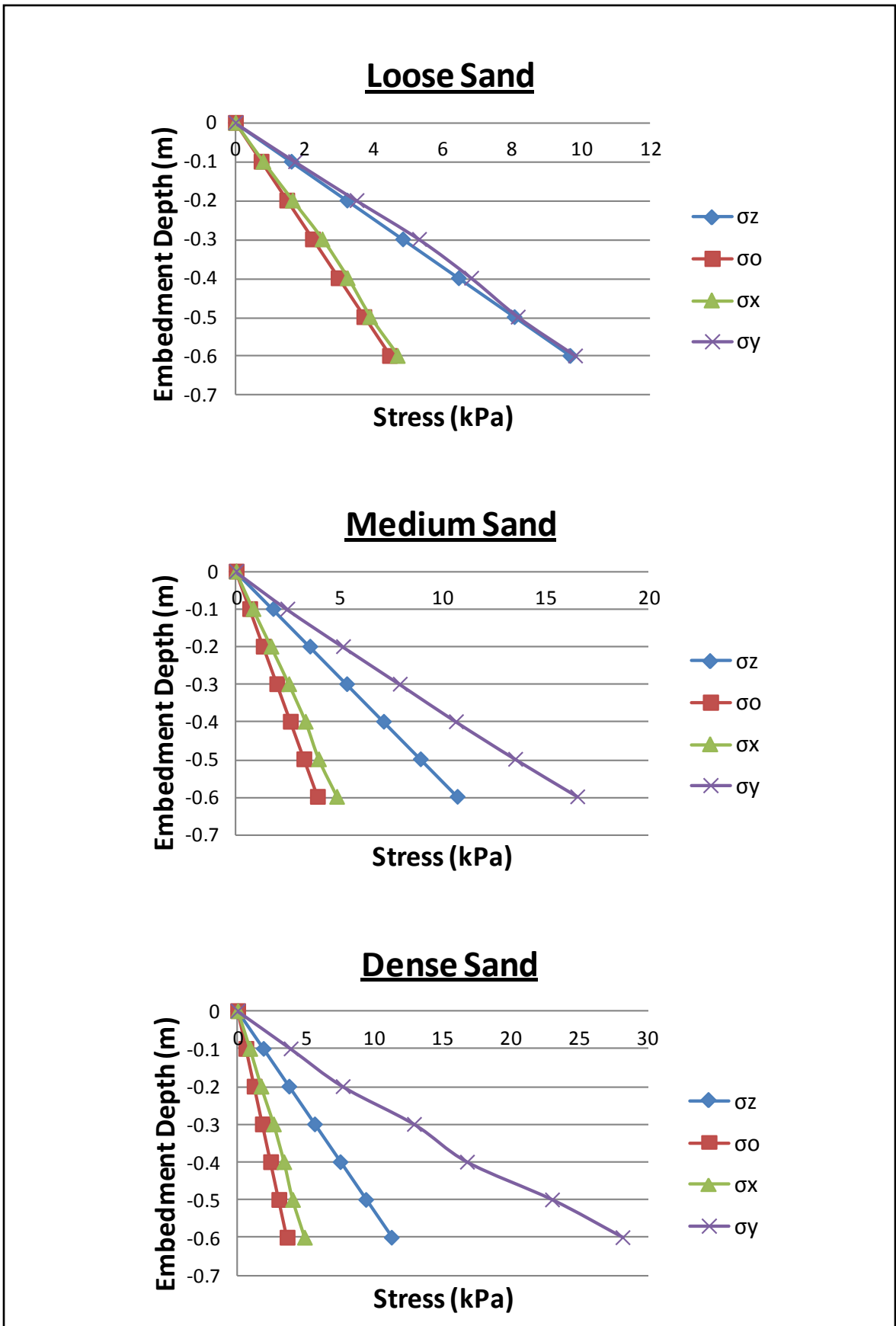


Figure 4.52. Sand Compaction Results for Vertical and Lateral Stresses.

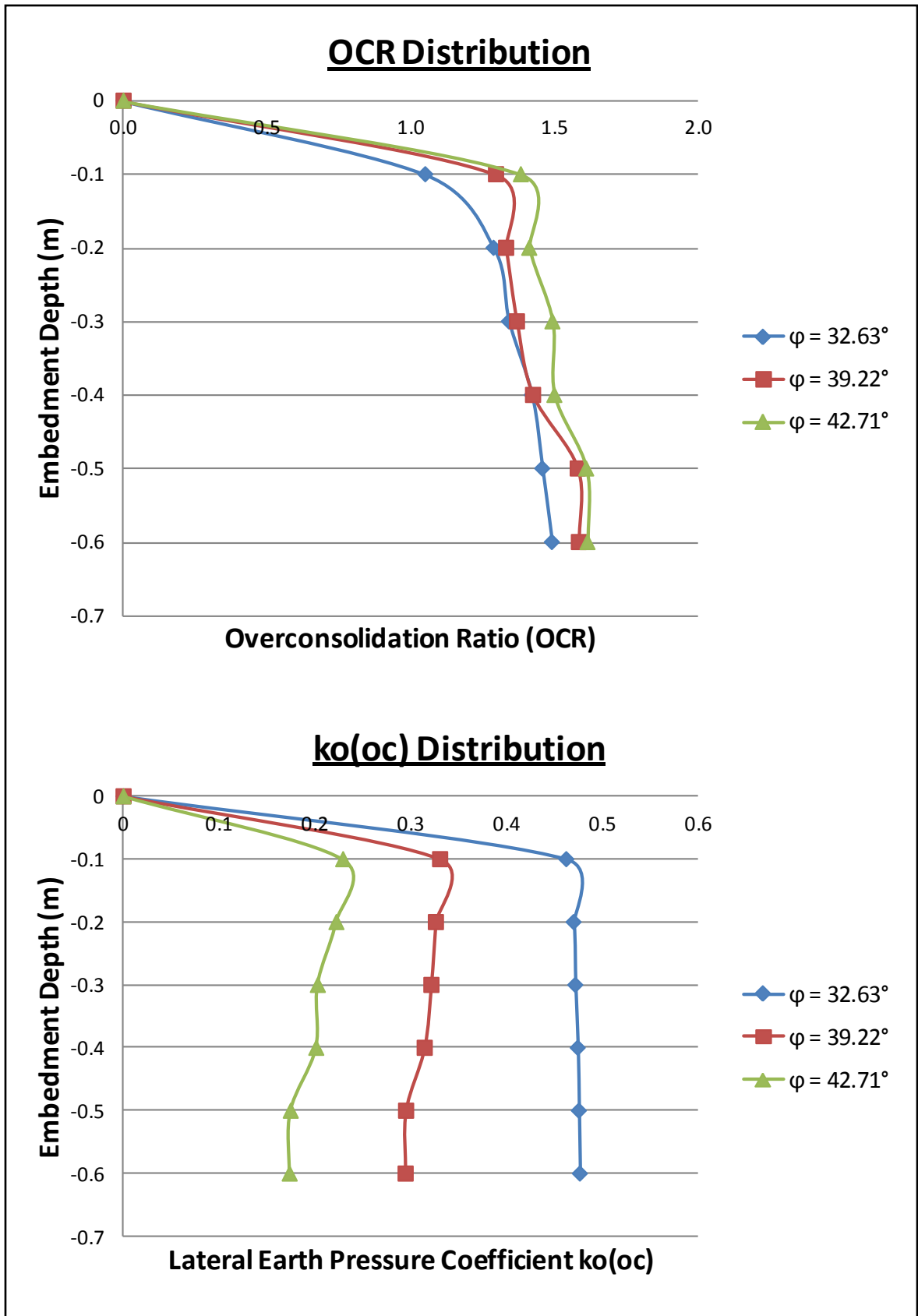


Figure 4.53. OCR and $k_{o(oc)}$ Distribution from Sand Compaction.

4.6 Soil–Shell Structure Interface

To obtain contact pressure diagrams, the 24 models should be tested at the surface of a sand bed that has been vibro–compacted in layers along with an embedment surcharge. For upright models the depth of embedment, D/b is kept at 0.83 while inverted models are to have embedment ratio's ranging from 0.50 – 0.85 during testing such that the lateral edge beams have full lateral support in keeping with field–like conditions. This is also commensurate with the numerical study to for validation purposes. Similarly, the soil conditions will be varied in loose, medium and dense sand conditions. This provides good indication of variation of contact pressures based on soil strength parameter, ϕ , the angle of shearing resistance.



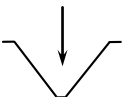

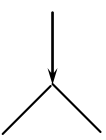

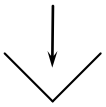

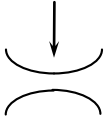
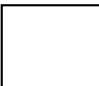
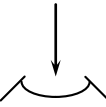

Shell No.	Footing Type	CONFIGURATION			Analysis
		Section	Plan	Shell Angle, θ (°)	
1	Plain Square			180	3D
2	Sinusoidal			36 D/B : 0.36	2D, 3D
3	V–Shaped (upright)			34 D/B : 0.42	2D
4	V–Shaped (inverted)			18	2D
				27	
				36	
				D/B : 0.40	
5	Cylindrical (upright) (inverted)			1:8	Proposed
				1:6	
				1:4	
				Sag/span–1:10	
6	Combined (upright)			1:8	Proposed
				1:6	
				1:4	
				18, S/S–1:14	

Table 4.13. Shell Model Cases Analyzed (3D using Shape Factors).

A total of 27 tests were conducted to obtain the results aside from the prerequisite pre-tests. To summarize the findings, Table 4.13 is presented for the developed shell footings including: type, configuration and type of analysis conducted.

One should note that the experimental results available and indicate with an asterisk (*) are for comparison. These shells can be tested under 3D conditions ($L = B$), but typically meant for use as strip 2D footings. The following table is used to summarize shell footings tested and based on contact pressure variations the one with the most uniform variation would be indicative as being optimal. The maximum value obtained may indicate the geometry with largest variation, however a block diagram of the results as described in the next section would reveal a full picture of the normal contact pressure distribution.

Shell No.	Footing Type	Rise-to-half-base ratio	Bearing Capacity (N/mm length of footing)	Settlement (at 1/3 BC, mm)	Min., Max. Contact pressure (at Full BC, kPa, Medium Sand)	Average Contact pressure (1/3 BC, kPa)
1	Flat Model	0.75	0.81	32.6	194, 402	189
2	V-shaped (upright)	0.83	1.12	27.5	274, 348	221
3	Sinusoidal (inverted)	0.82	1.45	23.8	327, 411	232
4	iShell18° (inverted)	0.52	0.95	31.2	305, 360	202
5	iShell27° (upright)	0.58	1.28	28.6	317, 384	236
6	iShell36° (inverted)	0.61	1.43	24.7	323, 402	248

Table 4.14. Bearing Capacity, Settlement and Contact Pressures under 2D Analysis.

Testing the transducers prior to use should be done by applying air pressure to the sand box setup. Any defective or inoperative transducer can be immediately identified and remedied as air pressure reading should be identical to pressure transducer readings. Testing the shell models themselves for rigidity requires attention at the outset as well. The elastic performance of the footing-soil system should be similar for the different models. To confirm this, a cyclic load-settlement diagram of the shell footing models can be conducted. If similar settlement characteristics are obtained then models are indicative of having sufficient rigidity and would not deflect structurally, thereby retaining its shape of

contact at all stages of loading. Moreover, this ensures the soil fails before failure of the model footings.

Assumptions:

1. Frictional forces at the base of shell at the shell–soil interface are present
2. No loading aside from that applied to the shell footing
3. Soil is semi–infinite and elastic

As alternatives, plexiglass or polycarbonate models have been scrutinized for use, however it has been determined from the outset that good measurement of soil contact pressure requires that soil be in perfect contact with the soil, especially in the core sections of the shell and that the shell model itself be substantially rigid enough to resist deformation. A lagging quality found in plexiglass and polycarbonates tendency to deform thereby affecting the results. Upright shell models would definitely introduce human error in sand placement to adequately fill the encased core directly beneath these shells which is a rather difficult task. The inverted shell models are free of this problematic ensuring much more accurate contact pressure results.

To study the development of the normal contact pressure distribution, the contact pressures need to be evaluated at several different loading stages. The load–settlement curve for each test can be divided, according to (Lambe and Whitman, 1979), into three main stages. The initial stage is that of load causing local shear failure, Q , where the load–settlement curve demonstrated non–linear tendency. The intermediate stage is at the bearing capacity load, Q_b , defined by a rapid slope change in which the rate of settlement greatly increases with small increase in the applied load. The last stage is that defined by the ultimate load, Q_u , in which is peak load where rupture is imminent.

Once the shell models have been loaded the readings of the normal contact pressure distribution were converted to obtain pressure readings typically in the form kg/cm^2 , N/mm^2 , kPa or a variation thereof and plotted. A three–dimensional plot, as the one

proposed below identifies the pressure variations between the pressure points strategically positioned beneath the model and is an acceptable way to visualize pressure variation. Graphically, the obtained normal contact pressure distribution beneath three-dimensional shell model would be as that presented in Figure 4.54.

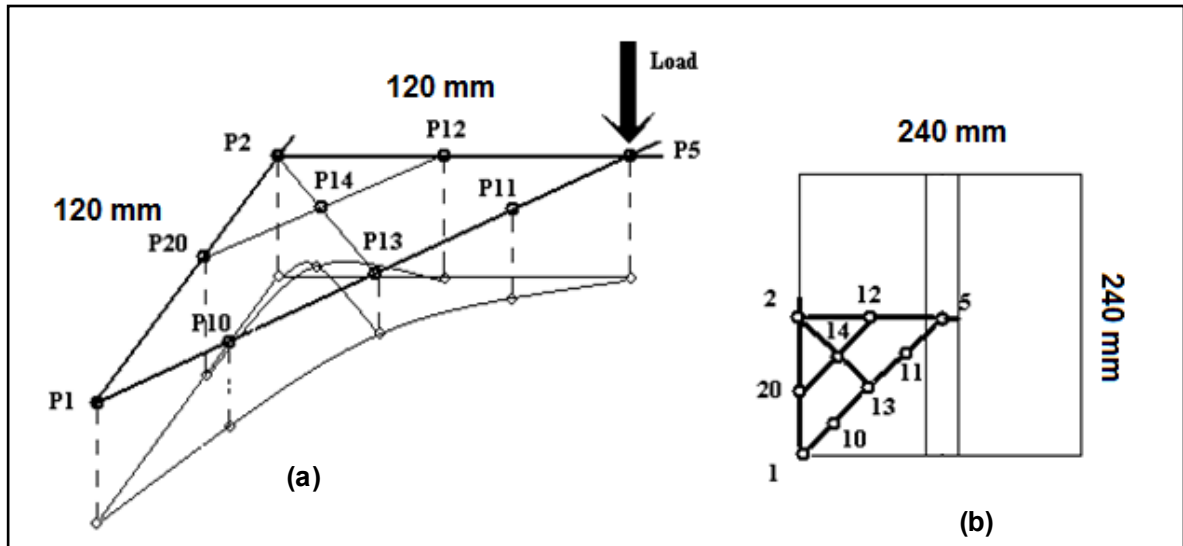


Figure 4.54. Normal Contact Pressure Distribution: (a) Block Diagram (b) Plan View.

If we consider the first model proposed we have an upright triangular shell with a shell angle of 18° . The readings as indicated beneath the iShell may be compiled to obtain a pressure diagram with model points as that illustrated in Figure 4.54(b) above.

The ultimate loads and settlement behaviour of the inverted shell test models (iShell #1 – 6) are analyzed and compared to that of the flat and upright and Sinusoidal shell models. In the analysis and prediction of performance, a shell efficiency factor, η_{is} and settlement factor, $F_{\delta(is)}$ for the inverted shell was developed as represented in the following equations:

$$\eta_{is} = \left(\frac{Q_{is} - Q_f}{Q_{us} - Q_f} \right)_u \times 100\% \quad (4.17)$$

$$F_{\delta(is)} = \left(\frac{\delta\gamma A_p}{Q_u} \right)_u \quad (4.18)$$

where,

$Q_{is, us, f}$: ultimate load of inverted, upright shells or flat (kN)

δ_u : settlement at ultimate load (mm)

γ : unit weight of soil (kN/m³)

A_p : area of planar shell footing projection (m²)

Q_u : ultimate load (kN)

The values of the test data calculations and load–settlement graphs obtained are summarized and presented in Table 4.15 and Figures 4.55 – 4.59 as follows:

PARAMETERS	Ultimate Load, Q_u (kN)			Settlement, δ (mm)			Settlement Factor, F_δ		
	Loose	Medium	Dense	Loose	Medium	Dense	Loose	Medium	Dense
MODEL \ ϕ_{soil}	32.6	39.2	42.7	32.6	39.2	42.7	32.6	39.2	42.7
Flat	6.12	10.78	17.35	16.32	21.05	21.21	2.48	2.01	1.32
Upright	6.75	11.84	18.34	15.15	20.89	21.47	2.09	1.81	1.26
Sinusoidal	7.89	13.42	20.31	14.38	19.85	21.51	1.70	1.52	1.14
iShell 1 – 18°	6.85	12.25	19.75	12.51	12.82	12.23	1.70	1.08	0.67
iShell 2 – 27°	7.15	12.94	19.89	12.49	12.22	13.38	1.62	0.97	0.73
iShell 3 – 36°	7.35	13.03	20.06	13.21	12.67	12.39	1.67	1.00	0.67
iShell 4 – 18°	6.95	12.28	19.76	12.73	13.34	13.22	1.70	1.12	0.72
iShell 5 – 27°	7.18	12.98	19.91	13.12	20.3	20.38	1.70	1.61	1.11
iShell 6 – 36°	7.43	13.12	20.08	12.25	19.21	20.42	1.53	1.51	1.10

Table 4.15. Load–Settlement Results for iShell Footing Models.

The results indicate the efficiency of inverted shell footings (η_{is}) decreases with increasing angle of shearing resistance of the soil. That is, more compact and dense the soil becomes, the less one benefits from the performance the shell footings have to offer. This confirms the premise that shells are reputedly better performers in weaker soils that necessitate a large load transferred to them. Another interesting result is the fact that the results are less than 5% margin of error with increasing shell thickness from 20 to 25 mm.

One can conclude that increasing shell thickness has only but mild effects as compared to the shell angle or continuum properties such as γ or $c - \phi$ variability of the bearing soil.

In terms of settlement, the factors of settlement indicate that the Sinusoidal shell model has best settlement characteristics having the lowest facot (F_δ). The inverted shells showed similar tendency, as their plots were in proximity with a 3% spread. All models showed that better settlement behaviour as the soils angle of internal friction increased as intuitively expected. Finally, it is observed overall that the inverted shells have better performance of the order of 3 – 9% over the upright shell and 42 – 45% better performance to that of their flat counterparts.

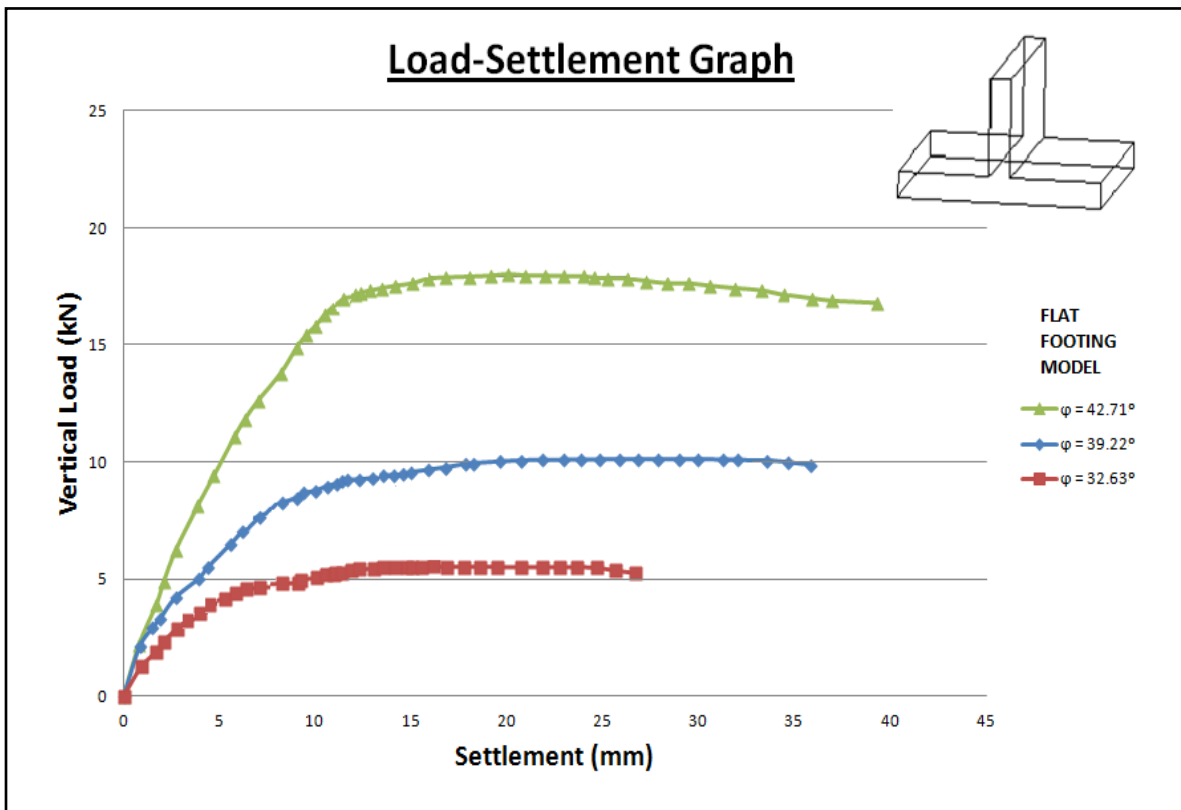


Figure 4.55. Load–Settlement Graph – Flat Footing Model.

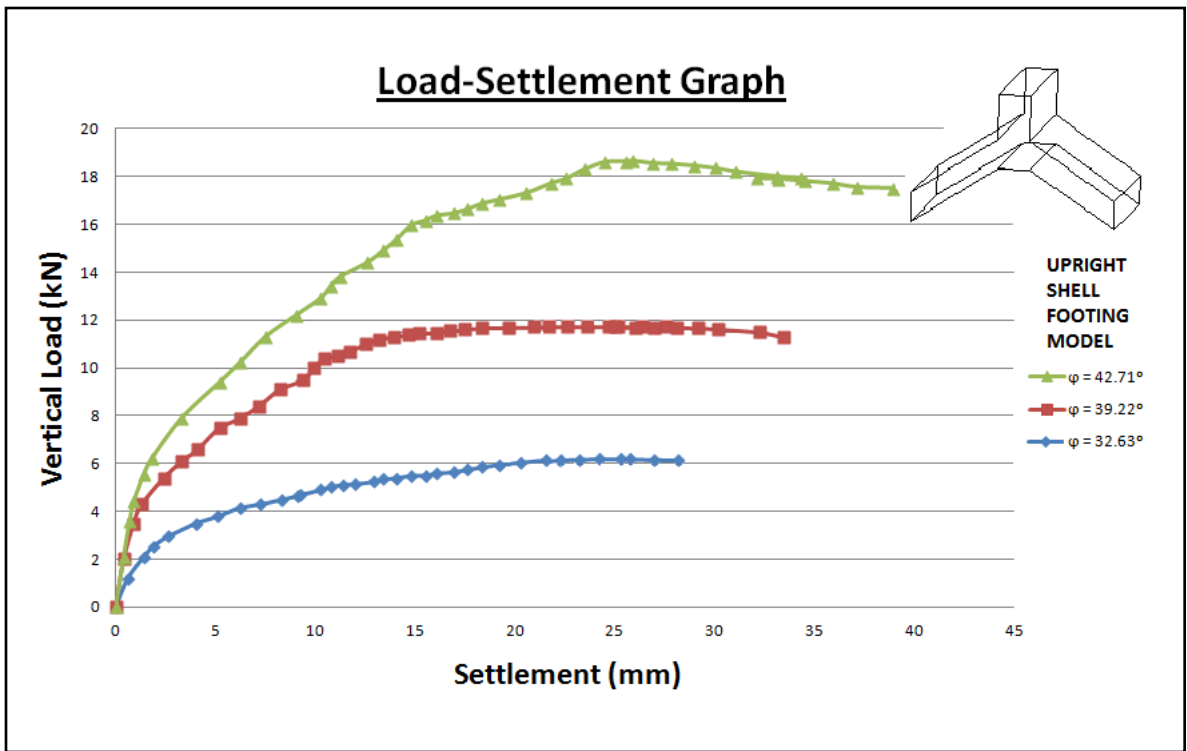


Figure 4.56. Load-Settlement Graph – Upright Footing Model.

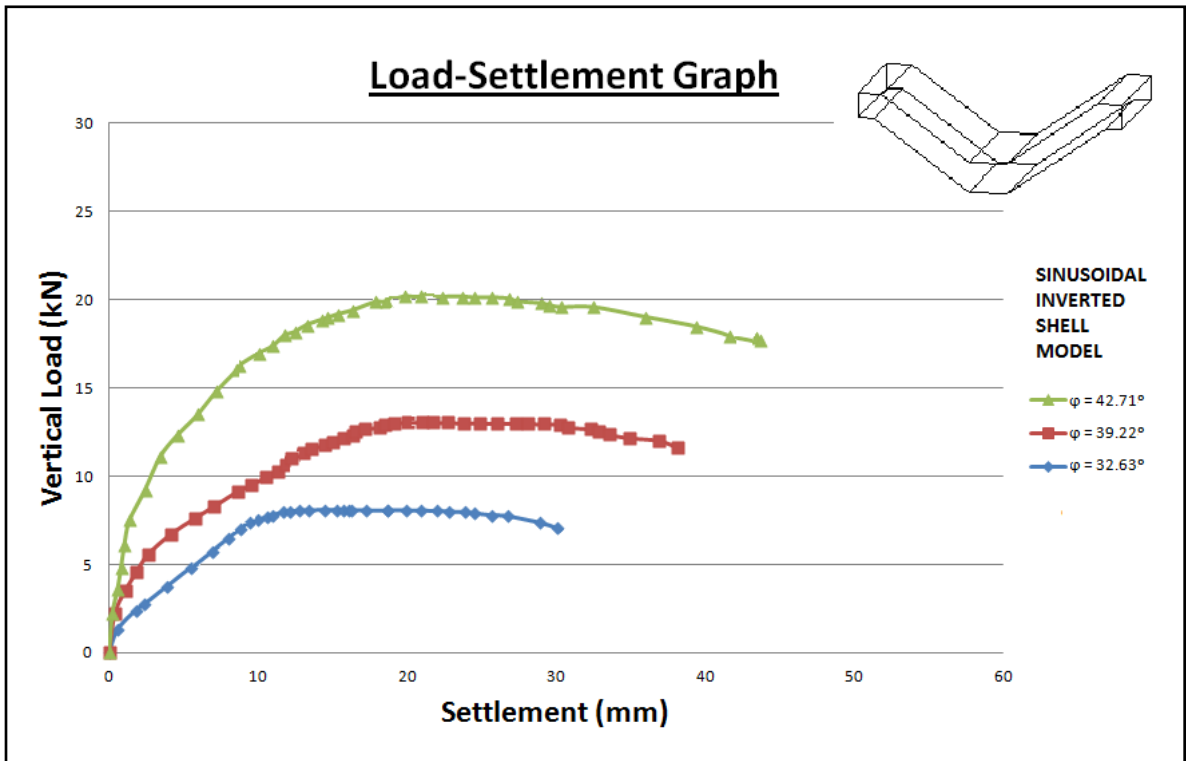


Figure 4.57. Load-Settlement Graph – Sinusoidal Footing Model.

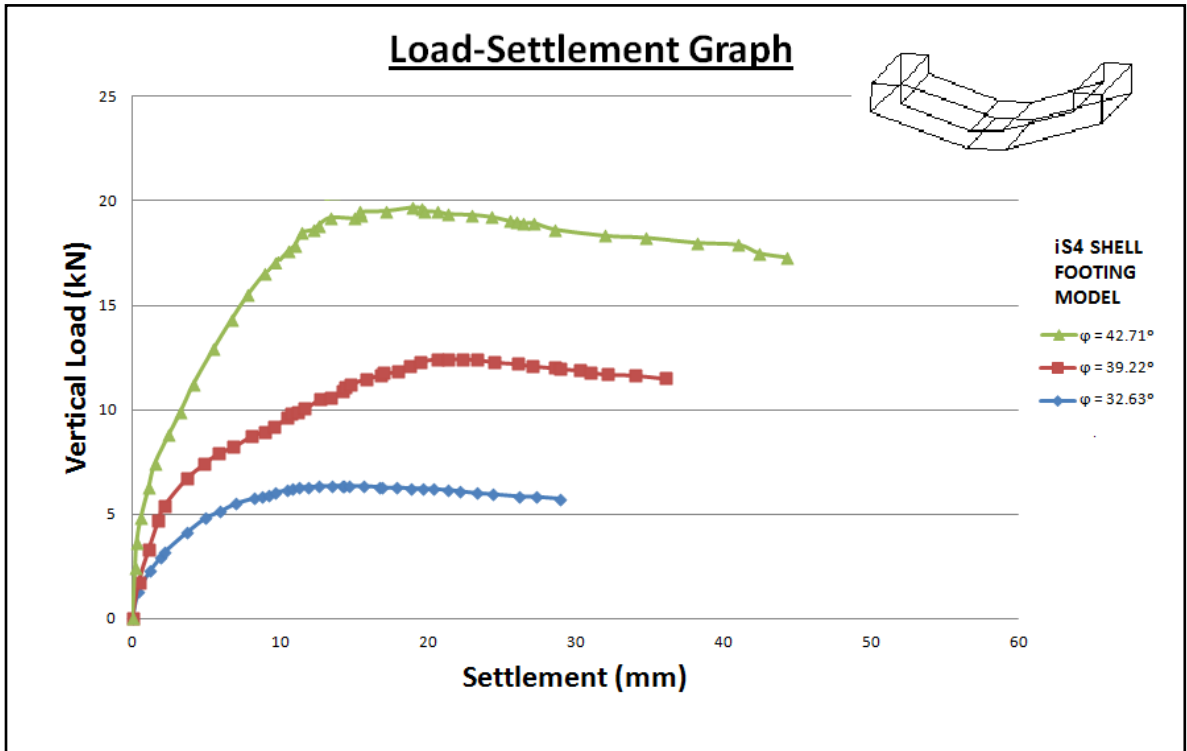


Figure 4.58. Load-Settlement Graph – iS4 Inverted Shell Footing Model.

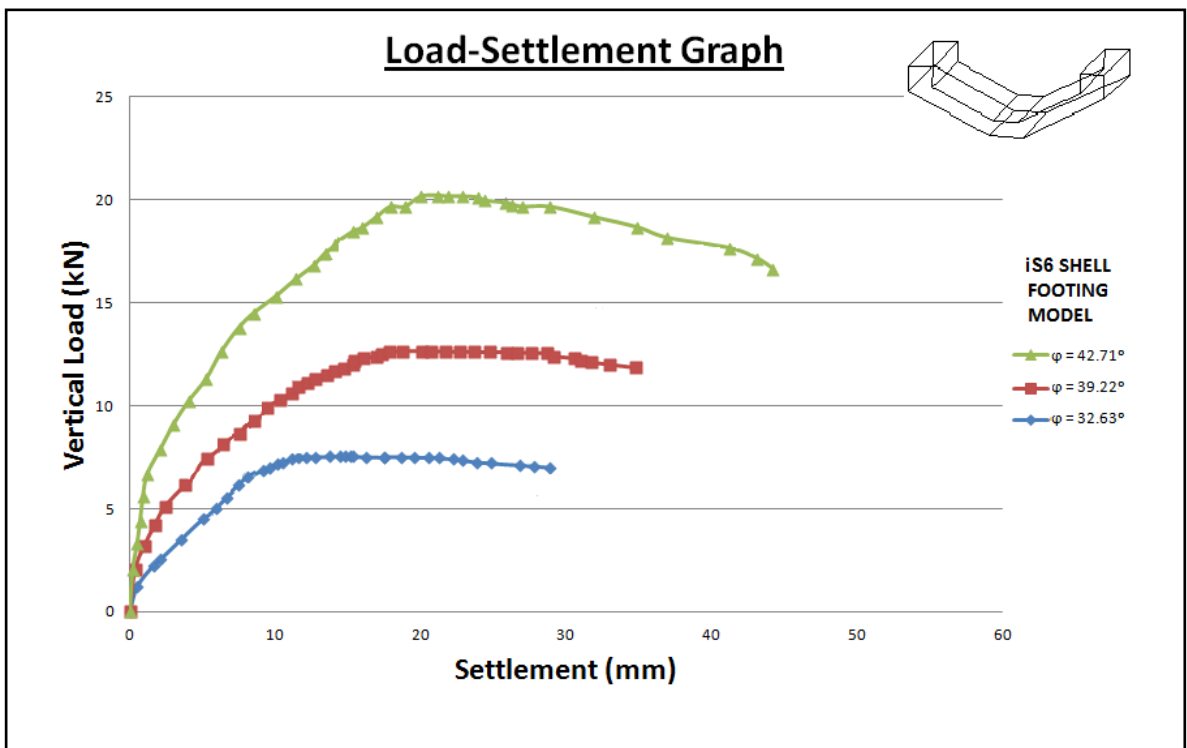


Figure 4.59. Load-Settlement Graph – iS6 Inverted Shell Footing Model.

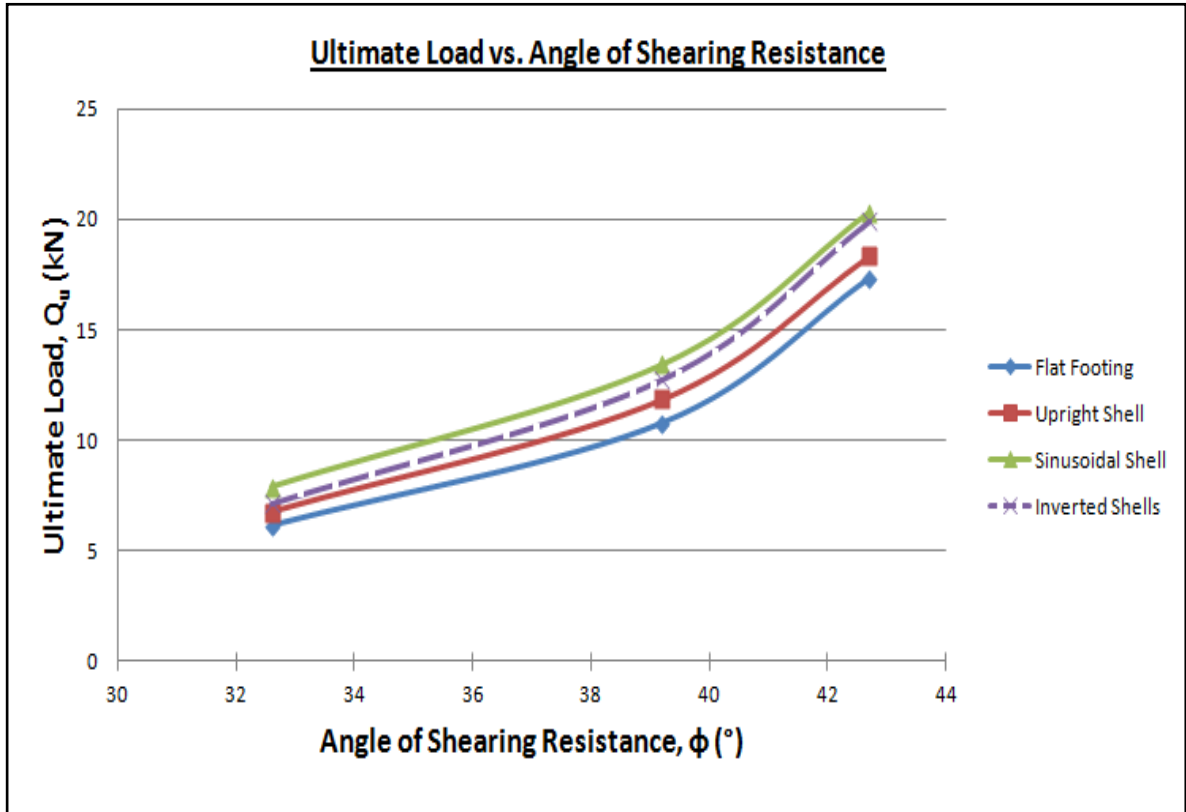


Figure 4.60. Ultimate Load (Q_u) vs. Angle of Shearing Resistance, $\phi(^{\circ})$.

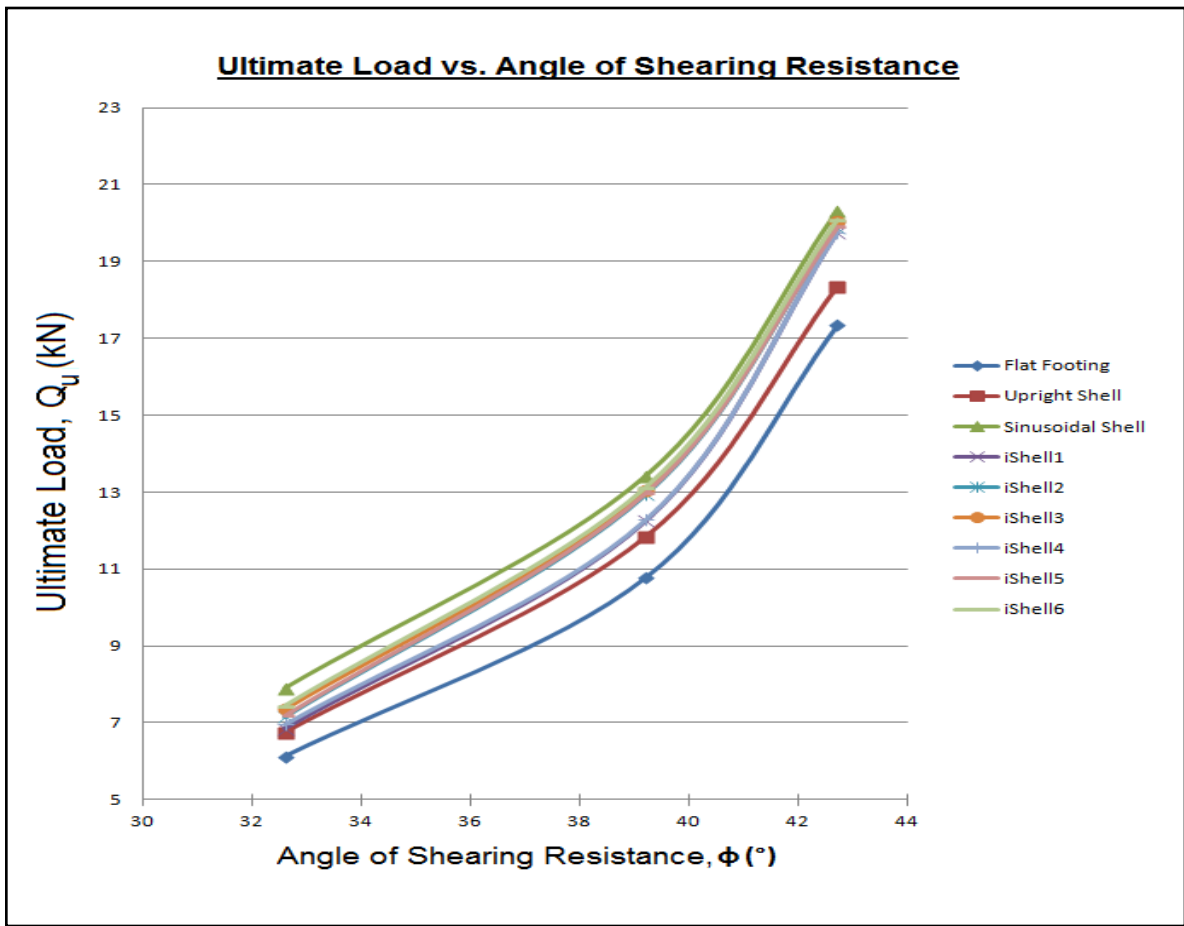


Figure 4.61. Ultimate Load (Q_u) vs. Angle of Friction, ϕ ($^{\circ}$) – Varia.

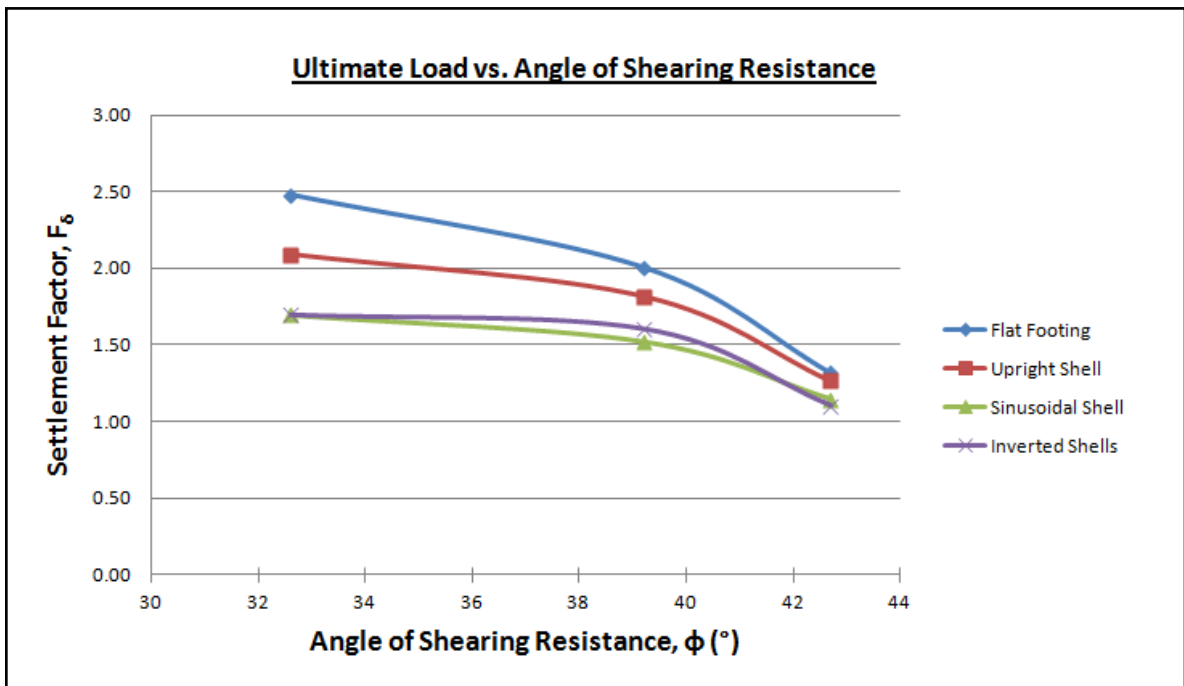


Figure 4.62. Ultimate Load (Q_u) vs. Settlement Factor, (F_{δ}).

Structure	Soil	Failure Load, Q (kPa)						Bearing Capacity, Q_b						Ultimate State, Q_u						Indices	
		C_L	P_1	P_2	P_3	Edge	C_L	P_1	P_2	P_3	Edge	C_L	P_1	P_2	P_3	Edge	Q/Q_u	Q_b/Q_u			
Footing	State	164	151	118	103	76	251	224	219	201	149	348	333	298	251	207	0.47	0.72			
Flat, Trail #1	Loose	230	215	202	123	73	402	395	398	292	223	546	540	505	496	399	0.42	0.74			
	Medium-Dense	406	379	368	205	181	625	571	522	448	423	875	864	756	706	686	0.46	0.71			
Flat, Trail #2	Dense	176	163	154	126	48	273	255	231	188	129	358	327	282	210	186	0.49	0.76			
	Loose	253	232	204	156	61	401	395	259	222	164	562	531	508	448	373	0.45	0.71			
Flat	Medium-Dense	419	382	262	229	287	626	586	512	429	420	878	871	822	711	705	0.48	0.71			
	Dense	170	157	136	115	62	262	240	225	195	139	353	330	290	231	197	0.48	0.74			
Flat	Medium-Dense	242	224	203	140	67	402	395	329	257	194	554	536	507	472	386	0.44	0.72			
	Dense	413	381	315	217	234	626	579	517	439	422	877	868	789	709	696	0.47	0.71			

Table 4.16. Contact Pressures for Axisymmetrical Condition for Embedded Flat Footings.

Structure	Soil	Failure Load, Q (kPa)						Bearing Capacity, Q_b						Ultimate State, Q_u						Indices	
		C_L	P_1	P_2	P_3	Edge	C_L	P_1	P_2	P_3	Edge	C_L	P_1	P_2	P_3	Edge	Q/Q_u	Q_b/Q_u			
Footing	State																				
	Loose	119	115	120	123	98	150	160	169	162	153	200	192	210	224	212	0.55	0.75			
	Medium-Dense	223	219	225	222	203	307	299	323	349	281	427	435	456	466	426	0.48	0.75			
Upright	Dense	248	255	263	253	241	441	522	565	549	496	752	874	830	805	728	0.30	0.65			
	Loose	137	135	129	112	121	210	192	185	171	175	276	265	255	211	202	0.50	0.76			
	Medium-Dense	258	286	237	242	225	405	394	361	363	325	551	562	512	503	450	0.51	0.72			
Sinusoidal	Dense	379	375	299	306	284	525	575	594	539	525	849	910	902	832	788	0.42	0.65			
	Loose	131	101	107	89	60	197	171	157	151	116	259	243	228	205	179	0.51	0.76			
	Medium-Dense	252	269	221	242	227	403	383	246	248	252	551	528	498	513	490	0.49	0.73			
iShell36	Dense	253	269	250	295	288	574	549	578	521	509	876	862	870	800	778	0.34	0.66			
	Loose	102	94	87	77	61	158	145	140	142	113	231	207	205	191	176	0.44	0.68			
	Medium-Dense	227	244	214	214	199	380	370	278	283	280	525	518	503	489	460	0.46	0.72			
iShell27	Dense	274	233.5	220.5	247.5	242	529.5	493	504	461.5	454	813	787	797	788	776.5	0.34	0.65			
	Loose	77	82	75	64	55	130	122	118	120	107	201	186	188	185	173	0.41	0.65			
	Medium-Dense	205	221	204	173	178	355	349	303	319	306	510	502	505	452	429	0.43	0.70			
iShell18	Dense	295	198	191	200	196	485	437	430	402	399	750	712	724	776	775	0.38	0.63			

Table 4.17. Contact Pressures for Axisymmetrical Condition for Embedded iShell Footings.

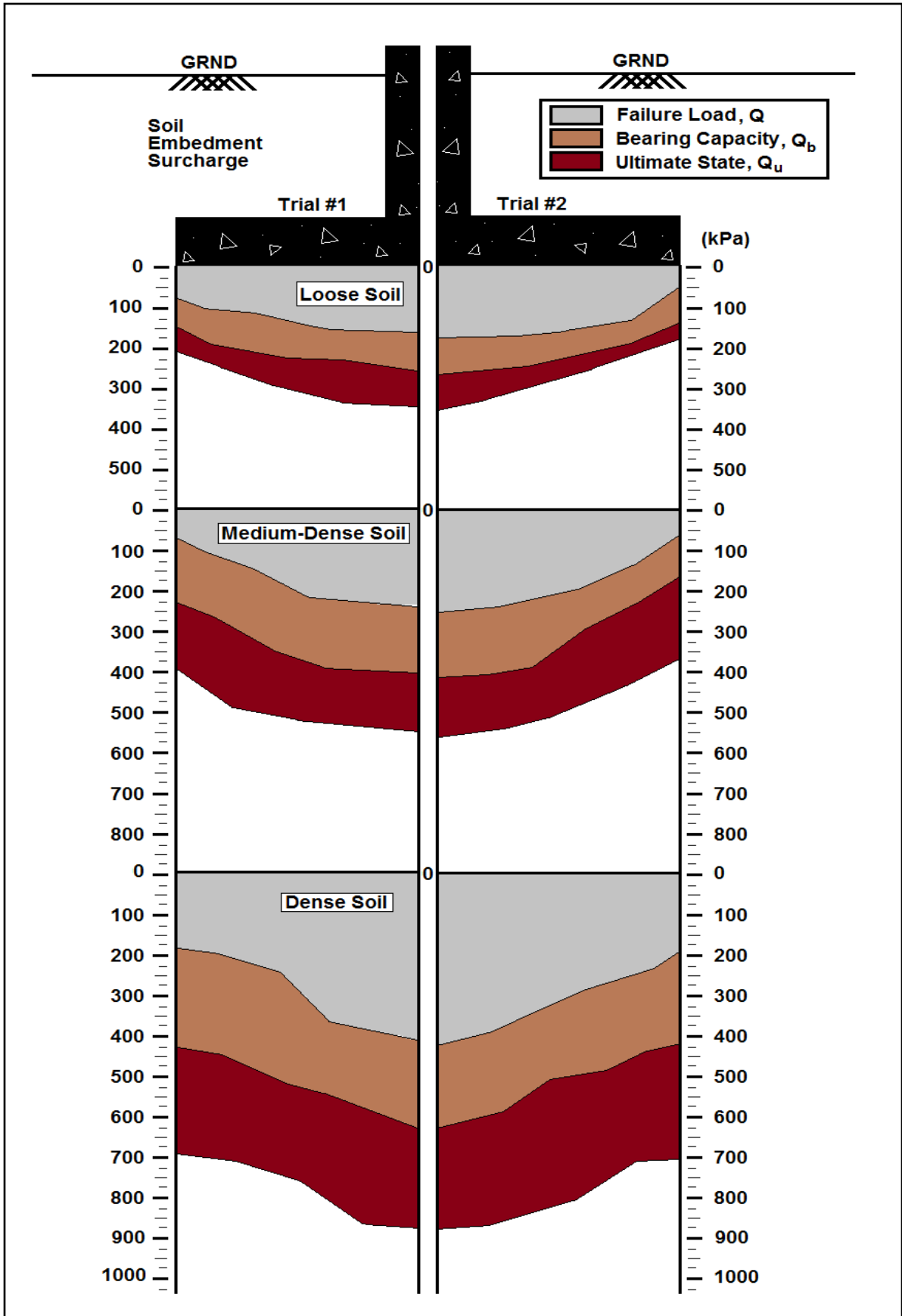


Figure 4.63. Contact Pressure Distribution for Flat Footing Model.

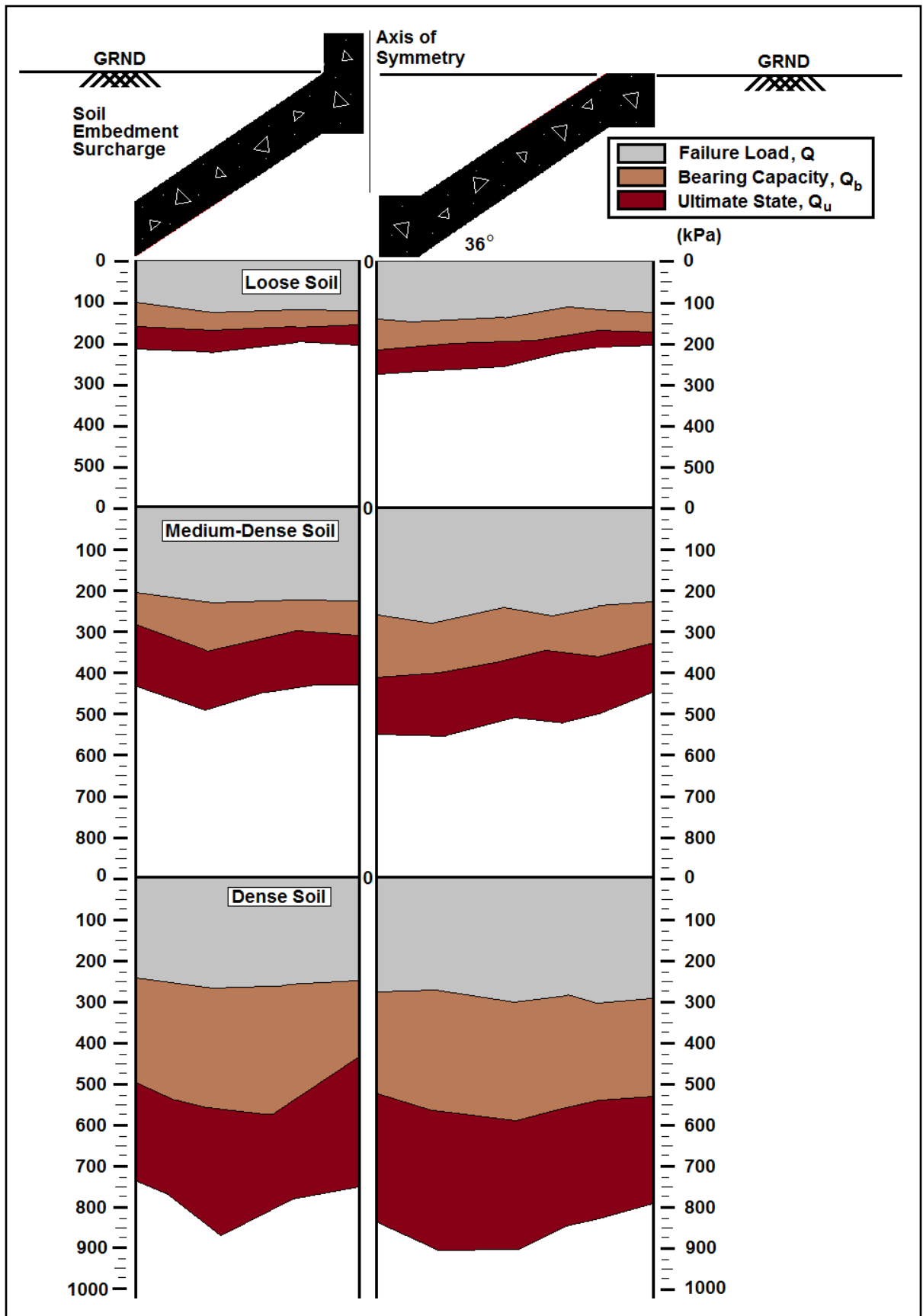


Figure 4.64. Contact Pressure Distribution for Upright and Sinusoidal Shell Footings.

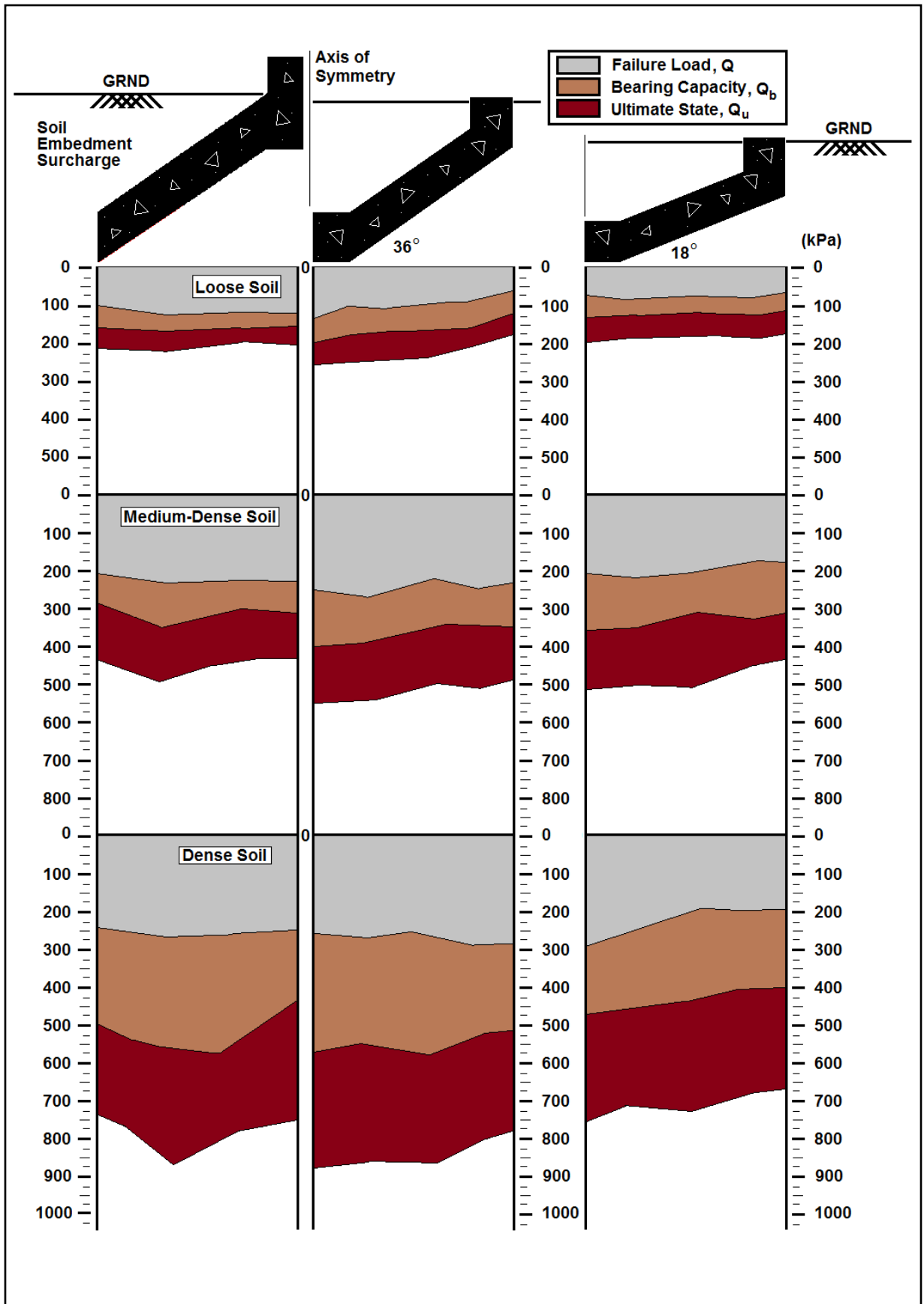


Figure 4.65. Contact Pressure Distribution for iShell18° (iS4) & iShell36° (iS6) Footings.

4.7 Summary

The hypothesis that the pattern of the elastic contact pressure distribution would most likely be some parabolic distribution along the principal plane was confirmed. Instinctively, the thought that edge concentrations would likely be expected was to be validated by the tests for conviction. For relatively loose soil, it was found that pressure distributions were relatively uniform whereas when densification of soil was modeled, the pressures seem to increase significantly at positions $B/3$ and $2B/3$ with high edge concentrations at the peripheries. The inverted shell, seems to exhibit similar magnitude stresses, however has tendency for high stress towards their centers at the inverted shells apex gradually decreasing over the footing width. This is seemingly more apparent in the medium dense soil and most apparent for the dense soil. An important element in this investigation would be the dispersion of contact pressures between the system of beams and the shell itself. The contact pressures at the center and edges would typically receive the majority of the load as the shell itself would mitigate the load to its boundaries. The values suggest edge concentrations as they may also indicate a tendency for centerline concentration as shown in several studies conducted by other researchers (Kurian, 1972; Abdel-Rahman, 1996). The higher magnitude of stress distributions of the inverted shells combined with deeper centerline penetration of the wedge suggests that higher bearing capacities of soil is obtained.

Conclusively, the contact pressure indicates a tendency for edge concentrations in the elastic stages of loading. The rigid edge beams absorb the load in this initial stages would be reason for their attention and application in the design stages of the shell footing. As loading continues a tendency for contact pressure may shift to the shell core regions in the inelastic stages. It has been suggested that a concentration of contact pressures towards the center has a positive effect on the ultimate strength as theories suggest. Moreover, in plotting results such as deflection (ω), or normal contact pressure (P), at a number of points on the shell, corresponding to a particular value of load separately on individual axes, it will be convenient to plot them together on a tridimensional block diagram as that aforementioned above. This produces a clearer portrait of the results and at the same time makes it visually more effective in appreciation of the physical response. Jeevan and

Kurian have developed software for the automatic plotting of such block diagrams which may be used however is not explored further in the present investigation.

Analysis Type	Foundation Type				
	Flat	Upright	Sinusoidal	iShell18°	iShell36°
Ultimate Load, Q_u (kN)					
Numerical	19.84	24.56	25.38	23.76	27.15
Experimental	17.35	19.56	20.31	19.76	20.08
Discrepancy, Q_u (%)	12.60	20.40	20.00	16.80	26.00
Shell Factor, S_f	1.00	1.21	1.26	1.05	1.24

Table 4.18. Ultimate Load Results for Numerical and Experimental Phase.

Comparisons are drawn between typical experimentally obtained results and those calculated in the numerical models. Load–settlement curves for each analysis are graphed and seemingly correlate fairly well within 12 – 26% discrepancy as upper bound with the numerical displaying more conservative results. As can be seen from results in Table 4.18, the higher numerical values correspond reasonably well and with good agreement between those of the laboratory model tests, validating the results obtained in either case. Discrepancies maybe attributed to experimental human error in compaction effort to achieve required density and other environmental factors associated with the laboratory setting. New shell configuration performance is difficult to evaluate taking into account soil response and the new geometry while optimizing shell parameters such as thickness or shell angle for instance. In order to investigate the effects these new shell configurations applicable to either upright or the inverted shell cases on the ultimate load Q_u , a shell factor (S_f) parameter may be introduced to classify performance as follows:

$$S_f = A_{Shell}/A_p \quad (1 < S_f \leq 2, S_f = 1 \text{ for flat footing}) \quad (4.19)$$

where,

A_{Shell}, A_p : areas of the shell base surface area and corresponding planar projection

This means that for increasing shell angle (θ) for either inverted or upright shell geometry, an increase in the shell factor (S_f) would be obtained as presented in Table 4.18, which can then be applied to the ultimate bearing capacity equations.

CHAPTER 5

THEORETICAL ISHELL MODELING

5.1 Introduction

Added insight into the behavioural response of bearing capacity for shell footings and their ultimate threshold from a mathematical perspective is of interest in this next section. A proposed failure trajectory within the soil medium for a given inverted shell and resulting soil geometry forms the basis for the following theoretical modeling work.

In a broad sense, foundations are a two-part system. The first part consists of the structural aspect of foundation design including support of shearing and bending stresses, for example. The second part consists of the geotechnical aspect of foundation design which is for the most part of interest in this research. Our focus is directed, therefore, to satisfying two fundamental foundation design requirements of the shell footings independently, namely bearing capacity and that of settlement. The more critical of the two being satisfied ensures both are satisfied and, in general, a safe foundation design from a geotechnical viewpoint is warrant. More importantly, however, is the bearing soil strength parameters which pertain to the natural foundation physical characteristics and are critical in determining the required plan dimensions of the foundation.

$$Q_f \leq (Q_{BC,S})_{\min} \quad (5.1)$$

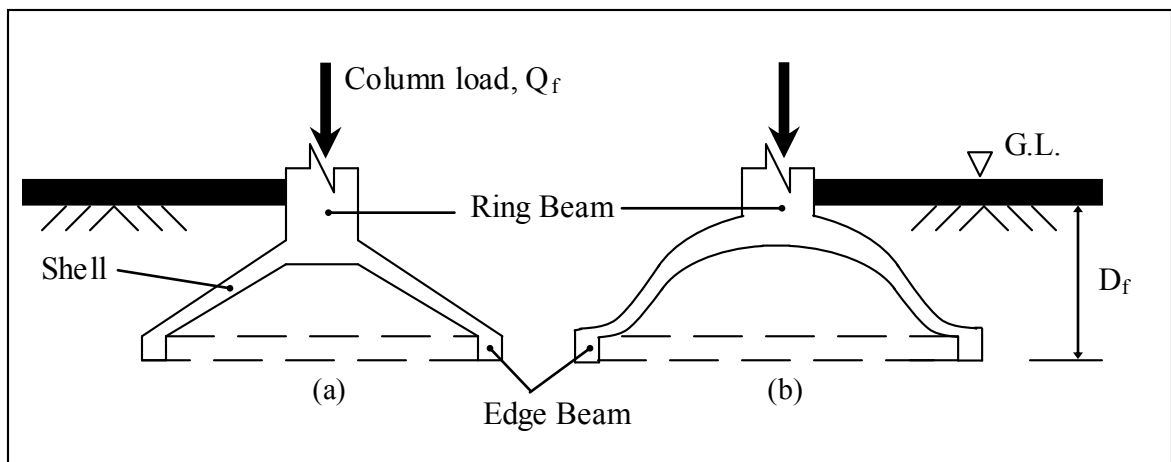


Figure 5.1. Shell Foundations: (a) Conical footing (b) Paraboloid of revolution footing.

5.1.1 Shell Behaviour

Owing to their light weight, graceful form, and high load resisting capacity, shells of various types are used for many structural purposes. Although shells with potential use in construction have been studied by numerous investigators, shell designers and builders have not been able to use structural optimization techniques that are presently available. As a result, we have limited basis for comparison in terms of structural optimization of shell footings. Computer models and analyses are now surging to develop form and dimensions of thin shell designs in an effort to make designs even more economical. Historically, the development of shells was experimental and forms for efficiency were in the constructability aspect of the shell. Parameters of construction included deflection tolerances, energy costs and form fluidity to ease construction process.

The soil–structure interface reactions may be seen in the following figure. As loading intensities diverge, an increase in eccentricity, e , either to the right or left, as the case may be, could result in soil contact pressures diverging as well. In the extreme case, where C_{ℓ} is significantly larger than C_{r} , the contact pressures being converted from compressive to tensile would result in a change of failure mode from that of slip to one of uplift. In either case, the combined footing would intuitively be a solution to the problem.

The rotational factor of safety is given by the equation:

$$FOS_r = \frac{M_o}{M_s} \geq 3 \quad (5.2)$$

where M_o = overturning moment (kN·m)

M_s = stabilizing moment (kN·m)

The overturning moment develops due to divergence of loading intensities C_{r} and C_{ℓ} creating eccentricity in the system, where:

$$V = C_{\ell} - C_r \quad (5.3)$$

$$\text{and } M_o = V \cdot e \quad (5.4)$$

The stabilising moment arises from the frictional forces developing beneath the shell, F , acting about point O . A rigorous expression for FOS_r has been developed (Dierks and Kurian, 1988) and is presented here as:

$$FOS_r = \frac{\mu}{(e/a)} f(\alpha) \quad (5.5)$$

where
$$f(\alpha) = \frac{\alpha^2}{\sin \alpha} (3/4 + \cot^2 \alpha) \quad (5.6)$$

From Figure 5.2, an increase in the angle ' α ' results in a decrease in the radial distance ' r ' from point ' O ' and a deeper shell depth, ' D_s '. The factor of safety drops considerably which becomes nearly constant for ' α ' values higher than 40° .

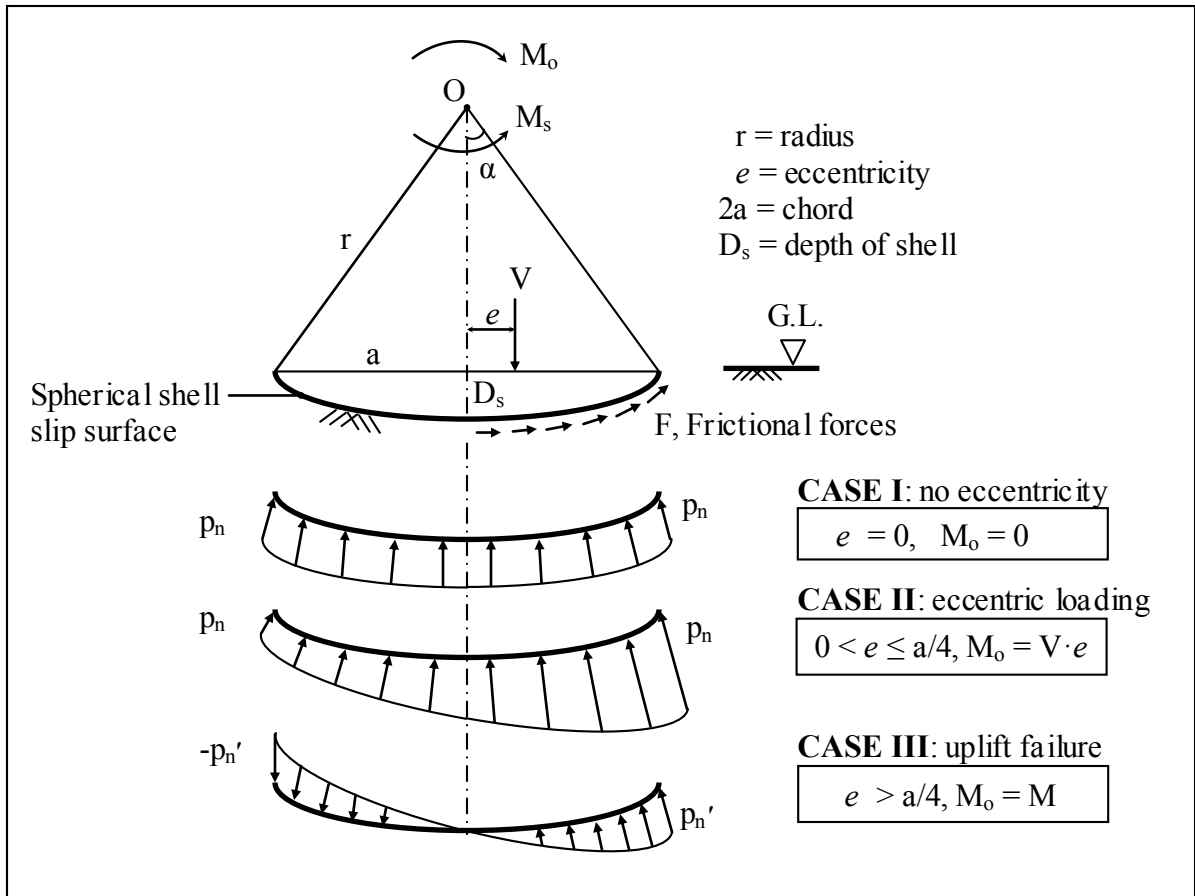


Figure 5.2. Inverted Spherical Shell Footing – Slip Stability.

In Equation (5.5) above, the location of the eccentricity value, ' e ' in the denominator for given values of μ and α , the FOS_r to (e/a) relationship is hyperbolic and is represented

in Figure 5.3 below. Upon inspection, one can immediately take note of a considerable drop in the factor of safety value for increasing eccentricity of the load initially and asymptotically approaching a constant value in the higher ranges.

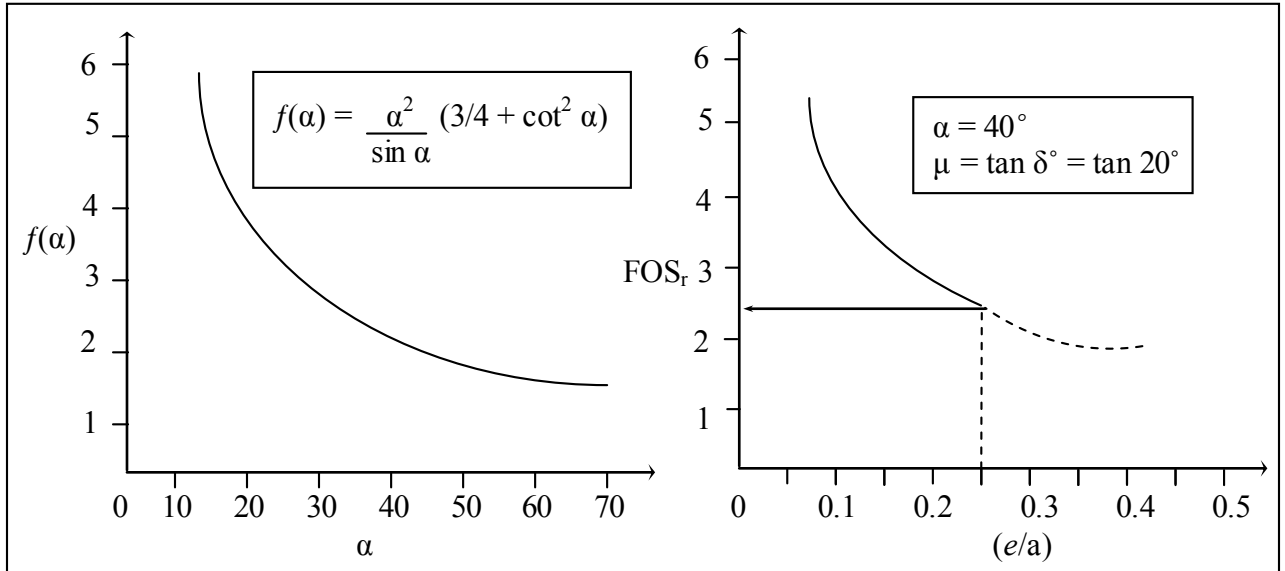


Figure 5.3. Spherical Shell Footing Behaviour: (a) $f(\alpha)$ vs. α (b) FOS_r vs. (e/a) .

From a structural point of view, the angle, ‘ α ’ is seldom designed to be above 45° as a limiting value following membrane stress theories. If we use $\alpha = 40^\circ$ conservatively, graphically we obtain $f(\alpha) = 1.643$ and the minimum factor of safety obtained would be:

$$FOS_{r, \min} = \frac{\mu}{(e/a)} f(\alpha) = \frac{\mu}{(e/a)} \times 1.6438 \quad (5.7)$$

With the conditions for uplift being satisfied, meaning we have no loss of contact between the shell and the soil, a limiting factor of 25% for the (e/a) ratio is allowable. Also, using $\delta = 20^\circ$ such that $\mu = \tan \delta = \tan 20^\circ = 0.364$, we obtain a $FOS_{r, \min} = 2.4$. Tabulated values are presented for consideration in Table 5.1 as follows.

Angle, $\alpha(^{\circ})$	FOS _r
40	2.4
35	2.9
30	3.3
25	4.0
20	4.5
15	5.8

Table 5.1 : Angle $\alpha(^{\circ})$ vs. FOS_r.

From the results, one can see that even for a considerably deep shell subject to high overturning moment, a reasonable FOS_r of 2.4 is obtained in the limiting case. Under normal loading conditions, one can conclude that the problem of stability against rotation for spherically inverted dome shell footings, for the most part, is not of appreciable concern with regards to use of this shell as a foundation structure.

As comfortable as the results are, a study of inverted shells having higher angles of α , namely those in the range of 30 – 45° is warranted and limited at the present time. Therefore, a raft footing composed of an inverted spherical or planar centre and the frustum of an inverted cone at each end or an inverted strip shell should be studied in those ranges.

5.2 Shell Footing Contact Pressure

Much of the work done on flat foundation serves as a great platform for application to shell contact pressures. The contact pressure beneath shells is inherently more complex due to the non-planar nature of the soil-shell interface. The soil contact pressure is a soil reaction that has mainly two components. At any point of soil-shell contact there would be a normal and a tangential component. If an elemental area beneath the shell is considered, the maximum value of the tangential component is limited to the coefficient of vertical surface friction multiplied by the normal component.

At any point on the shell, two curves pass through it one having maximum curvature and the other having the minimum. The planar surfaces of these curves carry the normal force of the shell and are mutually perpendicular. Therefore, the tangents to the two curves and the normal form an orthogonal system consisting of three mutually perpendicular straight lines. For convenience, one would resolve the tangential component of contact pressure along the directions of the principal tangents. The contact pressure at any point, therefore, would have generally three components, the normal and two principal tangents called N , T_1 and T_2 correlated to coordinate components x , y and z on elemental area, dA , respectively.

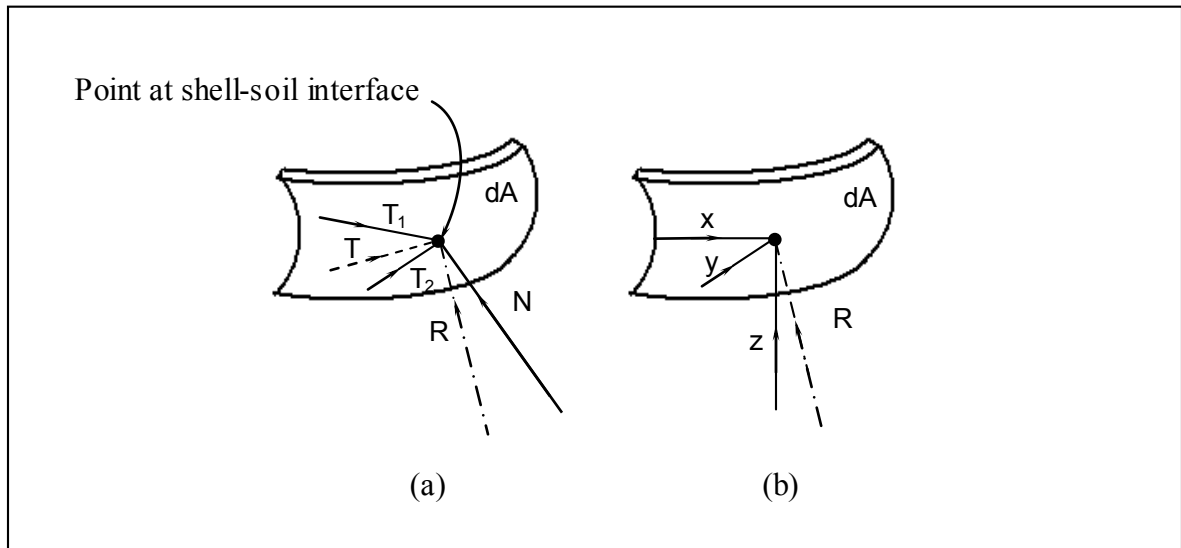


Figure 5.4. Contact Pressure Components: (a) Principal (b) Coordinate.

The distribution of pressure or the magnitudes of contact pressure components over the shell surface are highly indeterminate due to the highly complex interaction that takes place between the shell and the soil under loading.

In a more practical sense, if the bearing soil beneath the shell were soft clay ($\phi \approx 0$) it would produce tangential components T_1 and T_2 to be zero. A nearly hydrostatic case in which the contact pressures are purely normal to the shell at every point along its surface would result. In reality, the distribution is not normal and non-uniform at every point, only the resultant contact pressure at any point is normal. In contrast, if a highly granular soil material, such as well-graded sand were used, the tangential forces may develop such that it would shift the normal resultant to a vertical or almost vertical direction. In such a case, the resultant $R = z$ at all points with x and y equal to zero. If the assumption is made that R is uniformly distributed (which it is not), would imply that:

$$R = z = P / A_p = p_v \quad (5.8)$$

That is the conventional assumption made in typical structural shell foundation design in granular soil. For the normal and soil reaction case, a similar result follows such that:

$$p_n = p_v = P / A_p \quad (5.9)$$

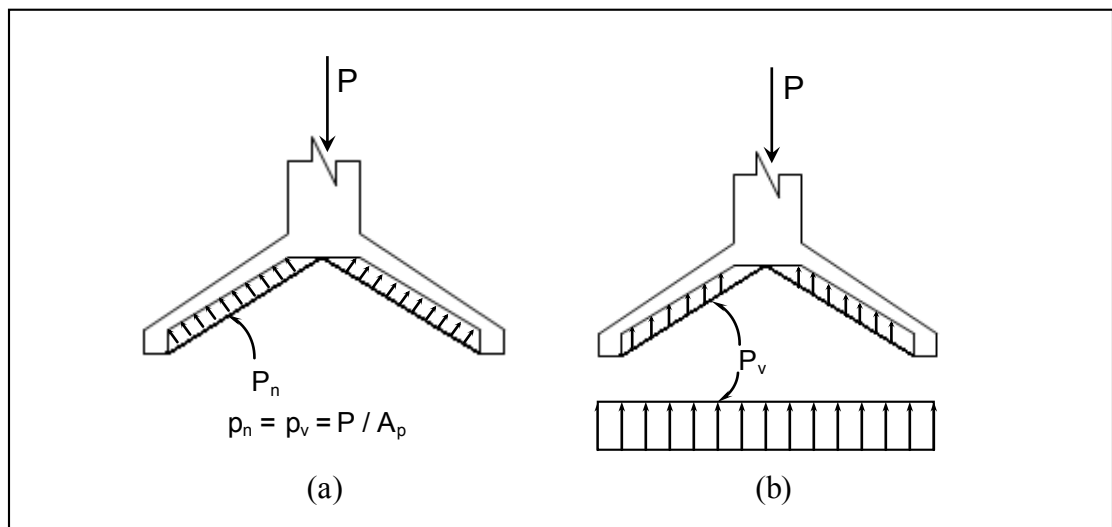
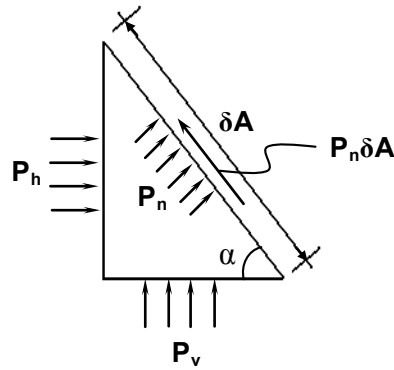


Figure 5.5. Shell Reactive Pressures: (a) Normal (b) Vertical.

Hydrostatic pressure situation is characterized as having the same intensity of pressure in all directions which is the case for soft–clayey soil. As proof, consider the elemental area on the tangent plane to be dA and unity (1) as the width as follows:



We have the elemental force $P_n \delta A$ and resolving into vertical and horizontal components, and dividing these components by the projected area, the following expressions for pressures applied are obtained:

$$P_v = \frac{P_n dA \cdot \cos \alpha}{dA \cdot \cos \alpha} = P_n \quad (5.10)$$

$$P_n = \frac{P_n dA \cdot \sin \alpha}{dA \cdot \sin \alpha} = P_n \quad (5.11)$$

A shell's structural behaviour is derived directly from its form, thus when designing a shell foundation, the fundamental consideration is the choice of geometry. This not only dictates the allowable load, but the overall efficiency and behaviour under load of the foundation system. To be economical, shells must essentially be designed properly as they are generally thin structures that look to optimize material. A look at the geotechnical behaviour as opposed to structural behaviour is of primordial concern with respect to deciding on shape. Being an iterative process, design based on soil considerations requires ample quality experimental testing to be conclusive for a shell shape to be an adequate foundation performer. Techniques for forming optimum shapes for pure tensile or compressive structures have been developed using physical models.

5.2.1 Contact Pressure Distribution

The actual pressure that the bearing soil experiences from a foundation footing is referred to the contact pressure as described in the foregoing sections and has received very limited attention in scarce research of shell footings. All structural foundation design work is based on assumption that the contact pressure is uniform over the entire base of the foundation, but a uniformly loaded foundation will not necessarily transmit a uniform contact pressure to the soil, nor will the soil respond uniformly to the incoming pressure.

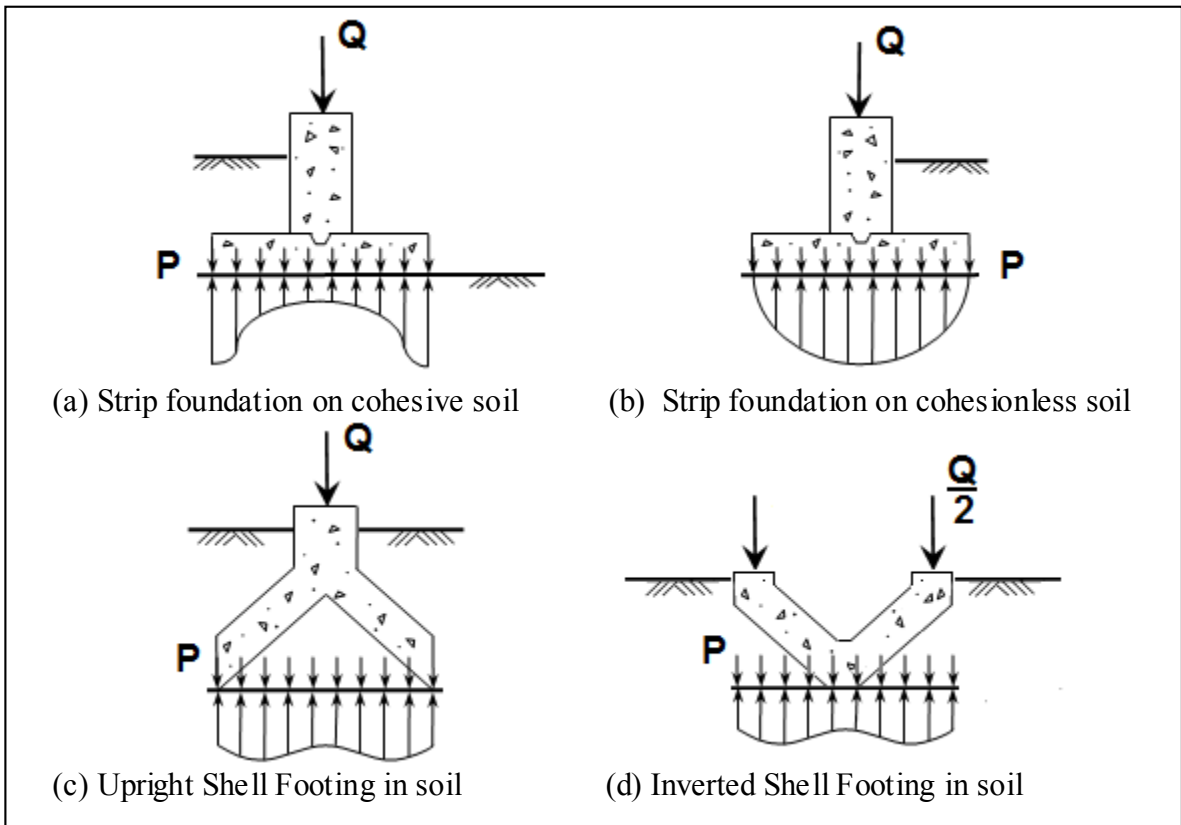


Figure 5.6. Contact Pressure Distribution Beneath Rigid Footings.

In all foregoing investigations this assumption is only plausible if the foundation is perfectly flexible. The contact pressure distribution depends upon the type and strength parameters of soil beneath it. Figures 5.6(a) and (b) depict the contact pressure distribution induced in a bearing soil that is cohesive (ie. clay) and cohesionless (ie. sand) respectively without consideration of the overburden pressure. Intuitively, overburden pressure would add stress to the toe of the footings as was observed in the numerical and experimental phases. Shell structural deformation under load as well as corresponding soil response are

important individual components each requiring rigorous mathematics for proper representations for each, let alone a model to represent their interaction. In this case, the shell footings are assumed to be both rigid and uniformly loaded so as to shift focus of the study to the geotechnical behaviour of the bearing soil as opposed to the structural component of the shell footing itself.

With the assumption that the vertical settlement of the foundation is uniform, it is observed from the elastic theory that the stress intensity at the edges of a foundation on cohesive soil is infinite. Actually, this can be interpreted to mean that local yielding at the outer boundaries of the foundation will occur until the resultant distribution reduces to that indicated in Figure 5.6(a). For the cohesive soil, when the soil mass is at its yield stress the soil has failed and the contact pressure distribution for this case tends to uniformity.

As for foundations sitting on cohesionless soil, the contact pressure distribution at the edges approaches zero. This is due to the fact that there is no overburden pressure to give the sand shear strength creating a roughly parabolic pressure distribution. Deviation from the assumed rectangular contact pressure distribution are most pronounced for surface loading and decrease with increasing footing depth and consequently increasing overburden pressure. With the inclusion of the overburden pressure, the shear strength will increase with increasing overburden at a rate that will render the contact pressure distribution relatively larger and more uniform at the contact interface.

Physically, a reinforced concrete foundation is neither perfectly flexible nor perfectly rigid but somewhere in between these two conditions depending on the degree of rigidity. Contact pressure distributions should be considered when designing for factored maximum shear (V_{\max}) and bending moments (M_{\max}) in a foundations structure. Nonetheless, to calculate shear and vertical stresses below the foundation, structural engineers have been using the gross assumption that a uniform load is inducing a rectangular uniform contact pressure shape beneath it. Since it is difficult to obtain qualitative data concerning the exact nature of the bearing soil, engineers have grossly estimated their designs. However, the effects should be recognized and accounted for since shear and more critically bending moments can be appreciably underestimated when assuming a straight-line distribution.

5.3 Bearing Capacity for iShell Footings

Historically, shell studies stem from the extensive work conducted on the ultimate bearing capacity for flat strip foundation footings dating as far back as the early 1920's. The earliest work on bearing capacity theory is perhaps the contributions made by Prandtl and Reissner between 1921 and 1924 (Das, 1988) whom have applied plastic equilibrium principles to soil penetration in variable layers. Since then, the evolution of shallow footings from traditional flat to that of shell footing foundations was continually improving. The development of upright shell footing bearing capacity, for example, has been theoretically developed in the past and was proven to be in favorable agreement with experimental results (Kurian and Varghese 1972; Kurian and Mohan 1981; Abdel-Rahman 1996). In the present investigation, the theoretical analysis for inverted shell footings is proposed and developed based on commensurate works in keeping with practice in treatment of shells as a shallow foundation footing.

5.3.1 Ultimate Bearing Capacity Theory

The first researcher to present a comprehensive theory for evaluating the ultimate bearing capacity of rough shallow foundations was Karl Terzaghi (1943). Vesic (1963) had proposed a relationship for the mode of failure based on bearing capacity for foundations resting on sands based on experimental results as shown in Figure 5.7. The general shear failure mode he proposed is based on the relative density of sand (D_r), embedment depth (D_f), width (B) and length (L) of foundation.

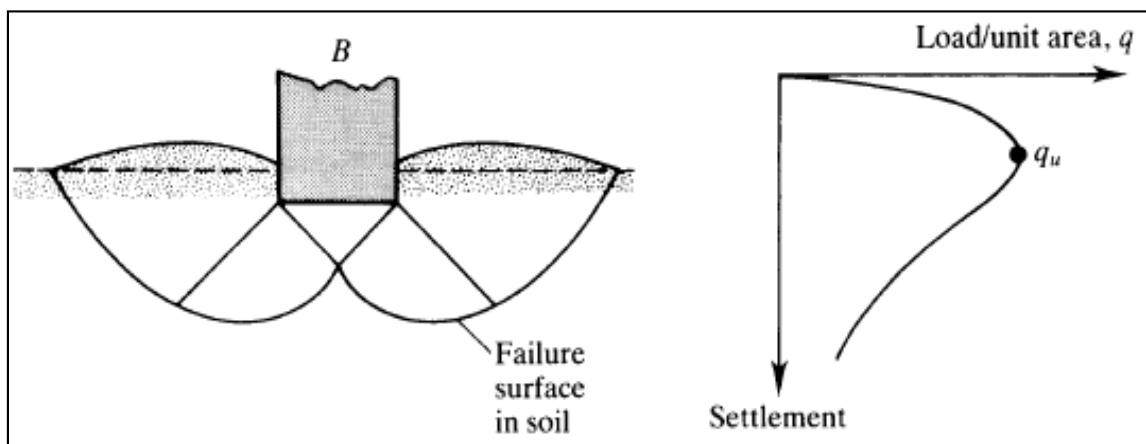


Figure 5.7. General Shear Failure Mode (Vesic, 1963).

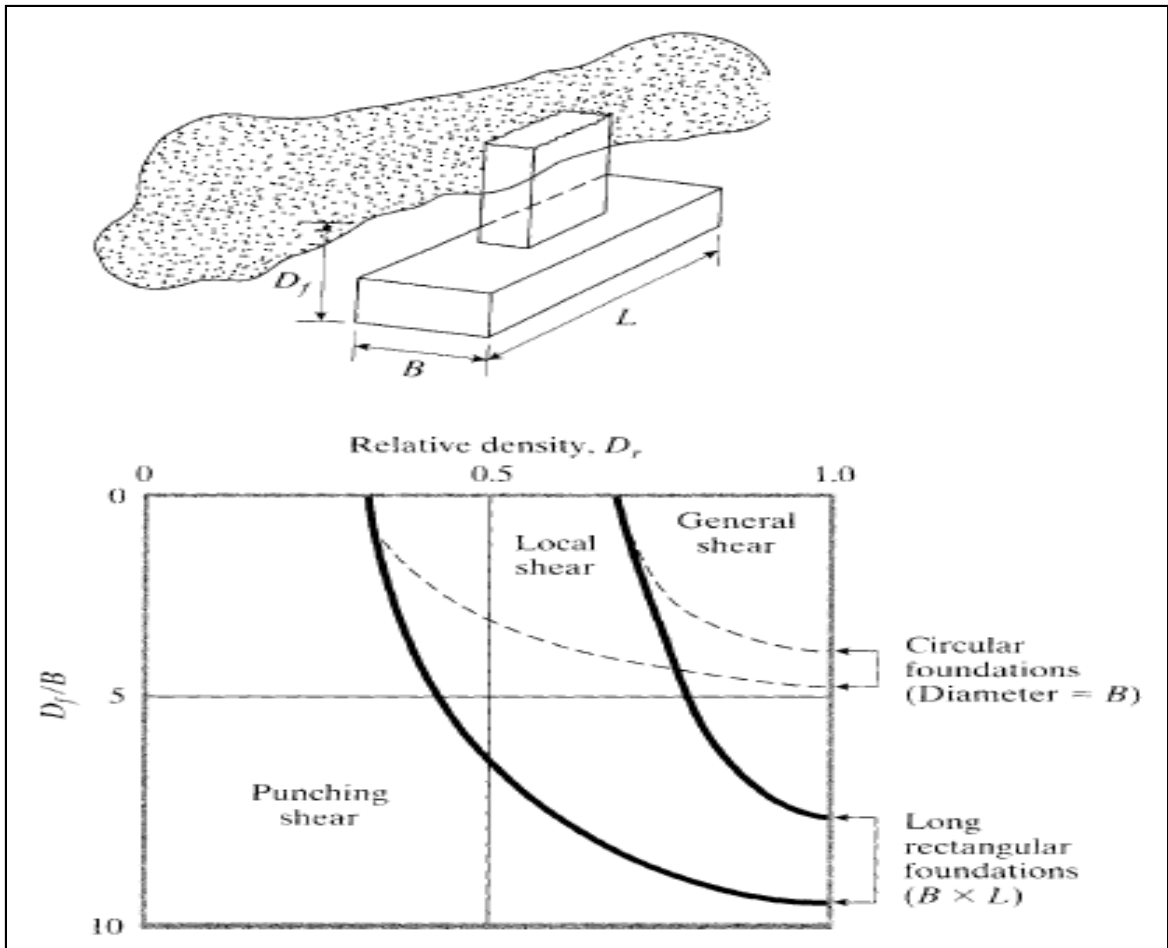


Figure 5.8. Foundation Failure Modes for Footings on Sand (Vesic, 1963).

There are no analytical solutions available to extend the bearing capacity equations to include the effects of unit weight of the foundation material. Numerous investigators have proposed relationships for the inclusion of the unit weight. They involve the application of an independent term (N_γ) to the ultimate gross bearing capacity equation. Analyses were developed by assuming the shapes of the failure surfaces and performing trial analyses until a solution was obtained. The ultimate gross bearing capacity equation for a rigid and centrally loaded continuous strip footing on a homogeneous granular material of unit weight γ developing general shear failure mode of behaviour as proposed by Terzaghi (1943) is as follows:

$$q_{ult} = cN_c + qD_fN_q + 0.5\gamma B_f N_\gamma \quad (5.12)$$

The basic fundamentals of the ultimate bearing capacity theories are based on the work of Prandtl and Reissner (Das, 1988). They investigated the problem of penetrating a metal punch into another softer, homogenous, isotropic material by applying the theory of plastic equilibrium. Karl Terzaghi was the pioneer to develop the first generalized ultimate bearing capacity theory and applied it to the field of geotechnical engineering. Since then, several contributions and modifications have been made by other researchers to refine and improve the bearing capacity theory. The solution of the ultimate bearing capacity is theoretically correct only if the system is statically and kinematically admissible. Static conditions are satisfied when all limit equilibrium equations are satisfied ($\Sigma X = 0$, $\Sigma Y = 0$, $\Sigma M = 0$), i.e., the shear stress on a soil element is equal to the shearing resistance of the said soil along the rupture surface. The conditions of kinematics are satisfied if the movement and displacement of soil elements along the rupture plane are feasible. The most common rupture surface used in the bearing capacity theories is composed of a soil wedge immediately located below the footing's base. The wedge is a rigid body which moves integrally with the footing during loading and remains in an elastic condition. A logarithmic spiral is originated from the point of intersection between the foundation's axis of symmetry and the elastic soil wedge. The logarithmic spiral is then connected with a plane surface until it intersects with the ground surface. The assumptions used in published theories lead to the final result and does not satisfy the basic requirements for either statics or kinematics conditions. However, these shortcomings are probably justified due to the fact that there are still a lot of uncertainties in the evaluation of the basic soil parameters employed in the calculation process of the ultimate bearing capacity.

Much like the development of the general bearing capacity equation to include depth, shape and load inclination factors by Meyerhof (1963); Hanna and Meyerhof (1981), the present study applies similar principals to inverted shells. The present analysis relies on some inherent assumptions. The introduction of a Shell Ratio (S_r) is conveniently used for best representation of a shell footing's configuration. The failure angle (α) depends on the said shell ratio, angle of shearing resistance (ϕ), and Mohr–Coulomb's failure envelope as used to establish the slope of the tangent of the rupture surface. Finally, Kötter's differential equation can be used to predict the ultimate bearing capacity of a foundation.

5.4 Theoretical Triangular iShell Model

The finite element models in the numerical study show the induced rupture surfaces for inverted strip shell footings as found in Chapter 3. This was similar to what was observed under initial testing of pigmented layered soil in the experimental phase. The respective theoretical cross section of inverted strip shell footing and rupture surfaces proposed follow these same results and is presented in Figure 5.10 for theoretical modeling in determination of the new inverted shell bearing capacity factors. It is worthwhile to note that similar failure mechanisms were employed by Balla (1962) and more recently by Rahman (1996) for the upright shell case. In the present investigation the failure surface is idealized and represented by a rupture surface composed of quasi-circular and plane surfaces found to have deeper penetration. The proposed rupture surface should satisfy the requirements for both static and kinematic conditions for inverted shell footings.

The projected rupture surface originates from the apex of the soil wedge (i.e. wedge (hij) shown in yellow in Figure 5.12) intersecting the inverted shell footing's axis of symmetry and the ground surface at angles satisfying static equilibrium. In order for the rupture surface to be kinematically admissible, only quasi-circular and planar surfaces were considered in its development. The inverted shell rupture surface proposed is shown in Figure 5.10 composed primarily of two parts; the circular surface (js) and plane surface (st). The circular rupture surface has central coordinates (x_o, z_o) from which moment equilibrium of all forces acting on the system is evaluated and given by the following expressions:

$$x_o = r_x \sin\left[\frac{\pi}{4} + \frac{\phi}{2}\right] \quad (5.13)$$

and

$$z_o = D - r \sin\left[\frac{\pi}{4} + \frac{\phi}{2}\right] \quad (5.14)$$

The principal objective of this theoretical study is to determine the geometry of the circular portion of failure which satisfies the equilibrium of all forces acting on the entire rupture surface. The deduced rupture surface will then be used to determine the inverted

shell bearing capacity coefficients (N_c , N_q , and N_γ) is and consequently the ultimate bearing capacity ($q_{u,Shell}$).

In the present analysis, the Shell Ratio (S_r) representing the shell footing's configuration in the vertical direction with respect to the shells apex in the horizontal direction is defined by Equation (5.15) as follows:

$$S_r = \frac{\pi + 2\theta}{\pi} \quad (5.15)$$

where, θ is the shell angle between shell bearing surface (hg) and the horizontal (hm) initiating from the inverted shells apex.

This ratio was selected to reflect the effect of shell configuration on the failure angle (α). The three extreme limits for (S_r) are $\{0, 1, 2\}$ with $S_r = 1$ for a flat foundation footing and $S_r = 0$ and 2 for piles or columns without a footing base. It is important to note that inverted shell footings have a shell ratio ranging between 1 and 2 while the upright counterparts range between 0 and 1 as summarized in Table 5.2 as follows.

Shell Angle, θ	Shell Ratio, S_r	Footing Type
0	1	Flat
$0 < \theta < \pi/2$	$1 < S_r < 2$	Inverted shell
$-\pi/2 < \theta < 0$	$0 < S_r < 1$	Upright shell
$\pm \pi/2$	0 & 2	Pile or column without base

Table 5.2. Shell Ratio's for Different Footing Configurations.

The failure angle (α) depends on the shell configuration represented by the shell ratio (S_r), and the angle of shearing resistance (ϕ). The following proposed empirical relationship for the failure angle (α) is based on experimental results deduced from the special loading tests conducted in the present investigation:

$$\alpha = \phi + (S_r - 1) \left[\frac{\pi}{4} - \frac{2\phi}{3} \right] \quad (5.16)$$

where,

α : vertical angle between shell surface level (ge) and the surface (eh) of the soil wedge (egh).

From Equation (5.15), for the case of the flat footing we have $\theta = 0^\circ$; $S_r = 1$, consequently the wedge failure angle $\alpha = \phi$. For the case of pile or columns where $\theta = \pm\pi/2$; $S_r = 0$ and 2, consequently $\alpha = (5\phi/3 - \pi/4)$ and $(\phi/3 + \pi/4)$ respectively. For the inverted shell footing case, ie, $S_r = 1$, is equal to the angle of shearing resistance $(4\phi/3 - \pi/8)$. The failure angle (α) for the case of a flat footing, ie, $S_r = 2$, is equal to the angle of shearing resistance (ϕ). For inverted shell footing with shell angle ($\theta = 45^\circ$), i.e., $S_r = 1.5$, the angle (α) is equal to $(4\phi/3 - \pi/8)$. For shell footing with shell angle ($\theta = \pi/2 + 45^\circ$), i.e., $S_r = 2.5$, the angle (α) is equal to $(2\phi/3 + \pi/8)$; and for deep foundation, ie., $S_r = 3$ and ($\theta = \pi^\circ$), the angle (α) is equal to $(\pi/4 + \phi/3)$. However, the present investigation is limited to shallow foundation where the shell angle (θ) is less than 90° . In order to determine the value of angle (ψ), which satisfies the conditions of limit equilibrium, Mohr Coulomb's envelope shown in Figure 5.9 was used to establish the slope of the tangent of the rupture surface at point (j) located on the axis of symmetry and point (t) on the ground surface. From this figure, the shear stress (τ_{xy}) can be presented as a function of the shear stress (τ) existing on Mohr's circle as follows:

$$\tau_{xy} = \tau \frac{\cos(\phi + 2\psi)}{\cos\phi} \quad (5.17)$$

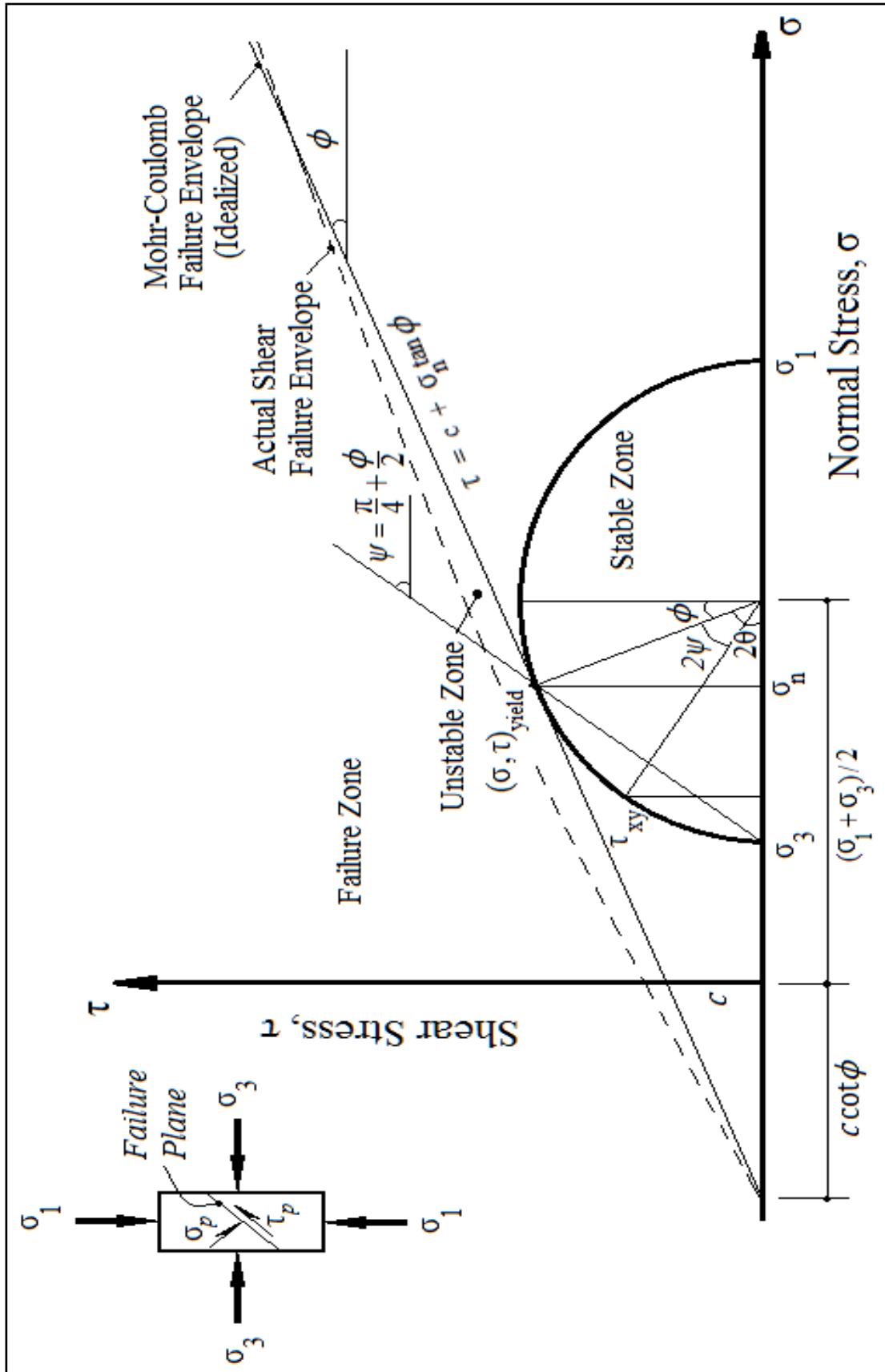


Figure 5.9. Mohr-Coulomb's Failure Criterion.

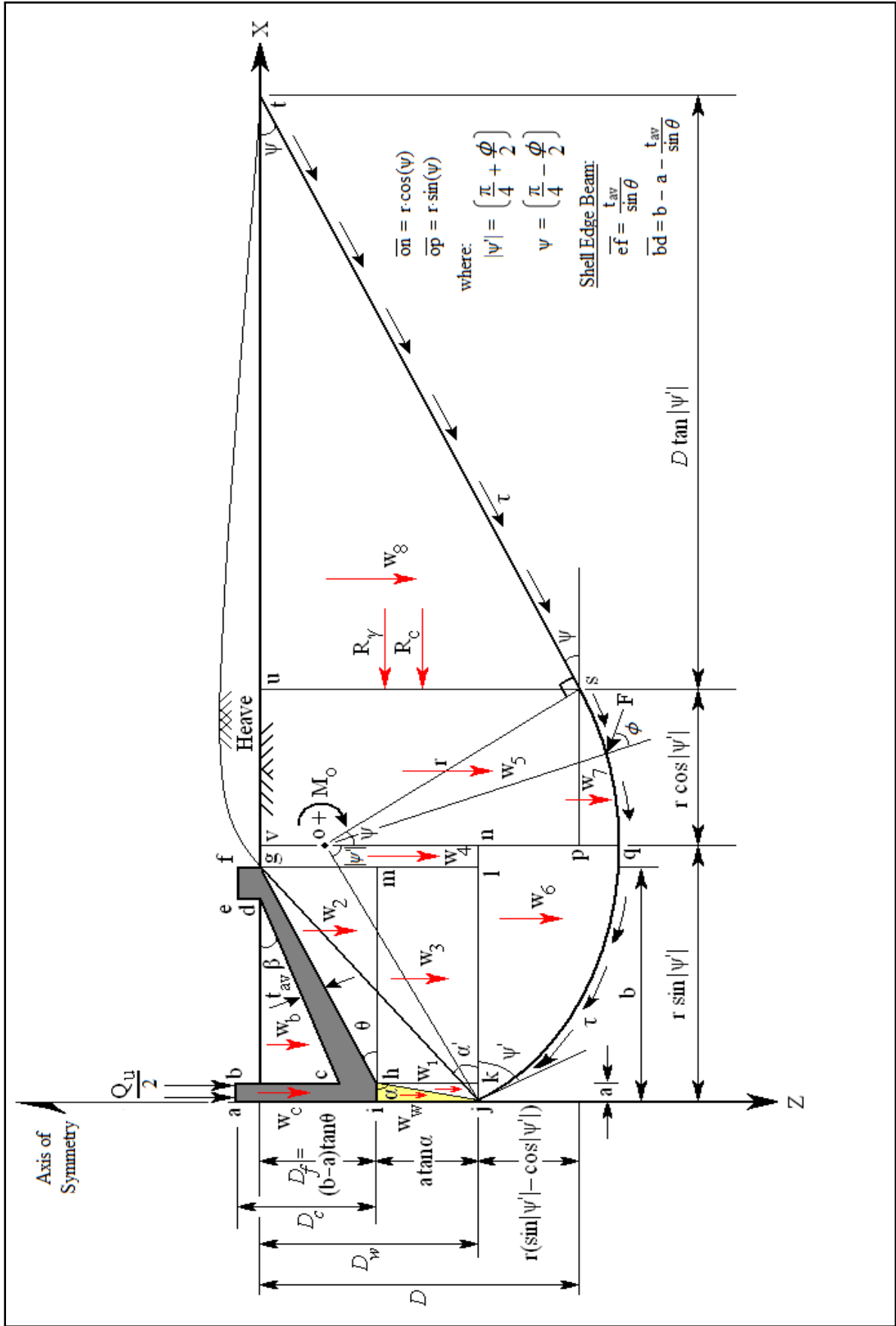


Figure 5.10. iShell Footing Rupture Surface.

The shear stress (τ_{xy}) on the axis of symmetry and on the ground surface, must be equal to zero, which is satisfied when $\cos(\phi + 2\psi) = 0$, i.e., when the angle $(\phi + 2\psi)$ is equal to $(\phi \pm \pi/2)$. According to the active and passive stress states, the associated slopes of the tangents at points (j) and (t) are noted respectively as:

$$\psi = \left[\frac{\pi}{4} - \frac{\phi}{2} \right] \quad (5.18)$$

and

$$\psi' = - \left[\frac{\pi}{4} + \frac{\phi}{2} \right] \quad (5.19)$$

The distribution of soil pressure and shear stress along an arc of a given rupture surface was investigated by Kötter (1888). He derived a mathematical solution which can be employed for any rupture surface (plane or curve). This solution can be adopted to define more accurately the location and shape of the rupture surface. However, due to the rigorous mathematical formulation, such as the set of hyperbolic-type differential equations, often referred to as the Kötter differential equations, this approach was rarely used by researchers in predicting the ultimate bearing capacity of a foundation.

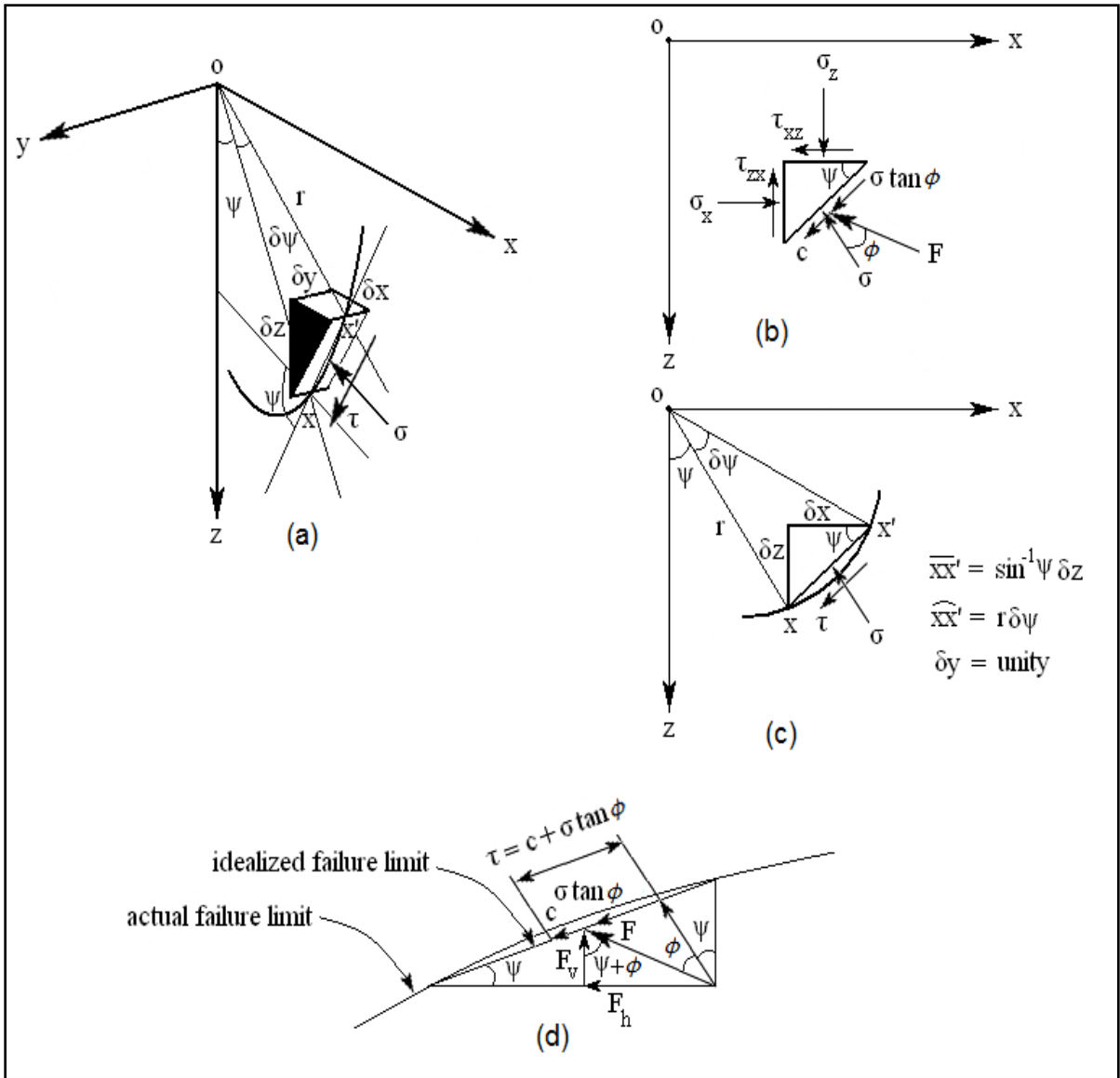


Figure 5.11. iShell-Soil Interface Equilibrium using Kötter's Parameters.

In the present investigation, in order to determine the distribution of shear stress acting along both parts of the rupture surface, Kötter's differential equation for the passive stress state will be utilized. Using the notations shown in Figure 5.11, Kötter's equation can be written as follows:

$$\frac{\partial \tau}{\partial s} + 2\tau \tan \phi \frac{\partial \psi}{\partial s} + \gamma \sin \phi \sin(\psi \pm \phi) = 0 \quad (5.20)$$

For the inclined plane rupture surface (mn): $\frac{\partial \psi}{\partial s} = 0$

Substituting with this boundary condition in Kötter's differential equation, the following is obtained:

$$\frac{\partial \tau_{pl}}{\partial s} - \gamma \sin \phi \sin(\psi + \phi) = 0 \quad (5.21)$$

or $\partial \tau_{pl} = \gamma \sin \phi \sin(\psi + \phi) \partial s$ (5.22)

and $\tau_{pl} = \gamma \sin \phi \sin(\psi + \phi) s + \lambda_1$ (5.23)

where, $\lambda_1 = \text{constant}$

From Figure 5.20(a) and substitute by $s = \frac{z}{\sin \psi}$

thus,

$$\tau_{pl} = \gamma \sin \phi \frac{\sin(\psi + \phi)}{\sin \psi} z + \lambda_1 \quad (5.24)$$

Substitute for the angle ψ by $(\pi/4 - \phi/2)$, as established from Equation (5.18):

$$\tau_{pl} = \gamma \sin \phi \tan \left[\frac{\pi}{4} + \frac{\phi}{2} \right] z + \lambda_1 \quad (5.25)$$

where λ_1 is equal to the shear stress (τ_{pl}) at the ground surface, ie. at $z = 0$.

$$\lambda_1 = (1 + \sin \phi) c \quad (5.26)$$

$$\tau_{pl} = \gamma \sin \phi \tan \left[\frac{\pi}{4} + \frac{\phi}{2} \right] z + (1 + \sin \phi) c \quad (5.27)$$

For the circular surface : $\frac{\partial s}{\partial \psi} = -r$

Multiplying the first and second terms of Kotter's equation by $\frac{\partial s}{\partial \psi}$ and the third term by $-r$, the following equation is obtained:

$$\frac{\partial \tau_{\text{cir}}}{\partial \psi} + 2\tau_{\text{cir}} \tan \phi = -r\gamma \sin(\psi + \phi) \quad (5.28)$$

in order to solve this equation, the following substitutions are employed:

$$M = 2 \tan \phi \quad (5.29)$$

$$N = r\gamma \sin \phi \sin(\psi + \phi) \quad (5.30)$$

Substituting with Equations (5.29) and (5.30) in Equation (5.28)

$$\partial \tau_{\text{cir}} + (M\tau_{\text{cir}} - N) \partial \psi = 0 \quad (5.31)$$

Multiplying Equation (5.31) by $\mu(\psi, \tau_{\text{cir}})$:

$$\mu \partial \tau_{\text{cir}} + (M\tau_{\text{cir}} - N)\mu \partial \psi = 0 \quad (5.32)$$

In order to obtain the exact solutions of Equation (5.21), the following relationships must be satisfied:

$$\frac{\partial \mu}{\partial \psi} = \frac{\partial (M\tau_{\text{cir}} - N)\mu}{\partial \tau_{\text{cir}}} \quad (5.33)$$

$$\frac{\partial \mu}{\partial \psi} = M\mu = 2\mu \tan \phi \quad (5.34)$$

$$\frac{\partial \mu}{\mu} = 2 \tan \phi \partial \psi \quad (5.35)$$

$$\ln(\mu) = 2\psi \tan \phi$$

or

$$\mu = e^{2\psi \tan \phi} \quad (5.36)$$

The final solution of the differential equation can be obtained as follows:

$$\mu\tau_{\text{cir}} = \int \mu N \partial\psi \quad (5.37)$$

$$e^{2\psi \tan\phi} \tau_{\text{cir}} = - \int e^{2\psi \tan\phi} r\gamma \sin\phi \sin(\psi + \phi) \partial\psi \quad (5.38)$$

To determine the shear stress for the circular part of the rupture surface (τ_{cir}), the integration in the right-hand side of Equation (5.38) is substituted by the following:

$$I = - \int e^{2\psi \tan\phi} r\gamma \sin\phi \sin(\psi + \phi) \partial\psi \quad (5.39)$$

To solve the integration (I) in Equation (5.39) the following calculations are performed:

$$I = \frac{e^{2\psi \tan\phi}}{2 \tan\phi} \sin(\psi + \phi) - \frac{1}{2 \tan\phi} \int e^{2\psi \tan\phi} \cos(\psi + \phi) \partial\psi \quad (5.40)$$

$$I = \frac{e^{2\psi \tan\phi}}{2 \tan\phi} \sin(\psi + \phi) - \frac{e^{2\psi \tan\phi}}{2 \tan\phi} \cos(\psi + \phi) - \frac{1}{4 \tan^2\phi} \int e^{2\psi \tan\phi} \cos(\psi + \phi) \partial\psi \quad (5.41)$$

$$I\left(1 + \frac{1}{4 \tan^2\phi}\right) = \frac{e^{2\psi \tan\phi}}{2 \tan\phi} \sin(\psi + \phi) - \frac{e^{2\psi \tan\phi}}{2 \tan\phi} \cos(\psi + \phi) \quad (5.42)$$

$$I = \frac{e^{2\psi \tan\phi}}{2 \tan^2\phi} (2 \tan\phi \sin(\psi + \phi) - \cos(\psi + \phi)) + \lambda_2 \quad (5.43)$$

where, $\lambda_2 = \text{constant}$

Substituting by the integration (I) in Equation (5.38), the shear stress (τ_{cir}), can be presented in the following form:

$$\tau_{\text{cir}} = \lambda_2 (e^{-2\psi \tan\phi}) - \frac{r\gamma \sin\phi}{1 + 4 \tan^2\phi} (2 \tan\phi \sin(\psi + \phi) - \cos(\psi + \phi)) + \lambda_2 \quad (5.44)$$

In order to determine the constant λ_2 , equate the shear stress from the plane part and the circular part, i.e, $\tau_{pl} = \tau_{cir}$, at the junction point (p) where the slope of the tangent is equal to $(\pi/4 - \phi/2)$, and the depth (z) at point (p) is equal to (D).

$$\gamma \sin\phi \tan\left[\frac{\pi}{4} + \frac{\phi}{2}\right]D + (1 + \sin\phi)c = \lambda_2(e^{-2\psi \tan\phi}) - \frac{r\gamma \sin\phi}{1 + 4 \tan^2\phi} (2\tan\phi \sin(\psi + \phi) - \cos(\psi + \phi)) \quad (5.45)$$

$$\lambda_2 = e^{2\left[\frac{\pi}{4} - \frac{\phi}{2}\right]\tan\phi} \left[\gamma \sin\phi \tan\left[\frac{\pi}{4} + \frac{\phi}{2}\right]H + (1 + \sin\phi)c \right] + e^{2\left[\frac{\pi}{4} - \frac{\phi}{2}\right]\tan\phi} \frac{r\gamma \sin\phi}{1 + 4\tan^2\phi} \left[2 \tan\phi \sin\left[\frac{\pi}{4} + \frac{\phi}{2}\right] - \cos\left[\frac{\pi}{4} + \frac{\phi}{2}\right] \right] \quad (5.46)$$

To further simplify the terms, constant factors (ζ_i) are introduced to replace expressions that are solely functions of the angle of friction (ϕ), summarized as:

$$\zeta_1 = (1 + \sin\phi) \quad (5.47)$$

$$\zeta_2 = \sin\left[\frac{\pi}{4} + \frac{\phi}{2}\right] - \cos\left[\frac{\pi}{4} + \frac{\phi}{2}\right] \quad (5.48)$$

$$\zeta_3 = \sin\phi \tan\left[\frac{\pi}{4} + \frac{\phi}{2}\right] \quad (5.49)$$

$$\zeta_4 = 1 + 4\tan^2\phi \quad (5.50)$$

$$\zeta_5 = e^{2\left[\frac{\pi}{4} - \frac{\phi}{2}\right]\tan\phi} \quad (5.51)$$

$$\zeta_6 = \sin\phi \left[2\tan\phi \sin\left[\frac{\pi}{4} + \frac{\phi}{2}\right] - \cos\left[\frac{\pi}{4} + \frac{\phi}{2}\right] \right] \quad (5.52)$$

$$\zeta_7 = \zeta_2\zeta_3 + (\zeta_6 / \zeta_4) \quad (5.53)$$

Bearing depth of soil (D) at point (s) on the rupture surface can be expressed as:

$$D = D_f + a \tan\alpha + r \left[\sin\left[\frac{\pi}{4} + \frac{\phi}{2}\right] - \cos\left[\frac{\pi}{4} + \frac{\phi}{2}\right] \right] \quad (5.54)$$

$$D_w = D_f + a \tan \alpha \quad (5.55)$$

$$D = D_w + r \zeta_2 \quad (5.56)$$

Simplification for the constant λ_2 can be expressed as:

$$\lambda_2 = \zeta_3(\gamma D_w \zeta_3 + r \zeta_7 + c \zeta_l) \quad (5.57)$$

As depicted in Figure 5.11(d), the vertical and horizontal components of the resultant force, F_v and F_h , respectively, can be obtained in consideration of shear stress, τ , as follows:

$$\tau = c + \sigma \tan \phi \quad (5.58)$$

$$\tau - c = \sigma \tan \phi = \left[\frac{\sigma}{\cos \phi} \right] \sin \phi = F \sin \phi \quad (5.59)$$

$$F = \left[\frac{\tau - c}{\sin \phi} \right] \quad (5.60)$$

$$F_v = \left[\frac{\tau - c}{\sin \phi} \right] \cos(\psi + \phi) \quad (5.61)$$

$$F_h = \left[\frac{\tau - c}{\sin \phi} \right] \sin(\psi + \phi) \quad (5.62)$$

Figure 5.11(d) depicts the partial derivative of the vertical component (∂F_v) acting over an elemental rupture surface can be expressed as:

$$\partial F_v = \left[\frac{\tau - c}{\sin \phi} \right] r \cos(\psi + \phi) \partial \psi \quad (5.63)$$

Substitution of shear stress (τ_{pl}) over the plane surface into Equation (5.63) above yields:

$$\partial F_{vp} = \left[c + \gamma z \tan \left(\frac{\pi}{4} + \frac{\phi}{2} \right) \right] \partial z \quad (5.64)$$

$$\text{where,} \quad \partial z = r \cos(\psi + \phi) \partial \psi \quad (5.65)$$

$$\text{so that,} \quad F_{vp} = cz + \frac{1}{2} \gamma z^2 \tan\left[\frac{\pi}{4} + \frac{\phi}{2}\right] \quad (5.66)$$

where F_{vp} is the resultant force vertical component acting on the planar portion of the rupture surface. Substitution of shear stress (τ_{cir}) over the circular surface into Equation (5.63) above yields:

$$\partial F_{vc} = \int_{-\left[\frac{\pi}{4} + \frac{\phi}{2}\right]}^{\left[\frac{\pi}{4} - \frac{\phi}{2}\right]} \left[\frac{\tau_{cir} - c}{\sin \phi} \right] \cos(\psi + \phi) r \partial \psi \quad (5.67)$$

Integration given by Equation (5.67) is divided into three parts ζ_1 , ζ_2 , and ζ_3 expressed as:

$$F_{vc} = \sum_{n=1}^3 \zeta_n \quad (5.68)$$

$$\zeta_1 = \int \left[\frac{\lambda_2 e^{-2\psi \tan \phi}}{\sin \phi} \right] r \cos(\psi + \phi) \partial \psi \quad (5.69)$$

$$\zeta_2 = - \int \left[\frac{r^2 \gamma}{1 + 4 \tan^2 \phi} \right] \left[2 \tan \phi \sin(\psi + \phi) - \cos(\psi + \phi) \right] \cos(\psi + \phi) \partial \psi \quad (5.70)$$

$$\zeta_3 = - \int \left[\frac{c r}{\sin \phi} \right] \cos(\psi + \phi) \partial \psi \quad (5.71)$$

Solving for each of the three parts yields the expressions:

$$\zeta_1 = \frac{\lambda_2 r}{\sin \phi} \left[\frac{e^{-2\psi \tan \phi}}{1 + 4 \tan^2 \phi} (\sin(\psi + \phi) - 2 \tan \phi \cos(\psi + \phi)) \right] \Bigg|_{-\left[\frac{\pi}{4} + \frac{\phi}{2}\right]}^{\left[\frac{\pi}{4} - \frac{\phi}{2}\right]} \quad (5.72)$$

$$\zeta_1 = \frac{\lambda_2 r e^{-2\left(\frac{\pi}{4} - \frac{\phi}{2}\right) \tan \phi}}{\sin \phi (1 + 4 \tan^2 \phi)} \cos\left(\frac{\pi}{4} + \frac{\phi}{2}\right) \left[e^{\pi \tan \phi} \tan^2\left(\frac{\pi}{4} + \frac{\phi}{2}\right) + \tan\left(\frac{\pi}{4} + \frac{\phi}{2}\right) - 2 \tan \phi \right] \quad (5.73)$$

$$\zeta_2 = - \frac{r^2 \gamma}{1 + 4 \tan^2 \phi} \left(\sin^2(\psi + \phi) + \psi + \frac{\sin^2(\psi + \phi)}{2} \right) \Bigg|_{-\left(\frac{\pi}{4} + \frac{\phi}{2}\right)}^{\left(\frac{\pi}{4} - \frac{\phi}{2}\right)} \quad (5.74)$$

$$\zeta_2 = - \frac{r^2 \gamma}{1 + 4 \tan^2 \phi} \left(\frac{\pi}{4} + \frac{\cos \phi}{2} - \tan \phi \sin \phi \right) \quad (5.75)$$

$$\zeta_3 = - \frac{c r}{\sin \phi} \left(\sin(\psi + \phi) \right) \Bigg|_{-\left(\frac{\pi}{4} + \frac{\phi}{2}\right)}^{\left(\frac{\pi}{4} - \frac{\phi}{2}\right)} \quad (5.76)$$

$$\zeta_3 = - \frac{c r \sqrt{2}}{\sin \phi} \cos\left(\frac{\phi}{2}\right) \quad (5.77)$$

Substitution of expressions for ζ_1 , ζ_2 , and ζ_3 obtained above into Equation (5.68) and solving for (F_{vc}) yields:

$$F_{vc} = \frac{\lambda_2 r e^{-2\left(\frac{\pi}{4} - \frac{\phi}{2}\right) \tan \phi}}{\sin \phi (1 + 4 \tan^2 \phi)} \cos\left(\frac{\pi}{4} + \frac{\phi}{2}\right) \left[e^{\pi \tan \phi} \tan^2\left(\frac{\pi}{4} + \frac{\phi}{2}\right) + \tan\left(\frac{\pi}{4} + \frac{\phi}{2}\right) - 2 \tan \phi \right] + \frac{r^2 \gamma}{1 + 4 \tan^2 \phi} \left(\frac{\pi}{4} + \frac{\cos \phi}{2} - \tan \phi \sin \phi \right) - \frac{c r \sqrt{2}}{\sin \phi} \cos\left(\frac{\phi}{2}\right) \quad (5.78)$$

$$\xi_8 = \cos\left[\frac{\pi}{4} + \frac{\phi}{2}\right] e^{-2\left[\frac{\pi}{4} - \frac{\phi}{2}\right] \tan\phi} \quad (5.79)$$

$$\xi_9 = e^{\pi \tan\phi} \tan^2\left[\frac{\pi}{4} + \frac{\phi}{2}\right] + \tan\left[\frac{\pi}{4} + \frac{\phi}{2}\right] - 2\tan\phi \quad (5.80)$$

$$\xi_{10} = \frac{\pi}{4} + \frac{\cos\phi}{2} - \tan\phi \sin\phi \quad (5.81)$$

$$\xi_{11} = -\frac{\sqrt{2}\cos\left[\frac{\phi}{2}\right]}{\sin\phi} \quad (5.82)$$

Substituting $\xi_8 - \xi_{11}$ inclusively into Equation (5.78) for (F_{vc}) yields:

$$F_{vc} = \frac{\lambda_2 r \xi_8 \xi_9}{\sin\phi \xi_4} + \frac{\lambda_2 r^2 \xi_{10}}{\xi_4} + cr \xi_{11} \quad (5.83)$$

$$\xi_{12} = \frac{\xi_3 \xi_5 \xi_8 \xi_9}{\sin\phi \xi_4} \quad (5.84)$$

$$\xi_{13} = \frac{\xi_5 \xi_7 \xi_8 \xi_9}{\sin\phi \xi_4} + \frac{\xi_{10}}{\xi_4} \quad (5.85)$$

$$\xi_{14} = \frac{\xi_1 \xi_5 \xi_8 \xi_9}{\sin\phi \xi_4} + \xi_{11} \quad (5.86)$$

The resultants force vertical component acting on the circular portion of the rupture surface (F_{vc}) is deduced and summarized as:

$$F_{vc} = \gamma r D_w \xi_{12} + \gamma r^2 \xi_{13} + cr \xi_{14} \quad (5.87)$$

The soils failure pattern is represented by the rupture surface proposed in Figure 5.10. The overall surface was divided into a series of soil prisms notated as (w_n) representing the soil weight and (l_n) for the corresponding lever arm which spans the center of the slip circle

at point (o) to the center of gravity of the soil prism. The soil weight and the resulting lever arm expressions are represented as:

For soil prism (*hjk*):

$$w_1 = \frac{1}{2} \gamma a^2 \tan \alpha \quad (5.88)$$

$$l_1 = r \sin \left[\frac{\pi}{4} + \frac{\phi}{2} \right] - \frac{2}{3} a \quad (5.89)$$

For soil prism (*ghm*):

$$w_2 = \frac{1}{2} \gamma (b - a)^2 \tan \theta \quad (5.90)$$

$$l_2 = r \sin \left[\frac{\pi}{4} + \frac{\phi}{2} \right] - \frac{1}{3} (a + 2b) \quad (5.91)$$

For soil prism (*hklm*):

$$w_3 = \gamma a (b - a) \tan \alpha \quad (5.92)$$

$$l_3 = r \sin \left[\frac{\pi}{4} + \frac{\phi}{2} \right] - \frac{1}{2} (a + b) \quad (5.93)$$

For soil prism (*glnv*):

$$w_4 = \gamma \left[r \sin \left[\frac{\pi}{4} + \frac{\phi}{2} \right] - b \right] D_w \quad (5.94)$$

$$l_4 = \frac{1}{2} \left[r \sin \left[\frac{\pi}{4} + \frac{\phi}{2} \right] - b \right] \quad (5.95)$$

For soil prism (*vpsu*):

$$w_5 = \gamma \left[r \cos \left[\frac{\pi}{4} + \frac{\phi}{2} \right] \right] D \quad (5.96)$$

$$l_5 = \frac{1}{2} r \cos\left[\frac{\pi}{4} + \frac{\phi}{2}\right] \quad (5.97)$$

For soil prism (*jnq*):

$$w_6 = \frac{1}{2} \gamma r^2 \sin\left[\frac{\pi}{4} + \frac{\phi}{2}\right] \left(1 - \cos\left[\frac{\pi}{4} + \frac{\phi}{2}\right]\right) \quad (5.98)$$

$$l_6 = \frac{2}{3} r \left(\frac{1 - \frac{3}{2} \cos\left[\frac{\pi}{4} + \frac{\phi}{2}\right] + \frac{1}{2} \cos^3\left[\frac{\pi}{4} + \frac{\phi}{2}\right]}{\sin\left[\frac{\pi}{4} + \frac{\phi}{2}\right] - \sin\left[\frac{\pi}{4} + \frac{\phi}{2}\right] \cos\left[\frac{\pi}{4} + \frac{\phi}{2}\right]} \right) \quad (5.99)$$

For soil prism (*pqs*):

$$w_7 = \frac{1}{2} \gamma r^2 \sin\left[\frac{\pi}{4} - \frac{\phi}{2}\right] \left(1 - \cos\left[\frac{\pi}{4} - \frac{\phi}{2}\right]\right) \quad (5.100)$$

$$l_7 = \frac{2}{3} r \left(\frac{1 - \frac{3}{2} \cos\left[\frac{\pi}{4} - \frac{\phi}{2}\right] + \frac{1}{2} \cos^3\left[\frac{\pi}{4} - \frac{\phi}{2}\right]}{\sin\left[\frac{\pi}{4} - \frac{\phi}{2}\right] - \sin\left[\frac{\pi}{4} - \frac{\phi}{2}\right] \cos\left[\frac{\pi}{4} - \frac{\phi}{2}\right]} \right) \quad (5.101)$$

For soil prism (*stu*):

$$w_8 = \frac{1}{2} \gamma D^2 \tan\left[\frac{\pi}{4} + \frac{\phi}{2}\right] \quad (5.102)$$

$$l_8 = r \cos\left[\frac{\pi}{4} + \frac{\phi}{2}\right] + \frac{1}{3} D \tan\left[\frac{\pi}{4} + \frac{\phi}{2}\right] \quad (5.103)$$

Summation of all weights (w_T) for the soil prism (*ghjqrst*), and the consequent moment (M_{w_T}) acting about the center of the circle at point (o) are expressed as:

$$w_T = \sum_{n=1}^8 w_n \quad (5.104)$$

$$M_{w_T} = \sum_{n=1}^8 w_n l_n \quad (5.105)$$

Normalizing the effects of the shell foundations total width (B) in the calculation of the radius of the rupture circle, the factor rho (ρ) is implemented by the following expression:

$$\rho = \frac{r}{b} \quad (5.106)$$

where,

r = radius of circle

and

$$b = \frac{1}{2} B = \text{one half of the shell foundations total width}$$

Solving Equation (5.105), under the normalized condition yields the resulting moment due to the soils total unit weight (M_{wT}) acting about the center of the circle (o) evaluated as:

$$\sum M_{wT} = 0$$

Yielding the following expression:

$$\begin{aligned} M_{wT} = & \frac{\gamma b^3}{6} \left[(\sin\psi - \cos\psi) \left(3\cos^2\psi + 3\tan\psi\cos\psi(\sin\psi - \cos\psi) + \tan^2\psi(\sin\psi - \cos\psi)^2 \right) \right. \\ & \left. - 3\sqrt{2} \sin\left(\frac{\phi}{2}\right) + \sin^3\psi - \cos\psi \right] \rho^3 + \frac{\gamma b^2}{2} \left[D_w(\cos^2\psi + 2\tan\psi\cos\psi(\sin\psi - \cos\psi) - \sin^2\psi) \right] \rho^2 \\ & + \frac{\gamma b}{2} \left[D_w^2 \tan\psi \left(\cos\psi + \tan\psi(\sin\psi - \cos\psi) \right) + \sin\psi \left(b^2 - a^2(1 - \tan\alpha) \right) \right] \rho \\ & + \frac{\gamma}{6} \left[(a^3 - 5b^3)\tan\theta - a^3\tan\alpha + D_w^2\tan^2\psi \right] \end{aligned} \quad (5.107)$$

The shell foundations total concrete weight (w_c) is divided into three segments (w_{c1} , w_{c2} , w_{c3}) having respective lever arms (l_1 , l_2 and l_3). The fixed column height (D_f) and width (a) of the foundation are illustrated in Figure 5.10. Moreover, the shell angle (θ) and the average shell thickness (t_{av}) over its inclined length constitute the main cross-sectional parameters used in the analysis. The unit weight of concrete (γ_c) for the foundations is

employed to determine the resulting moment about the center of the circle due to the total weight of the shell foundations concrete (Mw_c) computed as:

$$w_{c1} = a D_f \gamma_c \quad (5.108)$$

$$l_1 = r \sin\left(\frac{\pi}{4} + \frac{\phi}{2}\right) - \frac{1}{2} a \quad (5.109)$$

$$w_{c2} = t_{av} H \gamma_c \quad (5.110)$$

where,

$$H = \left(b - a - \frac{t_{av}}{\sin\theta} \right) \left(\frac{1}{\cos\theta} \right)$$

$$l_2 = r \sin\left(\frac{\pi}{4} + \frac{\phi}{2}\right) + \frac{t_{av}}{2\sin\theta} - \frac{1}{2} (a + b) \quad (5.111)$$

$$w_{c3} = \frac{1}{2} \gamma_c \left(\frac{t_{av}^2}{\cos\theta \sin\theta} \right) \quad (5.112)$$

$$l_3 = r \sin\left(\frac{\pi}{4} + \frac{\phi}{2}\right) - b + \frac{2t_{av}}{3\sin\theta} \quad (5.113)$$

$$Mw_C = \sum_{n=1}^3 w_{C_n} l_n \quad (5.114)$$

After simplification, yielding the following expression:

$$Mw_C = \left[a b t_{av} \sin\left(\frac{\pi}{4} + \frac{\phi}{2}\right) \left[\gamma_c \left[\frac{D_f}{t} + \frac{t_{av}}{2a \cos\theta \sin\theta} \right] + \frac{1}{\cos\theta} \left[\frac{b}{a} - 1 - \frac{t_{av}}{a \sin\theta} \right] \right] \right] \rho + \frac{bt^2}{\cos\theta \sin\theta} \left(1 - \frac{\gamma_c}{2} \right) + \frac{t_{av}}{2\cos\theta} (a^2 - b^2) + \frac{t^3}{6\cos\theta \sin^2\theta} (2\gamma_c - 3) - \frac{1}{2} a^2 D_f \gamma_c \quad (5.115)$$

$$l_b = r \sin\left[\frac{\pi}{4} + \frac{\phi}{2}\right] - \frac{1}{3}(2a + b) - \frac{t}{\sin\theta} \quad (5.117)$$

Yielding the simplified expression for backfill weight as:

$$\begin{aligned} M_{w_b} &= w_b l_b \\ &= \left[b \sin\left[\frac{\pi}{4} + \frac{\phi}{2}\right] \left(\gamma \tan\theta \left[\frac{1}{2}(a^2 + b^2) - ab \right] + \frac{\gamma t}{\cos\theta} \left[a - b + \frac{t}{2\sin\theta} \right] \right) \right] \rho + \\ &\quad \left(\gamma \tan\theta \left[\frac{1}{2}(a^2 + b^2) - ab \right] + \frac{\gamma t}{\cos\theta} \left[a - b + \frac{t}{2\sin\theta} \right] \right) \left[-\frac{1}{3}(2a + b) - \frac{t}{\sin\theta} \right] \end{aligned} \quad (5.118)$$

Similarly, for the concentrated soil wedge section:

$$w_w = \frac{1}{2} \gamma a^2 \tan\alpha \quad (5.119)$$

$$l_w = r \sin\left[\frac{\pi}{4} + \frac{\phi}{2}\right] - \frac{a}{3} \quad (5.120)$$

Yielding the simplified expression for soils wedge weight as:

$$M_{w_w} = w_w l_w = \left[\frac{1}{2} \gamma a^2 b \tan\alpha \sin\left[\frac{\pi}{4} + \frac{\phi}{2}\right] \right] \rho - \frac{a^3 b \gamma}{6} \tan\alpha \quad (5.121)$$

The Rankine passive earth pressure (R_p) counteracts the radial shear zone region horizontally acting over the vertical section (su) as shown in Figure 5.11. The passive pressure consists of cohesion (R_c) and unit weight (R_γ) components deduced from Rankine Passive Earth pressure theory (Das, 2005) formulated as:

$$\sigma_p = \sigma_v \tan^2\left[\frac{\pi}{4} + \frac{\phi}{2}\right] + 2c \tan\left[\frac{\pi}{4} + \frac{\phi}{2}\right] \quad (5.122)$$

whereas here,

$$R_\gamma = \frac{1}{2} \gamma D^2 \tan^2\left[\frac{\pi}{4} + \frac{\phi}{2}\right] \quad (5.123)$$

$$R_c = 2cD \tan\left[\frac{\pi}{4} + \frac{\phi}{2}\right] \quad (5.124)$$

having respective lever arms,

$$l_\gamma = r \sin\left(\frac{\pi}{4} + \frac{\phi}{2}\right) - \frac{1}{3} D \quad (5.125)$$

$$l_c = r \sin\left(\frac{\pi}{4} + \frac{\phi}{2}\right) - \frac{1}{2} D \quad (5.126)$$

so that when added forms the total passive earth pressure generating the resulting moment (M_{Rp}) about the center of the circle at point (o) as follows:

$$M_{Rp} = R_\gamma l_\gamma + R_c l_c \quad (5.127)$$

$$= Db \tan\psi \left[\frac{1}{2} \gamma D \tan\psi + 2c \right] \rho - D^2 \tan\psi \left[c - \frac{1}{6} \gamma D \tan^3\psi \right] \quad (5.128)$$

$$\begin{aligned} M_{Rp} = & \frac{1}{2} b^3 \tan^2\psi \xi_1 \left[\frac{1}{3} \tan^2\psi \xi_1^2 + \sin\psi \right] \rho^3 + \left[\frac{1}{2} b^2 \tan\psi (\gamma D_w \tan^3\psi - 2c) \xi_1^2 + \right. \\ & \left. b^2 \tan\psi (\gamma D_w \tan\psi \sin\psi + 2c \sin\psi) \xi_1 \right] \rho^2 + \left[\frac{1}{2} b D_w \tan\psi (\gamma D_w \tan^3\psi - 4c) \xi_1 + \right. \\ & \left. 2b D_w \tan\psi \sin\psi \left(\frac{1}{4} \gamma D_w \tan\psi + c \right) \right] \rho + D_w^2 \tan\psi \left(\frac{1}{6} \gamma D_w \tan^3\psi - c \right) \quad (5.129) \end{aligned}$$

The shear stress (τ) acting along the circular rupture surface is the only parameter generating moment (M_F) since the normal stresses (σ_r) acting over the same surface and directed along the radius of the circle are concurrent and therefore do not contribute to the moment developing at the center of the circle (o), thereby producing the following equation:

$$M_F = \int_{-\left(\frac{\pi}{4} + \frac{\phi}{2}\right)}^{\left(\frac{\pi}{4} - \frac{\phi}{2}\right)} r^2 \tau d\psi \quad (5.130)$$

$$M_F = - \frac{r^2 \lambda_2}{2 \tan \phi} \left(e^{-2 \tan \phi \left[\frac{\pi}{4} - \frac{\phi}{2} \right]} - e^{-2 \tan \phi \left[\frac{\pi}{4} + \frac{\phi}{2} \right]} \right) - \frac{r^3 \gamma \sin \phi \sqrt{2}}{1 + 4 \tan^2 \phi} \left(2 \tan \phi \sin \left[\frac{\phi}{2} \right] - \cos \left[\frac{\phi}{2} \right] \right) \quad (5.131)$$

Employing the following eight equations as a function of (ϕ) and substituting back into Equation (5.131) above, the resulting moment (M_F) developing about the center of the circle at point (o) due to shear stress is obtained as the expression of Equation (5.135):

$$\xi_{15} = -2 \tan \phi \quad (5.132)$$

$$\xi_{16} = \frac{1}{\xi_{15}} \left(e^{\xi_{15} \left[\frac{\pi}{4} - \frac{\phi}{2} \right]} - e^{-\xi_{15} \left[\frac{\pi}{4} + \frac{\phi}{2} \right]} \right) \quad (5.133)$$

$$\xi_{17} = - \frac{\sin \phi}{\xi_4} \sqrt{2} \left(2 \tan \phi \sin \left[\frac{\phi}{2} \right] - \cos \left[\frac{\phi}{2} \right] \right) \quad (5.134)$$

$$M_F = r^2 (\lambda_2 \xi_{16} + r \gamma \xi_{17}) \quad (5.135)$$

$$M_F = r^2 \xi_{16} \xi_5 (\gamma D_w \xi_3 + \gamma \rho b \xi_7 + c \xi_1) + r^3 \gamma \xi_{17} \quad (5.136)$$

$$\xi_{18} = \xi_{17} + \xi_5 \xi_7 \xi_{16} \quad (5.137)$$

$$\xi_{19} = \xi_3 \xi_5 \xi_{17} \quad (5.138)$$

$$\xi_{20} = \xi_1 \xi_5 \xi_{17} \quad (5.139)$$

$$M_F = \gamma b^3 \xi_{18} \rho^3 + \gamma b^2 D_w \xi_{19} \rho^2 + c b^2 \xi_{20} \rho^2 \quad (5.140)$$

Considering,
$$+\downarrow \sum F_z = 0$$

yields,

$$T_v = F_{vc} + F_{vp} - c_v \sum_{n=1}^7 w_n \quad (5.141)$$

Static equilibrium of soil prism ($ghjqst$) is maintained in the vertical direction when Equation (5.141) holds true. Consequently, substitution of the following equations and from the fact that $r = \rho b$, the vertical equilibrium equation for (T_v) may be simplified and expressed by Equation (5.146):

$$\xi_{21} = \frac{\pi}{2} - 2\sin\left[\frac{\pi}{4} + \frac{\phi}{2}\right]\cos\left[\frac{\pi}{4} + \frac{\phi}{2}\right] \quad (5.142)$$

$$\xi_{22} = \xi_{13} - \xi_2 \cos\left[\frac{\pi}{4} + \frac{\phi}{2}\right] - \frac{1}{2}\xi_{21} \quad (5.143)$$

$$\xi_{23} = \xi_{12} - \left[\sin\left[\frac{\pi}{4} + \frac{\phi}{2}\right] + \cos\left[\frac{\pi}{4} + \frac{\phi}{2}\right]\right] \quad (5.144)$$

$$\xi_{24} = \xi_2 + \xi_{14} \quad (5.145)$$

$$\begin{aligned} T_v &= \gamma r^2 \xi_{22} + \gamma r D_w \xi_{23} + c r \xi_{24} + \gamma b D_w - \frac{1}{2} \gamma a^2 \tan \alpha \\ &= \gamma \rho^2 b^2 \xi_{22} + \gamma a \tan \alpha \left[b(1 + \rho \xi_{23}) - \frac{1}{2} a \right] + b \left[\gamma D_f (1 + \rho \xi_{23}) + c \rho \xi_{24} \right] \end{aligned} \quad (5.146)$$

$$c_v = c a \tan \alpha \quad (5.147)$$

If we consider equilibrium of the inverted shell footing in the vertical direction with all forces acting on the shell proper as per Figure 5.10, the equation for the ultimate capacity (q_u) may be determined as simplified in Equation (5.149) as follows:

Considering,
$$+\downarrow \sum F_z = 0$$

yields,

$$q_u b = T_v + c_v - w_w \quad (5.148)$$

$$\begin{aligned} &= \gamma \rho^2 b^2 \xi_{22} + \gamma a \tan \alpha \left[b(1 + \rho \xi_{23}) - \frac{1}{2} a \right] + b \left[\gamma D_f (1 + \rho \xi_{23}) + c \rho \xi_{24} \right] \\ &\quad + c a \tan \alpha - \frac{1}{2} \gamma a^2 \tan \alpha \\ q_u &= \gamma b \left[\xi_{22} \rho^2 + \frac{a}{b} \tan \alpha \left(\xi_{23} \rho + \left[\frac{b^2 - a}{b} \right] \right) \right] + \gamma D_f (1 + \xi_{23} \rho) + c (\xi_{24} \rho + \frac{a}{b} \tan \alpha) \quad (5.149) \end{aligned}$$

If the ultimate bearing capacity of Equation (5.149) developed for the inverted shell foundation were to take the form proposed by Terzaghi (1943) as per Equation (5.12), the following bearing capacity factors would be obtained:

$$N_c = \xi_{24} \rho + \frac{a}{b} \tan \alpha \quad (5.150)$$

$$N_q = \xi_{23} \rho + 1 \quad (5.151)$$

$$N_\gamma = \xi_{22} \rho^2 + \frac{a}{b} \tan \alpha \left[\xi_{23} \rho + \left[\frac{b^2 - a}{b} \right] \right] \quad (5.152)$$

The bearing capacity factors developed are a function of the angle of shearing resistance (ϕ), failure angle (α), shell angle (θ), shell width ($B = 2b$), shell column thickness (a). They also depend on the factor (ρ) which in turn is a function of the radius (r) of the circular component of the rupture surface which relies on soil cohesion (c), soil unit weight (γ), and finally the embedment and shell ratio's (ER) and (S_r) respectively.

In order to maintain consistency with the direction of stresses developing along side the proposed slip failure surface the clockwise direction is assigned to be positive in terms of sign convention. Therefore, based on equilibrium at the base of the inverted shell

footing, the moment developing about the center of the circle due to the resultant force (T) is given as:

Considering, $\sum M_T = 0$

yields,

$$M_T = -q_u b \left[r \sin \left(\frac{\pi}{4} + \frac{\phi}{2} \right) - \frac{b}{2} \right] - \frac{1}{2} \gamma a^2 \tan^2 \alpha \left[r \sin \left(\frac{\pi}{4} + \frac{\phi}{2} \right) - \frac{a}{3} \right] + c a r \left[\tan \alpha \sin \left(\frac{\pi}{4} + \frac{\phi}{2} \right) - \cos \left(\frac{\pi}{4} + \frac{\phi}{2} \right) \right] \quad (5.153)$$

Consequently, substituting Equation (5.183) and ($r = \rho b$) into Equation (5.198) yields,

$$M_T = \left[-\gamma b^3 \xi_{22} \sin \left(\frac{\pi}{4} + \frac{\phi}{2} \right) \right] \rho^3 - \left[b^2 \xi_{24} \sin \left(\frac{\pi}{4} + \frac{\phi}{2} \right) (\gamma a \tan \alpha - c) - \frac{1}{2} \gamma b^3 \xi_{22} \right] \rho^2 + \left[\gamma D_f b^2 \sin \left(\frac{\pi}{4} + \frac{\phi}{2} \right) (1 + \xi_{23}) \right] \rho + \left[\frac{1}{2} \left[b^2 \xi_{24} (\gamma a \tan \alpha - c) - \gamma a^2 b \tan^2 \alpha \right] \right] \rho + \left[a b \tan \alpha \sin \left(\frac{\pi}{4} + \frac{\phi}{2} \right) \left[\gamma (a - b^2) + 2c \right] \right] \rho + \left[-c a b \cos \left(\frac{\pi}{4} + \frac{\phi}{2} \right) \right] \rho - \frac{\gamma b^2}{2} \left[D_f (1 + \xi_{23}) + \left[a \tan \alpha \left(b - \frac{a}{b} - \frac{c}{\gamma b} + \frac{a^2}{3b^2} \tan \alpha \right) \right] \right] \quad (5.154)$$

Final substitution of all forces developing within the soil medium satisfying the requirements of moment equilibrium including the summation of M_{WT} , M_{WC} , M_{Wb} , M_{Rp} , M_F and M_T acting about the center of the rupture circle at point (o) produces the final moment (M_o) in a third degree equation of factor (ρ) expressed as:

$$\sum M_o = 0$$

yielding,

$$M_{WT} + M_{WC} + M_{Wb} + M_{Rp} + M_F + M_T = 0 \quad (5.155)$$

5.5 iShell Bearing Capacity Coefficients

Using the coefficient of the bearing capacity for inverted triangular shell footings obtained in the previous section, the tables of the coefficient with respect to the friction angle and shell angle of shell configurations were prepared using the equations developed earlier. Appendix (II) shows the algorithm used in determining values of $(N_c, N_q, N_\gamma)_{iS}$. The values are obtained by a trial and error system built into the program to converge on their values by satisfying equilibrium of the iShell–soil system. Appendix (III) provides bearing capacity factors for inverted shell (iShell) footings. These are critical in design of such footings to evaluate ultimate bearing capacity, and optimize the shell footing design for the soil situation encountered.

The comparison between the program test results and FE results compared with that results obtained using the developed formula are presented in Table 5.2 for flat and inverted triangular shell footings. It can be observed that the results obtained using the developed formula for flat footing and inverted shell footings are correlated well with that results calculated using Terzaghi's formula for shallow footings and the results obtained using FE models for inverted triangular shell.

5.5.1 iShell Depth and Shape Factors

In order to evaluate the ultimate bearing capacity for soil loaded vertically the conventional form of Terzaghi's equation described earlier can be re-written to include the embedment surcharge and shape distinction (Meyerhof, 1963) in a more explicit form as:

$$q_u = cN_cF_{cs}F_{cd} + \gamma D_f N_q F_{qs}F_{qd} + 0.5\gamma B_f N_\gamma F_{\gamma s}F_{\gamma d} \quad (5.156)$$

As a corollary, in consideration of embedded shell footings with the newly proposed soil rupture surface model illustrated in Figure 5.10 from a theoretical perspective, a new ultimate bearing capacity shell equation, $(q_{u,Shell})$ is introduced for cohesionless granular soil as:

$$q_{u,Shell} = q N_{qiS} S_f (F_{qs} F_{qd})_{Shell} + 0.5 \gamma B_f N_{\gamma iS} (F_{\gamma s} F_{\gamma d})_{Shell} \quad (5.157)$$

where,

- $q_{u,Shell}$: ultimate bearing capacity for a shell footing
- q : embedment surcharge
- c : cohesion of soil
- γ : unit weight of soil
- B : width or diameter of footing
- $(N_c, N_q, N_\gamma)_{iS}$: shell bearing capacity coefficients
- S_f : shell factor
- $(F_{cs}, F_{qs}, F_{\gamma s})_{Shell}$: shell shape factors
- $(F_{cd}, F_{qd}, F_{\gamma d})_{Shell}$: shell depth factors

These new shell–shape and shell–depth factors were derived experimentally for the axisymmetrical condition employed in the tests. The shell depth factors obtained experimentally in the lab are presented in Figure 5.13 wherefrom corresponding bearing capacity coefficients $(N_q, N_\gamma)_{iS}$ with $(N_c)_{iS}$ unattributed due to the absence of cohesive component in the system. Consequently, the shape factors $(F_{qs}, F_{\gamma s})_{Shell}$ were calculated from the experimental results under the same axisymmetrical conditions and are presented in Figures 5.13 and 5.14. At last, iShell software employing C–code and algorithm was used to generate design charts based on the angle of shearing resistance of the soil, $\phi(^{\circ})$ and the shell angle $\theta(^{\circ})$ for the embedded case.

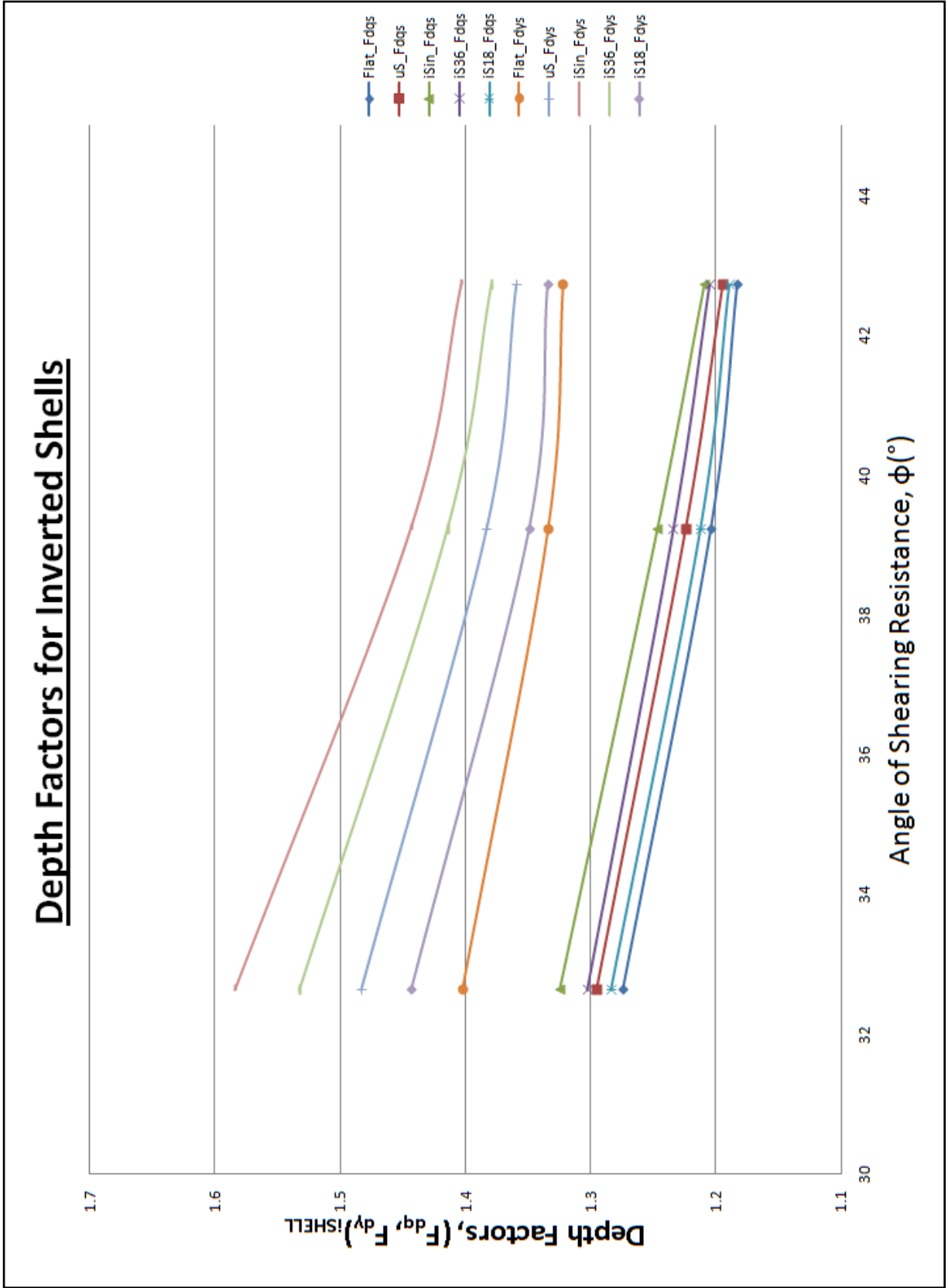


Figure 5.13. iShell Depth Factors (F_{dq} , F_{dy})_{iShell}.

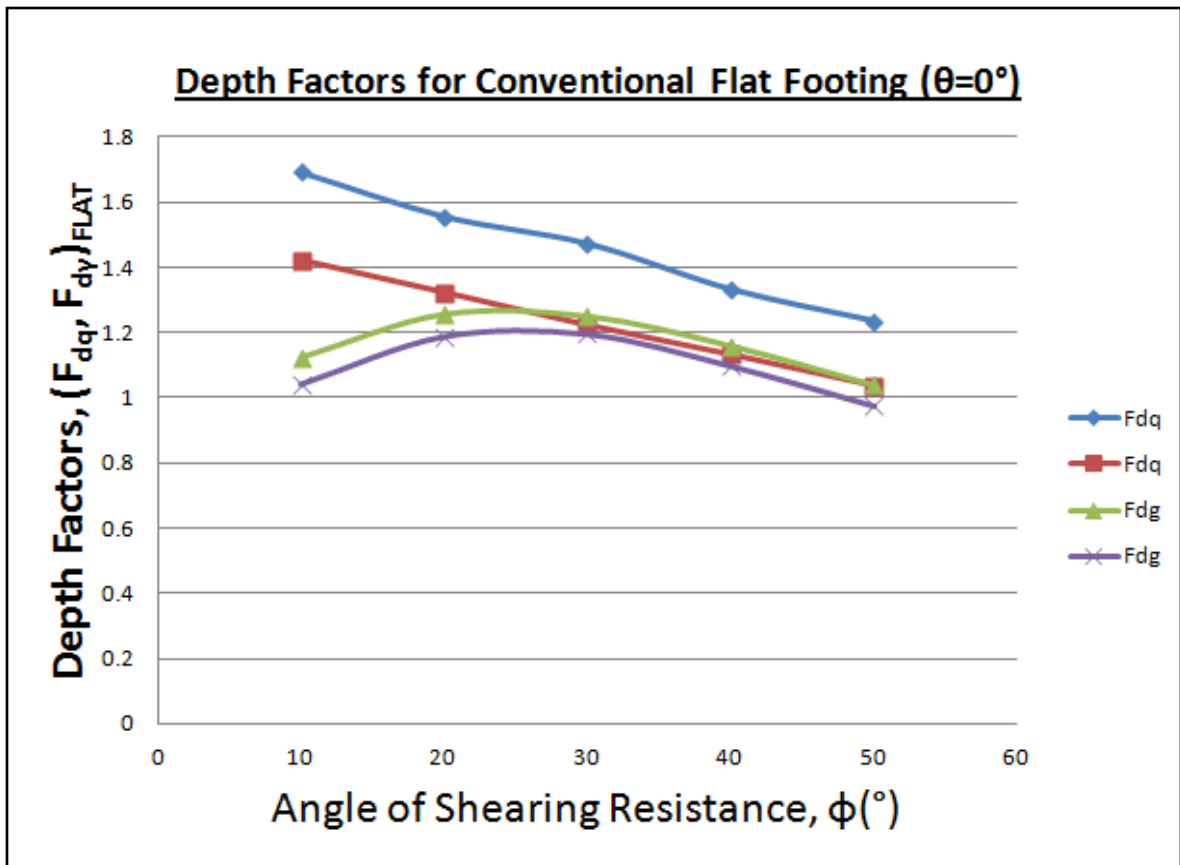


Figure 5.14. Flat Footing Depth Factors (F_{dq} , F_{dy}).

5.6 Concluding Remarks

Theoretical model for the ultimate bearing capacity of inverted triangular shell footing was developed. The derivation of this equations were presented step by step taking into account the most important parameters that affect the geotechnical behaviour of any soil. The coefficients for the ultimate bearing capacity of soil for shell footings (N_c , N_q and N_γ)_{IS} were presented. Application of this equation was presented in detail for variable soil densities and different shell angles. It can be observed that the results obtained using the developed formula for flat footing and inverted shell footings correlate well with those results calculated using Terzaghi's formula for shallow footings and the results obtained using finite element models for inverted triangular shell.

CHAPTER 6

iSHELL INNOVATION

6.1 Introduction

The inverted shell footing foundation concept has an important history in its development in Canada like no other, but this is not where true inspiration for innovation is to be found. It is the belief that an optimum foundation design is a careful combination of its type including shape and configuration for the local soil encountered and material make-up as selected. Employing the use of a shell footing means one is seeking to harness full soil strength potential to achieve maximum bearing capacity and reduce settlement as key to any optimized foundation solution. Bound together by modern concrete and steel material, shell footings help empower the design engineer by providing a reliable option as the latest newcomers in foundation engineering field; the use of shell structural footings as a viable foundation alternative. As well-appreciated, the behaviour of soil at any project location and the interactions of the earth materials during and after construction of the project have a major influence on the success, economy, and safety of the work. Therein, lies the utility and beauty of opting for a structural shell footing.

6.2 iShell Economy

Assessing shell shape and material selection yields two-fold economy: time and money. The immediate economic benefit found is reduced initial cost of construction which falls directly in-line with present times of economic hardship. Scarce public funds and low-risk private investors are always receptively keen to cost-effective solutions that yield maximum output. Secondly, benefits in the reduction of lead-time in schedules to achieve equivalent or improved results is possible. Reduced time of construction means quicker turnaround in interest on initial investment which permits for improved cash flow. Moreover, shells can experience immediate benefit from shape exploration and material engineering research such as composites and Fibre-Reinforced Polymers (FRP) making it a genuine leader in innovation. In principal, as an agent of change and in pursuit of improved performance, shells efficient use of soil with minimal use of material and labor thereby reducing environmental toll makes it an economically feasible solution.

6.3 iShell Construction Methods

Adoption of shells has historically been found to be an attractive economic alternative especially where labor is relatively cheap and materials expensive due to lagging material availability. However, this trend is quickly dissipating as material prices continue to soar on account of the increase in crude oil prices, wage parity, competitiveness and other world economies clashing in a global market. Engineering solutions optimizing use of material such as the shell-option offers means increasingly gravitating towards a conservation mentality affecting all countries and not just the isolated or developing ones. Figure 6.1 below illustrates the economy achievable by opting for shell footing solution.

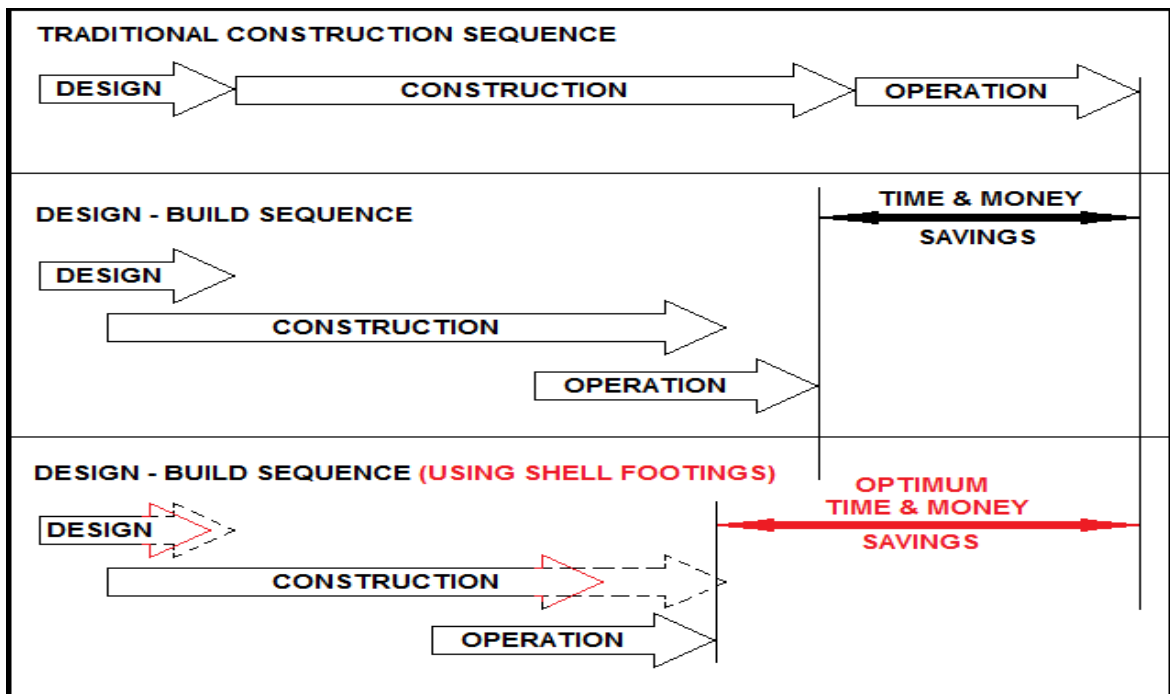


Figure 6.1. Economical Contrast in Opting for Shell Footing Foundations.

The figure shows that savings in the design phase on account of reduced shell size and continuity may help reduce design effort. Main economy, however, is experienced in the construction phase providing possibility for an earlier start in operation of the facility. Opting for shell footings rather than pile foundations to circumvent problematic soil is one example. Heavy pile-driving equipment contributing to green house gas emissions, for example, is conveniently replaced with pre-cast shells to start the superstructure earlier.

6.4 iShell Concrete Mix

The use of innovative composite materials is a serious initiative to help reduce life-cycle costs particularly in the case of new construction and facilitate rehabilitation of our deteriorating civil infrastructure in existence. Incorporating new fibrous materials and modern construction techniques, green designs are developed and negative environmental impacts are contained. The primary research objective here is incorporation and implementation of this advanced technology for the construction and strengthening of shell footing structures. Key elements in support of this endeavour are the use of corrosion-resistant, lightweight fibre reinforced polymers (FRP's) currently making major breakthroughs in mechanical and aeronautical structural applications. FRP utilization is a proven cost-effective state-of-the-art technology in the repair and strengthening of such structures. To exploit the same advantages in foundations, a new concrete mix design proposes to further explore this possibility.

The effectiveness of FRP addition to a cementitious mix generates virtually non-porous concrete which is a major cause of present-day deterioration. This addition allows for reduction in shell structure thickness without compromising strength and overall rigidity. The use of modern concrete would be clearly demonstrated through the following experimental research explored here and would form a basis for full-scale field testing application in the future. Despite their suggested advantages, rehabilitation techniques using FRP's have still seen rather limited application in North America. Reservations exist primarily because of unresolved questions concerning their performance; long-term cost-effectiveness and durability of retrofit techniques in severe winter climatic conditions.

The principal objective of the experimental research program is to optimize FRP material selection for shell footings, and develop an innovative product useful for foundations and other cognate structures. The two focus areas of the research program are structured to accomplish this objective. FRPs are increasingly being used in civil infrastructures in applications ranging from reinforcing rods and tendons to wraps for seismic retrofit of columns. Research conducted has led to many corrosion-free and economical structural components, including concrete decks that can be devoid of tensile

reinforcement. Three generations of hybrid FRP/concretes used in other civil structures such as decks and bridges have been developed using pultrusion (a continuous process of manufacturing of composite material with constant cross section whereby reinforced fibers are pulled through a resin otherwise known as extrusion) and filament-winding techniques that show excellent potential to be used as lightweight, corrosion-free, strong decks for short and medium-span structures, as well as for long-span structures. To date, there is no work done using composite concrete in shell footing applications, let alone test results from such research. Moreover, it is important to consider that tests using ultra-high performance concrete without aggregates nor reinforcement bars has never been undertaken based on the literature review. And so this is the first time an attempt is made to employ such a mix either in the laboratory or in the field in an earth-shell application.

Over the long term, the impact of this research is to promote and advocate us of shell footings even in developed northern climates and not just developing countries as done thus far. The results would have impact on North American infrastructure design and foundation footing construction will undoubtedly have achieved much more substantial technological advances over predecessor footings of the past. The potential savings and economic benefits could be unprecedented. Foundation structures and possibly infrastructure that lasts much longer and requires less maintenance is destined to have a positive impact in our northern economy, by advancing knowledge of new technologies by foundation designers in this specialty sector.

6.4.1 Innovation Incentives

In lieu of present economic privation and advances in material science, the significance of material and labor costing, now more than ever, has been scrutinized and found to be of paramount importance. Design decisions impact the trade workforce, impacting the construction industry, which in turn impact societies and ultimately reflected in our economy's lagging performance. Leading edge technological advances seem to be the plausible first step in development of feasible solutions as structural engineers are repeatedly challenged to "do more with less." In shell foundation engineering, our focus is

drawn to overcoming cost hurdle which in the case of shell footings has high labor intensity element as its main culprit against warranting its use.

To counteract migration of cheap construction labour, domestic solutions must be developed creatively to reverse adoption of foreign alternatives. We are therefore urgently prompted to optimize designs, use innovative thinking, newly engineered materials and lean construction methodologies to remain competitive. This next chapter serves to spur innovation and entice new construction alternatives in shell foundation design over that currently available or which has been previously studied. Loads, loading frequency and load patterns are increasingly on the rise, our development of shell footing solutions must follow in tandem. Vibrations, load reversals and exposure to the ever-evolving climactic conditions are some sensitive issues influencing not just the structure but the state of the bearing soil. The use of composite materials, such as fiber reinforced polymers (FRP), high-density polyethylene (HDPE), have found their place in many structural applications and have evolved recently to address weight distribution and aggressive loading requirement issues. Wind tunnel aerodynamics and flow problems have been addressed, for example, in the aerospace and automotive industries using such composites. The results are lighter structures that can take more load and more importantly costs less to produce simply on merit of lean composite geometry.

6.4.2 iShell Footing Innovation

This study introduces two new innovative alternatives to concrete and even high-strength concretes currently available that have been traditionally used in the past employing resin-based products. The objective is to meet and exceed loading capacities, reduce material quantities, optimize field constructability and drive down the labor element of costs associated with previous shell footings proposed. Suffice to say, based on existing literature, to-date the concept of composites applied to shells is non-existent, much less the use of fibrous material or plastics in combination with footings. The methods that follow outlined techniques which have never been attempted in the past and thus have garnered attention here.

The primary material engineering objectives here are:

- a) To investigate the use of the newly develop shells employing the mix on the geotechnical performance side
- b) To develop an economical and practical concrete mix designed specifically for shell footings
- c) To promote shell footing use as reputable foundations in industry

With today's construction projects becoming more and more complex and costly, a major project cannot succeed or at least remain competitive without proper consideration of project alternatives otherwise known as "opportunity lost." The objectives listed above help serve as an economic alternative over traditional methods. By utilizing novel shape with correct material, a shell's value in savings (S_i) may be measured using the formula:

$$S_i = \frac{\text{shape} + \text{performance} + \text{material quality}}{\text{cost}} \quad (6.1)$$

with the numerator cost functions weighted according to the needs of the particular project.

6.4.3 iShell Mix Design

Part of the economy discussed thus far relates to a proper mix design specially developed here for shell footings. Structural strength of material is maintained to cast the prototypes used in this study. The method follows pre-casting technique employing a highly cementitious blend with very little to no aggregates in the mix into pre-defined formworks developed in house. The blend, referred to here as iShell Mix (iSM) is pumped and vibrated much like traditional concrete but mixed using fiber-like resins as the interlocking mechanism in the matrix. iSM is a proprietary ultra-high performance concrete mix whose physical characteristics far exceed those of traditional concrete used in contemporary structural applications. iSM has high compressive strength and flexural

resistance compared to traditional concretes. It also has high durability, abrasion resistance, and chemical/environmental resistances (e.g. freeze and thaw, salt water, etc.). Due to these enhanced strength properties, iSM can be used in thinner cross-sections and in more varied shell applications than common concrete on account of oftentimes involved geometries. This new mix is almost self-levelling and is best suited for precast elements or in-situ repair and upgrade or maintenance works. The constituents of iSM are cement, fine sand, silica fume and silica flour as a filler, additive and water, using a low water cement ratio and may include high-strength steel fibers or non-metallic fibers.

iSM is a ductile material with aesthetic flexibility element that possesses ultra high compressive strength, high tensile strength and high durability together with high fatigue performance. It also has excellent impact, blast and abrasion resistance. The type and quantities of special materials used in SM result in a superior material that can provide innovative and valuable solutions for a wide range of shell applications. Why would one develop a high-performing shell mix? The reasons are numerous, but perhaps the best premise for its development is doing away with steel reinforcing bars and eliminating traditional aggregates to further reduce shell thickness. In theory, this would translate to reduction in transportation, handling and installation time on account of lighter sections. Furthermore, the materials pliability and shape-ability to almost any imaginable form is now possible. Finally, these characteristics are enhanced without compromising strength; in fact contrary to popular thinking, strength is increased, as this study aims to confirm.

iShell Mix is comparable in strength to powdered concrete composed of high grade Portland cement (1/3 – 3/8 parts), homogenous fine sand (1/3 – 3/8 parts), flyash (1/3 part), silica fume and fiber-reinforced with PVA fibers (1 – 3% by volume), with improved homogeneity. The fine sand replacing traditional coarse-to-fine aggregates have particle sizes in the 100 – 400 μ m (1 – 4 tenths of a millimeter). The outstanding strength-to-weight characteristic means theoretically that it can be sliced thin (up to 10 mm in thickness) and still maintain its integrity.

To develop cost-savings, the mix requires production of extruded plastic shapes into which the iSM batch can be poured. Since aggregates are non-existent, its fluid nature

enables auto-placement and set thereby completing the curved or complex shapes. The idea of producing a thinner, longer, sleeker and ultimately shapelier shell section requires a matrix whereby the steel element is replaced by an equivalent.

Normal concrete for instance offers very little to negligible flexural strength while a shell mix may exhibit significant strength to overcome diagonal shell cracking trajectories as found by previous researchers such as Varghese, (1971). While steel maintains a significant advantage in tensile and flexural strength, the replacement fibers would outperform traditional reinforcing bars by being more apt at fitting the space confinement synonymous with the shell footing forms. This is highly related to the material's ability to bend, within finite limits, without breaking, a property otherwise known as its ductility. Unlike conventional concrete, the Shell Mix will deflect as it reaches its load limit, providing as well, an added margin of safety.

Yet another alternative are reactive powder concretes (RPC), a special type of ultra high strength, superplasticized concrete whose properties are attractive because compressive strengths up to 800 MPa [116 ksi] have been recorded, but more typically in excess of 200 MPa [29 ksi] (Richard and Cheyrezy, 1994); (Baché, 1981); Coppola *et al.* L'Industria Ital Cemento 707 : 112–125 (1996); (Blais and Couture, 1999).

The second method is using Shell Liner Plates (SLP) much like tunnel liner plates or a bin-wall construction for abutments. The plates may be corrugated steel sheets (CSS) or high-density polyethylene (HDPE) material shaped into shell forms for on-site construction. The main attraction and distinction of this method from the first is that of direct and indirect contact. Precast iSM units are much like traditional shell construction in direct contact with the prepared bearing soil. By introducing a liner to the shell, not only is the composite footing concept developed, an immediate 'Active' or direct protection against the earth elements is created. Traditional concrete cover designs of shells account for the lagging 'Passive' protection. High water table introducing high acidity levels, alkali reactivity and geo-weathering are examples of geo-earth aggression. Shell mix being synonymous to a material having high tensile strength, high modulus, high bonding strength like steel, carbon, aramid fibers and fiberglass, PVA fibers have a modulus of

elasticity (resistance to stretching) greater than concrete, making them truly structural fibers. Unlike other structural fibers, PVA is hydrophilic, causing it to form a molecular bond with the matrix during hydration and curing. In summary, we can theorize that the structures longevity, durability and reduced maintenance element of the structure is improved. As a result, enhanced development of soil response beneath the shell footings is achievable.

Composite shells would otherwise be extremely durable, impermeable, corrosion resistant, stain resistant, and so free-flowing and self-leveling that it can be placed without vibration or other forms of consolidation. It is so finely textured it may perfectly replicate any casting surface, even a mirror finish. The iShell mix is conceivably the ideal material for shell foundation footings having huge flow advantage over granular counterpart. Strength is dependant on the type of fibers used, and whether or not a secondary heat treatment is used to further develop compressive strength. The cured concrete has the capability to sustain deformations and resist flexural and tensile stresses, even after initial cracking.

6.4.3.1 Research and Development

iShell Mix® is a fluid concrete that came to reality based on innovation and latest material technology available. The mix is destined for shell footing structures in foundation engineering substructure applications as an alternative to conventional footings. The mix is developed on the principle of cost saving techniques and most beneficial for customized shapes of restricted thicknesses.

So what exactly is iShell Mix? The newest and latest breed of innovation in concreting materials is the fruit of the last past decade in research and development arenas. iShell Mix is a Super Highly Engineered Light Liquid Mix (iSHELL Mix®) which incorporates fiber reinforced polymers in the blend. Moreover, diverging from typical mixes, iShell Mix contains absolutely no aggregates and depends on reactive powders in forming its matrix. The name iShell Mix reflects a highly ductile material of unique and improved behavioural performance over that of conventional mixes.

6.4.3.2 Batch Composition

iShell Mix is a compound ultra-high strength product stemming from similar liquefied super-concretes developed in recent years such as reactive powder concrete (RPC), ultra-high performance fiber-reinforced concrete (UHPC or UHPFRC) and SuperCrete (SC) developed to meet restrictive demands of high-strength structures. Therefore, this blend has been found apt at fulfilling the requirements for shell footings representing confined, restrictive spaces. It is made up of commonly available ingredients found in concrete, namely, cement, silica, quartz powder, fine sands, Wollastonite fibers, superplasticizers and water.

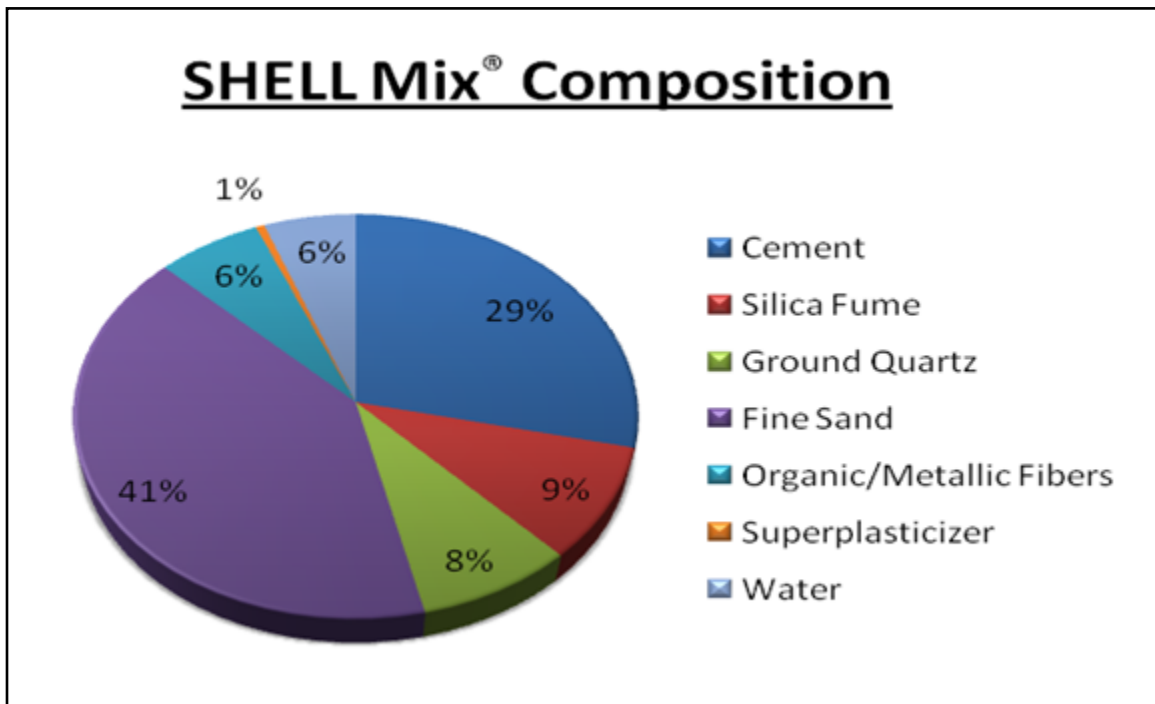


Figure 6.2. iShell Mix Constituents Composition.

A highly blended general use Portland Cement composed primarily of hydraulic calcium silicates is the type used in the iShell Mix design. Much like typical cements it forms a binder paste with water to hold together the fine granular material.

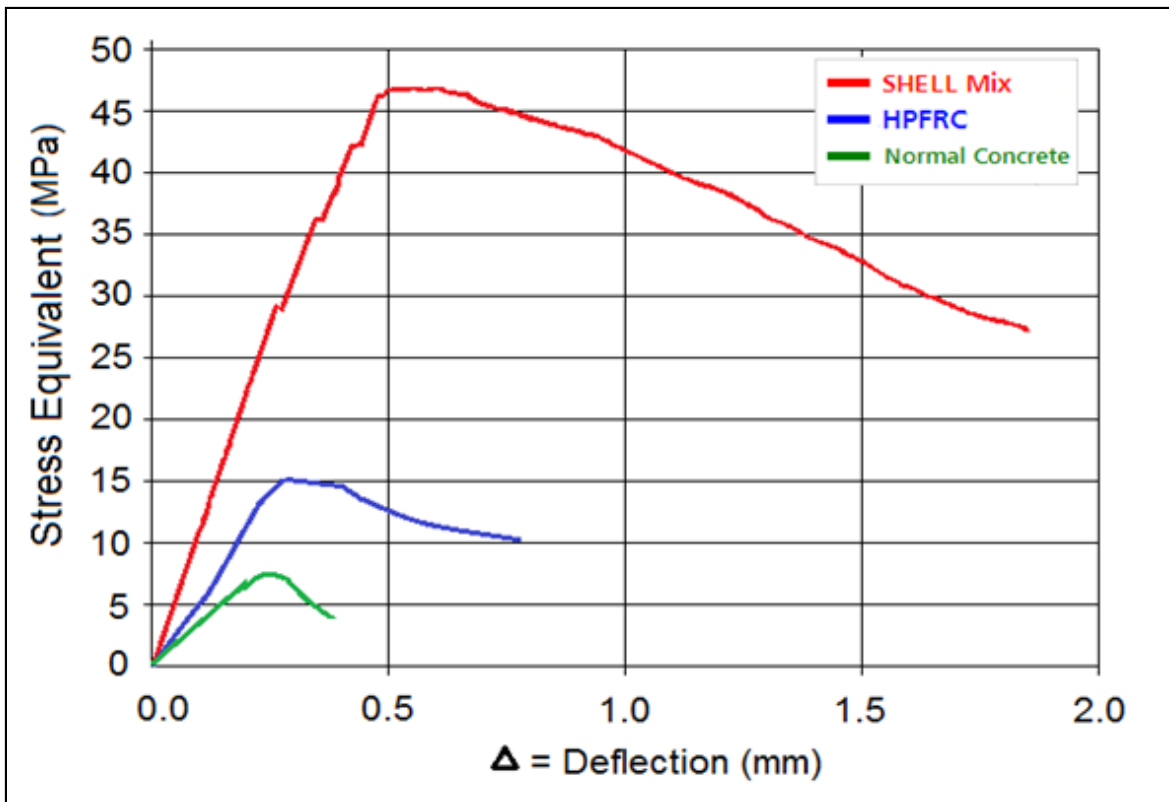


Figure 6.3. Load–Deflection Curve for Various Concrete Mixes.

6.4.3.3 Increase of Dry–Compact Density

Increasing the dry–compact density of the solids will reduce water content in a concrete mix. In traditional concretes for example, an increase in the dry compacted density is achieved by using superplasticizers and silica fume. An increase of dry compact density of up to 6% can be attained by applying a post–mould pressure during the setting period (Richard & Cheyrezy, 1994). This pressure acts to remove entrapped air and expel excess water. It also partially compensates for chemical shrinkage during the first few hours of setting by inducing micro–cracks in the sample.

As one can denote from Figure 6.4 below, the main problem with traditional type mixes is the abrupt haphazard arrangement of the mixes’ fines leaves very little room for effective arrangement of the conglomerating fibers whose main function is to offer the much needed bonding and tensile strength. By optimizing the design parameters one makes available much needed space for increased amounts of fiber reinforcements such as

PVA's to react with themselves as well as encompassing cementitious mix ingredients. We hypothesize therefore, an increased contact surface area of the fibers results in direct correlation to an increase in strengthening of the concrete a significant trademark and milestone of the iShell Mix design.

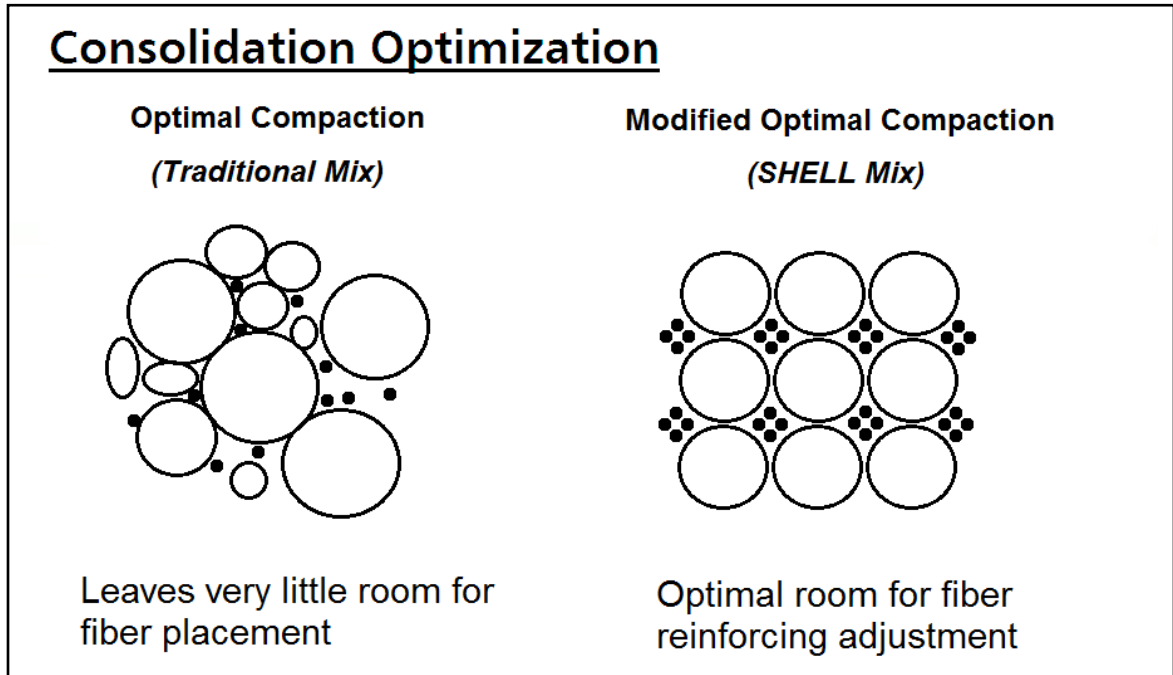


Figure 6.4. Matrix Consolidation Optimization Strategy.

6.4.3.4 Microstructure Improvement

Silica fume encourages pozzolanic reactions within the cement past. These pozzolanic reactions are activated by temperature. Richard and Cheyrezy (1994) observed a 30% resistance gain by curing 90°C for two days while decreasing the size of pores. They also found that, when using ground quartz, a higher curing temperature of 250 – 400°C results in transformation of amorphous cement hydration products to crystalline products resulting in dehydration and significant decrease in weight.

The following figure shows an enlarged view of micro-cracks within the hardened concrete after load is applied. It is worthwhile to mention the consistency is made up of lean material with little to no air pockets, although nearly impossible to completely eliminate, there may still be very limited quantities of pore inclusions. The tendency would

then be for cracking pattern to develop as to link the pores under loading of the concrete element. Here, then, the important behavioural response of the fibers comes into play.

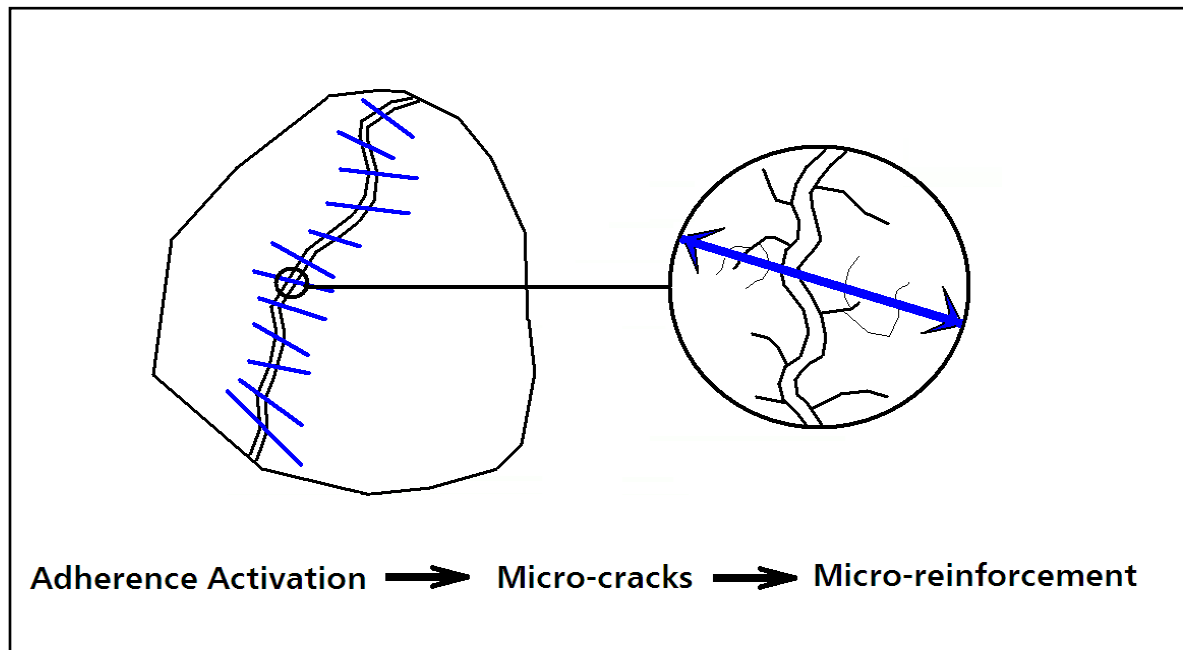


Figure 6.5. Micro-Crack Reinforcement Behaviour.

The continuous fiber strains across any possible aperture, as shown above in Figure 6.5, is depicted as stitching across two faces of the matrix ensuing strength. This is an important offensive mechanism, as it tends to elongate in a manner as if to mend the adjacent fascias together maintaining bond strength otherwise explained as a self-repair or auto-healing process. The resulting micro-reinforcement achieved by interlocking of the fibers creates the interwoven structural mesh regarded as the structural steel reinforcement bars counterparts.

6.4.4 iShell Mix Characteristics

An increase in temperatures of high-performing concrete mix such as iShell Mix is due to the exothermic reaction of Portland cement hydration. This increase within the concrete structural element depends on geometrical and thermodynamic factors, such as its shape and size, the ambient temperature and the heat exchange rate through the forms and the top surface, which depends on the ambient temperature (Schaller *et al.*, 1992; Lachemi,

Lessard and Aïtcin, 1996). The literature is clear about concerns with high temperature gradients for particularly high–cemenet content batches for thick massive structures such as gravity damns or massive piers. Costly solutions for treatment include liquid nitrogen cooling or use of crushed ice replacing the same water mass within the mix with the former being most expensive. Where either of these options are simply unavailable, use of a retarder may be an alternative. Nonetheless, given the inherent nature of shells being typically thin–slabbed, these problems are clearly unapplicable and at best negligible. An important correlation is drawn from the preceding in adopting the shell option as a foundation solution. This advantage coupled with other noble characteristics of iShell Mix high–performance concrete has to offer as enlisted herein below makes it a worthwhile contender:

- High Strength: Similar strength to steel yet weighs about 60% less
- Chemical Resistance: When treated with appropriate resins, composites with outstanding resistance to chemicals can be developed. The glass fiber resists attack from most chemicals
- Compatibility: Accepts different types of sizes enabling it to be compatible with many synthetic resins as well as mineral matrices like cement, plaster, etc.
- Workability: Requires less water exhibiting positive consolidation
- Durability: Does not degrade, or deteriorates as insects or rodents cannot attack them
- Fatigue Life: Exhibits very good fatigue properties and can undergo very long cyclic loads without fatigue
- Incombustible: Being a mineral material is neither combustible nor supports combustion (when exposed to heat, it neither emits smoke nor toxic gases)
- Inherent resistance to microbiological attack, corrosion and erosion
- Acceptable cost level
- Lightweight: Enables pre–casting capability into single parts of a complete shape or single complex dimensional shape as distinct advantages

As a direct result of these important characteristics, listed below are some of the beneficial milestones now attainable with the development of this new iShell Mix designed specifically for shell footing foundations which is discussed in the subsequent sections :

- Homogeneity improvement
- Dimensional stability (high strength)
- Absence of capillary pores promoting an optimal material
- Impermeability to water and gas (unconnected trace pores)
- Resistance to carbon dioxide CO₂, Chlorides and other aggressive soil agents
- Resistance to freeze/thaw cycling and deicing salts
- Auto-repair of any micro-crack development increasing bond strength
- Absence of adverse alkali reactions (longer life in severe environments)
- Corrosion and acidity resistance (resistance to chemical attack)
- Improved resistance to fire, radiation and radioactive ion diffusions
- Improved impact resistance
- Volume Stability (compaction without segregation)

6.4.4.1 Homogeneity Improvement

iShell Mix relies on the homogeneous nature of its “aggregates” to enhance its physical properties. Common aggregates and traditional sands found in heterogeneous cement mixes are virtually eliminated and replaced with finely ground quartz. Large aggregates form a rigid skeleton and prevent global shrinkage while smaller aggregates can move relative to the paste decreasing the voids present in the end product. The Young’s modulus of the cement paste is also increased in the mix with values ranging from 55 to 75 GPa. This eliminates modulus variance between the quartz and the surrounding paste (Richard & Cheyrezy, 1994) and easily conveys the transfer of mechanical properties between the two mediums.

6.4.4.2 Dimensional Stability

Drying shrinkage and creep in concrete structures have been given a great deal of attention throughout the literature. The basic principle is to quantify the long-term deformation and behaviour of the concrete once it cures. This affects not only the overall geometry of the shape but induces new internal stresses in the footings. Drying shrinkage may be defined as volume reduction suffered by concrete as a result of moisture migration when exposed to lower relative humidity environment than the initial one in its own pore system. For forming and workability purposes of the iShell Mix in consolidating the concrete, the amount of water added to the mixture is slightly higher than that strictly needed for normal hydration of the concrete. As a result, when curing is complete the added water coupled with the resulting relative humidity gradient develops moisture migration out of the footings. The advantage iShell Mix offers is that this phenomenon is greatly reduced if not virtually eliminated since almost no volume reduction is allowed having a non-porous concrete. Accordingly, in much the same way, swelling occurs when the opposite happens. That is, a volume increase is experienced from increase in moisture content due to absorption of the water. This is also limited by the composition of the mix.

Creep is the time-dependant strain that occurs due to imposed and constant stresses over time. Its counterpart mechanism is referred to relaxation which is the time-dependant reduction of the stress due to a constantly maintained deformation level over time. It is worthwhile to mention that other delayed strains in uncured concrete may be experienced such as thermal, plastic and autogenous shrinkage of primarily early volume change during hydration.

The following is a summary of the delayed strains in concrete and more specifically, the time-dependant deformations due to drying and creep phenomena in cementitious material such as the iShell Mix developed.

6.4.4.3 Heat Treatment

The effects of heat treatment, essential to the formation of the high strengths seen in iShell mix concrete are briefly discussed. As identified herein after, the benefits of such treatment are:

- Faster strength evolution
- Zero long-term shrinkage and significantly less creep
- Considerably improved durability

In quantitative terms the first point negates the need for a 28 day compression test before use. As a result, a structural element may be ready for installation in as little as three to four days from time of pouring. In addition, both compressive and tensile strengths are typically 10% higher than the 28-day strength with storage and exposure to water. For the second point, the creep coefficient may be reduced by as much as 75% from 0.8 down to 0.2. Lastly, heat treatment causes a reduction in the void ratio, which in durability terms means a higher radiation, contamination and chemical penetration resistance.

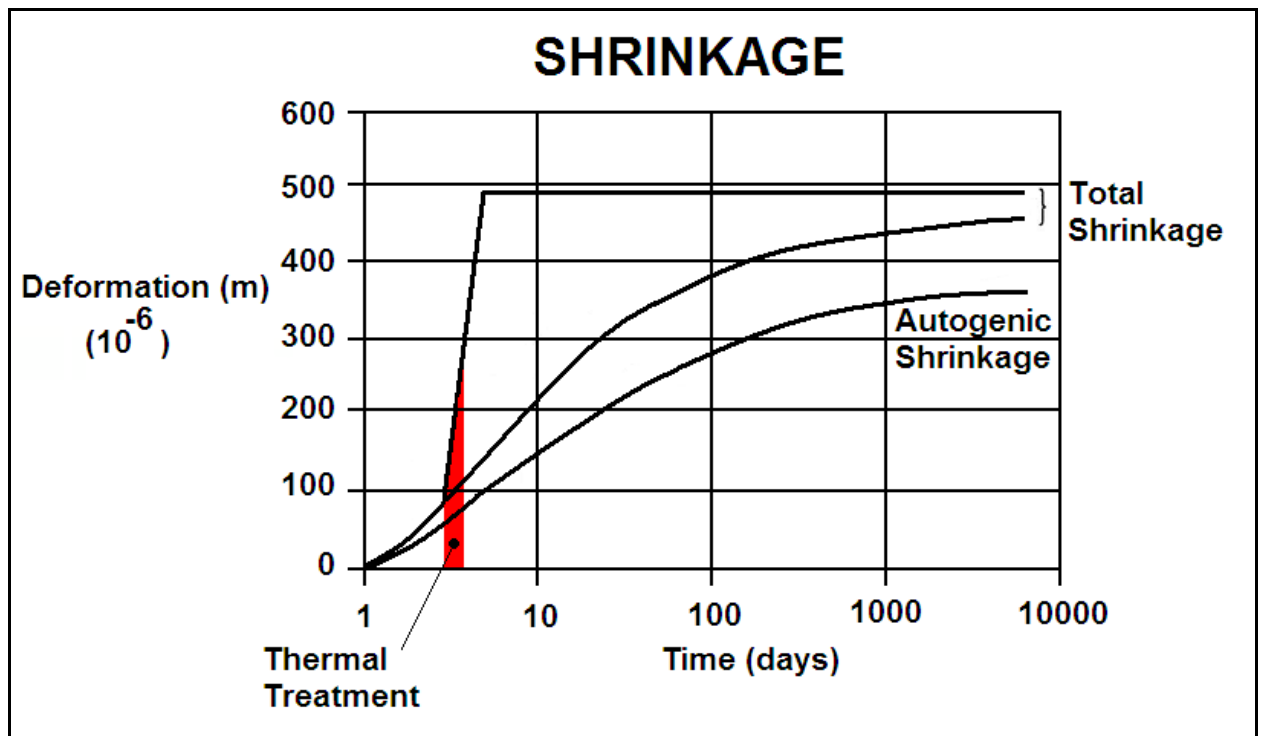


Figure 6.6. Shrinkage of iShell Mix Concrete.

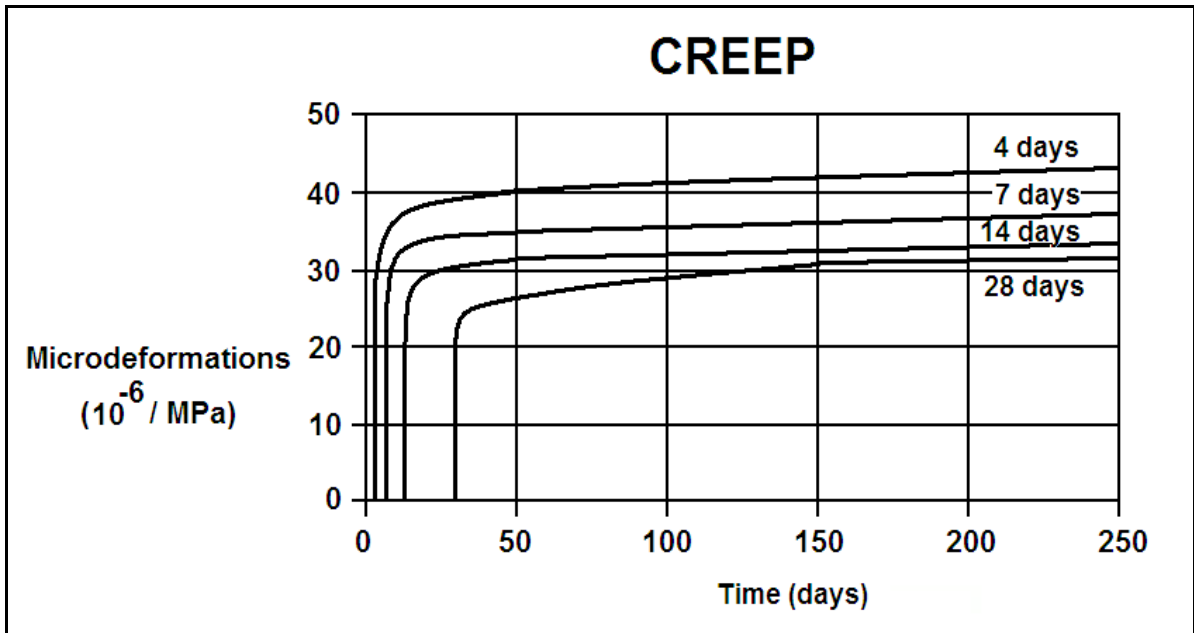


Figure 6.7. Creep of iShell Mix Concrete.

6.4.4.4 Capillary Porosity

Porosity is basically attributed to several factors and tends to decrease generally over time during the curing process. The curing process itself, w/c ratio and the environment in which it is exposed are major factors in determining the capillary porosity of a concrete. Aside from larger voids capillary, cement paste contains pores within the solid hydrates and is dependant upon the w/c ratio and the rate of hydration. Microcracking often related to shrinkage while capillary porosity is an internal material characteristic. The following graph shows the comparative distribution of the sizes of pores for normal, high-performance and iShell Mix concretes.

A closer look at concretes microstructure, one is able to cipher the difference between traditional concrete mixes used in the past and the newly proposed mix. The product of hydration is such that porosity has been significantly reduced from as high as 25% interconnected capillary porosity to as little as 2% virtually eliminating potential for nodal cracking. The result therefore is a deviation from porous concrete to non-porous concrete.

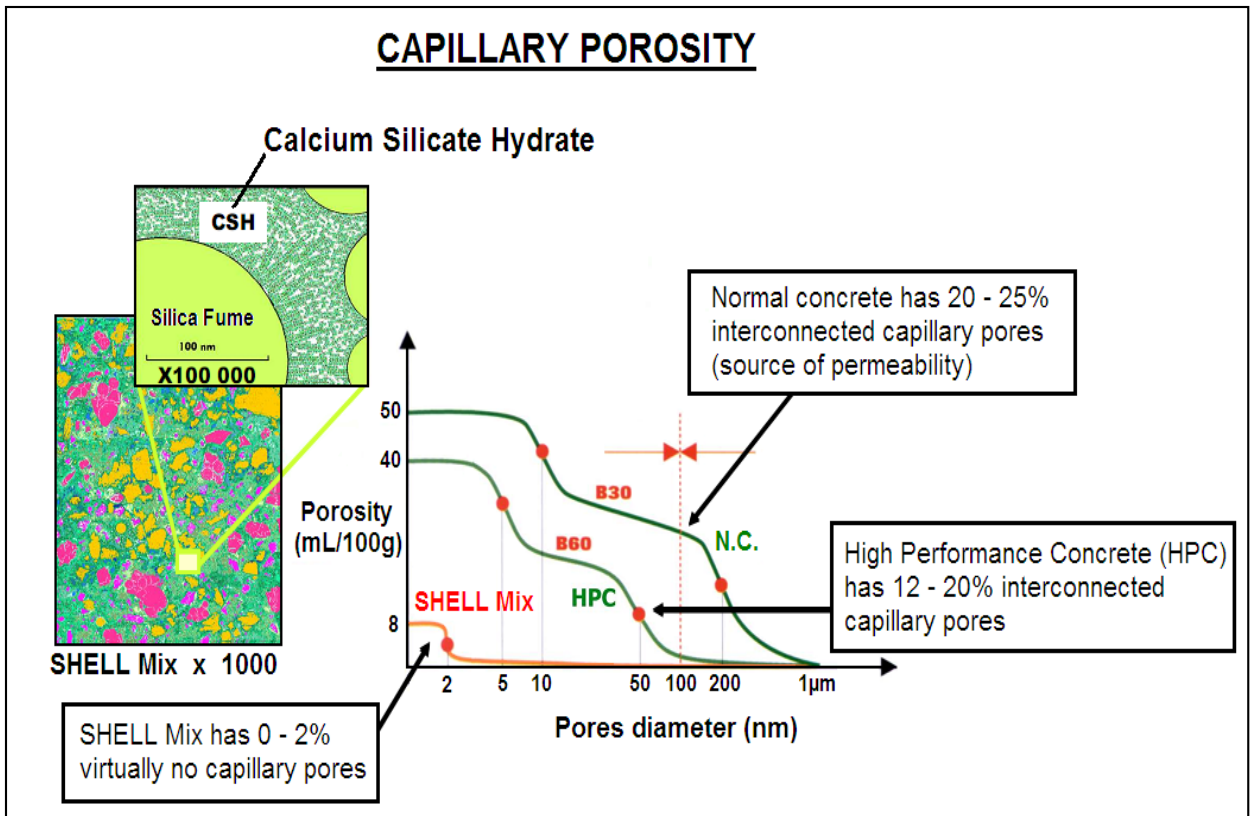


Figure 6.8. Capillary Porosity of iShell Mix Concrete.

Impermeability

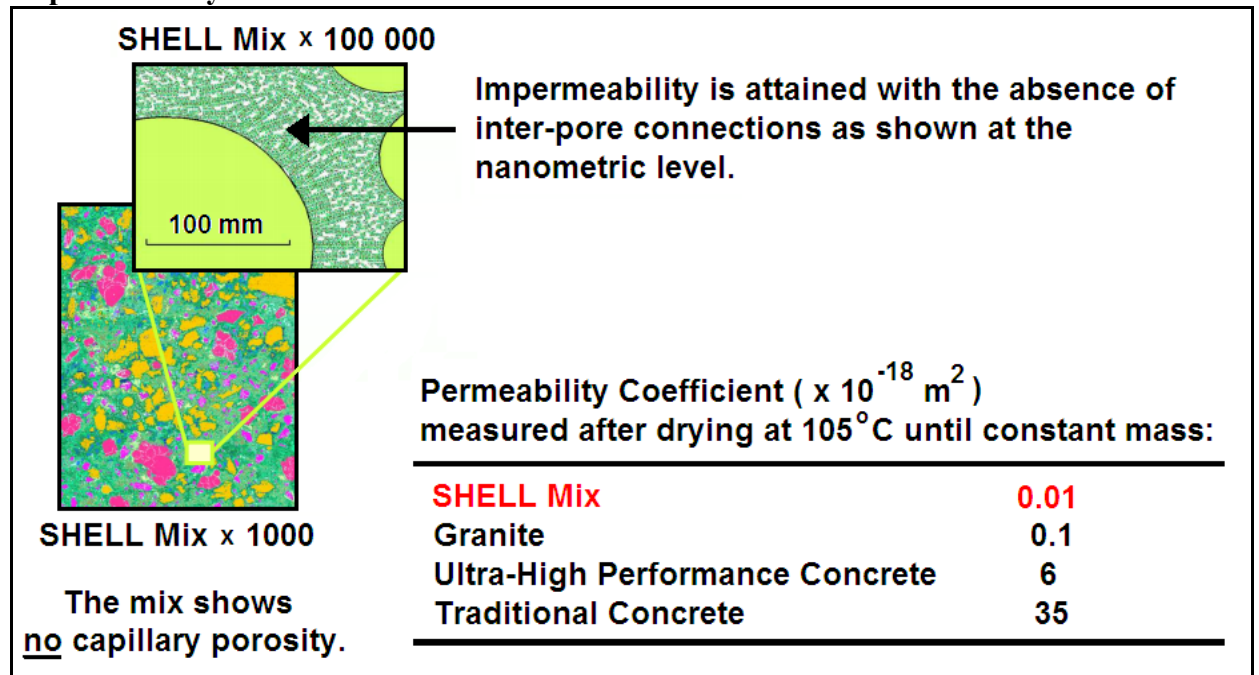


Figure 6.9. iShell Mix Permeability.

6.4.4.5 Acid, Fire and Corrosion Resistance

iShell Mix concrete is capable of resisting highly aggressive soil environments where ordinary concretes may have been severely damaged by deterioration. Samples of the iShell Mix batch have been exposed to different aggressive elements (calcium sulfate, sodium sulfate, acetic acid, ammonium sulfate, nitrates, salt and distilled water). The results indicate great resistance to penetration and attack.

Much like other ultra-high performance mixes, iShell Mix has admirable fire resistance characteristics. First, being deprived of reinforcement bars working in tension, fire and more importantly heat propagation is contained by increasing fire penetration times. The metal fibers ensure high strength even at high temperature. This increases exposure time allowed without jeopardizing the structural integrity of the element. Second, the fire-retardant rating is much higher on account of its high density and low porosity traits. As a result, this formula is not susceptible to spalling and so a calculation-based approach may be adopted.

High-strength concrete is specified where reduced weight is an important factor or where architectural considerations call for support elements of minimal thickness. Carrying loads more efficiently than normal-strength concrete, high-strength concrete also reduces the total amount of material placed and lowers the overall cost of the structure. Further to this, the iShell Mix is developed not only reduce amount of material, but to come up with a carefully optimized batch that would allow auto-placement in confined spaces without compromising strength, durability and integrity.

6.5 Concluding Remarks

Project managers and engineers require innovation in various areas of construction to save time and money for their clients. Considerable savings may be ascertained early on in the design phase as far as foundation selection is concerned. The option of using a shell footing was developed to make available a novel alternative that is both innovative and economical. The iShell Mix concrete design presented, for instance, is an option for optimum use of fibrous additives for the concrete material resting on soil of limited bearing capacity. Shells are proponents in innovation as contemporary solutions where in some cases using conventional methods is costly, burdensome and simply impractical to build. Replacing a conventional deep foundation for a shallow one employing shell footings, for example, in isolated or raft forms may be used to circumvent problematic soil situations and to accomplish the foundation construction cost-effectively. The admirable contributions shells offer is motivation to further investigate their proprietary traits as the topic is a distinguished one and steadily growing throughout the world.

CHAPTER 7

CONCLUSIONS & RECOMMENDATIONS

7.1 Summary

Shell footings have been employed effectively in different parts of the world because of their admirable performance and cost effectiveness. Their structural capacity is manifested by sustainment of direct membrane stresses from applied loads owing to their streamlined form. The geometry of shell foundation footings plays a major role in increasing the ultimate carrying capacity of bearing soil generated by the shell footings. The usage of inverted strip shell footing for problematic soil environments is therefore a plausible alternative to conventional or even upright shell footings. The objectives of this study were to investigate the geotechnical behaviour of the inverted triangular strip model as compared to upright and similar conventional models used previously. The data obtained in this study supports the merits of the iShell as having admirable geotechnical performance by making efficient use of bearing soils strength based on shape. This translates to improved material cost efficiency and thereby resulting in a most efficient foundation design. Inverted shell footings are therefore decisively most economical where labor costs are low and construction materials are expensive. Assurance and reliability offered from newly developed concrete mix investigated offers a maximum strength option for the iShells developed contributing to geometrical optimization and consequently added economic benefit.

Theoretical, numerical and experimental investigations have been carried out in this present investigation to study the impact of several parameters. Shell thickness, shell angle and soil's angle of internal friction were key parameters used to determine the impact on the geotechnical behaviour, namely, load carrying capacity and settlement. The behaviour of the Sinusoidal shell model has also been investigated as the latest shape to study its soil-structure interaction under static vertical and monotonic load. The Sinusoidal shell has outperformed both the inverted and the upright shells investigated. The inverted strip shells following plan-strain conditions have been found to be the most economical shell over the upright forms and more so over the flat plain foundation. Upon thorough investigation, this was concluded on the basis of producing the most uniform contact

pressure distribution curve at depth making effective use of soil by producing a more uniform stress distribution curve. Moreover, a higher load bearing capacity and reduced settlement have been obtained for the inverted shell model iShell36°. On the merit of improved soil response from iShell footings, these three-dimensional structures as foundations have proven to sustain applied loads and perform admirably in variable soil conditions particularly for those with higher shell angles.

7.1.1 Geotechnical Behaviour of iShell Footings

The inverted shell footing versus its upright counterpart has been studied from a geotechnical performance point of view. The observed soil–structure interaction examined by load–settlement measurements and stress–load distributions across the bearing soil strata have shown reasonable results in good agreement through parallel forms of study. From the numerical output, based on finite element analysis, the vertical static load as applied to the end beams under monotonic uniform loading revealed a 20% improvement in settlement reduction and a 25% increase in bearing capacity as compared to upright shells.

The applicability of the adopted FE model was first validated using the model test data presented in Chapter 3. In the parametric study, the shell thickness was alternated between 19 mm [3/4 in.] and 25 mm [1 in.] for various shell angles including 18, 27 and 36 degrees to observe its behaviour. The influence of shell thickness and shell angle on the load carrying capacity of the inverted shells revealed that the Sinusoidal model performs best followed by the inverted shell Model iS#6 having shell angle $\theta = 27^\circ$, representing a 3% and 8% advantage over the iS#4 & iS#5 models respectively. Overall, a 3 – 5% increase in bearing capacity over the upright shell model was found. In order to fully appreciate the results, full–scale field tests may be conducted on the optimum shapes with models of similitude respecting size, dimensional metrics and material parameters. This would further validate the model tests conducted in this present investigation.

The influence of soil properties was investigated to study the effects of the elasticity modulus on the behaviour of the shell footings. The influence of shell thickness has shown approximately 13% increase in load carrying capacity of the shells by varying the thickness

from 19 mm to 25 mm. Adding edge beam in shell footings for the upright shells was found to cause stress concentrations at their ends. The Sinusoidal model showed improved performance likely due to the toe edge beam presence. Investigation of this effect of stress distribution in the shell footings in the presence of edge beams has been carried out. For this purpose, edge beam addition to the shell footings may be investigated further to elaborate and confirm its effectiveness at variable locations subjected to similar loads. Stress distribution below the shell footings at various distances from the center of the shell has been obtained to check stress uniformity. Intuitively, increasing embedment ratio (D/b) will tend to increase the shell's bearing capacity as stronger layered soil is generally present at depth. Embedment depth of shell over one-half shell rise for the footings were considered as being limited between 0.52 and 0.83 and given the confined range, this parameter was thought to have only mild influence on stress distributions.

The soil–structure interaction of 2D shell foundations following plane–strain conditions was investigated. The applicability of the finite element model was first elaborated using available data. It was further validated with experimental model test data from the experimental phase. The resulting model was then used to test the behaviour of 2D shell footing models analytically. The results of the findings indicate that the upright shell model with shell angle of 34° exhibited higher stress concentrations at the edge of the shell whereas the inverted shells demonstrated better stress distribution over the shell contact surface. The rupture surface obtained from the 2D finite element for inverted strip shell footing was employed in the theoretical analysis. The rupture surfaces comprise of a circular and plain surface, and provide kinematical and statically admissible solution. Kotter's differential equations were effectively employed to simulate the shear stress distributions along the circular as well as plane parts of the rupture surface. The shell ratio (S_r) was proposed and incorporated in the analysis to take into account the effect of shell configuration on the failure mechanism and accordingly, the ultimate bearing capacity. Finally, a new ultimate bearing capacity equation ($q_{u,Shell}$) was introduced with the newly developed iShell bearing capacity factors to be implemented therein.

7.2 Conclusion

From the theoretical, numerical and experimental results obtained in this study, the following conclusions can be drawn about the geotechnical behaviour of the newly adopted inverted shell (iShell) footings:

1. The proposed FE models simulated the behaviour of shell footings with acceptable accuracy found to be in good agreement with experimental results. Preliminary FE analysis showed iShell footings had higher bearing capacity than upright models.
2. The load carrying capacity of the inverted shell was found to increase with increase in shell angle and shell thickness. From the parametric study, an optimum cross-section for inverted shell footings was identified and used in the experimental investigation. As well, an increase in shell thickness showed tendency to improve shell load-carrying capacity. Intuitively, a limiting thickness should be considered beyond which the shell concept would be undermined.
3. An ultra-high strength concrete was developed expressly for shell footings using latest fiber-reinforcements available for use in the experimental test phase. The mix developed showed admirable performance in both compression and flexural tests. A 40% increase over conventional high performance concrete was obtained. Applicability to shell footings showed admirable performance as no aggregates and no steel reinforcements are required maintaining rigidity and high performance similar to metallic prototypes.
4. Experimental results showed that triangular shell footing exhibited higher stress concentration in the edge beams, however, for inverted triangular shell, stress was better distributed over the shell its in which no stress concentration was observed.
5. The inverted triangular shell footing model load carrying capacity based on load-settlement results was found to be 15% and 28% higher than the upright shell and conventional flat footing specimens respectively.

6. The developing contact pressure distribution behaved in a linear fashion as a function of the applied load. Maximum pressure was observed towards the ends for flat footing, which inverted shells showed a more uniform distribution with maximum values having tendency towards the central regions of the shell.
7. Using layered sand, a distinguishable rupture surface was visualized to validate that proposed in the theoretical study. The rupture surfaces have shown to go deeper with increasing both shell angle and shell thickness in the parametric study. This translates to an increase in the ultimate load carrying capacity of the inverted shell model.
8. Using Mohr–Coulomb’s failure criterion on an elastic perfectly plastic soil model generated good representation of the behaviour of soil–structure interaction in a cohesionless soil as confirmed by the experimental study.
9. The results generated from the numerical, theoretical and experimental models were compared, presented and proved to be in overall agreement with one another.
10. An interactive shell modeling algorithm called ‘iShell’ was programmed to predict the ultimate bearing capacity based on the theoretical findings for inverted shell footings.
11. The results confirm admirable performance of shells based not only on geometry alone, but coupled with modern composite concretes employing fiber–reinforcements makes optimal and efficient use of the shell concept. Inverted shell footings utilizing high–performance concretes should be widely considered as serious contenders as shallow shell footing foundations.
12. This study led to the conclusion that for a rise–to–base ratio greater than 0.5 for the shells, which is typically normal values used in the field, an increase in shell thickness does not substantially increase the stiffness of the entire footing or postpone the onset of concrete cracking.

7.3 Recommendations for Further Research

Conceiving of the proper methodology to approach further shell footing studies should be well-scrutinized beforehand. Many challenges arise as experienced in this present study. Micro-concrete modeling, for example, as initially considered with required mould preparation can take significantly more time than anticipated. Wood moulds require shop-drawings and construction. The micro-concrete would require 28 days minimum for attaining 95% of concrete strength, f_c' and for concrete curing. Concerns about aggregate size and keeping material proportions in check can be a limiting task for shell conception. Problems of creep and shrinkage are ever-present due to time constraints. The cage reinforcement also requires special attention in terms of position and cover which in itself can be a restraining factor in ones scaled design. Moreover, material test specimens for the concrete and steel must be developed in order to control material quality in testing. This is main reasoning behind alternative developments of shell model from which iShell Mix concrete was borne. Primarily, in overcoming such obstacles while maintaining the high level of rigidity required for this research. Finally, the inability to retest a model after loading has its drawbacks. While cracking and failure patterns are interesting to see, their investigation is beyond the scope of this present study. The combination of all these factors would greatly delay the experimental testing phase and have therefore been left for future field studies.

One should realize that in the final analysis, what remains true is the fact that the physical behaviour of the structure is unique, and that we are actually trying to interpret and understand the same by analytical tools at various levels of sophistication. Thus membrane and contact pressure theories themselves are two theoretical approaches to understand the same physical phenomenon exhibited by the prototype shell models. The physical approach as a tool, however, lacks the philosophical drive and abstraction of the analytical approach. Continued study of shell footings as admirable foundation performers has great merit. Influence of shape defining contact surface areas generating more data on the bearing capacity, settlement and load distribution on the soil justifies a need and warrants considerable study to validate such criteria for rational shell footing design.

As shell shapes and concrete materials evolve, experimental investigations will prove to become increasingly less attractive as time and cost constraints associated with their development are significant factors to consider. Deviation from laboratorial studies will undoubtedly be replaced by more sophisticated numerical studies as processing power of computers have already well surpassed even the most rigorous closed–formed analytical solutions available. However, it is safe to say that experimental work would be most effective when used in validating a particular behavioural aspect, be it regarding the structural shell or the soil continuum on which it rests. Field–testing using full–scale models is one example of further developing the experimental investigation for inverted shell performance. Experiencing questionable results in a preliminary numerical study, for example, may be reason to introduce an experimental study to validate an unknown or dubious result. Despite challenges arising from similitude such as material and/or geometrical aspects, experimental investigations remain a primitive source of critical information and raw data. Moreover, gross errors associated with scaling effects, boundary conditions and the human factor are ever–present. Whether experimental, theoretical or numerical research approach is pursued, the methodology and results shed light on the subject and should be complementary. In spearheading the advancement of knowledge for shell foundations and to advocate their design implementation in industry, the following topics of investigation are recommended for future study:

1. Shell foundation behaviour under lateral load to simulate wind and/or seismic load conditions. The design of tall slender structures having thin–shell foundation supports often require a lateral load analysis such as silos, tanks and chimney stacks, for example due to wind and/or seismic effects. Possible lateral–load factors modifying the bearing capacity and settlement equations may be introduced representing non–axisymmetric loading cases for shell footings for their adoption in earthquake and/or high–wind prone zones.
2. Numerical investigation on shell footings using finite–difference software versus existing FEM investigations in a comparative study. An advanced geotechnical software package such as FLAC3D may be utilized in an explicit finite difference formulation that may model complex behaviours not readily suited to FEM codes

such as: problems that consist of several stages, large displacements and strains, non-linear material behaviour and unstable systems; even cases of yield/failure over large areas, or total collapse.

3. Conduct field-testing of shell foundation models under variable loading conditions. To further validate theoretical and numerical models presented, development of experimental prototype models of similar shapes may be tested outdoors to better simulate field-like conditions. A full-scale model test respecting properties of similitude would provide supportive insight in the behaviour of inverted or newly proposed shell configurations.
4. Develop factors of safety for sliding, overturning and bearing capacity of shell foundation footings used beneath retaining wall structures. A study of the three types of lateral earth pressures including at rest, active and passive pressures applied to a shell supported retaining wall may be undertaken describing how each may be calculated. The total force resulting from lateral earth pressure may be investigated and how these forces may be used to determine such factors of safety.
5. Study the composite behavioural response of shell footings over a pile group. A numerical investigation into shell-pile group combinations and their behaviour upon loading may be undertaken. As well, the development of a theoretical model may be used as comparison since experimental investigations are non-existent.
6. Investigate the geotechnical behaviour of shells on reinforced collapsible soil. Comparisons between dry and inundated soils of the problematic type and their behaviour when subject to hydrostatic pressures exerted on a shell and its response as a foundation footing may be studied. Moreover, the shell-soil response when the bearing soil is mechanically improved using geo-synthetic reinforcements may be investigated. Ground water table rise may be used as the main parameter beneath the shell footing foundation.

REFERENCES

- [1] ACI Committee 318 (2008). “Building Code Requirements for Structural Concrete (ACI 318-08),” *American Concrete Institute*.
- [2] Anonymous (1974). “Model Studies on the Behaviour of Sand under Two- and Three-Dimensional Shell Foundations,” *International Journal of Rock Mechanics and Mining Science & Geomechanics Abstracts*, 11(4), pp. 86–87.
- [3] Anonymous (1965). “R.C. Shells in Roof & Foundations of Factory Buildings,” *Bulletin Int. Association for Shell and Spatial Structures*, (22), pp. 55–58.
- [4] Abdel-Rahman, M. M., and Hanna, A. M. (2000). “Extension of the Classical Bearing Capacity Theory for Shell Foundations,” *Proceeding of the 53rd Canadian Geotechnical Conference*, Canada, pp. 15–20.
- [5] Abdel-Rahman, M. M. (1996). “Geotechnical Behavior of Shell Foundations,” *Ph.D. Thesis, Civil Engineering, Concordia University*, Montreal, Quebec, Canada, pp. 126–137.
- [6] Abdel-Rahman, M. M., and Hanna, A. M. (1994). “Vertical Displacement Induced in Soil by Conical Shell Foundations,” *Proceedings of the Conference on Vertical and Horizontal Deformations of Foundations and Embankments. Part 2 (of 2), Jun 16–18*, ASCE, New York, NY, USA, College Station, TX, USA, pp. 937–948.
- [7] Anderson, A. R. (1960). “Precast, Prestressed Stadium Floats on Hyperbolic-Paraboloids,” *Engineering News Record*, No.164(7), pp. 62–63.
- [8] Agarwal, K. B. & Gupta, R. N. (1977). “Soil-structure Interaction in Shell Foundations,” *Proc. International Workshop on Soil Structure Interaction*. University of Roorkee, Roorkee, India. Vol. 2, pp. 110–112.
- [9] Alpan, I. (1967). “The Empirical Evaluation of the Coefficient K_o and K_{oR} ,” *Soils and Foundations*, 7(1), pp. 31–40.
- [10] Ayyar, T. S. R., Rao, N. R., and Nair, T. K. G. (1979). “Stress Distribution Below Funicular Shell Foundations,” *Bulletin of the International Association for Shell and Spatial Structures*, 20–1(69), pp. 35–38.

- [11] Baché, H. H. (1981). “Densified Cement/Ultra-Fine Particle-Based Materials,” *Proceedings of the 2nd international Conference on Superplasticizers in Concrete*, Ottawa, Ontario, Canada, pp. 35–41.
- [12] Balla, A. (1962). “Bearing Capacity of Foundations,” *Journal of Soil Mechanics and Foundations Division*, ASCE, Vol. 88, No. SM5, pp. 13–34.
- [13] Bell, F. G. (1993). “Engineering Geology,” *Blackwell Scientific Publications*, p. 358.
- [14] Bhattacharya, B., and Ramaswamy, G. S. (1977). “A Finite Element Analysis of Funicular Shells on a Two Parameter Foundation Model,” *Bulletin of Int’l. Ass. on Shell and Spatial Structures*, 18(65), pp. 45–54.
- [15] Bolton, M. D., (1991). “Geotechnical Stress Analysis for Bridge Abutment Design,” *Report 270*, Transport and Road Research Laboratory, Crowthorne, UK.
- [16] Bolton, M. D., (1986). “The Strength and Dilatancy of Sands,” *Géotechnique* 36, No. 1, pp. 65–78.
- [17] Blais, P. Y., and Couture, M. (1999). “Precast, Prestressed Pedestrian Bridge – World’s First Reactive Powder Concrete Structure,” *PCI Journal*, Vol. 44, No. 5, pp. 60–71.
- [18] Brooker, E. W., and Ireland, H. O. (1965). “Earth Pressure at Rest Related to Stress History,” *Canadian Geotechnical Journal*, 2(1), pp. 1–15.
- [19] Candela, F. (1958). “Stress Analysis for any Hyperbolic Paraboloid,” *Architectural Record*, August, pp. 205–207.
- [20] Candela, F. (1955). “Structural Applications of Hyperbolic Paraboloidal Shells,” *Journal of The American Concrete Institute*, Vol. 26, No. 5, pp. 397–415.
- [21] Coppola, L., Troli, R., Colleparidi, S., Borsoi, A., Cerulli, T., and Colleparidi, M. (1996). “Innovative Cementitious Materials. From HPC to RPC. Part II. The Effect of Cement and Silica Fume Type on the Compressive Strength of Reactive Powder Concrete,” *L’Industria Italiana del Cemento*, Vol. 707, pp. 112–125.
- [22] Das, B. M., and Hanna, A. M. (1988). “Model Tests for Shallow Strip Foundation on Granular Soil,” *Special Topics in Foundations*, ASCE Geotechnical Special Publication, No. 16, pp. 110–124.

- [23] Dawoud, R. H., and Fareed, A. (1972). "Shallow Thin Shells of Revolution on an Elastic Foundation," (50), pp. 31–38.
- [24] Das, Y. C., and Kedia, K. K. (1977). "Shells on Elastic Foundations," *Transactions of 4th Int'l. Conference Structural Mech. In Rector Technology*, San Francisco, USA, M(3/6), pp. 1–11.
- [25] Dierks, K., and Kurian, N. P. (1988). "Zum Verhalten von Kugel- und Doppelkegelschalenfundamenten unter zentrischer und exzentrischer Belastung; Behaviour of Spherical and Double Cone Shell Foundations Under Concentric and Eccentric Loads," *Bauingenieur*, 63(7), pp. 325–333.
- [26] Dierks, K., and Kurian, N. P. (1981). "Zum Verhalten von Kegelschalenfundamenten unter zentrischer und exzentrischer Belastung; Behavior of Conical Shell Foundations Subjected to Axial and Eccentric Loads," *Bauingenieur*, 56(2), pp. 61–65.
- [27] Enriquez, R. R., and Fierro, A. (1963). "A New Project for Mexico City," *Civil Engineering*, Vol. 33, No. 6, pp. 36–38.
- [28] Fareed, A., and Dawoud, R. H. (1979). "Cylindrical Shells on Elastic Foundation," *World Congress on Shell and Spatial Structures*. Madrid, Spain, pp. 5.33–5.46.
- [29] Feng, T. W., and Huang, Y. H. (2009). "Disc Shear of Loose Sands in a Test Tank," *International Offshore and Polar Engineering Conference*, Osaka, Japan, Proc. 19th, June 21–26, p. 51.
- [30] Goncharov, B. V., and Rybakov, A. V. (2001). "Shell Foundations on Tamped Soil Beds," *Soil Mechanics and Foundation Engineering*, 38(5), pp. 167–171.
- [31] Goncharov, Y. M. (1990). "Experience with Construction and Operation of Residential Buildings on Shell-Foundations in Igarka," *Soil Mechanics and Foundation Engineering*, 27(3), pp. 96–101.
- [32] Goncharov, Y. M., Shaparov, G. V., and Tarasyuk, V. G. (1983). "New Type of Shell Foundation for Permafrost Soils," *Soil Mechanics and Foundation Engineering (English Translation of Osnovaniya, Fundamenty i Mekhani)*, 20(2), pp. 13–57.
- [33] Graybeal, B., and Davis, M. (2008). "Cylinder or Cube: Strength Testing of 80 to 200 MPa UHPFRC," *ACI Materials Journal*, 105(6), pp. 603–609.

- [34] Gupta, V. K., Kaushik, S. K., and Roy, S. (1997). "Behavior of Ferrocement Hypar Shell Foundations with Precast Column Elements," *Journal of Ferrocement*, 27(4), pp. 275–289.
- [35] Hadid, W. H. (1983). "New Foundation Models," *M.Eng. Thesis, Civil Engineering, Concordia University, Montreal, Quebec, Canada*.
- [36] Hanley, J. T. (1964). "Interaction Between a Sand and Cylindrical Shells Under Static and Dynamic Loading," *Proceedings of the Symposium on Soil-Structure Interaction*, pp. 487–528.
- [37] Hanna, A. M. (1988). "Shell Foundations: The Future Alternative," *International Journal for Housing Science and its Applications*, Vol. 12, No. 4, pp. 289–295.
- [38] Hanna, A. M. (1981). "Foundations on Strong Sand Overlying Weak Sand," *Journal of the Geotechnical Engineering Division, ASCE*, Vol. 107, No. GT7, pp. 915–927.
- [39] Hanna, A. M., and Abdel-Rahman, M. M. (1998). "Experimental Investigation of Shell Foundations on Dry Sand," *Canadian Geotechnical Journal*, 35(5), pp. 847–857.
- [40] Hanna, A. M., and Abdel-Rahman, M. M. (1990). "Ultimate Bearing Capacity of Triangular Shell Strip Footings on Sand," *Journal of Geotechnical Engineering*, 116(12), pp. 1851–1863.
- [41] Hanna, A. M., and Hadid, W. H. (1987). "New Models of Shallow Foundations," *International Journal of Mathematical Modeling*, 4, pp. 799–811.
- [42] Hanna, A. M., and Meyerhof, G. G. (1981). "Experimental Evaluation of Bearing Capacity of Footings Subjected to Inclined Loads," *Canadian Geotechnical Journal*, 18(4), pp. 599–603.
- [43] He, Chongzhang (1984). "Hollow Conic Shell Foundation and Calculation," *Proceedings of the 5th Engrg. Mech. Div., Specialty Conf. in Mech./Civil Engineering, ASCE, University of Wyoming, Laramie, Wyoming, USA*, (1), pp. 535–538.
- [44] Holzer, C. E., Garlock, M. E., Prevost, J. H. (2008). "Structural Optimization of Felix Candela's Chapel Lomas de Cuernavaca," *5th International Conference on Thin-Walled Structures*, Brisbane, Australia.

- [45] Hooks, J. M. (2001). “Innovative Materials for Bridges of the 21st Century,” *International SAMPE Symposium and Exhibition (Proceedings)*, 46(II), pp. 1352–1363.
- [46] Huang, Yih (1984). “The Theory of Conical Shell and its Applications,” *Proceedings of the 5th Engrg. Mech. Div., Specialty Conf. in Mech./Civil Engineering*, ASCE, University of Wyoming, Laramie, Wyoming, USA, (1), pp. 539–542.
- [47] Huat, B. B. K. and Thamer, A. M. (2006). “Finite Element Study Using FE Code (PLAXIS) on the Geotechnical Behavior of Shell Footings,” *Journal of Computer Science*, 2(1), pp. 104–108.
- [48] IS: 456 (2000) & IS: 9456 (1980). “Plain and Reinforced Concrete—Code of Practice for Design and Construction,” *Bureau of Indian Standards*, New Delhi.
- [49] Iyer, T. S. R., and Rao, N. R. (1970). “Model Studies on Funicular Shells as Rafts on Sands,” *Proceedings of the symposium on shallow foundations*, Bombay, India, (1), pp. 149–156.
- [50] Jain, V. K., Nayak, G. C., and Jain, O. P. (1977). “General Behaviour of Conical Shell Foundations,” *Proceedings of the 3rd International Symposium on Soil-Structure Interaction*, University of Roorkee, India, Vol. 2, pp. 53–61.
- [51] Jaky, J. (1944). “The Coefficient of Earth Pressure at Rest,” *Journal of the Society of Hungarian Architects and Engineers*, Budapest, Hungary, pp. 355–358.
- [52] Jamiolkowski, M., Lancellota, R., Marchetti S., Nova R., and Pasqualini, E. (1979). “Design Parameters for Clays,” *State-of-the-art Report*, 7th European Conference in Soil Mechanics, Brighton.
- [53] Joedicke, J., Benersfeld, W., and Kupfer, H. (1963). “Shell Architecture,” Reinhold Publishing Corp., New York.
- [54] Kaimal, S. S. (1967). “Hypar Footings for a Housing Project in India,” *Bulletin of the International Association for Shell and Spatial Structures*, (32), pp. 7–12.
- [55] Kaimal, S. S. (1971). “Hyperbolic Paraboloid Shell Foundations,” 4(6), pp. 370–3.
- [56] Kidder, F. E. (1905). “Building, Construction and Superintendence,” *W. T. Comstock*, Chapter III, pp. 87–126.

- [57] Konrad, J. M. (1998). "Sand State from Cone Penetrometer Tests: A Framework Considering Grain Crushing Stress," *Géotechnique*, 48(2), pp. 201–215.
- [58] Kötter, F. (1903). "Die Bestimmung des Drucks an gekrümmten Gleitflächen, eine Aufgabe aus der Lehre vom Erddruck," *Sitzungsberichte der Akademie der Wissenschaften*, Berlin, pp. 229–233.
- [59] Krishna Mohan Rao, S. V., and Appa Rao, T. V. S. R. (1994). "Stress Resultants in Hyperboloid Cooling Tower Shells Subjected to Foundation Settlement," *Computers and Structures*, 52(4), pp. 813–827.
- [60] Kurian, N. P. (2006). "Shell Foundations: Geometry, Analysis, Design and Construction," *Alpha Science International Ltd.*, Madras Chennai, India.
- [61] Kurian, N. P. (1994). "Behaviour of Shell Foundations Under Subsidence of Core Soil," *Proceedings of the 13th International Conference on Soil Mechanics and Foundation Engineering. Part 2 (of 3), Jan. 5–10*, A. A. Balkema, New Delhi, India, p. 591.
- [62] Kurian, N. P. (1971). "Studies on the Strength and Performance of Hyperbolic Paraboloidal Shell Footings on Sand," *Ph.D. Thesis*, Department of Civil Engineering, Indian Institute of Technology, Masdras.
- [63] Kurian, N. P., and Jayakrishna Devaki, V. M. (2005). "Analytical studies on the geotechnical performance of shell foundations," *Canadian Geotechnical Journal*, 42(2), pp. 562–573.
- [64] Kurian, N. P., and Jeyachandran, S. R. (1972). "Model Studies on the Behavior of Sand Under Two and Three Dimensional Shell Foundations," *Indian Geotechnical Journal*, Vol. 2, No. 1, pp. 79–90.
- [65] Kurian, N. P., and Mishra, P. K. (1985). "Ultimate Strength of Inverted Dome Shell Foundations with Free Edges," *Bulletin of the International Association for Shell and Spatial Structures*, 26–3(89), pp. 29–37.
- [66] Kurian, N. P., and Mohan, C. S. (1983). "Ultimate Strength of Hyperbolic Paraboloidal Shell Foundations Under Vertical Loads and Moments," *Bulletin of the International Association for Shell and Spatial Structures*, 24–1(81), pp. 27–42.

- [67] Kurian, N. P., and Mohan, C. S. (1981). "Contact Pressures Under Shell Foundations," *Proceedings of the International Conference on Soil Mechanics and Foundation Engineering*, (2), pp. 165–168.
- [68] Kurian, N. P., and Shah, S. H. (1984). "Economy of Conical and Inverted Dome Shell Foundations," *Journal of the Institution of Engineers (India), Part CI: Civil Engineering Division*, (64), pp. 281–286.
- [69] Kurian, N. P., and Shah, S. H. (1984). "Ultimate Strength of Spherical Shell Raft under Vertical Loads and Moments," *Bulletin of the International Association for Shell and Spatial Structures*, 25(86), pp. 35–45.
- [70] Kurian, N. P., and Shah, S. H. (1984). "Model Studies on Conical and Spherical Shell Foundations," *Indian Institute of Technology, Madras, II*, pp. 33–40.
- [71] Kurian, N. P., and Sharma, A. K. (1984). "Ultimate Strength of Dome-Cum-Cone Combined Shell Foundations," *Indian Concrete Journal*, 58(9), pp. 239–248.
- [72] Kurian, N. P., and Sridevi, M. (1999). "Nonlinearisation of the winkler model for the analysis of shells on elastic foundations," *Journal of the International Association for Shell and Spatial Structures*, 40(130), pp. 93–102.
- [73] Kurian, N. P., and Varghese, P. C. (1972). "The Ultimate Strength of Reinforced Concrete Hyperbolic Paraboloid Footings," *The Indian Concrete Journal*, Vol. 46, pp. 513–519.
- [74] Lachemi, M., Lessard, M. and Aïtcin, P. C., (1996). "Early-Age Temperature Developments in a High-Performance Concrete Viaduct," *ACI SP-167*, pp. 149–179.
- [75] Lambe, T. W., and Whitman, R. V. (1979). "Soil Mechanics," *John Wiley and Sons Inc.*, New York, N.Y.
- [76] Mackey, R. D. (1966). "Active and Passive Pressures on Curved Surfaces," *Sols-Soil*, No. 17, pp. 31–40.
- [77] Maharaj, D. K. (2004). "Finite Element Analysis of Conical Shell Foundation," *Elect. Journal Geotechnical Engineering*, 9A, Paper No. 348.
- [78] Martin, I., and Ruiz, S. (1955). "Folded Plate Raft Foundation for 24-Storey Building," *Journal of The American Concrete Institute*, Vol. 31, pp. 121–126.

- [79] Mayne P. W., and Kulhawy F. H. (1982). “ K_o -OCR Relationships in Soils,” *Journal of Geotechnical Engineering*, Vol. 108, No. 6, pp. 851–872.
- [80] Melerski, E. (1988). “Thin Shell Foundation Resting on Stochastic Soil,” *Journal of Structural Engineering*, ASCE. 114 (12), pp. 2692–2709.
- [81] Meyerhof, G. G. (1976). “Bearing Capacity and Settlement of Pile Foundations,” *Journal of Geotechnical Engineering*, ASCE Vol. 102, No. GT3, pp. 197–228.
- [82] Nath, Y., and Jain, R. K. (1985). “Orthotropic Annular Shells on Elastic Foundations,” *Journal of Engineering Mechanics*, ASCE III(10), pp. 1242–1256.
- [83] Nie, G. H. (2003). “Analysis of Non-linear Behaviour of Imperfect Shallow Spherical Shells on Pasternak Foundation by the Asymptotic Iteration Method,” *International Journal of Pressure Vessels and Piping*, 80(4), pp. 229–235.
- [84] Paliwal, D. N. (1994). “Large Deflection in a Shallow Spherical Shell on an Elastic Foundation Under a Concentrated Load at the Centre,” *International Journal of Pressure Vessels and Piping*, 57(2), pp. 131–133.
- [85] Paliwal, D. N., and Bhalla, V. (1993). “Large Deflection Analysis of Cylindrical Shells on a Pasternak Foundation,” *International Journal of Pressure Vessels and Piping*, 53(2), pp. 261–271.
- [86] Paliwal, D. N. and Rai, R. N. (1986). “Shallow Spherical Shell on Pasternak Foundation Subjected to Elevated Temperature,” *Journal of Thin-walled structures*, 5(S), pp. 343–349.
- [87] Paliwal, D. N., Sinha, S. N. (1986). “Static and Dynamic Behaviour of Shallow Spherical Shells on Winkler Foundation,” *Journal of Thin-walled structures*, Vol. 4, No. 6, pp. 411–422.
- [88] Paliwal, D. N., Sinha, S. N., and Ahmad, A. (1992). “Hypar Shell on Pasternak Foundation,” *Journal of Engineering Mechanics*, Vol. 118, No. 7, pp. 1303–1316.
- [89] Paliwal, D. N., and Srivastava, R. (1994). “Large Deflection of Cylindrical Shells on a Kerr Foundation,” *International Journal of Pressure Vessels and Piping*, Vol. 57, No. 1, pp. 1–5.
- [90] Paliwal, D. N., and Srivastava, R. (1993). “Nonlinear Static Behaviour of Shallow Spherical Shell on a Kerr Foundation,” *International Journal of Pressure Vessels and Piping*, Vol. 55, No. 3, pp. 481–494.

- [91] Pandian, N. S., and Ranganatham, B. V. (1970). “Hyperbolic Paraboloidal Shell Foundations,” *Proceedings of Symposium on Shallow Foundations*, Bombay, India (1), pp. 142–148.
- [92] Poorooshasb, H. B., Holubec, I., and Sherbourne, A. N. (1967). “Yielding and Flow of Sand in Triaxial Compression, Part 2 and 3,” *Canadian Geotechnical Journal*, Vol. 4, No. 4, pp. 376–397.
- [93] Rad, N. S., and Tumay, M.T. (1987). “Factors Affecting Sand Specimen Preparation by Raining,” *Geotechnical Testing Journal*. Vol. 10, No. 1, pp. 31–37.
- [94] Ramiah, B. K., Purushothamaraj, P., Chickanagappa, L. S., and Pinto Adrian, R. (1977). “Experimental Studies on Shell Foundations,” *Proceedings – Annual Allerton Conference on Circuit and System Theory*, pp. 299–306.
- [95] Richard, P., and Cheyrezy, M. H. (1994). “Reactive Powder Concretes with High Ductility and 200–800 MPa Compressive Strength,” *ACI Special Publication*, Vol. 144, pp. 507–518.
- [96] Sankar, R., Paliwal, D. N., and Jha, D. (2003). “Free vibrations of a Cylindrical Shell Resting on an Elastic Foundation,” *Journal of Structural Engineering*, Madras, Vol. 30, No. 3, pp. 139–146.
- [97] Schaller, I., de Larrard, F., Sudret, J.P., Acker, P. and LeRoy, R. (1992). “Experimental Monitoring of the Joigny Bridge in High-Performance Concrete: From Material to Structure,” *Ed. Y. Malier, E & FN SPON*, London, pp. 432–457.
- [98] Schmidt, B. (1966). “Discussion of Earth Pressure at Rest Related to Stress History,” *Canadian Geotechnical Journal*, Vol. 3, No. 4, pp. 239–242.
- [99] Sharma, A. K. (1984). “Economy in Shell Foundations in Soft Soils,” *West Indian Journal of Engineering*, Vol. 9, No. 2, pp. 20–26.
- [100] Simpson, B. (1992). “Retaining Structures: Displacement and Design,” *Géotechnique*, 42(4), pp. 541–576.
- [101] Stuit, H. G. (1995). “Sand in the Geotechnical Centrifuge,” *Ph.D. Thesis. Delft University of Technology*, Netherlands, pp. 45–76.
- [102] Terzaghi, K. (1943). “Theoretical Soil Mechanics,” *John Wiley and Sons Inc.*, New York, London.

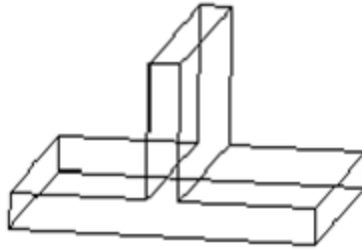
- [103] Vaid Y. P., and Negussey D. (1984). “Relative Density of Pluviated Sand Samples,” *Soils and Foundations*, Vol. 24, No. 2, pp. 101–105.
- [104] Varghese, P. C., and Kurian, N. P. (1971) “Strength and Performance of Reinforced Concrete Precast Hypar Footings,” *Journal of the Indian National Group of the International Ass. for Bridge and Structural Engineering*, Madras, Vol. 1, No. 2, pp. 49–66.
- [105] Vesic, A. S. (1963). “Bearing Capacity of Deep Foundations in Sand,” *Highway Research Record*, No. 39, National Academy of Sciences, pp. 112–153.
- [106] Vishay (2001). “StrainSmart® Manual and System 5000 Hardware & Software,” *Vishay Measurements Group, Inc.*, Canada, pp. 1–49.
- [107] Wang, C. (1985). “Design and Construction of M-Type Shell Structure Foundation for Spheroidal Tank,” *Proceedings of the International Association for Shell and Spatial Structures*, Application of Shells in Engineering Structures, Moscow, USSR, Vol. 3, pp. 390–403.
- [108] Wikipedia (2008). “Sydney Opera House at Night,” *Web-based Encyclopedia*, http://www.en.wikipedia.org/wiki/Sydney_Opera_House, & “Hoover Dam,” http://www.en.wikipedia.org/wiki/File:Hoover_dam_from_air.jpg
- [109] Wroth, C. P. (1972). “In-Situ Measurements on Initial Stress and Deformation Characteristics,” *Proceedings, In-Situ Measurement of Soil Properties*, North Carolina State University, Geotechnical Engineering Division, pp. 181–230.

APPENDIX I

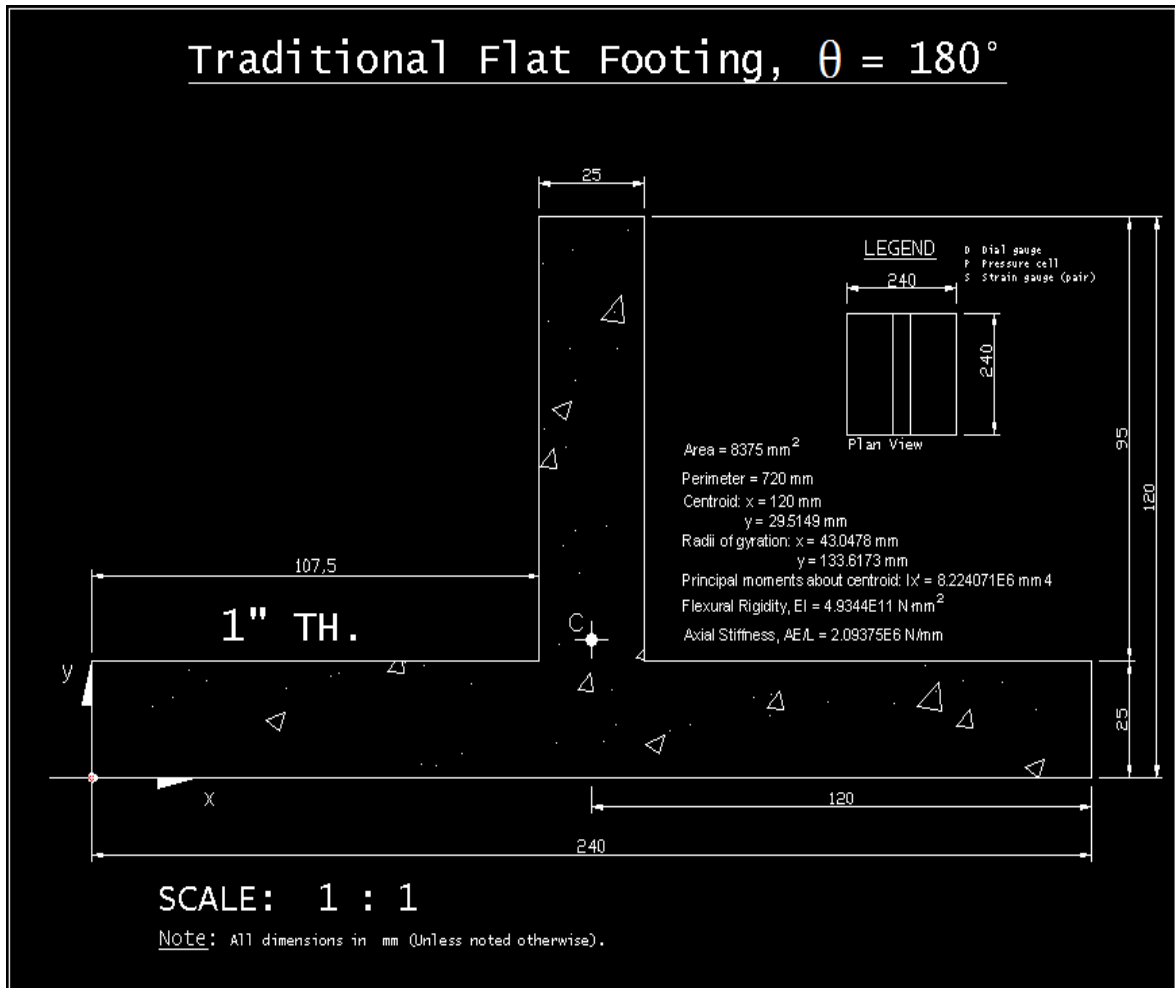
iShell Prototypes

iShell Prototypes

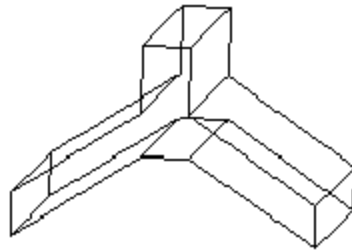
- Prototype 1 : Flat Footing Model, $\theta = 180^\circ$
- Prototype 2 : Upright Triangular Shell Footing Model, $\theta = 34^\circ$
- Prototype 3 : Sinusoidal iShell Footing Model ($t_s = 25$ mm, $\theta = 36^\circ$)
- Prototype 4 : iShell Footing Model iS#1 ($t_s = 19$ mm, $\theta = 18^\circ$)
- Prototype 5 : iShell Footing Model iS#2 ($t_s = 19$ mm, $\theta = 27^\circ$)
- Prototype 6 : iShell Footing Model iS#3 ($t_s = 19$ mm, $\theta = 36^\circ$)
- Prototype 7 : iShell Footing Model iS#4 ($t_s = 25$ mm, $\theta = 18^\circ$)
- Prototype 8 : iShell Footing Model iS#5 ($t_s = 25$ mm, $\theta = 27^\circ$)
- Prototype 9 : iShell Footing Model iS#6 ($t_s = 25$ mm, $\theta = 36^\circ$)



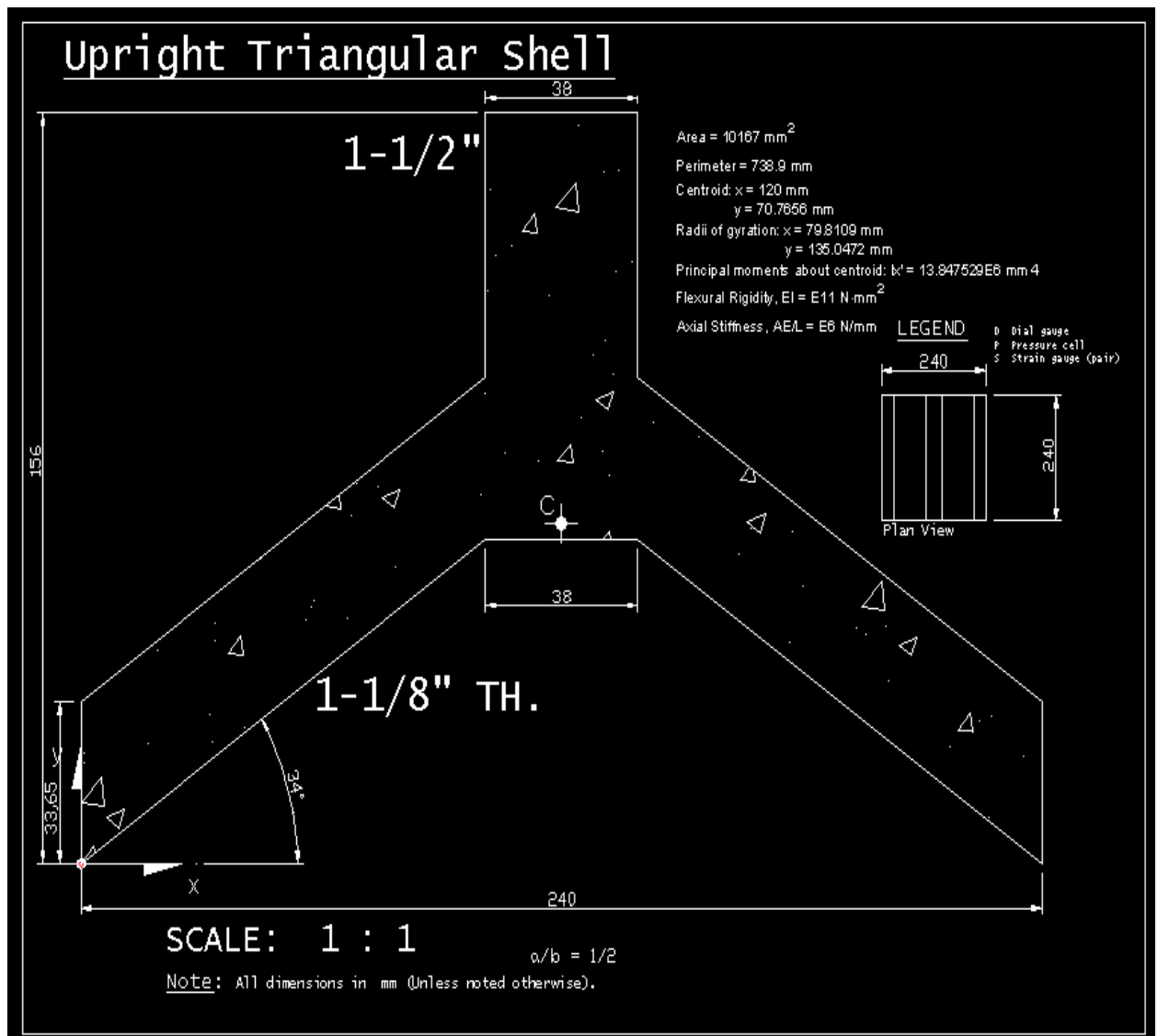
Isometric View – Flat Footing Model.



Prototype 1. Flat Footing Model, $\theta = 180^\circ$.



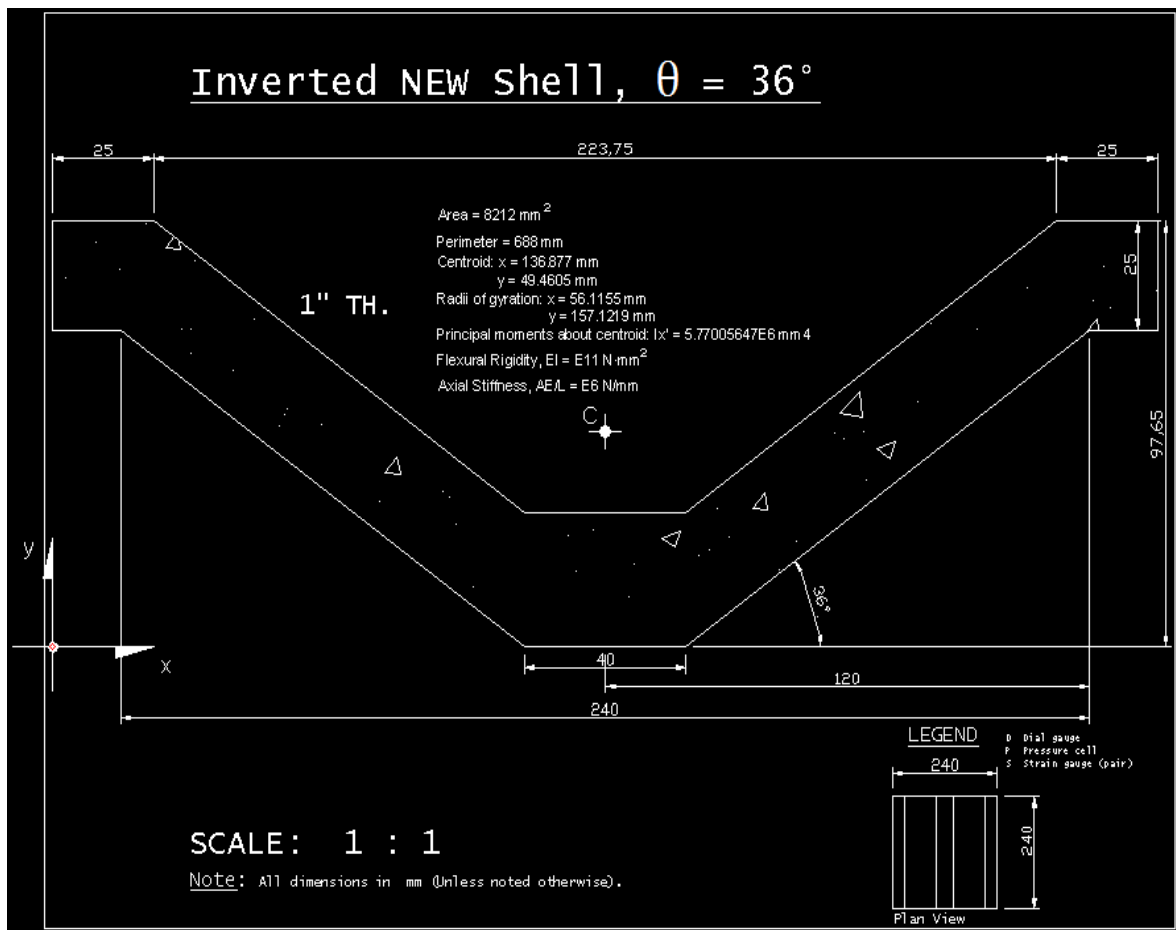
Isometric View – Upright Triangular Shell Footing Model.



Prototype 2. Upright Triangular Shell Footing Model, $\theta = 34^\circ$.



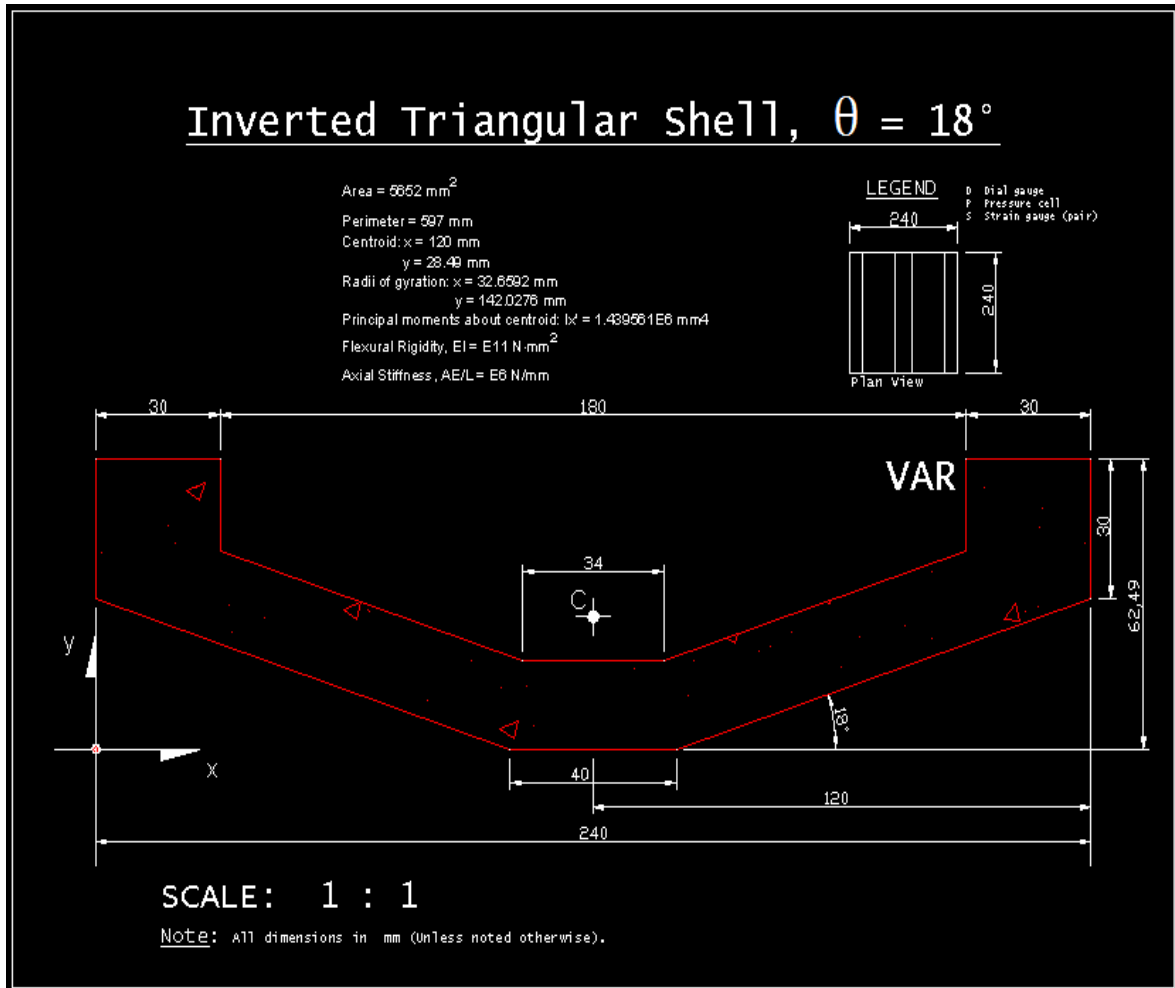
Isometric View – Sinusoidal iShell Footing Model.



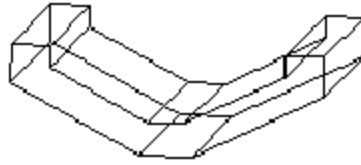
Prototype 3. Sinusoidal iShell Footing Model ($t_s = 25$ mm, $\theta = 36^\circ$).



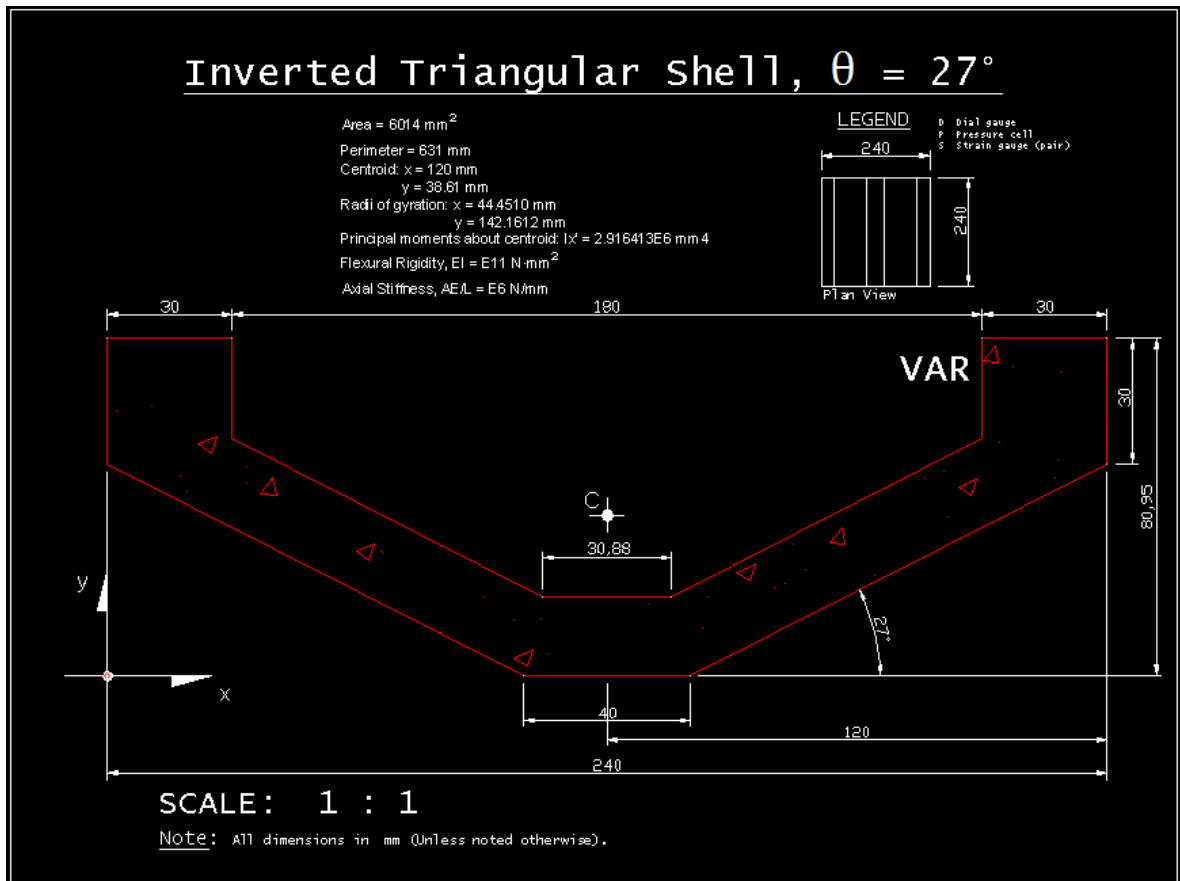
Isometric View – iShell Footing Model iS#1.



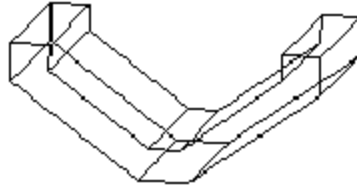
Prototype 4. iShell Footing Model iS#1 ($t_s = 19$ mm, $\theta = 18^\circ$).



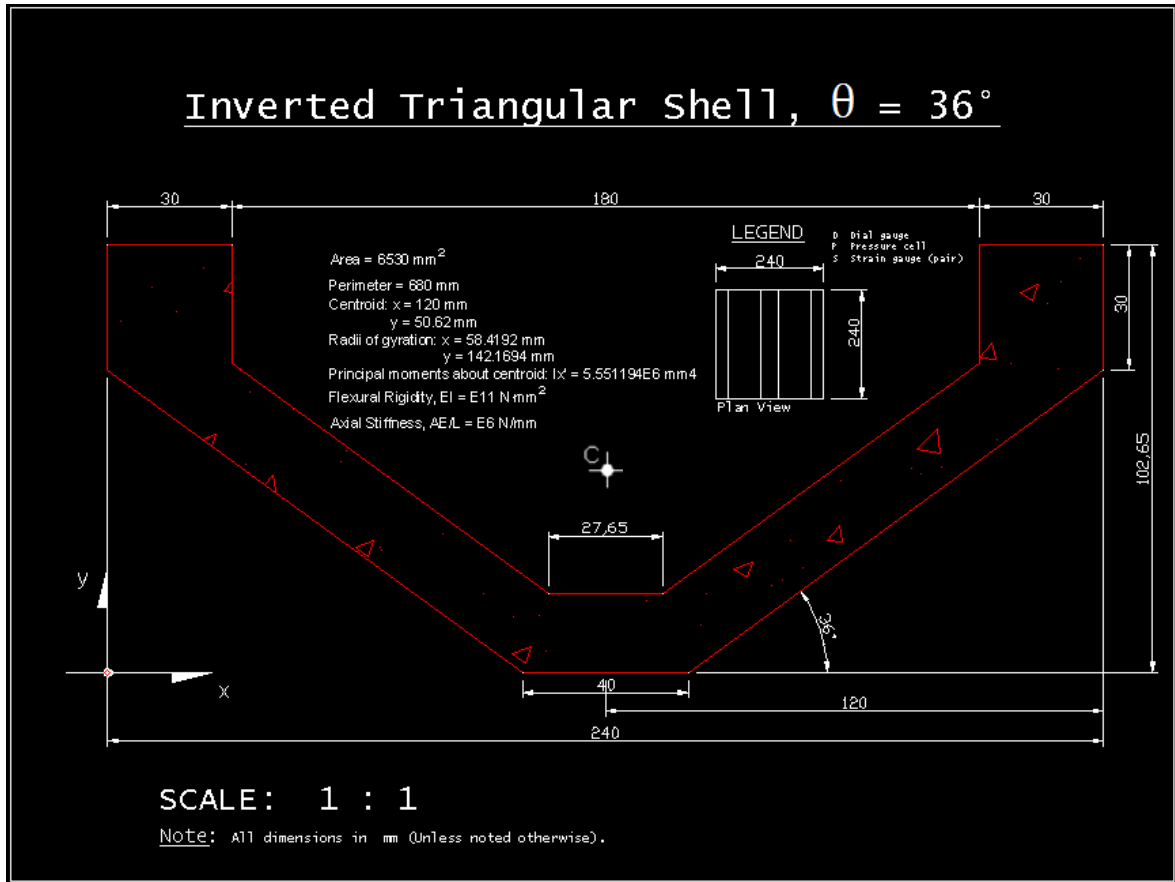
Isometric View – iShell Footing Model iS#2.



Prototype 5. iShell Footing Model iS#2 ($t_s = 19$ mm, $\theta = 27^\circ$).



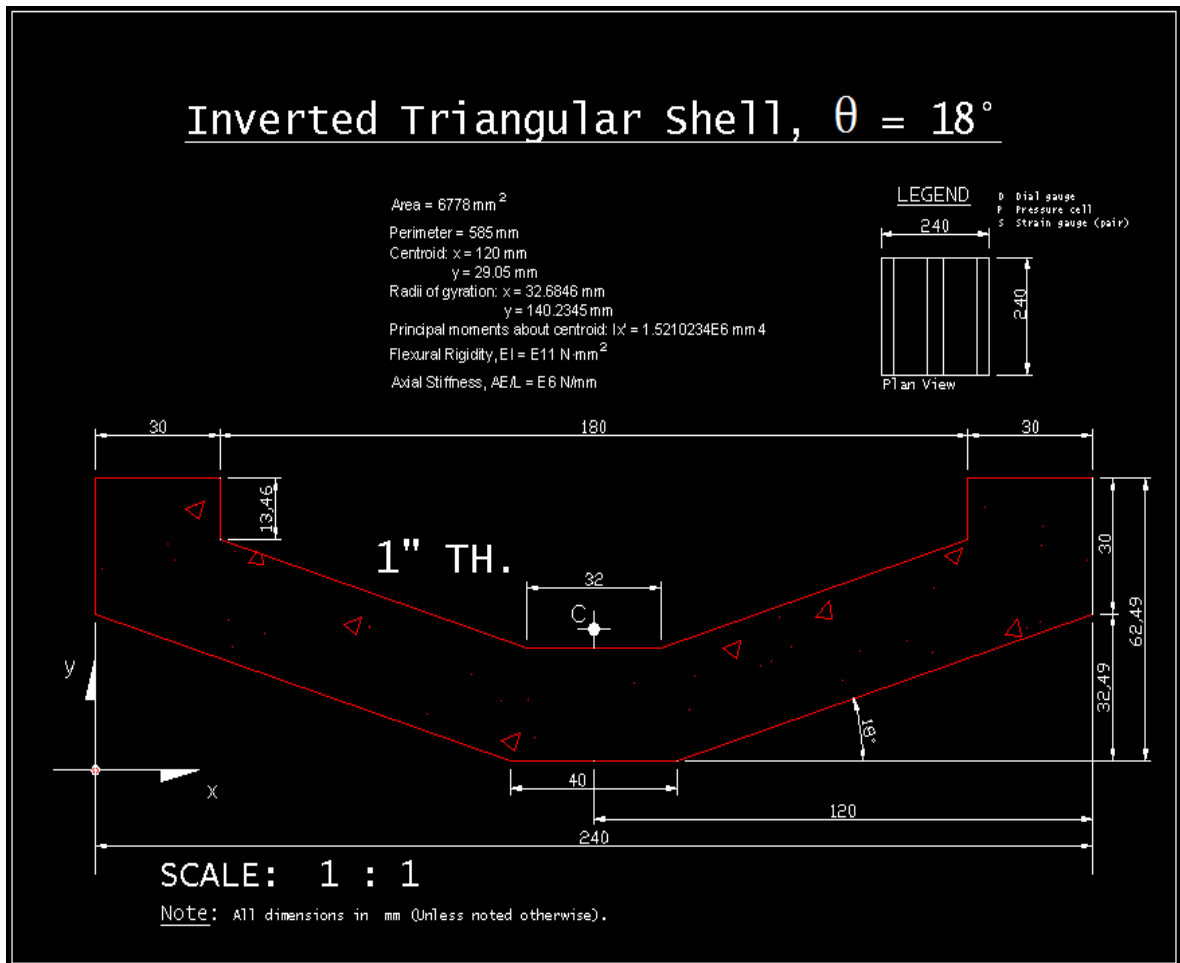
Isometric View – iShell Footing Model iS#3.



Prototype 6. iShell Footing Model iS#3 ($t_s = 19$ mm, $\theta = 36^\circ$).



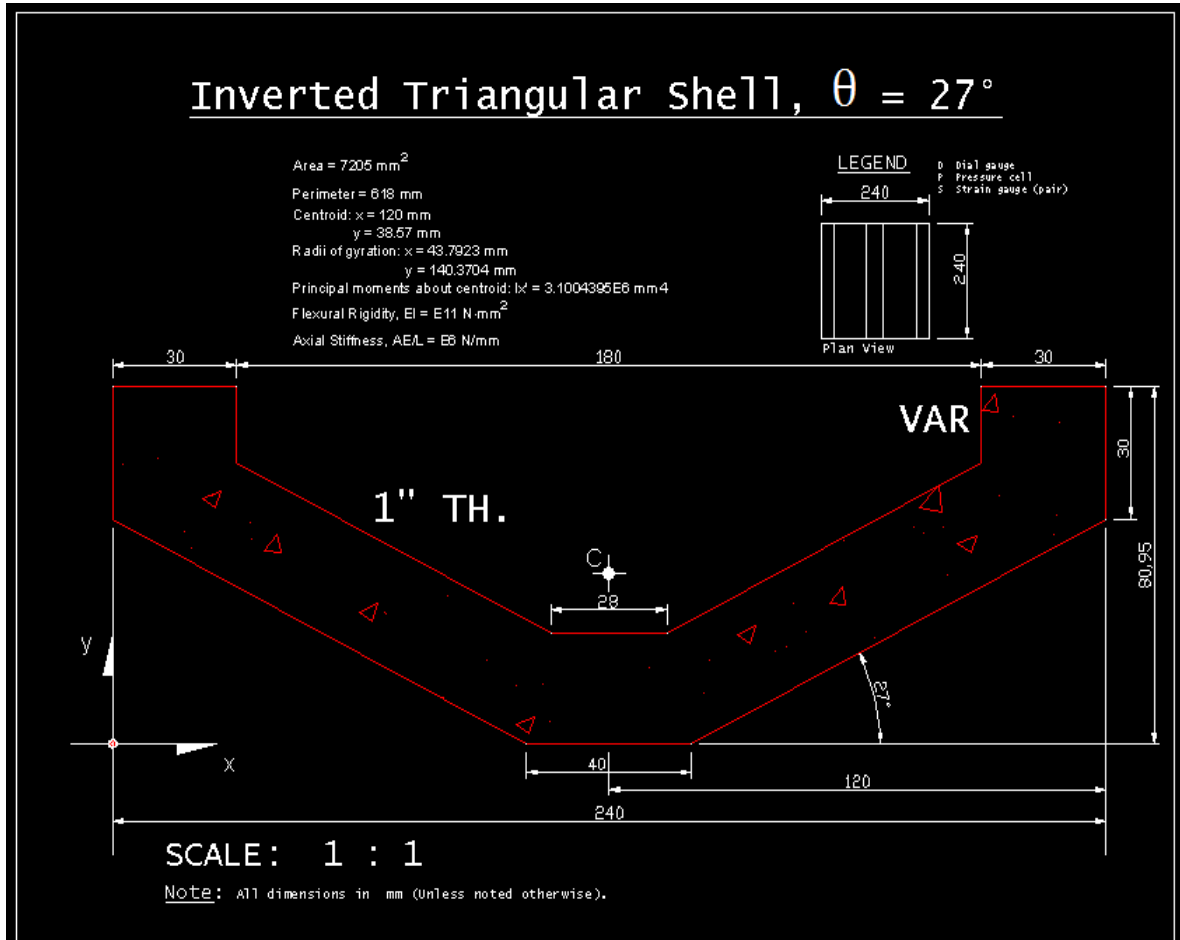
Isometric View – iShell Footing Model iS#4.



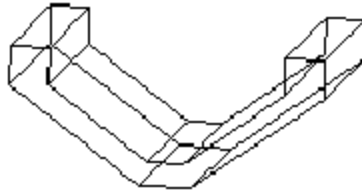
Prototype 7. iShell Footing Model iS#4 ($t_s = 25$ mm, $\theta = 18^\circ$).



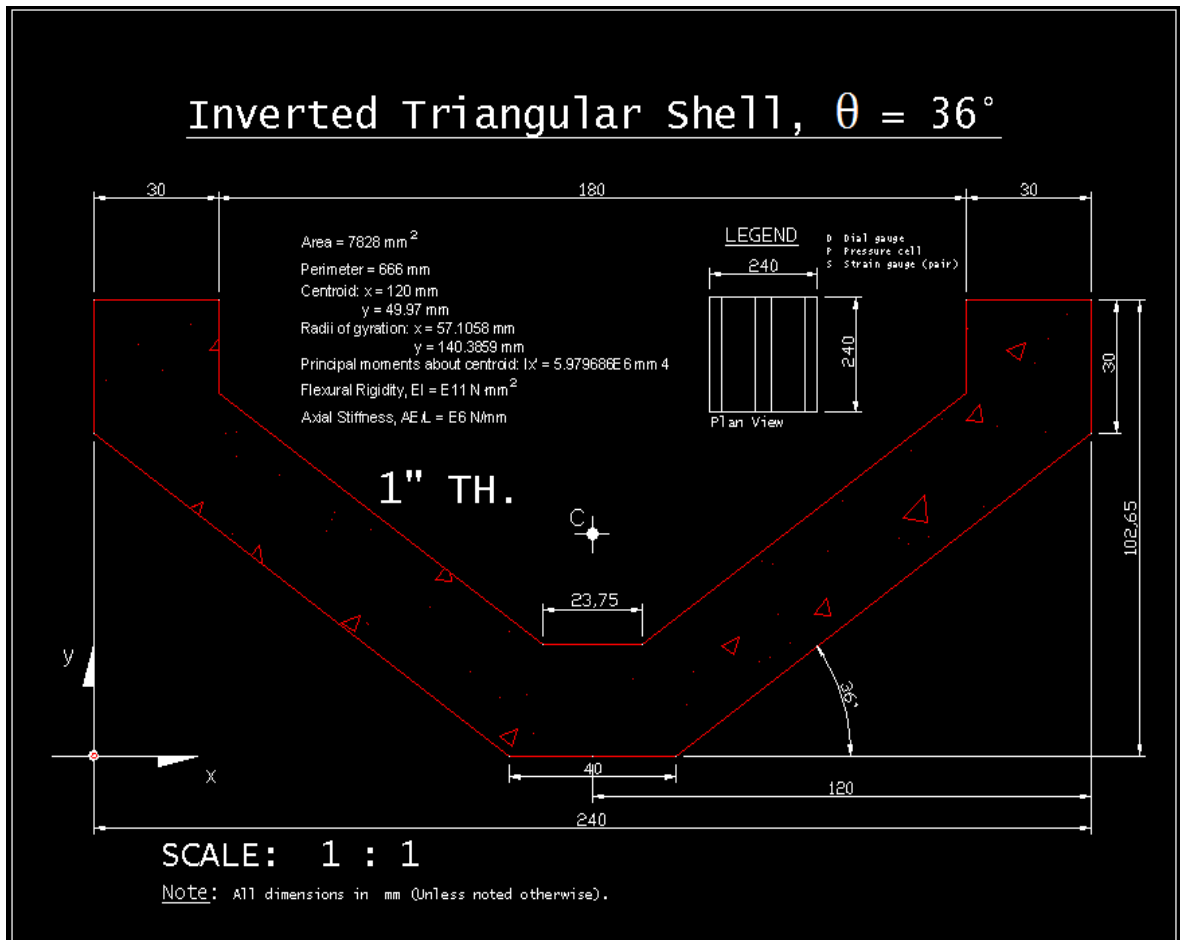
Isometric View – iShell Footing Model iS#5.



Prototype 8. iShell Footing Model iS#5 ($t_s = 25$ mm, $\theta = 27^\circ$).



Isometric View – iShell Footing Model iS#6.



Prototype 9. iShell Footing Model iS#6 ($t_s = 25 \text{ mm}$, $\theta = 36^\circ$).

APPENDIX II

iShell Bearing Capacity Program

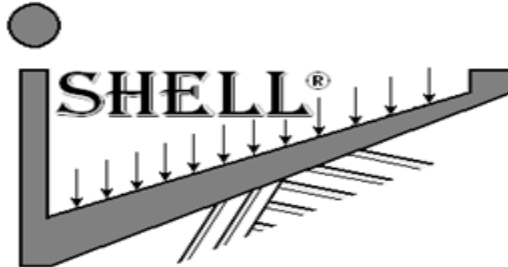
iShell Bearing Capacity Program

Development of iShell® software generates $(N_c, N_q \text{ \& } N_\gamma)_{iS}$ values for bearing capacity determination for inverted shell footings. A preliminary coding in excel using macros was formulated to establish consistency in the evaluation of individual equations and to easily verify dependency between parameters. A typical screen-shot of the spreadsheet used is illustrated in Figure 1.

HI7		$f_k = [quf] * breadth_b * (SoilG / G(2) * breadth_b * (2 * TAN(alpha) + TAN(Theta(R)))) - cohesion_c * breadth_b * TAN(alpha)$																
A	B	C	D	E	F	G	H	I	J	K	L	M	N					
	SoilG	Theta	Phi(R)	CIT	CST	Thickness (t)	Breadth (B)	ConcreteG (Gc)	GravityAccel	Radius	Theta (T1, T2, stepT)							
1																		
2	Constants:	G1	12	C1	0.1	0.24	2.4	20	9.81	1.2								
3		G2	22	C2	0.3													
4																		
5	Average G		17	Average C	0.2	0.12	1.2											
6	(Phi, Theta)	Phi	Theta	Phi(R)	CIT	CST	c1	c2	c3	c4	c5	c6	c7	c8				
7	(10,0)	10	0	0.174532925	0.872664626	0.698131701	1.173648178	0.123256833	0.20694584	1.124364817	1.360359003	-0.064708084	-0.032043301	0.50250999				
8	(10,10)	10	10	0.174532925	0.872664626	0.698131701	1.173648178	0.123256833	0.20694584	1.124364817	1.360359003	-0.064708084	-0.032043301	0.50250999				
9	(10,20)	10	20	0.174532925	0.872664626	0.698131701	1.173648178	0.123256833	0.20694584	1.124364817	1.360359003	-0.064708084	-0.032043301	0.50250999				
10	(10,30)	10	30	0.174532925	0.872664626	0.698131701	1.173648178	0.123256833	0.20694584	1.124364817	1.360359003	-0.064708084	-0.032043301	0.50250999				
11	(10,40)	10	40	0.174532925	0.872664626	0.698131701	1.173648178	0.123256833	0.20694584	1.124364817	1.360359003	-0.064708084	-0.032043301	0.50250999				
12	(10,50)	10	50	0.174532925	0.872664626	0.698131701	1.173648178	0.123256833	0.20694584	1.124364817	1.360359003	-0.064708084	-0.032043301	0.50250999				
13	(10,60)	10	60	0.174532925	0.872664626	0.698131701	1.173648178	0.123256833	0.20694584	1.124364817	1.360359003	-0.064708084	-0.032043301	0.50250999				
14	(10,70)	10	70	0.174532925	0.872664626	0.698131701	1.173648178	0.123256833	0.20694584	1.124364817	1.360359003	-0.064708084	-0.032043301	0.50250999				
15	(10,80)	10	80	0.174532925	0.872664626	0.698131701	1.173648178	0.123256833	0.20694584	1.124364817	1.360359003	-0.064708084	-0.032043301	0.50250999				
16	(10,90)	10	90	0.174532925	0.872664626	0.698131701	1.173648178	0.123256833	0.20694584	1.124364817	1.360359003	-0.064708084	-0.032043301	0.50250999				
17	(11,0)	11	0	0.191986218	0.881391272	0.689405055	1.190808995	0.135546363	0.231469821	1.151134818	1.408675943	-0.064131088	-0.024336296	0.48653459				
18	(11,10)	11	10	0.191986218	0.881391272	0.689405055	1.190808995	0.135546363	0.231469821	1.151134818	1.408675943	-0.064131088	-0.024336296	0.48653459				
19	(11,20)	11	20	0.191986218	0.881391272	0.689405055	1.190808995	0.135546363	0.231469821	1.151134818	1.408675943	-0.064131088	-0.024336296	0.48653459				
20	(11,30)	11	30	0.191986218	0.881391272	0.689405055	1.190808995	0.135546363	0.231469821	1.151134818	1.408675943	-0.064131088	-0.024336296	0.48653459				
21	(11,40)	11	40	0.191986218	0.881391272	0.689405055	1.190808995	0.135546363	0.231469821	1.151134818	1.408675943	-0.064131088	-0.024336296	0.48653459				
22	(11,50)	11	50	0.191986218	0.881391272	0.689405055	1.190808995	0.135546363	0.231469821	1.151134818	1.408675943	-0.064131088	-0.024336296	0.48653459				
23	(11,60)	11	60	0.191986218	0.881391272	0.689405055	1.190808995	0.135546363	0.231469821	1.151134818	1.408675943	-0.064131088	-0.024336296	0.48653459				
24	(11,70)	11	70	0.191986218	0.881391272	0.689405055	1.190808995	0.135546363	0.231469821	1.151134818	1.408675943	-0.064131088	-0.024336296	0.48653459				
25	(11,80)	11	80	0.191986218	0.881391272	0.689405055	1.190808995	0.135546363	0.231469821	1.151134818	1.408675943	-0.064131088	-0.024336296	0.48653459				
26	(11,90)	11	90	0.191986218	0.881391272	0.689405055	1.190808995	0.135546363	0.231469821	1.151134818	1.408675943	-0.064131088	-0.024336296	0.48653459				

Figure 1. iShell Spreadsheet for Parameter Evaluation and Dependency.

The following algorithm written in C++ code is used to obtain new shell bearing capacity factors as modeled theoretically based on the numerical and experimental work. The use of Armadillo C++ linear algebra open-source library is acknowledged as having been accessed from <http://arma.sourceforge.net/>



```
#include <iostream>,<string>,<sstream>,<fstream>
#define org1 "iSHELL FOUNDATIONS\n\n"
#define org2 "ULTIMATE BEARING CAPACITY PROGRAM\n\n"
#define org3 "(C) R. Rinaldi, 2012\n"
#define orgDec
"%%%%%%%%%%%%%%%%%%%%%%%%%%%%%%%%%%%%%%%%%%%%%%%%%%%%%%%%%\n"
#define orgDec2
"*****\n"
#define PI 3.14159
#define g 9.80665
#define TH
using namespace std;
void centerText(char*t);

int main() {
    centerText(orgDec);
    centerText(org1);
        centerText(org2);
            centerText(org3);
                centerText(orgDec);
    cout<< endl;
    system("Pause");
return 0;

}

void centerText(char*t){
    int l=strlen(t);
    int p=(int)((80-l)/2);
    for(int i=0;i<p;i++)
        cout<<" ";
    cout<<t<<endl;

}

#include "ShellOptimization.h"
#include <fstream>

using namespace arma;
using namespace std;
```

```

vec Phi , Theta, Ones;
double SoilG_G, cohesion_c, Thickness_t, WedgeThickness_a, Breadth_B,
breadth_b, ConcreteG__Gc, Radius_Ro;

int main()
{
    // input phi, theta, Radius of soil stress lines Ro, average soil
    density G, average soil cohesion C, Thickness t and wedge thickness a,
    breadth b and Breadth B, Concrete Density Gc
    SoilG_G = 17, cohesion_c = 0.2, Thickness_t = 0.24,
    WedgeThickness_a = 0.12,
    Breadth_B = 2.4, breadth_b = 1.2, ConcreteG__Gc = 20,
    Radius_Ro = 1.2;
    int phil = 55, phi0 = 10, dphi = 1;
    int thetal = 90, theta0 = 0, dtheta = 10;
    cout << "MAKE SURE TO SEPARATE CONSECUTIVE VALUES BY A SPACE!" <<
    endl;

    cout << "Enter lower, upper and delta phi followed by Return" <<
    endl;
    cin >> phi0 >> phil >> dphi;
    cout << "Enter lower, upper and delta theta followed by Return" <<
    endl;
    cin >> theta0 >> thetal >> dtheta;
    cout << "Enter values for Radius Ro, Soil and Concrete G, cohesion
    c, Thickness t, "
    << "Wedge Thickness a, Breadth B and breadth b followed by
    Return" << endl;
    cin >> Radius_Ro >> SoilG_G >> ConcreteG__Gc >> cohesion_c >>
    Thickness_t >> WedgeThickness_a >>
    Breadth_B >> breadth_b;
    cout << "Thank you. Your values will now be saved to
    OutputTable.txt" << endl;
    cout << "..." << endl;
    Phi.set_size(((phil-phi0)/dphi+1)*((thetal-theta0)/dtheta+1));
    Theta.set_size(((phil-phi0)/dphi+1)*((thetal-theta0)/dtheta+1));
    Ones = ones(((phil-phi0)/dphi+1)*((thetal-theta0)/dtheta+1));
    for(int phi = phi0; phi <= phil; phi+=dphi){
        for (int theta = theta0; theta <= thetal; theta+=dtheta){
            Phi((phi-phi0)*((thetal-theta0)/dtheta+1) +(theta-
            theta0)/dtheta) = phi* PI()/180;
            Theta((phi-phi0)*((thetal-theta0)/dtheta+1) +(theta-
            theta0)/dtheta) = theta*PI()/180;
        }
    }
    vec PhiD , ThetaD, NG, NQ, NC, TANPHI;
    PhiD = Phi*180/PI();
    ThetaD = Theta*180/PI();
    NG = Ng();
    NQ = Nq();
    NC = Nc();
    TANPHI = tan(Phi);
    // output results to outputtable.txt
    ofstream fout("OutputTable.xls");
    cout << setw(5) << "Phi" << setw(10) << "Theta" << setw(30) << "Ng"
    << setw(10) << "Nq" << setw(10) << "Nc" << setw(10) << "tan(Phi)" <<
    endl;
}

```

```

    cout << "" << endl;
    //wchar_t buff[] = "φ";
    fout << "Phi" << '\t' << "Theta" << '\t' << "Ng" << '\t' << "Nq"
    << '\t' << "Nc" << '\t' << "tan(Phi)" << endl;

    for (int i = 0; i < Phi.n_elem; i++){
        cout.unsetf(ios::fixed);
        fout.unsetf(ios::fixed);
        if(i>0 && PhiD(i)==PhiD(i-1)){
            cout << setw(5) << " " << setw(10) << ThetaD(i) <<
            fixed << setprecision(2) << setw(30) << NG(i) << setw(10) << NQ(i) <<
            setw(10) << NC(i) << setw(10) << TANPHI(i) << endl;
            fout << '\t' << ThetaD(i) << fixed << setprecision(2)
            << '\t' << NG(i) << '\t' << NQ(i) << '\t' << NC(i) << '\t' << TANPHI(i)
            << endl;
        }else{
            cout << setw(5) << PhiD(i) << setw(10) << ThetaD(i) <<
            fixed << setprecision(2) << setw(30) << NG(i) << setw(10) << NQ(i) <<
            setw(10) << NC(i) << setw(10) << TANPHI(i) << endl;
            fout << PhiD(i) << '\t' << ThetaD(i) << fixed <<
            setprecision(2) << '\t' << NG(i) << '\t' << NQ(i) << '\t' << NC(i) <<
            '\t' << TANPHI(i) << endl;
        }
    }
    fout.close();
    cout << "Output has been sucessfully written to OutputTable.txt" <<
    endl;
    cout << "END of execution" << endl;
    return 0;
}

double PI ()
{
    static double ret = 0;
    if (!ret)
        ret = atan2(0.0, -1.0);
    return ret;
}

vec CIT ()
{
    static vec ret;
    if (ret.empty())
        ret=PI()/4.0 + (Phi/2.0);
    return ret;
}

vec CST ()
{
    static vec ret;
    if (ret.empty())
        ret=PI()/4.0 - (Phi/2.0);
    return ret;
}

vec c1 ()
{
    static vec ret;

```

```

        if (ret.empty())
            ret=1+sin(Phi);
        return ret;
    }
vec c2 ()
{
    static vec ret;
    if (ret.empty())
        ret=sin(CIT())-cos(CIT());
    return ret;
}
vec c3 ()
{
    static vec ret;
    if (ret.empty())
        ret=sin(Phi)%tan(CIT());
    return ret;
}
vec c4 ()
{
    static vec ret;
    if (ret.empty())
        ret=1+(4*pow(tan(Phi), 2));
    return ret;
}
vec c5 ()
{
    static vec ret;
    if (ret.empty())
        ret=exp(2*CIT()%tan(Phi));
    return ret;
}
vec c6 ()
{
    static vec ret;
    if (ret.empty())
        ret=sin(Phi)%((2*tan(Phi)%sin(CIT()))-cos(CIT()));
    return ret;
}
vec c7 ()
{
    static vec ret;
    if (ret.empty())
        ret=(c2()%c3())+(c6()/c4());
    return ret;
}
vec c8 ()
{
    static vec ret;
    if (ret.empty())
        ret=cos(CIT())%(exp(-2*CST())%tan(Phi));
    return ret;
}
vec c9 ()
{
    static vec ret;
    if (ret.empty())

```



```

        ret=(exp(PI()*tan(Phi))%pow(tan(CIT()),2))+tan(CIT())-
(2*tan(Phi));
        return ret;
}
vec c10 ()
{
    static vec ret;
    if (ret.empty())
        ret=(PI()/4.0)+(cos(Phi)/2.0)-(tan(Phi)%sin(Phi));
    return ret;
}
vec c11 ()
{
    static vec ret;
    if (ret.empty())
        ret=-sqrt((double)2)*cos(Phi/2.0)/sin(Phi);
    return ret;
}
vec c12 ()
{
    static vec ret;
    if (ret.empty())
        ret=(c3()%c5()%c8()%c9())/sin(Phi)%c4();
    return ret;
}
vec c13 ()
{
    static vec ret;
    if (ret.empty())
        ret=((c5()%c7()%c8()%c9())/sin(Phi)%c4())+(c10()/c4());
    return ret;
}
vec c14 ()
{
    static vec ret;
    if (ret.empty())
        ret=((c1()%c5()%c8()%c9())/sin(Phi)%c4())+c11();
    return ret;
}
vec c15 ()
{
    static vec ret;
    if (ret.empty())
        ret=-2*tan(Phi);
    return ret;
}
vec c16 ()
{
    static vec ret;
    if (ret.empty())
        ret=(1/c15())%(exp(c15()%(CST()))-exp(-c15()%(CIT())));
    return ret;
}
vec c17 ()
{
    static vec ret;
    if (ret.empty())

```

```

        ret=-
        ((sin(Phi)*sqrt((double)2))/c4())%(2*tan(Phi)%sin(Phi/2.0)-cos(Phi/2.0));
        return ret;
    }
vec c18 ()
{
    static vec ret;
    if (ret.empty())
        ret=c17()+(c5()%c7()%c16());
    return ret;
}
vec c19 ()
{
    static vec ret;
    if (ret.empty())
        ret=c3()%c5()%c17();
    return ret;
}
vec c20 ()
{
    static vec ret;
    if (ret.empty())
        ret=c1()%c5()%c17();
    return ret;
}
vec c21 ()
{
    static vec ret;
    if (ret.empty())
        ret=(PI()/2.0)-(2.0*sin(CIT())%cos(CIT()));
    return ret;
}
vec c22 ()
{
    static vec ret;
    if (ret.empty())
        ret=c13()-(c2()%cos(CIT()))-(0.5*c21());
    return ret;
}
vec c23 ()
{
    static vec ret;
    if (ret.empty())
        ret=c12()-(sin(CIT())+cos(CIT()));
    return ret;
}
vec c24 ()
{
    static vec ret;
    if (ret.empty())
        ret=c2()%c14();
    return ret;
}
vec DepthConcrete_Dc ()
{
    static vec ret;

```

```

        if (ret.empty())
            ret=(breadth_b-WedgeThickness_a)*tan(Theta);
        return ret;
    }
vec ShellRatio_Sr ()
{
    static vec ret;
    if (ret.empty())
        ret=(PI()+2.0*Theta)/PI();
    return ret;
}
vec alpha ()
{
    static vec ret;
    if (ret.empty())
        ret=Phi +( ShellRatio_Sr()-1)%((PI()/4.0)-(2.0*Phi/3.0));
    return ret;
}
vec DepthFooting_Df ()
{
    static vec ret;
    if (ret.empty())
        ret=(breadth_b-WedgeThickness_a)*tan(Theta);
    return ret;
}
vec DepthWedge_Dw ()
{
    static vec ret;
    if (ret.empty())
        ret=DepthFooting_Df()+ (WedgeThickness_a*tan(alpha()));
    return ret;
}
vec DepthbfMin_dbf ()
{
    static vec ret;
    if (ret.empty())
        ret=DepthFooting_Df()/ (WedgeThickness_a);
    return ret;
}
vec DepthbfMax_Dbf ()
{
    static vec ret;
    if (ret.empty())
        ret=DepthFooting_Df()+tan(alpha());
    return ret;
}
vec x0 ()
{
    static vec ret;
    if (ret.empty())
        ret=Radius_Ro*sin(CIT());
    return ret;
}
vec z0 ()
{
    static vec ret;
    if (ret.empty())

```

```

        ret=DepthFooting_Df()-x0();
    return ret;
}
vec H ()
{
    static vec ret;
    if (ret.empty())
        //ret=(breadth_b-WedgeThickness_a - (Theta?
Thickness_t/sin(Theta):0))/cos(Theta);
        ret=(breadth_b-WedgeThickness_a -
Thickness_t/sin(Theta))/cos(Theta);
    return ret;
}
vec Depth_D ()
{
    static vec ret;
    if (ret.empty())
        ret=DepthWedge_Dw() + (Radius_Ro*(sin(CIT())-cos(CIT())));
    return ret;
}
vec WSoil1_w1 ()
{
    static vec ret;
    if (ret.empty())
        ret=SoilG_G/2*pow(WedgeThickness_a,2)*tan(alpha());
    return ret;
}
vec WSoil2_w2 ()
{
    static vec ret;
    if (ret.empty())
        ret=SoilG_G/2*pow(breadth_b-WedgeThickness_a,2)*tan(Theta);
    return ret;
}
vec WSoil3_w3 ()
{
    static vec ret;
    if (ret.empty())
        ret=SoilG_G*WedgeThickness_a*(breadth_b-
WedgeThickness_a)*tan(alpha());
    return ret;
}
vec WSoil4_w4 ()
{
    static vec ret;
    if (ret.empty())
        ret=SoilG_G*(Radius_Ro*sin(CIT())-breadth_b)%DepthWedge_Dw();
    return ret;
}
vec WSoil5_w5 ()
{
    static vec ret;
    if (ret.empty())
        ret=SoilG_G*(Radius_Ro*cos(CIT()))%Depth_D();
    return ret;
}
vec WSoil6_w6 ()

```

```

{
    static vec ret;
    if (ret.empty())
        ret=(SoilG_G/2)*(pow(Radius_Ro,2))*(sin(CIT()))%(1-
cos(CIT()));
    return ret;
}
vec WSoil7_w7 ()
{
    static vec ret;
    if (ret.empty())
        ret=(SoilG_G/2)*pow(Radius_Ro,2)*(sin(CST()))%(1-cos(CIT()));
    return ret;
}
vec WSoil8_w8 ()
{
    static vec ret;
    if (ret.empty())
        ret=(SoilG_G/2)*pow(Depth_D(),2)*(tan(CIT()));
    return ret;
}
vec Wtotal ()
{
    static vec ret;
    if (ret.empty())

        ret=WSoil1_w1()+WSoil2_w2()+WSoil3_w3()+WSoil4_w4()+WSoil5_w5()+WSo
il6_w6()+WSoil7_w7()+WSoil8_w8();
    return ret;
}
vec x1 ()
{
    static vec ret;
    if (ret.empty())
        ret=(Radius_Ro*sin(CIT()))-(2*WedgeThickness_a)/3.0;
    return ret;
}
vec x2 ()
{
    static vec ret;
    if (ret.empty())
        ret=(Radius_Ro*sin(CIT()))-
(WedgeThickness_a+(2*breadth_b))/3.0;
    return ret;
}
vec x3 ()
{
    static vec ret;
    if (ret.empty())
        ret=(Radius_Ro*sin(CIT()))-
((WedgeThickness_a+breadth_b)/2.0);
    return ret;
}
vec x4 ()
{
    static vec ret;
    if (ret.empty())

```

```

        ret=((Radius_Ro*sin(CIT()))-breadth_b)/2.0;
    return ret;
}
vec x5 ()
{
    static vec ret;
    if (ret.empty())
        ret=(Radius_Ro*cos(CIT()))/2.0;
    return ret;
}
vec x6 ()
{
    static vec ret;
    if (ret.empty())
        ret=(1-((3.0/2.0)*cos(CIT()))+((1.0/2.0)*pow(cos(CIT()),3)));
    return ret;
}
vec x7 ()
{
    static vec ret;
    if (ret.empty())
        ret=(sin(CIT()))-(sin(CIT())%cos(CIT()));
    return ret;
}
vec x8 ()
{
    static vec ret;
    if (ret.empty())
        ret=((2.0*Radius_Ro)/3.0)*(x6()/x7());
    return ret;
}
vec x9 ()
{
    static vec ret;
    if (ret.empty())
        ret=(1.0-
((3.0/2.0)*cos(CST()))+((1.0/2.0)*pow(cos(CST()),3.0)));
    return ret;
}
vec x10 ()
{
    static vec ret;
    if (ret.empty())
        ret=(sin(CST()))-(sin(CST())%cos(CST()));
    return ret;
}
vec x11 ()
{
    static vec ret;
    if (ret.empty())
        ret=((2.0*Radius_Ro)/3.0)*(x9()/x10());
    return ret;
}

```

```

vec x12 ()
{
    static vec ret;
    if (ret.empty())
        ret=(Radius_Ro*cos(CIT()))+(1.0/3.0)*Depth_D()%(tan(CIT()));
    return ret;
}
vec Mw1 ()
{
    static vec ret;
    if (ret.empty())
        ret=-ConcreteG__Gc*WedgeThickness_a*((breadth_b-
WedgeThickness_a)*tan(Theta))%(Radius_Ro*sin(CIT))-
(WedgeThickness_a/2.0));
    return ret;
}
vec Mw2 ()
{
    static vec ret;
    if (ret.empty())
        ret=(-
ConcreteG__Gc*H()*Thickness_t%(Radius_Ro*sin(CIT))+(Thickness_t/2.0*sin
(Theta))-(0.5*(WedgeThickness_a+breadth_b)));
    return ret;
}
vec Mw3 ()
{
    static vec ret;
    if (ret.empty())
        ret=(1.0/2.0)*(-ConcreteG__Gc)*(pow(Thickness_t,
2)/(cos(Theta)%sin(Theta))%(Radius_Ro*sin(CIT))-
breadth_b+((2.0*Thickness_t)/3.0*sin(Theta)));
    return ret;
}
vec Mw4 ()
{
    static vec ret;
    if (ret.empty())
        ret=-(1.0/2.0)*SoilG_G*((breadth_b-
WedgeThickness_a)*tan(Theta)-(Thickness_t/(cos(Theta))))%(breadth_b-
WedgeThickness_a-(Thickness_t/sin(Theta))%(Radius_Ro*sin(CIT))-
((1.0/3.0)*((2*WedgeThickness_a)+breadth_b))-(Thickness_t/(sin(Theta))));
    return ret;
}
vec Mwedge ()
{
    static vec ret;
    if (ret.empty())
        ret=(-
(1.0/2.0)*SoilG_G*(pow(WedgeThickness_a,2))*tan(alpha))%(Radius_Ro*sin(
CIT))-(WedgeThickness_a/3.0));
    return ret;
}
vec MwFooting ()
{
    static vec ret;

```

```

        if (ret.empty())
            ret=Mw1()+Mw2()+Mw3()+Mw4();
        return ret;
    }
vec Mw ()
{
    static vec ret;
    if (ret.empty())

        ret=MwFooting()+ (WSoil5_w5 () %x5 ())+(WSoil7_w7 () %x11 ())+(WSoil8_w8 ()
%x12 ())-
        ((WSoil1_w1 () %x1 ())+(WSoil2_w2 () %x2 ())+(WSoil3_w3 () %x3 ())+(WSoil4_w4 () %x4
        ())+ (WSoil6_w6 () %x8 ()));
        return ret;
    }
vec Rc ()
{
    static vec ret;
    if (ret.empty())
        ret=2*cohesion_c*Depth_D () %tan (CIT ());
    return ret;
}
vec Rg ()
{
    static vec ret;
    if (ret.empty())
        ret=((SoilG_G/2.0) *(pow (Depth_D (), 2) ) % (pow (tan (CIT ()), 2) ));
    return ret;
}
vec Rh ()
{
    static vec ret;
    if (ret.empty())
        ret=Rc () +Rg ();
    return ret;
}
vec ec ()
{
    static vec ret;
    if (ret.empty())
        ret=Radius_Ro*sin (CIT ()) - (Depth_D () /2.0);
    return ret;
}
vec eg ()
{
    static vec ret;
    if (ret.empty())
        ret=Radius_Ro*sin (CIT ()) - (Depth_D () /3.0);
    return ret;
}
vec Mrp ()
{
    static vec ret;
    if (ret.empty())
        ret=(Rc () %ec ()) + (Rg () %eg ());
    return ret;
}

```



```

vec Tau1 ()
{
    static vec ret;
    if (ret.empty())
        ret=cohesion_c*c1();
    return ret;
}
vec Tau2 ()
{
    static vec ret;
    if (ret.empty())

        ret=c5()%(Radius_Ro*SoilG_G*c7()+SoilG_G*DepthWedge_Dw()%c3()+cohes
ion_c*c1());
    return ret;
}
vec Taup ()
{
    static vec ret;
    if (ret.empty())
        ret=SoilG_G*sin(Phi)%tan(CIT())%Depth_D()+Tau1();
    return ret;
}
vec Tauc ()
{
    static vec ret;
    if (ret.empty())
        ret=Tau2()%exp(-2*CST())%tan(Phi)-
(Radius_Ro*SoilG_G*c6())/c4());
    return ret;
}
vec Mf ()
{
    static vec ret;
    if (ret.empty())

        ret=(pow(Radius_Ro,2))*Tau2()%c20()+ (pow(Radius_Ro,3))*SoilG_G*c21(
);
    return ret;
}
vec Cv ()
{
    static vec ret;
    if (ret.empty())
        ret=cohesion_c*DepthWedge_Dw();
    return ret;
}
vec Tpv ()
{
    static vec ret;
    if (ret.empty())

        ret=(SoilG_G/2.0)*tan(CIT())%(pow(Depth_D(),2))+cohesion_c*Depth_D(
);
    return ret;
}
vec Tcv ()

```

```

{
    static vec ret;
    if (ret.empty())

        ret=(SoilG_G*Radius_Ro*DepthWedge_Dw()%c12())+(SoilG_G*(pow(Radius_
Ro,2))*c13()+cohesion_c*Radius_Ro*c14());
        return ret;
}
vec Pv ()
{
    static vec ret;
    if (ret.empty())
        ret=(Tpv()+Tcv()-Cv()-Wtotal());
    return ret;
}
vec Pvfg ()
{
    static vec ret;
    if (ret.empty())

        ret=SoilG_G*pow(breadth_b,2)*(c16()*(Radius_Ro/pow(breadth_b,2))+c1
7()*Radius_Ro/breadth_b*tan(alpha()))+(tan(alpha())/2.0);
        return ret;
}
vec Pvfq ()
{
    static vec ret;
    if (ret.empty())

        ret=SoilG_G*Depth_D()*breadth_b*(Radius_Ro/breadth_b*c17()+1);
        return ret;
}
vec Pvfc ()
{
    static vec ret;
    if (ret.empty())
        ret=cohesion_c*breadth_b*Radius_Ro/breadth_b*c18();
    return ret;
}
vec Pvft ()
{
    static vec ret;
    if (ret.empty())
        ret=Pvfg()+Pvfq()+Pvfc();
    return ret;
}
vec Quq ()
{
    static vec ret;
    if (ret.empty())

        ret=SoilG_G*breadth_b*((Radius_Ro/pow(breadth_b,2))*c16()+Radius_Ro
/breadth_b*tan(alpha()))%c17()-(tan(Theta)/2.0);
        return ret;
}
vec Quq ()
{

```

```

        static vec ret;
        if (ret.empty())
            ret=SoilG_G*DepthFooting_Df()%(Radius_Ro/breadth_b*c17()+1);
        return ret;
    }
vec Quc ()
{
    static vec ret;
    if (ret.empty())
        ret=cohesion_c*(Radius_Ro/breadth_b*c18()+tan(alpha()));
    return ret;
}
vec Qu ()
{
    static vec ret;
    if (ret.empty())
        ret=Qug()+Quq()+Quc();
    return ret;
}
vec Pvq ()
{
    static vec ret;
    if (ret.empty())

        ret=Qu()*breadth_b+(SoilG_G/2)*pow(breadth_b,2)*(tan(alpha()+tan(T
heta))-cohesion_c*breadth_b*tan(alpha()));
        return ret;
}
vec Ph ()
{
    static vec ret;
    if (ret.empty())
        ret=Pv()%tan(alpha()-Phi);
    return ret;
}
vec Mt1 ()
{
    static vec ret;
    if (ret.empty())
        ret=-Qu()*breadth_b*(Radius_Ro*sin(CIT())-(breadth_b/2.0));
    return ret;
}
vec Mt2 ()
{
    static vec ret;
    if (ret.empty())
        ret=-
        (SoilG_G/2.0)*(pow(WedgeThickness_a,2))*(tan(alpha()+tan(Theta))%((Radiu
s_Ro*sin(CIT()))-(WedgeThickness_a/3.0)));
        return ret;
}
vec Mt3 ()
{
    static vec ret;
    if (ret.empty())

```

```

        ret=cohesion_c*WedgeThickness_a*Radius_Ro*((tan(alpha())%sin(CIT()))
)-cos(CIT()));
        return ret;
    }
vec Mt ()
{
    static vec ret;
    if (ret.empty())
        ret=Mt1()+Mt2()+Mt3();
    return ret;
}
vec Mtot ()
{
    static vec ret;
    if (ret.empty())
        ret=(Mw()+Mf ())+ (Mrp ()+Mt ()) + Mwedge();
    return ret;
}
vec FRow3i ()
{
    static vec ret;
    if (ret.empty())
        ret=(SoilG_G*(pow(breadth_b,3))/6.0)*(sin(CIT())-cos(CIT()));
    return ret;
}
vec FRow3a ()
{
    static vec ret;
    if (ret.empty())
        ret=FRow3i ()%(3*pow(cos(CIT()),2));
    return ret;
}
vec FRow3b ()
{
    static vec ret;
    if (ret.empty())
        ret=FRow3i ()*3*tan(CIT())%cos(CIT())%(sin(CIT())-cos(CIT()));
    return ret;
}
vec FRow3c ()
{
    static vec ret;
    if (ret.empty())
        ret=FRow3i ()%pow(tan(CIT()),2)%pow(sin(CIT())-cos(CIT()),2);
    return ret;
}
vec FRow3d ()
{
    static vec ret;
    if (ret.empty())
        ret=-
(SoilG_G*pow(breadth_b,3)/6.0)*(3*sqrt((double)2)*sin(Phi/2));
    return ret;
}
vec FRow3e ()
{

```

```

        static vec ret;
        if (ret.empty())
            ret=(SoilG_G*pow(breadth_b,3)/6.0)*pow(sin(CIT()),3);
        return ret;
    }
vec FRow3f ()
{
    static vec ret;
    if (ret.empty())
        ret=-(SoilG_G*pow(breadth_b,3)/6.0)*(cos(CIT()));
    return ret;
}
vec FRow3 ()
{
    static vec ret;
    if (ret.empty())
        ret=FRow3a()+FRow3b()+FRow3c()+FRow3d()+FRow3e()+FRow3f();
    return ret;
}
vec FRof3 ()
{
    static vec ret;
    if (ret.empty())
        ret=SoilG_G*pow(breadth_b,3)*c18();
    return ret;
}
vec FRorp3 ()
{
    static vec ret;
    if (ret.empty())
        ret.set_size(Phi.n_rows);
        ret.fill(0);
    return ret;
}
vec FRorp3a ()
{
    static vec ret;
    if (ret.empty())

        ret=0.5*pow(breadth_b,3)*pow(tan(CIT()),2)*(1.0/3.0)%pow(tan(CIT()),
,2)%pow(c1(),3);
        return ret;
}
vec FRorp3b ()
{
    static vec ret;
    if (ret.empty())
        ret=0.5*pow(breadth_b,3)*pow(tan(CIT()),2)%c1()%sin(CIT());
    return ret;
}
vec FRorp32 ()
{
    static vec ret;
    if (ret.empty())
        ret=FRorp3a()+FRorp3b();
    return ret;
}

```

```

vec FRot3 ()
{
    static vec ret;
    if (ret.empty())
        ret=-(SoilG_G*pow(breadth_b, 3) *c22 () %sin (CIT ()) );
    return ret;
}
vec FRo3 ()
{
    static vec ret;
    if (ret.empty())
        ret=FRow3()+FRof3()+FRorp3 () +FRof3 ();
    return ret;
}
vec FRow2i ()
{
    static vec ret;
    if (ret.empty())
        ret=(0.5*SoilG_G*pow (breadth_b, 2)) *DepthWedge_Dw ();
    return ret;
}
vec FRow2a ()
{
    static vec ret;
    if (ret.empty())
        ret=FRow2i () %pow (cos (CIT ()), 2);
    return ret;
}
vec FRow2b ()
{
    static vec ret;
    if (ret.empty())
        ret=FRow2i () % (2*tan (CIT ()) %cos (CIT ()) % (sin (CIT ()) -
cos(CIT())));
    return ret;
}
vec FRow2c ()
{
    static vec ret;
    if (ret.empty())
        ret=FRow2i () % (-pow (sin (CIT ()), 2));
    return ret;
}
vec FRow2 ()
{
    static vec ret;
    if (ret.empty())
        ret=FRow2a () +FRow2b () +FRow2c ();
    return ret;
}
vec FRof2a ()
{
    static vec ret;
    if (ret.empty())
        ret=SoilG_G*pow (breadth_b, 2) *DepthWedge_Dw () %c19 ();
    return ret;
}

```

```

vec FRof2b ()
{
    static vec ret;
    if (ret.empty())
        ret=cohesion_c*pow(breadth_b,2)*c20();
    return ret;
}
vec FRof2 ()
{
    static vec ret;
    if (ret.empty())
        ret=FRof2a()+FRof2b();
    return ret;
}
vec FRorp2a ()
{
    static vec ret;
    if (ret.empty())

        ret=0.5*pow(breadth_b,2)*tan(CIT())%(SoilG_G*DepthWedge_Dw())%pow(tan(CIT()),3)%pow(c1(),2)%Mrp();
    return ret;
}
vec FRorp2b ()
{
    static vec ret;
    if (ret.empty())
        ret=-0.5*pow(breadth_b,2)*tan(CIT())%pow(c1(), 2)%Mrp();
    return ret;
}
vec FRorp2c ()
{
    static vec ret;
    if (ret.empty())

        ret=pow(breadth_b,2)*tan(CIT())*SoilG_G*DepthWedge_Dw()%tan(CIT())%sin(CIT())%c1()%Mrp();
    return ret;
}
vec FRorp2d ()
{
    static vec ret;
    if (ret.empty())

        ret=pow(breadth_b,2)*tan(CIT())*2*cohesion_c%sin(CIT())%c1()%Mrp();
    return ret;
}
vec FRorp2 ()
{
    static vec ret;
    if (ret.empty())
        ret=FRorp2a()+FRorp2b()+FRorp2c()+FRorp2d();
    return ret;
}
vec FRot2a ()
{
    static vec ret;

```

```

        if (ret.empty())
            ret=-
pow(breadth_b,2)*c24()%sin(CIT())%(SoilG_G*WedgeThickness_a*tan(alpha()))
;
        return ret;
    }
vec FRot2b ()
{
    static vec ret;
    if (ret.empty())
        ret=pow(breadth_b,2)*c24()%sin(CIT())*cohesion_c;
    return ret;
}
vec FRot2c ()
{
    static vec ret;
    if (ret.empty())
        ret=-0.5*SoilG_G*pow(breadth_b,3)*c22();
    return ret;
}
vec FRot2 ()
{
    static vec ret;
    if (ret.empty())
        ret=FRot2a()+FRot2b()+FRot2c();
    return ret;
}
vec FRow2 ()
{
    static vec ret;
    if (ret.empty())
        ret=FRow2()+FRowf2()+FRowrp2()+FRot2();
    return ret;
}
vec FRowli ()
{
    static vec ret;
    if (ret.empty())
        ret = 0.5*SoilG_G*breadth_b*Ones;
    return ret;
}
vec FRowlii ()
{
    static vec ret;
    if (ret.empty())
        ret=FRowli()%pow(DepthWedge_Dw(),2)%tan(CIT());
    return ret;
}
vec FRowliii ()
{
    static vec ret;
    if (ret.empty())

        ret=WedgeThickness_a*breadth_b*Thickness_t*sin(CIT())*ConcreteG__Gc
;
    return ret;
}

```



```

vec FRowliv ()
{
    static vec ret;
    if (ret.empty())
        ret=1.0/ (cos (Theta));
    return ret;
}
vec FRowlv ()
{
    static vec ret;
    if (ret.empty())
        ret=breadth_b*sin(CIT())*SoilG_G*tan(alpha ());
    return ret;
}
vec FRowlvi ()
{
    static vec ret;
    if (ret.empty())
        ret=(SoilG_G*Thickness_t)/cos(Theta);
    return ret;
}
vec FRowla ()
{
    static vec ret;
    if (ret.empty())
        ret=FRowlii()%((cos(CIT())));
    return ret;
}
vec FRowlb ()
{
    static vec ret;
    if (ret.empty())
        ret=FRowlii()%tan(CIT())%(sin(CIT())-cos(CIT()));
    return ret;
}
vec FRowlc ()
{
    static vec ret;
    if (ret.empty())
        ret=FRowli ()%sin(CIT ())*pow(breadth_b,2);
    return ret;
}
vec FRowld ()
{
    static vec ret;
    if (ret.empty())
        ret=-FRowli()%sin(CIT())*(pow(WedgeThickness_a,2));
    return ret;
}
vec FRowle ()
{
    static vec ret;
    if (ret.empty())
        ret=FRowli ()%sin(CIT ())*pow(WedgeThickness_a,2)%tan(CIT());
    return ret;
}
vec FRowlf ()

```

```

{
    static vec ret;
    if (ret.empty())
        ret=FRowliii()%(DepthFooting_Df()/Thickness_t);
    return ret;
}
vec FRowlg ()
{
    static vec ret;
    if (ret.empty())

        ret=FRowliii()%(Thickness_t/(2.0*WedgeThickness_a*cos(Theta)%sin(Th
eta)));
    return ret;
}
vec FRowlh ()
{
    static vec ret;
    if (ret.empty())
        ret=FRowliv()*(breadth_b/WedgeThickness_a);
    return ret;
}
vec FRowlj ()
{
    static vec ret;
    if (ret.empty())
        ret=-FRowliv();
    return ret;
}
vec FRowlk ()
{
    static vec ret;
    if (ret.empty())
        ret=-FRowliv()%(Thickness_t/(WedgeThickness_a*sin(Theta)));
    return ret;
}
vec FRowll ()
{
    static vec ret;
    if (ret.empty())
        ret=FRowlv()*(0.5*pow(WedgeThickness_a,2));
    return ret;
}
vec FRowlm ()
{
    static vec ret;
    if (ret.empty())
        ret=FRowlv()*(0.5*pow(breadth_b,2));
    return ret;
}
vec FRowln ()
{
    static vec ret;
    if (ret.empty())
        ret=-FRowlv()*(WedgeThickness_a*breadth_b);
    return ret;
}

```

```

vec FRowlo ()
{
    static vec ret;
    if (ret.empty())
        ret=FRowlvi()%sin(CIT())*WedgeThickness_a*breadth_b;
    return ret;
}
vec FRowlp ()
{
    static vec ret;
    if (ret.empty())
        ret=-FRowlvi()%sin(CIT())*pow(breadth_b,2);
    return ret;
}
vec FRowlq ()
{
    static vec ret;
    if (ret.empty())

        ret=FRowlvi()*breadth_b*sin(CIT())%(Thickness_t/(2*sin(Theta)));
    return ret;
}
vec FRowlr ()
{
    static vec ret;
    if (ret.empty())
        ret=FRowli()*pow(WedgeThickness_a,2)%tan(alpha())%sin(CIT());
    return ret;
}
vec FRowl ()
{
    static vec ret;
    if (ret.empty())

        ret=FRowla()+FRowlb()+FRowlc()+FRowld()+FRowle()+FRowlf()+FRowlg()+
FRowlh()+FRowlj()+FRowlk()+FRowll()+FRowlm()+FRowln()+FRowlo()+FRowlp()+F
Rowlq()+FRowlr();
    return ret;
}
vec FRowf1 ()
{
    static vec ret;
    if (ret.empty())
        ret = 0*Ones;
    return ret;
}
vec FRorpla ()
{
    static vec ret;
    if (ret.empty())

        ret=0.5*breadth_b*pow(DepthWedge_Dw(),2)%pow(tan(CIT()),4)*SoilG_G%
c1()%Mrp();
    return ret;
}
vec FRorplb ()
{

```

```

        static vec ret;
        if (ret.empty())
            ret=-
2*breadth_b*DepthWedge_Dw()%tan(CIT())*cohesion_c%c1 () %Mrp ();
        return ret;
    }
vec FRorplc ()
{
    static vec ret;
    if (ret.empty())

        ret=0.5*breadth_b*SoilG_G*pow(DepthWedge_Dw(), 2) %pow (tan (CIT ()), 2) %
sin(CIT())%Mrp ();
        return ret;
    }
vec FRorpld ()
{
    static vec ret;
    if (ret.empty())

        ret=2*breadth_b*DepthWedge_Dw()%tan(CIT())%sin(CIT())*cohesion_c%Mr
p ();
        return ret;
    }
vec FRorpl ()
{
    static vec ret;
    if (ret.empty())
        ret=FRorpla()+FRorplb()+FRorplc()+FRorpld();
    return ret;
}
vec FRotla ()
{
    static vec ret;
    if (ret.empty())
        ret=SoilG_G*DepthFooting_Df()*pow(breadth_b, 2) %sin (CIT ());
    return ret;
}
vec FRotlb ()
{
    static vec ret;
    if (ret.empty())
        ret=FRotla () %c23 ();
    return ret;
}
vec FRotlc ()
{
    static vec ret;
    if (ret.empty())

        ret=0.5*pow(breadth_b, 2) *c24 () *SoilG_G*WedgeThickness_a%tan(alpha()
);
        return ret;
    }
vec FRotld ()
{
    static vec ret;

```

```

        if (ret.empty())
            ret=-0.5*pow(breadth_b,2)*c24()*cohesion_c;
        return ret;
    }
vec FRotle ()
{
    static vec ret;
    if (ret.empty())
        ret=-
0.5*SoilG_G*pow(WedgeThickness_a,2)*breadth_b*pow(tan(alpha()),2);
    return ret;
}
vec FRotlf ()
{
    static vec ret;
    if (ret.empty())

        ret=WedgeThickness_a*breadth_b*tan(alpha())%sin(CIT())*SoilG_G*Wedg
eThickness_a;
    return ret;
}
vec FRotlg ()
{
    static vec ret;
    if (ret.empty())
        ret=-
WedgeThickness_a*breadth_b*tan(alpha())%sin(CIT())*SoilG_G*pow(breadth_b,
2);
    return ret;
}
vec FRotlh ()
{
    static vec ret;
    if (ret.empty())

        ret=WedgeThickness_a*breadth_b*tan(alpha())%sin(CIT())*2*cohesion_c
;
    return ret;
}
vec FRotli ()
{
    static vec ret;
    if (ret.empty())
        ret=-cohesion_c*WedgeThickness_a*cos(CIT());
    return ret;
}
vec FRotl ()
{
    static vec ret;
    if (ret.empty())

        ret=FRotla()+FRotlb()+FRotlc()+FRotld()+FRotle()+FRotlf()+FRotlg()+
FRotlh()+FRotli();
    return ret;
}
vec FRol ()
{

```

```

        static vec ret;
        if (ret.empty())
            ret=FRow1()+FRowf1()+FRorpl()+FRot1();
        return ret;
    }
vec FRow0i ()
{
    static vec ret;
    if (ret.empty())
        ret=(SoilG_G/6.0)*tan(Theta);
    return ret;
}
vec FRow0a ()
{
    static vec ret;
    if (ret.empty())
        ret=FRow0i()*pow(WedgeThickness_a,3);
    return ret;
}
vec FRow0b ()
{
    static vec ret;
    if (ret.empty())
        ret=FRow0i()*(-5*pow(breadth_b,3));
    return ret;
}
vec FRow0c ()
{
    static vec ret;
    if (ret.empty())
        ret=-(SoilG_G/6.0)*pow(WedgeThickness_a,3)*tan(alpha());
    return ret;
}
vec FRow0d ()
{
    static vec ret;
    if (ret.empty())
        ret=(SoilG_G/6.0)*pow(DepthWedge_Dw(),2)%pow(tan(CIT()),2);
    return ret;
}
vec FRow0e ()
{
    static vec ret;
    if (ret.empty())
        ret=(breadth_b*pow(Thickness_t,2))/(cos(Theta)%sin(Theta));
    return ret;
}
vec FRow0f ()
{
    static vec ret;
    if (ret.empty())
        ret=-FRow0e()*(0.5*ConcreteG__Gc);
    return ret;
}
vec FRow0g ()
{
    static vec ret;

```

```

        if (ret.empty())
            ret=(Thickness_t*(pow(WedgeThickness_a,2)))/(2.0*cos(Theta));
        return ret;
    }
vec FRow0h ()
{
    static vec ret;
    if (ret.empty())
        ret=-(Thickness_t*pow(breadth_b,2))/(2.0*cos(Theta));
    return ret;
}
vec FRow0j ()
{
    static vec ret;
    if (ret.empty())

        ret=(pow(Thickness_t,3)*ConcreteG__Gc)/(3.0*cos(Theta)%pow(sin(Theta),2));
    return ret;
}
vec FRow0k ()
{
    static vec ret;
    if (ret.empty())

        ret=(pow(Thickness_t,3)*ConcreteG__Gc)/(2.0*cos(Theta)%pow(sin(Theta),2));
    return ret;
}
vec FRow0l ()
{
    static vec ret;
    if (ret.empty())
        ret=-
0.5*(pow(WedgeThickness_a,2))*DepthFooting_Df()*ConcreteG__Gc;
    return ret;
}
vec FRow0ii ()
{
    static vec ret;
    if (ret.empty())
        ret=(1/(6.0*cos(Theta)%pow(sin(Theta),2)));
    return ret;
}
vec FRow0iii ()
{
    static vec ret;
    if (ret.empty())
        ret=(3*sin(Theta)*pow(WedgeThickness_a,2)*breadth_b)-
sin(Theta)*pow(breadth_b,3)-2*sin(Theta)*pow(WedgeThickness_a,3)-
3*sin(Theta)%pow(cos(Theta),2)*pow(WedgeThickness_a,2)*breadth_b+sin(Theta)
a)%pow(cos(Theta),2)*pow(breadth_b,3)+2*sin(Theta)%pow(cos(Theta),2)*pow(
WedgeThickness_a,3)-
8*WedgeThickness_a*pow(Thickness_t,2)*sin(Theta)+5*breadth_b*pow(Thicknes
s_t,2)*sin(Theta)+Thickness_t*pow(cos(Theta),2)*pow(breadth_b,2)+7*Thickn
ess_t*pow(cos(Theta),2)*pow(WedgeThickness_a,2)-3*pow(Thickness_t,3)-
7*pow(WedgeThickness_a,2)*Thickness_t-

```

```

8*Thickness_t*pow(cos(Theta),2)*WedgeThickness_a*breadth_b+8*WedgeThickne
ss_a*Thickness_t*breadth_b-pow(breadth_b,2)*Thickness_t;
    return ret;
}
vec FRow0m ()
{
    static vec ret;
    if (ret.empty())
        ret=FRow0ii()%FRow0iii();
    return ret;
}
vec FRow0n ()
{
    static vec ret;
    if (ret.empty())
        ret=-
(1.0/6.0)*pow(WedgeThickness_a,3)*breadth_b*SoilG_G*tan(alpha());
    return ret;
}
vec FRow0 ()
{
    static vec ret;
    if (ret.empty())

        ret=FRow0a()+FRow0b()+FRow0c()+FRow0d()+FRow0e()+FRow0f()+FRow0g()+
FRow0h()+FRow0j()+FRow0k()+FRow0l()+FRow0m()+FRow0n();
    return ret;
}
vec FRof0 ()
{
    static vec ret;
    if (ret.empty())
        ret = 0*Ones;
    return ret;
}
vec FRorp0a ()
{
    static vec ret;
    if (ret.empty())

        ret=(pow(DepthWedge_Dw(),3)/6.0)*SoilG_G*pow(tan(CIT()),4)%Mrp();
    return ret;
}
vec FRorp0b ()
{
    static vec ret;
    if (ret.empty())
        ret=-pow(DepthWedge_Dw(),2)%tan(CIT())*cohesion_c%Mrp();
    return ret;
}
vec FRorp0 ()
{
    static vec ret;
    if (ret.empty())
        ret=FRorp0a()+FRorp0b();
    return ret;
}

```



```

vec FRot0i ()
{
    static vec ret;
    if (ret.empty())
        ret=-0.5*SoilG_G*pow(breadth_b,2)*Ones;
    return ret;
}

vec FRot0a ()
{
    static vec ret;
    if (ret.empty())
        ret=FRot0i ()%DepthFooting_Df ();
    return ret;
}

vec FRot0b ()
{
    static vec ret;
    if (ret.empty())
        ret=FRot0i ()%c23 ();
    return ret;
}

vec FRot0c ()
{
    static vec ret;
    if (ret.empty())
        ret=FRot0i ()*WedgeThickness_a*breadth_b*tan(alpha());
    return ret;
}

vec FRot0d ()
{
    static vec ret;
    if (ret.empty())
        ret=FRot0i ()*(-
pow(WedgeThickness_a,2)/breadth_b)%tan(alpha());
    return ret;
}

vec FRot0e ()
{
    static vec ret;
    if (ret.empty())
        ret=FRot0i ()*(-
WedgeThickness_a*cohesion_c)/(SoilG_G*breadth_b)%tan(alpha());
    return ret;
}

vec FRot0f ()
{
    static vec ret;
    if (ret.empty())

        ret=FRot0i ()*(pow(WedgeThickness_a,3)/pow(breadth_b,2))%tan(alpha()
);
    return ret;
}

vec FRot0 ()
{

```

```

        static vec ret;
        if (ret.empty())
            ret=FRot0a()+FRot0b()+FRot0c()+FRot0d()+FRot0e()+FRot0f();
        return ret;
    }
vec FRo0 ()
{
    static vec ret;
    if (ret.empty())
        ret=FRow0()+FRof0()+FRorp0()+FRot0();
    return ret;
}
vec FRo ()
{
    static vec ret;
    if (ret.empty())

        ret=(FRo3()*(Radius_Ro/pow(breadth_b,3)))+(FRo2()*(Radius_Ro/pow(breadth_b,2)))+(FRo1()*Radius_Ro/breadth_b)+FRo0();
        return ret;
}
vec FRod1 ()
{
    static vec ret;
    if (ret.empty())

        ret=3.0*(Radius_Ro/pow(breadth_b,2))*FRo3()+2*Radius_Ro/breadth_b*FRo2()+FRo1();
        return ret;
}
vec DRo ()
{
    static vec ret;
    if (ret.empty())
        ret=-FRo()/FRod1();
    return ret;
}
vec Rof ()
{
    static vec ret;
    if (ret.empty())
        ret = Radius_Ro/breadth_b*Ones;
    return ret;
}
vec Rf ()
{
    static vec ret;
    if (ret.empty())
        ret = Radius_Ro*Ones;
    return ret;
}
vec FRof ()
{
    static vec ret;
    if (ret.empty())
        ret=FRo();
    return ret;
}

```

```

}
vec Mtotf ()
{
    static vec ret;
    if (ret.empty())
        ret=Mtot ();
    return ret;
}
vec qufg ()
{
    static vec ret;
    if (ret.empty())

        ret=SoilG_G*breadth_b*(pow(Rof(),2)%c16()+Rof()*tan(alpha())%c17() -
(tan(Theta)/2.0));
    return ret;
}
vec qufq ()
{
    static vec ret;
    if (ret.empty())
        ret=SoilG_G*DepthFooting_Df()%(Rof() %c17()+1);
    return ret;
}
vec qufc ()
{
    static vec ret;
    if (ret.empty())
        ret=cohesion_c*(Rof()%c18()+tan(alpha()));
    return ret;
}
vec quf ()
{
    static vec ret;
    if (ret.empty())
        ret=qufg()+qufq()+qufc();
    return ret;
}
vec Fht ()
{
    static vec ret;
    if (ret.empty())
        ret=quf()*breadth_b*tan(Theta)-cohesion_c*breadth_b;
    return ret;
}
vec Pvq2 ()
{
    static vec ret;
    if (ret.empty())

        ret=quf()*breadth_b+(SoilG_G/2.0)*pow(breadth_b,2)*(tan(alpha())+ta
n(Theta))-cohesion_c*breadth_b*tan(alpha());
    return ret;
}
vec L ()
{
    static vec ret;

```

```

        if (ret.empty())

            ret=breadth_b*(Rof()+DepthFooting_Df()*sin(CIT()))/cos(CIT());
            return ret;
    }
    vec Ng ()
    {
        static vec ret;
        if (ret.empty())
            ret=pow(Rof(),2)%c16()+Rof()*tan(alpha())%c17()-
(tan(Theta)/2.0);
            return ret;
    }
    vec Nq ()
    {
        static vec ret;
        if (ret.empty())
            ret=1+Rof()%c17();
            return ret;
    }
    vec Nc ()
    {
        static vec ret;
        if (ret.empty())
            ret=Rof()%c18()+tan(alpha());
            return ret;
    }
    vec qux ()
    {
        static vec ret;
        if (ret.empty())

            ret=cohesion_c*Nc()+DepthFooting_Df()*SoilG_G*Nq()+breadth_b*SoilG_
G*Nq();
            return ret;
    }
    vec Qut ()
    {
        static vec ret;
        if (ret.empty())
            ret=qux()%pow(Depth_D(),2);
            return ret;
    }
    vec Mxw ()
    {
        static vec ret;
        if (ret.empty())

            ret=pow(Rof(),3)%FRow3()+pow(Rof(),2)%FRow2()+Rof()%FRow1()+FRow0()
;
            return ret;
    }
    vec Mxf ()
    {
        static vec ret;
        if (ret.empty())

```

```

        ret=pow(Rof(),3)%FRot3()+pow(Rof(),2)%FRof2()+Rof()%FRof1()+FRof0()
;
        return ret;
}
vec Mxrp ()
{
    static vec ret;
    if (ret.empty())

        ret=pow(Rof(),3)%FRorp3()+pow(Rof(),2)%FRorp2()+Rof()%FRorp1()+FRor
p0();
        return ret;
}
vec Mxt ()
{
    static vec ret;
    if (ret.empty())

        ret=pow(Rof(),3)%FRot3()+pow(Rof(),2)%FRot2()+Rof()%FRot1()+FRot0()
;
        return ret;
}
vec Mxtotal ()
{
    static vec ret;
    if (ret.empty())
        ret=Mxw()+Mxf()+Mxrp()+Mxt();
    return ret;
}
/////double Mwftg-Mtot ()
///// {
/////     static double ret = 0;
/////     if (ret.empty())
/////         ret=MwFooting()-Mtot();
/////     return ret;
///// }
//cout << "Phi:" << Phi << endl;
//cout << "Theta:" << Theta << endl;
//cout << setprecision(15);
//cout << CIT() << endl;
//cout << CST() << endl;
//cout << c3() << endl;
//cout << c2() << endl;
//cout << c3() << endl;
//cout << c4() << endl;
//cout << c5() << endl;
//cout << c6() << endl;
//cout << c7() << endl;
//cout << c8() << endl;
//cout << c9() << endl;
//cout << c10() << endl;
//cout << c11() << endl;
//cout << c12() << endl;
//cout << c13() << endl;
//cout << c14() << endl;
//cout << c15() << endl;

```

```

//cout << c16() << endl;
//cout << c17() << endl;
//cout << c18() << endl;
//cout << c19() << endl;
//cout << c20() << endl;
//cout << c21() << endl;
//cout << c22() << endl;
//cout << c23() << endl;
//cout << c24() << endl;
//cout << endl;
//cout << DepthConcrete_Dc() << endl;
//cout << ShellRatio_Sr() << endl;
//cout << alpha() << endl;
//cout << DepthFooting_Df() << endl;
//cout << DepthWedge_Dw() << endl;
//cout << DepthbfMin_dbf() << endl;
//cout << DepthbfMax_Dbf() << endl;
//cout << x0() << endl;
//cout << z0() << endl;
//cout << H() << endl;
//cout << Depth_D() << endl;
//cout << WSoil1_w1() << endl;
//cout << WSoil2_w2() << endl;
//cout << WSoil3_w3() << endl;
//cout << WSoil4_w4() << endl;
//cout << WSoil5_w5() << endl;
//cout << WSoil6_w6() << endl;
//cout << WSoil7_w7() << endl;
//cout << WSoil8_w8() << endl;
//cout << Wtotal() << endl;
//cout << x1() << endl;
//cout << x2() << endl;
//cout << x3() << endl;
//cout << x4() << endl;
//cout << x5() << endl;
//cout << x6() << endl;
//cout << x7() << endl;
//cout << x8() << endl;
//cout << x9() << endl;
//cout << x10() << endl;
//cout << x11() << endl;
//cout << x12() << endl;
//cout << Mw1() << endl;
//cout << Mw2() << endl;
//cout << Mw3() << endl;
//cout << Mw4() << endl;
//cout << Mwedge() << endl;
//cout << MwFooting() << endl;
//cout << Mw() << endl;
//cout << Rc() << endl;
//cout << Rg() << endl;
//cout << Rh() << endl;
//cout << ec() << endl;
//cout << eg() << endl;
//cout << Mrp() << endl;
//cout << Tau1() << endl;
//cout << Tau2() << endl;

```

```

//cout << Taup() << endl;
//cout << Tauc() << endl;
//cout << Mf() << endl;
//cout << Cv() << endl;
//cout << Tpv() << endl;
//cout << Tcv() << endl;
//cout << Pv() << endl;
//cout << Pvfg() << endl;
//cout << Pvfq() << endl;
//cout << Pvfc() << endl;
//cout << Pvft() << endl;
//cout << Quq() << endl;
//cout << Quq() << endl;
//cout << Quc() << endl;
//cout << Qu() << endl;
//cout << Pvq() << endl;
//cout << Ph() << endl;
//cout << Mt1() << endl;
//cout << Mt2() << endl;
//cout << Mt3() << endl;
//cout << Mt() << endl;
//cout << Mtot() << endl;
//cout << FRow3i() << endl;
//cout << FRow3a() << endl;
//cout << FRow3b() << endl;
//cout << FRow3c() << endl;
//cout << FRow3d() << endl;
//cout << FRow3e() << endl;
//cout << FRow3f() << endl;
//cout << FRow3() << endl;
//cout << FRow3() << endl;
//cout << FRorp3() << endl;
//cout << FRorp3a() << endl;
//cout << FRorp3b() << endl;
//cout << FRorp32() << endl;
//cout << FRow3() << endl;
//cout << FRow3() << endl;
//cout << FRow2i() << endl;
//cout << FRow2a() << endl;
//cout << FRow2b() << endl;
//cout << FRow2c() << endl;
//cout << FRow2() << endl;
//cout << FRow2a() << endl;
//cout << FRow2b() << endl;
//cout << FRow2() << endl;
//cout << FRorp2a() << endl;
//cout << FRorp2b() << endl;
//cout << FRorp2c() << endl;
//cout << FRorp2d() << endl;
//cout << FRorp2() << endl;
//cout << FRow2a() << endl;
//cout << FRow2b() << endl;
//cout << FRow2c() << endl;
//cout << FRow2() << endl;
//cout << FRow2() << endl;
//cout << FRow1i() << endl;
//cout << FRow1ii() << endl;

```



```

//cout << FRorp0a() << endl;
//cout << FRorp0b() << endl;
//cout << FRorp0 () << endl;
//cout << FRot0i () << endl;
//cout << FRot0a () << endl;
//cout << FRot0b () << endl;
//cout << FRot0c () << endl;
//cout << FRot0d () << endl;
//cout << FRot0e () << endl;
//cout << FRot0f () << endl;
//cout << FRot0() << endl;
//cout << FRo0 () << endl;
//cout << FRo () << endl;
//cout << FRod1 () << endl;
//cout << DRo () << endl;
//cout << Rof () << endl;
//cout << Rf () << endl;
//cout << FRof () << endl;
//cout << Mtotf () << endl;
//cout << qufg () << endl;
//cout << qufq () << endl;
//cout << qufc () << endl;
//cout << quf () << endl;
//cout << Fht () << endl;
//cout << Pvq2 () << endl;
//cout << L () << endl;
//cout << Ng () << endl;
//cout << Nq () << endl;
//cout << Nc () << endl;
//cout << qux () << endl;
//cout << Qut () << endl;
//cout << Mxw () << endl;
//cout << Mxf () << endl;
//cout << Mxrp () << endl;
//cout << Mxt () << endl;
//cout << Mxtotal () << endl;
//cout << Mwftg-Mtot () << endl;

```

APPENDIX III

iShell Bearing Capacity Factor Tables

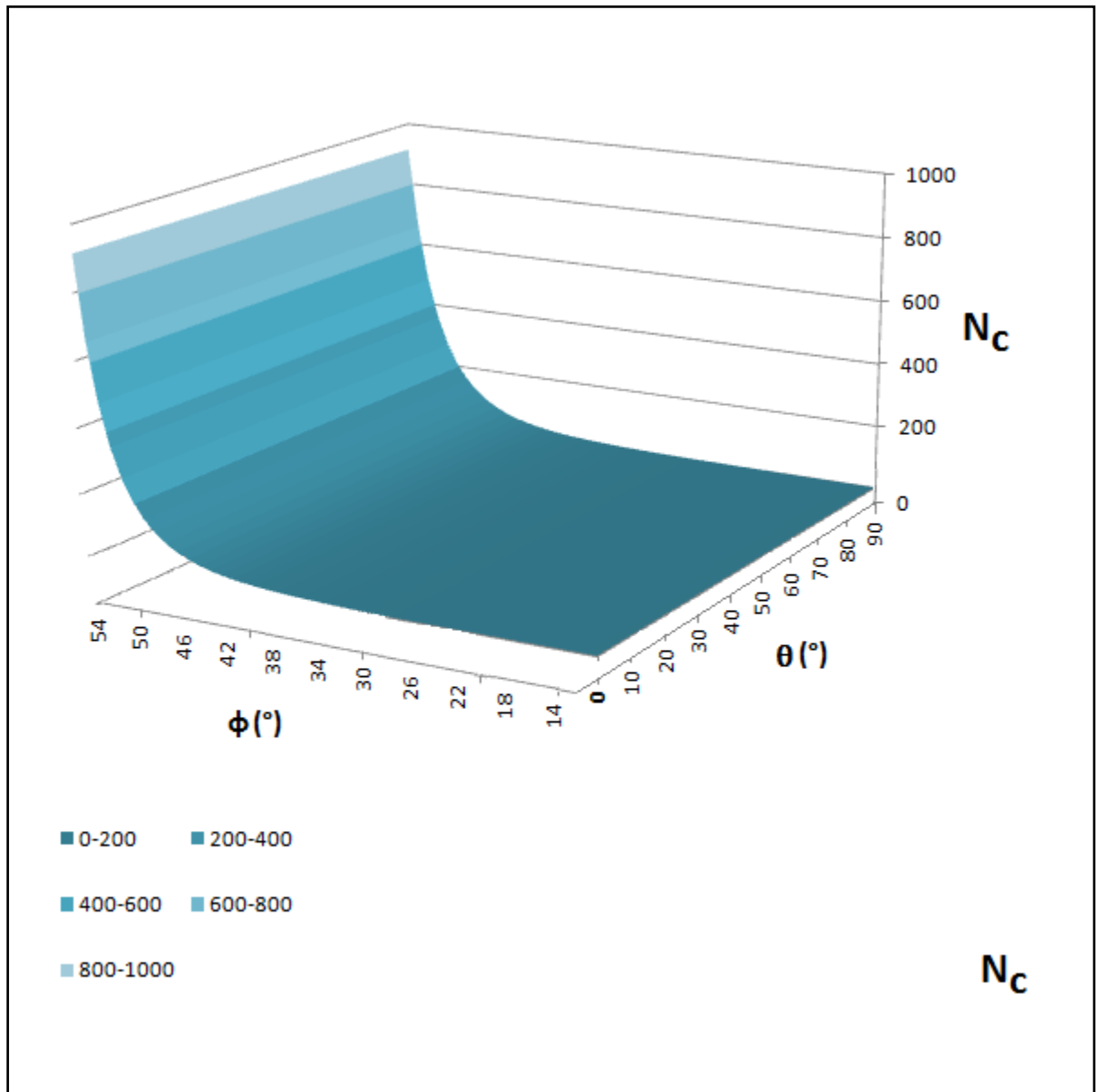


Figure 1. iShell – Bearing Capacity Factor, N_c for Cohesion.

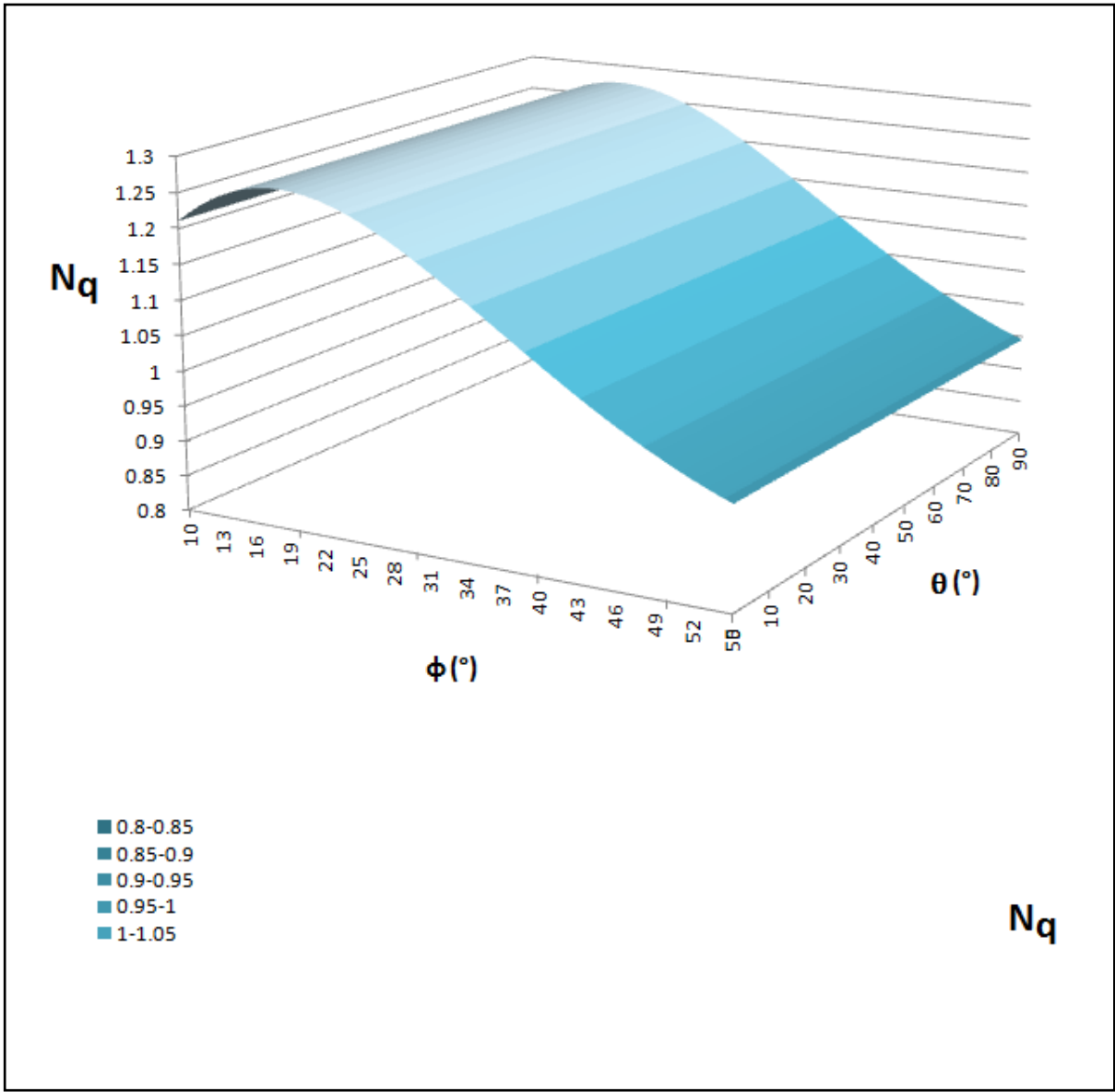


Figure 2. iShell – Bearing Capacity Factor, N_q for Overburden Pressure.

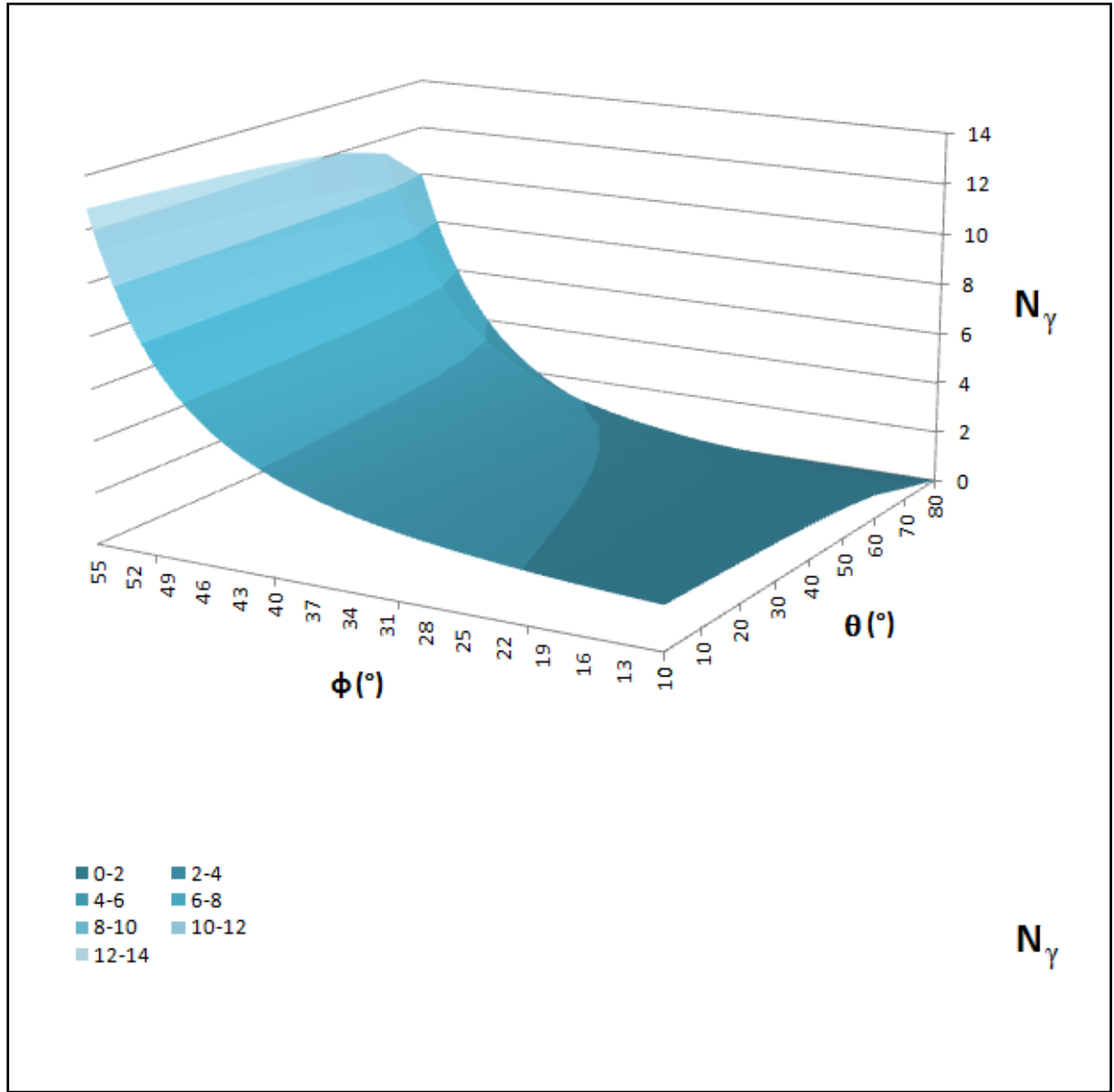


Figure 3. iShell – Bearing Capacity Factor, N_γ for Soil.